Direct Imaging and Spectral Characterisation of Long Period Exoplanets and Brown Dwarfs

Rickman, Emily Louise

UNIVERSITÉ DE GENEVE
Département d'Astronomie

FACULTÉ DES SCIENCES
Dr Damien Ségransan

Direct Imaging and Spectral Characterisation of Long Period Exoplanets and Brown Dwarfs

THÈSE

présentée à la Faculté des Sciences de l'Université de Genève
pour obtenir le grade de Docteur ès sciences,
mention Astronomie et Astrophysique

par

Emily Louise RICKMAN

de

Shoreham-by-Sea (UK)

Thèse N^{O} 5483

GENÈVE
Département d'Astronomie de l'Université de Genève
2020

“You’re braver than you believe, stronger than you seem, and smarter than you think."
— Christopher Robin

RESUMÉ

Les planètes géantes et naines brunes à séparation orbitale au-delà de 5 UA nous sont encore étrangères; très peu de choses sont connues à propos de ces objets. Pourtant, ils sont d'une importance certaine afin de contraindre les incertitudes qui accompagnent les modèles de formation et d'évolution des planètes géantes.

En outre, ces modèles souffrent d'un manque de comparaison observationnelle. La chimie moléculaire complexe des atmosphères des planètes géantes et naines brunes, par exemple, laisse aux modèles un vaste champ de possibilités. Afin de limiter l'espace des paramètres de ces modèles d'évolution, une contribution majeure serait de compléter la corrélation masse-luminosité à l'aide de mesures précises de ces deux grandeurs. Actuellement, les masses dynamiques d'une poignée de naines brunes uniquement sont connues, donnant à toute nouvelle détection une grande importance pour les modèles de ces objets. De plus, les naines brunes constituent des analogues pertinents pour la caractérisation des exoplanètes géantes.

Les mesures de vitesses radiales apportent une limite inférieure uniquement sur les masses, résultat de l'inclinaison orbitale inconnue du système. Aussi des observations supplémentaires en imagerie directe, en plus des vitesses radiales, sont-elles nécessaires afin de lever l'incertitude sur la masse dynamique des compagnons.

Dans cette thèse, j'ai notamment sélectionnné les cibles les plus prometteuses pour l'imagerie directe sur base du survey CORALIE pour les planètes extra-solaires de l'hémisphère sud bénéficiant de plus de 20 années de données en vitesses radiales. Ce survey représente 1647 étoiles de séquence principale à faible masse et à moins de 50 parsec de distance. Imager les compagnons de ces étoiles nous permettrait de combler le fossé séparant les détections d'exoplanètes par vitesses radiales et les détections d'exoplanètes et naines brunes par imagerie directe.

Cette thèse décrit les progrès effectués pour la détection, caractérisation et le suivi des planètes géantes et naines brunes à grande séparation de l'étoile hôte, couplant les techniques d'imagerie directe et de vitesses radiales. Les détections de plusieurs planètes géantes à longue période via des mesures en vitesses radiales seront présentées, ainsi que l'imagerie directe de quelques uns de ces compagnons avec VLT/SPHERE et la découverte d'une naine brune de référence de type T et de masse $\sim 50\ M_{\rm Jup}$. La découverte d'objets de référence, tel celui mentionné, constitue une source précieuse pour les modéles avancés d'évolution. Les progrès technologiques nous permettant d'imager des objects de plus en plus petits, ces derniers jouent un role important en vue de tester les modèles atmospheriques.

Les intérêts à détecter des compagnons massifs et à longues périodes d'étoiles sont certains. D'une part, cela permet de sonder une région de l'espace des paramètres encore très peu explorée, surtout en termes de masse, séparation par rapport à l'étoile hôte et âge de cette dernière. Apporter de nouvelles détections permettrait de préciser le taux d'occurence de ces objets. Par ailleurs, ces observations servent d'étapes nécessaires vers la découverte d'exoplanètes de plus en plus petites et utilisant les deux techniques de détection.

FOREWORD

Very little is known about giant planets and brown dwarfs at an orbital separation greater than 5 AU. And yet, these are important puzzle pieces needed for constraining the uncertainties that exist in giant planet formation and evolutionary models.

Furthermore, evolutionary models of giant planets and brown dwarfs are plagued by a lack of observational constraints. The complex molecular chemistry of their atmospheres leaves a relatively wide parameter space for models to span. Placing accurate mass and luminosity data to observationally populate the mass-luminosity relationship provides a major contribution to an understanding of brown dwarf and giant planet evolutionary models. To date, individual dynamical masses are known for only a handful of brown dwarfs, therefore any new detections contributes greatly to brown dwarf models. In addition, they can act as important analogues for the characterisation of giant exoplanets.

Radial velocity measurements provide only a lower limit on the measured masses due to the unknown orbital inclination. Therefore directly imaging candidates from radial velocities is needed to break that degeneracy and provide constraints on the dynamical masses of companions.

As a part of this thesis, I have selected targets ideal for direct imaging using the CORALIE survey for southern extra-solar planets with over 20 years worth of radial-velocity data. This survey contains a volume-limited sample of 1647 low-mass main sequence stars within 50 parsecs. Detecting these giant companion candidates allows us to start bridging the gap between radial-velocity-detected exoplanets and directly-imaged planets and brown dwarfs.

This thesis describes progress towards the detection, characterisation and monitoring of widely-separated giant planets and brown dwarfs through both direct imaging and long-period radial-velocities. This includes the detection of several long-period radial-velocity giant planets and brown dwarfs, as well as the direct imaging of some of these companions with VLT/SPHERE and the discovery of a benchmark $\sim$50 $M_{\rm Jup}$ T-type brown dwarf. The discovery of benchmark sources provides a powerful and critical tool of advanced evolutionary models. As we move toward imaging smaller and smaller objects it is important to use these objects as a laboratory to test theoretical atmospheric models.

The components of detecting long-period massive-companions helps to probe a parameter space in mass, separation and age where the occurrence rate of these objects is not well understood. They also serve as a stepping stone towards detecting smaller and smaller exoplanets using both of these methods of detection.

ACKNOWLEDGEMENTS

This journey has certainly been interesting. It started with the Brexit referendum and ended with the COVID-19 global pandemic, yet somehow I made it here.

I would like to start by thanking Damien for your guidance, support, and providing me with the opportunity to embark on this journey. I really appreciate the independence and confidence that you gave me to grow as a scientist. Also thanks to Anthony, Janis, and Sébastien who all helped me along the way to answer my questions, point me in the right direction when I needed it, and believed in me. Your support is greatly appreciated. Thank you to my jury – Damien, Stéphane, Corinne, Sascha, and Vincent for taking the time to read my thesis and asking such insightful questions.

There are so many people that I've met along the way with whom I have created great memories. A special thanks to Louise, Heather, Marianne, Karina, Helen, Nico, Manu, Oli, Julia, Anne, JP, Leo, Ati, Lorenzo, Alejandro, George, Anthony, Dan, and many others for the karaoke, BBQs, hiking, caves ouvertes, #postergate, and board games. Every single one of you made these past few years unique in a different way, and I will always treasure that.

An additional thank you to Helen for proofreading and providing feedback, and to Manu for helping me shape the resumé of my thesis. Thank you to Heather for being a mentor, and being an inspiration for so many women in science, I aspire to follow in your footsteps some day.

Thank you to every woman that stood before me to blaze the trail, and to every single ally of women in science that I met both in person and via Twitter. You gave me the energy to continue when I didn't think that I belonged.

A special thanks to two of my rocks back in the UK – Kirsty and Jess. I simply would not have made it without your support. The hysterical phone calls, visits, travelling, distractions and motivation. Thank you both for being there, you are two of the most awesome people and inspirational women that I know.

And last, but by no means least, I would like to thank my Mum, Dad, sister Katie and (soon-to-be) brother-in-law Jason for your endless support, words of encouragement, and plenty of wine through the difficult times. I will forever be in your debt for the amount that you have done for me over the years to get me to where I am today.

TABLE OF CONTENTS

CHAPTER 1

INTRODUCTION

"You dig deeper and it gets more and more complicated, and you get confused, and it's tricky and it's hard, but... it is beautiful."

— Brian Cox

1.1 The big picture

The discovery of the first exoplanet around a sun-like star (51 Peg b, Mayor & Queloz 1995), opened up a whole unexplored field of hunting for other worlds outside of our Solar System. Since then, over 4000 exoplanets have been discovered, enabling us to characterise these exoplanets, their occurrence rates, and distributions in order to understand the formation and evolution of our own Solar System.

However, the detection techniques used to discover most exoplanets to date typically favour planets orbiting close to their host star (< 5 AU). This leaves a wide parameter space of long-period exoplanets where their formation scenarios and occurrence rates are not well understood. However, detecting such companions can prove a challenge.

In the same year as the discovery of 51 Peg b, the first clear detection of the substellar objects known as brown dwarfs (Basri & Marcy 1995; Basri et al. 1996; Nakajima et al. 1995; Oppenheimer et al. 1995; Rebolo et al. 1995, Fig. 1.1), sparked the expansion of a research field to understand these strange objects. One interesting aspect about these substellar objects, that has been discovered more recently, is that ultracool ($\lesssim$2000 K) brown dwarfs overlap in both mass and temperature range with giant gaseous exoplanets (Faherty et al. 2016) and possess similar atmospheric properties (Faherty et al. 2013; Liu et al. 2013; Showman & Kaspi 2013).

This opened up an additional avenue in exploring massive companions orbiting stars. Because ultracool brown dwarfs share this mass and temperature range with giant planets, they can be used as analogues in being able to understand their physical properties.

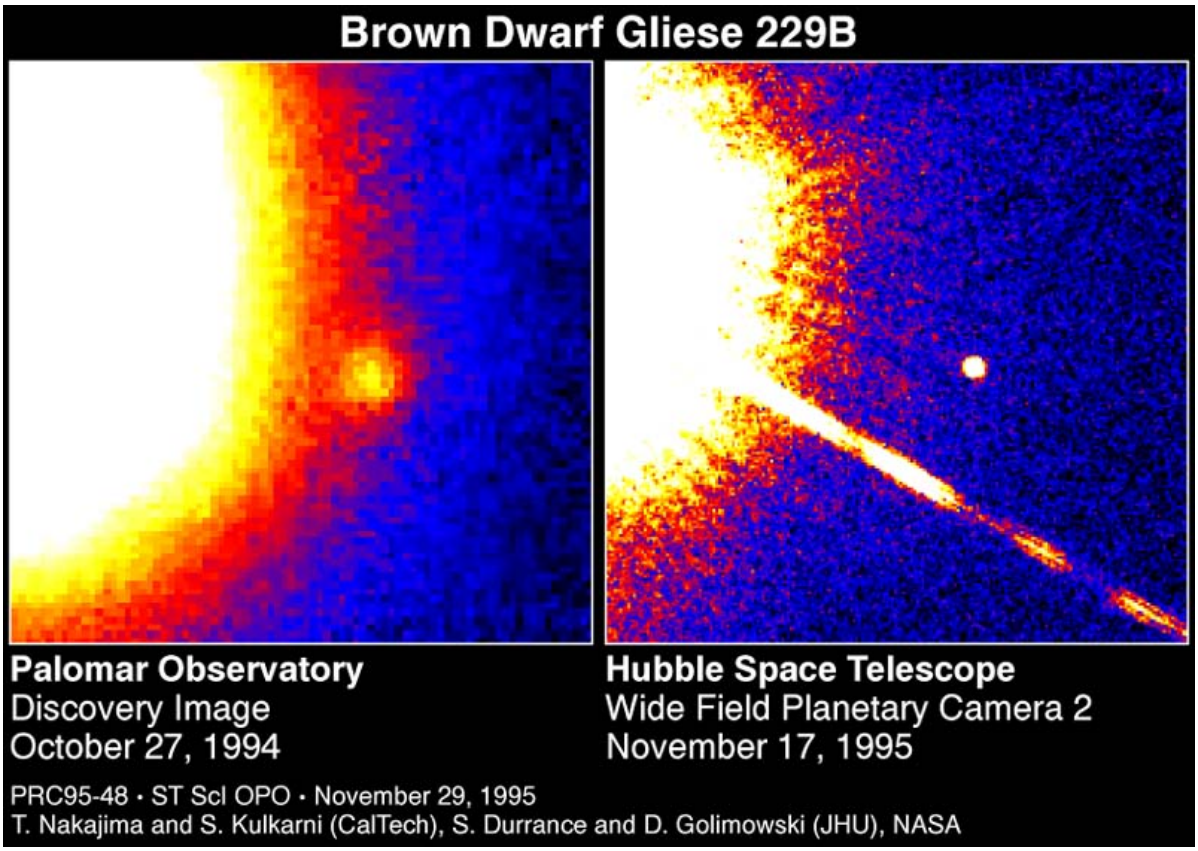

Fig. 1.1 The detection of the first brown dwarf, GJ 229 B by Nakajima et al. (1995).

By constraining physical properties of these companions we can start to ask some important astrophysical questions. What are the formation and evolutionary scenarios for giant planets and brown dwarfs at wide separations? And what are the occurrence rates of such objects?

To be able to answer these questions, it is necessary to establish a systematic search to hunt for such companions. Firstly, by establishing the best detection techniques to do so, but more importantly by combining these techniques to not just *detect* planets, but to *characterise* them.

1.2 Exoplanet detection techniques

There are several methods to detect exoplanets, both directly and indirectly. To date, the indirect methods of detecting exoplanets, primarily the transit method (described in section 1.2.3) and the radial velocity method (described in section 1.2.2), have been the most successful in terms of the number of detections. These two methods, however, primarily probe separations of exoplanets that are very close to their host star (see Fig. 1.2). To understand exoplanet populations, their formation scenarios, and occurrence rates, it is necessary to probe separations beyond those favourable to these two techniques.

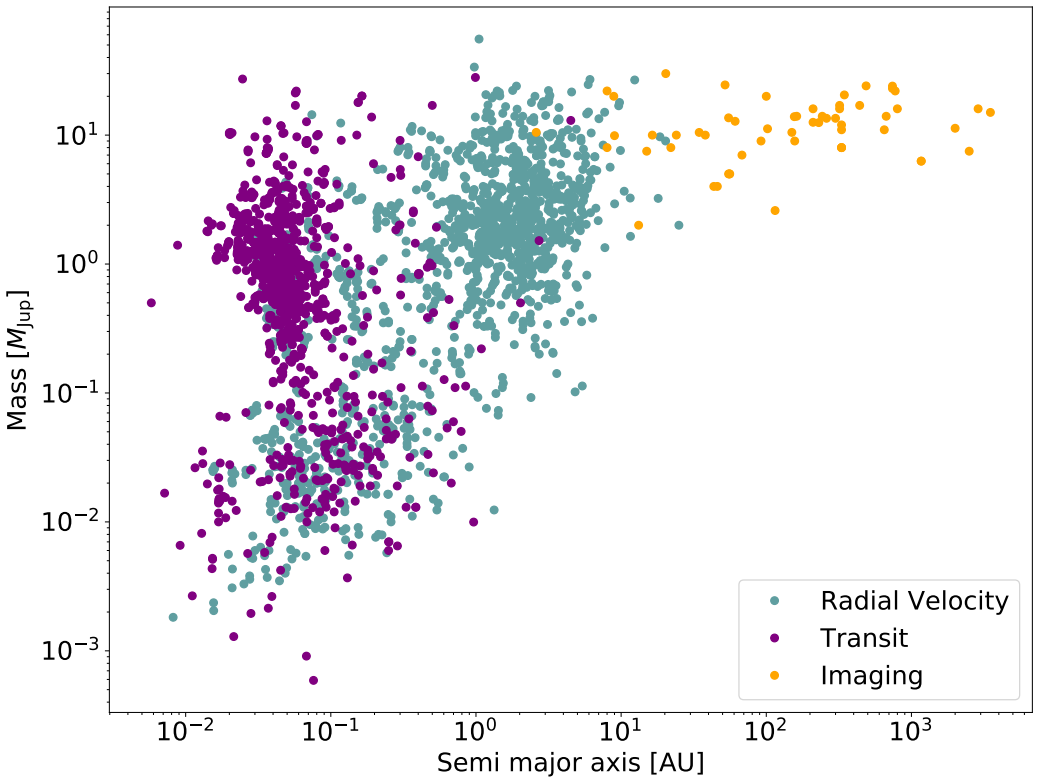

Fig. 1.2 The mass-separation space of detected exoplanets as of April 2020 from the NASA Exoplanet Archive (Akeson et al. 2013). The exoplanets detected using the radial velocity method are coloured in teal; the transit method in purple, and direct imaging in orange.

Direct imaging (described in section 1.2.1) allows us to hunt for long period companion candidates and understand the full picture of exoplanet demographics. Furthermore, combining exoplanet detection techniques is invaluable to pull out additional information about these detected exoplanets.

For this thesis I have combined the radial velocity technique with direct imaging to hunt for new long-period giant exoplanets and brown dwarfs, which probe an unexplored parameter space in both mass and separation (see Fig. 1.2). This furthers our understanding of the occurrence rate of such massive orbital companions at wide separations.

By combining these techniques, I broke the degeneracy of orbital parameters in order to constrain the properties of these companions. I detected new companions, including a benchmark brown dwarf, that can be spectrally characterised to derive a temperature, in addition to its dynamical mass being constrained. These objects are tools to test atmospheric, formation, and evolutionary models of giant planets and brown dwarfs. Ultimately, constraining the parameters of such objects means that they can be placed on a mass-luminosity-age sequence of brown dwarfs that is currently not well understood.

1.2.1 Direct imaging

The focus of this thesis uses a direct method of detecting exoplanets, called direct or high-contrast imaging. This involves, as the name suggests, taking a direct image of a planet or substellar companion next to its host star. This, however, is not an easy task to do.

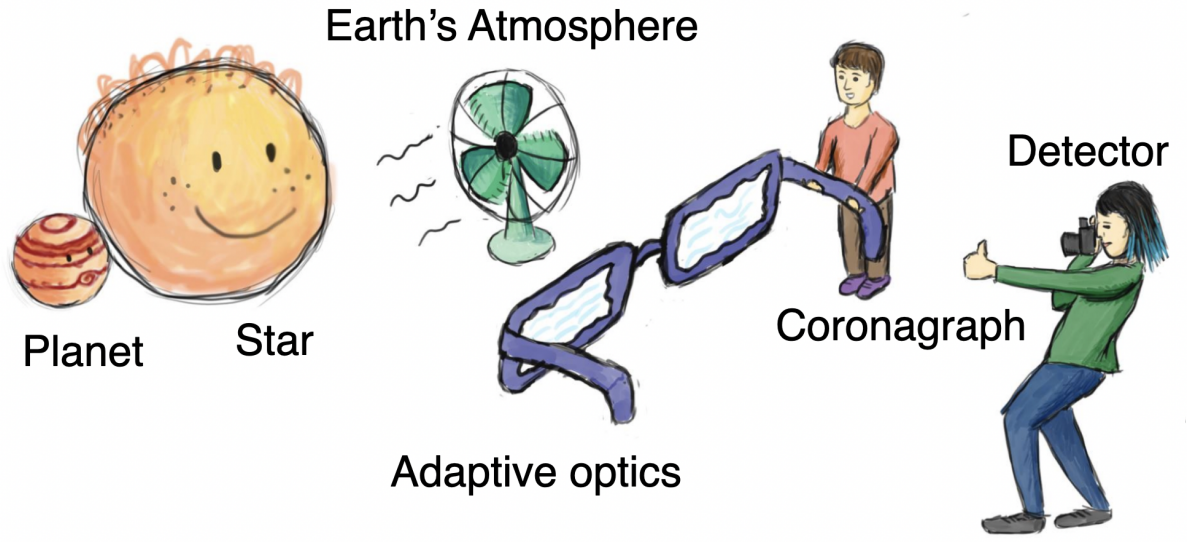

Fig. 1.3 A schematic of the basic principles of direct imaging. In order to try and observe a faint planet next to a bright star, a coronagraph is necessary to remove as much of the starlight as possible. In addition, to account for the turbulence of Earth's atmosphere, adaptive optics are used. Finally, the image is read out using a detector. Adapted image from Jason Wang, GPI.

Any substellar companion orbiting close to its host star will be hidden by the luminosity of the star. So in order to directly image a substellar companion, as much starlight needs to be removed from the image as possible to be able to detect any extremely faint companions. This is the role of the coronagraph shown in Fig. 1.3, which is discussed in detail in Chapter 2.3.

Another difficulty in trying to directly image substellar companions is correcting for the turbulence of the Earth's atmosphere, which causes the star to appear as a mess of speckles rather than a point source. In order to correct for this, adaptive optics (AO, see reviews by e.g. Davies & Kasper 2012; Guyon 2018) are used. The principles and role of adaptive optics is discussed in depth in Chapter 2.2.

Because of the extreme contrast ratio in luminosity between the star and any substellar companion, direct imaging typically favours companions that are massive, self-luminous (i.e. young) and are widely-separated from their host star.

As this is the primary detection technique discussed in this thesis, I will save the full discussion and details of the key components of direct imaging for Chapter 2.

1.2.2 Radial velocities

The radial velocity (RV) method utilises the Doppler Shift effect (Einstein 1905) where it is possible to measure the shift in the spectrum of a star, as a planet or brown dwarf companion and stellar host orbit around their centre-of-mass (see Fig. 1.4). As the star moves towards and away the Earth, the spectrum is blue- and red- shifted respectively.

The change in the velocity can be measured by measuring the shift in the wavelength of the stellar spectrum by:

$$v_r = \frac{\lambda_{\rm obs} - \lambda_0}{\lambda_0} c \tag{1.1}$$

where v_r is the radial velocity, λ_0 is the rest-frame wavelength, $\lambda_{\rm obs}$ is the observed wavelength and c is the speed of light. The radial-velocity of the star is usually quantified in terms of the semi-amplitude, K, of the radial-velocity signal. It can be derived from Kepler's Laws and written as:

$$K_s = \frac{28.4}{\sqrt{1-e^2}} \left(\frac{m_{\rm pl} \sin i}{M_{\rm Jup}}\right) \left(\frac{M_*}{M_\odot}\right)^{-2/3} \left(\frac{P}{\rm year}\right)^{-1/3} [\rm m/s] \tag{1.2}$$

where $m_{\rm pl}$ is the mass of the orbiting companion, M_* is the mass of the host star, P is the orbital period of the system, e is the eccentricity, and i is the inclination with respect to the observer. As the inclination of an observed system is unknown, the radial-velocity method provides a minimum mass of the companion, given by $m \sin i$, where m is the true or dynamical mass of the companion.

In order to get the true mass of an orbiting companion, it is necessary to combine detection techniques. For example, combining measurements from the radial velocity method with astrometric measurements of the orbiting companion from direct imaging breaks the degeneracy of the inclination, giving the true mass. This is discussed more in Chapter 2.7.

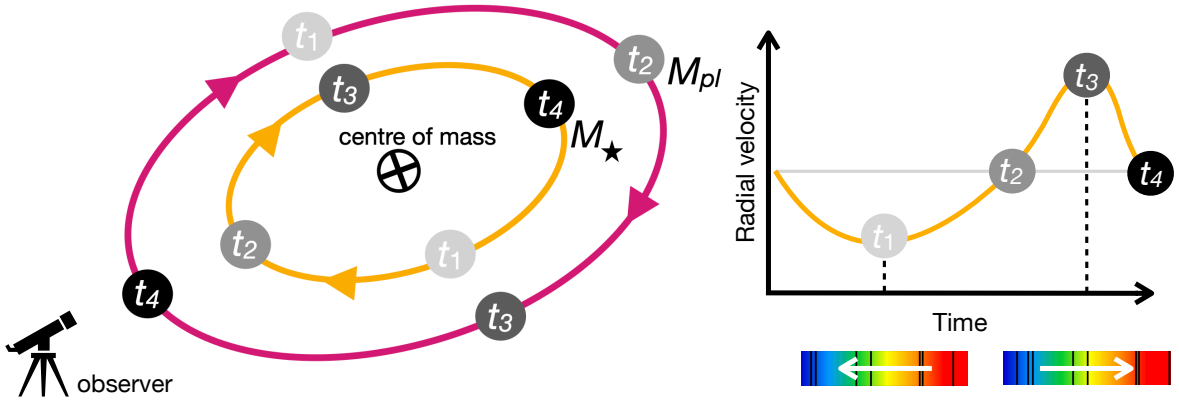

Fig. 1.4 *Left:* A planet and star orbiting around their centre of mass 'the barycentre'. *Right:* How the measured radial velocity of the star changes as it orbits the centre of mass. As the star moves towards the observer, the light leaving the star is 'compressed' and the spectral lines move towards the blue end of the spectrum. As the star moves away from us, the light leaving the star is 'stretched' and the spectral lines move towards the red end of the spectrum. Figure adapted from Perryman (2018).

Because there are many factors that can contaminate the stellar spectrum, these need to be taken into account when measuring the radial velocity of a star. Stellar activity indicators, such as R'_{HK} (Wilson 1963, 1968), can be used to measure the level of stellar activity in order to detrend the radial velocity measurements to search for potential companions hidden in the data.

The optimal targets for the radial velocity method are bright stars that are not too young, have low stellar activity, and are slow rotators. With the latest generation of spectrographs being able to measure to down less than 1 m/s, identifying planets can still pose a challenge, even for the most optimal targets (e.g. Dumusque et al. 2011).

Since the discovery of 51 Peg b (Mayor & Queloz 1995) using the radial-velocity method with the ELODIE spectrograph (Baranne et al. 1996), the hunt for planets using this technique exploded. It led to several large surveys to hunt for planetary companions of nearby stars. This included the ELODIE-SOPHIE search (Perrier et al. 2003; Bouchy et al. 2009); the Lick planet search (Fischer et al. 2014) and the Keck-HIRES search (Vogt et al. 2000).

A new spectrograph, CORALIE, was built and placed upon the Swiss-Euler 1.2 m telescope at La Silla Observatory, Chile; this marked the start of the ongoing CORALIE search for extra-solar planets (Queloz et al. 2000; Udry et al. 2000). It is this ongoing radial-velocity search that is the basis for the detection of the long period companions discussed in this thesis. Because of the continuous monitoring, with more than 20 years of observations, we are able to hunt for long-period companions that aren't typically detected by the radial velocity method. This is because the semi-amplitude we measure decreases with longer and longer orbital periods, as $K \propto P^{-1/3}$. The CORALIE survey is discussed in depth in Chapter 3.

Following on from the success of CORALIE, a new spectrograph called HARPS (High Accuracy Radial velocity Planet Searcher), was installed on the ESO 3.6 m telescope, also at La Silla Observatory

in 2003 (Mayor et al. 2003), and this marked the start of the HARPS search for southern extra-solar planets (Pepe et al. 2004).

Due to the success of HARPS, an improved copy was built for the northern hemisphere, named HARPS-N (Cosentino et al. 2012), and placed on the Telescopio Nazionale Galileo (TNG) in La Palma, Spain.

More recently, a new state-of-the-art spectrograph was installed on the Very Large Telescope (VLT) at Paranal Observatory, Chile, called ESPRESSO (Pepe et al. 2010). It aims to reach a precision of 10 cm/s and will contribute significantly to finding planets with smaller and smaller masses.

1.2.3 Other methods

Transit method

The transit method to detect exoplanets is an indirect method, whereby we measure the amount of flux from a host star over time. If a planet passes in front of the stellar disk, i.e. the planet transits the star, then we can detect this dip in the flux received from the star due to the planet. An illustration of this is shown in Fig. 1.5.

Because there is a specific geometric configuration required to observe a transit, the probability of observing a transit is low. For this reason, most transit surveys use the approach of observing a large amount of stars (e.g. Wheatley et al. 2013; Ricker et al. 2015). Furthermore, the probability of observing a transit is highly sensitive to the orbital period, whereby the probability decreases with increasing orbital period. As a result, most planets discovered by the transit method have short periods, as seen in Fig. 1.2.

The measured dip in the flux of the star ΔF, as shown in Fig. 1.5, is related to the radius of the planet by

$$\Delta F = \left(\frac{R_{\rm pl}}{R_*}\right)^2 \tag{1.3}$$

where R_{pl} is the radius of the planet and R_* is the radius of the star. Therefore, the measured light curve is able to provide an estimate of the planet's radius. Because of this, the bulk density of an exoplanet can be estimated from its radius and mass measurements when combined with the RV method, and this can tell us something about the composition of an exoplanet. This was the case when the first transit of an exoplanet, HD 209458, was detected by Henry et al. (2000), and independently confirmed by Charbonneau et al. (2000). It confirmed that a short period planet had a similar radius and density as gas giants in our own Solar System, which led to the commonly used term today of *'hot Jupiters'*.

In addition, we can learn about atmospheres of exoplanets using this method, as some of the starlight passes through the planets atmosphere as it transits. This can be measured with transmission spectroscopy, which was first done by Charbonneau et al. (2002). On the other side of the planet's orbit, it can be observed as it passes behind the star, and from this the thermal emission of a planet can be observed where absorption features can be measured (e.g. Charbonneau et al. 2005).

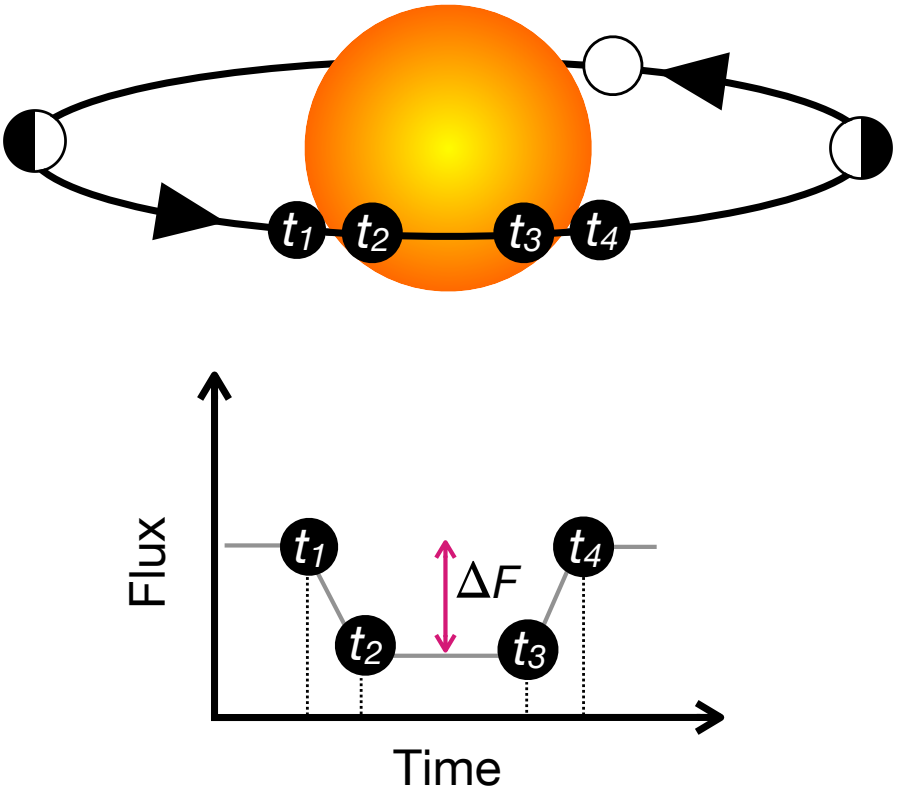

Fig. 1.5 *Top:* a planet orbiting around a star with key components of the transit marked $t_1 - t_4$. *Bottom:* The flux we expect to measure over time as the planet transits the star where the points correspond to where the planet is in the orbit indicated above it with the points going from $t_1 - t_4$. The dip in the flux measured as the planet transits the star is denoted by ΔF.

To date, the transit method has discovered the most amount of exoplanets with 3176 confirmed transiting exoplanets as of April 2020 (NASA Exoplanet Archive, Akeson et al. 2013). This is mostly thanks to the *Kepler* space mission (Borucki et al. 2010; Koch et al. 2010), launched in 2009, which has was discovered over 2000 exoplanets alone, with many more candidates to be confirmed.

Astrometry

The astrometic method of detection is similar to the RV method in that it relies on measuring the displacement of the host star from its barycentre due to an orbiting companion. However, rather than measuring the one dimensional radial motion, astrometry measures the tangential, two dimensional motion by measuring the position of the star in the sky over time.

It works by observing the path of a star across the sky over several years. As stars move through the galaxy, they trace out a linear path across the sky, as shown by the dotted straight line in Fig. 1.6. The spiral-like shape in Fig. 1.6 is caused by the motion of Earth around the Sun. Any perturbations

from this expected path in the sky can be caused by an orbiting companion and this displacement can be measured to determine the mass and period of such a companion.

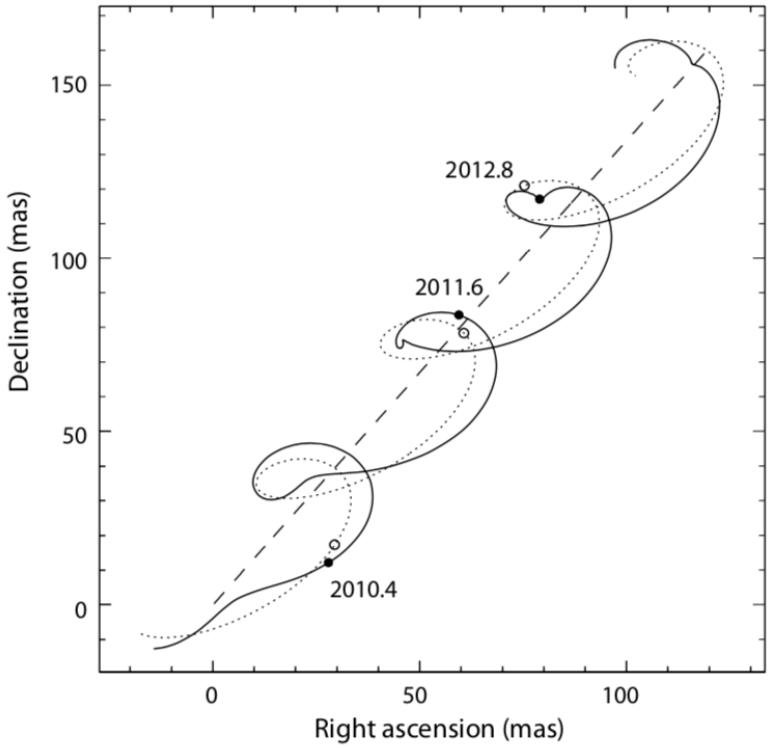

Fig. 1.6 An illustration of the astrometric method of detecting exoplanets. The straight dashed line shows the path that a star makes as it moves through the galaxy. The thin dotted spiral line shows the path the star would take if there was no orbiting companion present. The solid line shows the motion of the star as a result of an orbiting companion. These measurements are taken over several years, like labelled on the figure, to confirm an astrometric signal. Figure from Perryman (2011).

From Kepler's Laws, simple geometry and taking the approximation that the planet's mass to be much smaller than the stellar mass ($m_{\rm pl} << M_*$), the astrometric signal is given by:

$$\theta_A = 3\mu{\rm as}\frac{m_{\rm pl}}{M_\oplus}\left(\frac{M_*}{M_\odot}\right)^{-2/3}\left(\frac{P}{\rm yr}\right)^{2/3}\left(\frac{d}{\rm pc}\right)^{-1}, \tag{1.4}$$

for a planet with an orbital period P, at a distance d from the observer.

Astrometry has already been proven to be successful at determining the true mass of previously detected exoplanets via the RV method (e.g. Sahlmann et al. 2011a,b). However, to date this method has not had any success in *discovering* a new planet. This will change significantly with the final data release from the space mission *Gaia* (Perryman et al. 2001; Gaia Collaboration et al. 2016a,b, 2018).

Gaia was launched in 2013 and started observing in 2014. It is seeking to measure the positions, distances and motions of stars to very high precision. It is predicted by Perryman et al. (2014) that *Gaia* will detect over 20,000 giant long-period planets from the primary five year mission alone. Going forward

this technique will become extremely powerful, especially as the discovery space of *Gaia* overlaps significantly with that of high-contrast imaging, and combining detection techniques is advantageous in the characterisation of exoplanets.

1.3 Giant planet formation

After the discovery of 51 Peg b was confirmed to be a 'hot Jupiter', the previously accepted theories of planet formation started to be questioned. The detection of many more hot Jupiters followed (Butler & Marcy 1996; Butler et al. 1997; Noyes et al. 1997; Butler et al. 1998; Delfosse et al. 1998; Fischer et al. 1999), and this led to a new development in planet formation and migration models.

The theory of giant planet formation continued to be put into question after more recent discoveries of widely-separated companions with direct imaging (Marois et al. 2008; Lagrange et al. 2010; Marois et al. 2010; Kuzuhara et al. 2013; Rameau et al. 2013).

This led to two possible theories to explain how giant planets form: core accretion and gravitational instability. Neither however, fully explain the formation of such massive companions at wide orbits.

1.3.1 Core accretion

Core accretion, sometimes called the 'bottom-up' approach (Pollack et al. 1996), is made up of four main stages, illustrated in Fig. 1.7.

The first stage consists of orbiting dust grains in a disk accreting into planetesimals, growing as they collide. As the planetesimals grow, they move to near-coplanar orbits to form planetary embryos. The gas-giant planets then continue to accrete gas before the disk disappears. Gas giants then scatter or accrete remaining planetesimals.

Whilst this mechanism can explain the formation of smaller planets (Wetherill 1980; Ida & Lin 2004; Alibert et al. 2005), for planets with a mass of a few Jupiter masses or more on wide-orbits, it fails to form these companions within the lifetime of the protoplanetary disk.

1.3.2 Gravitational instability

Another possible formation scenario for giant planets is through gravitational instability (e.g. Cameron 1978; Bodenheimer et al. 1980; Adams & Benz 1992; Boss 1997, 2006). Contrary to the core accretion model, gravitational instability is extremely fast (Mordasini et al. 2010).

In this model, illustrated in Fig. 1.7, a protoplanetary disk of gas and dust forms around a young star. Instabilities in the gravitational disk then cause clumps of gas to form that become self-gravitating. Dust grains then coagulate to the centre of the protoplanet, forming a core. The giant planet then continues to sweep out a wide gap as it continues to feed on gas in the disk.

It is possible to measure such dust and gas distributions in planet-forming disks with the use of, for example, the Atacama Large Millimeter/submillimeter Array (ALMA) observatory, allowing informative

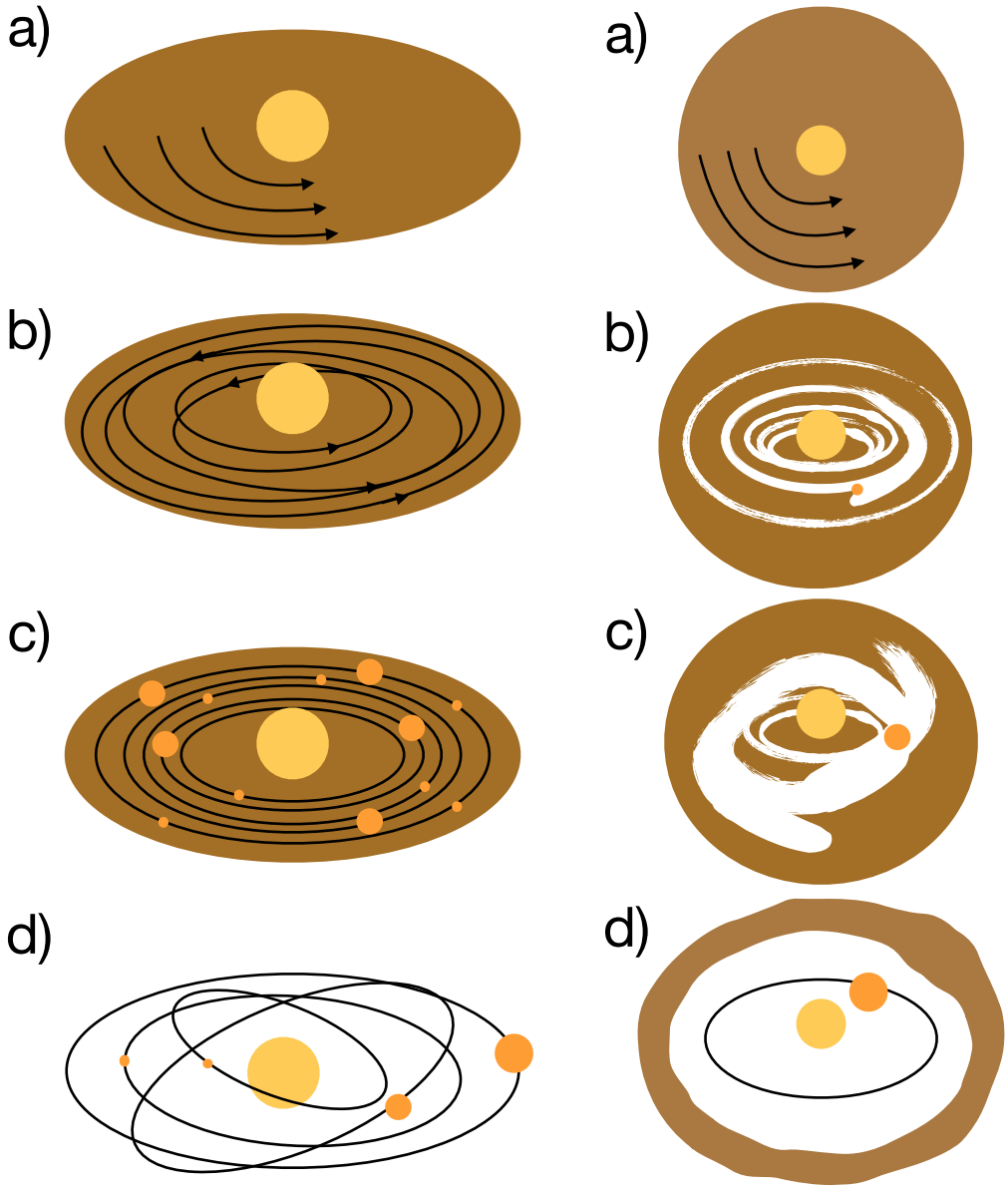

Fig. 1.7 The two main possible formation scenarios for giant planets. The central star is shown in both cases by the central yellow circle. *Left:* Core accretion formation scenario. (a) Dust grains orbiting in a disk start accreting into planetesimals. (b) As the planetesimals grow, they move to co-planar orbits (c) The gas-giant planets continue to accrete gas before the disk disappears (d) Any remaining planetesimals are either accreted or scattered. *Right:* Gravitational instability formation scenario. (a) A disk of gas and dust forms around a young star. (b) Instabilities in this large disk cause clumps of gas to start forming that become self-gravitating. (c) Dust grains coagulate towards the centre of the protoplanetary clump forming a core. (d) The giant planet continues to sweep out wide gaps in the disk as it continues to feed on the gas in the disk.

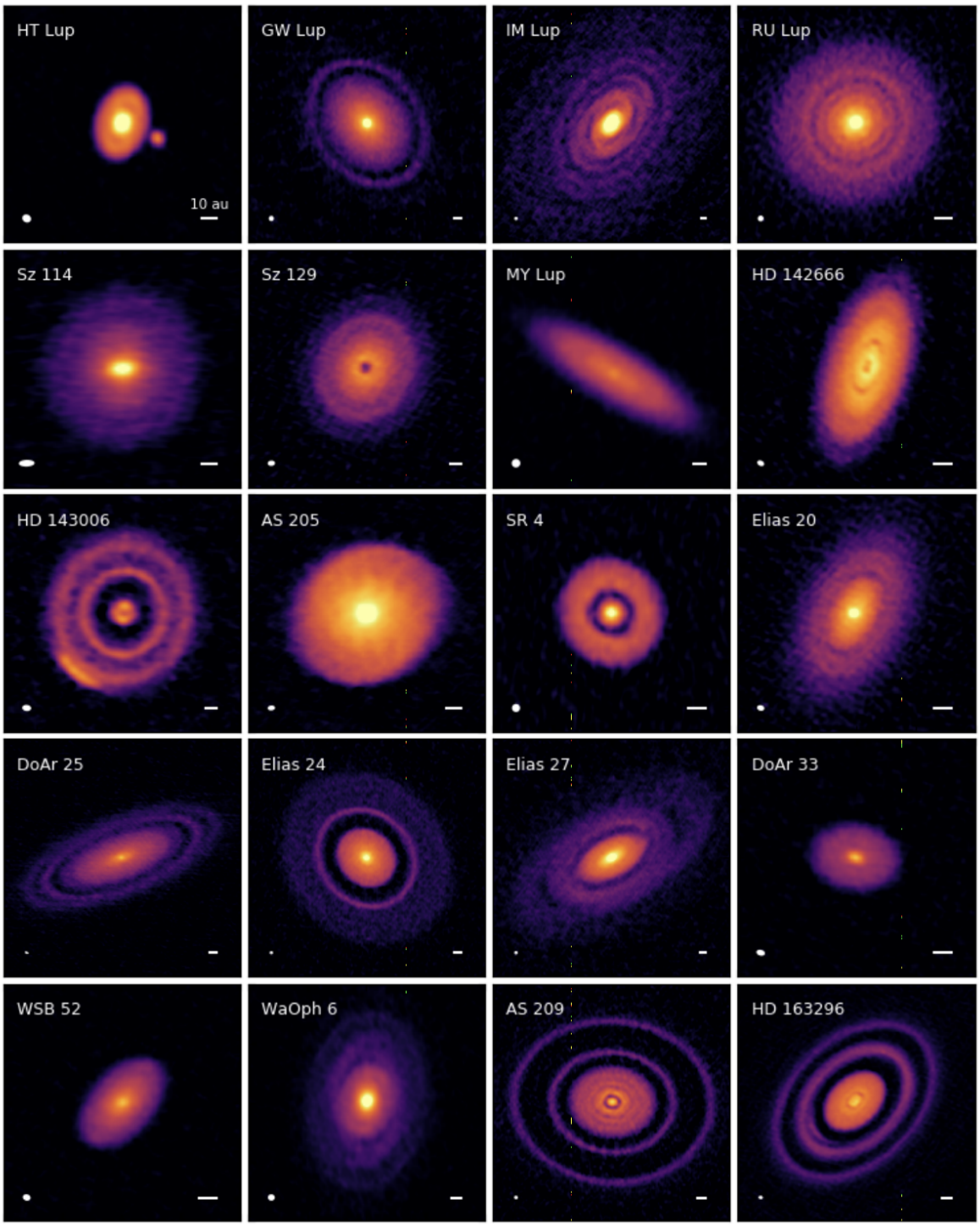

Fig. 1.8 Gallery of 1.25 mm continuum emissions images from ALMA in the DSHARP sample. Figure from Andrews et al. (2018).

images of such disks like shown in Fig. 1.8. This can contribute to our understanding of gas and dust dynamics in disks.

The gravitational instability formation scenario is, however, not without problems. In order for gravitational instability to be viable, it requires a cool and massive disk that is not compatible with current disk models and observations (Vigan et al. 2017). For this reason, it fails to explain giant companions on such wide orbits. Therefore, it is necessary that some other mechanism needs to be considered or that a combination of these mechanisms is required to explain how giant planets get on such wide orbits.

1.3.3 Observational signatures

Marley et al. (2007) proposed that young giant planets formed by core accretion in a protoplanetary disk should have a much lower entropy content at young ages than objects of the same mass and age formed by gravitational instability.

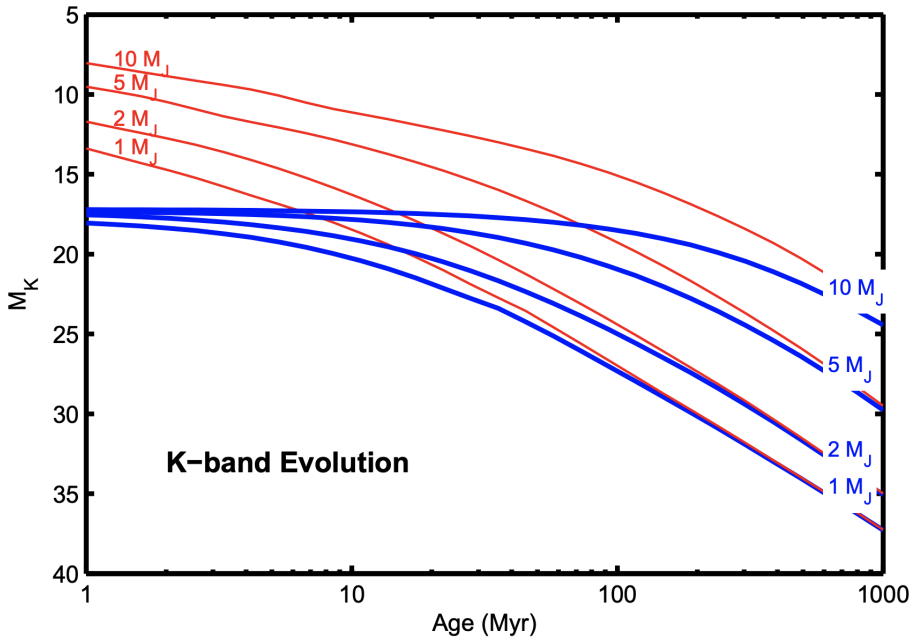

Fig. 1.9 The K-band magnitude of a giant planet as a function of age shown for hot-start (in red) and cold-start (in blue) models. Figure from Spiegel & Burrows (2012).

As a result, objects formed via core accretion should be smaller, cooler and fainter at young ages than those formed via gravitational instability. This led to the coined terms of 'hot-start' vs. 'cold-start' scenarios to describe gravitational instability and core accretion respectively.

Spiegel & Burrows (2012) defined some spectral and photometric features to differentiate between hot-start and cold-start models, especially when a giant planet is very young (<10 Myr), one of which is shown in Fig. 1.9. Therefore, being able to directly detect such young objects helps to differentiate the formation scenario in which a giant planet could have formed.

These theories do not come without caveats though. They are extremely dependent on the initial conditions of their formation, which are not well understood (e.g. Mordasini et al. 2012; Mordasini 2013; Spiegel & Burrows 2012).

1.4 Brown dwarfs

Brown dwarfs are substellar objects, that the International Astronomical Union (IAU) defined as objects that are capable of burning deuterium but not hydrogen in their core (Boss et al. 2003). Models show that this typically covers the mass range $\sim 13-80\ M_{\rm Jup}$ (Fig 1.11, Saumon et al. 1996; Burrows et al. 2001). Therefore, they sit in a mass regime that is between that of planets and stars.

Brown dwarfs were defined this way as $13\ M_{\rm Jup}$ is the minimum mass where deuterium fusion can occur (Burrows et al. 1993), while the upper mass limit is defined as the minimum mass where hydrogen fusion can occur (Chabrier et al. 2000). However, this mass limit is widely debated, as many factors including the initial conditions makes this boundary more blurred.

So what really are brown dwarfs? Are they failed stars or super-planets? How do they form and evolve? What do their atmospheres look like? How common are such objects?

In this section, I briefly outline the history and context of the prediction and discovery of brown dwarfs; the physics of these substellar objects, and discuss both field brown dwarfs as well as brown dwarfs as companions.

1.4.1 History and context

The existence of brown dwarfs was first proposed by Kumar (1962a,b) as the answer to the pre-main sequence phase of stellar evolution. Prior to the consideration of brown dwarfs, previous theoretical calculations of the gravitational contraction phase of stellar evolution were done treating the interior as an ideal gas (Levee 1953; Henyey et al. 1955).

However, it came to the realisation of Kumar (1962b, 1963a,b) that this could no longer be the case for a sufficiently low-mass star. Knowing that the stellar core temperature, T, is proportional to M/R, and the stellar core density, ρ is proportional to M/R^3, where M and R are the mass and radius of the star respectively, a limit of rapidly-rising central density and a slow-rising central temperature means that the gas could no longer be treated as 'ideal'. The central density reaches a limit that causes the gas to become partially degenerate before becoming hot enough for hydrogen burning to commence. The initial calculations made by Kumar (1963b) put this limit of hydrogen-burning minimum mass at $\sim 0.1\ M_{\odot}$, whilst more detailed evolutionary calculations were made later by Grossman et al. (1974) who placed the limit at $\sim 0.085\ M_{\odot}$.

After the short initial hot contracting phase of the low-mass star, it begins to slowly cool down and evolves towards a completely degenerate configuration, which Kumar (1962b, 1963a) referred to as a 'black dwarf'.

Fig. 1.10 Image credit: Joergens (2014).

It wasn't until 1975 that the term 'brown dwarf' was first coined by Tarter (1975), and felt that the term was appropriate as these objects were thought to have no colour (which later turned out to not really be the case).

After the proposition of these enigmatic objects by Kumar (1962b), it seemed logical that these low-luminosity brown dwarfs could hide a significant proportion of our Galaxy's dark matter. This, however, was disputed (Tinney 1999) after the first discoveries of these objects (Basri & Marcy 1995; Basri et al. 1996; Nakajima et al. 1995; Oppenheimer et al. 1995; Rebolo et al. 1995), as the mass-function for brown dwarfs was determined to be too shallow to account for the amount of dark matter in the Galaxy (Reid & Gizis 1997; Kroupa 1998; Tinney 1995).

The cartoon shown in Fig. 1.10 emphasises the way in which brown dwarfs were viewed as 'failed stars' - especially when they were first discovered in 1995:

> *"Face it – in this town, either you're a star or you're just another brown dwarf."*

but little was it known at the time, that the science of these substellar objects is weird and wonderful, and stretched the boundaries in the following decades of our the understanding of interesting astrophysical concepts, including becoming a key analogue for understanding giant exoplanets.

1.4.2 The physics of brown dwarfs

So what's to say that a 13 $M_{\rm Jup}$ planet is any different from a 13 $M_{\rm Jup}$ brown dwarf? The *fundamental* difference is their formation scenarios. It was highlighted on several occasions (Kumar 1972, 1974,

1994, 1995) that to discuss the nature of such objects, it is necessary to understand their formation mechanisms.

The discussion of the formation of giant planets is already presented in Chapter 1.3. Contrary to giant planets, brown dwarfs are thought to form like stars in either systems (as stellar binaries) or as isolated objects. Stars form when a molecular cloud starts to fragment into smaller entities, once they reach their Jeans mass (Jeans 1902). The cloud isothermally collapses until it becomes optically thick so that is no longer able to radiate heat away and compression heating exceeds radiative cooling, causing the fragment to heat up and continue to accrete material. It is vital, however, that a mechanism has to come into play to prevent a pre-stellar core from accreting enough material to become a hydrogen-burning star and that the initial mass of the collapsing fragment is more massive than a brown dwarf.

Turbulence in molecular clouds has been suggested to create high density regions in a molecular cloud, causing a lower Jeans mass (Padoan & Nordlund 2004; Hennebelle & Chabrier 2008). Several mechanisms have been considered that halt accretion once a low-mass fragment has formed. These include hierarchical fragmentation (Boss et al. 2000; Whitehouse & Bate 2006), disk fragmentation, with resulting binaries being disrupted by passing stars (Goodwin & Whitworth 2007), premature ejection of protostellar embryos from their natal cores, halting post-formation accretion (Whitworth et al. 2007) as well as cores that are photoeroded by an ionisation front of an HII region from the wind of a nearby supernovae or OB stars (Whitworth & Zinnecker 2004).

It is thought that a combination of these mechanisms contribute to the population of (isolated) brown dwarfs. However, the amount that each formation scenario contributes to the overall population or, whether there is a dominant formation mechanism, is still not defined.

During the very first stages of a brown dwarf's life ($\lesssim$20 Myr), brown dwarfs with masses greater than $\sim 0.012\,M_{\odot}$ are able to burn deuterium in their core (Saumon et al. 1996) producing nuclear energy via:

$$\mathrm{p} + \mathrm{d} \longrightarrow \gamma + {}^{3}\mathrm{He} \tag{1.5}$$

After the initial and brief phase of deuterium-burning, brown dwarfs no longer have a source of energy and therefore the remainder of a brown dwarf's life is spent cooling off. This is primarily characterised by its luminosity and temperature (see Fig. 1.11). This is contrary to stars that stabilise their luminosity due to nuclear burning in their core. Just like the luminosities of brown dwarfs, after the peak core temperature is reached, the temperature continues to decrease with age, which are assigned to approximate spectral types.

The main building blocks of a brown dwarf are hydrogen (H) and helium (He) that are placed under such extreme density that they become partially degenerate. This is due to the Pauli exclusion principle where two identical electrons can't occupy the same space, forcing electrons to higher momentum states (i.e. contributing to the pressure). This restriction on the number density of each state is the source of degeneracy pressure.

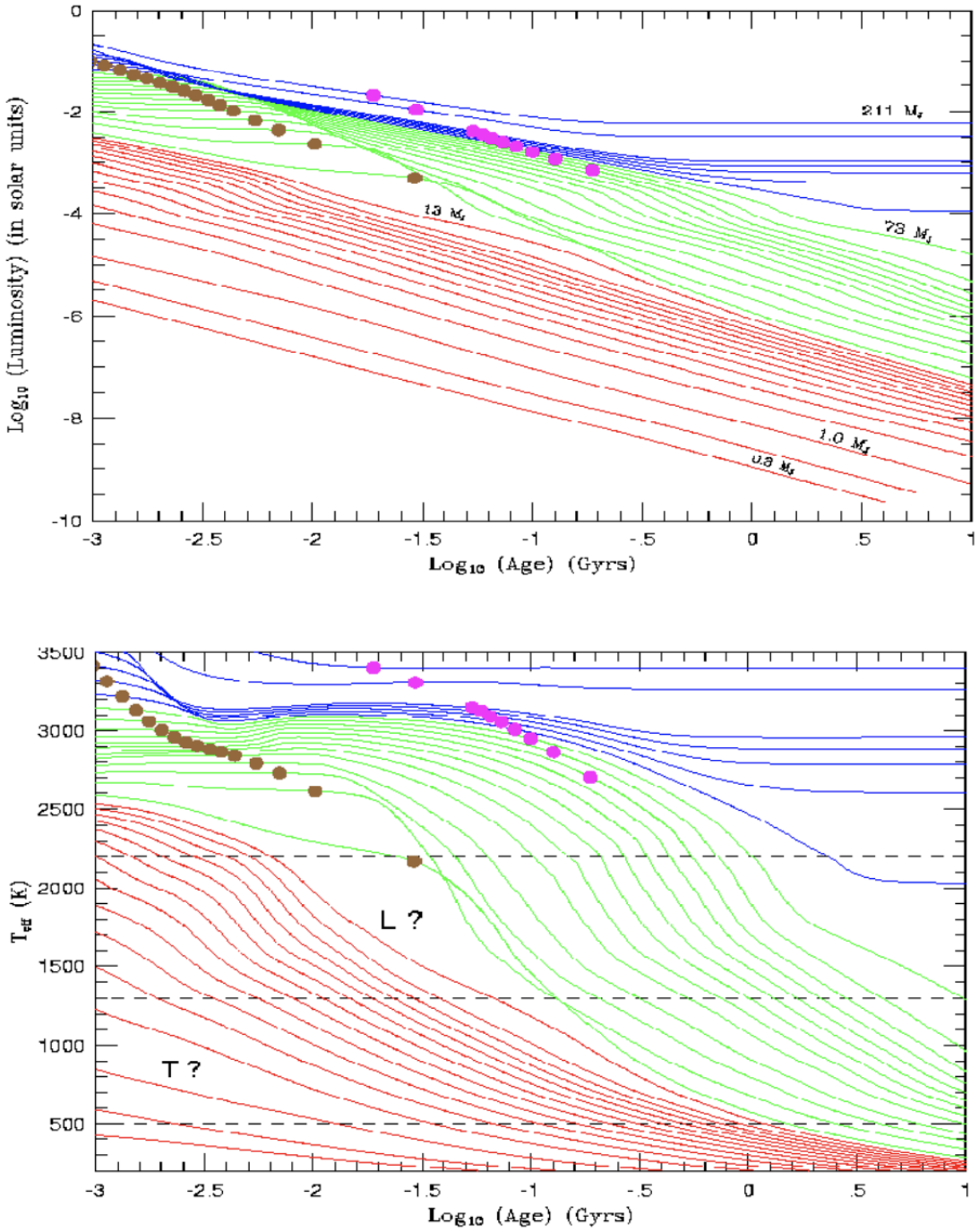

Fig. 1.11 Evolution of the luminosity of stellar and substellar objects as a function of their age. The blue, green and red lines represent stellar objects ($> 80\ M_{\rm Jup}$), brown dwarfs ($15 - 80\ M_{\rm Jup}$), planets ($< 15\ M_{\rm Jup}$) respectively. Figure from Burrows et al. (1997).

In order to understand the complexities of such matter, an equation of state is required to understand the relationship between pressure, temperature, and density profiles. The most widely used equation of state for brown dwarfs to date has been the semi-analytical H/He model of Saumon et al. (1995). More recently, Chabrier et al. (2019) outlined a new equation of state in the domain of pressure ionisation.

Hydrogen-burning stars contain radiative cores. Brown dwarfs, however, are so optically thick that energy transport by radiation is negligible. Instead, the primary process to transport energy from deep hot layers to its surface where it is radiated away, producing the observable luminosity, is convection. This fully convective state (and negligible radiation) results in a quasi-adiabatic thermal profile with the adiabatic gradient fixed by the equation of state (Chabrier & Baraffe 2000).

Due to the degeneracy of brown dwarfs, the variation in the radii over its lifetime is not so severe. This is due to the competition between the Coulomb pressure and electron degeneracy in the equation of state (Saumon et al. 1995). The mechanical structure (defined by the equation of state) of a brown dwarf defines the mass-radius relationship. As the density of the most massive brown dwarfs is set by electron degeneracy pressure, whilst the least massive brown dwarfs the density is set by Coulomb pressure, the radii of brown dwarfs have a low mass dependence of $R \propto M^{-1/8}$ (Chabrier & Baraffe 2000), placing the radii of all brown dwarfs at approximately 1 $R_{\rm Jup}$. This can be seen in Fig. 1.12 where the radius as a function of mass is relatively flat. Consequently, the surface gravity, g, of a brown dwarf, varies incredibly by mass and defined by:

$$g = \frac{GM}{R^2} \tag{1.6}$$

where G is the gravitational constant ($\approx 6.6743 \times 10^{-8}\mathrm{cm}^3\mathrm{g}^{-1}\mathrm{s}^{-2}$), M is the mass of the brown dwarf and R is the radius of the brown dwarf. The surface gravity affects the spectral features of brown dwarfs significantly. For example, young objects possess redder colours in the near infrared compared to their older counterparts. This is due to the inefficiency of dust sedimentation because of their low surface gravities, leaving dust high in their atmospheres.

What is interesting to note is that giant planets are described by the same equation of state as brown dwarfs, as they share the same pressure-temperature parameter space (Fortney et al. 2011) and have similar radii ($\sim 1\ R_{\rm Jup}$) that is also dictated by the equation of state.

As a brown dwarf cools over time, its spectrum resembles a giant planet more and more, which agrees with the theoretical expectation that a cooling brown dwarf will eventually end up as a cold fully degenerate object, just like giant planets (Metchev 2006).

But what are the stages of a brown dwarf before it reaches that point? Brown dwarfs undergo an evolution that is described by a spectral sequence of M $\rightarrow$ L $\rightarrow$ T $\rightarrow$ Y. Each of these spectral types are used to characterise brown dwarfs and can be placed on a colour-magnitude diagram to define its sequence (as seen in Fig. 1.13)

The modern classification of M dwarfs is based on Boeshaar (1976), which was further extended by Kirkpatrick et al. (1991). The optical part of the spectrum of M dwarfs is mostly characterised by strong

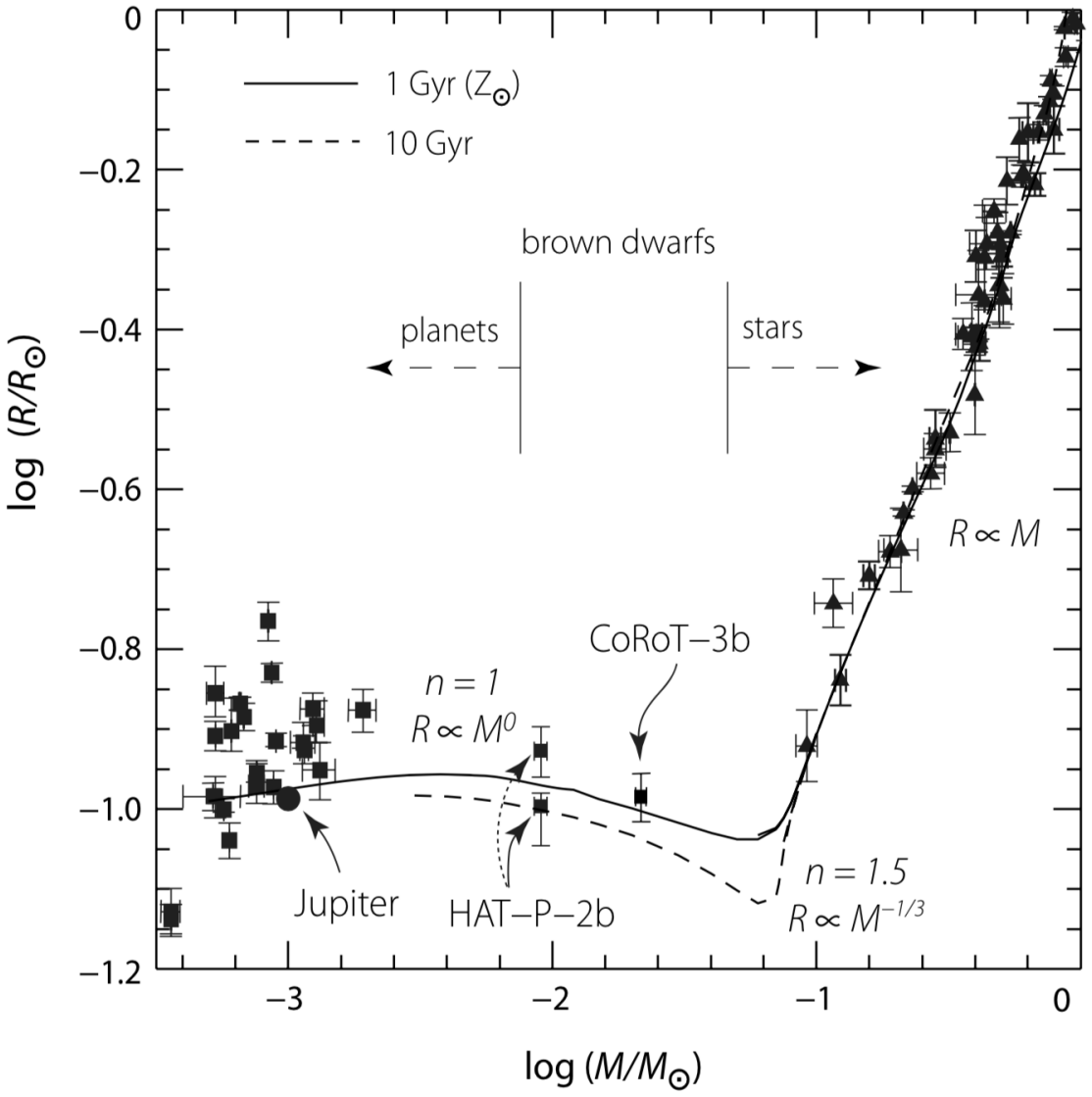

Fig. 1.12 The radius of brown dwarfs has a relatively flat mass dependence, due to very different densities are either end of the mass scale. Figure modified by Perryman (2011) from Chabrier et al. (2009).

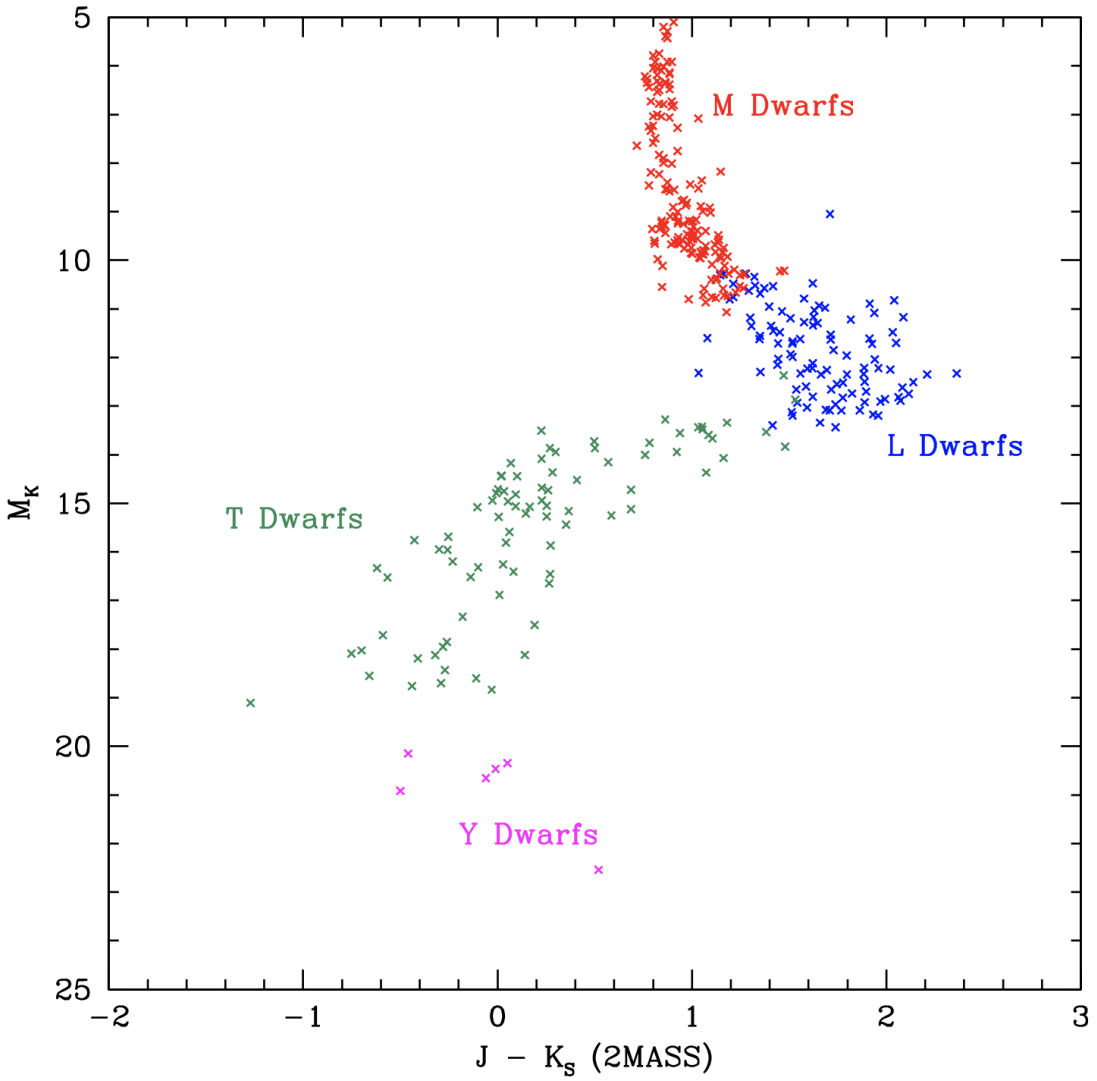

Fig. 1.13 Colour-magnitude diagram of the spectral type of observed field brown dwarfs. M dwarfs are shown in red, L dwarfs are shown in blue, T dwarfs in green, and Y dwarfs in pink. Figure from Bailey (2014).

oxide bands, and in the near-infrared part, spectra exhibit strong water (H_2O), carbon monoxide (CO), and iron hydride (FeH) features that can be seen in Fig. 1.14.

Further down the evolutionary sequence, as brown dwarfs cool, the transition from M dwarf to L dwarf is defined by the formation of condensates ($\lesssim$2000 K). These condensates are thought to be responsible for the dust clouds that are necessary to explain the spectra and colours of L dwarfs (Allard et al. 2001; Marley et al. 2002). L dwarfs become increasingly redder through later spectral types and the titanium oxide (TiO) and vanadium oxide (VO) present in M dwarf spectra disappear by mid-L types. The atmospheres of L dwarfs have been reproduced by the so-called 'Dusty' models (Allard et al. 2001), where dust in the atmosphere is uniformly mixed.

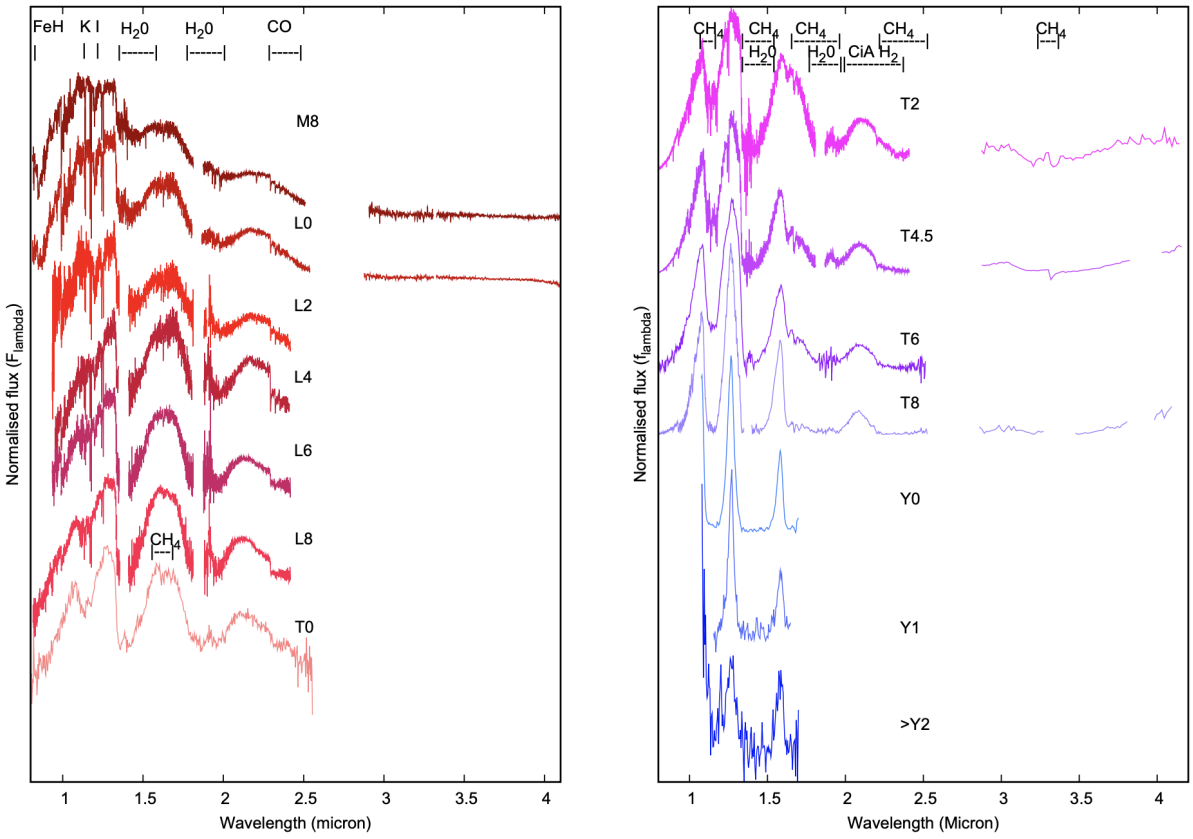

Fig. 1.14 The spectral features of brown dwarf atmospheres shown during the different spectral types (which correspond to an evolutionary path). Figure from Helling & Casewell (2014).

As the sequence moves towards T dwarfs (classified by Burgasser et al. (2006)), the presence of methane (CH_4) in the near-infrared becomes abundantly clear (see Fig. 1.14).

This dominance of CH_4 takes over from carbon monoxide (CO) in M and L dwarfs, as the temperature decreases and the pressure increases. The transition from CO to CH_4 occurs around 1100 K (Fegley & Lodders 1996) and is governed by the transition:

$$CH_4 + H_2O \rightleftharpoons CO + 3\,H_2 \tag{1.7}$$

With increasing T-type, the broad CH_4 and H_2O absorption features become deeper, leaving triangular peaks as seen in the T6 and T8 types in Fig. 1.14. The 'Cond' models Allard et al. (2001) reproduce the atmospheric features present in T dwarfs, as the models deal with an atmosphere where the dust has completely settled down into an optically-thick region.

Modelling the spectra of the transition between L and T dwarfs is, however, difficult to replicate. The transition is seen as a distinctive feature in the colour-magnitude diagram of brown dwarfs (Fig. 1.13).

The transition is thought to be associated with the clearing of dust clouds that dominate L dwarfs. Allard et al. (2001) proposed the 'Settl' models as an intermediate phase to the Dusty and Cond models. More recent work has questioned whether the spectra of brown dwarfs may be explained by convection mechanisms rather than condensate clouds (Tremblin et al. 2015, 2016, 2017). There still remains no consensus about the physical mechanism of the L/T transition, and it is a widely discussed topic.

Burrows et al. (2003) discussed the possibility of an even colder spectral class of brown dwarfs, called Y dwarfs that were discovered in the past decade by Cushing et al. (2011) and furthered defined by Kirkpatrick et al. (2012). The transition from T to Y is marked by the presence of ammonia (NH_3). This transitions occurs around 600-700 K and is governed by the transition:

$$N_2 + 3\,H_2 \rightleftharpoons NH_3 \tag{1.8}$$

There are only a handful of Y dwarfs that have been detected to date as cooler objects become more difficult to detect. One of the detections so far include the coldest known brown dwarf with a temperature of just 250 K (Luhman 2014). As the spectral sequence becomes increasingly closer to giant planets in temperature, they serve as great analogues for understanding gaseous exoplanets and challenge our understanding of such atmospheres (Morley et al. 2018; Leggett et al. 2019).

What is evident when discussing brown dwarfs, is that the formation, evolution, structure, atmospheric properties, and physical properties like surface gravity, are entwined in such a way that it is impossible to model such objects without taking all of these factors into account. But it is this wonderful mixture of physics that makes them so much more interesting than being so-called 'failed stars'.

1.4.3 Field brown dwarfs

To further understand the nature of brown dwarfs, it became key to detect many more after the initial discoveries. Consequently, several deep, wide-field infrared sky surveys were carried out to hunt for such objects. These include:

- The Deep Near-Infrared Southern Sky Survey (DENIS, Epchtein et al. 1997; Delfosse et al. 1999b)
- The Two Micron All Sky Survey (2MASS, Skrutskie et al. 2006; Kirkpatrick et al. 1999; Burgasser et al. 1999)
- The Sloan Digital Sky Survey (SDSS, York et al. 2000)
- Wide Field Infrared Explorer (WISE, Wright et al. 2010) and ALLWISE (Kirkpatrick et al. 2014)

The detections from these surveys constitute the vast majority of known brown dwarfs, with these wide-area imaging surveys detecting primarily isolated, or field, brown dwarfs.

Whilst surveying field brown dwarfs allows us to study their atmospheric properties in depth, the problem comes with an inability to measure the masses of these objects. The mass can be estimated using evolutionary tracks of brown dwarfs, which require a measured luminosity and distance. But furthermore, an age is also required, which means it is beneficial to observe brown dwarfs that are part of stellar associations with known ages.

The exception to this is if the brown dwarf is in a binary system where the dynamical masses can be measured (e.g. Dupuy & Liu 2012; Lane et al. 2001; Dupuy et al. 2014).

However, the binarity of brown dwarfs is not beneficial for this task with only about 10-20% of L and T dwarfs in binary systems (Gizis et al. 2003; Burgasser 2007; Goldman et al. 2008) with evidence that the multiplicity decreases with increasing spectral type (Fontanive et al. 2018).

With such a low frequency of binary systems, they are not so easy to detect and they rely on being wide enough to spatially resolve with a telescope (without the use of coronagraphy discussed in Chapter 2.3). Furthermore, observing the radial velocity of a brown dwarf binary is an extremely difficult task due to their low-luminosity and being fast rotators.

1.4.4 Brown dwarfs as companions

Some of the problems outlined in discussing field brown dwarfs are the unknown parameters of age, leading to an uncertainty on the mass of the brown dwarf. To eliminate this problem, observing brown dwarfs as companions to solar-type stars means that the age of the system can be determined from the star itself and the (minimum) mass can be measured using the radial velocity technique as described in Chapter 1.2.2.

Furthermore, combining the radial velocity and direct imaging techniques means that a true dynamical mass that is model independent can be measured, establishing critical benchmark brown dwarfs. Moreover, direct imaging of such objects at different evolutionary stages is crucial in trying to disentangle the formation scenario that created them. One aspect of this is being able to spectroscopically examine such objects (e.g. Cheetham et al. 2018b; Peretti et al. 2019) to retrieve clues of their formation from their atmospheres. This, however, isn't trivial as such measurements can often be hindered by clouds and non-equilibrium chemistry (Helling et al. 2008; Baraffe et al. 2010).

Some of the first brown dwarfs that were discovered via the radial velocity method were from Marcy et al. (2001) and Udry et al. (2002). However, even from these early radial-velocity surveys for exoplanets, it became clear that there is a dearth of companions in the mass range between $\sim 13-80\,M_{\rm Jup}$ at close separations ($\lesssim$ 5 AU). Companions in this mass range are so close to their star that they would be easily detectable via the radial-velocity method. Statistical analyses of the occurrence rates of companions with different masses orbiting close to their host star were carried out, such that Udry & Santos (2007) and Mayor et al. (2011) found that $\sim$ 14% of solar-type stars have planets within 4.5 AU in the mass range between $0.15-13\,M_{\rm Jup}$. On the other end of the mass range, Halbwachs et al. (2003)

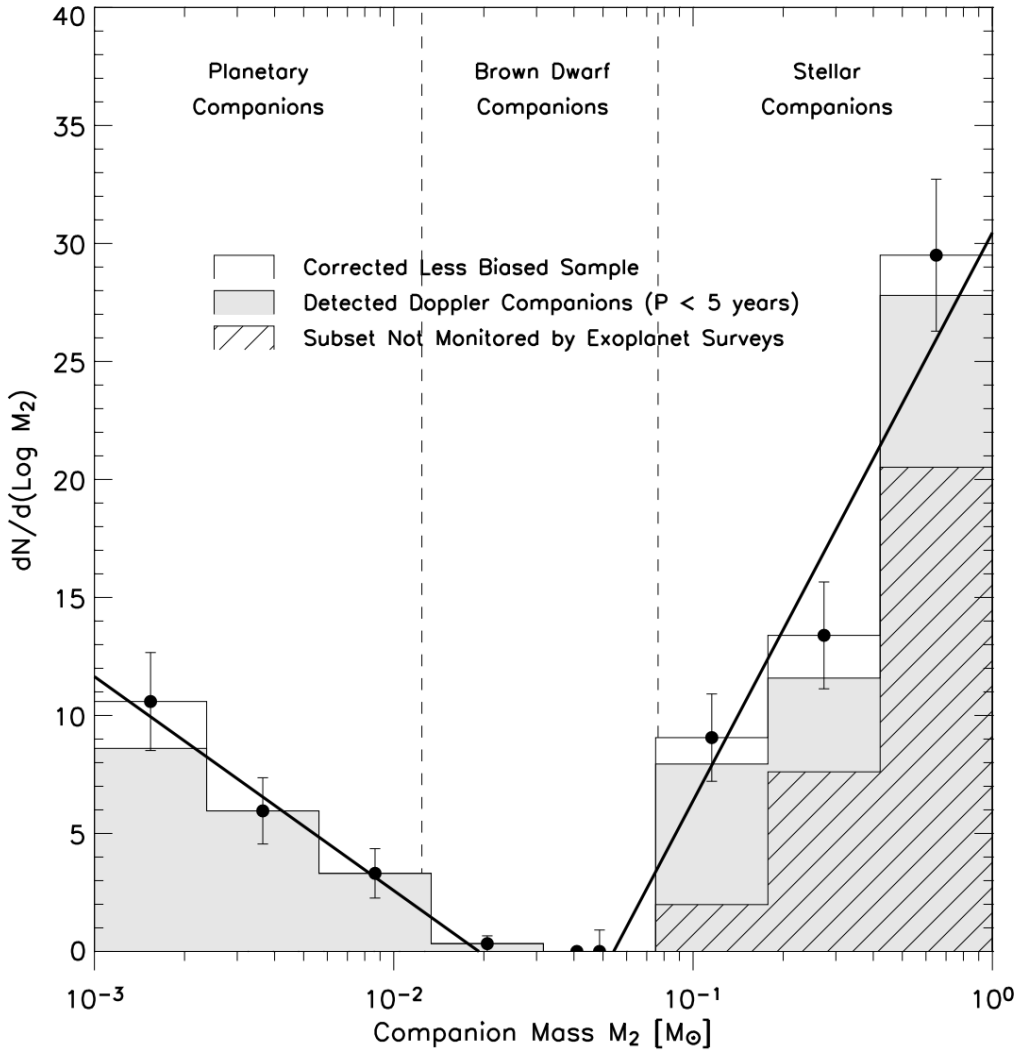

Fig. 1.15 A histogram showing the comparative number of closely-separated planetary companions on the left, brown dwarf companions and in the middle, and stellar companions on the right. There is a clear dearth of brown dwarf companions at such separations, called the 'brown dwarf desert'. Figure from Grether & Lineweaver (2006).

found that $\sim 13\%$ have stellar companions ($m \sin i > 80\ M_{\rm Jup}$) within 10 AU. However, Sahlmann et al. (2011b) found that only 0.6% have companions in the brown dwarf mass regime ($13 - 80\ M_{\rm Jup}$) in the same separation range. The lack of brown dwarf companions close to their stars became known as the 'brown dwarf desert' (Fig. 1.15, Marcy & Butler 2000; Mayor & Udry 2000; Grether & Lineweaver 2006).

The brown dwarf desert clearly indicates separate formation scenarios for planetary and stellar companions (Chabrier et al. 2014). Furthermore, the occurrence rate of the brown dwarf population on wide orbits is not yet understood, or the extent of the brown dwarf desert, which means that there is still an ongoing debate about the formation scenario for such companions (Wagner et al. 2019).

In recent studies it has been found that the formation mechanism of brown dwarfs as companions to stars may differ depending on their separation. Ma & Ge (2014) and Bowler et al. (2020) have both found that brown dwarfs above and below the brown dwarf desert possess a different eccentricity distribution, not only confirming that the desert is real, but also implying that the close-in brown dwarfs may form in the protoplanetary disk through gravitational instabilities, whereas widely-separated brown dwarfs may dominantly form like a stellar binary through molecular cloud fragmentation.

It has been the recent advancement in direct imaging that allows us to probe this widely-separated region. As a result there are still only a few directly imaged brown dwarf companions, and especially those with a known mass and age, as well as physical properties like temperature, $\log g$ and radius. This highlights the importance of detecting brown dwarf companions through the combination of the radial-velocity and direct imaging methods as they can provide us with these physical parameters, and act as benchmarks to compare to models of formation and evolution.

For this reason, the detection and characterisation of long-period exoplanets and brown dwarfs are key in contributing to the occurrence rates of these objects, as well as providing critical benchmarks for model comparison, and ultimately helping to investigate the formation mechanisms that create such widely-separated massive companions.

1.5 This thesis

Due to technical challenges, to date, the number of ultracool companions to solar-type stars directly imaged is very low. However, once detected, these few targets represent an ideal laboratory to test the complex physics of cool atmospheres as well as the structure and the evolution of substellar objects. In addition, the study of brown dwarf companions to solar-type stars gives access to key information about the system such as its age, metallicity as well as dynamical masses.

The work I have carried out in this thesis combines the radial velocity and direct imaging techniques to hunt for ultracool giant planet and brown dwarf companions[1]. I have probed an unconstrained parameter space in mass and separation, as well as provided accurate dynamical masses on these companions to contribute to just a small number of such detected objects. I primarily probe the

[1] As the focus of this thesis is on the detection of brown dwarf companions, whenever I refer to brown dwarfs throughout this thesis, it can be assumed that I am talking about brown dwarf companions.

separation range greater than 5 AU where the occurrence rate of giant exoplanets and brown dwarfs is not yet well understood.

Ultimately, the planets and brown dwarfs presented in this thesis contribute to just a short list of such objects and help to populate the mass-luminosity-age relationship with well defined physical parameters.

In Chapter 2, I go into detail about high-contrast imaging, including the instrumentation, data processing and analysis I have used. In Chapter 3, I present five new long period companions that I have published from a radial-velocity search. In Chapter 4, I outline the follow-up monitoring and imaging of these radial velocity companions and the results of this. In Chapter 5, I present the direct detection and spectral characterisation of a new benchmark brown dwarf. In Chapter 6, I present an ongoing high-contrast imaging survey around young stars and some early results. And finally in Chapter 7, I outline the conclusions of this work along with the outlook and future perspectives.

CHAPTER 2

HIGH-CONTRAST IMAGING

"If we assume we've arrived: we stop searching, we stop developing."

— Jocelyn Bell Burnell

2.1 Introduction

In Chapter 1.2.1 I briefly discussed the direct method to detect exoplanets, also known as high-contrast imaging. There are, like any other detection method, many pros and cons to using this method to hunt for exoplanets. One advantage of high-contrast imaging is the ability to directly observe the spectrum of the planet or brown dwarf without the need to worry so much about stellar contamination. Furthermore, images of disks can be taken (e.g. Milli et al. 2017; Keppler et al. 2018), which can give us hints towards the formation of such systems.

A large drawback of high-contrast imaging is the difficulty to detect new planets. This is mostly due to the fact that the detection space is primarily limited to young, widely-separated ($\gtrsim$10 AU), massive planets where the occurrence rate of such companions is thought to not be so high (Bowler 2016). Despite this drawback, it serves as a crucial parameter space to explore in order to understand the demographics of *all* exoplanets, providing a detection method that complements other methods that typically favour much closer companions, like the radial-velocity method discussed in Chapter 1.2.2.

High-contrast imaging, however, is not an easy task to do. Trying to image something that is a million times fainter than its host star and is tens of parsecs away has been described by Perryman (2012) as:

> *"...trying to detect a moth dancing around a lighthouse seen from several kilometers distance."*

There are several steps both during the observations themselves, as well as in post-processing, that are used to try and hunt for these buried signals in the glare of their stellar host's starlight. This chapter

introduces and explains the steps of how we can discover planets despite the difficulties involved. And I also explain how it is possible to characterise such detections, as well as combine the method of high-contrasting imaging with the radial-velocity method to further constrain such detections.

2.2 Adaptive optics

A necessary part of high-contrast imaging as discussed in briefly in Chapter 1.2.1, is the use of adaptive optics (AO). Adaptive optics allow us to spatially resolve objects at a much closer angular separation, towards the diffraction limit of the telescope.

When the light of a star passes through the circular aperture of a telescope, this transforms the light from a point source into a diffraction pattern, called an Airy Disk (see Fig. 2.1). The shape and size of the response function of the telescope observing a point source of light is called the Point-Spread Function (PSF). Two objects of similar brightness can be considered to be spatially resolved, according to the Rayleigh criterion, if the peaks of each PSF are separated by:

$$\theta \simeq \frac{1.22\lambda}{D} \tag{2.1}$$

where D is the diameter of the aperture of the telescope and λ is the wavelength of light at which you are observing in. This is the separation of the first Airy disk minimum, which is where the factor of 1.22 is derived from. An example of this is shown in Fig. 2.1.

Assuming we were observing with an 8.2 m telescope, at a wavelength of 1.5μm, we could reach an angular resolution of 46 mas, and for a star at a distance of 20 pc that corresponds to just under 1 AU, for two objects of a similar apparent brightness.

In reality, this is far more challenging. Most ground-based telescopes don't operate at the diffraction limit. This is due to atmospheric turbulence that distorts the wavefront of light arriving from a distance star. It is necessary to correct for this to be able to reach the resolution required for high-contrast imaging.

A technique was developed by Labeyrie (1970) in order to resolve closely-separated binary stars using a large telescope, which I will describe briefly. This technique, called 'speckle imaging', uses information of the high-contrast images in the Fourier space, by using the correlations between the speckle patterns seen on the images, to subsequently be used to reconstruct a spatially resolved image.

For my work, however, I have made use of adaptive optics on large telescopes to correct for atmospheric turbulence. The concepts of adaptive optics are shown in Fig. 2.2. Light emitted from distant stars arrive at the Earth as as a plane wavefront. This wavefront is perturbed by atmospheric turbulence, which creates a corrugated or distorted wavefront to enter the aperture of the telescope. A fraction of the light from this wavefront is read into a wavefront sensor by the use of a beam-splitter and then analysed by a real-time high-speed computer that records the shape of the incoming wavefront. This information is then fed back to the deformable mirror to correct the wavefront, which is ultimately

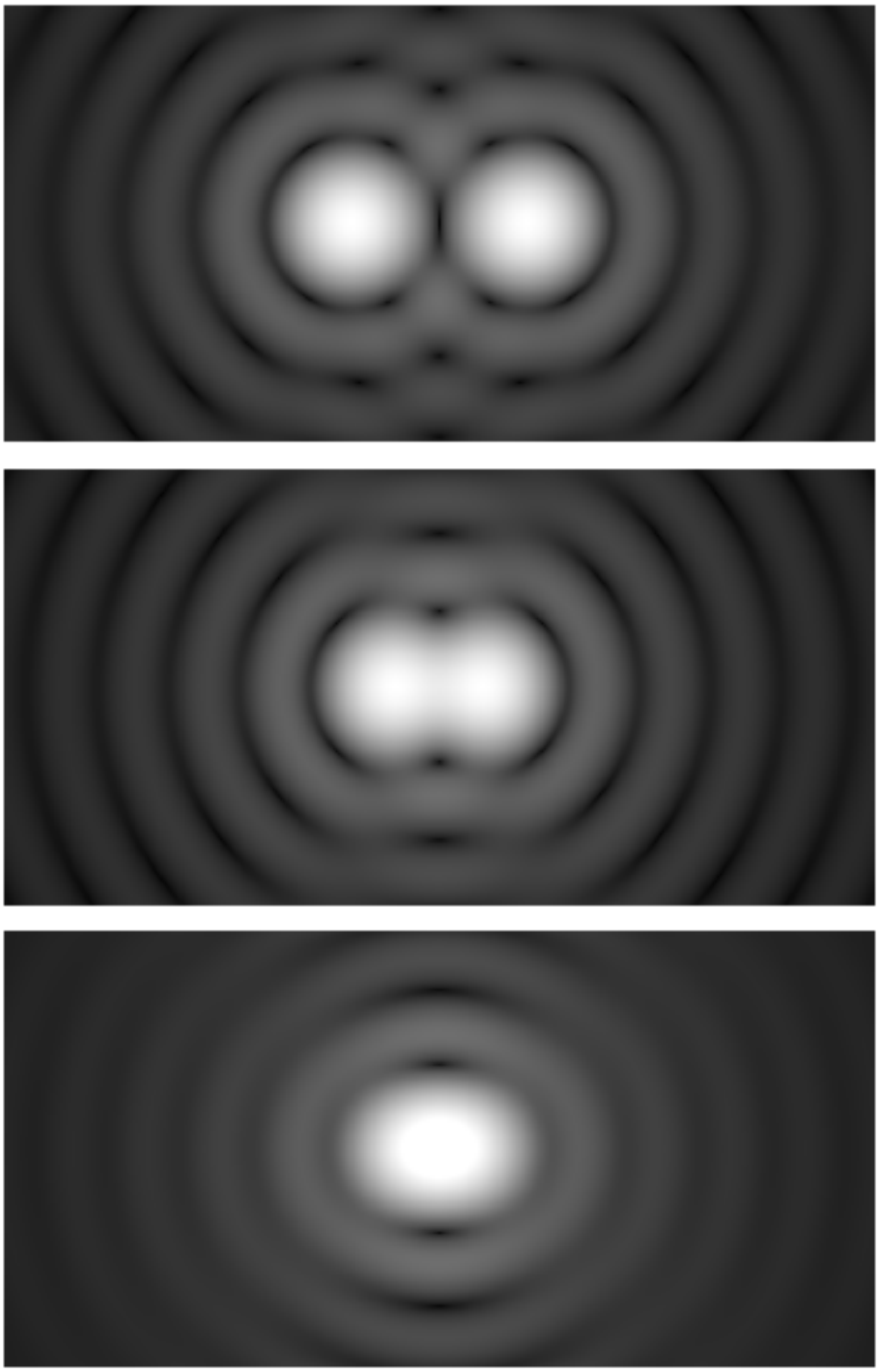

Fig. 2.1 Two equally bright PSFs with an Airy Disk diffraction pattern observed at different separations. The top image shows two clearly resolved PSFs. The middle image shows the two PSFs meeting the Rayleigh criterion described by Equation 2.1 and the bottom image shows the two PSFs below the Rayleigh criterion and are therefore indistinguishable. Image credit: Wikimedia commons.

guided into the detector. This loops round at a rate of several hundred to thousands of times per second during observations to continuously correct for the incoming wavefront.

The first adaptive optics was installed on the ESO 3.6 metre telescope at La Silla Observatory, Chile (Rigaut et al. 1991), which was used for testing before the VLT came online. Later a dedicated camera, COMIC, was used as a testbed to install new cameras in the near and mid-infrared (Lacombe et al. 1998). During this time period, one of the best AO instruments on sky was PUEO (Rigaut et al. 1998), installed at the Canada-France-Hawaii Telescope, which under median observing conditions, could already achieve near diffraction-limited images in the H and K band.

The effect of the atmosphere on the PSF is called the 'seeing'. Atmospheric turbulence is caused by variations in density and temperature, which consequently vary the refractive index of the atmosphere at different points. The size of a turbulent cell in the atmosphere is quantified by the *Fried parameter* (Fried 1966). The Fried parameter, r_0 is characterised by the scale of the turbulence structure (Kolmogorov 1941) and is given by:

$$r_0 = 0.185\lambda^{6/5}\cos^{3/5}z\left(\int_0^\infty C_n^2(h)\mathrm{d}h\right)^{-3/5} \tag{2.2}$$

where λ is the wavelength in metres, z is the zenith distance, h is the altitude in the atmosphere, and C_n^2 is the turbulence structure constant as a function of altitude. Therefore the seeing has a wavelength dependence of $r_0 \propto \lambda^{6/5}$. This means that for longer wavelengths, the size of the turbulent cells will be much larger, thus reducing the influence of the atmosphere on observations. For this reason, it is beneficial to observe at longer wavelengths, i.e. in the infrared compared to the visible. Furthermore, observing closer to the zenith, i.e. at a lower airmass, is beneficial as it reduces the length of the path that the light has to take through the atmosphere.

This means that the diffraction limit is given by the diameter of the stable wavefront, r_0 rather than the diameter of the telescope. Therefore, Equation 2.1 becomes:

$$\theta \simeq \frac{\lambda}{r_0} \tag{2.3}$$

Another parameter that needs to be considered for the correction of the wavefront is the coherence time, τ_0. It can be derived from the Fried parameter and defined as:

$$\tau_0 = 0.31\frac{r_0}{v_0} \tag{2.4}$$

where v_0 is the wind speed perpendicular to the line-of-sight (Roddier 1981), where a mean weighted turbulence profile can be used (e.g. Poyneer et al. 2009) to take into account wind speed at different altitudes. As the coherence time indicates the time it takes for one turbulent cell to be replaced by the next, then ideally the correction by AO needs to be faster than this. Therefore, it is an important parameter to define at what frequency the AO system has to perform to correct the distorted wavefront.

Of course, there are limitations in what an AO system can achieve. If the AO system is not able to correct faster than the coherence time, for example observing in high wind speeds, or if there is a delay

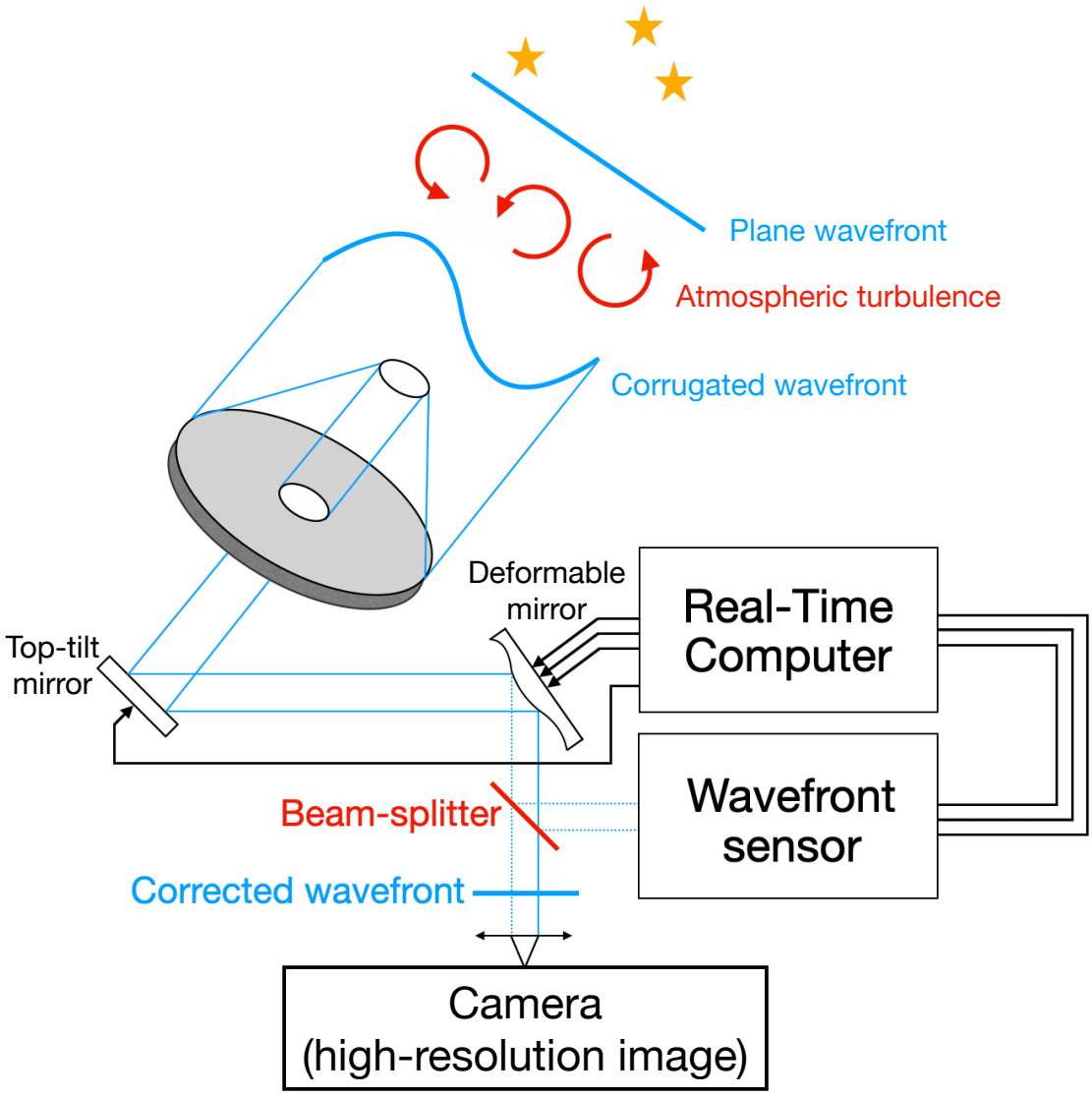

Fig. 2.2 A schematic of the principles of adaptive optics. The plane wavefront from distant stars is perturbed by atmospheric turbulence. The corrugated wavefront enters the telescope, where some of the light is directed to a wavefront sensor with the use of a beam-splitter. The wavefront sensor then records the incoming wavefront which is analysed by a real-time computer and the corrections are sent to the deformable mirror. The corrected wavefront then enters the detector. Figure adapted from Kaufer (2008).

between the wavefront analysis and the correction of the deformable mirror, this can cause speckles to appear on the images. These speckles evolve on different time scales, which can depend on the observing conditions, as well as the variations in the optics of the system (e.g. Racine et al. 1999; Macintosh et al. 2005; Hinkley et al. 2007; Milli et al. 2016).

By the use of AO, it has been shown that it is possible to achieve close to the diffraction limit (e.g. Close et al. 2012, 2013; Rigaut et al. 2014) and it is certainly necessary to achieve the resolution required to detect faint companions around bright stars with direct imaging. An example of the performance that can be achieved with AO from Close et al. (2003) is shown in Fig. 2.3.

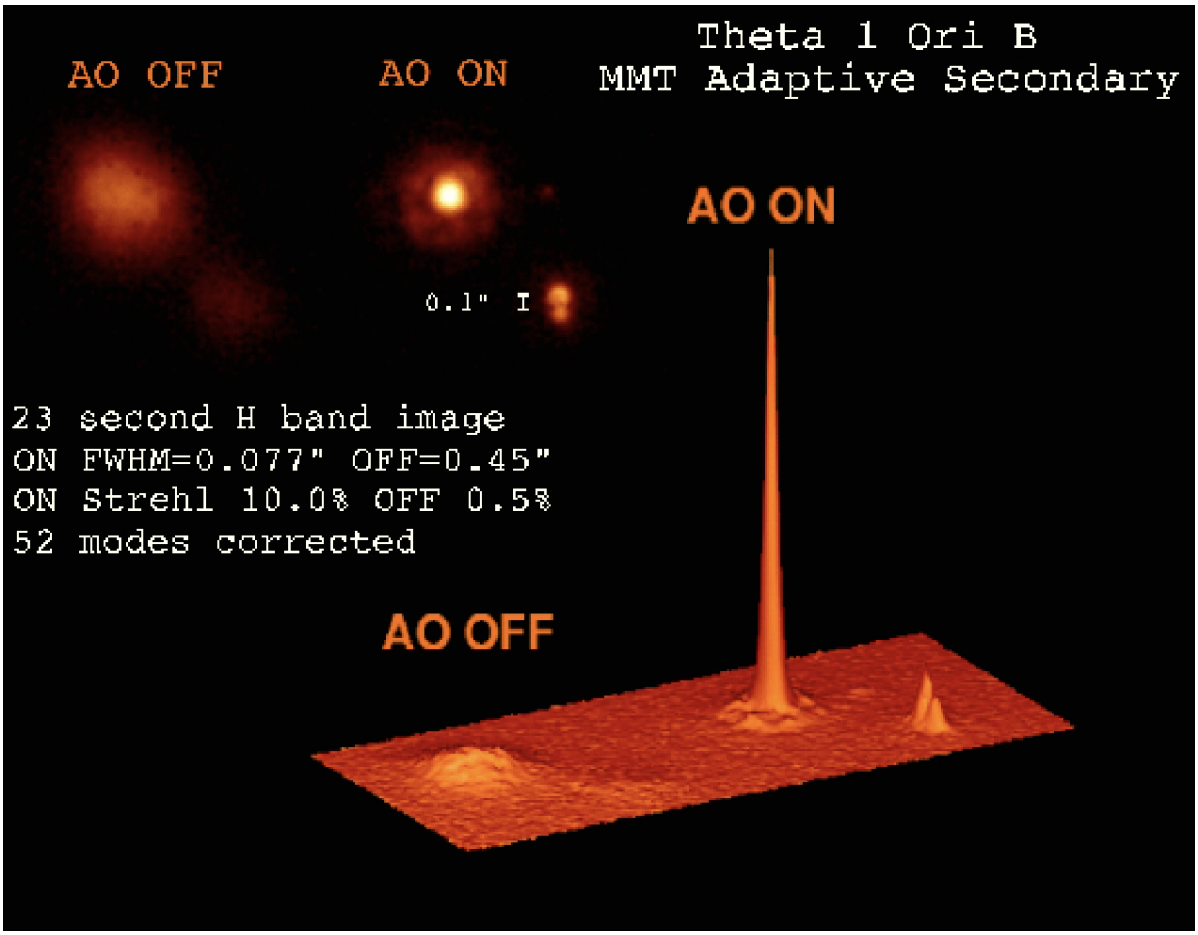

Fig. 2.3 An observation of θ^1 Ori B using the MMT in the *H* band. The left image shows the observation without the use of the AO system and the right images shows the same observation with the use the AO system, where the companions can be resolved. The 3D PSFs are also shown corresponding the AO off and AO on respectively. Figure from Close et al. (2003).

One way to measure the performance of an AO system is by the *Strehl ratio*. The Strehl ratio is defined as the ratio of the measured peak intensity of an imaged point source, over the expected peak intensity from an ideal diffraction limited system. Therefore, a Strehl ratio of 100% corresponds to a perfect optical system. Without adaptive optics, a ground-based observatory will not typically exceed

1% (like seen in the left image of Fig. 2.3), compared to with adaptive optics in the near-infrared that can increase the value to between 20% and 60% (Fig. 2.3, Rousset et al. 2003). The latest generation of extreme adaptive optics (XAO) can achieve Strehl ratios of more than 90%, and this is case for VLT/SPHERE which is discussed in Chapter 2.4.

2.3 Coronagraphy

An additional component that is necessary for high-contrast imaging is to reduce as much of the starlight as possible to reveal any faint companions hidden by the luminosity of the host star. The coronagraph, invented by Lyot (1939), does just that. It was originally invented for the purpose of blocking out the light of the Sun to observe its corona without the need to wait for a solar eclipse. It is now frequently used for directly imaging exoplanets.

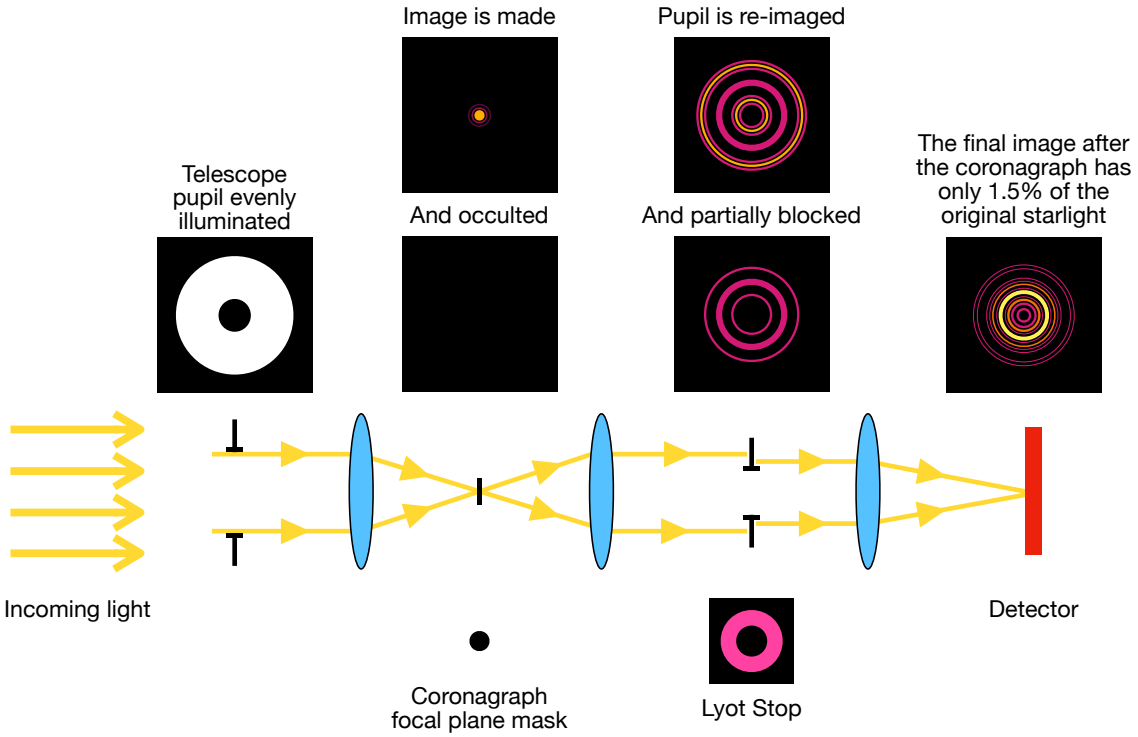

Fig. 2.4 A schematic of the basic principles of a coronagraph. The incoming light from a star enters the telescope. A coronagraph focal plane mask is placed at the first image plane which suppresses the starlight. The diffracted starlight is then blocked using a Lyot stop before the final image then enters the detector with only 1.5% of the original starlight. Figure adapted from Sivaramakrishnan et al. (2001).

A schematic of the basic principles of a coronagraph is shown in Fig. 2.4. The light from a distant star enters the pupil of the telescope. A focal plane mask is put at the first image plane in order to suppress the stellar light. However, because the light gets diffracted in the re-imaged plane due to

the sharp edges of the focal plane mask, a Lyot stop is placed to block out the diffracted light. The final image then enters the detector with a significantly reduced amount of starlight (of the order of $\sim 0.5 - 1.5\%$).

Developments in coronagraphy include replacing a mask with sharp edges, with apodised edges. This reduces the amount of scattered light from the first image plane. Interferometric masks were also developed to act on the phase of the light rather than the amplitude (Gay & Rabbia 1996; Roddier & Roddier 1997), which is particularly important for telescopes that are not limited by atmospheric seeing (e.g. space-based telescopes or with the use of adaptive optics). More recent advances include an Annular Groove Phase (AGPM) vortex coronagraph (Mawet et al. 2005; Absil et al. 2013), which is used on VLT/NACO, discussed in Chapter 6. Furthermore, detailed overviews of coronagraphic designs can be found in Guyon et al. (2006) and Martinache (2019).

Using a coronagraph is necessary for high-contrast imaging to reach angular separations that are close to the host star and to remove as much of the unwanted starlight as possible. To enhance this even further, coupling AO with the use of a coronagraph allows for high-contrast imaging to reach further capabilities. This was first carried out by Beuzit et al. (1998).

But as with any method, it does not coming without problems. Residual speckles can still remain due to diffracted starlight, and often these will be brighter than any potential companion. In order to try and suppress these speckles, complex post-processing techniques are necessary. The different types of image processing that are used are discussed in Chapter 2.5.

2.4 Spectro-Polarimetric High-contrast Exoplanet REsearch (SPHERE)

The Spectro-Polarimetric High-contrast Exoplanet REsearch (SPHERE, Beuzit et al. 2019) is a high-contrast near-infrared imager mounted on the VLT/UT3 at Paranal, Chile (shown in Fig. 2.5). SPHERE makes use of an apodised Lyot coronagraph (Soummer 2005) to block out as much star light as possible from the host star as discussed in Chapter 2.3. It hosts an extreme adaptive optics system with a deformable mirror to correct for atmospheric turbulence at a frequency of 1.38 kHz (Beuzit et al. 2019).

SPHERE hosts several advanced capabilities that are advantageous to high-contrast imaging as well as low-resolution spectroscopic and polarimetric characterisation. It contains an Integral Field Spectrograph (IFS, Claudi et al. 2008) in addition to an Infra-Red dual Imaging and Spectrograph (IRDIS, Dohlen et al. 2008), and the Zurich Imaging Polarimeter (ZIMPOL, Schmid et al. 2018).

SPHERE has been at the forefront in the direct detection and characterisation of numerous planets (e.g. Chauvin et al. 2017), as well as brown dwarfs (e.g. Cheetham et al. 2018b), disks (e.g. Lagrange et al. 2016), and even witnessing the formation of a newborn planet (Keppler et al. 2018).

Many detections from VLT/SPHERE have come from the SpHere INFrared survey for Exoplanets (SPHERE-SHINE, Chauvin et al. 2017), which is a 200-night Guaranteed Time Observations (GTO) survey. There are several aims of the survey that include determining the frequency of giant planets in the 10-50 AU range as a function of stellar host mass and age, in addition to studying the atmospheres of exoplanets and contributing to the understanding of giant planet formation. I have worked as a

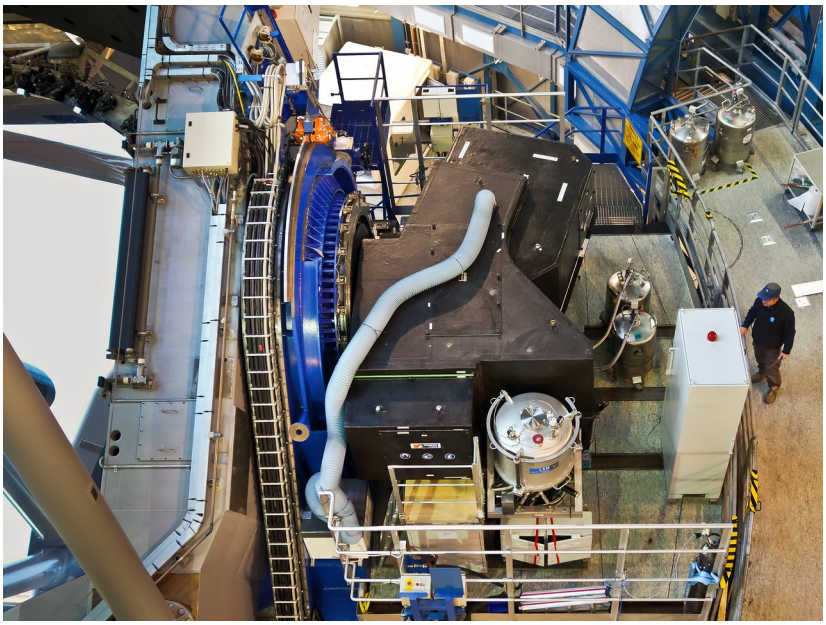

Fig. 2.5 SPHERE is mounted on VLT/UT3 at the Nasmyth focus. Image credit: ESO.

collaborator for the SPHERE-SHINE survey and survey papers where I have made contributions are listed in Appendix A.2.

As part of this thesis I have used SPHERE to take follow-up images of radial-velocity-detected giant planets and brown dwarfs, which is discussed in depth in Chapters 4 and 5. This has been done using the IRDIS and IFS modes of SPHERE in order to utilise the high-contrast and precise astrometry that can be retrieved using the narrow-band filters with IRDIS and the spectral information that can retrieved using the IFS. Furthermore, SPHERE has two CCDs, which means that it is capable of observing using IRDIS and IFS simultaneously, allowing the detection and characterisation of a companion to be done using one observation.

IRDIS operates with narrow band filters in the wavelength range from 0.95 μm - 2.32μm and can be used in four observing modes: Classical Imaging (CI), Dual-Band Imaging (DBI, Vigan et al. 2010), Long-Slit Spectroscopy (LSS, Vigan et al. 2008), and Dual Polarisation Imaging (DPI, de Boer et al. 2020; van Holstein et al. 2020). For my observations in this thesis I have utilised the DBI mode to make use of spectral differential imaging (SDI, see Chapter 2.5.2).

IFS operates in the wavelength range 0.95 μm $-$ 1.65 μm across 39 wavelength channels, and can operate either in the $Y-J$ range with a resolution of $\sim$ 54 or the $Y-H$ range with a spectral resolution of $\sim$ 30 referred to as the IFS extended mode.

Observing using IRDIS and IFS means that I can select a band where we expect a larger amount of flux from an ultracool object (e.g. the J or H-band with IRDIS), whilst simultaneously characterising a detected companion by extracting the spectral information from the IFS data, which is crucial to pull out physical parameters of ultracool objects like effective temperature and surface gravity (see Chapter 2.6).

2.5 Data processing and analysis

As mentioned previously, in order to detect faint signals of potential companion candidates orbiting around bright stars it is necessary to combine the use of adaptive optics (Chapter 2.2), coronagraphy (Chapter 2.3) and various sophisticated data post-processing techniques which are discussed here. Post-processing techniques of high-contrast imaging was first done by Christou et al. (1998), who demonstrated by recovering the point spread function of Io in thermal imaging. The intricacies of various post-processing techniques of high-contrast imaging data are described in the following sections.

2.5.1 Angular Differential Imaging

Angular Differential Imaging (ADI, Marois et al. 2006) is a technique applied to high-contrast imaging data in order to suppress speckles and noise present in images in order to detect faint signals of potential companion candidates. Marois et al. (2008) applied this technique to successfully detect the first directly imaged multi-planetary system, HR 8799. The principle of the idea is that an altitude-azimuth mounted telescope's de-rotator is switched off (i.e. it observes in pupil tracking mode) during an observation of a target star.

Any companion around the observed star will appear to rotate around it as the field rotates due to the rotation of the Earth tracking a star like shown in Fig. 2.6. The angle position between the field of view's rotation and the telescope's pupil orientation is called the 'parallactic angle' as seen in Fig. 2.6, which depends on the latitude of the observatory as well as the declination and hour angle of the target.

During an observing sequence as the field rotates, continuous images are taken which lead to a sequence of images with the sky rotated around the target star. But whilst any companion rotates as a function of the parallactic angle in the image (shown by the blue dot in Fig. 2.7), the diffraction pattern, and quasi-static speckles stay relatively stable throughout the observation (shown by the yellow dots in Fig. 2.7). A median of the observing sequence in taken to give the average noise pattern throughout the observation. The median is then subtracted from each image to remove the noise and preserve the signal of the companion. Then to increase the signal of any companion candidates, the images are de-rotated (to take into account rotation over time) and stacked upon one another to amplify any signals. The median of this rotated stack is then taken to give the final detection image. This method is known as 'classical Angular Differential Imaging' or cADI.

Sufficient field rotation between frames is required to use this technique, otherwise the signal of the planet will be subtracted from itself, as shown in Fig. 2.8. This is especially problematic at radii close to the star. For this reason, it is important to observe the target as it is passing through its highest point in the sky, known as its 'meridian passage', where it is closest to the zenith and therefore experiences a faster rate of field rotation.

Furthermore, to account for self-subtraction, Marois et al. (2006) built upon the idea of cADI to formulate 'smart ADI' or sADI. In sADI the same principle is used but it builds a systematic

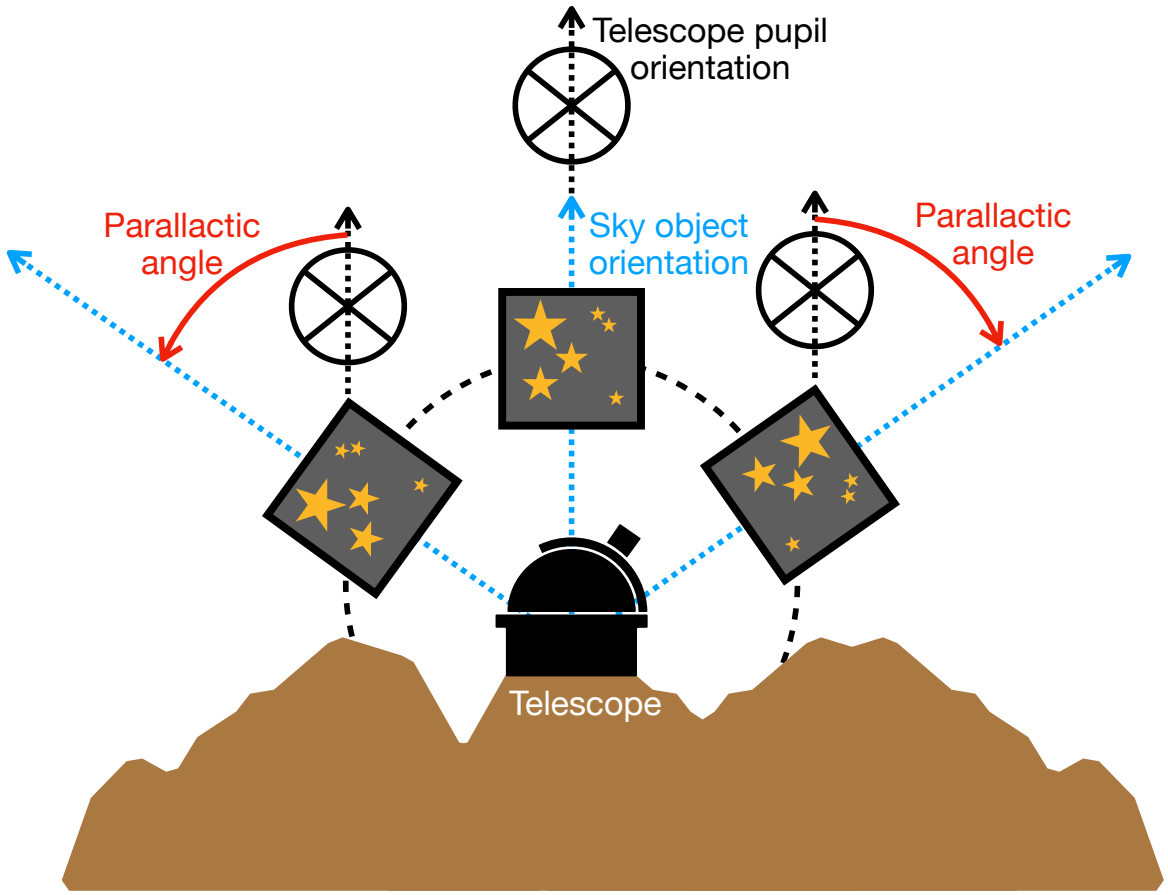

Fig. 2.6 A schematic of the principles of pupil tracking mode. An altitude-azimuth mounted telescope follows a target in the sky whilst disabling field tracking mode. Because of this the field-of-view of the sky rotates with respect to the telescope pupil orientation, meaning that any companion candidate to the target star rotates around it as a function of the parallactic angle, whilst the diffraction pattern and quasi-static speckles remain in a fixed position.

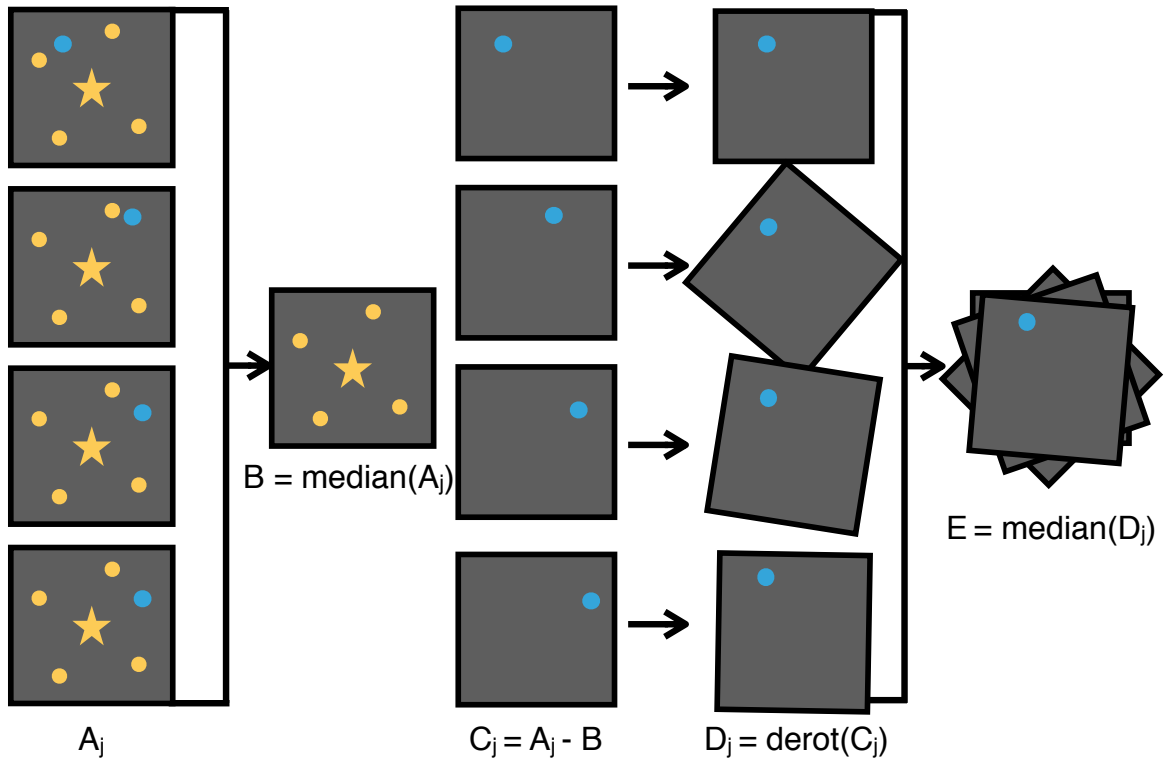

Fig. 2.7 Schematic of the principles of angular differential imaging. The blue dot in each image represents a signal from a companion candidate. The central yellow star represents the primary target. The yellow dots represent noise or speckles in the images. The stack of images is taken over an observing sequence, shown by A_j. The median of these images is taken to give the noise pattern over the observing sequence, shown by B. Image B is then subtracted from each of the images in A_j to eliminate the noise whilst preserving the signal of the companion, which gives a new stack of images shown by C_j. The images of C_j are then de-rotated to stack the signal of the companion on top of one another shown by D_j. Finally, a median of D_j is taken to give the final detection image with suppressed noise and stacked companion signal shown by E.

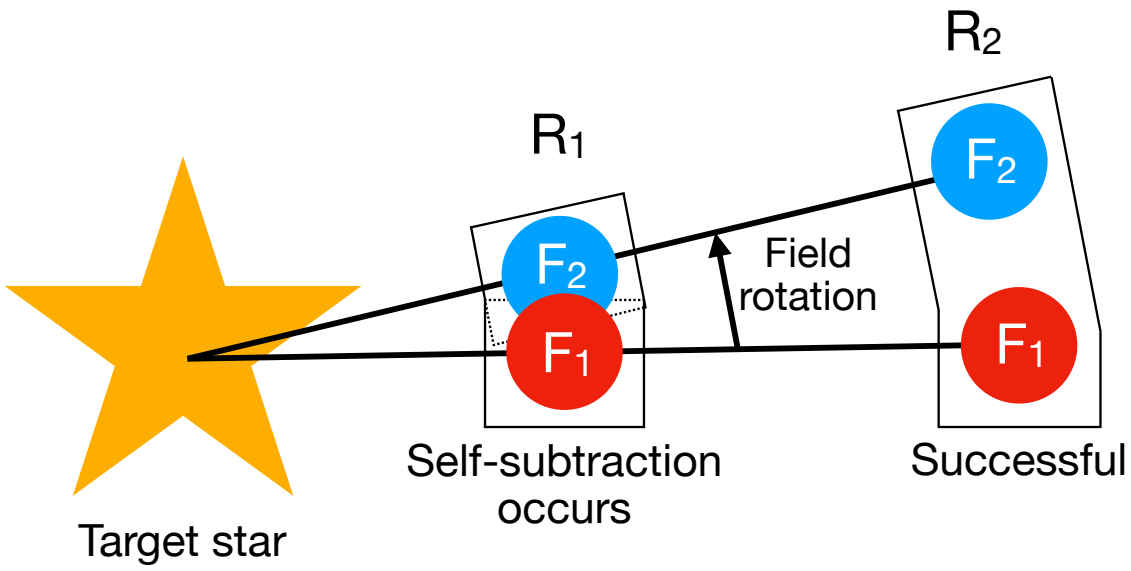

Fig. 2.8 A schematic of the principles of self-subtraction. A companion rotates across two frames, F_1 and F_2 around the target star. At radius R_1 from the star the subtraction area contains an overlap of the companion between F_1 and F_2 leading to a partial subtraction of the companion signal. Whereas at radius, R_2 the field rotation is sufficient that in the subtraction area the companion signal in F_1 and F_2 do not overlap and therefore the signal is not self-subtracted.

model for each frame, using only frames that have rotated by at least $1\lambda/D$ to minimise the effect of self-subtraction.

Another technique that makes use of ADI that is used to suppress the noise in high-contrast imaging is Principal Component Analysis (PCA). It was first proposed for the use of high-contrast imaging by Soummer et al. (2012) and Amara & Quanz (2012) independently. The method of PCA constructs a reference point spread function by converting the stack of science images taken into principal, orthogonal, linearly, uncorrelated components. The uncorrelated structures are removed to model the residual background serving as a reference frame to subtract from each science image. Therefore, all of the similar or correlated noise between the images will be removed, whereas any companion candidate in the image would have moved over time by using ADI. This means that the quasi-static speckles and relatively stable residual noise is removed, whilst the signal from a moving companion is preserved. The frames are then de-rotated and co-added, like in cADI and sADI.

2.5.2 Spectral Differential Imaging

In addition to angular diversity being used to further enhance a signal from a companion candidate, spectral diversity can also be used. This led to a technique called spectral differential imaging (SDI), that exploits the use of observing in several different spectral bands, like in DBI mode using SPHERE, or across multiple wavelengths using IFS on SPHERE.

There are two different ways in which spectral differential imaging can be carried out. The first of those is to observe in two narrow bands close in wavelength to one another such that one of the wavelengths aligns with an absorption band of a molecule present in the atmosphere of the observed companion (e.g. Rosenthal et al. 1996; Racine et al. 1999; Lenzen et al. 2004; Marois et al. 2005). In the atmospheres of ultracool brown dwarfs and giant exoplanets, molecular absorption due to methane or water is expected.

SPHERE makes use of strong methane absorption bands at several wavelengths of ultra-cool companions (like shown in Fig. 2.9). Imaging simultaneously in two narrow bands (DBI) means that one image will have a significant amount of flux from the companion, whereas due to molecular absorption, the other image will have a very small amount of flux from the companion. However, the stellar light and speckles should be relatively stable between these two bands, and so if one image is subtracted from the other the noise is removed whilst preserving the signal of the companion, as shown in Fig. 2.9. However, one obvious pitfall to this method is that it relies on the companion having strong molecular absorption its atmosphere.

Subsequently, Marois et al. (2005) developed an SDI method using spectral deconvolution. This makes use of the fact that the diffraction pattern from stellar light and speckles scale radially outward, proportional to the increase in wavelength, whilst the signal from a companion candidate remains at the same separation independent of wavelength and can therefore be distinguished from the noise pattern.

Multiple images can be taken over several different wavelengths and re-scaled to the size of a reference wavelength (see Fig. 2.10). This reference is then subtracted to remove the speckles and stray stellar light whilst preserving the signal from a companion. This can be done across several wavelengths to obtain a low resolution spectrum of the companion (e.g. Thatte et al. 2007). Modern advancements in direct imaging instruments like IFS on SPHERE (Claudi et al. 2008) or the Gemini Planet Imager (GPI, Macintosh et al. 2008) allow for this method to be used. It is extremely beneficial as it allows for the companion to be characterised at the same time as its detection. This is crucial for determining physical parameters of ultracool companions, as the depth and shape of absorption bands vary greatly for temperature, surface gravity, and radius. For this reason the IFS on SPHERE covers a region of multiple absorption bands as seen in Fig. 2.10.

Similarly to the self-subtraction issue of ADI, it is necessary to only subtract wavelengths where the companion signal will not overlap when the image is re-scaled. This can be overcome by not using the images that are closest in wavelengths to one another.

The most efficient way to suppress noise in high-contrast imaging is to combine angular and spectral diversities by using a combination of both ADI and SDI, whilst using instruments like SPHERE, that make use of adaptive optics and coronagraphy as discussed in Chapter 2.2 and 2.3 respectively.

For the high-contrast imaging data throughout this thesis, I have use of the Geneva Reduction and Analysis Pipeline for High-Contrast Imaging of planetary Companions (GRAPHIC), which was developed by Hagelberg et al. (2016). GRAPHIC incorporates cADI, PCA and SDI as discussed here.

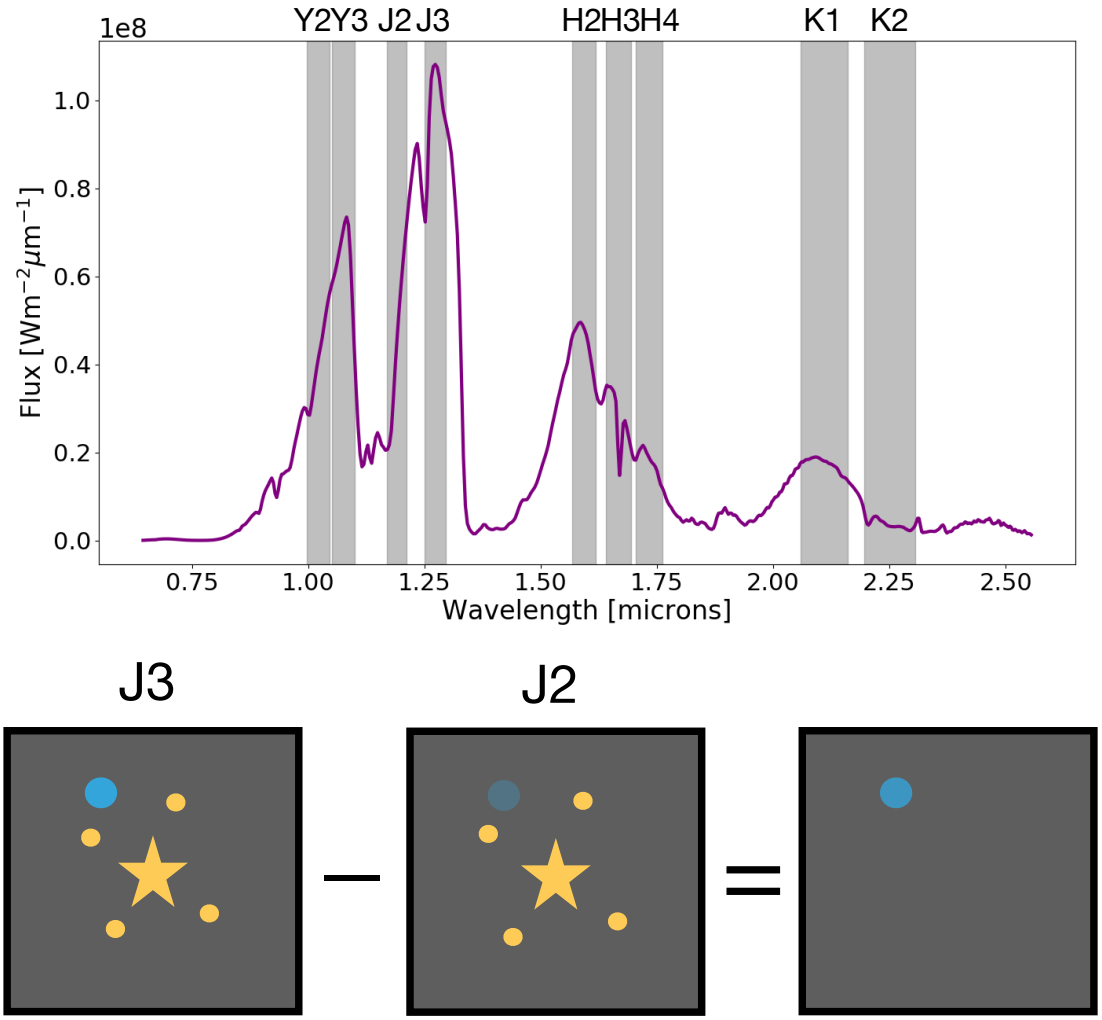

Fig. 2.9 A schematic of the principles of spectral differential imaging using DBI. *Top:* A spectrum of an ultracool T4 type brown dwarf (Morley et al. 2012). The grey highlighted bands indicate the narrow-band filters available for DBI with IRDIS on SPHERE. Each group of bands sits over a methane absorption band such that one narrow band filter receives a significant amount of flux of the companion whilst the other receives a lot less flux. *Bottom:* Two schematic images taken in the $J3$ and $J2$ bands. The central star represents the primary target, the yellow dots represent speckles and the blue dot represents a PSF of a companion. The $J2$ image with methane absorption from the companion is subtracted from the $J3$ image and the result is the removal of noise whilst preserving the signal of the companion.

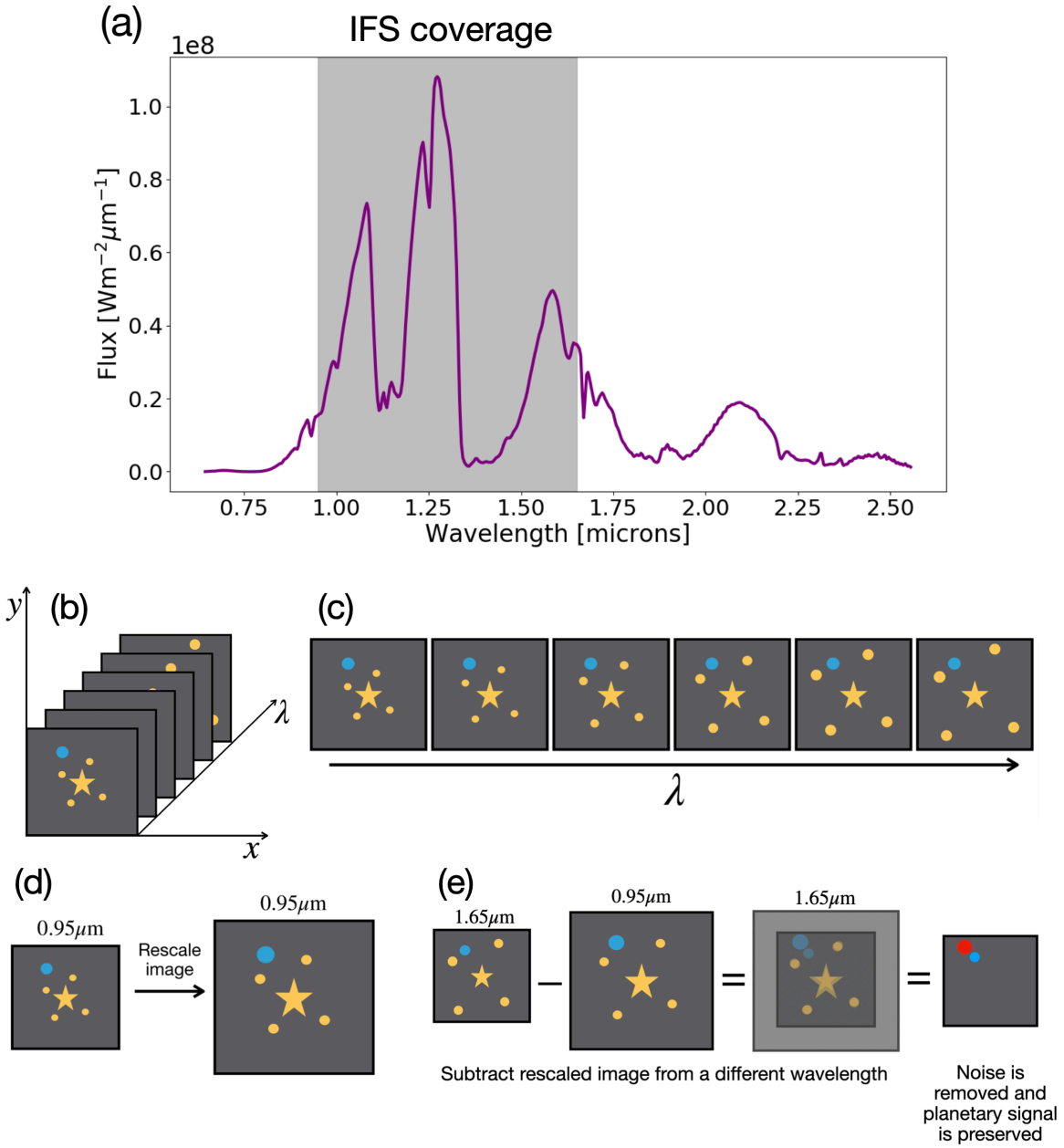

Fig. 2.10 Schematic of the principles of spectral differential imaging using spectral deconvolution. (a) Shows the spectrum of an ultracool T4 type brown dwarf (Morley et al. 2012) with the grey shaded area showing the wavelength coverage of IFS on SPHERE. This is split in 39 wavelength channels, which creates an image cube of increasing wavelength, λ shown by (b). The central star represents the primary target, the yellow dots represents speckles and the blue dot represents the PSF of a companion. In (c) it is shown that the diffraction and speckle pattern scale as a function of wavelength whilst the companion PSF is fixed. In (d), an image from wavelength 0.95μm is rescaled with respect to the stellar PSF centre to the size of a longer wavelength (1.65μm). In (e) the rescaled image is then subtracted from the longer wavelength, which removes the noise whilst preserving the PSF of the companion. The blue dot shows where the companion signal is and the red dot shows the subtraction of the companion signal from the image (i.e. negative flux).

2.6 Physical parameters

I have spoken about *how* we can detect companions using high-contrast imaging but what exactly can we learn about such detections? Several key physical parameters of detected companions can be derived using high-contrast imaging data.

2.6.1 Astrometry and photometry

The position of the companion in an image can be determined using a 'negative fake planet injection' (NEGFC, Lagrange et al. 2010; Marois et al. 2010; Bonnefoy et al. 2011). For this method, a PSF image of the target star without the coronagraph is taken during the observing sequence. This provides an estimate of what the shape of the companion's PSF looks like, as they are observed using the same optical system. The inverse of this stellar PSF is injected into the cube of science images with varying separation, position angle, and flux across a grid of parameters in order to minimise the χ^2 of the residuals in a small aperture centered on the injection position.

The NEGFC method determines the position of the companion on the image, which provides a projected separation between the companion and the star. The projected and physical separation of a detected companion is calculated using the distance to the target and the small angle approximation such that:

$$\theta[''] = \frac{a[\mathrm{AU}]}{d[\mathrm{pc}]} \tag{2.5}$$

where θ is the projected separation in arcseconds, a is the physical separation in AU and d is the distance to the star in parsecs.

Moreover, using the NEGFC technique, the PSF is scaled to fit the size of the companion's PSF. This determines the number of counts coming directly from the companion which is compared to the number of counts measured from the star which gives the contrast ratio of the amount between the companion and the primary star. This contrast ratio is then converted to a magnitude difference, Δm, using:

$$\Delta m = m_* - m_{\mathrm{pl}} = -2.5 \log\left(\frac{m_*}{m_{\mathrm{pl}}}\right) \tag{2.6}$$

where m_* is the apparent magnitude of the star and m_{pl} is the apparent magnitude of the companion. This can then be converted to an absolute magnitude using the distance modulus:

$$\mu = m_{\mathrm{pl}} - M_{\mathrm{pl}} = 5 \log\left(\frac{d}{10\ \mathrm{pc}}\right) \tag{2.7}$$

where μ is the distance modulus, m_{pl} is the apparent magnitude of the companion, M_{pl} is the absolute magnitude of the companion and d is the distance in parsecs.

The absolute magnitude of the companion can then be converted to a mass estimate using giant planet and brown dwarf evolutionary models, like those of Baraffe et al. (2003) and Baraffe et al. (2015).

This relies on having a good estimate of the age of the star, which is often the source of the largest uncertainty on the mass estimate of a companion.

2.6.2 Atmospheric spectral fitting

Atmospheric information can be determined using the IFS on SPHERE. The IFS observes in the wavelength range 0.95μm - 1.65μm that is split into 39 wavelength channels. For a wavelength channel where there is substantial flux from the companion, the position of the companion is fitted using the NEGFC method. This allows for the position to be fixed and just the flux to be fitted for each wavelength channel. Fitting for the position in a high-flux image allows the separation and position angle to be determined, so that in a wavelength channel where there is little or no flux, the position of where you expect the companion to be seen is known. These 39 images from each channel are analysed separately and the flux at each wavelength outputs a spectrum.

In order to convert the spectrum of the companion from contrasts to physical fluxes in each channel, a model spectrum of the host star needs to be fit taking into account the spectral energy distribution (SED) of the star using known fluxes at different wavelengths (e.g. from, Perryman et al. 1997; Høg et al. 2000; Cutri et al. 2003; Cutri & et al. 2013), as well as taking into account filter transmission curves for the instrument used[1].

This spectrum can then be fitted to models or observed field brown dwarfs to determine the companion's effective temperature, surface gravity, and metallicity. The atmospheric characterisation in this thesis is carried out using the 'SpeX Prism Library Analysis Toolkit' (Splat, Burgasser et al. 2016) which makes use of the SpeX prism library (Burgasser 2014) that contains more than 1000 low-resolution near-infrared spectra of ultracool M, L, T and Y dwarfs.

Splat contains a routine, `modelFitGrid()`, that compares the observed spectrum of an object to a model grid over a range of effective temperatures, surface gravities, and metallicities using a χ^2 statistic and outputs the best-fitted spectrum. This can be done for spectral models (e.g. Hauschildt et al. 1999; Allard et al. 2001; Burrows et al. 2006; Witte et al. 2011; Madhusudhan et al. 2011; Allard et al. 2012; Morley et al. 2012; Saumon et al. 2012; Morley et al. 2014) which cover a varying range of temperatures, surface gravities and metallicities, as well as sedimentation efficiency and cloud coverage fractions. The measured spectrum can also be compared to observed spectra of field brown dwarfs, which have known observed physical parameters, from the either the SpeX prism library or a variety of other libraries, including but not limited to: 2MASS (Cutri et al. 2003); SDSS (Ahn et al. 2012); WISE (Cutri & et al. 2012); ALLWISE (Cutri & et al. 2014); UKIDSS (Lawrence et al. 2007); and DENIS (DENIS Consortium 2005).

The best-fitted model or observed spectra determines the most likely effective temperature, surface gravity, metallicity, and spectral type of the companion, as well as molecular absorption features present in ultracool companions like CH_4 or H_2O.

[1]The SPHERE filter transmission curves can be found at https://www.eso.org/sci/facilities/paranal/instruments/sphere/inst/filters.html

2.6.3 Spectral characterisation

When a companion is observed using two different bands, the magnitude of the companion can be determined in each band using the NEGFC method. From this, the spectral type of the companion can be determined in a separate way from the atmospheric spectral fitting by placing it on a colour-magnitude or colour-colour diagram by measuring the difference in magnitude between two different bands.

Fig. 2.11 shows the placement of several directly imaged giant planets and brown dwarfs (Luhman et al. 2006; Marois et al. 2008; Lagrange et al. 2010; Bailey et al. 2014; Mawet et al. 2015; Samland et al. 2017; Keppler et al. 2018; Cheetham et al. 2018a, 2019) on a colour-magnitude diagram in addition to a sequence of field brown dwarfs. The colour-magnitude sequence of field brown dwarfs is well defined, and so by comparing the placement of brown dwarf companions on this sequence, its spectral type can be determined.

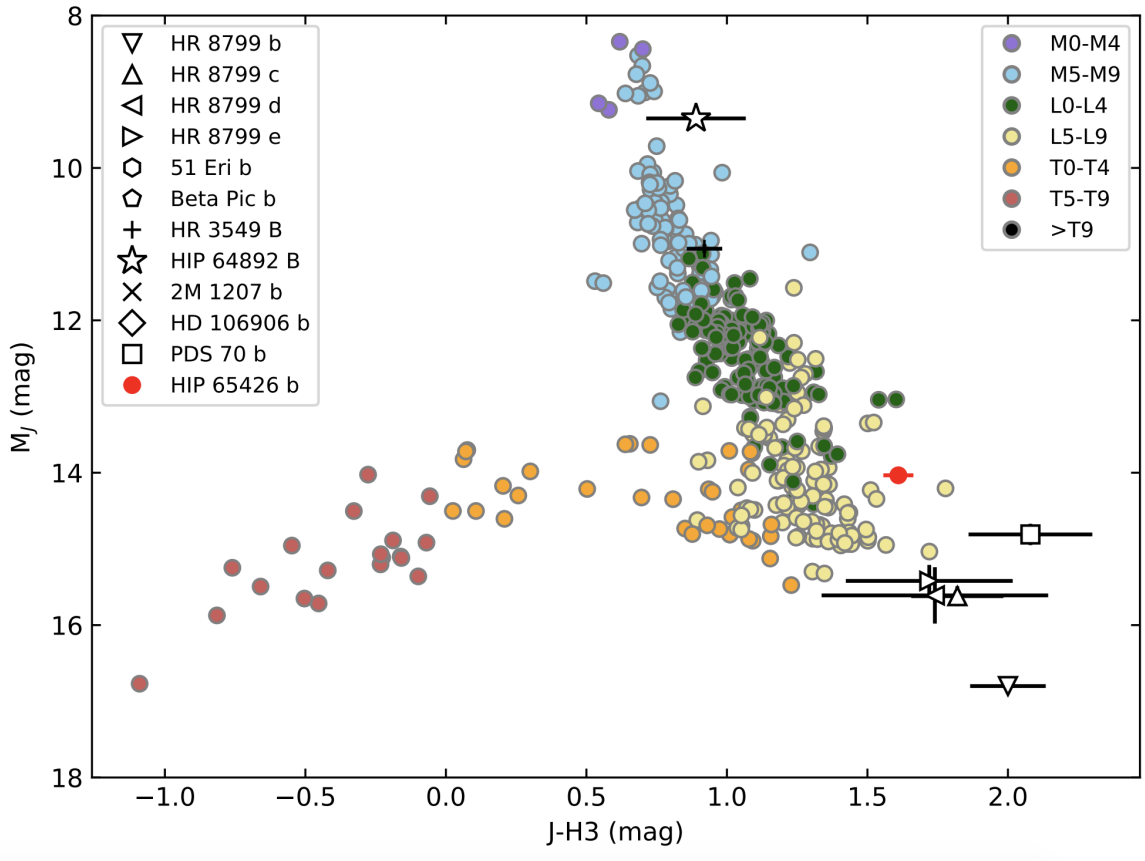

Fig. 2.11 A colour-magnitude diagram with a sequence of field brown dwarfs shown in coloured circles and the placement of several directly imaged giant planets and brown dwarfs on the sequence. Figure from Cheetham et al. (2019).

2.7 Combining detection techniques

Further to the physical parameters listed in Chapter 2.6, combining several detection techniques (as described in Chapter 1.2) allows even more information to be extracted about the detection of a companion as each detection technique provides different information about a companion.

As described in Chapter 2.6.1, the mass of the companion can be estimated from its absolute magnitude and using giant planet and brown dwarf evolutionary models. However, large uncertainties on this mass estimate remain if the age of the star is not well constrained, and doesn't take into account that the model may make assumptions that may affect the mass estimate.

For this thesis, I have focused on bridging the gap between the radial-velocity method (see Chapter 1.2.2) and the direct imaging method discussed throughout this Chapter. What is really paramount about combining these two detection techniques is that a true dynamical mass of a companion can be determined that is model independent. This is done by simultaneously fitting the radial velocity data, which provides a lower limit on the mass of the companion ($M \sin i$) due to the unknown inclination i, with the astrometric information (separation and position angle) from the direct detection, breaking the mass degeneracy due to the inclination.

The first set of observations to use a combination of these two techniques was done by Delfosse et al. (1999a); Forveille et al. (1999); Ségransan et al. (2000), which have contributed to building an accurate observational mass-luminosity relation for M-dwarfs (Ségransan et al. 2003).

This highlights the importance of detecting such companions using both of these methods as any detections can serve as benchmark objects with known masses, effective temperatures, surface gravities, and spectral types; which can be used to compare with giant planet and brown dwarf models of formation, evolution and atmospheres.

Moreover, combining detection techniques allows a wider mass-separation parameter space to be probed, as different detection techniques favour different parameter spaces as shown in Fig. 1.2.

CHAPTER 3

THE CORALIE SEARCH FOR EXTRA-SOLAR PLANETS

"You get a planet! And you get a planet!
Everybody gets a planet!"

— Louise Nielsen

3.1 Introduction and background

The CORALIE search for extra-solar planets is an ongoing radial-velocity survey with more than 20 years of observations of F8-K0 type main-sequence stars. It is a volume-limited sample consisting of 1647 stars within 50 pc to search for extra-solar planets in the Southern Hemisphere (Udry et al. 2000; Queloz et al. 2000) using the Swiss-Euler 1.2 metre telescope at La Silla Observatory, Chile.

Thanks to long-term efforts with the CORALIE spectrograph and more than 20 years of continuous observations; this data now allows us to probe the outer reaches of extra-solar systems where we have detected massive planets and brown dwarfs with angular separations amenable to direct imaging. Ultimately this means that we can close the gap between young, directly imaged objects, and those discovered through the radial-velocity technique.

For the past ~ 3 years I have been responsible for the monitoring and co-ordination of observations of the long-period (> 5 AU) companion search with the CORALIE spectrograph. From this, I identified several interesting giant planet and brown dwarf candidates for continuous monitoring observations using CORALIE. The selected objects of this study already show significant orbital progression, with periods of $\sim 20-50$ years. For follow-up of previously-detected companions or to monitor new candidates, the observing strategy was to observe each target approximately every 2 weeks with CORALIE (corresponding to $\sim$1 RV measurement per observing mission); except for in the case of high-priority targets where they would be observed more frequently as necessary. For targets showing long-term linear drifts in the data, these would be observed less frequently with some observed just once per year to monitor any changes in the observed drift.

As a result of these monitoring efforts, we have detected and published several interesting companions. In Rickman et al. (2019) we present the discovery of three new giant planets and two low-mass brown dwarfs with separations greater than 5 AU from the CORALIE spectrograph. In addition, we have also combined published RV measurements from other spectrographs, including HARPS (Mayor et al. 2003), HIRES (Vogt et al. 1994), and Hamilton (Vogt 1987).

Several of these companion candidates published in Rickman et al. (2019) are promising candidates for follow-up with high-contrast imaging with VLT/SPHERE (which is discussed in depth in Chapter 4), or with ELT/METIS in the future (Carlomagno et al. 2016).

3.2 The CORALIE search for southern extra-solar planets XIII. Three new massive planets and two low-mass brown dwarfs at greater than 5 AU separation

Details of the discovery of three new giant planets and two low-mass brown dwarfs with separations larger than 5 AU are outlined in Rickman et al. (2019) below.

A&A 625, A71 (2019)
https://doi.org/10.1051/0004-6361/201935356

Astronomy & Astrophysics

The CORALIE survey for southern extrasolar planets

XVIII. Three new massive planets and two low-mass brown dwarfs at greater than 5 AU separation★,★★

E. L. Rickman[1], D. Ségransan[1], M. Marmier[1], S. Udry[1], F. Bouchy[1], C. Lovis[1], M. Mayor[1], F. Pepe[1], D. Queloz[1], N. C. Santos[2,3], R. Allart[1], V. Bonvin[4], P. Bratschi[1], F. Cersullo[1], B. Chazelas[1], A. Choplin[1], U. Conod[1], A. Deline[1], J.-B. Delisle[1], L. A. Dos Santos[1], P. Figueira[5,2], H. A. C. Giles[1], M. Girard[1], B. Lavie[1], D. Martin[1,★★★,6], F. Motalebi[1], L. D. Nielsen[1], H. Osborn[7,8], G. Ottoni[1], M. Raimbault[1], J. Rey[1,9], T. Roger[1,10], J. V. Seidel[1], M. Stalport[1], A. Suárez Mascareño[1,11], A. Triaud[12], O. Turner[1], L. Weber[1], and A. Wyttenbach[1,13]

(Affiliations can be found after the references)

Received 25 February 2019 / Accepted 2 April 2019

ABSTRACT

Context. Since 1998, a planet-search around main sequence stars within 50 pc in the southern hemisphere has been underway with the CORALIE spectrograph at La Silla Observatory.
Aims. With an observing time span of more than 20 yr, the CORALIE survey is able to detect long-term trends in data with masses and separations large enough to select ideal targets for direct imaging. Detecting these giant companion candidates will allow us to start bridging the gap between radial-velocity-detected exoplanets and directly imaged planets and brown dwarfs.
Methods. Long-term precise Doppler measurements with the CORALIE spectrograph reveal radial-velocity signatures of massive planetary companions and brown dwarfs on long-period orbits.
Results. In this paper, we report the discovery of new companions orbiting HD 181234, HD 13724, HD 25015, HD 92987 and HD 50499. We also report updated orbital parameters for HD 50499b, HD 92788b and HD 98649b. In addition, we confirm the recent detection of HD 92788c. The newly reported companions span a period range of 15.6–40.4 yr and a mass domain of 2.93–26.77 $M_{\rm Jup}$, the latter of which straddles the nominal boundary between planets and brown dwarfs.
Conclusions. We report the detection of five new companions and updated parameters of four known extrasolar planets. We identify at least some of these companions to be promising candidates for imaging and further characterisation.

Key words. techniques: radial velocities – planets and satellites: detection – binaries: visual – planetary systems

1. Introduction

Little is known about massive giant planets and brown dwarfs at orbital separations between 5 and 50 AU due to their low occurrence rate (Bowler 2016) and to the lower sensitivity of the different observing methods in this separation range. Indeed, radial velocity (RV) and transit techniques are extremely efficient at detecting planets around older stars at short separations (Fischer et al. 2014). On the other hand, direct imaging is most efficient at detecting younger planets at separations larger than several times the diffraction limit of the telescope (typically 5–10 λ/D). This translates into several tens of astronomical units for the closest young stellar associations (e.g. β Pic and 51 Eri as part of the β Pic moving group (Zuckerman et al. 2001; Feigelson et al. 2006) and HR 8799 as part of the Columba association (Zuckerman et al. 2011). Nevertheless, the population of massive giant exoplanets at intermediate orbital separations between 5 and 50 AU is an important puzzle piece needed for constraining the uncertainties that exist in planet formation and evolution models.

The historical CORALIE planet-search survey has been ongoing for more than 20 yr in the southern hemisphere and monitors a volume-limited sample of 1647 main sequence (MS) stars from F8 down to K0 located within 50 pc of the Sun (Udry et al. 2000). With an individual measurement precision ranging between 3.5 and 6 ms^{-1}, CORALIE has permitted (or has contributed to) the detection of more than 140 extra-solar planet candidates (Pepe et al. 2002; Udry et al. 2002; Tamuz et al. 2008; Ségransan et al. 2010; Marmier et al. 2013). Such a long and continuous monitoring of nearby MS stars is unique among all planet search surveys; it allows us to detect massive giant planets at separations larger 5 AU as well as to identify small RV drifts

★ The radial velocity measurements and additional data products discussed in this paper are available on the DACE web platform at https://dace.unige.ch/radialVelocities. See the appendix for a direct link to the individual target data products. A copy of the data is also available at the CDS via anonymous ftp to cdsarc.u-strasbg.fr (130.79.128.5) or via http://cdsarc.u-strasbg.fr/viz-bin/qcat?J/A+A/625/A71

★★ Based on observations collected with the CORALIE spectrograph mounted on the 1.2 m Swiss telescope at La Silla Observatory and with the HARPS spectrograph on the ESO 3.6 m telescope at La Silla (ESO, Chile).

★★★ Fellow of the Swiss National Science Foundation.

hinting at the presence of low-mass companions at even wider separations.

These are indeed very useful targets for direct imaging, as such old and very-low-mass companions are rare and very difficult to search for blindly. Cheetham et al. (2018) has shown with the discovery of the ultra-cool brown dwarf companion orbiting the planet host star HD 4113 A that long-term RV surveys are an extremely useful tool to select targets to image. Not only does it allow us to start filling in a largely unexplored parameter space, but through combining RV and direct imaging we can now expect to measure the masses of these companions using Kepler's laws. By constraining the mass, we are able to place additional constraints on the evolution of the companion, both in terms of temperature and atmospheric composition (Crepp et al. 2018; Peretti et al. 2019).

In this paper we report the discovery of four new giant planets and brown dwarfs orbiting HD 181234, HD 13724, HD 25015, and HD 92987, together with the updated CORALIE orbital elements for an already known exoplanet around HD 98649 (Marmier et al. 2013). We also report updated orbital parameters for HD 50499b (Vogt et al. 2005), as well as the detection of HD 50499c, which has previously been noted by Vogt et al. (2005), Butler et al. (2017), and Barbato et al. (2018). We also report the updated orbital parameters of HD 92788b detected by Fischer et al. (2001) and confirm the recent detection of HD 92788c (Wittenmyer et al. 2019).

The paper is organised as follows. The properties of the host stars are summarised in Sect. 2. In Sect. 3 we present our RV data and the inferred orbital solution of the newly detected companions. In Sect. 4 we present the CORALIE updated parameters of already known exoplanets with new detections in two of these systems. The results are discussed in Sect. 5 with some concluding remarks.

2. Stellar characteristics

Spectral types, V band magnitude and colour indices are taken from the HIPPARCOS catalogue (Perryman et al. 1997) while astrometric parallaxes (π) and luminosities are taken from the second *Gaia* date release (Gaia Collaboration 2018). Effective temperatures, gravities, and metallicities are derived using the same spectroscopic methods as applied in Santos et al. (2013), whilst the $v \sin(i)$ is computed using the calibration of CORALIE's cross correlation function (CCF; Santos et al. 2001; Marmier 2014).

The mean chromospheric activity index – $\log(R'_{\rm HK})$ – of each star is computed by co-adding the corresponding CORALIE spectra to improve the signal-to-noise ratio (S/N) which allows us to measure the Ca II re-emission at λ = 3933.66 Å. We derived an estimate of the rotational period of the star from the mean $\log(R'_{\rm HK})$ activity index using the calibration of Mamajek & Hillenbrand (2008).

Stellar radii and their uncertainties are derived from the *Gaia* luminosities and the effective temperatures obtained from the spectroscopic analysis. A systematic error of 50 K was quadratically added to the effective temperature error bars and was propagated in the radius uncertainties.

The mass and the age of the stars, as well as their uncertainties, are derived using the Geneva stellar-evolution models (Ekström et al. 2012; Georgy et al. 2013). The interpolation in the model grid was made through a Bayesian formalism using observational Gaussian priors on $T_{\rm eff}$, $M_{\rm V}$, $\log g$, and [Fe/H] (Marmier 2014).

The observed and inferred stellar parameters for newly detected host stars to planetary companions are summarised in Table 1 and host stars to brown dwarf companions in Table 2.

3. Radial velocities and orbital solutions

The CORALIE observations span over more than 20 yr, from June 1998 to December 2018. During that time, CORALIE went through two major upgrades in June 2007 (Ségransan et al. 2010) and in November 2014 to increase overall efficiency and accuracy of the instrument. These changes introduced small offsets in the measured RVs that depend on several parameters such as the spectral type of the star and its systemic velocity. For this reason, we decided to consider CORALIE as three different instruments, corresponding to the different upgrades: the original CORALIE as CORALIE-98 (C98), the first upgrade as CORALIE-07 (C07), and the latest upgrade as CORALIE-14 (C14).

In addition to the RV time series, the CORALIE automated pipeline also provides several useful indicators that help pinpoint the origin of observed periodic signals. These are the CCF full width at half maximum (FWHM), the bisector, and the H_α chromospheric activity indicator.

We are also using published RVs taken with other spectrographs, namely HARPS (Mayor et al. 2003), HIRES (Vogt et al. 1994), and HAMILTON (Vogt 1987). The data products presented in this paper are available at the Data and Analysis Center for Exoplanets (DACE)[1].

We perform an initial modelling of the RV time series using the online DACE platform. Keplerian model initial conditions are computed using the formalism described in Delisle et al. (2016). The stellar activity detrending and the modelling of the instrumental noise and the stellar jitter follow the formalism described in Díaz et al. (2016) and Delisle et al. (2018). Analytical false-alarm probabilities (FAPs) are computed on the periodogram of the residuals following Baluev (2008) and numerical FAP values which are used in this paper are computed by permutation of the calendar. Periodic signals with a FAP lower than 0.1% are considered significant and are added to the model. For each periodogram shown, the three lines represent the 10, 1, and 0.1% FAP in ascending order.

Once the RV time series is fully modelled using DACE online tools, we run a Markov chain Monte Carlo (MCMC) analysis of each system using the algorithm described in Díaz et al. (2014, 2016) and Delisle et al. (2018) to obtain the posterior distributions of the model parameters. Each MCMC simulation is run with 10 000 000 iterations drawing the proposal solution obtained using DACE. The parameter confidence intervals are computed for a 68.27% confidence level.

Gaussian priors are set for the instrument offsets and stellar mass with uniform priors for the orbital elements. In the cases where the minimum RV ($T_{V_{\rm min}}$) or the maximum RV ($T_{V_{\rm max}}$) is well sampled, we perform the fit using either of these instead of fitting the phase.

In this section we present the orbital solutions for newly reported giant planets and brown dwarfs from the CORALIE survey. A summary of the orbital solutions can be found in Table 3 for the newly detected companions and the fully probed MCMC parameter space is shown in the appendix.

[1] The data are available at the Data and Analysis Center for Exoplanets (DACE) which can be accessed at https://dace.unige.ch

Table 1. Observed and inferred stellar parameters for host stars to the planet candidates: HD 181234, HD 25015, HD 50499, HD 92788, and HD 98649.

Parameters	Units	HD 181234	HD 25015	HD 50499	HD 92788	HD 98649
Spectral type [a]		G5	K1V	G1V	G6V	G3/G5V
V [a]		8.59	8.87	7.21	7.31	8.00
$B-V$ [a]		0.841	0.899	0.614	0.694	0.658
π [b]	(mas)	20.9 ± 0.06	26.7 ± 0.05	21.58 ± 0.03	28.83 ± 0.05	23.7 ± 0.05
L [b]	($L_\odot$)	0.80 ± 0.003	0.41 ± 0.001	2.38 ± 0.005	1.25 ± 0.003	0.98 ± 0.003
$T_{\rm eff}$ [c]	(K)	5386 ± 60	5160 ± 63	6099 ± 43	5744 ± 24 [e]	5790 ± 58
$\log g$ [c]	(cgs)	4.25 ± 0.11	4.40 ± 0.14	4.42 ± 0.05	4.39 ± 0.04	4.51 ± 0.09
[Fe/H] [c]	(dex)	0.32 ± 0.05	0.04 ± 0.04	0.38 ± 0.03	0.27 ± 0.02 [e]	0.05 ± 0.04
$\log R'_{\rm HK}$ [c]		−5.17 ± 0.01	−4.48 ± 0.002	−5.08 ± 0.004	−4.98 ± 0.01 [f]	−5.06 ± 0.005
$P_{\rm rot}$	(days)	50.8 ± 2.0	13.6 ± 2.3	22.4 ± 1.0	31.0 ± 1.4 [g]	27.7 ± 1.2
$v \sin i$ [d]	(km s^{-1})	2.105	3.485	4.313	2.719	2.218
M_*	($M_\odot$)	1.01 ± 0.06	0.86 ± 0.05	1.31 ± 0.07	1.15 ± 0.07	1.03 ± 0.06
R_*	($R_\odot$)	1.05 ± 0.07	0.83 ± 0.04	1.42 ± 0.02	1.14 ± 0.02	1.01 ± 0.02
Age	(Gyr)	6.32 ± 2.58	4.00 ± 3.41	2.40 ± 0.56	2.55 ± 1.51	2.42 ± 1.62

Notes. [a] Parameters taken from HIPPARCOS (Perryman et al. 1997). [b]Parameters taken from *Gaia* data release 2 (Gaia Collaboration 2018). [c]Parameters derived using CORALIE spectra. [d]Parameters derived using CORALIE CCF. [e]Parameters taken from Sousa et al. (2008). [f]Parameters derived using HARPS spectra. [g]From the calibration of the rotational period vs. activity (Mamajek & Hillenbrand 2008).
Refrences. (1) Gaia Collaboration (2018); (2) Mamajek & Hillenbrand (2008); (3) Perryman et al. (1997); (4) Sousa et al. (2008).

Table 2. Observed and inferred stellar parameters for host stars to the brown dwarf candidates: HD 13724 and HD 92987.

Parameters	Units	HD 13724	HD 92987
Spectral type [a]		G3/G5V	G2/G3V
V [a]		7.89	7.03
$B-V$ [a]		0.667	0.641
π [b]	(mas)	23.0 ± 0.03	22.9 ± 0.03
L [b]	($L_\odot$)	$1.14^{+0.001}_{-0.002}$	2.55 ± 0.006
$T_{\rm eff}$ [c]	(K)	5868 ± 27 [e]	5770 ± 36 [f]
$\log g$ [c]	(cgs)	4.44 ± 0.07 [g]	4.00 ± 0.15 [f]
[Fe/H] [c]	(dex)	0.23 ± 0.02 [e]	−0.08 ± 0.08 [f]
$\log R'_{\rm HK}$ [c]		−4.76 ± .003	−5.090 ± 0.006
$P_{\rm rot}$	(days)	20.2 ± 1.2	26.2 ± 1.1
$v \sin i$ [d]	(km s^{-1})	3.025	2.616
M_*	($M_\odot$)	1.14 ± 0.06	1.08 ± 0.06
R_*	($R_\odot$)	1.07 ± 0.02	1.58 ± 0.04
Age	(Gyr)	0.76 ± 0.71	7.75 ± 0.31

Notes. [a]Parameters taken from HIPPARCOS (Perryman et al. 1997). [b]Parameters taken from *Gaia* data release 2 (Gaia Collaboration 2018). [c]Parameters derived using CORALIE spectra. [d]Parameters derived using CORALIE CCF. [e]Parameters taken from Gomes da Silva et al. (2014). [f]Parameters taken from Bond et al. (2006). [g]Parameters taken from Porto de Mello et al. (2014).
References. (1) Bond et al. (2006); ; (2) Gaia Collaboration (2018); (3) Gomes da Silva et al. (2014); (4) Perryman et al. (1997); (5) Porto de Mello et al. (2014).

3.1. HD 181234 (LTT 5654, HIP 95015)

HD 181234 was observed with CORALIE at La Silla Observatory since May 2000. Fifteen measurements were taken with CORALIE-98, 21 additional RV measurements were obtained with CORALIE-07, and 59 additional RV measurements were obtained with CORALIE-14. HD 181234 has also been observed with Keck/HIRES (Butler et al. 2017) with 20 RV measurements from June 1999 to August 2014.

The best-fit Keplerian, as shown in Fig. 1, shows that we are looking at a highly eccentric system with an eccentricity of 0.73. It has an orbital period of 20.4 yr with a minimum mass of 8.4 $M_{\rm Jup}$. The orbital solutions are summarised in Table 3. Figure 1 shows the CORALIE RVs and the corresponding best-fit Keplerian model along with the RV residuals and a periodogram of the residuals. The results from the fully probed parameter space from the MCMC are shown in the appendix.

3.2. HD 92987 (HIP 52472)

HD 92987 was observed with CORALIE at La Silla Observatory since January 1999. Fifty-three measurements were taken with CORALIE-98, 18 additional RV measurements were obtained with CORALIE-07, and 22 additional RV measurements were obtained with CORALIE-14.

HD 92987b is one of the brown dwarf candidates with a minimum mass of 16.88 $M_{\rm Jup}$ and a semi-major axis of 9.62 AU, making it a promising candidate for direct imaging. The orbital solutions for HD 92987 are summarised in Table 3. Figure 2 shows the CORALIE RVs and the corresponding best-fit Keplerian model along with the RV residuals and a periodogram of the residuals. The results from the fully probed parameter space from the MCMC are shown in the appendix.

3.3. HD 25015 (HIP 18527)

HD 25015 was observed with CORALIE at La Silla Observatory since May 2001. Twenty-two measurements were taken with CORALIE-98, 32 additional RV measurements were obtained with CORALIE-07, followed by 56 additional RV measurements obtained with CORALIE-14.

Table 3. Best-fitted solutions for the substellar companions orbiting HD 13724, HD 181234, HD 25015, and HD 92987.

Parameters	Units	HD 13724b	HD 181234b	HD 25015b	HD 92987b
P	(yr)	$40.42^{+13.42}_{-4.38}$	$20.43^{+0.22}_{-0.21}$	$16.48^{+1.86}_{-0.72}$	$28.35^{+1.51}_{-0.74}$
K	(ms^{-1})	$214.3^{+21.5}_{-10.2}$	$126.8^{+1.8}_{-1.6}$	$60.1^{+3.1}_{-3.2}$	$152.7^{+2.3}_{-2.7}$
e		$0.34^{+0.09}_{-0.05}$	0.73 ± 0.01	$0.39^{+0.09}_{-0.07}$	$0.21^{+0.02}_{-0.01}$
ω	(deg)	$187.5^{+2.9}_{-1.7}$	$93.3^{+1.7}_{-1.8}$	$77.7^{+9.8}_{-8.6}$	$195.1^{+6.7}_{-8.4}$
T_p	(JD)	6189.1^{+73}_{-54}	$7668.7^{+5.5}_{-5.0}$	5852^{+160}_{-140}	7889^{+130}_{-180}
$M. \sin i$	(M_{Jup})	$26.77^{+4.4}_{-2.2}$	$8.37^{+0.34}_{-0.36}$	$4.48^{+0.30}_{-0.28}$	$16.88^{+0.69}_{-0.65}$
a	(AU)	$12.40^{+2.6}_{-0.9}$	$7.52^{+0.16}_{-0.16}$	$6.19^{+0.45}_{-0.23}$	$9.62^{+0.36}_{-0.26}$
N_{RV}		167	115	110	93
ΔT	(yr)	19.3	18.6	17.6	19.9

Notes. For each parameter, the mode of the posterior is considered, with error bars computed from the MCMC chains with 10 000 000 iterations using a 68.27% confidence interval. ΔT is the time interval between the first and last measurements. C98 stands for CORALIE-98, C07 for CORALIE-07 and C14 for CORALIE-14. N_{RV} is the number of RV measurements. T_P is shown in BJD-2 450 000.

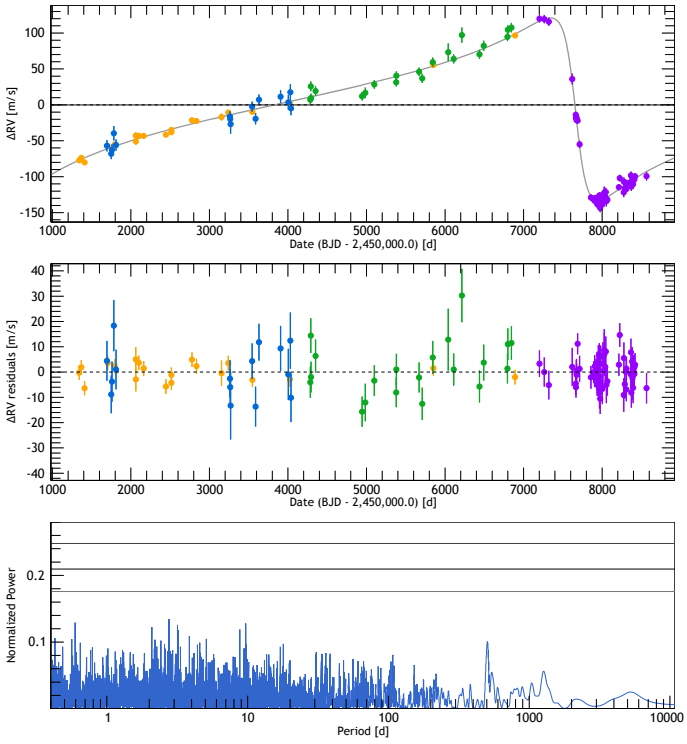

Fig. 1. *Top*: HD 181234 RV measurements as a function of Julian Date obtained with CORALIE-98 (blue), CORALIE-07 (green), CORALIE-14 (purple) and HIRES data (Butler et al. 2017) in orange. The best single-planet Keplerian model is represented as a black curve. *Middle*: RV residuals of HD 181234. *Bottom*: periodogram of the residuals for HD 181234. The three black lines represent the 10, 1, and 0.1% FAPs in ascending order.

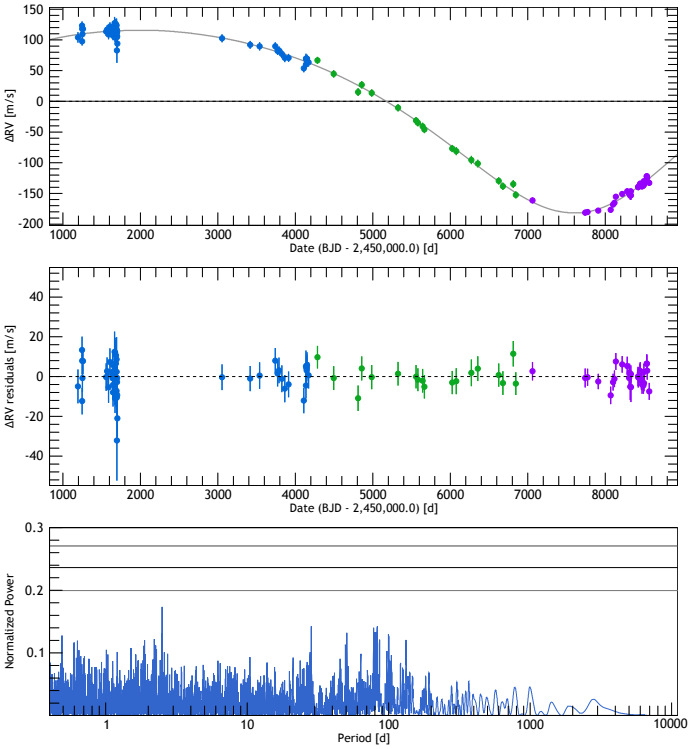

Fig. 2. *Top*: HD 92987 RV measurements as a function of Julian Date obtained with CORALIE-98 (blue), CORALIE-07 (green) and CORALIE-14 (purple). The fitted single-planet Keplerian model is represented as a black curve. *Middle*: RV residuals of HD 92987. *Bottom*: periodogram of the residuals for HD 92987. The three black lines represent the 10, 1 and 0.1% FAPs in ascending order.

We note here that all of the stars in our sample are very quiet with the exception of HD 25015. When we plot the H_α versus time, we see that some periodicity exists in the periodogram at a FAP of greater than 10%, as seen in Fig 3 at approximately 370.26 days. We do not see a periodicity in the FWHM or bisector, therefore we cannot exclude that there is telluric line contamination in the H_α index with CORALIE. We detrend the RV from the stellar activity using the H_α indicators. A scale factor is adjusted to the smoothed H_α (using a Gaussian filter at 0.1 yr), as well as an additional jitter term proportional to the activity trend.

The orbital solutions for HD 25015 are summarised in Table 3. Figure 3 shows the CORALIE RVs and the corresponding best-fit Keplerian model along with the RV residuals, the periodogram of the residuals and a periodogram for H_α

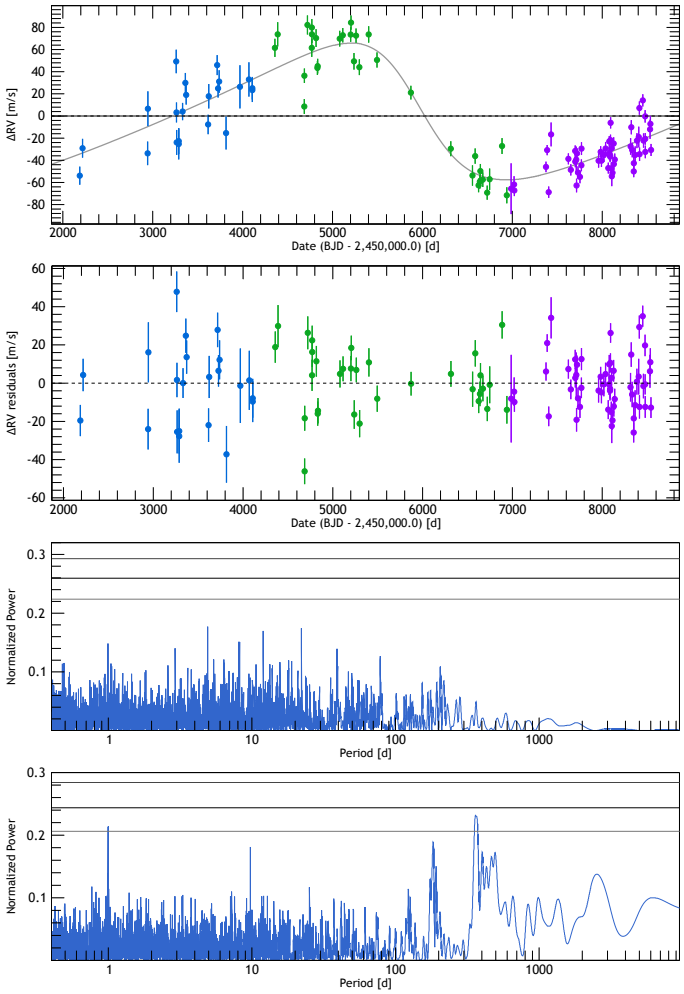

Fig. 3. *Top*: HD 25015 RV measurements as a function of Julian Date obtained with CORALIE-98 (blue), CORALIE-07 (green) and CORALIE-14 (purple). The fitted single-planet Keplerian model is represented as a black curve. *Second figure*: RV residuals of HD 25015. *Third figure*: periodogram of the residuals for HD 25015 after the signal has been removed showing no significant signals. The three black lines represent the 10, 1 and 0.1% FAPs in ascending order. *Bottom*: periodogram of H_α before detrending. The three black lines represent the 10, 1 and 0.1% FAPs in ascending order, showing a significant peak above the 10% FAP at 370.26 days.

before detrending. The results from the fully probed parameter space from the MCMC are shown in the appendix.

3.4. HD 13724 (HIP 10278)

HD 13724 has been observed with CORALIE at La Silla Observatory since August 1999. It is a relatively young star at 0.76 ± 0.71 Gyr old.

During the past 19.3 yr, 167 Doppler measurements were taken on this target with 70 RV measurements taken with CORALIE-98, 19 with CORALIE-07, 48 with CORALIE-14 and 30 with HARPS. HD 13724b is a brown dwarf companion with a minimum mass of 26.77 $M_{\rm Jup}$ and a semi-major axis of 12.4 AU, making it a promising candidate for direct imaging.

The orbital solutions for HD 13724 are summarised in Table 3. Figure 4 shows the CORALIE RVs and the corresponding best-fit Keplerian model along with the RV residuals and a periodogram of the residuals. The results from the fully probed parameter space from the MCMC are shown in the appendix.

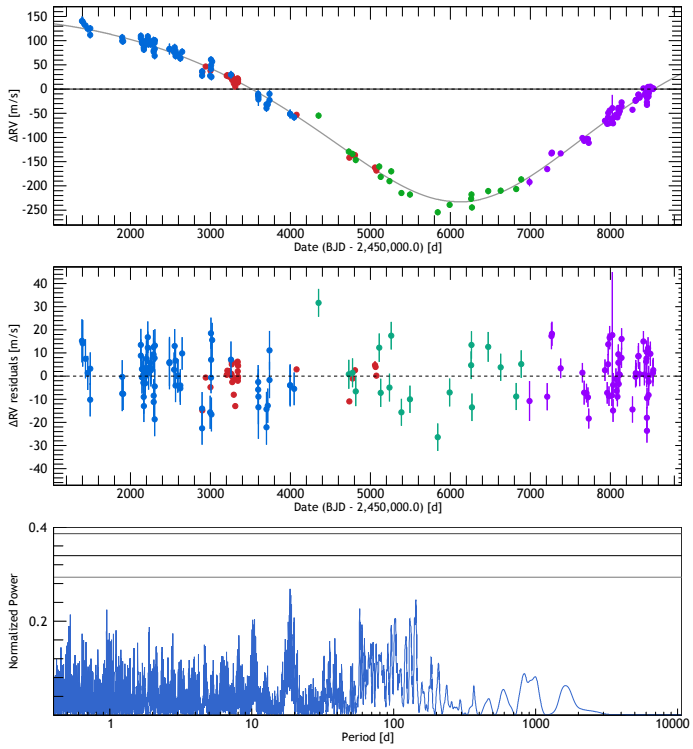

Fig. 4. *Top*: HD 13724 RV measurements as a function of Julian Date obtained with CORALIE-98 (blue), CORALIE-07 (green), CORALIE-14 (purple) and HARPS (red). The best single-planet Keplerian model is represented as a black curve. *Middle*: RV residuals of HD 13724. *Bottom*: periodogram of the residuals for HD 13724 after the signal has been removed showing no significant signals. The three black lines represent the 10, 1 and 0.1% FAPs in ascending order.

4. Updated parameters for known exoplanets

We present updated orbital parameters for a known exoplanet around HD 98649 (Marmier et al. 2013). We also report updated orbital parameters for HD 92788b (Fischer et al. 2001) and confirm the detection of HD 92788c (Wittenmyer et al. 2019). Moreover, we report the discovery of a new planet around HD 50499 and report updated orbital parameters for HD 50499b (Vogt et al. 2005).

The RV data is fitted in the same way as described in Sect. 3. The stellar parameters for these systems are summarised in Table 1. For HD 50499 we also report the discovery of a new exoplanet.

The orbital parameters for HD 98649, HD 50499, and HD 92788 are summarised in Table 4. The probed physical parameters using the MCMC for each target are shown in the appendix.

4.1. A companion of 7 $M_{\rm Jup}$ on an eccentric orbit of 15 yr around HD 98649 (LTT 4199, HIP 55409)

We report updated parameters for a known exoplanet detected by Marmier et al. (2013). The star HD 98649 is of G3/G5V type at 42.19 ± 0.09 pc from the Sun. The star properties are summarised in Table 4.

HD 98649 has been observed with CORALIE at La Silla Observatory since February 2003. Fourteen measurements were taken with CORALIE-98, 42 additional RV measurements were obtained with CORALIE-07, followed by 12 additional RV measurements obtained with CORALIE-14.

Table 4. Best-fitted solution for the substellar companions orbiting HD 50499, HD 92788, and HD 98649.

Parameters	Units	HD 50499b	HD 50499c	HD 92788b	HD 92788c	HD 98649b
P	(yr)	6.80 ± 0.05	$23.6^{+7.18}_{-1.11}$	0.892 ± 0.0001	$31.79^{+13.84}_{-2.48}$	$16.49^{+1.13}_{-0.70}$
K	(ms^{-1})	$18.94^{+0.82}_{-0.86}$	$24.23^{+3.79}_{-0.95}$	$108.24^{+0.89}_{-0.84}$	$33.29^{+2.33}_{-1.94}$	$140.1^{+33.1}_{-6.1}$
e		$0.27^{+0.04}_{-0.03}$	$0.00^{+0.14}_{-0.02}$	$0.35^{+0.004}_{-0.005}$	$0.46^{+0.12}_{-0.03}$	$0.86^{+0.04}_{-0.02}$
ω	(deg)	$259.32^{+7.89}_{-10.19}$	$[-115, +161]$	$-82.17^{+1.01}_{-1.16}$	$-25.71^{+6.63}_{-8.92}$	$252.61^{+1.97}_{-7.03}$
T_p	(JD)	$6172.9^{+50.4}_{-67.5}$	11832^{+3731}_{-2885}	$5647.14^{+0.73}_{-0.73}$	6858^{+133}_{-202}	$5121.7^{+16.8}_{-28.1}$
$M. \sin i$	(M_{Jup})	1.45 ± 0.08	$2.93^{+0.73}_{-0.18}$	$3.76^{+0.16}_{-0.15}$	$3.67^{+0.30}_{-0.25}$	$6.79^{+0.53}_{-0.31}$
a	(AU)	3.93 ± 0.07	$9.02^{+1.73}_{-0.33}$	0.97 ± 0.02	$10.50^{+2.90}_{-0.55}$	$6.57^{+0.31}_{-0.23}$
N_{RV}		214		214		68
ΔT	(yr)	19.9		18.8		15.8

Notes. For each parameter, the mode of the posterior is considered, with error bars computed from the MCMC chains with 10 000 000 iterations using a 68.27% confidence interval. ΔT is the time interval between the first and last measurements. C98 stands for CORALIE-98, C07 for CORALIE-07, and C14 for CORALIE-14. N_{RV} is the number of RV measurements. Because the ω for HD 50499c is not very well constrained, we only provide the 68.27% confidence interval here. The fully probed parameters from the MCMC can be found in the appendix. T_P is shown in BJD-2 450 000.

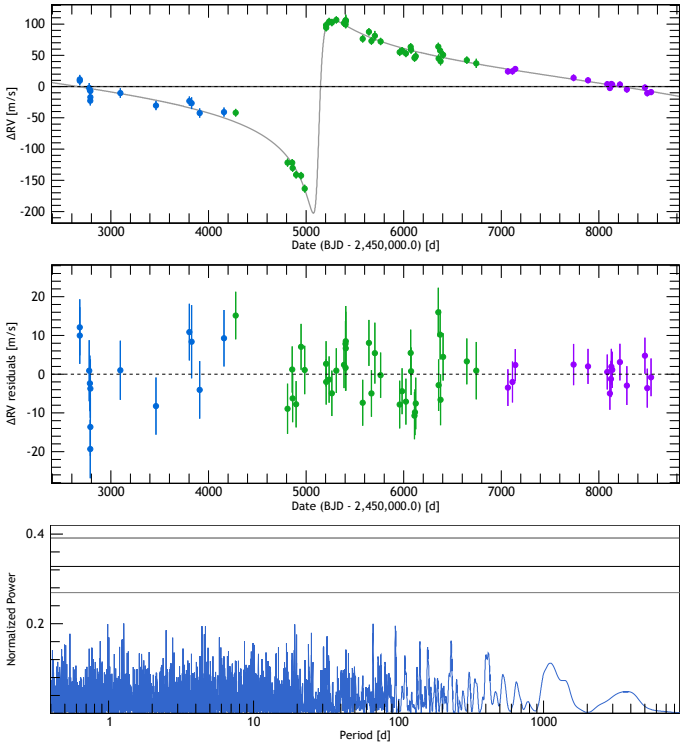

Fig. 5. *Top*: HD 98649 RV measurements as a function of Julian Date obtained with CORALIE-98 (blue), CORALIE-07 (green) and CORALIE-14 (purple). The best single-planet Keplerian model is represented as a black curve. *Middle*: RV residuals of HD 98649. *Bottom*: periodogram of the residuals for HD 98649 showing no significant signals remaining. The three black lines represent the 10, 1 and 0.1% FAP in ascending order.

HD 98649b is an extremely eccentric planet with an eccentricity of $0.86^{+0.04}_{-0.02}$. The orbital parameters agree well with Marmier et al. (2013) who reported a period of $P = 13.56^{+1.66}_{-1.27}$ yr and a mass of $M \sin i = 6.8 \pm 0.5\ M_{Jup}$.

The orbital solutions for HD 98649 are summarised in Table 4. Figure 5 shows the CORALIE RVs and the corresponding best-fit Keplerian model along with the RV residuals and a periodogram of the residuals. The results from the fully probed parameter space from the MCMC are shown in the appendix.

4.2. HD 50499 (HIP 32970)

HD 50499 is a G1V star at 46.34 ± 0.06 pc from the Sun. The star properties are summarised in Table 1.

We report updated orbital parameters for a known exoplanet around HD 50499b previously detected by Vogt et al. (2005). We also report the discovery of a new exoplanet in this system.

HD 50499 was observed with CORALIE at La Silla Observatory since January 1999. Forty-four measurements were taken with CORALIE-98, 39 additional RV measurements with CORALIE-07, followed by 40 additional RV measurements obtained with CORALIE-14. There are also 5 measurements taken with HARPS, as well as an additional 86 RV points publicly available from HIRES.

The outer signal was previously noted by Vogt et al. (2005). It was also reported by Butler et al. (2017) who noted that the outer trend is parabolic with additional data points from HIRES. In addition, Barbato et al. (2018) fits the RV data for a single Keplerian orbit plus a quadratic term obtaining a best-fit curve where lower limits for the outer companion are derived. Here we provide additional data points from CORALIE, which allows us to further constrain this outer planet.

We derive the orbital solution for HD 50499 using two Keplerians as seen in Fig. 6. The orbital solutions for HD 50499 are summarised in Table 4. Figure 6 shows the CORALIE, HARPS, and HIRES RVs and the corresponding best-fit Keplerian models along with the periodogram of the residuals. Figure 7 shows the phase-folded RV diagrams for HD 50499b and HD 50499c. The results from the fully probed parameter space from the MCMC are shown in the appendix.

These parameters agree well with Vogt et al. (2005) who reports that HD 50499b has a period of 6.80 ± 0.30 yr and a mass of $1.71 \pm 0.2\ M_{Jup}$.

Because not all of the outer planet period is covered, the uncertainties on the period of the second Keplerian remain relatively large with an unconstrained ω.

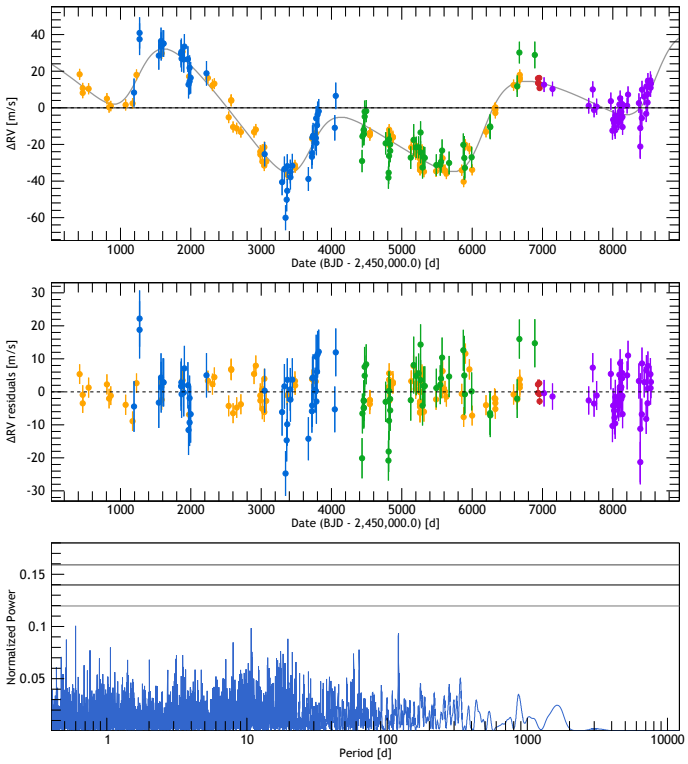

Fig. 6. *Top*: HD 50499 RV curves. Blue: CORALIE-98 data; green: CORALIE-07; purple: CORALIE-14 data; red: HARPS data; and orange: HIRES data (Butler et al. 2017). The Keplerian models are represented by black curves. *Middle*: RV residuals of HD 50499. *Bottom*: periodogram of the residuals of HD 50499 after the two planetary signals were removed, indicating that there are no more significant signals remaining in the data. The three black lines represent the 10, 1 and 0.1% FAPs in ascending order.

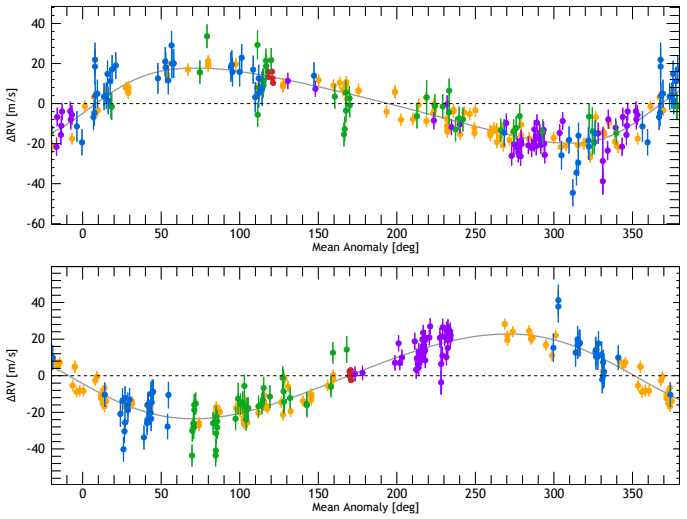

Fig. 7. Phase-folded RV curves for HD 50499. Blue: CORALIE-98 data; green: CORALIE-07; purple: CORALIE-14 data; red: HARPS data; orange: HIRES data. The Keplerian models are represented by black curves. *Top*: phase-folded curve for HD 50499b. *Bottom*: phase-folded curve for HD 50499c.

The parameters we obtain for HD 50499c agree with Barbato et al. (2018) who report that the quadratic trend corresponds to a planet with an orbital period of $P \geq 22.61$ yr and a minimum mass of $M \sin i \geq 0.942\, M_{\rm Jup}$.

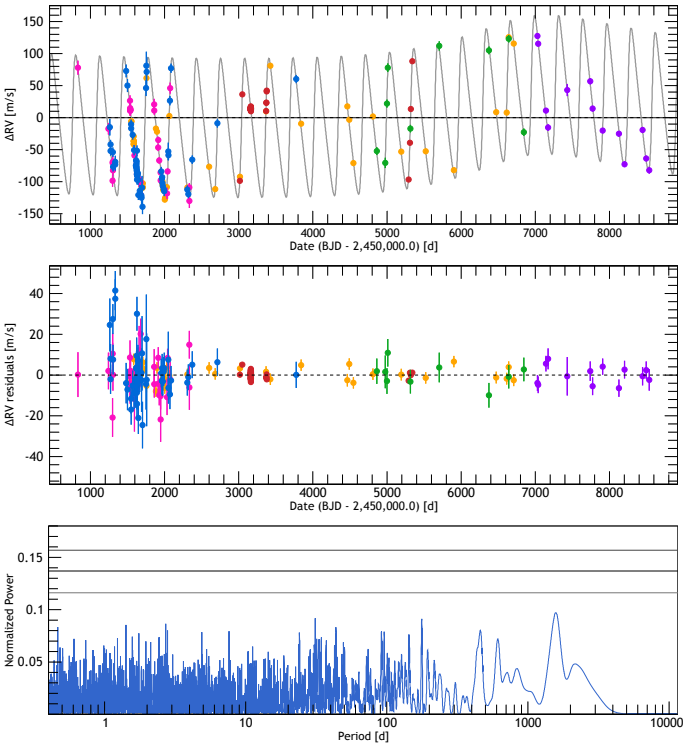

Fig. 8. *Top*: HD 92788 RV measurements as a function of Julian Date obtained with CORALIE-98 (blue), CORALIE-07 (green), CORALIE-14 (purple), HARPS (red), HIRES (orange; Butler et al. 2017) and HAMILTON (pink; Butler et al. 2006). The best single-planet Keplerian model is represented by black curve. *Middle*: RV residuals of HD 92788. *Bottom*: periodogram of the residuals for HD 92788 after the signal was removed showing no significant signals. The three black lines represent the 10, 1, and 0.1% FAPs in ascending order.

4.3. HD 92788 (HIP 52409)

We report updated orbital parameters for HD 92788b (Fischer et al. 2001) and confirm the detection of HD 92788c (Wittenmyer et al. 2019). HD 92788 is a G6V star at 28.83 ± 0.05 pc from the Sun. The star properties are summarised in Table 4.

HD 92788 was observed with CORALIE at La Silla Observatory since March 1999, 59 RV measurements were obtained with CORALIE-98, an additional 10 RV measurements were obtained with CORALIE-07, and an additional 11 RV measurements were obtained with CORALIE-14. There are also 61 measurements taken with HARPS, 42 RV points publicly available from HIRE, and an additional 31 RV points from HAMILTON.

The orbital solutions for HD 92788 are summarised in Table 4. Figure 8 shows the CORALIE, HARPS, HIRES, and HAMILTON RVs and the corresponding best-fit Keplerian models along with a time series of the residuals and a periodogram of the residuals. Figure 9 shows the phase-folded RV diagram for HD 92788b and the time series for HD 92788c. The results from the fully probed parameter space from the MCMC are shown in the appendix.

The orbital parameters for HD 92788b agree well with Fischer et al. (2001) who reported a period of $P = 0.894 \pm 0.009$ yr and a minimum mass of $M \sin i = 3.34\, M_{\rm Jup}$ and also agree well with the recently reported parameters by Wittenmyer et al. (2019) who report HD 92788b to have an orbital period of 0.892 ± 0.00008 yr and a minimum mass of $M \sin i = 3.78 \pm 0.18 M_{\rm Jup}$.

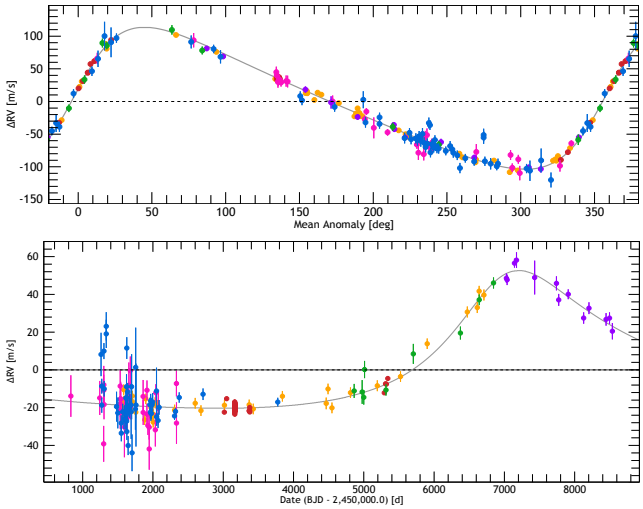

Fig. 9. Blue: CORALIE-98 data; green: CORALIE-07 data; purple: CORALIE-14 data; red: HARPS data; orange: HIRES data; pink: HAMILTON data. The Keplerian models are represented by black curves. *Top*: phase-folded curve for HD 92788b. *Bottom*: time series for HD 92788c.

Wittenmyer et al. (2013) tested the system for a potential additional planet with a period of 162 days which they found by limiting the eccentricity of the Keplerian model of HD 92788b. This is because fitting Keplerians can be biased towards fitting an increased eccentricity, especially when the semi-amplitude is small or the system has not been sampled well (Shen & Turner 2008). Although Wittenmyer et al. (2013) suggested that there is a possible additional planet in the system, when we fitted the Keplerian the signal was not significant above the noise (lower than a 10% FAP) to claim an additional planet at this period, as seen in Fig. 8 and therefore we do not detect this signal.

We do however detect the signal of another planet in the system, HD 92788c, as was recently discovered by Wittenmyer et al. (2019). We confirm this planet with orbital parameters that agree with Wittenmyer et al. (2019), who report a period of 26.99 ± 2.54 yr and a minimum mass of $M \sin i$ of 3.64 ± 0.69 $M_{\rm Jup}$.

5. Discussion and conclusion

Here we report the discovery of five new giant planets and brown dwarf candidates discovered with the CORALIE spectrograph mounted on 1.2 m Euler Swiss telescope at La Silla Observatory as well as updated orbital parameters for four previously detected planets. CORALIE time series combined with the published data sets independently confirms the existence of these four already published companions. In addition, we do not find any significant evidence for the exoplanet HD 92788c suggested by Wittenmyer et al. (2013). The newly reported companions span a period range of 15.6–40.4 yr and a mass domain of 2.93–26.77 $M_{\rm Jup}$.

Most of the parent stars in this paper have a metallicity excess, as seen in Fig. 10. Despite the small size of our sample, our results seem to agree with previous observations that giant planets appear to occur significantly around stars that are more metal-rich, which has been noted before by Santos et al. (2004), Fischer & Valenti (2005), Mayor et al. (2011) and Boisse et al. (2012).

The focus of this paper is on long-period exoplanets, where all of the newly reported planets have periods over 15 yr. This contributes to the relatively small number of previously known planets with periods in this range, where according to the NASA

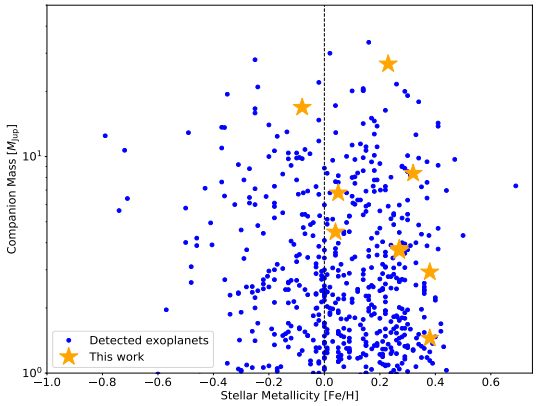

Fig. 10. Companion mass in the limits 1–50 $M_{\rm Jup}$ as a function of the host star metallicity. The new companions presented in this paper are shown by the orange stars. Previously detected planets and brown dwarfs are shown in blue[2]. The black dashed line shows the metallicity of the Sun. Most of the stars with detected companions in this paper have a significant metallicity excess.

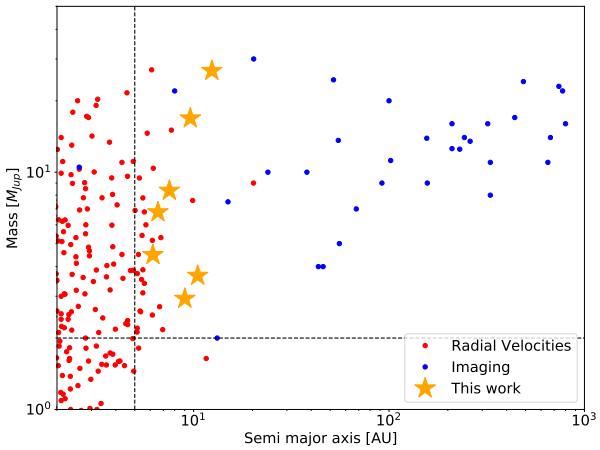

Fig. 11. Mass of detected exoplanets and brown dwarfs as a function of separation. The new companions presented in this paper are shown by the orange stars. Previously detected imaged planets and brown dwarfs are shown in blue and the RV-detected planets are shown in red[2]. The black dashed lines show the limits for companions that are in a potential detectable parameter space with imaging, i.e., giant planets more massive than 2 $M_{\rm Jup}$ and planets at a separation larger than 5 AU.

Exoplanet Archive[3] there are only 26 known exoplanets with a period greater than 15 yr.

As seen in Fig. 11, the planets and brown dwarfs presented in this paper are bridging the gap between the RV detected exoplanets and the directly imaged exoplanets. As we achieve deeper detection limits and smaller inner working angles in imaging with new instrumentation and telescopes, and span longer base lines with RV techniques, this gap in separation will decrease.

Combining RV and direct imaging data has previously been done, for example by Kane et al. (2014), Rodigas et al. (2016a,b) and Crepp et al. (2012). More recently, these two techniques have been combined for two candidates from the CORALIE RV survey with the detection of HD 4747 B by Peretti et al. (2019) and with the discovery of an ultra-cool brown dwarf companion to HD 4113 A by Cheetham et al. (2018).

[2] Companions taken from the NASA Exoplanet Archive.
[3] The NASA Exoplanet Archive can be accessed at https://exoplanetarchive.ipac.caltech.edu/index.html

With future direct imaging detections of these candidates presented here, we aim to follow the same method as Cheetham et al. (2018) and Peretti et al. (2019), and perform an atmospheric retrieval analysis of carbon and oxygen abundances, as demonstrated by Lavie et al. (2017). The CORALIE survey plays an important step in identifying promising targets for such observations, making CORALIE a unique instrument in being able to carry out such a long continuous survey at high precision. Furthermore, the stars in the CORALIE sample are older than the commonly and directly imaged targets, and so the substellar companions probed in this paper represent a new and complementary parameter space.

A great many attempts have been made to detect these long-period companions through imaging as part of a 15-yr effort using VLT/NACO with little success. Now with the capabilities of VLT/SPHERE with a contrast limit of $\sim 10^{-3}$–10^{-4} at a separation of 0.1 arcsec (Beuzit et al. 2019) we are able to start detecting these massive planets and brown dwarfs.

Some of these targets may be challenging for SPHERE, but where this is the case, they should be within the capabilities of ELT/METIS, where METIS should achieve a 10^{-5} contrast at 0.1 arcseconds (Carlomagno et al. 2016). In addition, combining astrometry that will be available from *Gaia* with RV data will allow us to further constrain the range of possible masses of these massive companions.

Acknowledgements. This work has been carried out within the framework of the National Centre for Competence in Research PlanetS supported by the Swiss National Science Foundation. The authors acknowledge the financial support of the SNSF. This publication makes use of the Data & Analysis Center for Exoplanets (DACE), which is a facility based at the University of Geneva (CH) dedicated to extrasolar planets data visualisation, exchange and analysis. DACE is a platform of the Swiss National Centre of Competence in Research (NCCR) PlanetS, federating the Swiss expertise in Exoplanet research. The DACE platform is available at https://dace.unige.ch. L.A.dS. and J.V.S. acknowledge the support from the European Research Council (ERC) under the European Union's Horizon 2020 research and innovation programme (project FOUR ACES, grant agreement No 724427). N.C.S. was supported by FCT – Fundação para a Ciência e a Tecnologia – through national funds and by FEDER through COMPETE2020 – Programa Operacional Competitividade e Internacionalização by these grants: UID/FIS/04434/2013 & POCI-01-0145-FEDER-007672; PTDC/FIS-AST/28953/2017 & POCI-01-0145-FEDER-028953 and PTDC/FIS-AST/32113/2017 & POCI-01-0145-FEDER-032113. This work has made use of data from the European Space Agency (ESA) mission *Gaia* (http://www.cosmos.esa.int/gaia), processed by the *Gaia* Data Processing and Analysis Consortium (DPAC, http://www.cosmos.esa.int/web/gaia/dpac/consortium). Funding for the DPAC has been provided by national institutions, in particular the institutions participating in the *Gaia* Multilateral Agreement.

References

Baluev, R. V. 2008, MNRAS, 385, 1279
Barbato, D., Sozzetti, A., Desidera, S., et al. 2018, A&A, 615, A175
Beuzit, J.-L., Vigan, A., Mouillet, D., et al. 2019, A&A, submitted, [arXiv:1902.04080]
Boisse, I., Pepe, F., Perrier, C., et al. 2012, A&A, 545, A55
Bond, J. C., Tinney, C. G., Butler, R. P., et al. 2006, MNRAS, 370, 163
Bowler, B. P. 2016, PASP, 128, 102001
Butler, R. P., Wright, J. T., Marcy, G. W., et al. 2006, ApJ, 646, 505
Butler, R. P., Vogt, S. S., Laughlin, G., et al. 2017, AJ, 153, 208
Carlomagno, B., Absil, O., Kenworthy, M., et al. 2016, in Adaptive Optics Systems V, Proc. SPIE, 9909, 990973
Cheetham, A., Ségransan, D., Peretti, S., et al. 2018, A&A, 614, A16
Crepp, J. R., Johnson, J. A., Howard, A. W., et al. 2012, ApJ, 761, 39
Crepp, J. R., Principe, D. A., Wolff, S., et al. 2018, ApJ, 853, 192
Delisle, J. B., Ségransan, D., Buchschacher, N., & Alesina, F. 2016, A&A, 590, A134
Delisle, J.-B., Ségransan, D., Dumusque, X., et al. 2018, A&A, 614, A133
Díaz, R. F., Almenara, J. M., Santerne, A., et al. 2014, MNRAS, 441, 983
Díaz, R. F., Ségransan, D., Udry, S., et al. 2016, A&A, 585, A134
Ekström, S., Georgy, C., Eggenberger, P., et al. 2012, A&A, 537, A146
Feigelson, E. D., Lawson, W. A., Stark, M., Townsley, L., & Garmire, G. P. 2006, AJ, 131, 1730
Fischer, D. A., & Valenti, J. 2005, ApJ, 622, 1102
Fischer, D. A., Marcy, G. W., Butler, R. P., et al. 2001, ApJ, 551, 1107
Fischer, D. A., Howard, A. W., Laughlin, G. P., et al. 2014, Protostars and Planets VI (Tucson: University of Arizona Press), 715
Gaia Collaboration (Brown, A. G. A., et al.) 2018, A&A, 616, A1
Georgy, C., Ekström, S., Eggenberger, P., et al. 2013, A&A, 558, A103
Gomes da Silva, J., Santos, N. C., Boisse, I., Dumusque, X., & Lovis, C. 2014, A&A, 566, A66
Kane, S. R., Howell, S. B., Horch, E. P., et al. 2014, ApJ, 785, 93
Lavie, B., Mendonça, J. M., Mordasini, C., et al. 2017, AJ, 154, 91
Mamajek, E. E., & Hillenbrand, L. A. 2008, ApJ, 687, 1264
Marmier, M. 2014, Ph.D. Thesis, Geneva Observatory, University of Geneva, Switzerland
Marmier, M., Ségransan, D., Udry, S., et al. 2013, A&A, 551, A90
Mayor, M., Pepe, F., Queloz, D., et al. 2003, The Messenger, 114, 20
Mayor, M., Marmier, M., Lovis, C., et al. 2011, ArXiv e-prints [arXiv:1109.2497]
Pepe, F., Mayor, M., Galland, F., et al. 2002, A&A, 388, 632
Peretti, S., Ségransan, D., Lavie, B., et al. 2019, A&A, accepted [arXiv:1805.05645]
Perryman, M. A. C., Lindegren, L., Kovalevsky, J., et al. 1997, A&A, 323, L49
Porto de Mello, G. F., da Silva, R., da Silva, L., & de Nader, R. V. 2014, A&A, 563, A52
Rodigas, T. J., Bergeron, P., Simon, A., et al. 2016a, ApJ, 831, 177
Rodigas, T. J., Arriagada, P., Faherty, J., et al. 2016b, ApJ, 818, 106
Santos, N. C., Israelian, G., & Mayor, M. 2001, A&A, 373, 1019
Santos, N. C., Israelian, G., & Mayor, M. 2004, A&A, 415, 1153
Santos, N. C., Sousa, S. G., Mortier, A., et al. 2013, A&A, 556, A150
Ségransan, D., Udry, S., Mayor, M., et al. 2010, A&A, 511, A45
Shen, Y., & Turner, E. L. 2008, ApJ, 685, 553
Sousa, S. G., Santos, N. C., Mayor, M., et al. 2008, A&A, 487, 373
Tamuz, O., Ségransan, D., Udry, S., et al. 2008, A&A, 480, L33
Udry, S., Mayor, M., Naef, D., et al. 2000, A&A, 356, 590
Udry, S., Mayor, M., Naef, D., et al. 2002, A&A, 390, 267
Vogt, S. S. 1987, PASP, 99, 1214
Vogt, S. S., Allen, S. L., Bigelow, B. C., et al. 1994, in Instrumentation in Astronomy VIII, eds. D. L. Crawford, & E. R. Craine, Proc. SPIE, 2198, 362
Vogt, S. S., Butler, R. P., Marcy, G. W., et al. 2005, ApJ, 632, 638
Wittenmyer, R. A., Wang, S., Horner, J., et al. 2013, ApJS, 208, 2
Wittenmyer, R. A., Clark, J. T., Zhao, J., et al. 2019, MNRAS, 484, 5859
Zuckerman, B., Song, I., Bessell, M. S., & Webb, R. A. 2001, ApJ, 562, L87
Zuckerman, B., Rhee, J. H., Song, I., & Bessell, M. S. 2011, ApJ, 732, 61

[1] Département d'astronomie, Université de Genève, 51 ch. des Maillettes, 1290 Versoix, Switzerland
e-mail: emily.rickman@unige.ch
[2] Instituto de Astrofísica e Ciências do Espaço, Universidade do Porto, CAUP, Rua das Estrelas, 4150-762 Porto, Portugal
[3] Departamento de Física e Astronomia, Faculdade de Ciências, Universidade do Porto, Rua do Campo Alegre, 4169-007 Porto, Portugal
[4] Institute of Physics, Laboratory of Astrophysics, École Polytechnique Fédérale de Lausanne (EPFL), Observatoire de Sauverny, 1290, Versoix, Switzerland
[5] European Southern Observatory, Alonso de Córdova 3107, Vitacura, Santiago, Chile
[6] Department of Astronomy and Astrophysics, University of Chicago, 5640 South Ellis Avenue, Chicago, IL 60637, USA
[7] Department of Physics, University of Warwick, Coventry CV4 7AL, UK
[8] Aix Marseille Université, CNRS, LAM (Laboratoire d'Astrophysique de Marseille) UMR 7326, 13388 Marseille, France
[9] Carnegie Institution for Science, Las Campanas Observatory, Casilla 601, Colina El Pino s/n, La Serena, Chile
[10] Physikalisches Institut, Universität Bern, Gesellschaftsstr. 6, 3012 Bern, Switzerland
[11] Instituto de Astrofísica de Canarias, 38205 La Laguna, Tenerife, Spain
[12] School of Physics & Astronomy, University of Birmingham, Edgbaston, Birmingham, B15 2TT, UK
[13] Leiden Observatory, Leiden University, Postbus 9513, 2300 RA Leiden, Netherlands

Appendix A: Direct access to the RVs and other data products

The RV measurements and additional data products discussed in this paper are available in electronic form on the DACE web platform for each individual target with each link. A copy of the data is also available at the CDS.

HD 13724: https://dace.unige.ch/radialVelocities/?pattern=HD13724
HD 181234: https://dace.unige.ch/radialVelocities/?pattern=HD181234
HD 25015: https://dace.unige.ch/radialVelocities/?pattern=HD25015
HD 50499: https://dace.unige.ch/radialVelocities/?pattern=HD50499
HD 92788: https://dace.unige.ch/radialVelocities/?pattern=HD92788
HD 92987: https://dace.unige.ch/radialVelocities/?pattern=HD92987
HD 98649: https://dace.unige.ch/radialVelocities/?pattern=HD98649

Appendix B: MCMC tables

We probed the model parameter space with the MCMC sampler described in (Díaz et al. 2014, 2016). For each MCMC simulation, we performed 10 000 000 iterations with initial conditions drawn from the solution obtained using DACE. The corresponding parameters and confidence intervals for each star are listed in Tables B.1–B.7 for HD 181234, HD 92987, HD 13724, HD 25015, HD 98649, HD 50499 and HD 92788 respectively.

Table B.1. Parameters probed by the MCMC used to fit the RV measurements of HD 181234.

Parameter	Units	Max(likelihood)	Mode	Mean	Std	Median	68.27%	95.45%	99.73%	Prior
log(likelihood)		−359.29	−365.26	−366.31	2.83	−365.95	[−369.09–363.55]	[−372.93–361.77]	[−377.96–360.46]	–
Star										
M_S	($M_\odot$)	1.0495	1.0117	1.0101	0.0601	1.0105	[0.9501–1.0704]	[0.8899–1.1296]	[0.8287–1.1895]	$\mathcal{U}$
Π_S	(mas)	21.093	20.916	20.915	0.209	20.915	[20.708–21.123]	[20.498–21.336]	[20.280–21.538]	$\mathcal{U}$
Offset										
$\gamma_{\mathrm{COR98(DRS-3.3)}}$	(m s^{-1})	−8.36	−5.47	−5.41	2.74	−5.44	[−8.14–2.69]	[−10.79–0.22]	[−13.61–3.38]	$\mathcal{N}(0,4)$
$\gamma_{\mathrm{HIRES(Pub-2017)}}$	(m s^{-1})	46701.91	46703.49	46703.39	2.42	46703.40	[46701.00–46705.79]	[46698.55–46708.24]	[46695.72–46711.05]	$\mathcal{U}$
$\gamma_{\mathrm{COR07(DRS-3.4)}}$	(m s^{-1})	−46664.21	−46664.26	−46664.23	1.99	−46664.23	[−46666.21–46662.23]	[−46668.23–46660.32]	[−46670.43–46658.23]	$\mathcal{U}$
$\gamma_{\mathrm{COR14(DRS-3.8)}}$	(m s^{-1})	15.82	14.32	14.40	3.31	14.38	[11.08–17.72]	[7.84–21.08]	[4.93–24.60]	$\mathcal{N}(12,4)$
Noise										
$\sigma_{\mathrm{COR98(DRS-3.3)}}$	(m s^{-1})	5.52	7.12	8.04	2.82	7.70	[5.40–10.67]	[3.39–14.71]	[1.18–20.48]	$\mathcal{U}$
$\sigma_{\mathrm{COR07(DRS-3.4)}}$	(m s^{-1})	8.13	8.15	8.82	2.14	8.57	[6.77–10.84]	[5.34–13.84]	[4.10–17.95]	$\mathcal{U}$
$\sigma_{\mathrm{HIRES(Pub-2017)}}$	(m s^{-1})	2.966	3.265	3.555	0.790	3.453	[2.803–4.300]	[2.287–5.447]	[1.845–6.988]	$\mathcal{U}$
$\sigma_{\mathrm{COR14(DRS-3.8)}}$	(m s^{-1})	2.846	3.378	3.413	0.815	3.394	[2.631–4.205]	[1.810–5.122]	[0.703–6.113]	$\mathcal{U}$
HD 181234b										
P	(d)	7515.1	7463.4	7465.4	80.7	7464.3	[7385.6–7545.4]	[7307.0–7632.1]	[7221.7–7718.5]	$\mathcal{U}$
K	(m s^{-1})	126.31	126.75	126.81	1.71	126.77	[125.11–128.52]	[123.49–130.32]	[122.00–132.26]	$\mathcal{U}$
e		0.72845	0.73177	0.73216	0.00710	0.73211	[0.72512–0.73925]	[0.71793–0.74649]	[0.71028–0.75311]	$\mathcal{U}$
ω	(°)	94.75	93.27	93.23	1.78	93.24	[91.46–95.01]	[89.62–96.75]	[87.88–98.58]	$\mathcal{U}$
T_{Vmin}	(BJD)	2460630.87	2457946.63	2457946.37	8.55	2457946.40	[2457937.94–2457954.82]	[2457928.94–2457963.58]	[2457919.90–2457972.50]	$\mathcal{U}$
a_S	(AU)	0.05978	0.05922	0.05926	0.00110	0.05925	[0.05816–0.06036]	[0.05711–0.06153]	[0.05605–0.06275]	–
a	(AU)	7.650	7.517	7.517	0.159	7.519	[7.359–7.676]	[7.192–7.828]	[7.019–7.976]	–
m	($M_\oplus$)	2737	2659	2656	111	2657	[2544–2767]	[2430–2877]	[2318–2986]	–
m	(M_J)	8.613	8.366	8.358	0.351	8.361	[8.006–8.707]	[7.648–9.053]	[7.294–9.395]	–
m	($M_\odot$)	0.008222	0.007986	0.007978	0.000335	0.007980	[0.007641–0.008311]	[0.007300–0.008641]	[0.006962–0.008968]	–
T_C	(BJD)	2460344.43	2457661.70	2457661.72	2.36	2457661.72	[2457659.38–2457664.06]	[2457656.97–2457666.45]	[2457654.32–2457669.15]	–
T_P	(BJD)	2460355.10	2457668.66	2457668.91	5.26	2457668.85	[2457663.69–2457674.13]	[2457658.52–2457679.58]	[2457653.25–2457685.35]	–

Notes. The maximum likelihood solution, median, mode, and standard-deviation of the posterior distribution for each parameter are shown, as well as the 68.27, 95.45, and 99.73% confidence intervals. The prior for each parameter can be of type: $\mathcal{U}$: uniform, $\mathcal{N}$: normal, or $\mathcal{TN}$: truncated normal. Reference epoch: 2455500.0 BJD.

Table B.2. Parameters probed by the MCMC used to fit the RV measurements of HD 92987.

Parameter	Units	Max(likelihood)	Mode	Mean	Std	Median	68.27%	95.45%	99.73%	Prior
log(likelihood)		−287.21	−292.23	−293.24	2.60	−292.89	[−295.76–290.72]	[−299.43–289.15]	[−303.96–288.07]	–
Star										
M_S	($M_\odot$)	1.0877	1.0795	1.0807	0.0601	1.0805	[1.0207–1.1409]	[0.9602–1.2010]	[0.9018–1.2590]	$\mathcal{U}$
Π_S	(mas)	22.860	22.943	22.943	0.228	22.944	[22.715–23.170]	[22.487–23.399]	[22.279–23.626]	$\mathcal{U}$
Offset										
$\gamma_{\mathrm{COR14(DRS-3.8)}}$	($\mathrm{m\,s^{-1}}$)	11.89	11.28	11.21	3.40	11.21	[7.80–14.61]	[4.35–18.01]	[0.77–21.33]	$\mathcal{N}(12,4)$
$\gamma_{\mathrm{COR98(DRS-3.3)}}$	($\mathrm{m\,s^{-1}}$)	10.38	5.65	5.73	2.82	5.73	[2.94–8.52]	[0.06–11.39]	[−2.92–14.40]	$\mathcal{N}(0,4)$
$\gamma_{\mathrm{COR07(DRS-3.4)}}$	($\mathrm{m\,s^{-1}}$)	4757.07	4759.04	4759.37	2.21	4759.25	[4757.21–4761.52]	[4755.31–4764.14]	[4753.41–4767.46]	$\mathcal{U}$
Noise										
$\sigma_{\mathrm{COR07(DRS-3.4)}}$	($\mathrm{m\,s^{-1}}$)	2.88	3.55	3.76	1.60	3.66	[2.25–5.26]	[0.71–7.32]	[0.03–10.30]	$\mathcal{U}$
$\sigma_{\mathrm{COR98(DRS-3.3)}}$	($\mathrm{m\,s^{-1}}$)	5.408	5.746	5.968	0.925	5.899	[5.065–6.876]	[4.315–8.029]	[3.656–9.431]	$\mathcal{U}$
$\sigma_{\mathrm{COR14(DRS-3.8)}}$	($\mathrm{m\,s^{-1}}$)	2.22	2.68	2.79	1.40	2.73	[1.38–4.13]	[0.26–5.85]	[0.02–8.18]	$\mathcal{U}$
HD 92987b										
$\log P$	(d)	4.0204	4.0150	4.0208	0.0175	4.0191	[4.0038–4.0376]	[3.9909–4.0607]	[3.9805–4.0921]	$\mathcal{U}$
$\log K$	($\mathrm{m\,s^{-1}}$)	2.17745	2.18372	2.18316	0.00709	2.18324	[2.17601–2.19025]	[2.16885–2.19710]	[2.16133–2.20394]	$\mathcal{U}$
$\sqrt{e}\cos\omega$		−0.4573	−0.4435	−0.4426	0.0260	−0.4428	[−0.4682–0.4169]	[−0.4939–0.3898]	[−0.5227–0.3615]	$\mathcal{U}$
$\sqrt{e}\sin\omega$		−0.1091	−0.1232	−0.1119	0.0580	−0.1154	[−0.1694–0.0541]	[−0.2173–0.0143]	[−0.2573-0.0857]	$\mathcal{U}$
T_{Vmin}	(BJD)	2457596.8	2457600.4	2457599.0	26.3	2457599.7	[2457573.1–2457625.1]	[2457543.7–2457649.7]	[2457513.1–2457674.0]	$\mathcal{U}$
a_S	(AU)	0.14139	0.14234	0.14371	0.00487	0.14321	[0.13900–0.14843]	[0.13550–0.15492]	[0.13232–0.16417]	–
a	(AU)	9.687	9.621	9.672	0.318	9.653	[9.362–9.981]	[9.093–10.365]	[8.849–10.841]	–
e		0.2210	0.2109	0.2125	0.0164	0.2118	[0.1966–0.2280]	[0.1817–0.2482]	[0.1657–0.2764]	–
K	($\mathrm{m\,s^{-1}}$)	150.47	152.67	152.48	2.49	152.49	[149.97–154.97]	[147.52–157.43]	[144.99–159.93]	–
ω	(°)	193.42	195.10	194.29	7.60	194.55	[186.68–201.84]	[178.30–208.69]	[169.69–214.64]	–
m	($M_\oplus$)	5312	5363	5369	214	5368	[5155–5583]	[4939–5796]	[4727–6002]	–
m	(M_J)	16.714	16.876	16.893	0.673	16.891	[16.222–17.566]	[15.541–18.238]	[14.874–18.887]	–
m	($M_\odot$)	0.015954	0.016108	0.016124	0.000643	0.016123	[0.015484–0.016767]	[0.014834–0.017409]	[0.014197–0.018028]	–
P	(d)	10482	10355	10499	428	10450	[10089–10904]	[9794–11501]	[9560–12362]	–
T_C	(BJD)	2455569.4	2455533.3	2455534.2	40.4	2455533.6	[2455493.9–2455574.5]	[2455455.4–2455617.2]	[2455416.6–2455662.2]	–
T_P	(BJD)	2457841	2457889	2457861	155	2457870	[2457708–2458015]	[2457530–2458147]	[2457331–2458264]	–

Notes. The maximum likelihood solution, median, mode, and standard-deviation of the posterior distribution for each parameter are shown, as well as the 68.27, 95.45, and 99.73% confidence intervals. The prior for each parameter can be of type: $\mathcal{U}$: uniform, $\mathcal{N}$: normal, or $\mathcal{TN}$: truncated normal. Reference epoch: 2455500.0 BJD.

Table B.3. Parameters probed by the MCMC used to fit the RV measurements of HD 13724.

Parameter	Units	Max(likelihood)	Mode	Mean	Std	Median	68.27%	95.45%	99.73%	Prior
log(likelihood)		−592.80	−599.41	−600.20	2.60	−599.89	[−602.74–597.67]	[−606.25–595.94]	[−610.74–594.59]	–
					Star					
M_S	($M_\odot$)	1.1744	1.1406	1.1397	0.0599	1.1396	[1.0798–1.1994]	[1.0202–1.2596]	[0.9580–1.3200]	$\mathcal{U}$
Π_S	(mas)	23.306	22.978	22.979	0.230	22.979	[22.749–23.208]	[22.520–23.441]	[22.302–23.663]	$\mathcal{U}$
					Offset					
$\gamma_{\rm HARPS03(DRS-3.5)}$	($m\,s^{-1}$)	44.00	41.66	41.57	3.59	41.59	[37.95–45.16]	[34.40–48.71]	[30.79–52.28]	$\mathcal{U}$
$\gamma_{\rm COR98(DRS-3.3)}$	($m\,s^{-1}$)	5.14	1.66	1.70	3.30	1.71	[−1.58–4.99]	[−4.97–8.25]	[−8.27–11.42]	$\mathcal{N}(0,4)$
$\gamma_{\rm COR14(DRS-3.8)}$	($m\,s^{-1}$)	26.96	15.28	15.28	3.84	15.28	[11.44–19.10]	[7.57–22.90]	[3.94–26.52]	$\mathcal{N}(12,4)$
$\gamma_{\rm COR07(DRS-3.4)}$	($m\,s^{-1}$)	20614.5	20597.2	20613.7	37.9	20608.9	[20578.6–20647.3]	[20549.7–20716.3]	[20535.6–20735.2]	$\mathcal{U}$
					Noise					
$\sigma_{\rm COR07(DRS-3.4)}$	($m\,s^{-1}$)	12.93	13.98	15.25	3.34	14.76	[12.11–18.37]	[10.08–23.44]	[8.60–30.19]	$\mathcal{U}$
$\sigma_{\rm HARPS03(DRS-3.5)}$	($m\,s^{-1}$)	5.622	5.493	5.772	0.859	5.671	[4.942–6.605]	[4.349–7.771]	[3.857–9.337]	$\mathcal{U}$
$\sigma_{\rm COR14(DRS-3.8)}$	($m\,s^{-1}$)	9.75	9.98	10.29	1.36	10.17	[8.96–11.63]	[7.92–13.38]	[7.08–15.51]	$\mathcal{U}$
$\sigma_{\rm COR98(DRS-3.3)}$	($m\,s^{-1}$)	8.340	8.723	8.884	0.963	8.821	[7.932–9.835]	[7.143–10.981]	[6.491–12.353]	$\mathcal{U}$
					HD 13724b					
$\log P$	(d)	4.2315	4.1727	4.2093	0.0979	4.1952	[4.1196–4.2941]	[4.0453–4.4723]	[4.0079–4.5266]	$\mathcal{U}$
$\log K$	($m\,s^{-1}$)	2.3447	2.3310	2.3414	0.0330	2.3396	[2.3098–2.3725]	[2.2780–2.4195]	[2.2580–2.4389]	$\mathcal{U}$
$\sqrt{e}\cos\omega$		−0.6095	−0.5767	−0.5881	0.0621	−0.5862	[−0.6446–0.5307]	[−0.7277–0.4578]	[−0.7525–0.4045]	$\mathcal{U}$
$\sqrt{e}\sin\omega$		−0.0557	−0.0812	−0.0824	0.0201	−0.0818	[−0.1020–0.0626]	[−0.1243–0.0439]	[−0.1538–0.0237]	$\mathcal{U}$
$T_{\rm Vmin}$	(BJD)	2456047.7	2456038.8	2456038.6	28.8	2456039.2	[2456009.9–2456067.5]	[2455979.1–2456093.7]	[2455943.9–2456120.6]	$\mathcal{U}$
a_S	(AU)	0.3212	0.2703	0.3157	0.0938	0.2954	[0.2367–0.3865]	[0.1889–0.6070]	[0.1679–0.6801]	–
a	(AU)	13.78	12.40	13.34	2.18	12.90	[11.47–15.04]	[10.21–19.86]	[9.56–21.73]	–
e		0.3745	0.3365	0.3569	0.0721	0.3507	[0.2896–0.4215]	[0.2214–0.5347]	[0.1776–0.5692]	–
K	($m\,s^{-1}$)	221.1	214.3	220.1	16.9	218.6	[204.1–235.8]	[189.7–262.7]	[181.1–274.7]	–
ω	(°)	185.22	187.45	188.13	2.50	187.86	[185.80–190.39]	[183.96–194.14]	[182.15–199.24]	–
m	($M_\oplus$)	9184	8507	8875	1126	8747	[7810–9899]	[6972–11785]	[6404–12781]	–
m	(M_J)	28.90	26.77	27.93	3.54	27.52	[24.58–31.15]	[21.94–37.08]	[20.15–40.22]	–
m	($M_\odot$)	0.02759	0.02555	0.02666	0.00338	0.02627	[0.02346–0.02973]	[0.02094–0.03540]	[0.01923–0.03839]	–
P	(d)	17040	14764	16637	4187	15673	[13170–19684]	[11099–29669]	[10185–33620]	–
T_C	(BJD)	2453671	2453723	2453662	174	2453686	[2453505–2453826]	[2453202–2453933]	[2452980–2454008]	–
T_P	(BJD)	2456152.0	2456189.1	2456199.0	66.5	2456195.2	[2456135.4–2456261.8]	[2456076.2–2456345.7]	[2456008.8–2456458.5]	–

Notes. The maximum likelihood solution, median, mode, and standard-deviation of the posterior distribution for each parameter are shown, as well as the 68.27, 95.45, and 99.73% confidence intervals. The prior for each parameter can be of type: $\mathcal{U}$: uniform, $\mathcal{N}$: normal, or $\mathcal{TN}$: truncated normal. Reference epoch: 2455500.0 BJD.

Table B.4. Parameters probed by the MCMC used to fit the RV measurements of HD 25015.

Parameter	Units	Max(Likelihood)	Mode	Mean	Std	Median	68.27%	95.45%	99.73%	Prior
log(Likelihood)		−430.28	−435.20	−436.10	2.51	−435.77	[−438.54–433.67]	[−442.07–432.17]	[−446.55–431.20]	–
					Star					
M_S	($M_\odot$)	0.8851	0.8598	0.8599	0.0502	0.8600	[0.8097–0.9103]	[0.7591–0.9597]	[0.7098–1.0082]	$\mathcal{U}$
Π_S	(mas)	26.651	26.695	26.685	0.266	26.684	[26.418–26.952]	[26.157–27.218]	[25.893–27.491]	$\mathcal{U}$
					Offset					
$\gamma_{\mathrm{COR07(DRS-3.4)}}$	($\mathrm{m\,s^{-1}}$)	28536.61	28537.76	28537.61	2.83	28537.63	[28534.79–28540.43]	[28531.85–28543.20]	[28528.97–28545.98]	$\mathcal{U}$
$\gamma_{\mathrm{COR14(DRS-3.8)}}$	($\mathrm{m\,s^{-1}}$)	15.62	12.81	12.77	3.80	12.76	[8.96–16.57]	[5.21–20.38]	[1.55–24.36]	$\mathcal{N}(12, 4)$
$\gamma_{\mathrm{COR98(DRS-3.3)}}$	($\mathrm{m\,s^{-1}}$)	2.76	−0.01	−0.06	3.86	−0.03	[−3.93–3.79]	[−7.81–7.67]	[−11.51–11.69]	$\mathcal{N}(0, 4)$
					Activity cycle					
$A_{H_\alpha\mathrm{,Gauss.,0.1yr,lowpass}}$	($\mathrm{m\,s^{-1}}$)	7.59	6.81	6.82	4.37	6.82	[2.49–11.15]	[−1.95–15.58]	[−6.98–20.36]	$\mathcal{U}$
					Noise					
$\sigma_{\mathrm{COR07(DRS-3.4)}}$	($\mathrm{m\,s^{-1}}$)	10.26	12.07	10.77	4.79	11.17	[5.57–15.48]	[0.95–19.66]	[0.05–24.44]	$\mathcal{U}$
Low act.	($\mathrm{m\,s^{-1}}$)	8.32	10.54	8.53	3.85	9.19	[3.96–12.36]	[0.61–14.85]	[0.04–17.16]	$\mathcal{U}$
$\sigma_{H_\alpha\mathrm{,Gauss.,0.1yr,lowpass}}$	($\mathrm{m\,s^{-1}}$)	14.60	14.31	13.98	6.73	14.01	[6.90–20.61]	[1.20–27.89]	[0.06–35.04]	$\mathcal{U}$
$\sigma_{\mathrm{COR98(DRS-3.3)}}$	($\mathrm{m\,s^{-1}}$)	16.12	16.47	16.35	5.92	16.40	[10.75–21.88]	[3.47–28.45]	[0.21–36.46]	$\mathcal{U}$
$\sigma_{\mathrm{COR14(DRS-3.8)}}$	($\mathrm{m\,s^{-1}}$)	5.53	8.28	6.48	3.87	6.41	[2.03–10.71]	[0.28–13.87]	[0.02–17.05]	$\mathcal{U}$
					HD 25015b					
$\log P$	(d)	3.7879	3.7821	3.7937	0.0353	3.7888	[3.7609–3.8259]	[3.7377–3.8807]	[3.7187–3.9585]	$\mathcal{U}$
$\log K$	($\mathrm{m\,s^{-1}}$)	1.7817	1.7796	1.7788	0.0236	1.7791	[1.7558–1.8016]	[1.7300–1.8254]	[1.7011–1.8552]	$\mathcal{U}$
$\sqrt{e}\cos\omega$		0.190	0.133	0.128	0.100	0.128	[0.027–0.228]	[−0.071–0.328]	[−0.171–0.432]	$\mathcal{U}$
$\sqrt{e}\sin\omega$		0.5950	0.6088	0.6054	0.0631	0.6070	[0.5449–0.6668]	[0.4712–0.7283]	[0.3832–0.7800]	$\mathcal{U}$
T_{Vmax}	(BJD)	2455258	2455209	2455210	122	2455209	[2455090–2455329]	[2454964–2455458]	[2454827–2455591]	$\mathcal{U}$
a_S	(AU)	0.03141	0.03112	0.03144	0.00227	0.03132	[0.02924–0.03361]	[0.02730–0.03639]	[0.02526–0.04051]	–
a	(AU)	6.309	6.193	6.311	0.373	6.260	[5.966–6.642]	[5.720–7.231]	[5.509–8.115]	–
e		0.3901	0.3883	0.3969	0.0785	0.3944	[0.3200–0.4745]	[0.2454–0.5622]	[0.1699–0.6497]	–
K	($\mathrm{m\,s^{-1}}$)	60.49	60.11	60.18	3.29	60.13	[56.99–63.33]	[53.71–66.90]	[50.25–71.65]	–
ω	(°)	72.29	77.65	78.20	9.32	78.13	[69.06–87.41]	[59.46–96.93]	[49.33–107.71]	–
m	($M_\oplus$)	1469.8	1424.3	1428.1	91.6	1427.0	[1336.7–1520.0]	[1249.5–1614.0]	[1162.7–1713.7]	–
m	(M_J)	4.625	4.482	4.494	0.288	4.490	[4.206–4.783]	[3.932–5.079]	[3.659–5.392]	–
m	($M_\odot$)	0.004415	0.004278	0.004289	0.000275	0.004286	[0.004015–0.004565]	[0.003753–0.004848]	[0.003492–0.005147]	–
P	(d)	6137	6021	6239	531	6149	[5766–6697]	[5467–7598]	[5233–9090]	–
T_C	(BJD)	2455962.9	2455936.9	2455940.6	97.7	2455939.6	[2455843.2–2456038.8]	[2455745.3–2456137.5]	[2455648.1–2456230.8]	–
T_P	(BJD)	2455840	2455852	2455861	149	2455858	[2455715–2456009]	[2455568–2456166]	[2455413–2456323]	–

Notes. The maximum likelihood solution, median, mode, and standard-deviation of the posterior distribution for each parameter are shown, as well as the 68.27, 95.45, and 99.73% confidence intervals. The prior for each parameter can be of type: $\mathcal{U}$: uniform, $\mathcal{N}$: normal, or $\mathcal{TN}$: truncated normal. Reference epoch: 2455500.0 BJD.

Table B.5. Parameters probed by the MCMC used to fit the RV measurements of HD 98649.

Parameter	Units	Max(Likelihood)	Mode	Mean	Std	Median	68.27%	95.45%	99.73%	Prior
log(Likelihood)		−201.70	−207.30	−208.21	2.60	−207.89	[−210.77–205.67]	[−214.31–204.03]	[−218.55–202.86]	–
					Star					
M_S	($M_\odot$)	0.9465	1.0296	1.0300	0.0599	1.0299	[0.9701–1.0899]	[0.9105–1.1501]	[0.8513–1.2099]	$\mathcal{U}$
Π_S	(mas)	23.995	23.688	23.684	0.236	23.684	[23.448–23.921]	[23.211–24.158]	[22.967–24.390]	$\mathcal{U}$
					Offset					
$\gamma_{\mathrm{COR98(DRS-3.3)}}$	($\mathrm{m\,s^{-1}}$)	−7.05	−1.94	−1.87	3.41	−1.87	[−5.29–1.52]	[−8.66–5.01]	[−11.97–8.58]	$\mathcal{N}(0,4)$
$\gamma_{\mathrm{COR14(DRS-3.8)}}$	($\mathrm{m\,s^{-1}}$)	20.61	16.33	16.18	2.86	16.22	[13.33–19.03]	[10.38–21.83]	[7.29–24.66]	$\mathcal{N}(12,4)$
$\gamma_{\mathrm{COR07(DRS-3.4)}}$	($\mathrm{m\,s^{-1}}$)	4281.50	4281.91	4282.18	2.27	4282.11	[4279.94–4284.45]	[4277.87–4286.97]	[4275.82–4289.55]	$\mathcal{U}$
					Noise					
$\sigma_{\mathrm{COR98(DRS-3.3)}}$	($\mathrm{m\,s^{-1}}$)	8.66	8.89	9.87	2.82	9.46	[7.25–12.47]	[5.51–16.73]	[4.17–23.36]	$\mathcal{U}$
$\sigma_{\mathrm{COR14(DRS-3.8)}}$	($\mathrm{m\,s^{-1}}$)	0.62	0.46	1.75	1.29	1.51	[0.47–3.00]	[0.07–4.90]	[0.00–7.73]	$\mathcal{U}$
$\sigma_{\mathrm{COR07(DRS-3.4)}}$	($\mathrm{m\,s^{-1}}$)	5.63	6.49	6.73	1.15	6.64	[5.61–7.85]	[4.73–9.32]	[3.95–11.07]	$\mathcal{U}$
					HD 98649b					
$\log P$	(d)	3.7508	3.7808	3.7848	0.0240	3.7834	[3.7611–3.8086]	[3.7409–3.8373]	[3.7222–3.8692]	$\mathcal{U}$
$\log K$	($\mathrm{m\,s^{-1}}$)	2.1918	2.1458	2.1817	0.0622	2.1650	[2.1272–2.2386]	[2.1061–2.3537]	[2.0906–2.4329]	$\mathcal{U}$
$\sqrt{e}\cos\omega$		−0.3301	−0.2764	−0.3155	0.0796	−0.2974	[−0.3900–0.2445]	[−0.5267–0.2028]	[−0.5957–0.1629]	$\mathcal{U}$
$\sqrt{e}\sin\omega$		−0.8689	−0.8808	−0.8715	0.0221	−0.8769	[−0.8885–0.8572]	[−0.8984–0.8016]	[−0.9072–0.7610]	$\mathcal{U}$
T_{Vmax}	(BJD)	2455271.6	2455264.7	2455262.2	14.1	2455263.5	[2455250.4–2455274.8]	[2455227.6–2455286.4]	[2455190.8–2455299.0]	$\mathcal{U}$
a_S	(AU)	0.04055	0.04129	0.04223	0.00280	0.04178	[0.03969–0.04477]	[0.03789–0.04939]	[0.03626–0.05465]	–
a	(AU)	6.097	6.570	6.609	0.277	6.594	[6.336–6.881]	[6.105–7.212]	[5.891–7.586]	–
e		0.8640	0.8556	0.8659	0.0253	0.8626	[0.8410–0.8927]	[0.8239–0.9223]	[0.8087–0.9403]	–
K	($\mathrm{m\,s^{-1}}$)	155.5	140.1	153.6	24.4	146.2	[134.0–173.2]	[127.7–225.8]	[123.2–270.9]	–
ω	(°)	249.20	252.61	250.16	4.99	251.29	[245.58–254.58]	[236.70–257.20]	[231.95–259.71]	–
m	($M_\oplus$)	2101	2157	2194	148	2175	[2059–2325]	[1954–2574]	[1856–2829]	–
m	(M_J)	6.610	6.788	6.905	0.466	6.843	[6.479–7.315]	[6.148–8.098]	[5.839–8.903]	–
m	($M_\odot$)	0.006309	0.006479	0.006591	0.000445	0.006532	[0.006184–0.006982]	[0.005868–0.007729]	[0.005574–0.008498]	–
P	(d)	5633	6024	6103	341	6073	[5769–6436]	[5506–6875]	[5274–7399]	–
T_C	(BJD)	2454102	2453718	2453924	410	2453860	[2453525–2454369]	[2453243–2454828]	[2452944–2454969]	–
T_P	(BJD)	2455128.3	2455121.7	2455116.0	22.1	2455117.9	[2455093.6–2455138.5]	[2455066.9–2455153.8]	[2455042.6–2455164.4]	–

Notes. The maximum likelihood solution, median, mode, and standard-deviation of the posterior distribution for each parameter are shown, as well as the 68.27, 95.45, and 99.73% confidence intervals. The prior for each parameter can be of type: $\mathcal{U}$: uniform, $\mathcal{N}$: normal, or $\mathcal{TN}$: truncated normal. Reference epoch: 2455500.0 BJD.

Table B.6. Parameters probed by the MCMC used to fit the RV measurements of HD 50499.

Parameter	Units	Max(Likelihood)	Mode	Mean	Std	Median	68.27%	95.45%	99.73%	Prior
log(Likelihood)		−668.22	−677.90	−678.84	3.49	−678.50	[−682.24–675.41]	[−686.79–672.90]	[−692.68–671.11]	–
					Star					
M_S	($M_\odot$)	1.3739	1.3102	1.3098	0.0699	1.3102	[1.2402–1.3795]	[1.1687–1.4483]	[1.0980–1.5220]	$\mathcal{U}$
Π_S	(mas)	99.91	100.03	99.99	1.00	100.00	[98.98–100.99]	[97.99–101.98]	[96.91–103.08]	$\mathcal{U}$
					Offset					
$\gamma_{\rm HIRES(Pub-2017)}$	($m\,s^{-1}$)	−36798.27	−36798.15	−36798.23	1.45	−36798.21	[−36799.68–36796.79]	[−36801.16–36795.38]	[−36802.59–36794.00]	$\mathcal{U}$
$\gamma_{\rm COR98(DRS-3.3)}$	($m\,s^{-1}$)	3.63	3.77	3.71	1.95	3.72	[1.76–5.68]	[−0.21–7.57]	[−2.15–9.55]	$\mathcal{N}(0,4)$
$\gamma_{\rm COR07(DRS-3.4)}$	($m\,s^{-1}$)	36813.30	36814.53	36817.23	6.52	36815.30	[36812.73–36821.25]	[36810.66–36838.24]	[36808.80–36850.47]	$\mathcal{U}$
$\gamma_{\rm HARPS03(DRS-3.5)}$	($m\,s^{-1}$)	32.74	31.73	31.76	2.32	31.75	[29.47–34.04]	[27.06–36.43]	[24.66–39.01]	$\mathcal{N}(32,4)$
$\gamma_{\rm COR14(DRS-3.8)}$	($m\,s^{-1}$)	17.56	16.71	16.80	2.60	16.78	[14.25–19.38]	[11.59–22.11]	[8.46–24.74]	$\mathcal{N}(12,4)$
					Noise					
$\sigma_{\rm HIRES(Pub-2017)}$	($m\,s^{-1}$)	3.956	4.178	4.247	0.410	4.220	[3.838–4.658]	[3.503–5.139]	[3.212–5.777]	$\mathcal{U}$
$\sigma_{\rm COR98(DRS-3.3)}$	($m\,s^{-1}$)	7.34	7.71	7.95	1.16	7.85	[6.81–9.09]	[5.93–10.53]	[5.12–12.29]	$\mathcal{U}$
$\sigma_{\rm COR07(DRS-3.4)}$	($m\,s^{-1}$)	7.42	7.52	7.84	1.22	7.73	[6.65–9.03]	[5.73–10.58]	[4.94–12.62]	$\mathcal{U}$
$\sigma_{\rm HARPS03(DRS-3.5)}$	($m\,s^{-1}$)	1.81	2.24	3.20	2.11	2.68	[1.71–4.49]	[1.12–8.72]	[0.67–18.95]	$\mathcal{U}$
$\sigma_{\rm COR14(DRS-3.8)}$	($m\,s^{-1}$)	4.79	5.04	5.19	1.02	5.12	[4.19–6.19]	[3.36–7.42]	[2.56–8.91]	$\mathcal{U}$
					HD 50499b					
$\log P$	(d)	3.39372	3.39533	3.39536	0.00333	3.39535	[3.39207–3.39867]	[3.38870–3.40205]	[3.38489–3.40537]	$\mathcal{U}$
$\log K$	($m\,s^{-1}$)	1.2733	1.2783	1.2766	0.0195	1.2772	[1.2573–1.2959]	[1.2361–1.3150]	[1.2148–1.3338]	$\mathcal{U}$
$\sqrt{e}\cos\omega$		−0.1092	−0.1029	−0.1038	0.0773	−0.1033	[−0.1813–0.0262]	[−0.2583–0.0484]	[−0.3288–0.1272]	$\mathcal{U}$
$\sqrt{e}\sin\omega$		−0.5199	−0.5129	−0.5060	0.0458	−0.5082	[−0.5507–0.4615]	[−0.5915–0.4069]	[−0.6298–0.3356]	$\mathcal{U}$
$T_{\rm Vmin}$	(BJD)	2455823.0	2455820.7	2455825.2	33.8	2455823.4	[2455791.7–2455858.5]	[2455762.5–2455898.4]	[2455733.0–2455940.5]	$\mathcal{U}$
a_S	(AU)	0.004096	0.004160	0.004153	0.000184	0.004154	[0.003971–0.004336]	[0.003784–0.004523]	[0.003595–0.004701]	–
a	(AU)	3.9830	3.9293	3.9288	0.0730	3.9298	[3.8567–4.0018]	[3.7783–4.0719]	[3.6983–4.1391]	–
e		0.2822	0.2725	0.2749	0.0382	0.2739	[0.2376–0.3124]	[0.2004–0.3549]	[0.1642–0.4003]	–
K	($m\,s^{-1}$)	18.763	18.944	18.927	0.850	18.930	[18.083–19.767]	[17.223–20.653]	[16.399–21.568]	–
ω	(°)	258.14	259.32	258.18	9.08	258.55	[249.13–267.21]	[238.96–275.11]	[227.46–283.12]	–
m	($M_\oplus$)	470.6	460.6	460.8	25.6	460.7	[435.4–486.4]	[410.1–512.8]	[385.2–540.9]	–
m	(M_J)	1.4809	1.4494	1.4501	0.0807	1.4497	[1.3699–1.5304]	[1.2905–1.6136]	[1.2121–1.7021]	–
m	($M_\odot$)	0.0014135	0.0013834	0.0013841	0.0000770	0.0013837	[0.0013076–0.0014608]	[0.0012318–0.0015402]	[0.0011569–0.0016247]	–
P	(d)	2475.8	2484.6	2485.3	19.1	2485.1	[2466.5–2504.2]	[2447.4–2523.8]	[2426.0–2543.1]	–
T_C	(BJD)	2455055.5	2455060.8	2455055.6	50.9	2455057.1	[2455004.9–2455106.4]	[2454950.1–2455153.9]	[2454889.1–2455194.6]	–
T_P	(BJD)	2457073.4	2456172.9	2456164.6	58.8	2456167.7	[2456105.4–2456223.3]	[2456040.3–2456273.6]	[2455966.5–2456322.7]	–
					HD 50499c					
$\log P$	(d)	3.9217	3.9390	3.9819	0.0949	3.9509	[3.9140–4.0506]	[3.8848–4.2905]	[3.8590–4.4037]	$\mathcal{U}$
$\log K$	($m\,s^{-1}$)	1.3722	1.3816	1.4081	0.0555	1.3917	[1.3670–1.4475]	[1.3473–1.5814]	[1.3297–1.6610]	$\mathcal{U}$
$\sqrt{e}\cos\omega$		0.086	−0.058	−0.103	0.220	−0.089	[−0.344–0.132]	[−0.549–0.279]	[−0.642–0.401]	$\mathcal{U}$
$\sqrt{e}\sin\omega$		0.197	0.099	0.080	0.117	0.085	[−0.046–0.204]	[−0.159–0.286]	[−0.256–0.349]	$\mathcal{U}$
$T_{\rm Vmin}$	(BJD)	2454510.8	2454559.9	2454549.0	73.8	2454551.4	[2454475.4–2454621.0]	[2454394.8–2454692.6]	[2454316.7–2454770.4]	$\mathcal{U}$
a_S	(AU)	0.0181	0.0191	0.0240	0.0115	0.0201	[0.0177–0.0286]	[0.0161–0.0634]	[0.0148–0.0970]	–
a	(AU)	8.96	9.02	9.78	1.68	9.24	[8.69–10.75]	[8.27–15.51]	[7.88–18.57]	–
e		0.0460	0.0000	0.0792	0.0761	0.0571	[0.0171–0.1365]	[0.0026–0.3079]	[0.0002–0.4259]	–
K	($m\,s^{-1}$)	23.56	24.23	25.82	3.78	24.64	[23.28–28.02]	[22.25–38.14]	[21.37–45.82]	–
ω	(°)	66	180	50	113	81	[−115–161]	[−177–177]	[−180–180]	–
m	($M_\oplus$)	923	932	1032	239	957	[874–1164]	[814–1801]	[759–2346]	–
m	(M_J)	2.904	2.932	3.246	0.751	3.011	[2.752–3.664]	[2.560–5.666]	[2.387–p7.382]	–
m	($M_\odot$)	0.002772	0.002799	0.003098	0.000717	0.002874	[0.002626–0.003497]	[0.002444–0.005408]	[0.002278–0.007046]	–
P	(d)	8350	8611	9861	2745	8932	[8204–11235]	[7671–19522]	[7228–25332]	–
T_C	(BJD)	2456009	2461130	2462211	2525	2461357	[2460705–2463463]	[2460175–2471070]	[2459652–2476577]	–
T_P	(BJD)	2455509	2461832	2462479	4026	2461969	[2458947–2465593]	[2456054–2474140]	[2455527–2479915]	–

Notes. The maximum likelihood solution, median, mode, and standard-deviation of the posterior distribution for each parameter are shown, as well as the 68.27%, 95.45%, and 99.73% confidence intervals. The prior for each parameter can be of type: $\mathcal{U}$: uniform, $\mathcal{N}$: normal, or $\mathcal{TN}$: truncated normal. Reference epoch: 2455500.0 BJD.

Table B.7. Parameters probed by the MCMC used to fit the RV measurements of HD 92788.

Parameter	Units	Max(Likelihood)	Mode	Mean	Std	Median	68.27%	95.45%	99.73%	Prior
log(Likelihood)		−625.86	−636.46	−637.60	3.58	−637.24	[−641.13–634.06]	[−645.81–631.54]	[−650.84–629.55]	–
Star										
M_S	($M_\odot$)	1.1684	1.1483	1.1500	0.0702	1.1500	[1.0805–1.2202]	[1.0089–1.2907]	[0.9272–1.3575]	$\mathcal{U}$
Π_S	(mas)	28.838	28.835	28.829	0.288	28.828	[28.541–29.120]	[28.254–29.406]	[27.958–29.662]	$\mathcal{U}$
Offset										
$\gamma_{\rm COR14(DRS-3.8)}$	($m\,s^{-1}$)	9.64	10.96	10.84	3.53	10.83	[7.32–14.39]	[3.89–17.94]	[0.33–21.77]	$\mathcal{N}(12,4)$
$\gamma_{\rm COR07(DRS-3.4)}$	($m\,s^{-1}$)	−4430.37	−4430.03	−4430.76	2.76	−4430.42	[−4433.39–4428.15]	[−4437.43–4426.17]	[−4440.86–4423.54]	$\mathcal{U}$
$\gamma_{\rm HAMILTON(Pub-2006)}$	($m\,s^{-1}$)	4448.46	4448.30	4448.04	2.68	4448.10	[4445.39–4450.72]	[4442.43–4453.25]	[4439.52–4455.84]	$\mathcal{U}$
$\gamma_{\rm COR98(DRS-3.3)}$	($m\,s^{-1}$)	−1.95	−2.24	−2.24	2.29	-2.21	[−4.51–0.03]	[−6.94–2.25]	[−9.77–4.46]	$\mathcal{N}(0,4)$
$\gamma_{\rm HARPS03(DRS-3.5)}$	($m\,s^{-1}$)	38.84	38.53	38.23	1.84	38.33	[36.45–40.02]	[34.19–41.68]	[31.45–43.36]	$\mathcal{N}(32,4)$
$\gamma_{\rm HIRES(Pub-2017)}$	($m\,s^{-1}$)	4470.60	4470.24	4470.10	1.93	4470.16	[4468.25–4472.01]	[4465.96–4473.73]	[4462.84–4475.55]	$\mathcal{U}$
Noise										
$\sigma_{\rm COR07(DRS-3.4)}$	($m\,s^{-1}$)	2.42	3.96	4.54	2.72	4.24	[1.90–6.99]	[0.33–10.98]	[0.02–17.75]	$\mathcal{U}$
$\sigma_{\rm HIRES(Pub-2017)}$	($m\,s^{-1}$)	3.521	3.752	3.831	0.531	3.788	[3.311–4.355]	[2.911–5.025]	[2.576–5.898]	$\mathcal{U}$
$\sigma_{\rm COR14(DRS-3.8)}$	($m\,s^{-1}$)	2.91	4.08	4.60	2.14	4.36	[2.65–6.52]	[0.96–9.71]	[0.07–14.94]	$\mathcal{U}$
$\sigma_{\rm HAMILTON(Pub-2006)}$	($m\,s^{-1}$)	4.85	5.16	5.08	2.22	5.09	[2.82–7.25]	[0.62–9.64]	[0.03–12.51]	$\mathcal{U}$
$\sigma_{\rm COR98(DRS-3.3)}$	($m\,s^{-1}$)	9.36	9.58	9.83	1.35	9.75	[8.49–11.17]	[7.40–12.78]	[6.42–14.65]	$\mathcal{U}$
$\sigma_{\rm HARPS03(DRS-3.5)}$	($m\,s^{-1}$)	1.431	1.491	1.535	0.194	1.523	[1.344–1.727]	[1.186–1.960]	[1.045–2.215]	$\mathcal{U}$
HD 92788b										
$\log P$	(d)	2.5128215	2.5128306	2.5128344	0.0000622	2.5128330	[2.5127722–2.5128955]	[2.5127131–2.5129638]	[2.5126589–2.5130376]	$\mathcal{U}$
$\log K$	($m\,s^{-1}$)	2.03396	2.03454	2.03446	0.00351	2.03447	[2.03100–2.03795]	[2.02741–2.04146]	[2.02355–2.04503]	$\mathcal{U}$
$\sqrt{e}\cos\omega$		0.0809	0.0797	0.0800	0.0113	0.0800	[0.0687–0.0912]	[0.0573–0.1026]	[0.0452–0.1144]	$\mathcal{U}$
$\sqrt{e}\sin\omega$		−0.58785	−0.58698	−0.58697	0.00398	−0.58699	[−0.59092–0.58302]	[−0.59485–0.57895]	[−0.59886–0.57446]	$\mathcal{U}$
λ_0	(°)	115.191	115.166	115.125	0.474	115.140	[114.656–115.591]	[114.128–116.041]	[113.540–116.525]	$\mathcal{U}$
a_S	(AU)	0.0030300	0.0030350	0.0030349	0.0000271	0.0030348	[0.0030080–0.0030619]	[0.0029814–0.0030896]	[0.0029521–0.0031194]	–
a	(AU)	0.9768	0.9720	0.9712	0.0198	0.9716	[0.9517–0.9910]	[0.9302–1.0097]	[0.9044–1.0267]	–
e		0.35211	0.35120	0.35108	0.00451	0.35108	[0.34660–0.35558]	[0.34200–0.36013]	[0.33750–0.36478]	–
K	($m\,s^{-1}$)	108.133	108.243	108.262	0.874	108.261	[107.400–109.131]	[106.516–110.016]	[105.571–110.926]	–
ω	(°)	−82.17	−82.27	−82.24	1.10	−82.24	[−83.33–81.16]	[−84.44–80.04]	[−85.61–78.90]	–
m	($M_\oplus$)	1208.0	1195.9	1196.7	50.0	1196.9	[1147.2–1247.0]	[1095.5–1295.0]	[1037.4–1343.4]	–
m	(M_J)	3.801	3.763	3.766	0.157	3.766	[3.610–3.924]	[3.447–4.075]	[3.264–4.227]	–
m	($M_\odot$)	0.003628	0.003592	0.003594	0.000150	0.003595	[0.003446–0.003745]	[0.003290–0.003890]	[0.003116–0.004035]	–
P	(d)	325.7028	325.7097	325.7125	0.0467	325.7114	[325.6659–325.7583]	[325.6215–325.8095]	[325.5809–325.8649]	–
T_C	(BJD)	2455470.50	2455470.61	2455470.65	1.29	2455470.64	[2455469.38–2455471.93]	[2455468.11–2455473.28]	[2455466.78–2455474.73]	–
T_P	(BJD)	2455543.031	2455647.141	2455647.142	0.736	2455647.139	[2455646.415–2455647.868]	[2455645.674–2455648.640]	[2455644.949–2455649.443]	–
HD 92788c										
$\log P$	(d)	4.077	4.065	4.122	0.107	4.094	[4.030–4.222]	[3.984–4.410]	[3.945–4.597]	$\mathcal{U}$
$\log K$	($m\,s^{-1}$)	1.5369	1.5238	1.5239	0.0278	1.5239	[1.4962–1.5517]	[1.4684–1.5805]	[1.4393–1.6035]	$\mathcal{U}$
$\sqrt{e}\cos\omega$		0.6302	0.6139	0.6196	0.0554	0.6185	[0.5676–0.6730]	[0.5065–0.7354]	[0.4308–0.7870]	$\mathcal{U}$
$\sqrt{e}\sin\omega$		−0.2734	−0.3134	−0.3152	0.0947	−0.3135	[-0.4112–0.2213]	[−0.5121–0.1313]	[−0.5867–0.0255]	$\mathcal{U}$
$T_{\rm Vmax}$	(BJD)	2457168.9	2457142.6	2457122.4	99.5	2457129.7	[2457025.2–2457220.2]	[2456899.1–2457298.5]	[2456754.7–2457390.4]	$\mathcal{U}$
a_S	[AU]	0.03328	0.03195	0.03578	0.00782	0.03359	[0.02964–0.04200]	[0.02686–0.05768]	[0.02452–0.08454]	–
a	(AU)	10.77	10.50	11.65	2.18	11.00	[9.95–13.40]	[9.24–17.84]	[8.65–23.92]	–
e		0.4719	0.4551	0.4952	0.0767	0.4793	[0.4241–0.5739]	[0.3805–0.6820]	[0.3427–0.7579]	–
K	($m\,s^{-1}$)	34.43	33.29	33.48	2.14	33.41	[31.35–35.62]	[29.40–38.06]	[27.50–40.13]	–
ω	(°)	−23.45	−25.71	−26.79	7.89	−26.49	[−34.63–19.08]	[−43.21–11.50]	[−52.07–2.23]	–
m	($M_\oplus$)	1203.2	1164.8	1172.1	87.7	1169.0	[1084.5–1260.1]	[1004.8–1356.5]	[929.2–1455.6]	–
m	(M_J)	3.786	3.665	3.688	0.276	3.678	[3.413–3.965]	[3.162–4.268]	[2.924–4.580]	–
m	($M_\odot$)	0.003614	0.003498	0.003520	0.000264	0.003511	[0.003257–0.003785]	[0.003018–0.004074]	[0.002791–0.004372]	–
P	(d)	11927	11610	13703	4106	12405	[10706–16666]	[9639–25718]	[8804–39575]	–
T_C	(BJD)	2461454	2458838	2458997	386	2458921	[2458666–2459320]	[2458452–2460040]	[2458240–2460932]	–
T_P	(BJD)	2456919	2456858	2456825	167	2456834	[2456656–2456991]	[2456473–2457133]	[2456281–2457257]	–

Notes. The maximum likelihood solution, median, mode, and standard-deviation of the posterior distribution for each parameter are shown, as well as the 68.27, 95.45, and 99.73% confidence intervals. The prior for each parameter can be of type: $\mathcal{U}$: uniform, $\mathcal{N}$: normal, or $\mathcal{TN}$: truncated normal. Reference epoch: 2455500.0 BJD.

3.3 Summary and conclusions

The paper describes the detection of three new massive planets and two low mass brown dwarfs at a separation greater than 5 AU. The companions were detected using the radial velocity method as part of the ongoing CORALIE survey for extra-solar planets in the southern hemisphere. This survey utilises the Swiss-Euler 1.2 m telescope in La Silla Observatory, Chile and has been ongoing for more than 20 years. It is the continuous observations over such a long time span that allow for the detection of these companions.

The detection of such long-period (>5 AU) planets and brown dwarfs is crucial towards understanding the occurrence rate of such objects. These five new detections join just a short list of widely-separated companions, and work towards bridging the gap between radial-velocity detected companions and directly imaged companions. Consequently, some of these detected companions have been imaged with VLT/SPHERE and are presented in Chapter 4 and Chapter 5. Probing this mass-separation parameter space is important to understand occurrence rates and demographics of *all* exoplanets and ultimately help paint the picture of how these systems formed.

CHAPTER 4

DIRECT IMAGING OF ULTRACOOL COMPANIONS

"Just get more data."

— Leonardo dos Santos

4.1 Introduction and background

Detecting massive, long-period companion candidates via the radial-velocity (RV) method provides promising candidates to follow-up with direct imaging as discussed in Chapter 3. Follow-up direct imaging of long-period RV-detected companions from CORALIE and HARPS has been an ongoing programme for the past $\sim$ 15 years. Montagnier (2008) and Hagelberg (2014) used VLT/NACO (described in Chapter 6) to follow-up RV targets and have reported previous detections, or placed constraints on the parameter space in which these companion candidates sit.

These continued efforts allow us to select the most promising candidates for a direct detection with the latest generation of high-contrast imagers like VLT/SPHERE. Monitoring a volume-limited sample of stars with long-period companion candidates allows us to work towards understanding the fraction of brown dwarfs and giant exoplanets at a given separation, specifically at wide separations, around Sun-like stars in the solar neighbourhood.

4.2 Previously imaged targets

In Table 4.1 is a complete list of long-period RV companions previously imaged with VLT/NACO (Montagnier 2008; Hagelberg 2014) from the CORALIE and HARPS samples. In some cases, there were candidates in the sample that then turned out to have a radial-velocity signal due to stellar activity and therefore were rejected as companion candidates by Hagelberg (2014); these have also been flagged with 'stellar act.' in the 'RV signal' column in Table 4.1. For targets where there has been a direct detection, the mass of the detected companion is listed in the 'direct detection' column. In the cases where the RV curve and/or images of the companion have been published, or if the target has been

removed from the sample due to stellar activity, the publication is specified in the 'reference' column. Where the RV curve has already been published, the minimum mass ($m \sin i$) and period is listed from the corresponding reference.

In the cases where there is more than one companion candidate, the period and minimum mass are stated only for the longest period companion of that system.

The current state of the best-fit solution for each target under column 'RV signal' can be either of the following: 'linear' if the solution is linear; 'quadratic' is there is curvature present in the Keplerian; 'almost complete' if there is substantial phase coverage of the orbit in order to fit a constrained RV model, and 'complete' if there is full phase coverage of the orbit.

The RV curves are fit using the online tool by the 'Data and Analysis Center for Exoplanets' (DACE)[1]. For the complete or almost complete orbits the period is fitted and the corresponding minimum mass is listed.

If the orbital period of a companion is unconstrained, the minimum period is listed. This is estimated by decreasing the orbital period in the DACE solution to find the minimised χ^2_r corresponding to that orbital period. The *minimum* mass corresponding to this fitted solution is listed in Table 4.1.

The plots of the RV curves for each target in Table 4.1 are shown in Fig. 4.1, except for the targets that have been removed from the sample due to stellar activity.

[1] DACE can be accessed at https://dace.unige.ch.

Table 4.1 Previously imaged long period companion candidates.

Target	Sp. type	$m \sin i$ $M_{\rm Jup}$	Period years	RV signal	Direct detection	Reference
HIP 948	K5V	7.3	> 19.4	linear	0.2 $M_\odot$	Hagelberg (2014)
HD 142	F7V	5.3	16.44 ± 1.31	quadratic	no	Wittenmyer et al. (2012)
HD 1388	G0V	22	> 28.5	quadratic	$0.49 M_\odot$	Montagnier (2008)
HD 361	G1V	3.93	23.65 ± 1.3	complete	no	-
HD 4113	G5V	64.4	$104.6^{+29.0}_{-17.9}$	quadratic	66 $M_{\rm Jup}$	Cheetham et al. (2018b)
HD 4747	G8V/K0V	50.7	33.08 ± 0.70	quadratic	70 $M_{\rm Jup}$	Peretti et al. (2019)
HD 9796	K0V	24.5	> 39	linear	0.5 $M_\odot$	Montagnier (2008)
HD 13724	G3/5V	50.5	123^{+103}_{-51}	almost complete	50 $M_{\rm Jup}$	Rickman et al. (2019, 2020)
HD 14044	G2V	47.0	> 66.0	linear	0.66 $M_\odot$	Montagnier (2008)
HD 68475	K2V	11.7	> 27.0	quadratic	no	-
HD 72760	K0V	31.6	> 60.0	quadratic	0.38 $M_\odot$	Montagnier (2008)
HD 74014	K0III	49.7	18.63 ± 0.14	complete	no	-
HD 78612	G3V	40.8	> 54.0	quadratic	0.29 $M_\odot$	Montagnier (2008)

continued ...

... continued

Target	sp. type	$m \sin i$ M_{Jup}	period years	RV signal	direct detection	reference
HD 78746	K2.5V	91.5	10.9 ± 0.01	complete	no	-
HD 85390	K1.5V	-	-	stellar act.	no	Hagelberg (2014)
HD 87359	G6V	18.9	> 27	almost complete	0.47 $M_{\odot}$	Montagnier (2008)
HD 92987	G2/G3V	20.03	$29.89^{+1.10}_{-0.89}$	almost complete	0.3 $M_{\odot}$	Rickman et al. (2019), this work
HD 93351	G6V	5.3	> 38	linear	2×0.3 $M_{\odot}$	Hagelberg (2014)
HD 97037	G1V	21.5	> 34	linear	0.18 $M_{\odot}$	Montagnier (2008)
HD 98356	K0V	244.0	17.9 ± 0.1	complete	no	-
HD 98649	G3/G5V	6.79	$16.49^{+1.13}_{-0.70}$	complete	no	Rickman et al. (2019)
HD 100508	K1IV	-	-	stellar act.	no	Hagelberg (2014)
HD 101339	G5V	4.8	> 21	linear	no	-
HD 104263	G8/K0V	6.0	> 40	linear	0.15 $M_{\odot}$	Hagelberg (2014)
HD 104304	G8IV	102	> 50	quadratic	0.3 $M_{\odot}$	Montagnier (2008)
HD 111031	G5V	16.7	> 59	linear	0.18 $M_{\odot}$	Hagelberg (2014)
HD 112863	K1V	73.7	21.6 ± 0.03	complete	no	-

continued ...

... continued

Target	sp. type	$m \sin i$ $M_{\rm Jup}$	period years	RV signal	direct detection	reference
HD 116920	K2+V	54.9	> 33	linear	0.26 $M_\odot$	Montagnier (2008)
HD 117939	G4V	1.3	11.6 ± 1.2	complete	no	-
HD 124553	F8V	1.2	12.9 ± 0.2	complete	no	-
HD 132569	K1V	0.5	> 15	quadratic	WDS Catalog, 0.3 $M_\odot$	Hagelberg (2014)
HD 135625	G3IV/V	1.9	11.0 ± 0.1	complete	no	-
HD 139189	K0V	10.6	> 23	quadratic	no	-
HD 139879	G3V	0.6	> 60	quadratic	no	-
HD 145666	G2V	0.9	9.4 ± 0.4	complete	no	-
HD 149192	K4V	69.3	> 35	linear	0.44 $M_\odot$	Montagnier (2008)
HD 150139	F8V	3.4	> 18	linear	$0.5 M_\odot$	Hagelberg (2014)
HD 150437	G5V	-	-	stellar act.	no	Hagelberg (2014)
HD 157338	F9.5V	-	-	quadratic	0.41 $M_\odot$	Montagnier (2008)
HD 161050	F8/G0V	100.3	> 40	linear	no	-
HD 168863	K2/3(III)	8.2	> 36	quadratic	no	-

continued ...

. . . continued

Target	sp. type	$m \sin i$ $M_{\rm Jup}$	period years	RV signal	direct detection	reference
HD 170209	K(2)V	1.6	> 17	quadratic	no	-
HD 171990	F8V	-	-	stellar act.	no	Hagelberg (2014)
HD 178340	G8V	1.0	7.6 ± 0.1	complete	no	-
HD 185615	G6IV/V	3.0	> 55	linear	136 $M_{\rm Jup}$	Hagelberg (2014)
HD 195010	G8/K0V	60.56	$46.14^{+7.05}_{-7.38}$	quadratic	0.26 $M_\odot$	Montagnier (2008), this work
HD 197823	K0IV-V	3.9	> 28	quadratic	0.25 $M_\odot$	Hagelberg (2014)
HD 203432	G8IV	-	-	stellar act.	no	Hagelberg (2014)
HD 205891	G6V	25.3	> 43	linear	0.085 $M_\odot$	Montagnier (2008)
HD 206630	K3V	-	-	stellar act.	no	Hagelberg (2014)
HD 207700	G4V	5.4	> 36	linear	0.11 $M_\odot$	Hagelberg (2014)
HD 212708	G6IV	11.1	> 23	linear	0.3 $M_\odot$	Hagelberg (2014)
HD 213941	G8V	3.9	> 71	quadratic	0.25 $M_\odot$	Hagelberg (2014)
HD 219077	G8V+	10.39	$15.06^{+0.36}_{-0.33}$	complete	no	Marmier et al. (2013)
HD 219509	K3.5V	162	> 49	linear	0.24 $M_\odot$	Montagnier (2008)

continued . . .

. . . continued

Target	sp. type	$m \sin i$ M_{Jup}	period years	RV signal	direct detection	reference
HD 221146	G1V	10.4	> 25.87	linear	no	-
HD 222595	G5V	-	-	stellar act.	no	Hagelberg (2014)

Fig. 4.1 Radial-velocity curves from Table 4.1 of long-period companion candidates that have been previously imaged with NACO by Montagnier (2008) and/or Hagelberg (2014).

HIP 948

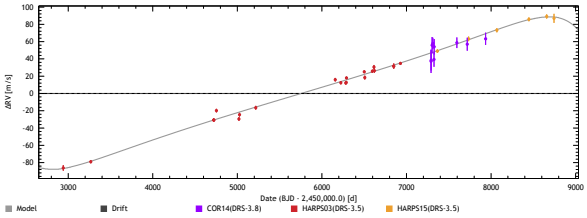

HD 142

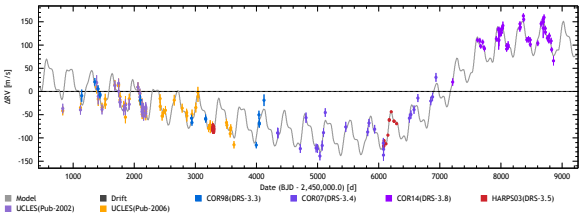

HD 1388

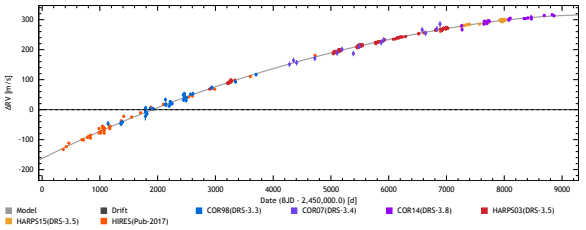

HD 361

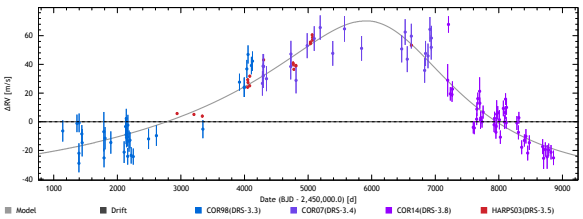

HD 4113

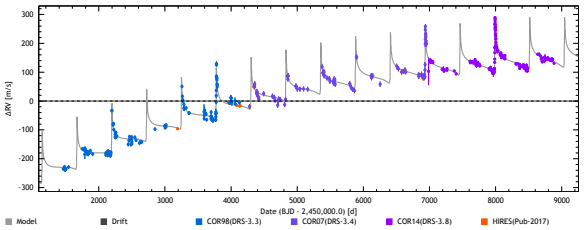

HD 4747

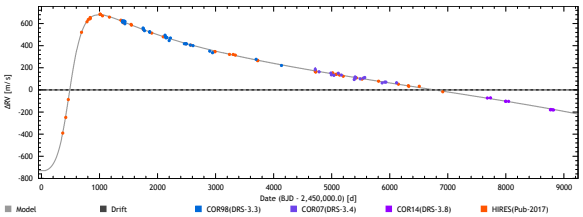

HD 9796

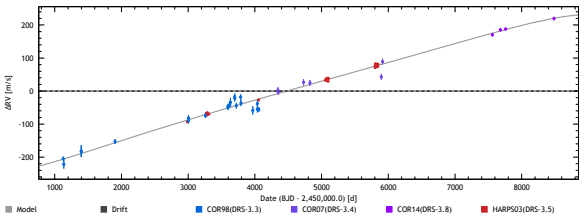

HD 13724

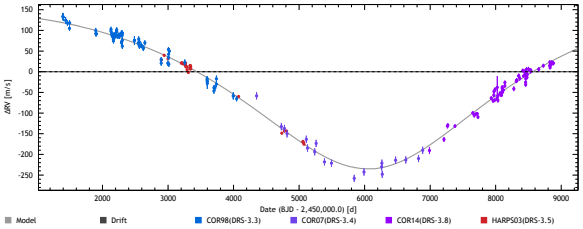

HD 14044

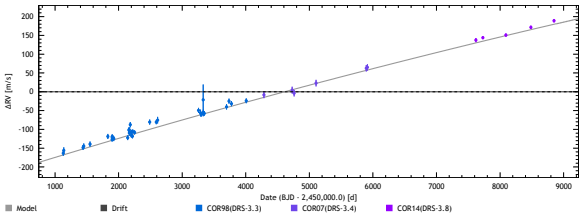

HD 68475

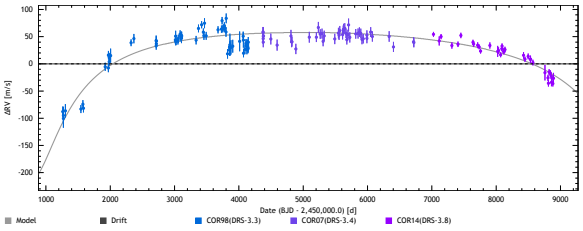

HD 72760

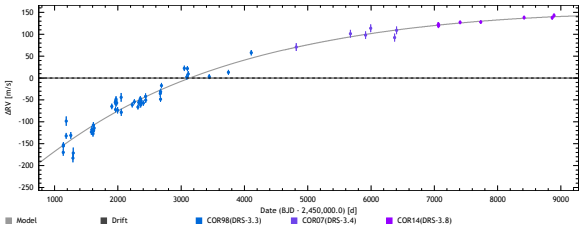

HD 74014

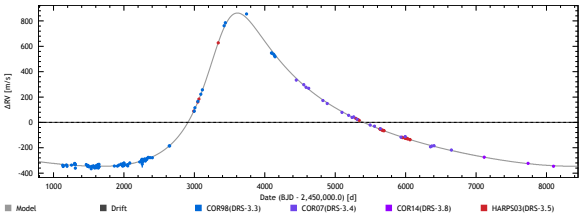

HD 78612

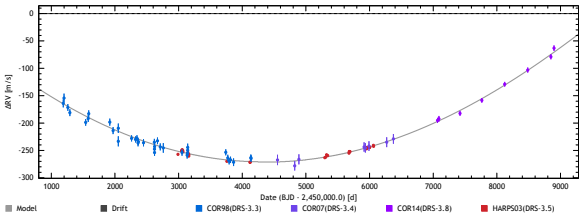

HD 78746

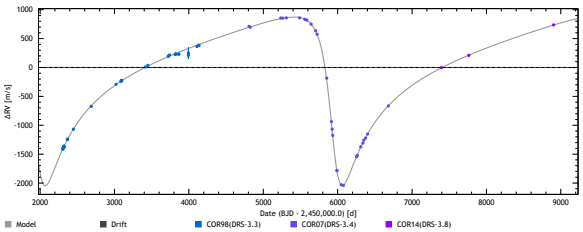

HD 87359

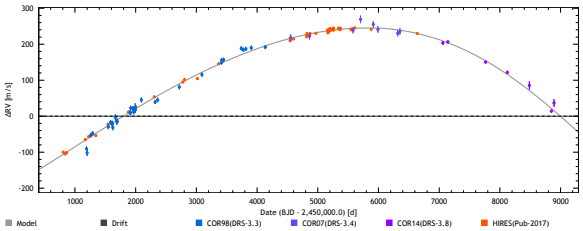

HD 92987

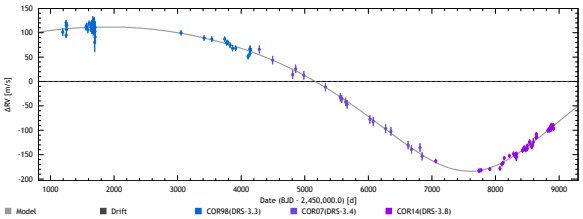

HD 93351

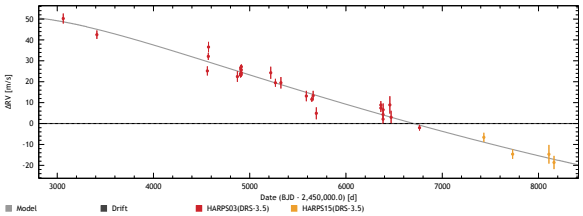

HD 97037

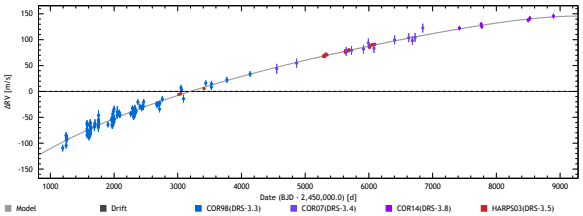

HD 98356

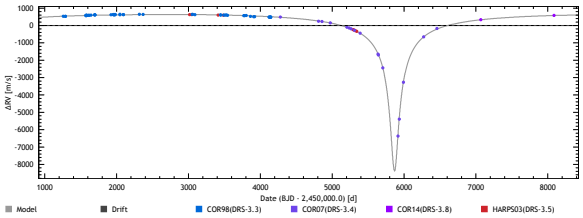

HD 98649

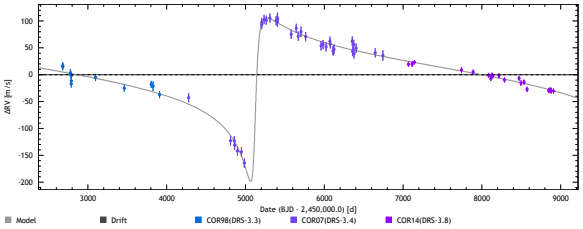

HD 101339

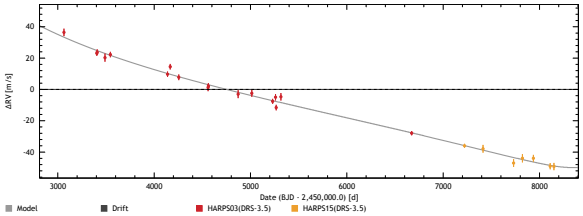

HD 104263

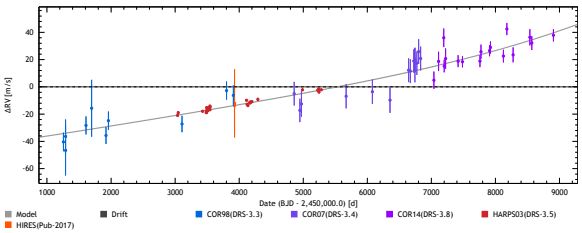

HD 104304

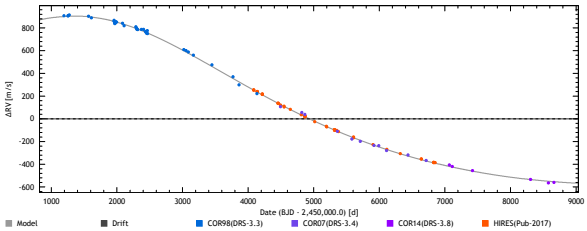

HD 111031

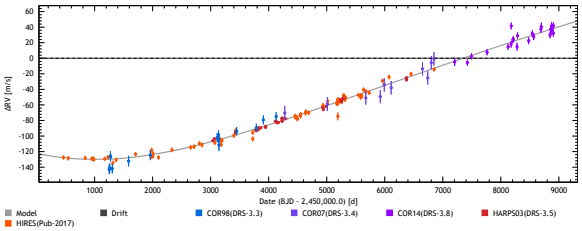

HD 112863

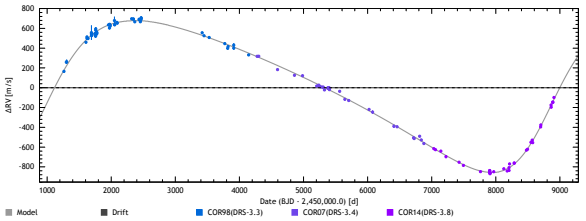

HD 116920

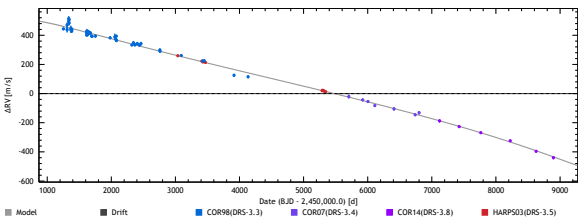

HD 117939

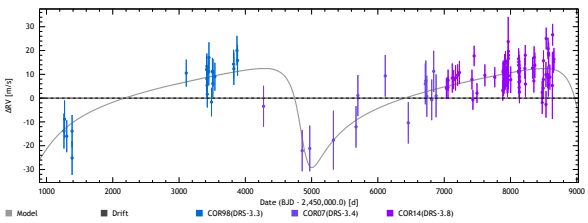

HD 124553

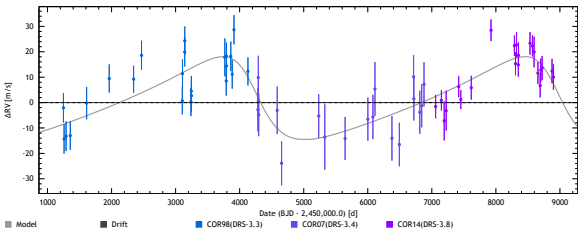

HD 132569

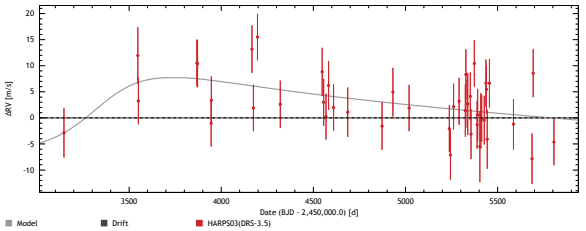

HD 135625

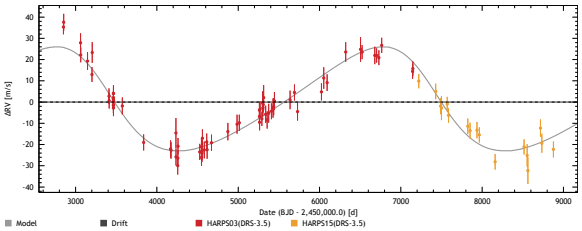

HD 139189

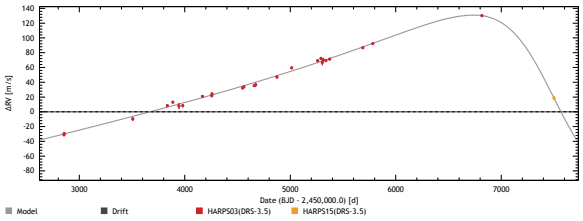

HD 139879

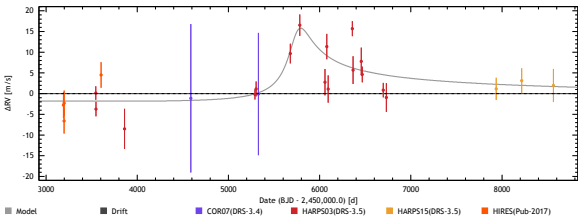

HD 145666

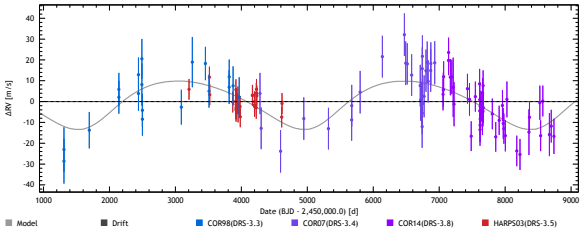

HD 149192

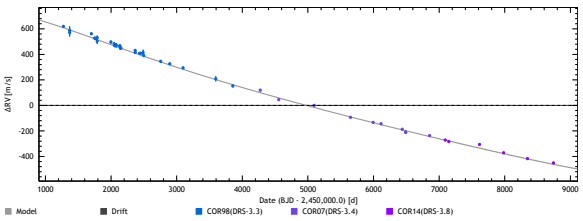

HD 150139

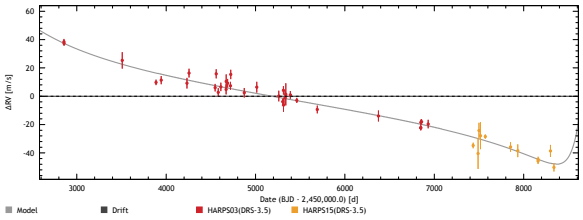

HD 157338

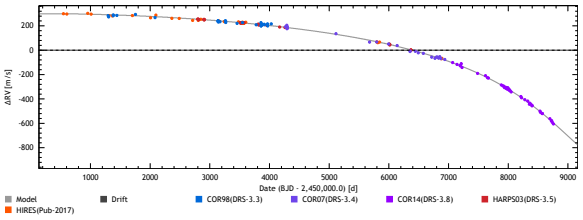

HD 161050

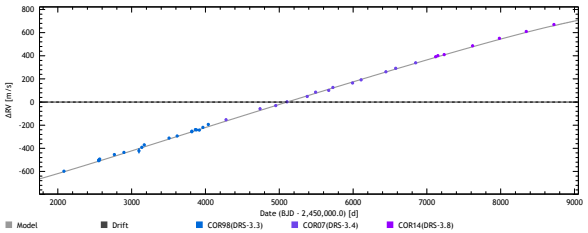

HD 168863

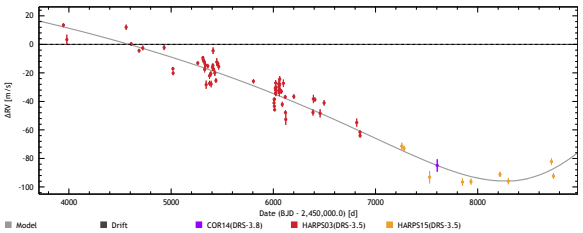

HD 170209

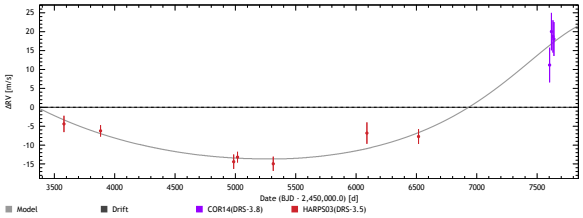

HD 178340

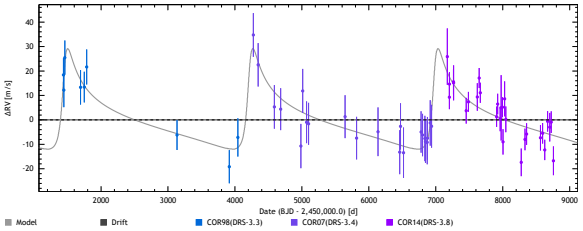

HD 185615

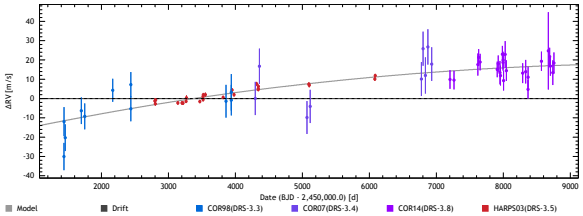

HD 195010

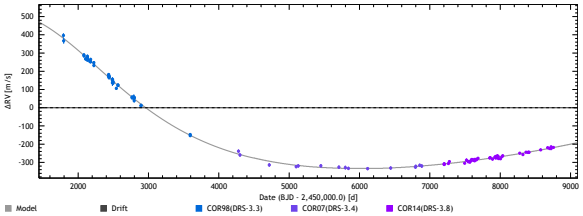

HD 197823

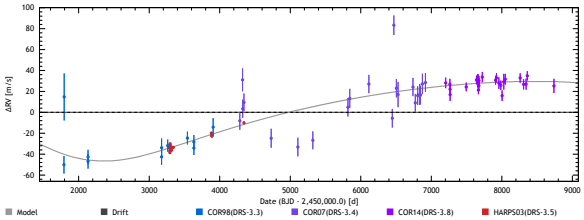

HD 205891

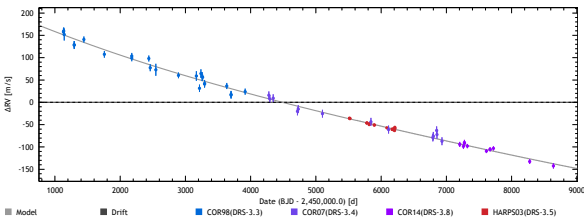

HD 207700

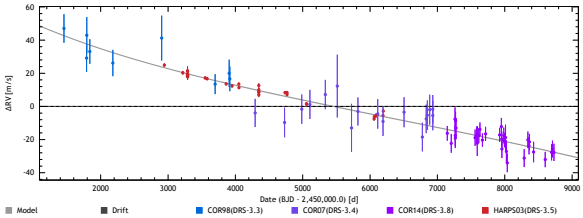

HD 212708

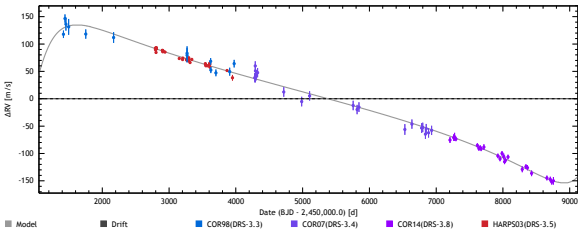

HD 213941

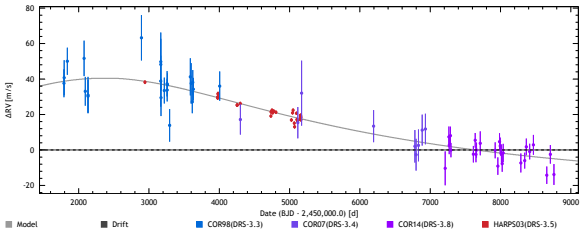

HD 219077

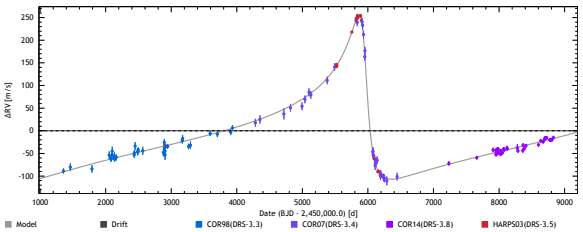

HD 219509

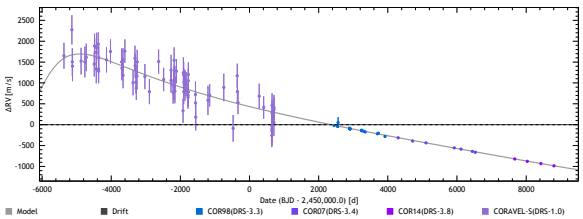

HD 221146

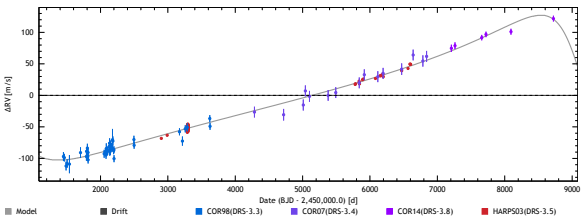

4.3 Target selection for SPHERE

As a follow-up to the direct imaging efforts with VLT/NACO, I coordinated the long-period search for exoplanets with CORALIE over the past ∼3 years and selected the most promising long-period RV companions reported in Rickman et al. (2019) and other unpublished RV curves from the CORALIE and HARPS samples to directly image using VLT/SPHERE. The aim of this is to either confirm the direct detection of the companion detected with RVs and characterise the orbit and dynamical mass, or narrow down the mass-separation parameter space in which a companion lies.

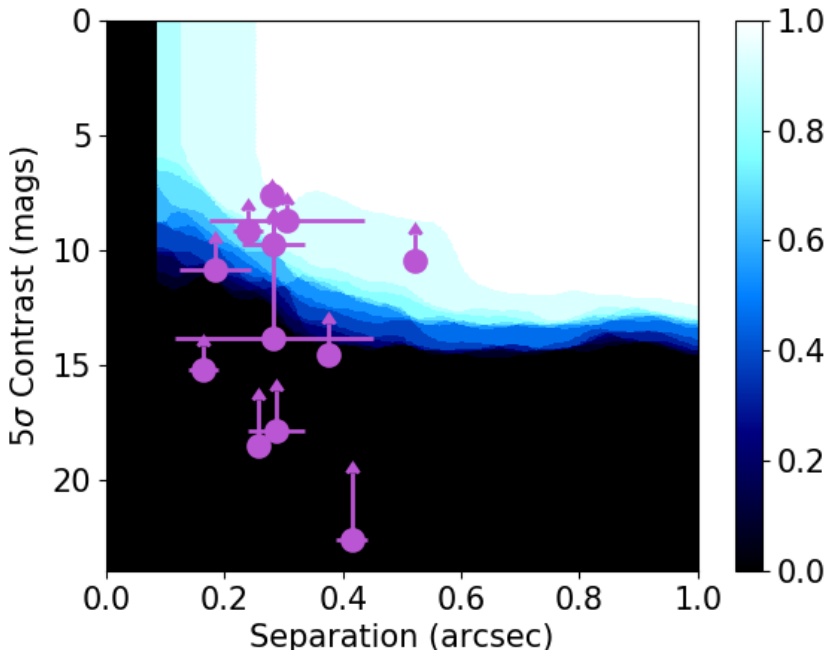

Fig. 4.2 Measured SPHERE $5-\sigma$ contrast curves with each observed or accepted target to be observed with VLT/SPHERE. The colour bar represents the likelihood of detecting a companion at $5-\sigma$ as a function of separation and contrast.

Over the course of my PhD, I wrote several observing proposals as principal investigator to follow-up these CORALIE and HARPS targets with VLT/SPHERE and was successful in being awarded observing time for all of them. Each target was selected according to their orbital configurations. An initial target selection was carried out to select targets with angular separation between the star and expected position of the companion, $\rho > 200$ mas, orbital period $P < 50$ yr and minimum mass $m \sin i > 8\ M_{\rm Jup}$. For each target, using the RV curves, I calculated the expected positions of each companion and the minimum mass ($m \sin i$) whilst simultaneously varying the unknown inclination angle from 0-90 degrees to give a minimum and maximum expected separation and mass of each companion. By combining the COND isochrones (Baraffe et al. 2003) for planetary and brown dwarf masses with the BHAC15 isochrones (Baraffe et al. 2015) for stellar masses, I estimated the contrast ratios for each system, allowing me to

judge the detectability of each companion candidate based on the measured SPHERE performance (see Fig. 4.2). The contrast range shown for each target is calculated for an age range of the host star between 1-4 Gyr, using the minimum mass ($m.\sin i$) taken from each RV curve, which provides an upper limit for the contrast ratio. The colour bar represents the likelihood of detecting the companion given the minimum mass from each RV curve.

4.4 Observing strategy

In order to use angular differential imaging on the data (see Chapter 2.5.1), it is important to gain as much field rotation as possible. Therefore, long exposures whilst the star passes through the meridian passage are necessary. This is important to help pull out a signal from an orbiting companion.

Building upon a pilot study of imaging ultracool brown dwarfs around main sequence stars with VLT/SPHERE (program ID: 099.C-0765(A), PI: Cheetham), we know that we can achieve $\Delta H \sim 13.5$ with ~ 3 hours of observations. Using the Exposure Time Calculator[2], I estimated the expected field rotation of each target over a 3 hour observation, which typically ranges from 40-120 degrees. This is sufficient to carry out ADI on the data.

For each observation, I chose to observe using the IRDIS in the $H23$ bands and IFS in its normal mode with the coronagraph (see Chapter 2.4 for details). This is because in order to achieve the required contrasts at such small angular separations, a combination of ADI and SDI techniques are required. The SPHERE IRDIFS mode allows sufficient spectral coverage to apply SDI to both IRDIS and IFS data, and enough spectral coverage to characterise any detected planets, while avoiding problems caused by the high thermal background apparent in the K band data taken in IRDIFS extended mode.

4.5 Data analysis

I performed an initial modelling of the RV time series using the online DACE platform. Initial Keplerian model conditions are computed using the formalism described in Delisle et al. (2016). The stellar-activity de-trending (where necessary) and the modelling of the instrumental noise and the stellar jitter follow the formalism described in Díaz et al. (2016) and Delisle et al. (2018). Analytical false-alarm probabilities (FAPs) are computed on the periodogram of the residuals following Baluev (2008). Periodic signals with a FAP lower than 0.1% are considered significant and are added to the model. For each periodogram shown in the following section, the three lines represent the 10, 1 and 0.1% FAP in ascending order.

For targets where we only have a signal from RV data and no direct detection, or targets that have not been imaged yet, the RV time series is first modelled using the DACE online tools. The model is fit with offsets between the different instruments with RV data (e.g. CORALIE, HARPS, Hamilton etc.). The CORALIE data is split into three different 'instruments' corresponding to two major upgrades since its installation in 1998 to increase overall efficiency and accuracy of the instrument. These were

[2]The SPHERE-IRDIS exposure time calculate can be found here: https://www.eso.org/observing/etc/bin/gen/form?INS.NAME=SPHERE+INS.MODE=IRDIS

carried out in 2007 and 2014 (Ségransan et al. 2010), and have caused known defined offsets between these three different time periods. The CORALIE data is therefore referred to as COR-98, COR-07, and COR-14 throughout this Chapter.

For each system I have ran a Markov Chain Monte Carlo (MCMC) analysis using the algorithm described in Díaz et al. (2014, 2016) and Delisle et al. (2018) to obtain the posterior distributions of the model parameters. Each MCMC simulation is run with 10,000,000 iterations drawing the proposal solution obtained using DACE. The parameter confidence intervals are computed for a 68.27% confidence level. A full description of the processing and analysis of the RV data can be found in Rickman et al. (2019).

The SPHERE imaging data is reduced using the Geneva Reduction and Analysis Pipeline for High-contrast Imaging of planetary Companions (GRAPHIC, Hagelberg et al. 2016). A full description of the high-contrast imaging data reduction, processing and analysis is described in Chapter 2.5.

4.6 Followed-up targets

In Table 4.2 all of the ESO VLT/SPHERE proposals that I have led to directly image these long-period RV companions are listed. Each proposal is listed with the ESO ID and awarded time with their corresponding target, time on target, observing mode, status of observation, date of observation, in addition to the field rotation achieved and the grade corresponding to the observing conditions when the target was observed. Grade A corresponds to when all of the constraints (weather or otherwise) are adhered to. Grade B corresponds to <10% violated constraints, which can be the case if the weather changes during the observation.

For each target in this section, I present the stellar parameters of each host star, the RVs, the high-contrast imaging data or future plans for high-contrast imaging data, and where relevant, a combined analysis of the RV and high-contrast imaging data. Along with the high-contrast imaging data, I also present calculated contrast curves which show the $5-\sigma$ contrast as a function of separation that is achieved on the high-contrast data for each target (similarly to the combined $5-\sigma$ contrast detectability map shown in Fig. 4.2). The contrast curve for high-contrast imaging data defines whether a signal of a companion candidate would be detectable at $5-\sigma$ at a given separation from the stellar host. This is of particular importance in the case of non-detections, where the contrast level determines an upper limit on the luminosity of a companion. In most cases of non-detection, this rules out a bright stellar companion as it would typically be brighter than the $5-\sigma$ contrast limit, and therefore one would expect to detect such an object in the high-contrast images.

In the following section I present updated RV measurements and orbital solutions for HD 92987 and HD 92788. I also present new direct detections of companions to HD 92987, HD 206505 and HIP 22059. Additionally, I present new RV companion candidates from the CORALIE sample and HARPS data for HD 216770, HIP 12436, HD 28185, HD 112863, HD 143616, HD 195010 and HD 157338. The only target listed in Table 4.2 that is not discussed in the following section is HD 13724, which is discussed in depth in Chapter 5.

Table 4.2 Complete list of proposed and accepted targets.

ESO ID	Awarded hours	Target	On target hours	Obs. mode	Status	Grade	Field rotation degrees	Date YYYY-MM-DD
0102.C-0236(A)	6.0	HD 13724	3.0	IRDIFS_H23	observed	A	70.02	2018-08-18
0102.C-0236(A)	6.0	HD 92987	3.0	IRDIFS_H23	observed	A	105.23	2018-01-16
0103.C-0199(A)	9.0	HD 112863	-	IRDIFS_H23	terminated	-	-	-
0103.C-0199(A)	9.0	HD 157338	-	IRDIFS_H23	terminated	-	-	-
0103.C-0199(A)	9.0	HD 206505	3.0	IRDIFS_H23	observed	B	38.81	2019-08-06
0104.C-0724(A)	10.0	HIP 12436	1.5	IRDIFS_H23	observed	A	18.39	2019-10-28
0104.C-0724(A)	10.0	HIP 12436	1.5	IRDIFS_H23	observed	B	13.17	2019-11-01
0104.C-0724(A)	10.0	HIP 22059	0.25	IRDIFS_H23	observed	A	9.21	2019-11-26
0104.C-0724(A)	10.0	HD 216770	1.5	IRDIFS_H23	observed	B	7.46	2019-10-12
0104.C-0724(A)	10.0	HD 216770	1.5	IRDIFS_H23	observed	B	9.28	2019-11-16
0104.C-0724(A)	10.0	HD 28185	1.5	IRDIFS_H23	observed	A	41.33	2019-12-11
0104.C-0724(A)	10.0	HD 28185	1.5	IRDIFS_H23	observed	A	15.78	2019-12-12
0104.C-0724(A)	10.0	HD 92788	1.5	IRDIFS_H23	observed	A	30.68	2020-01-11
0105.C-0072(A)	12.0	HD 112863	-	IRDIFS_H23	accepted	-	-	-
0105.C-0072(A)	12.0	HD 143616	-	IRDIFS_H23	accepted	-	-	-
0105.C-0072(A)	12.0	HD 157338	-	IRDIFS_H23	accepted	-	-	-
0105.C-0072(A)	12.0	HD 195010	-	IRDIFS_H23	accepted	-	-	-

4.7 Direct detections

4.7.1 HD 92987

The stellar characteristics of HD 92987 are listed in Table 4.3. The spectral type, V band magnitude and colour index are taken from *Hipparcos* (Perryman et al. 1997). The parallax π, luminosity, radius and effective temperature are taken from the second *Gaia* data release (Gaia Collaboration et al. 2018). The mass and age of HD 92987 are taken from Rickman et al. (2019) which were derived using the Geneva stellar-evolution models (Ekström et al. 2012; Georgy et al. 2013).

Table 4.3 Stellar characteristics of HD 92987.

Parameter	Units	HD 92987	Reference
Spectral Type		G2/3V	Perryman et al. (1997)
V		7.03	Perryman et al. (1997)
$B-V$		0.641	Perryman et al. (1997)
$T_{\rm eff}$	[K]	5770 ± 36	Rickman et al. (2019)
[Fe/H]	[dex]	-0.08 ± 0.08	Rickman et al. (2019)
Mass	[$M_{\odot}$]	1.08 ± 0.06	Rickman et al. (2019)
π	[mas]	22.94 ± 0.04	Gaia Collaboration et al. (2018)
Age	[Gyr]	7.75 ± 0.31	Rickman et al. (2019)
Radius	[$R_{\odot}$]	1.58 ± 0.04	Gaia Collaboration et al. (2018)
Luminosity	[$L_{\odot}$]	2.55 ± 0.006	Gaia Collaboration et al. (2018)

Radial velocities

HD 92987 has been observed with CORALIE since January 1999. Since Rickman et al. (2019) we have taken an additional 18 RV points, increasing the time baseline by $\sim$ 1 year. From the RV data alone, we get a minimum mass ($m \sin i$) of $\sim$ 16 $M_{\rm Jup}$, which made it a top priority companion candidate to directly image with VLT/SPHERE.

The fit to the RV data, along with the corresponding residuals, phase-folded diagram and periodogram after removing the long-period signal is seen in Fig. 4.3. We see that most of the orbital period is covered which already allows us to place constraints on the orbital parameters of the companion.

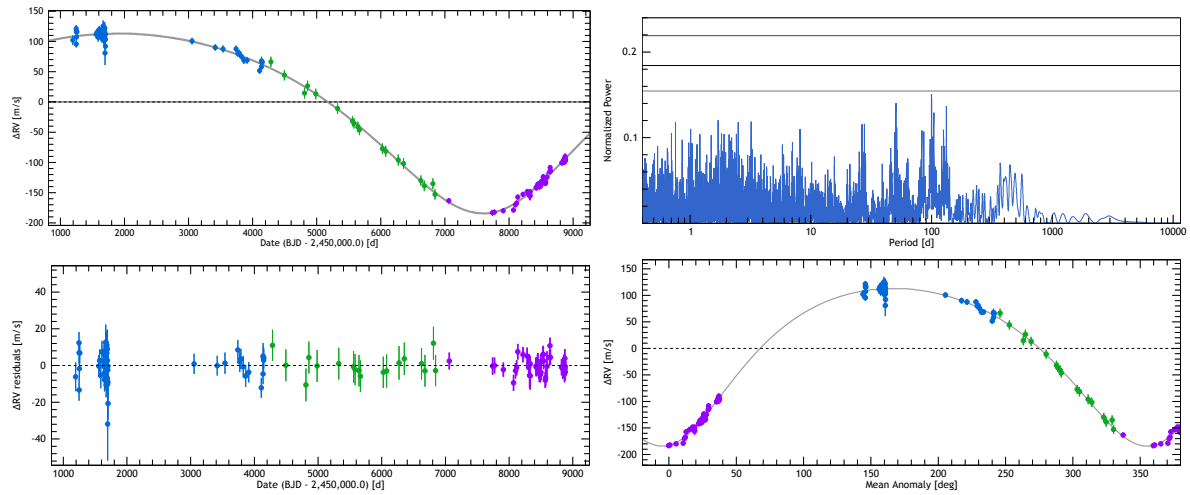

Fig. 4.3 *Top left:* HD 92987 RV measurements as a function of Julian Date. The blue data are COR-98; the green data are COR-07 and the purple data are COR-14. *Bottom left:* The residuals. *Top right:* The periodogram of the residuals of HD 92987 after the planetary signal has been removed, indicating that there are no more significant signals remaining in the data. The three black lines represent the 10, 1 and 0.1% FAPs in ascending order. *Bottom right:* Phase-folded curve for HD 92987 B.

High-contrast imaging

HD 92987 was observed with VLT/SPHERE (program ID: 0102.C-0236(A), PI: Rickman) in the $H2$ ($\lambda_{H2} = 1.58888\mu$m) and $H3$ ($\lambda_{H3} = 1.6671\mu$m) bands on 16-01-2018. The observing conditions at Paranal Observatory fluctuated between clear and thin clouds, but otherwise the constraints of the observations were met and the weather was relatively stable with an average seeing of 0.52" during the observation.

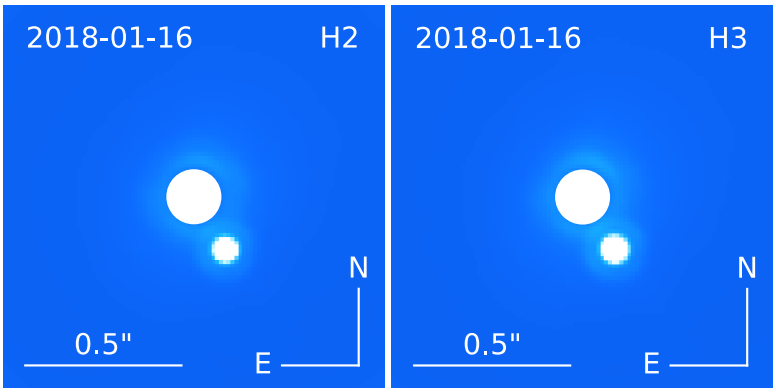

Fig. 4.4 Classical angular differential high-contrast images of HD 92987 in $H2$ and $H3$ bands.

The imaging data were reduced using the classical ADI method with the GRAPHIC pipeline (Hagelberg et al. 2016) described in Chapter 2.5. In the reduced high-contrast images we see a clear detection of a massive companion. We fit for the separation (in pixels), position angle (in degrees) and

contrast ratio between the star and the companion using a negative fake planet injection (Bonnefoy et al. 2011). To convert from pixels to separation in milliarcseconds (mas) and to correct to the True North angle offset, we use the calibration given in Maire et al. (2016). We correct for the Neutral Density (ND) transmission using the SPHERE ND filter curves.[3]

We obtain a contrast ratio between the star and the companion of 5.12 ± 0.01 mag which corresponds to an isochronal mass estimate of $\sim 314\ M_{\rm Jup}$ or $\sim 0.3\ M_{\odot}$, if the age of the system is taken to be 8 Gyr (Baraffe et al. 2015), meaning that the companion is of stellar nature. The classical ADI images in the $H2$ and $H3$ band are shown in Fig. 4.4. A $5-\sigma$ contrast curve corresponding to the $H2$ band is shown in Fig. 4.5.

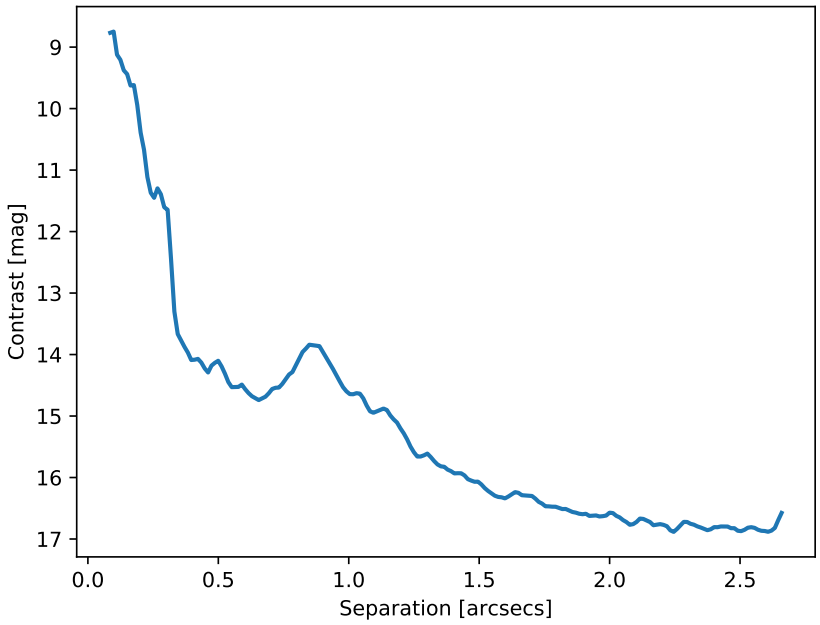

Fig. 4.5 $H2$ Contrast curve for HD 92987.

Combined analysis

The direct detection of the companion in the image agrees with a companion that is causing the signal in the RV curve. As we have a clear detection of HD 92987 B in the images, we do a combined fit for the RV and imaging data, which includes fitting for the inclination of the system in order to obtain a dynamical mass of the companion. For the combined fit we use the astrometry derived from the IRDIS $H2$ images along with the RV measurements. A full description is given in Chapter 2.7.

[3] ND filter curves are given at https://www.eso.org/sci/facilities/paranal/instruments/sphere/inst/filters.html.

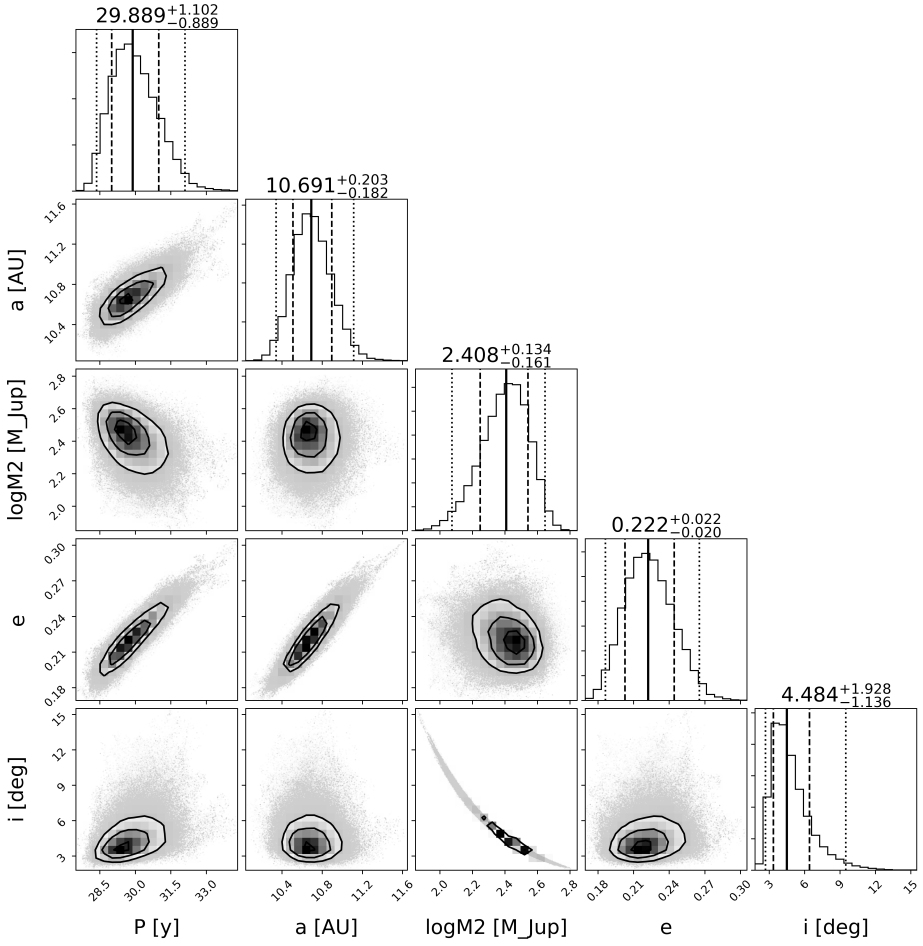

Fig. 4.6 Marginalised 1D and 2D posterior distributions for HD 92987 of the orbital period, the semi-major axis, the log of the companion mass, as well as the eccentricity and inclination corresponding to the global fit of the RV and direct-imaging models. Confidence intervals at 2.275%, 15.85%, 50.0%, 84.15%, 97.725% are overplotted on the 1D posterior distributions, while the median $\pm 1\sigma$ values are given at the top of each 1D distribution. Here, the 1, 2, and 3 σ contour levels are overplotted on the 2D posterior distribution.

From the combined fit, we obtain a dynamical mass of 257^{+90}_{-79} $M_{\rm Jup}$ within the 95% confidence interval, which is in agreement with the isochronal mass estimate. The posterior distributions of the physical parameters obtained from the combined fit are shown in Fig. 4.6.

Because $T_{V_{\rm min}}$ is better constrained than $T_{V_{\rm max}}$, $T_{V_{\rm min}}$ is used as a prior in the global fitting of the RV and imaging data. From the combined fit, we obtain an orbital period of $29.89^{+1.10}_{-0.89}$ years. The system has a small inclination ($4.48^{+1.93}_{-1.14}$ deg) meaning that the companion is close to a face-on orbit. The full list of orbital parameters are listed in Table 4.4.

From the posterior distributions shown in Fig 4.6, we can see that there are strong correlations between certain orbital parameters, for example $\log M_2$ and the inclination. This is expected, as the dynamical mass is strongly dependent on the inclination of the system. In addition, we see a correlation between the eccentricity and the orbital period and semi-major axis. Again this is expected, as the orbital period and semi-major axis have a strong dependency on the eccentricity of the system. To further constrain these variables, follow-up observations of HD 92987 B would be required, adding an additional epoch of astrometric data to the combined fit.

Table 4.4 Orbital parameters of HD 92987 B.

Parameter	Units	HD 92987 B
P	[years]	$29.89^{+1.10}_{-0.89}$
K	[m/s]	$153.10^{+3.78}_{-3.91}$
e		0.22 ± 0.02
ω_0	[deg]	$-172.26^{+10.48}_{-6.51}$
$T_{V_{\rm min}}$	[BJD]	$57588.67^{+51.53}_{-55.07}$
$m \sin i$	[$M_{\rm Jup}$]	$20.03^{+1.11}_{-1.04}$
$\log m_2$	[$M_{\rm Jup}$]	$2.41^{+0.13}_{-0.16}$
a	[AU]	$10.69^{+0.42}_{-0.34}$
i	[deg]	$4.48^{+1.93}_{-1.14}$

4.7.2 HIP 22059

The stellar characteristics of HIP 22059 are listed in Table 4.5. The spectral type, V band magnitude and colour index are taken from *Hipparcos* (Perryman et al. 1997). The parallax π, luminosity, radius and effective temperature are taken from the second *Gaia* data release (Gaia Collaboration et al. 2018). The mass and age of HIP 22059 are taken from Soto & Jenkins (2018).

Table 4.5 Stellar characteristics of HIP 22059.

Parameter	Units	HIP 22059	Reference
Spectral Type		K5V	Perryman et al. (1997)
V		9.57	Perryman et al. (1997)
$B-V$		0.95	Perryman et al. (1997)
$T_{\rm eff}$	[K]	$4698.81^{+165.29}_{-97.31}$	Gaia Collaboration et al. (2018)
[Fe/H]	[dex]	-0.35 ± 0.17	Soto & Jenkins (2018)
Mass	[$M_\odot$]	$0.68^{+0.03}_{-0.02}$	Soto & Jenkins (2018)
π	[mas]	32.16 ± 0.03	Gaia Collaboration et al. (2018)
Age	[Gyr]	$12.98^{+4.52}_{-6.46}$	Soto & Jenkins (2018)
Radius	[$R_\odot$]	$0.65^{+0.03}_{-0.04}$	Gaia Collaboration et al. (2018)
Luminosity	[$L_\odot$]	0.19 ± 0.0002	Gaia Collaboration et al. (2018)

Radial velocities

HIP 22059 has been observed with CORALIE since January 2001. There is also HARPS data from December 2003 until August 2007. It has a minimum mass of $158.83^{+39.36}_{-36.97}$ $M_{\rm Jup}$ placing in it in the stellar regime. We fit for a stellar jitter parameter when fitting the Keplerian. As the $T_{V_{\rm max}}$ is well covered, this is used as a prior in the global fit of the RV and imaging data. The fitted RV curve, phase-foleded diagram, the residuals and periodogram are shown in Fig. 4.7. The fitted orbital parameters are listed in Table 4.6.

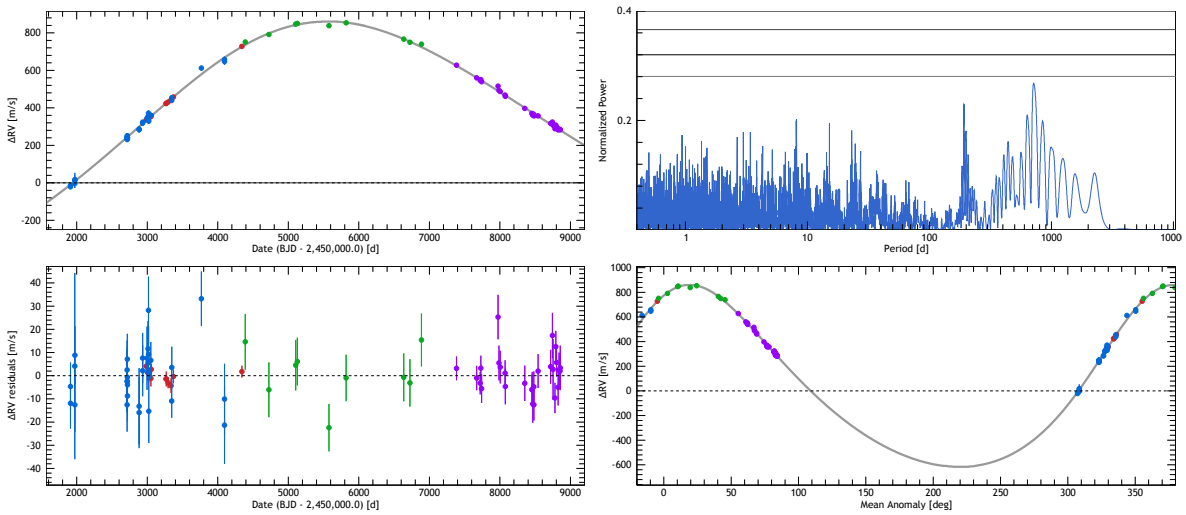

Fig. 4.7 *Top left:* HIP 22059 RV measurements as a function of Julian Date. The blue data are COR-98; the green data are COR-07, the red data are HARPS and the purple data are COR-14. *Bottom left:* The residuals. *Top right:* The periodogram of the residuals of HIP 22059 after the planetary signal has been removed, indicating that there are no more significant signals remaining in the data. The three black lines represent the 10, 1 and 0.1% FAPs in ascending order. *Bottom right:* Phase-folded curve for HIP 22059 B.

High-contrast imaging

HIP 22059 was observed with VLT/SPHERE (program ID: 0104.C-0724(A), PI: Rickman) on 26-11-2019 in the $H2$ ($\lambda_{H2} = 1.58888\ \mu$m) and $H3$ ($\lambda_{H3} = 1.6671\ \mu$m) bands. The observation was aborted after approximately 15 minutes due to a bright stellar companion in the raw images which can be seen in the classical ADI $H2$ and $H3$ band images in Fig. 4.8. The weather was good with photometric conditions during the time of observation and seeing around 0.60". The $5-\sigma$ contrast curve from the $H2$ band image can be seen in Fig. 4.9.

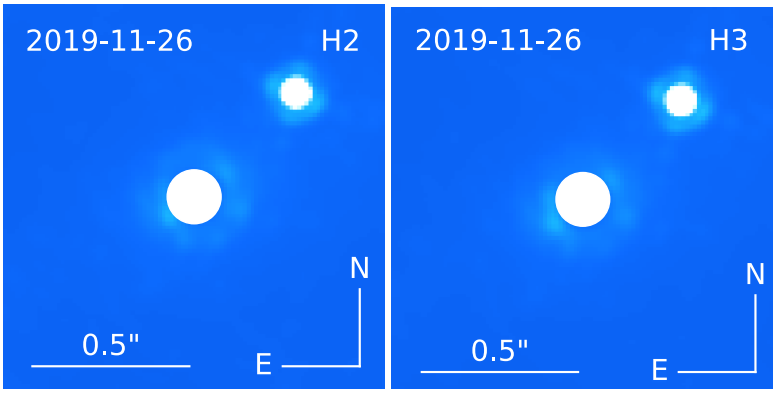

Fig. 4.8 $H2$ and $H3$ band high-contrast images of HIP 22059.

We fit for the separation (in pixels), position angle (in degrees) and contrast ratio between the star and the companion using a negative fake planet injection (Bonnefoy et al. 2011). To convert from pixels to separation in mas and to correct for the True North angle offset, we use the calibration given in (Maire et al. 2016). We correct for the ND transmission using the SPHERE ND filter curves.

From the negative fake planet injection fit, we obtain a contrast ratio between HIP 22059 and the companion of 3.40 ± 0.01 mag which corresponds to an isochronal mass estimate of $\sim 0.3\ M_{\odot}$ (Baraffe et al. 2015), meaning that HIP 22059 B is a low-mass star.

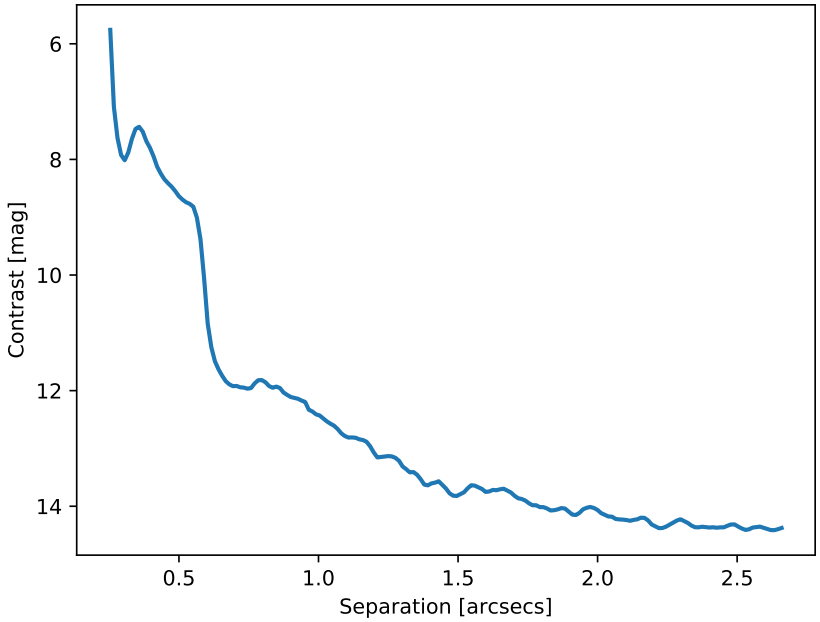

Fig. 4.9 $H2$ Contrast curve for HIP 22059.

Combined analysis

The direct detection seen in Fig. 4.8 agrees with the companion measured by the RV curve. We do a combined fit for the RV and imaging data, including fitting for the inclination of the system in order to obtain a dynamical mass of the companion. For the combined fit we use the astrometry derived from the IRDIS $H2$ images along with the RV measurements. A full description is given in Chapter 2.7.

From the combined fit, we obtain a dynamical mass of $281.84^{+125.54}_{-12.69}\ M_{\rm Jup}$, which agrees with the isochronal mass estimate. The upper mass of the companion is not so well constrained as the RV measurements themselves are not so well constrained as only a small span of the orbital phase is covered as seen in the phase-folded diagram in Fig. 4.7.

As $T_{V_{\rm max}}$ is somewhat constrained, we use this as a prior in the global fit of the RV and imaging data. From the combined fit, we obtain an orbital period of $111.75^{+76.07}_{-48.16}$ years, where the period covers a wide

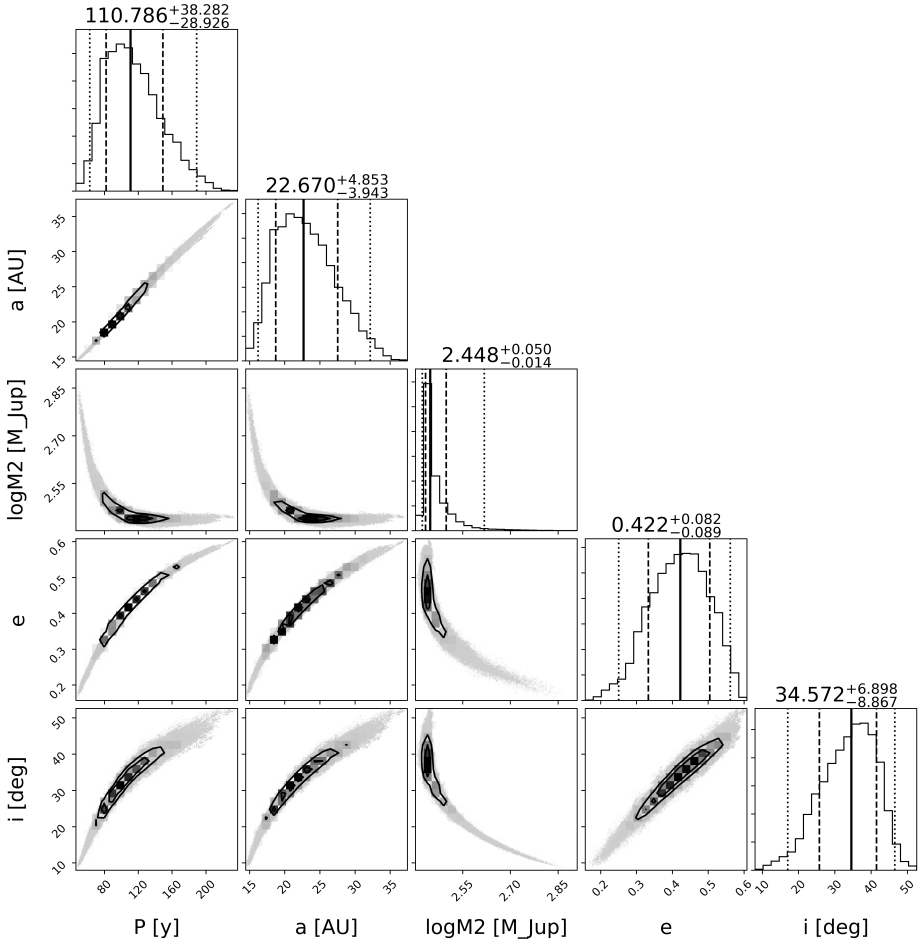

Fig. 4.10 Marginalised 1D and 2D posterior distributions for HIP 22059 of the orbital period, the semi-major axis, the log of the companion mass, as well as the eccentricity and inclination corresponding to the global fit of the RV and direct-imaging models. Confidence intervals at 2.275%, 15.85%, 50.0%, 84.15%, 97.725% are overplotted on the 1D posterior distributions, while the median $\pm 1\sigma$ values are given at the top of each 1D distribution. Here, the 1, 2, and 3 σ contour levels are overplotted on the 2D posterior distribution.

span due to mostly unconstrained RV measurements. An additional epoch of imaging data where the companion has moved significantly would help further constrain the mass and period of HIP 22059 B.

Table 4.6 Orbital parameters of HIP 22059.

Parameter	Units	HIP 22059 B
P	[years]	$111.75^{+76.07}_{-48.16}$
K	[m/s]	$1073.82^{+166.24}_{-216.73}$
e		$0.43^{+0.14}_{-0.17}$
ω_0	[deg]	$-15.82^{+2.66}_{-6.66}$
$T_{V_{\rm max}}$	[BJD]	$55570.009^{+24.08}_{-25.36}$
$m \sin i$	[$M_{\rm Jup}$]	$158.83^{+39.36}_{-36.97}$
$\log m_2$	[$M_{\rm Jup}$]	$2.45^{+0.16}_{-0.02}$
a	[AU]	$22.79^{+9.19}_{-6.47}$
i	[deg]	$34.79^{+11.58}_{-17.31}$

From the posterior distributions shown in Fig. 4.10, we can see that there are strong correlations across many of the physical parameters. Therefore, being able to constrain even just one of these parameters would already constrain the parameter space of the other physical parameters.

4.7.3 HD 206505

The stellar characteristics of HD 206505 are listed in Table 4.7. The spectral type, V band magnitude and colour index are taken from *Hipparcos* (Perryman et al. 1997). The metallicity is taken from Mata Sánchez et al. (2014). The parallax π, luminosity, radius and effective temperature are taken from the second *Gaia* data release (Gaia Collaboration et al. 2018). The mass and age of HD 206505 are derived using the Geneva stellar-evolution models (Ekström et al. 2012; Georgy et al. 2013).

Table 4.7 Stellar characteristics of HD 206505.

Parameter	Units	HD 206505	Reference
Spectral Type		K0V	Perryman et al. (1997)
V		8.73	Perryman et al. (1997)
$B-V$		0.819	Perryman et al. (1997)
$T_{\rm eff}$	[K]	$5377^{+50.33}_{-58.10}$	Gaia Collaboration et al. (2018)
[Fe/H]	[dex]	0.11 ± 0.03	Mata Sánchez et al. (2014)
Mass	[$M_{\odot}$]	0.93 ± 0.02	Ekström et al. (2012); Georgy et al. (2013)
π	[mas]	22.72 ± 0.03	Gaia Collaboration et al. (2018)
Age	[Gyr]	4.32 ± 2.76	Ekström et al. (2012); Georgy et al. (2013)
Radius	[$R_{\odot}$]	0.89 ± 0.02	Gaia Collaboration et al. (2018)
Luminosity	[$L_{\odot}$]	0.595 ± 0.001	Gaia Collaboration et al. (2018)

Radial velocities

HD 206505 has been observed with CORALIE since October 2001. It has a minimum mass of $75.04^{+2.98}_{-2.09}$ $M_{\rm Jup}$, placing it in a mass regime between a high-mass brown dwarf or a very low-mass star. The system is quite eccentric with an eccentricity of 0.61 ± 0.01. The $T_{V_{\rm max}}$ of the HD 206505 B is quite well constrained, so this is used to fit the RV data.

The resulting RV curve fit, the residuals, phase-folded diagram and the periodogram after the RV signal has been removed are shown in Fig. 4.11. The orbital parameters from the global RV and imaging data are shown in Table 4.8.

High-contrast imaging

HD 206505 was observed with VLT/SPHERE (program ID: 0103.C-0199(A), PI: Rickman) in the $H2$ ($\lambda_{H2} = 1.58888\mu$m) and $H3$ ($\lambda_{H3} = 1.6671\mu$m) bands on 06-08-2019. The requested observing

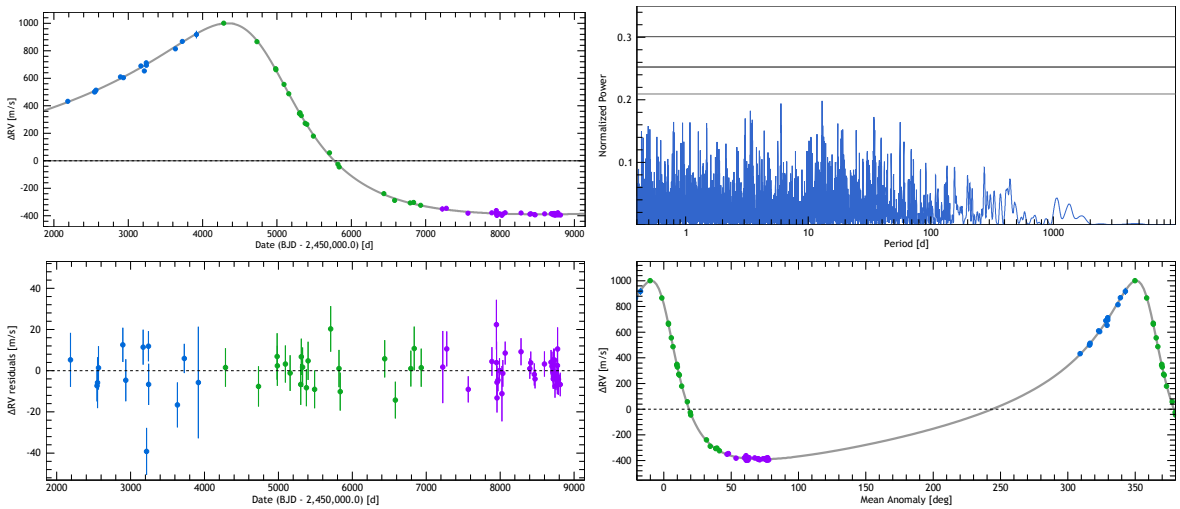

Fig. 4.11 *Top left:* HD 206505 RV measurements as a function of Julian Date. The blue data are COR-98; the green data are COR-07 and the purple data are COR-14. *Bottom left:* The residuals. *Top right:* The periodogram of the residuals of HD 206505 after the planetary signal has been removed, indicating that there are no more significant signals remaining in the data. The three black lines represent the 10, 1 and 0.1% FAPs in ascending order. *Bottom right:* Phase-folded curve for HD 206505 B.

constraints were mostly met, with photometric conditions throughout most of the observation and seeing between 0.6"-1.0" during the observation.

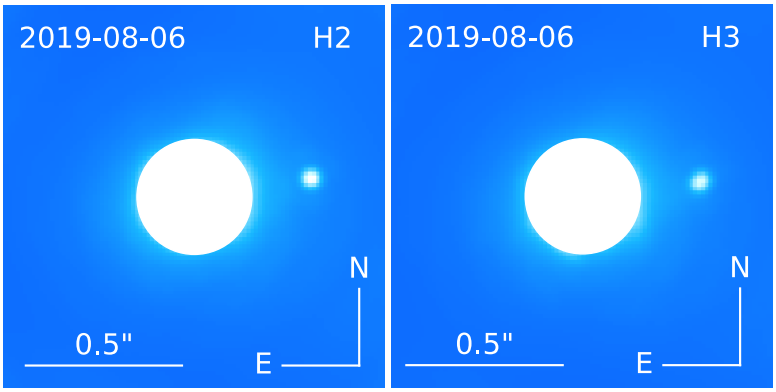

Fig. 4.12 High-contrast image of HD 206505.

The imaging data were reduced using the classical ADI method with the GRAPHIC pipeline (Hagelberg et al. 2016) described in Chapter 2.5. In the reduced high-contrast images shown in Fig. 4.12 we see a clear detection of a companion. We fit for the separation (in pixels), position angle (in degrees) and contrast ratio between the star and the companion using a negative fake planet injection (Bonnefoy et al. 2011). To convert from pixels to separation in mas and to correct for the True North angle offset, we use the calibration given in Maire et al. (2016). We correct for the ND transmission using the SPHERE ND filter curves.

We obtain a contrast ratio between the star and the companion of 7.56 ± 0.02 mag which corresponds to an isochronal mass estimate of $\sim 80\ M_{\rm Jup}$ if we take the age of the system to be 4 Gyr (Baraffe et al. 2015), which sits close to the border between a high-mass brown dwarf and a very low-mass star. The measured $5-\sigma$ corresponding to the $H2$ band is shown in Fig. 4.13.

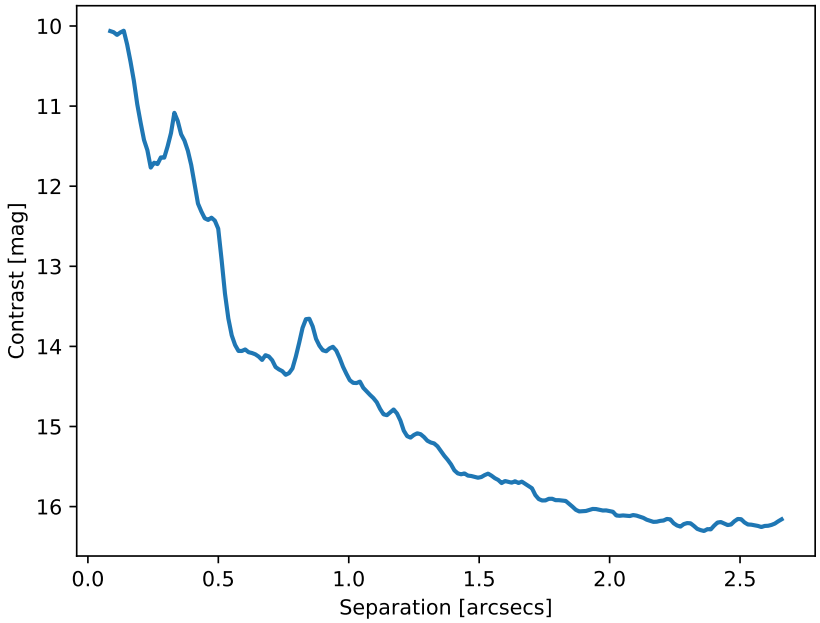

Fig. 4.13 $H2$ contrast curve for HD 206505.

Combined analysis

The direct detection of the companion in the image agrees with the companion that is measured by the RV curve. As we have a clear direct detection of HD 206505 B, we do a combined fit for the RV and imaging data, which includes fitting for the inclination of the system in order to obtain a dynamical mass of the companion. For the combined fit we use the astrometry derived from the IRDIS $H2$ images along with the RV measurements. A full description is given in Chapter 2.7.

From the combined fit, we obtain a dynamical mass of $83.18^{+29.02}_{-9.05} M_{\rm Jup}$, which agrees with the isochronal mass estimate. The mass is interesting as it sits at the border of what is considered a high-mass brown dwarf and what is considered a very low-mass star. In order to study the nature of this companion in more depth, additional imaging data would help constrain the dynamical mass, in addition analysing the spectral data would decipher the spectral type of the companion.

Because $T_{V_{\rm max}}$ is well constrained, this is used as a prior in the global fitting of the RV and imaging data. From the combined fit, we obtain an orbital period of $54.24^{+1.83}_{-1.80}$ years. The system is highly inclined, with an inclination angle of $90.17^{+37.21}_{-37.57}$ deg, meaning that the companion is closer to an

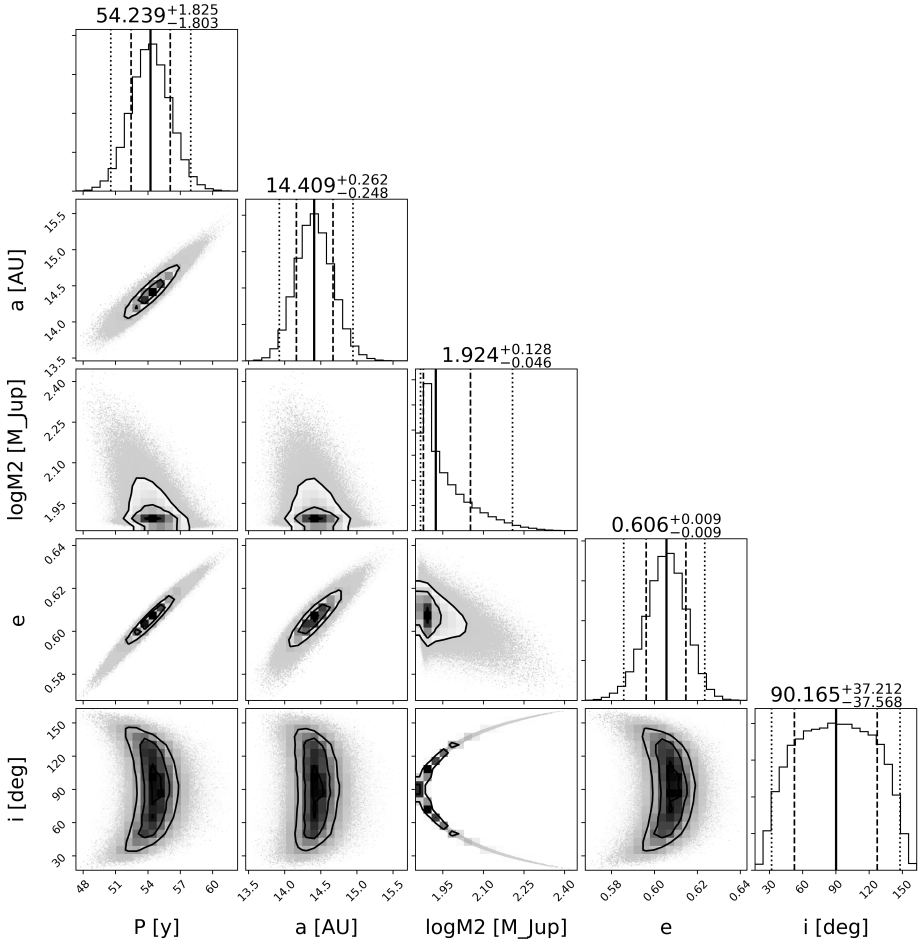

Fig. 4.14 Marginalised 1D and 2D posterior distributions for HD 206505 of the orbital period, the semi-major axis, the log of the companion mass, as well as the eccentricity and inclination corresponding to the global fit of the RV and direct-imaging models. Confidence intervals at 2.275%, 15.85%, 50.0%, 84.15%, 97.725% are overplotted on the 1D posterior distributions, while the median $\pm 1\sigma$ values are given at the top of each 1D distribution. Here, the 1, 2, and 3 σ contour levels are overplotted on the 2D posterior distribution.

edge-on orientation. The companion also is also relatively eccentric with an eccentricity of 0.61 ± 0.01. The full list of orbital parameters are listed in Table 4.8.

Table 4.8 Orbital parameters of HD 206505 B.

Parameter	Units	HD 206505 B
P	[years]	$54.24^{+1.83}_{-1.80}$
K	[m/s]	$700.851^{+6.82}_{-13.53}$
e		0.61 ± 0.01
ω_0	[deg]	44.29 ± 1.29
$T_{V_{\max}}$	[BJD]	$54299.122^{+14.65}_{-14.96}$
$m \sin i$	[$M_{\rm Jup}$]	$75.04^{+2.98}_{-2.09}$
$\log m_2$	[$M_{\rm Jup}$]	$1.92^{+0.13}_{-0.05}$
a	[AU]	$14.41^{+0.26}_{-0.25}$
i	[deg]	$90.17^{+37.21}_{-37.57}$

From the posterior distributions shown in Fig. 4.14, we can see that there is a strong correlation between the eccentricity and the period and semi-major axis of the companion which is expected as both the period and semi-major axis are highly dependent on the eccentricity of the system. In addition, the inclination probes a relatively wide parameter space, which is high correlated with the mass of the companion. Again, we expect this as the inclination of the system determines the mass with a high dependency. To further constrain these variables, follow-up observations of HD 206505 B would be required. Adding an additional epoch astrometric data to the fit would help constrain the orbital period, eccentricity, inclination and therefore the dynamical mass of the companion.

4.8 Radial-velocity detections

4.8.1 HD 216770

The stellar characteristics of HD 216770 are listed in Table 4.9. The spectral type, V band magnitude and colour index are taken from *Hipparcos* (Perryman et al. 1997). The parallax π, luminosity, radius and effective temperature are taken from the second *Gaia* data release (Gaia Collaboration et al. 2018). The mass and age of HD 216770 are derived using the Geneva stellar-evolution models (Ekström et al. 2012; Georgy et al. 2013).

Table 4.9 Stellar characteristics of HD 216770.

Parameter	Units	HD 216770	Reference
Spectral Type		K0V	Perryman et al. (1997)
V		8.10	Perryman et al. (1997)
$B-V$		0.821	Perryman et al. (1997)
$T_{\rm eff}$	[K]	$5385.33^{+58.67}_{-76.33}$	Gaia Collaboration et al. (2018)
[Fe/H]	[dex]	0.24 ± 0.04	Sousa et al. (2008)
Mass	[$M_\odot$]	0.98 ± 0.03	Ekström et al. (2012); Georgy et al. (2013)
π	[mas]	27.25 ± 0.07	Gaia Collaboration et al. (2018)
Age	[Gyr]	5.86 ± 3.30	Ekström et al. (2012); Georgy et al. (2013)
Radius	[$R_\odot$]	0.97 ± 0.02	Gaia Collaboration et al. (2018)
Luminosity	[$L_\odot$]	0.71 ± 0.002	Gaia Collaboration et al. (2018)

Radial velocities

HD 216770 has been observed with CORALIE since September 2000. In addition, it has been observed with HARPS between October 2003 and November 2013. It has a short period planet discovered by Mayor et al. (2004).

Table 4.10 Orbital parameters of HD 216770 b and HD 216770 c.

Parameter	Units	HD 216770 b	HD 216770 c
P	[years]	0.318 ± 0.042	$102.56^{+41.13}_{-48.21}$
K	[m/s]	20.85 ± 0.96	$99.2^{+47.7}_{-52.4}$
e		0.20 ± 0.03	$0.17^{+0.11}_{-0.12}$
ω_0	[deg]	-83.6 ± 9.8	23^{+109}_{-77}
T_0	[BJD]	2455568.16 ± 2.92	$2476121^{+20037}_{-16847}$
$m \sin i$	[$M_{\rm Jup}$]	0.49 ± 0.03	$16.26^{+57.54}_{-9.94}$
a	[AU]	0.47 ± 0.01	$21.50^{+6.18}_{-7.14}$

We fit for both the short and long period planets simultaneously, giving HD 216770 b an orbital period of 0.318 ± 0.042 days and a minimum mass of 0.49 ± 0.03 $M_{\rm Jup}$. The long period companion has a fairly unconstrained orbit with a period of $102.56^{+41.13}_{-48.21}$ years and a minimum mass of $16.26^{+57.54}_{-9.94}$ $M_{\rm Jup}$. Because of the wide separation of HD 216770 c from its host star and its mass, it was selected as a

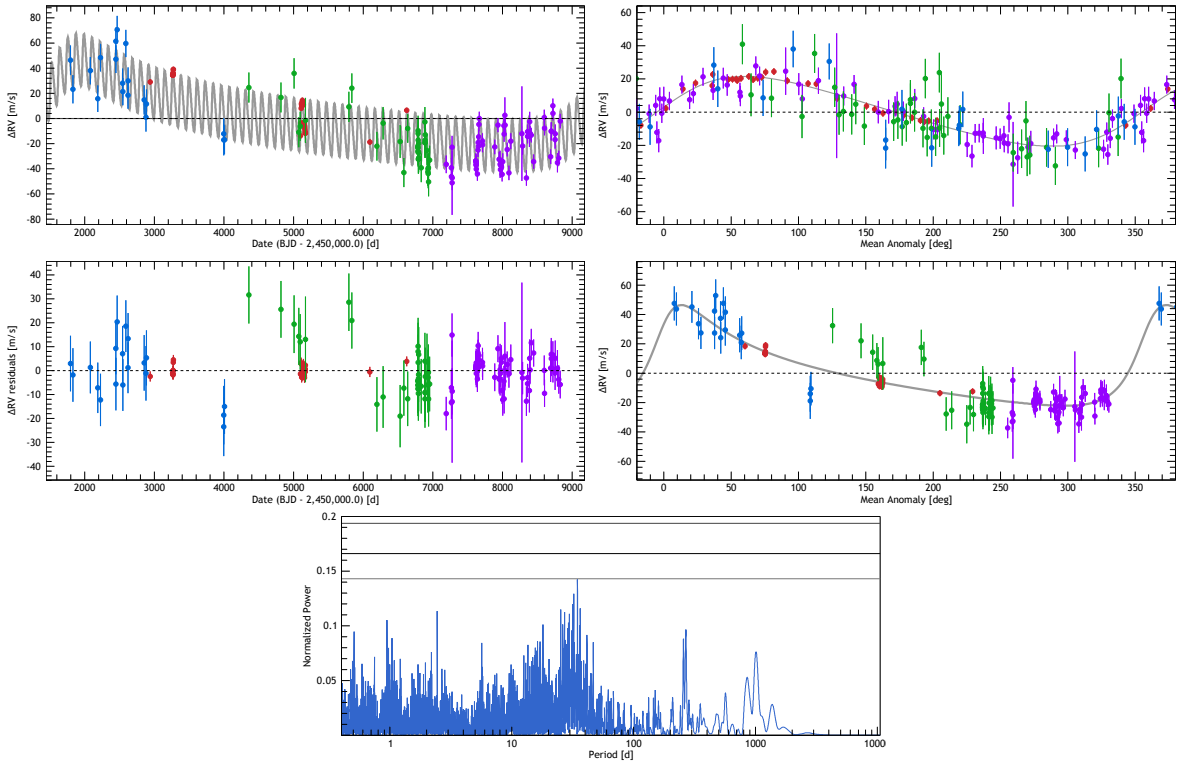

Fig. 4.15 *Top left:* HD 216770 RV measurements as a function of Julian Date. The blue data are COR-98; the green data are COR-07; the purple data are COR-14 and the red data are HARPS. *Middle left:* The residuals after the two planetary signals have been removed. *Top right:* Phase-folded curve for HD 216770 b. *Middle right:* Phase-folded curve for HD 216770 c. *Bottom:* The periodogram of the residuals of HD 216770 after the planetary signal has been removed, indicating that there are no more significant signals remaining in the data. The three black lines represent the 10, 1 and 0.1% FAPs in ascending order.

candidate for follow-up high-contrast imaging. The fitted RV curve for both companions and the residuals can be seen in Fig. 4.15 and the fitted orbital parameters are listed in Table 4.10.

High-contrast imaging

HD 216770 was observed with VLT/SPHERE (program ID: 0104.C-0724(A), PI: Rickman) on 12-10-2019 and 16-11-2019. Due to observing scheduling constraints from Paranal Observatory, they requested that the observations be split into two lots of 1.5 hour observations. The first observation was taken on 12-10-2019 and had clear but windy conditions with a seeing fluctuating between 0.6"-1.0". A second observation of HD 216770 was carried out on 16-11-2019 with clear weather conditions and seeing of about 1.0"-1.4".

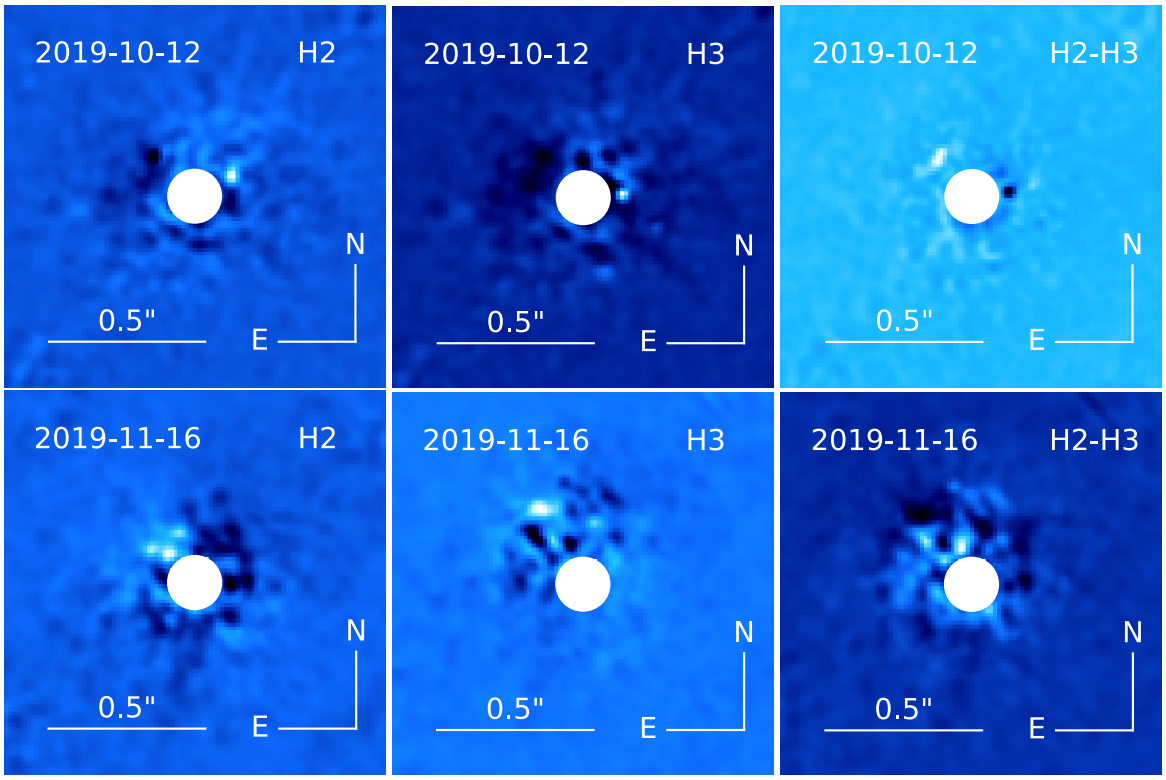

Fig. 4.16 ADI and SDI high-contrast images of HD 216770.

The ADI and SDI high-contrast images are shown in Fig. 4.16. We do not see a detection of a companion in either set of the images. The resulting $5-\sigma$ contrast curve from the $H2$ band image (where we would expect to see the greatest signal) is shown in Fig. 4.17.

Because the observations of HD 216770 were cut in half to be two lots of 1.5 hour observations, we do not reach the desired amount of field rotation, only achieving 7.46 deg and 9.28 deg for each observation. In addition, both observations were listed as grade B due to windy conditions and the seeing was quite high. Both of these factors in turn mean that the level of contrast level that we are able to achieve is not as high as expected, especially at small separations where we still see lots of residual

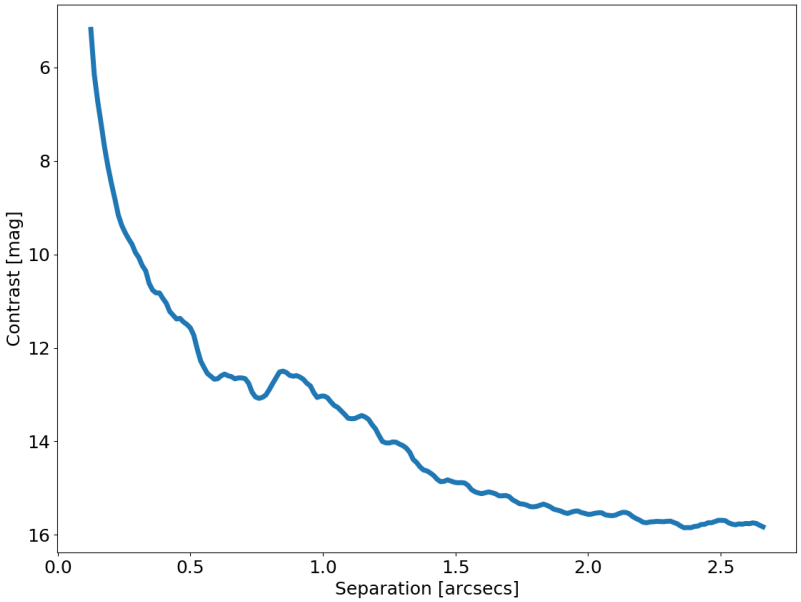

Fig. 4.17 $H2$ contrast curve for HD 216770.

noise in Fig. 4.16. This is particularly true in the observations taken on 16-11-2019 where the seeing was quite high ($\sim 1.0" - 1.4"$) giving less than ideal observing conditions.

HD 216770 c is a likely brown dwarf expected at a wide separation, so should be within the possibility of directly imaging this companion. Future observations with more time on target to achieve a significant increase in the field rotation and therefore the contrast ratio with better observing conditions will increase the possibility of detecting this companion with VLT/SPHERE.

4.8.2 HIP 12436

The stellar characteristics of HIP 12436 are listed in Table 4.11. The spectral type, V band magnitude and colour index are taken from *Hipparcos* (Perryman et al. 1997). The parallax π, luminosity, radius and effective temperature are taken from the second *Gaia* data release (Gaia Collaboration et al. 2018). The mass and age of HIP 12436 are derived using the Geneva stellar-evolution models (Ekström et al. 2012; Georgy et al. 2013).

Table 4.11 Stellar characterisatics of HIP 12436.

Parameter	Units	HIP 12436	Reference
Spectral Type		K3V	Perryman et al. (1997)
V		9.46	Perryman et al. (1997)
$B-V$		1.027	Perryman et al. (1997)
$T_{\rm eff}$	[K]	$4851.67^{+91.83}_{-103.00}$	Gaia Collaboration et al. (2018)
[Fe/H]	[dex]	0.16 ± 0.04	Delgado Mena et al. (2017)
Mass	[$M_{\odot}$]	0.82 ± 0.02	Ekström et al. (2012); Georgy et al. (2013)
π	[mas]	25.14 ± 0.03	Gaia Collaboration et al. (2018)
Age	[Gyr]	5.15 ± 3.98	Ekström et al. (2012); Georgy et al. (2013)
Radius	[$R_{\odot}$]	0.78 ± 0.03	Gaia Collaboration et al. (2018)
Luminosity	[$L_{\odot}$]	0.305 ± 0.001	Gaia Collaboration et al. (2018)

Radial velocities

HIP 12436 has been observed with HARPS since November 2003, with an additional three data points with CORALIE in December 2015. From fitting a single Keplerian to the RV data, we find that HIP 12436 has an orbital period of $28.08^{+1.16}_{-1.17}$ years a minimum mass of 8.66 ± 0.30 $M_{\rm Jup}$. The companion is quite eccentric with an eccentricity of 0.68 ± 0.01. All of the fitted orbital parameters are listed in Table 4.12. The fitted RV curves and corresponding residuals and periodogram can be seen in Fig. 4.18.

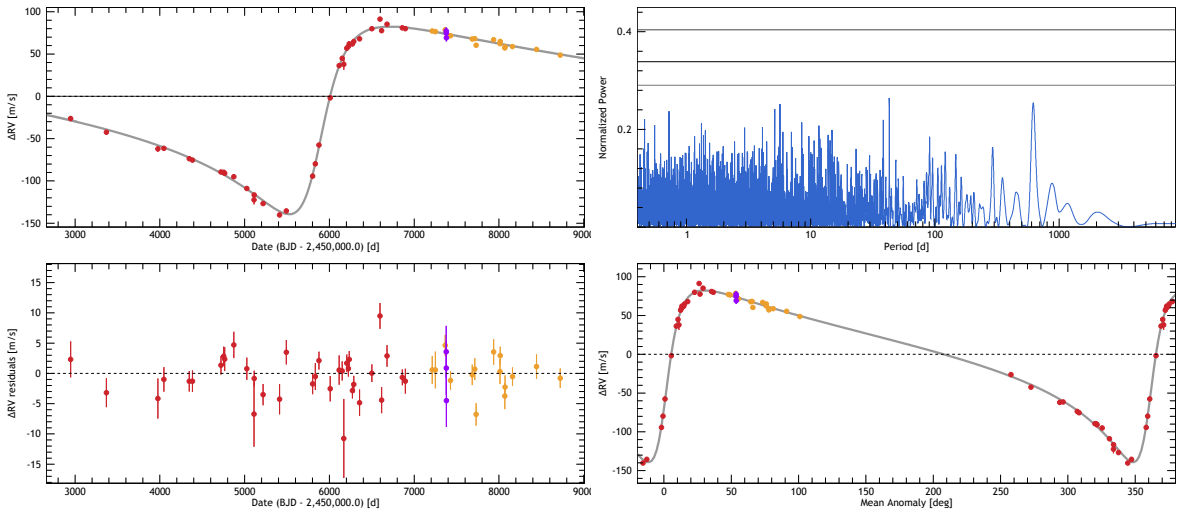

Fig. 4.18 *Top left:* HIP 12436 RV measurements as a function of Julian Date. The purple data are COR-14; the red data are HARPS-03 and the yellow data are HARPS-15. *Bottom left:* The residuals after the planetary signal has been removed. *Top right:* The periodogram of the residuals of HIP 12436 after the planetary signal has been removed, indicating that there are no more significant signals remaining in the data. The three black lines represent the 10, 1 and 0.1% FAPs in ascending order. *Bottom right:* Phase-folded curve for HIP 12436 b.

Table 4.12 Orbital parameters of HIP 12436 b.

Parameter	Units	HIP 12436 b
P	[years]	$28.08^{+1.16}_{-1.17}$
K	[m/s]	$110.91^{+0.65}_{-0.66}$
e		0.68 ± 0.01
ω_0	[deg]	$247.89^{+0.83}_{-0.85}$
T_0	[BJD]	$2455854.03^{+5.23}_{-5.29}$
$m \sin i$	$[M_{\rm Jup}]$	8.66 ± 0.30
a	[AU]	9.26 ± 0.30

High-contrast imaging

HIP 12436 was observed with VLT/SPHERE (program ID: 0104.C-0724(A), PI: Rickman) on 28-10-2019 and 01-11-2019. Similarly to HD 216770, the observations were split into two lots of 1.5 hour observations. The first observation taken on 28-10-2019 had clear conditions throughout the entire observation with a seeing of about 0.6"-0.8". The second observation was carried out on 01-11-2019 also with clear conditions and a seeing of 0.9"-1.3".

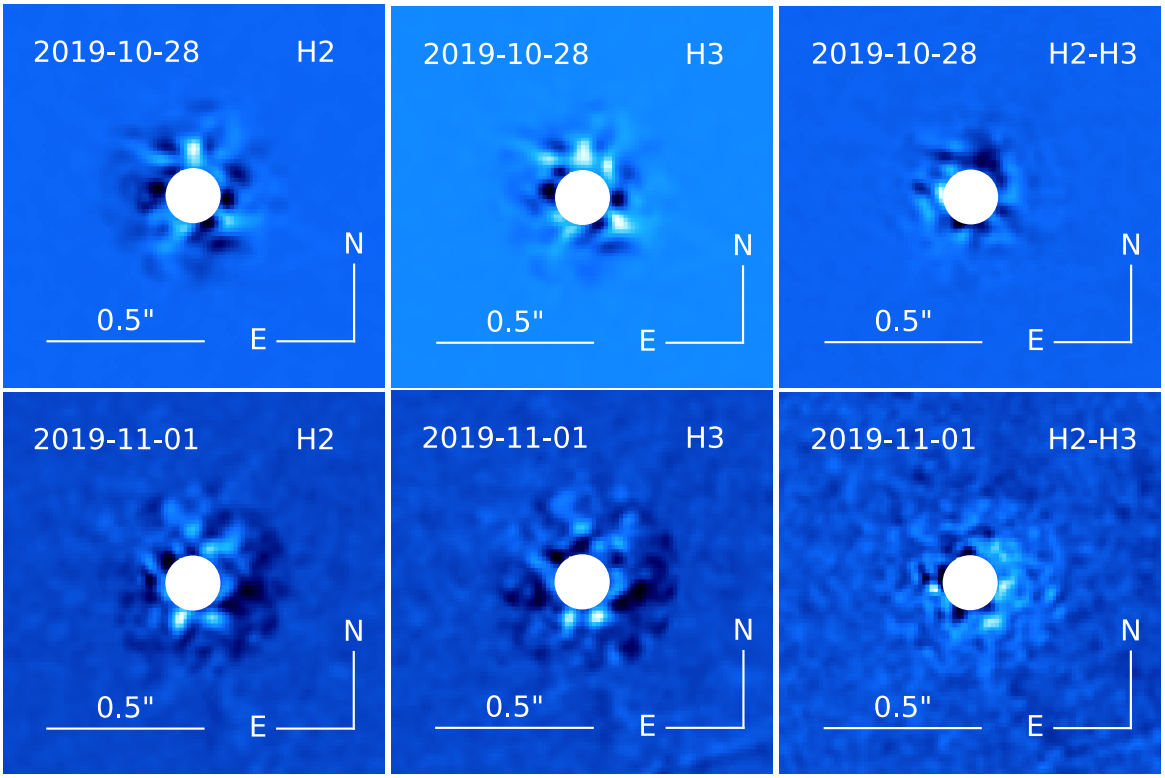

Fig. 4.19 IRDIS images of HIP 12436 in $H2$ ADI, $H3$ ADI and $H2$-$H3$ SDI. The star is masked by a white circle.

As the observation was split into two lots of 1.5 hour observations, instead of one 3 hour long observation, we only achieve a field rotation of 18.39 deg and 13.17 deg. If we had gained more field rotation then the we could achieve a higher contrast level. From the SPHERE images, we can already rule out a massive stellar companion or high-mass brown dwarf.

The reduced ADI and SDI images are shown in Fig. 4.19. There is no clear detection of a companion in any of the images. The $H2$ band $5-\sigma$ contrast curve is shown in Fig. 4.20.

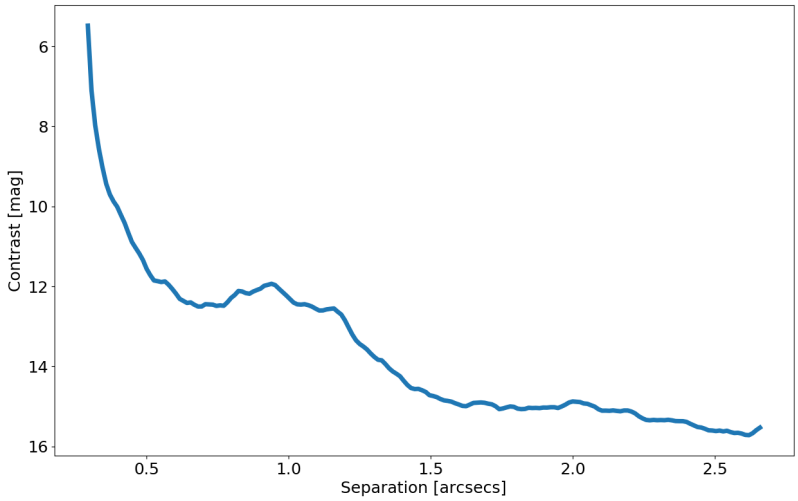

Fig. 4.20 $H2$ contrast curve for HIP 12436.

4.8.3 HD 28185

The stellar characteristics of HD 28185 are listed in Table 4.13. The spectral type, V band magnitude and colour index are taken from *Hipparcos* (Perryman et al. 1997). The parallax π, luminosity, radius and effective temperature are taken from the second *Gaia* data release (Gaia Collaboration et al. 2018). The mass and age of HD 28185 are derived using the Geneva stellar-evolution models (Ekström et al. 2012; Georgy et al. 2013).

Radial velocities

HD 28185 has been observed with CORALIE since October 1999. In addition, it has been observed with MIKE since June 1997 (Minniti et al. 2009), with HARPS from December 2003 to September 2004, with HRS from October 2005 to November 2007 (Wittenmyer et al. 2009) and with HIRES from January 2004 to September 2014 (Butler et al. 2017).

HD 28185 has two companions detected via the RV method. We fit for both the short and long period planets simultaneously. The resulting orbital fits can be seen in Fig. 4.21 and the orbital parameters are listed in Table 4.14.

The short period planet, first detected by Santos et al. (2001), has an orbital period of 1.06 ± 0.0001 years and a minimum mass of $5.99^{+0.20}_{-0.21}$ $M_{\rm Jup}$. The long period companion has a period of $34.14^{+1.93}_{-2.07}$ years and a minimum mass of 8.21 ± 0.50 $M_{\rm Jup}$.

Due to the expected wide separation of HD 28185 c, it was selected as a candidate for direct imaging with VLT/SPHERE. The fitted RV curves for both companions along with the corresponding residuals and periodogram are shown in Fig. 4.21. The fitted orbital parameters are listed in Table 4.14.

Table 4.13 Stellar characteristics of HD 28185.

Parameter	Units	HD 28185	Reference
Spectral type		G5	Perryman et al. (1997)
V		7.81	Perryman et al. (1997)
$B-V$		0.750	Perryman et al. (1997)
$T_{\rm eff}$	[K]	5665^{+171}_{-62}	Gaia Collaboration et al. (2018)
[Fe/H]	[dex]	0.21 ± 0.02	Sousa et al. (2008)
Mass	[$M_{\odot}$]	1.05 ± 0.03	Ekström et al. (2012); Georgy et al. (2013)
π	[mas]	25.36 ± 0.04	Gaia Collaboration et al. (2018)
Age	[Gyr]	4.74 ± 1.91	Ekström et al. (2012); Georgy et al. (2013)
Radius	[$R_{\odot}$]	$1.06^{+0.02}_{-0.06}$	Gaia Collaboration et al. (2018)
Luminosity	[$L_{\odot}$]	1.037 ± 0.002	Gaia Collaboration et al. (2018)

Table 4.14 Orbital parameters of HD 28185 b and HD 28185 c.

Parameter	Units	HD 28185 b	HD 28185 c
P	[years]	1.06 ± 0.0001	$34.14^{+1.93}_{-2.07}$
K	[m/s]	$167.49^{+0.45}_{-0.90}$	$72.04^{+2.53}_{-2.54}$
e		0.068 ± 0.003	0.04 ± 0.03
ω_0	[deg]	7.47 ± 2.36	$175.6^{+100.0}_{-106.1}$
T_0	[BJD]	$2455742.87^{+2.49}_{-2.50}$	2461956^{+3004}_{-2304}
$m \sin i$	[$M_{\rm Jup}$]	$5.99^{+0.20}_{-0.21}$	8.21 ± 0.50
a	[AU]	1.04 ± 0.02	$10.54^{+0.44}_{-0.46}$

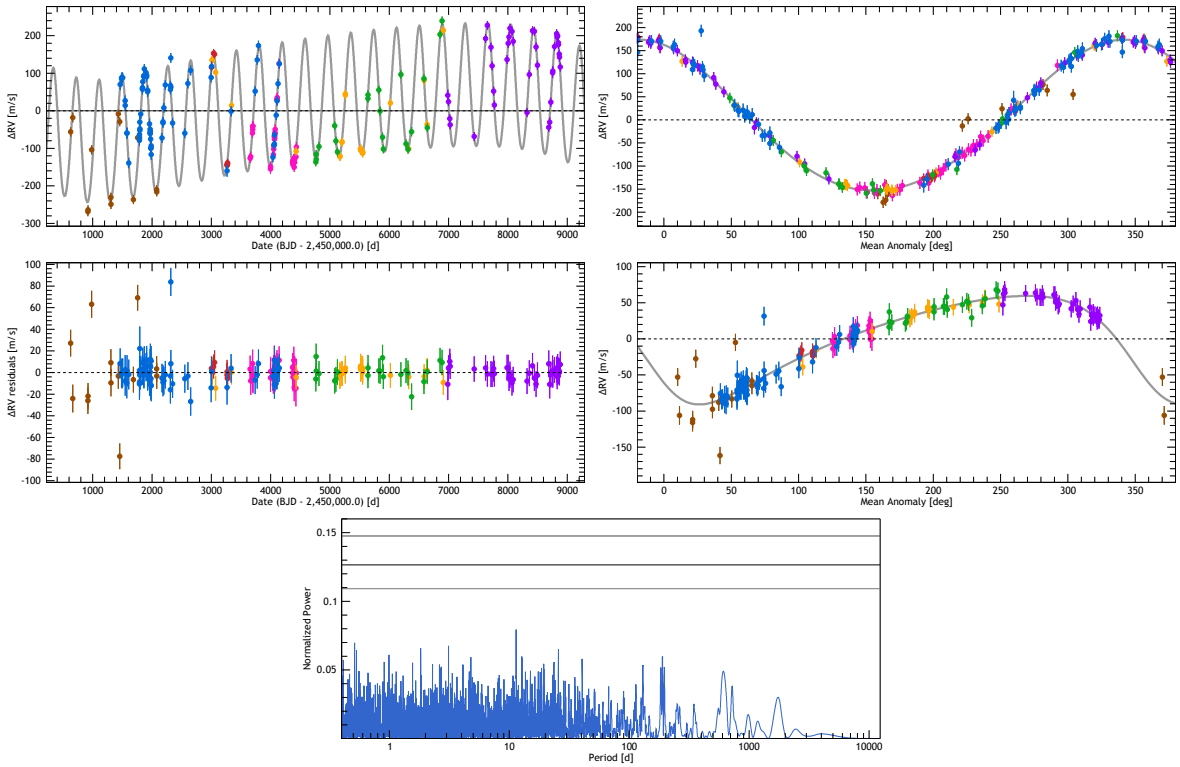

Fig. 4.21 *Top left:* HD 28185 RV measurements as a function of Julian Date. The blue data are COR-98; the green data are COR-07; the purple data are COR-14 and the red data are HARPS. *Middle left:* The residuals after the two planetary signals have been removed. *Top right:* Phase-folded curve for HD 28185 b. *Middle right:* Phase-folded curve for HD 28185 c. *Bottom:* The periodogram of the residuals of HD 28185 after the planetary signal has been removed, indicating that there are no more significant signals remaining in the data. The three black lines represent the 10, 1 and 0.1% FAPs in ascending order.

High-contrast imaging

HD 28185 was observed with VLT/SPHERE (program ID: 0104.C-0724(A), PI: Rickman) on 11-12-2019 and 12-12-2019. Similarly to the cases for HD 216770 and HIP 12436, the observations were split into two lots of 1.5 hour observations. The conditions for both sets of observations were good with clear conditions on 11-12-2019 and an average seeing around 0.6", and photometric conditions on 12-12-2019 and seeing fluctuating around 0.6"-1.0".

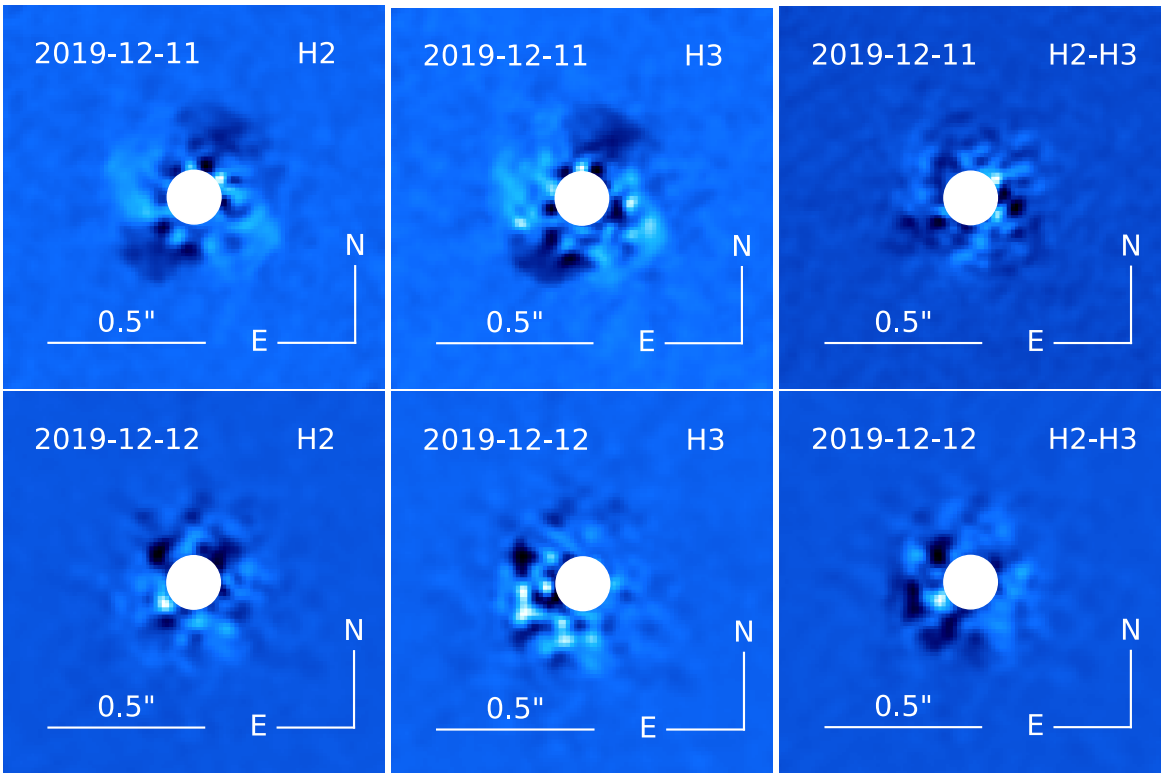

Fig. 4.22 High-contrast images of HD 28185.

The ADI and SDI high-contrast images are shown in Fig. 4.22. We do not see a detection of a companion in either set of the images. Because the observation was split up into two lots of 1.5 hour observations, we do not achieve the same amount of field rotation if the observation had been carried out for the full 3 hours non-stop, and we therefore we do not achieve as high a contrast level. The resulting $5-\sigma$ contrast curve from the $H2$ band image (where we would expect to see the greatest signal) is shown in Fig. 4.23.

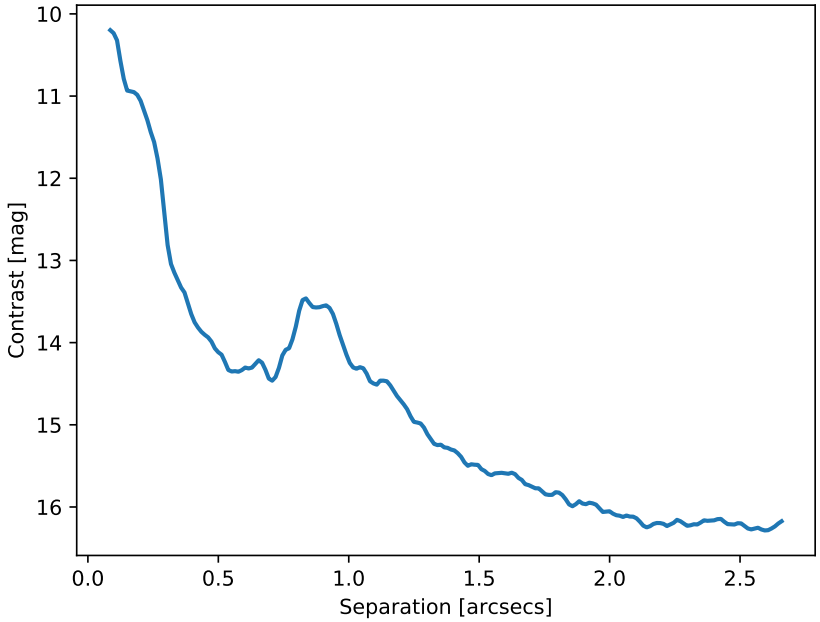

Fig. 4.23 $H2$ contrast curve for HD 28185.

4.8.4 HD 92788

The stellar characteristics of HD 92788 are listed in Table 4.15. The spectral type, V band magnitude and colour index are taken from *Hipparcos* (Perryman et al. 1997). The parallax π, luminosity, radius and effective temperature are taken from the second *Gaia* data release (Gaia Collaboration et al. 2018). The mass and age of HD 92788 are derived using the Geneva stellar-evolution models (Ekström et al. 2012; Georgy et al. 2013).

Radial velocities

HD 92788 has been observed with CORALIE since March 1999. In addition, it has been observed with HAMILTON from January 1998 to March 2002 (Butler et al. 2006), HIRES from January 2000 to February 2014 (Butler et al. 2017) and HARPS from January 2004 to May 2010.

HD 92788 hosts two planets. HD 92788 b was detected by Fischer et al. (2001) and an updated orbital fit is provided in Rickman et al. (2019). The orbital fit of HD 9788 c, detected by Wittenmyer et al. (2019), is also outlined in Rickman et al. (2019). Here we increase the baseline of observations by ~ 1 year. For fit for HD 92788 b and HD 92788 c simultaneously and for HD 92788 b we get an orbital period of 0.89 ± 0.0001 years and a minimum mass of $3.448^{+0.118}_{-0.177}$ $M_{\rm Jup}$ and for HD 92788 c an orbital period of $31.49^{+2.21}_{-2.38}$ years and a minimum mass of 3.36 ± 0.27 $M_{\rm Jup}$. The RV fits are shown in Fig. 4.24. The fitted orbital parameters are listed in Table 4.16.

Table 4.15 Stellar characteristics of HD 92788.

Parameter	Units	HD 92788	Reference
Spectral Type		G6V	Perryman et al. (1997)
V		7.31	Perryman et al. (1997)
$B-V$		0.694	Perryman et al. (1997)
$T_{\rm eff}$	[K]	5744 ± 24	Rickman et al. (2019)
[Fe/H]	[dex]	0.27 ± 0.02	Rickman et al. (2019)
Mass	[$M_\odot$]	1.15 ± 0.07	Rickman et al. (2019)
π	[mas]	28.83 ± 0.05	Gaia Collaboration et al. (2018)
Age	[Gyr]	2.55 ± 1.51	Rickman et al. (2019)
Radius	[$R_\odot$]	1.14 ± 0.02	Gaia Collaboration et al. (2018)
Luminosity	[$L_\odot$]	1.25 ± 0.003	Gaia Collaboration et al. (2018)

Table 4.16 Orbital parameters of HD 92788 b and HD 92788 c.

Parameter	Units	HD 92788 b	HD 92788 c
P	[years]	0.89 ± 0.0001	$31.49^{+2.21}_{-2.38}$
K	[m/s]	$108.73^{+0.59}_{-0.60}$	$33.78^{+2.27}_{-2.29}$
e		0.350 ± 0.003	0.44 ± 0.03
ω_0	[deg]	-82.68 ± 0.72	$-28.57^{+4.34}_{-4.40}$
T_0	[BJD]	$2455646.997^{+0.471}_{-0.469}$	2456788^{+142}_{-140}
$m \sin i$	[$M_{\rm Jup}$]	$3.448^{+0.118}_{-0.117}$	3.36 ± 0.27
a	[AU]	0.93 ± 0.02	$9.97^{+0.50}_{-0.53}$

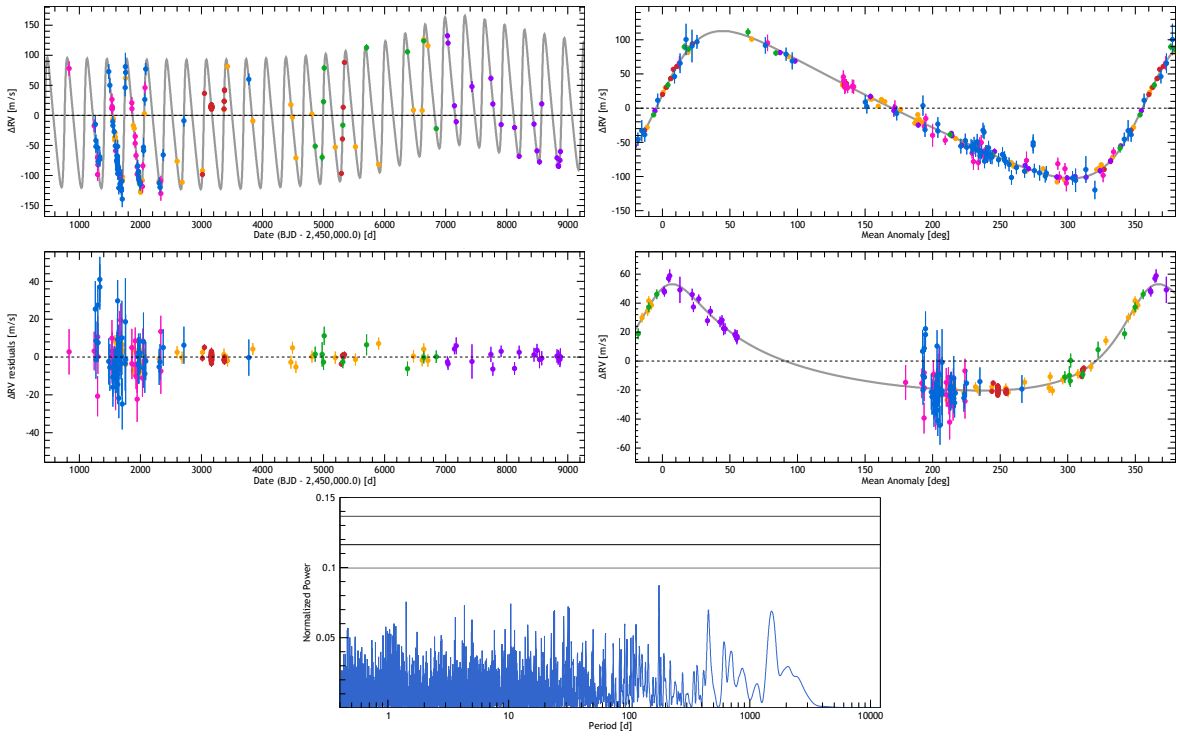

Fig. 4.24 *Top left:* HD 92788 RV measurements as a function of Julian Date. The blue data are COR-98; the green data are COR-07; the purple data are COR-14 and the red data are HARPS. *Middle left:* The residuals after the two planetary signals have been removed. *Top right:* Phase-folded curve for HD 92788 b. *Middle right:* Phase-folded curve for HD 92788 c. *Bottom:* The periodogram of the residuals of HD 216770 after the planetary signal has been removed, indicating that there are no more significant signals remaining in the data. The three black lines represent the 10, 1 and 0.1% FAPs in ascending order.

High-contrast imaging

Due to HIP 22059 hosting a massive companion that could be seen on the Real-Time Display (RTD) at Paranal Observatory, the observation was subsequently aborted early. For this reason, ESO asked if we had another companion that we would like to image with VLT/SPHERE as a replacement. Therefore, we requested to try and directly image HD 92788 c. HD 92788 was observed with VLT/SPHERE (program ID: 0104.C-0724(A), PI: Rickman) on 11-01-2020. The observing conditions were okay with thin clouds and a seeing around 0.7".

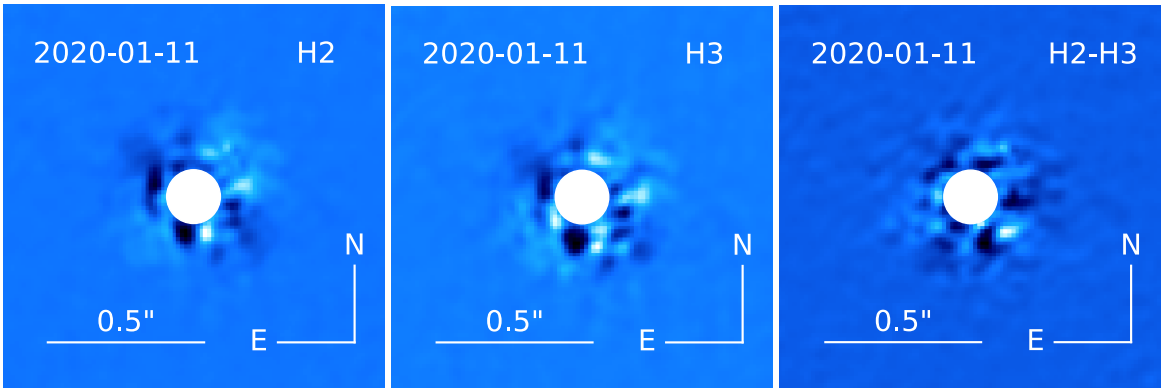

Fig. 4.25 IRDIS images of HD 92788 in $H2$ ADI, $H3$ ADI and $H2$-$H3$ SDI. The star is masked by a white circle.

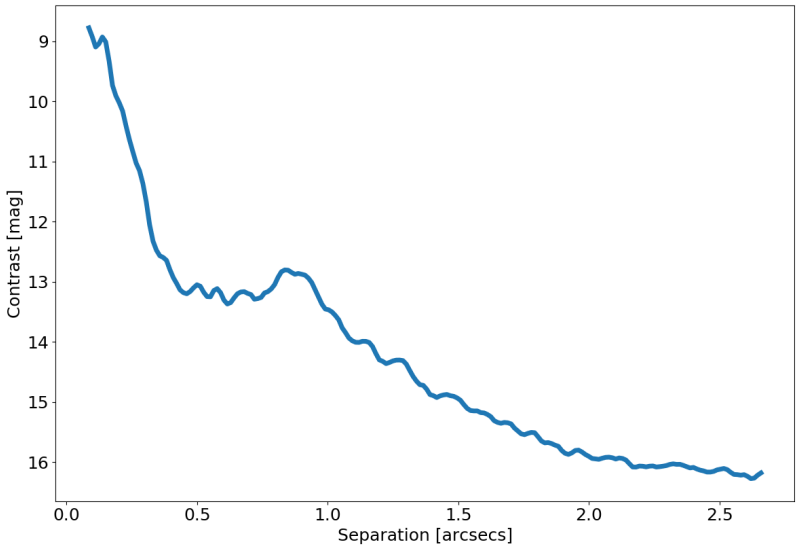

Fig. 4.26 $H2$ contrast curve for HD 92788.

The ADI and SDI high-contrast images are shown in Fig. 4.25. We do not see a detection of a companion in any of the images. The resulting $5-\sigma$ contrast curve from the $H2$ band (where we would expect to see the greatest signal) is shown in Fig. 4.26. As HD 92788 c has a relatively low mass with an $m \sin i = 3.36 \pm 0.27\ M_{\rm Jup}$, then a high level of contrast would be required to detect it. As it was selected as a quick target change, the observing strategy was not optimised to be able to detect the companion, with a field rotation of only 30.68 deg. Even with a significant amount of field rotation, HD 92788 c would not be easy to detect with SPHERE. Even from the images alone, we can rule out any massive companions, like high-mass brown dwarfs. Going forward, HD 92788 c will be a promising candidate to directly image with the next generation of telescopes and instrumentation.

4.9 Proposed targets

4.9.1 HD 112863

The stellar characteristics of HD 112863 are listed in Table 4.17. The spectral type, V band magnitude and colour index are taken from *Hipparcos* (Perryman et al. 1997). The parallax π, luminosity, radius and effective temperature are taken from the second *Gaia* data release (Gaia Collaboration et al. 2018). The mass and age of HD 112863 are derived using the Geneva stellar-evolution models (Ekström et al. 2012; Georgy et al. 2013).

Table 4.17 Stellar characteristics of HD 112863.

Parameter	Units	HD 112863	Reference
Spectral Type		K1V	Perryman et al. (1997)
V		8.69	Perryman et al. (1997)
$B-V$		0.779	Perryman et al. (1997)
$T_{\rm eff}$	[K]	$5342.00^{+76.33}_{-43.00}$	Gaia Collaboration et al. (2018)
[Fe/H]	[dex]	-0.11 ± 0.03	Mata Sánchez et al. (2014)
Mass	[$M_\odot$]	0.85 ± 0.02	Ekström et al. (2012); Georgy et al. (2013)
π	[mas]	27.08 ± 0.05	Gaia Collaboration et al. (2018)
Age	[Gyr]	3.61 ± 3.51	Ekström et al. (2012); Georgy et al. (2013)
Radius	[$R_\odot$]	$0.76^{+0.01}_{-0.02}$	Gaia Collaboration et al. (2018)
Luminosity	[$L_\odot$]	0.429 ± 0.001	Gaia Collaboration et al. (2018)

Radial velocities

HD 112863 has been observed with CORALIE since March 1999. We fit a Keplerian to the RV data as shown in Fig. 4.27. From the fit we obtain an orbital period of 21.60 ± 0.03 years which is well constrained as we have full phase coverage of the orbit. The companion has a minimum mass of $70.36^{+2.41}_{-2.40}$ $M_{\rm Jup}$, making it a promising candidate for a direct detection with SPHERE. The fitted orbital parameters are listed in Table 4.18.

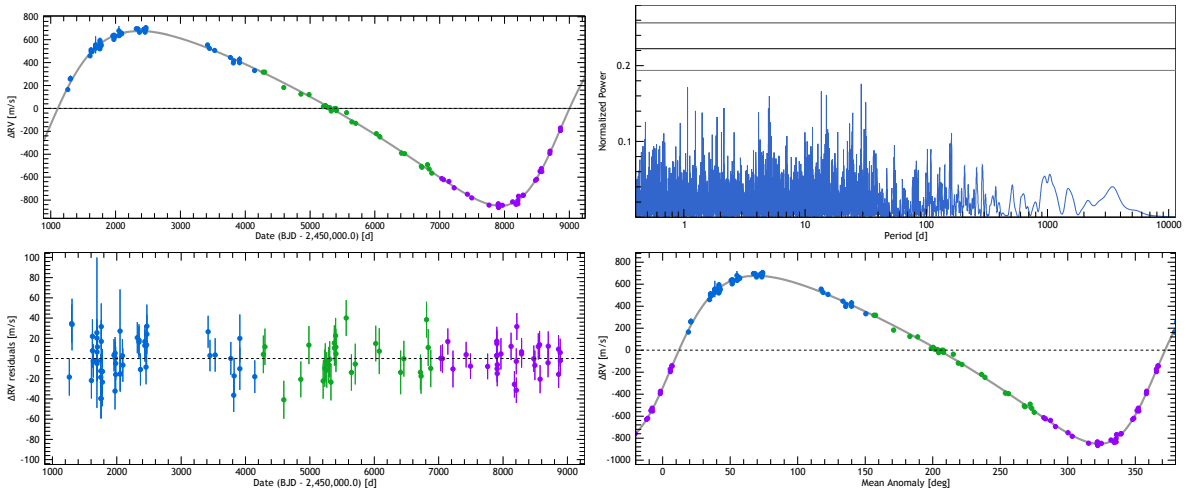

Fig. 4.27 *Top left:* HD 112863 RV measurements as a function of Julian Date. The blue data are COR-98; the green data are COR-07 and the purple data are COR-14. *Bottom left:* The residuals after the planetary signal has been removed. *Top right:* The periodogram of the residuals of HD 112863 after the planetary signal has been removed, indicating there that are no more significant signals remaining in the data. The three black lanes represent the 10, 1 and 0.1% FAPs in ascending order. *Bottom right:* Phase-folded curve for HD 112863.

Table 4.18 Orbital parameters of HD 112863 b.

Parameter	Units	HD 112863 b
P	[years]	21.60 ± 0.03
K	[m/s]	$766.68^{+4.75}_{-4.74}$
e		0.348 ± 0.002
ω_0	[deg]	$250.54^{+0.48}_{-0.49}$
T_0	[BJD]	$2458736.91^{+6.60}_{-6.63}$
$m \sin i$	[$M_{\rm Jup}$]	$70.36^{+2.41}_{-2.40}$
a	[AU]	7.92 ± 0.13

High-contrast imaging

HD 112863 has been accepted to be observed with VLT/SPHERE in P105 (01-04-2020 - 30-09-2020) under Program: 0105.C-0072(A), PI: Rickman. Due to its massive $m \sin i$ of $70.36^{+2.41}_{-2.40}$ $M_{\rm Jup}$ and wide expected separation, we expect to directly detect a high-mass brown dwarf or very low-mass star.

4.9.2 HD 143616

The stellar characteristics of HD 143616 are listed in Table 4.19. The spectral type, V band magnitude and colour index are taken from *Hipparcos* (Perryman et al. 1997). The parallax π, luminosity, radius and effective temperature are taken from the second *Gaia* data release (Gaia Collaboration et al. 2018). The mass and age of HD 143616 are derived using the Geneva stellar-evolution models (Ekström et al. 2012; Georgy et al. 2013).

Table 4.19 Stellar characteristics of HD 143616.

Parameter	Units	HD 143616	Reference
Spectral Type		G6/8V	Perryman et al. (1997)
V		8.26	Perryman et al. (1997)
$B-V$		0.700	Perryman et al. (1997)
$T_{\rm eff}$	[K]	$5530.00^{+33.63}_{-46.88}$	Gaia Collaboration et al. (2018)
[Fe/H]	[dex]	-0.08 ± 0.05	Bensby et al. (2014)
Mass	[$M_\odot$]	0.91 ± 0.02	Ekström et al. (2012); Georgy et al. (2013)
π	[mas]	23.95 ± 0.05	Gaia Collaboration et al. (2018)
Age	[Gyr]	8.80 ± 2.05	Ekström et al. (2012); Georgy et al. (2013)
Radius	[$R_\odot$]	$0.97^{+0.02}_{-0.01}$	Gaia Collaboration et al. (2018)
Luminosity	[$L_\odot$]	0.786 ± 0.002	Gaia Collaboration et al. (2018)

Radial velocities

HD 143616 has been observed with CORALIE since April 2003. It is an extremely eccentric system with an eccentricity of $0.968^{+0.002}_{-0.004}$. The $T_{V_{\rm min}}$ is used to fit the RV measurements as it is quite well constrained, leading to a relatively well constrained $m \sin i$ of 193.14 ± 6.7 $M_{\rm Jup}$, meaning that the companion is in the stellar regime. The fitted RV curve, residuals, periodogram and phase-folded diagram can be seen in Fig. 4.28. The orbital parameters are listed in Table 4.20.

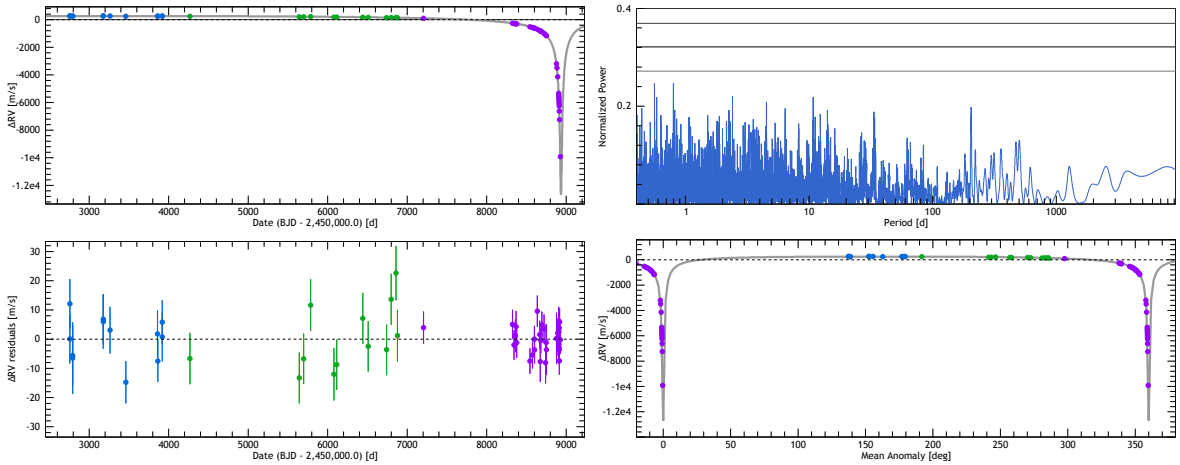

Fig. 4.28 *Top left:* HD 143616 RV measurements as a function of Julian Date. The blue data are COR-98; the green data are COR-07 and the purple data are COR-14. *Bottom left:* The residuals after the planetary signal has been removed. *Top right:* The periodogram of the residuals of HD 143616 after the planetary signal has been removed, indicating there that are no more significant signals remaining in the data. The three black lanes represent the 10, 1 and 0.1% FAPs in ascending order. *Bottom right:* Phase-folded curve for HD 143616.

Table 4.20 Orbital parameters of HD 143616 b.

Parameter	Units	HD 143616 b
P	[years]	$37.58^{+2.87}_{-5.61}$
K	[m/s]	$6539.8^{+56.8}_{-59.0}$
e		$0.968^{+0.002}_{-0.004}$
ω_0	[deg]	$182.07^{+0.33}_{-0.30}$
$T_{V_{\min}}$	[BJD]	$2458936.29^{+0.22}_{-0.24}$
$m \sin i$	$[M_{\rm Jup}]$	193.14 ± 6.7
a	[AU]	$11.86^{+0.65}_{-1.23}$

High-contrast imaging

HD 143616 has been accepted to be observed with VLT/SPHERE in P105 (01-04-2020 - 30-09-2020) under Program: 0105.C-0072(A), PI: Rickman. When HD 143616 was initially proposed to be imaged with VLT/SPHERE the RV signal was not as significant. However, since early 2020 the RV semi-amplitude has increased substantially and we expect to directly detect a companion of stellar nature.

4.9.3 HD 195010

The stellar characteristics of HD 195010 are listed in Table 4.21. The spectral type, V band magnitude and colour index are taken from *Hipparcos* (Perryman et al. 1997). The parallax π, luminosity, radius and effective temperature are taken from the second *Gaia* data release (Gaia Collaboration et al. 2018). The mass and age of HD 195010 are derived using the Geneva stellar-evolution models (Ekström et al. 2012; Georgy et al. 2013).

Table 4.21 Stellar characteristics of HD 195010.

Parameter	Units	HD 195010	Reference
Spectral Type		G8/K0V	Perryman et al. (1997)
V		8.82	Perryman et al. (1997)
$B-V$		0.779	Perryman et al. (1997)
$T_{\rm eff}$	[K]	$5352.33^{+84.17}_{-74.26}$	Gaia Collaboration et al. (2018)
[Fe/H]	[dex]	0.02 ± 0.02	Casagrande et al. (2011)
Mass	[$M_{\odot}$]	0.90 ± 0.02	Ekström et al. (2012); Georgy et al. (2013)
π	[mas]	19.88 ± 0.04	Gaia Collaboration et al. (2018)
Age	[Gyr]	10.27 ± 2.90	Ekström et al. (2012); Georgy et al. (2013)
Radius	[$R_{\odot}$]	0.95 ± 0.03	Gaia Collaboration et al. (2018)
Luminosity	[$L_{\odot}$]	0.672 ± 0.002	Gaia Collaboration et al. (2018)

Radial velocities

HD 195010 has been observed with CORALIE since September 2000. From fitting a Keplerian to the RV data as shown in Fig. 4.29, HD 195010 has a massive companion on a $46.14^{+7.05}_{-7.38}$ year period with a minimum mass of $60.56^{+9.91}_{-10.52}$ $M_{\rm Jup}$. The fitted orbital parameters are listed in Table 4.22. The fitted RV curve along with the corresponding residuals and periodogram are shown in Fig. 4.29.

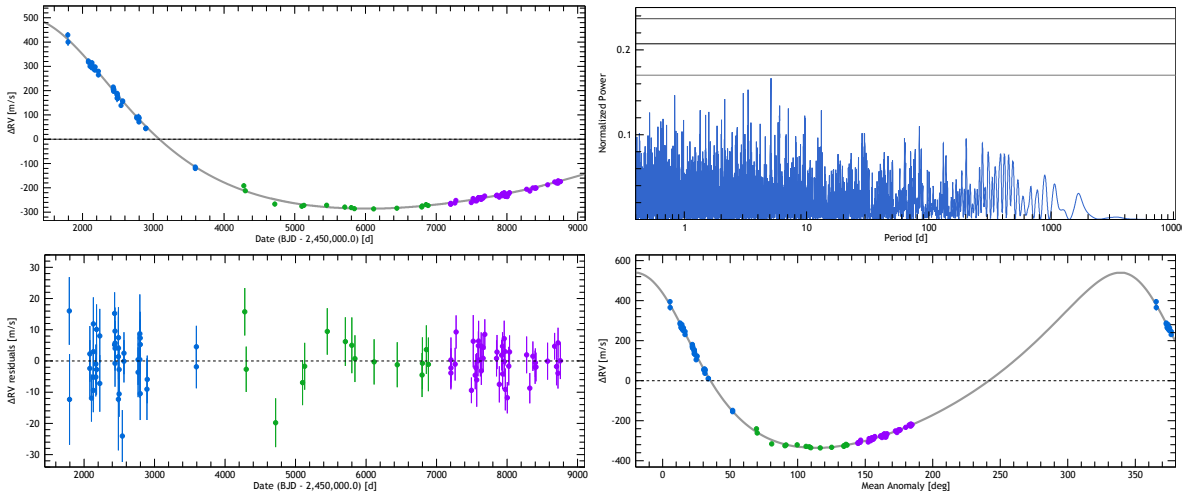

Fig. 4.29 *Top left:* HD 195010 RV measurements as a function of Julian Date. The blue data are COR-98; the green data are COR-07 and the purple data are COR-14. *Bottom left:* The residuals after the planetary signal has been removed. *Top right:* The periodogram of the residuals of HD 195010 after the planetary signal has been removed, indicating there that are no more significant signals remaining in the data. The three black lanes represent the 10, 1 and 0.1% FAPs in ascending order. *Bottom right:* Phase-folded curve for HD 195010.

Table 4.22 Orbital parameters of HD 195010 b.

Parameter	Units	HD 195010 b
P	[years]	$46.14^{+7.05}_{-7.38}$
K	[m/s]	$503.0^{+56.0}_{-60.9}$
e		0.31 ± 0.01
ω_0	[deg]	$53.8^{+12.8}_{-13.0}$
T_0	[BJD]	2468445^{+2641}_{-2730}
$m \sin i$	[$M_{\rm Jup}$]	$60.56^{+9.91}_{-10.52}$
a	[AU]	$13.07^{+1.39}_{-1.46}$

High-contrast imaging

HD 195010 has been accepted to be observed with VLT/SPHERE in P105 (01-04-2020 - 30-09-2020) under Program: 0105.C-0072(A), PI: Rickman. We expect to directly detect the long-period companion due to its massive nature ($60.56^{+9.91}_{-10.52}$ $M_{\rm Jup}$) and its wide separation.

4.9.4 HD 157338

The stellar characteristics of HD 157338 are listed in Table 4.23. The spectral type, V band magnitude and colour index are taken from *Hipparcos* (Perryman et al. 1997). The parallax π, luminosity, radius and effective temperature are taken from the second *Gaia* data release (Gaia Collaboration et al. 2018). The mass and age of HD 157338 are derived using the Geneva stellar-evolution models (Ekström et al. 2012; Georgy et al. 2013).

Table 4.23 Stellar characteristics of HD 157338.

Parameter	Units	HD 157338	Reference
Spectral Type		F9.5V	Perryman et al. (1997)
V		6.92	Perryman et al. (1997)
$B-V$		0.588	Perryman et al. (1997)
$T_{\rm eff}$	[K]	$6055.0^{+63.3}_{-54.0}$	Gaia Collaboration et al. (2018)
[Fe/H]	[dex]	-0.12 ± 0.04	Aguilera-Gómez et al. (2018)
Mass	[$M_\odot$]	1.05 ± 0.03	Ekström et al. (2012); Georgy et al. (2013)
π	[mas]	30.18 ± 0.05	Gaia Collaboration et al. (2018)
Age	[Gyr]	4.71 ± 1.13	Ekström et al. (2012); Georgy et al. (2013)
Radius	[$R_\odot$]	1.14 ± 0.02	Gaia Collaboration et al. (2018)
Luminosity	[$L_\odot$]	1.584 ± 0.004	Gaia Collaboration et al. (2018)

Radial velocities

HD 157338 has been observed with CORALIE since April 1999. In addition, it has been observed with HIRES since April 1997 (Butler et al. 2017) and with HARPS from June 2003 to March 2013. We fit a Keplerian to the RV data shown in Fig. 4.30 and obtain an orbital period of $51.12^{+4.11}_{-3.96}$ years and a minimum mass of $86.19^{+9.79}_{-10.02}$ $M_{\rm Jup}$. The orbital parameters are listed in Table 4.24. The fitted RV curve along with the corresponding residuals and periodogram are shown in Fig. 4.30.

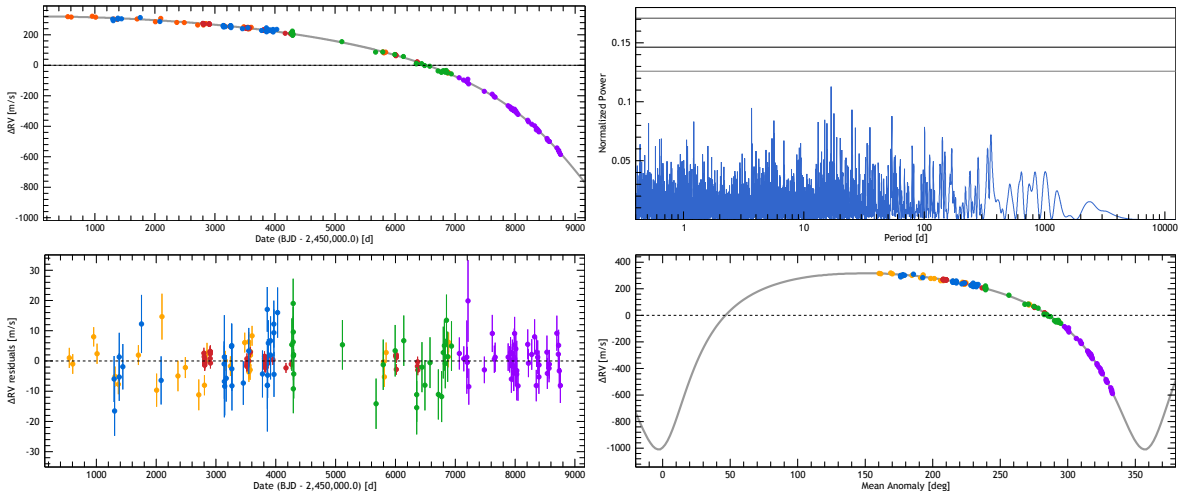

Fig. 4.30 *Top left:* HD 157338 RV measurements as a function of Julian Date. The blue data are COR-98; the green data are COR-07; the purple data are COR-14; the orange data are from HIRES and the red data are from HARPS. *Bottom left:* The residuals after the planetary signal has been removed. *Top right:* The periodogram of the residuals of HD 157338 after the planetary signal has been removed, indicating there that are no more significant signals remaining in the data. The three black lanes represent the 10, 1 and 0.1% FAPs in ascending order. *Bottom right:* Phase-folded curve for HD 157338.

Table 4.24 Orbital parameters of HD 157338 B.

Parameter	units	HD 157338 b
P	[years]	$51.12^{+4.11}_{-3.96}$
K	[m/s]	$796.2^{+79.9}_{-81.8}$
e		0.56 ± 0.01
ω_0	[deg]	$188.32^{+3.27}_{-3.38}$
$T_{\rm P}$	[BJD]	2460297^{+142}_{-151}
$m \sin i$	[$M_{\rm Jup}$]	$86.19^{+9.79}_{-10.02}$
a	[AU]	$14.13^{+0.81}_{-0.79}$

High-contrast imaging

HD 157338 has been accepted to be observed with VLT/SPHERE in P105 (01-04-2020 - 30-09-2020) under Program: 0105.C-0072(A), PI: Rickman. Due to the minimum mass being substantial ($51.12^{+4.11}_{-3.96}\ M_{\rm Jup}$) and its wide orbit, we expect to get a detection of this long-period companion.

4.10 Summary and conclusions

I present here the results of previous imaging campaigns with VLT/NACO to seek direct detections of RV-detected companions with CORALIE and HARPS. For the past $\sim$3 years, I have been responsible for the continuous monitoring of the massive long-period companions from the CORALIE sample. From this sample and using information from the previous VLT/NACO observing campaigns, I have proposed and carried out several observing campaigns with VLT/SPHERE to hunt for direct detections.

As a result of this, I present new direct detections of three massive companions to HD 92987, HD 206505 and HIP 22059. In addition, I provide updated orbital parameters from RV measurements of HD 216770, HIP 12436, HD 28185, HD 92788, HD 112863, HD 143616, HD 195010 and HD 157338. Of these targets HD 216770, HIP 12436, HD 28185 and HD 92788 have been directly imaged with VLT/SPHERE with no detection. The other four targets, HD 112863, HD 143616, HD 195010 and HD 157338, have been awarded observing time and are due to be imaged with VLT/SPHERE in P105 (01-04-2020 - 30-09-2020).

Monitoring the stars in the CORALIE and HARPS samples will allow us to carry out a statistical analysis in the future about the fraction of binaries, brown dwarfs and giant planets at wide separations. For example, deriving the eccentricity of companions around nearby stars in a volume-limited sample can place constraints on the formation process of ultracool companions. Bowler et al. (2020) has carried out a similar study on directly imaged companions where they found that there are two lots of eccentricity distributions above and below the brown dwarf desert, implying formation via gravitational instability and by molecular cloud fragmentation respectively. Long-lasting radial velocity surveys can help inform distributions even further by placing tighter constraints on orbital parameters and the dynamical masses of such objects.

In addition, combining RV data from CORALIE and HARPS with the forthcoming *Gaia* data release will open up a new parameter space and allow us to further constrain the fraction of widely-separated companions to Sun-like stars in the Solar neighbourhood and their parameters. Combining astrometric data from proper motion anomalies between *Hipparcos* and *Gaia* data to derive orbital inclinations and mass estimates. This is a technique that has been utilised by Kervella et al. (2020) for Proxima c, and will stand to be complementary technique to help inform future studies of exoplanets beyond the information given by radial velocities and direct imaging alone.

CHAPTER 5

SPECTRAL AND ATMOSPHERIC CHARACTERISATION OF A NEW BENCHMARK BROWN DWARF

"Science progresses best when observations force us to alter our preconceptions."

— Vera Rubin

5.1 Introduction and background

As part of the CORALIE survey for extra-solar planets (Udry et al. 2000) discussed in Chapter 3, one of the promising companion candidates identified for direct imaging was HD 13724. It was first observed with VLT/SPHERE in IRDIFS_H23 mode on 18-08-2018 as part of program 0102.C-0236(A) (PI: Rickman). As a result we identified a bright target in the SDI-reduced images. In addition, we extracted the spectral data measured using IFS on SPHERE and identified the target as a brown dwarf companion.

Following on from this, we proposed follow-up VLT/SPHERE observations of HD 13724 to observe the companion using additional bands (J and K bands) to help further constrain its atmospheric properties and to obtain an additional astrometric point to fit the orbit of HD 13724 B in order to derive a dynamical mass. Consequently, HD 13724 was observed again on 12-10-2019 and 18-10-2019 (program ID: 0104.C-0724(A), PI: Rickman) in the J and K bands respectively. The detected companion, HD 13724 B, had moved significantly in just over the one year between epochs, which meant that we were able to confirm that the companion is responsible for the RV signal that we detect, and allowed us to place good constraints on the spectral type, orbital and atmospheric properties of the brown dwarf.

HD 13724 B joins just a short list of brown dwarfs that have both an RV signal measured by its host star, in addition to a direct detection. It is now one of only five T-type brown dwarfs with both RVs and a direct detection alongside GJ 758 B (Thalmann et al. 2009; Bowler et al. 2018), HD 4113 C (Cheetham et al. 2018b), GJ 229 B (Nakajima et al. 1995; Brandt et al. 2019), and HD19467 (Maire et al. 2020). These objects act as crucial benchmarks, providing powerful and critical tools for testing atmospheric models of cool substellar objects which ultimately act as analogues for giant exoplanetary atmospheres.

5.2 Spectral and orbital characterisation of a new benchmark brown dwarf HD 13724 B

The full analysis of the direct detection, including the spectral and orbital characterisation is outlined in Rickman et al. (2020) below.

A&A 635, A203 (2020)
https://doi.org/10.1051/0004-6361/202037524

Astronomy & Astrophysics

Spectral and atmospheric characterisation of a new benchmark brown dwarf HD 13724 B⋆,⋆⋆

E. L. Rickman[1], D. Ségransan[1], J. Hagelberg[1], J.-L. Beuzit[2], A. Cheetham[1], J.-B. Delisle[1], T. Forveille[3], and S. Udry[1]

[1] Départment d'astronomie de l'Université de Genève, 51 ch. des Maillettes Sauverny, 1290 Versoix, Switzerland
e-mail: emily.rickman@unige.ch
[2] Aix Marseille Univ., CNRS, CNES, LAM, Marseille, France
[3] Univ. Grenoble Alpes, CNRS, IPAG, 38000 Grenoble, France

Received 17 January 2020 / Accepted 18 February 2020

ABSTRACT

Context. HD 13724 is a nearby solar-type star at 43.48 ± 0.06 pc hosting a long-period low-mass brown dwarf detected with the CORALIE echelle spectrograph as part of the historical CORALIE radial-velocity search for extra-solar planets. The companion has a minimum mass of $26.77^{+4.4}_{-2.2}$ $M_{\rm Jup}$ and an expected semi-major axis of ∼240 mas making it a suitable target for further characterisation with high-contrast imaging, in particular to measure its inclination, mass, and spectrum and thus establish its substellar nature.
Aims. Using high-contrast imaging with the SPHERE instrument on the Very Large Telescope (VLT), we are able to directly image a brown dwarf companion to HD 13724 and obtain a low-resolution spectrum.
Methods. We combine the radial-velocity measurements of CORALIE and HARPS taken over two decades and high-contrast imaging from SPHERE to obtain a dynamical mass estimate. From the SPHERE data we obtain a low-resolution spectrum of the companion from Y to J band, as well as photometric measurements from IRDIS in the J, H, and K bands.
Results. Using high-contrast imaging with the SPHERE instrument at the VLT, we report the first images of a brown dwarf companion orbiting the host star HD 13724. It has an angular separation of 175.6 ± 4.5 mas and an H-band contrast of 10.61 ± 0.16 mag, and using the age estimate of the star to be ∼1 Gyr gives an isochronal mass estimate of ∼44 $M_{\rm Jup}$. By combining radial-velocity and imaging data we also obtain a dynamical mass of $50.5^{+3.3}_{-3.5}$ $M_{\rm Jup}$. Through fitting an atmospheric model, we estimate a surface gravity of $\log g = 5.5$ and an effective temperature of 1000 K. A comparison of its spectrum with observed T dwarfs estimates a spectral type of T4 or T4.5, with a T4 object providing the best fit.

Key words. planetary systems – binaries: visual – techniques: radial velocities – techniques: high angular resolution – brown dwarfs

1. Introduction

Evolutionary models of brown dwarfs are plagued by a lack of observational constraints in addition to model degeneracies. The complex molecular chemistry of their atmospheres leaves a relatively wide parameter space for models to span. For this reason, the detection of brown dwarfs is vital to testing the complex atmospheres, structure, and evolution of these substellar objects (Baraffe et al. 2003, 2015). Furthermore, it is important to characterise brown dwarfs that are orbiting stars, where the age of the system can be constrained, unlike field brown dwarfs. In addition, brown dwarfs orbiting stars provide an opportunity to monitor the radial velocity (RV) of these systems which allows us to place constraints on their dynamical masses over time (Boden et al. 2006).

With over 20 yr worth of RV measurements from the CORALIE survey for extrasolar planets (Udry et al. 2000), HD 13724 has been identified as a promising candidate for observational follow-up with direct imaging (Rickman et al. 2019) due to its minimum mass ($26.77^{+4.4}_{-2.2}$ $M_{\rm Jup}$) and expected semi-major axis (∼240 mas), which was calculated from the orbital period, itself derived from RV measurements.

The CORALIE RV survey is a volume-limited sample of 1647 main sequence stars from F8 down to K0 located within 50 pc of the Sun. Such a long base line of observations allows us to detect massive giant planets at separations of larger than 5 AU. This in turn identifies golden targets for direct imaging, as such companions are rare and are very difficult to search for blindly. Selecting long-period candidates to image from RV surveys has proven to be valuable (see Cheetham et al. 2018; Peretti et al. 2019).

Radial-velocity measurements provide a lower limit on the measured masses due to the unknown orbital inclination. Therefore, directly imaging long-period RV candidates allows us to break that degeneracy and provide constraints on the dynamical mass of the companion.

Not only does combining these two detection techniques allow us to start filling in a largely unexplored parameters space, but through combining RV and direct imaging data we can now expect to dynamically measure the mass of such companions. By constraining the mass, we are able to place additional constraints on the evolution of the companion, both in terms of temperature and atmospheric composition (e.g. see Maire et al. 2016a; Vigan et al. 2016).

⋆ Based on observations collected with SPHERE mounted on the VLT at Paranal Observatory (ESO, Chile) under programmes 0102.C-0236(A) (PI: Rickman) and 0104.C-0702(B) (PI: Rickman) as well as observations collected with the CORALIE spectrograph mounted on the 1.2 m Swiss telescope at La Silla Observatory and with the HARPS spectrograph on the ESO 3.6 m telescope at La Silla (ESO, Chile).
⋆⋆ The radial-velocity measurements, reduced images and additional data products discussed in this paper are available on the DACE web platform at https://dace.unige.ch/

To date, individual dynamical masses from combining radial velocity and imaging measurements are known for only a handful of brown dwarfs (Thalmann et al. 2009; Sahlmann et al. 2011; Crepp et al. 2012, 2014, 2016; Dupuy & Liu 2017; Peretti et al. 2019; Bowler et al. 2018; Cheetham et al. 2018; Brandt et al. 2019; Maire et al. 2020), therefore any new detections contribute significantly to brown dwarf models in addition to providing important analogues for the characterisation of exoplanets. This forms part of a larger effort to determine the giant planet upper mass limit and lower mass limit for brown dwarfs, especially in the ~20 $M_{\rm Jup}$−40 $M_{\rm Jup}$ range where there is a dearth of observed companions (Sahlmann et al. 2011). Detecting brown dwarfs in this parameter space can help us to understand the formation of these objects, whether they formed via gravitational instability like binary systems or via core-accretion, as in the case of planets. This is crucial to understanding the formation processes of such systems and to defining the boundary between massive planets and low-mass brown dwarfs.

To determine the mass of an imaged brown dwarf companion, the key parameter for the evolution of substellar objects, we usually rely on evolutionary models (Marley et al. 1996; Baraffe et al. 2003; Allard et al. 2012; Morley et al. 2012). These models still need to be tested and properly calibrated through observations and the discovery of benchmark sources provides a powerful and critical tool to achieve this. Furthermore, as we move toward imaging increasingly small objects it is important to use them to test theoretical atmospheric models.

Typically, the conditions around young stars are more favourable to direct imaging because any companion will still be bright and hot and therefore easier to detect. In contrast, the RV method is typically suited to older stars where the RV signal is not too contaminated from variability caused by stellar activity in young and active stars. Consequently, combining these two techniques allows us to not only probe a mass-separation parameter space that is largely unexplored, but also bridge the gap between younger and older companion candidates.

Here, we report the first images and low-resolution spectrum of the benchmark brown dwarf HD 13724 B. In addition, we extend the time baseline of the RV observations. When combined with the imaging data, this allows constraints to be placed on the mass and orbital parameters of the brown dwarf companion. Thanks to the high precision of the RV data and the number of points, the minimum mass is well constrained, meaning that only a few astrometric points from high-contrast imaging were necessary to ensure a high-precision orbit and dynamical mass.

The paper is organised as follows. The properties of the host star are summarised in Sect. 2. In Sect. 3 we summarise the observations and data analysis procedures for the RV and high-contrast imaging data. In Sect. 4 we present the results of the imaging data analysis and derived companion properties, and give an overview of the results from the combined orbital fitting. The results are discussed in Sect. 5 with some concluding remarks.

2. Stellar characterisation

The observed and inferred stellar parameters for HD 13724 are summarised in Table 1. The spectral type, V band magnitude, and colour index are taken from the HIPPARCOS and *Tycho* catalogues (Hoeg et al. 1997; Perryman et al. 1997), while the astrometric parallax (π) and luminosity are taken from the second *Gaia* data release (Gaia Collaboration 2018). The effective temperature, gravity and metallicities were derived using the same spectroscopic methods as applied in Santos et al. (2013), whilst the $v \sin i$ is computed using the calibration of CORALIE's Cross Correlation Function (CCF; Santos et al. 2001; Marmier 2014).

Table 1. Stellar parameters of HD 13724.

Parameters	Units	HD 13724
Spectral type [a]		G3/G5V
V [a]		7.89
$B-V$ [a]		0.667
π [b]	[mas]	23.0 ± 0.03
M_v		4.70
T_{Gaia} [b]	[K]	$5775.33^{+49.67}_{-74.33}$
$\log g$	[cgs]	4.44 ± 0.07
[Fe/H]	[dex]	0.23 ± 0.02
$v \sin i$ [c]	[km s^{-1}]	3.025
M_*	[$M_\odot$]	1.14 ± 0.06
L_{Gaia} [b]	[$L_\odot$]	$1.14^{+0.001}_{-0.002}$
R_{Gaia} [b]	[$R_\odot$]	1.07 ± 0.02
$\log R'_{\rm HK}$ [c]		−4.76 ± 0.003
$P_{\rm rot}$	[days]	20.2 ± 1.2
Age	[Gyr]	1.04 ± 0.88

Notes. [a]Parameters taken from HIPPARCOS and *Tycho* (Perryman et al. 1997; Hoeg et al. 1997). [b]Parallaxes taken from *Gaia* data release 2 (Gaia Collaboration 2018). [c]Parameters derived using CORALIE CCF.

The mean chromospheric activity index – $\log(R'_{\rm HK})$ – is computed by co-adding the corresponding CORALIE spectra to improve the signal-to-noise ratio (S/N) which allows us to measure the Ca II re-emission at λ = 3933.66 Å. We derived an estimate of the rotational period of the star from the mean $\log(R'_{\rm HK})$ activity index using the calibration of Mamajek & Hillenbrand (2008).

The stellar radius and uncertainties are derived from the *Gaia* luminosities and the effective temperatures are obtained from the spectroscopic analysis. A systematic error of 50 K was quadratically added to the effective temperature error bars and propagated in the radius uncertainties.

The mass and age of HD 13724, as well as the uncertainties, were derived using the Geneva stellar evolution modes (Ekström et al. 2012; Georgy et al. 2013). The interpolation in the model grid was made through a Bayesian formalism using observational Gaussian priors on $T_{\rm eff}$, M_V, $\log g$, and [Fe/H] (Marmier 2014).

3. Observations and data reduction

Radial-velocity and direct imaging observations were combined to constrain the orbit of HD 13724 B. Furthermore, the extensive orbital coverage of the RV time series allows us to precisely constrain its orbital parameters. Combined with several direct imaging observations we are able to derive the orbital inclination i and thus the mass. In addition, the SPHERE high-contrast IRDIS observations provide six narrow-band-width photometric measurements in the J, H, and K bands and IFS observations allow us to obtain a low-resolution spectrum of the brown dwarf companion in the $Y-J$ bands.

3.1. Radial velocities

HD 13724 has been observed since August 1999 with the CORALIE spectrograph (Queloz et al. 2000) installed on the

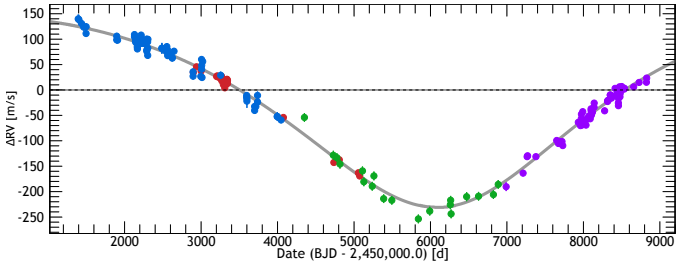

Fig. 1. HD 13724 RV measurements as a function of Julian Dates obtained with CORALIE-98 (blue), CORALIE-07 (green), and CORALIE-14 (purple). The HARPS-03 data are shown in red. The best single-planet Keplerian model is represented as a black curve.

Table 2. Orbital elements of HD 13724 B derived from the MCMC posterior distributions.

Param	Unit	Med	Std	CI (2.5%)	CI (97.5%)
P	yr	123	41	72	226
K	m s^{-1}	278	13	251	299
e		0.63	0.07	0.5	0.75
ω	deg	184.9	1.1	182.8	187.0
Ω	deg	16.4	4.2	7.3	23.9
i	deg	57.4	1.7	53.6	60.9
a_r	AU	26.3	5.6	18.3	39.5
$T_{V_{min}}$	d [(a)]	56034	21	55993	56074
M_B	M_{Jup}	50.5	3.3	43.7	56.7

Notes. [(a)]The date is expressed as BJD-2 400 000.0.

1.2 m EULER Swiss telescope at La Silla observatory (Chile) and HARPS (Mayor et al. 2003) on the ESO/3.6 m telescope to obtain RVs.

The RV data analysis presented in this paper was accomplished using a set of online tools hosted by the Data and Analysis Center for Exoplanets (DACE)[1], which performs a Keplerian fit to the data as described in Delisle et al. (2016). The 179 measurements obtained between August 1999 and December 2019 are shown in Fig. 1 with the corresponding Keplerian model.

Following on from Rickman et al. (2019) we obtained five more RV measurements over ~10 months. We also added four historical and low-precision (~300 m s^{-1}) CORAVEL measurements to increase the overall time-span of the RV measurements by 10 yr and to provide an upper bound constraint on the minimum mass of the companion. The RV data products presented in this paper are available at DACE with the new orbital parameters shown in Table 2. The full description of the RV data is outlined in Rickman et al. (2019).

3.2. SPHERE high-contrast imaging

HD 13724 was observed with SPHERE, the extreme adaptive optics system at the VLT (Beuzit et al. 2019) on 18 Aug. 2018, 12 Oct. 2019, and 18 Oct. 2019. Observations were taken using the IRDIFS mode, which allows the Integral Field Spectrograph (IFS; Mesa et al. 2015) and the InfraRed Dual-Band Imager and Spectrograph (IRDIS; Dohlen et al. 2008) modules to be used simultaneously. The IFS data cover a range of wavelengths from $Y-J$ (0.96–1.34 μm, spectral resolution $R \sim 54$). The IRDIS data were taken in dual-band imaging mode (Vigan et al. 2010) using the $H2$ and $H3$ filters (λ_{H2} = 1.58888 μm, λ_{H3} = 1.6671 μm), as well as using the $J2$ and $J3$ filters (λ_{J2} = 1.190 μm, λ_{J3} = 1.273 μm) and the $K1$ and $K2$ band filters (λ_{K1} = 2.110 μm and λ_{K2} = 2.251 μm), such that the $J2$, $H3$, and $K2$ bands align with methane absorption bands.

The observing sequence consisted of long-exposure images taken with an apodized Lyot coronagraph (Soummer et al. 2003). To measure the position of the star behind the coronograph, several exposures were taken with a sinusoidal modulation applied to the deformable mirror (to generate satellite spots around the star) at the beginning and at the end of the sequence. To estimate the stellar flux and the shape of the point-spread function (PSF) during the sequence, several short-exposure images were taken with the star moved from behind the coronograph, and using a neutral-density (ND) filter with a ~10% transmission[2], also at the beginning and end of the sequence. In addition, several long-exposure sky frames were taken to estimate the background flux and help identify bad pixels on the detector.

The SPHERE Data Reduction and Handling pipeline (Pavlov et al. 2008) was used to perform the wavelength extraction for the IFS data, turning the full-frame images of the lenslet spectra into image cubes. The remainder of the data reduction and analysis was completed using the Geneva Reduction and Analysis Pipeline for High-contrast Imaging of planetary Companions (GRAPHIC) (Hagelberg et al. 2016). The data were first sky subtracted, flat fielded, cleaned of bad pixels, and corrected for distortion (following Maire et al. 2016b). We then ran a principal component analysis (PCA) PSF substraction algorithm (Soummer et al. 2012; Amara & Quanz 2012) which is run separately for images at each wavelength channel and for each IRDIS channel. The resulting frames were derotated and median combined to produce a final PSF-substracted image.

In addition to this, we performed a spectral differential imaging (SDI) reduction for both the IFS and IRDIS datasets. The same PCA algorithm was then performed on the resulting images. The resulting PCA-reduced and SDI IRDIS and IFS images are shown in Fig. 2.

4. Results

4.1. Astrometry and photometry

The relative astrometry and photometry were calculated using a negative fake-planet injection on the images (Bonnefoy et al. 2011). An initial Nelder-Mead minimisation routine (Gao & Han 2012) was used to find a first-order estimation of the separation (in pixels), position angle (in degrees), and contrast ratio between the star and the companion. We then fitted over a 3D grid of parameters for the position and the flux of the fake negative PSF to minimise the residuals and to numerically derive the χ^2 with the associated 68.27% confidence interval. Subsequently, we corrected for the pixel scale and true north angle given in Maire et al. (2016b). The resulting parameters are listed in Table 3.

The IFS data were taken in the wavelength range 0.96–1.34 μm which is split into 39 wavelength channels, giving 39 images across the wavelength range. Because of the low S/N in

[1] The DACE platform is available at https://dace.unige.ch where the online tools to analyse RV data can be found in the section Observations->Radial Velocities.

[2] The corrections for the ND filter transmission are done using the ND filter curves given at https://www.eso.org/sci/facilities/paranal/instruments/sphere/inst/filters.html

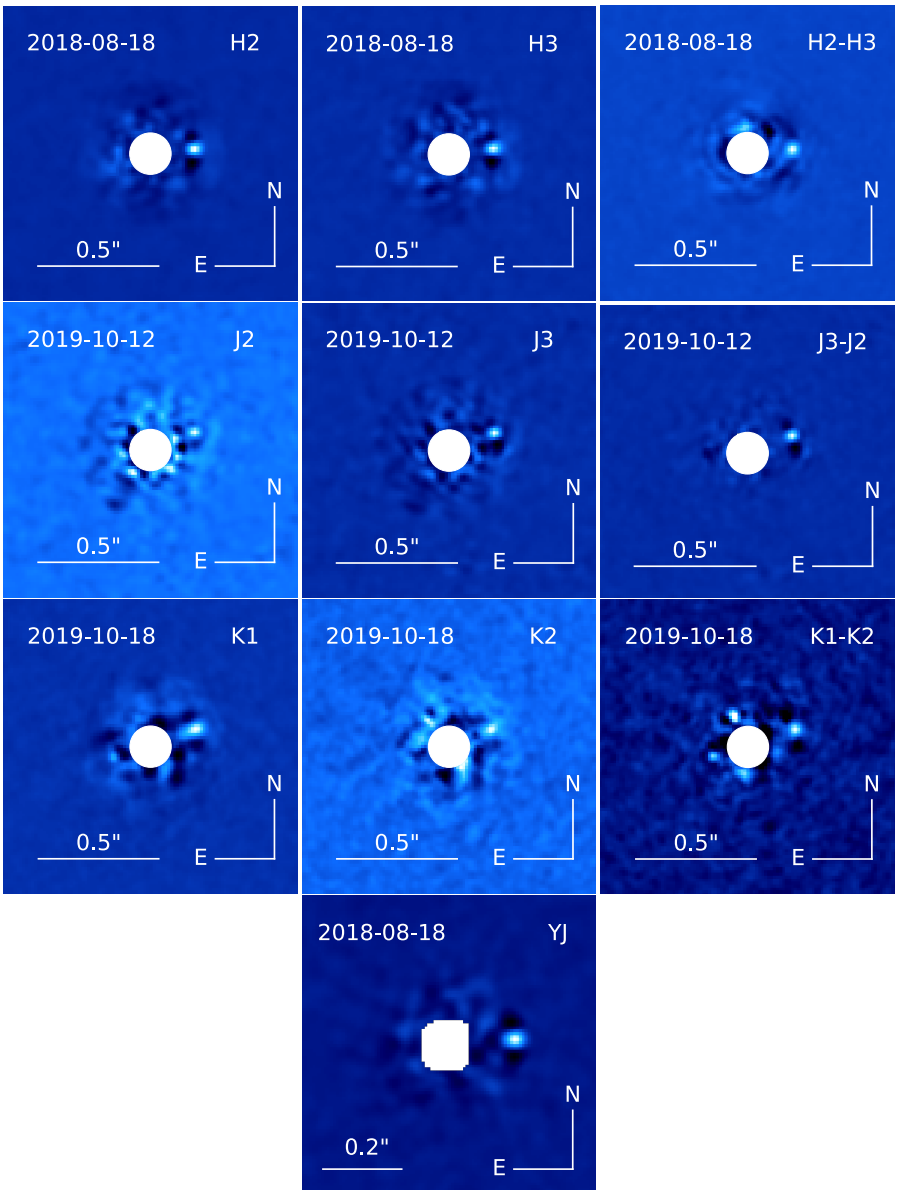

Fig. 2. IRDIS and IFS images of HD 13724. The star is masked by the white circle. We also show a weighted combination of the IFS SDI image. Each IFS wavelength channel was weighted by the average flux predicted by the best-fitting BT-Settl model (Allard et al. 2012).

Table 3. Measured relative astrometry and photometry of HD 13724 B from the SPHERE observations.

Instrument	Filter	Date	BJD [(a)]	ρ (mas)	θ (deg)	Contrast (mag)
IRDIS	*H*2	2018-08-18	58 349.29438	175.61 ± 4.45	272.15 ± 1.06	10.61 ± 0.16
IRDIS	*H*3	2018-08-18	58 349.29438	178.85 ± 4.56	272.50 ± 1.71	11.34 ± 0.32
IRDIS	*H*2–*H*3	2018-08-18	58 349.29438	177.70 ± 4.41	270.75 ± 1.76	11.71 ± 0.35
IRDIS	*J*2	2019-10-12	58 768.16564	179.9 ± 12.69	289.92 ± 2.49	11.50 ± 0.40
IRDIS	*J*3	2019-10-12	58 768.16564	188.90 ± 4.98	288.75 ± 1.05	10.37 ± 0.04
IRDIS	*J*3–*J*2	2019-10-12	58 768.16564	187.59 ± 1.60	288.25 ± 0.58	10.82 ± 0.09
IRDIS	*K*1	2019-10-18	58 774.20206	190.55 ± 9.05	288.75 ± 1.51	10.29 ± 0.18
IRDIS	*K*2	2019-10-18	58 774.20206	192.12 ± 15.84	288.75 ± 2.52	11.10 ± 0.46
IRDIS	*K*1–*K*2	2019-10-18	58 774.20206	200.32 ± 16.15	288.58 ± 2.62	11.15 ± 0.43

Notes. [(a)]The date are expressed as BJD-2 400 000.0.

some of the spectral channels, we used a different approach to measure the companion flux. For the IFS data, we performed a fit for the separation and position angle using the negative fake-planet injection using a stacked image across all of the wavelength channels in order to have a high S/N for the companion fit. Using this fitted position on the image, we then fitted for the contrast ratio between the companion and the star at each wavelength channel in order to extract the spectrum.

Table 4. The measured absolute photometry of HD 13724 B with the derived mass and temperature using Baraffe et al. (2003).

Band	App. mag	Abs. mag	Mass ($M_{\rm Jup}$)	Temp. (K)
$H2$	17.09 ± 0.16	13.90 ± 0.16	43.9 ± 1.8	1306 ± 48
$H3$	17.82 ± 0.32	14.63 ± 0.32	36.7 ± 3.0	1128 ± 74
$J2$	18.23 ± 0.40	15.04 ± 0.40	32.4 ± 4.0	1020 ± 99
$J3$	17.10 ± 0.05	13.91 ± 0.05	44.0 ± 0.6	1310 ± 18
$K1$	16.67 ± 0.18	13.48 ± 0.18	47.5 ± 2.2	1399 ± 56
$K2$	17.48 ± 0.46	14.29 ± 0.46	39.0 ± 4.3	1184 ± 106

4.2. Orbit determination and dynamical mass

To constrain the orbital parameters of the brown dwarf, we performed a combined fit to the RV and direct-imaging data. For this we used the IRDIS $H2$, $H3$, $J2$, $J3$, $K1$ and $K2$ astrometry $\{\rho(t), \theta(t)\}$ where $\rho(t)$ is the observed separation in mas and $\theta(t)$ is the position angle in degrees (see Table 4). This allows us to place constraints on the period, eccentricity, and inclination of the system.

Due to two major upgrades to CORALIE in June 2007 (Ségransan et al. 2010) and in November 2014, we consider CORALIE as three different instruments, corresponding to the different upgrades: the original CORALIE as CORALIE-98 (C98), the first upgrade as CORALIE-07 (C07), and the latest upgrade as CORALIE-14 (C14).

The observed RV signal was modelled with a single Keplerian and five RV offsets (corresponding to one offset for each RV instrument). HARPS-03 was chosen as the reference instrument while RV offsets were adjusted between CORAVEL, CORALIE-98, CORALIE-07, CORALIE-14, and HARPS-03; where each of the instrumental offsets were margnialised over for the fit.

A linear correlation is observed between the H_α activity index time series and the observed RVs which allows us to carry out a first-order detrending of the observed RV measurements using a linear scale factor between the H_α index time series and the modelled RVs (Delisle et al. 2018). A RV nuisance parameter – corresponding to the white noise component of the stellar activity – is added to the noise model of the likelihood function and is adjusted in the MCMC.

Regarding the Keplerian motion, we choose to adjust the natural log of the period and of the RV semi-amplitude to increase the efficiency of the MCMC due to the partial coverage of the orbit. We also probe the eccentricity and the argument of periastron through $\sqrt{e}.\cos\omega$ and $\sqrt{e}.\sin\omega$ variables. We use a uniform prior on these variables which also corresponds to a uniform prior in eccentricity and ω. The longitude of the ascending node, Ω, the inclination, i, and the relative orbit semi-major axis expressed in milli-arcseconds are also adjusted. The conversion from angles to astronomical units is done using the *Gaia* parallax as a Gaussian prior. The orbit phase reference was chosen as the time at which the RV is minimum, $T_{V_{\rm min}}$, since it is well defined by the RV observations (see Fig. 1).

We probe the full parameter space, composed of 16 parameters, using an MCMC with an adaptive Metropolis (Haario et al. 2001) and an adaptive scaling (Andrieu & Thoms 2008) which is particularly efficient at probing parameters with linear correlations. Additional tables and figures illustrating the results of the MCMC analysis are provided in the appendix.

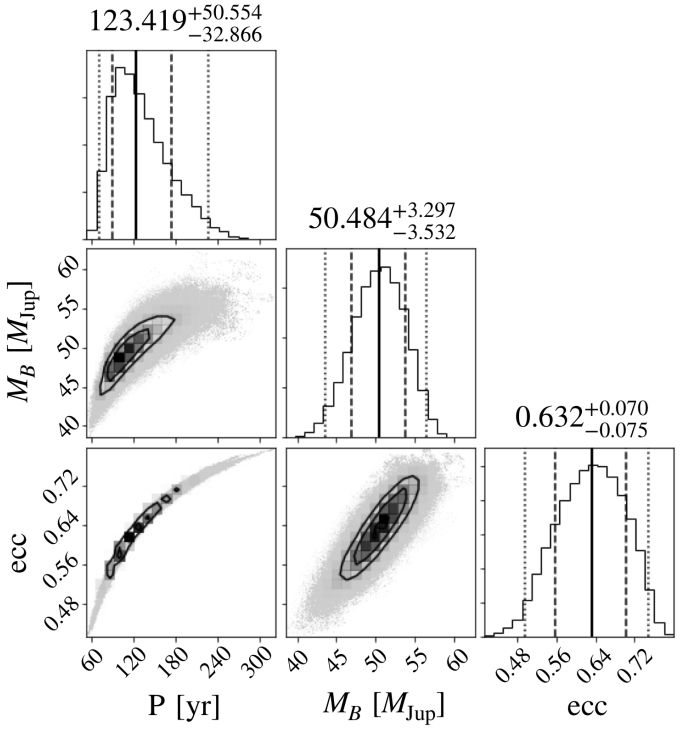

Fig. 3. Marginalised 1D and 2D posterior distributions of the orbital period, as well as the eccentricity and the companion mass corresponding to the global fit of the RV and direct-imaging models. Confidence intervals at 2.275, 15.85, 50.0, 84.15, 97.725% are overplotted on the 1D posterior distributions, while the median $\pm1\sigma$ values are given at the top of each 1D distribution. Here, 1, 2, and 3σ contour levels are overplotted on the 2D posterior distribution.

From combining the RV and direct imaging measurements we were able to bring good constraints on the geometry of the orbit and the mass of HD 13724 B. Based on the MCMC posterior distribution, we are able to set confidence intervals for the orbital elements and physical parameters of HD 13724 B. The 95% confidence interval for the period ranges from 72 to 226 yr, its semi-major axis between 18 and 40 AU, and its mass between 43 and 56 $M_{\rm Jup}$. Orbital elements values and confidence intervals are given in Table 2 while the full list of parameters adjusted in the MCMC is provided in the Appendix (Table A.1). A mass-period-eccentricity corner plot based on the marginalised 2D posterior distribution is presented in Fig. 3 and illustrates the wide range of orbits still compatible with our data. However, the nature of HD 13724 B is undoubtedly well below the hydrogen burning limit.

We note that these orbital solutions have higher eccentricities and longer periods than those published in Rickman et al. (2019). This is explained by (1) the SPHERE measurements that rule out the shortest periods and (2) a significant improvement in our MCMC implementation that increases the efficiency with which we can probe correlated parameter spaces (see Fig. A.1).

4.3. Companion properties

To allow a consistent comparison with other objects and to estimate the mass of HD 13724 B, we converted the $H2$, $H3$, $J2$, $J3$, $K1$ and $K2$ fluxes into absolute magnitudes using the *Gaia*-measured distance of HD 13724 (Gaia Collaboration 2018) shown in Table 1. We then used the COND (Baraffe et al. 2003) substellar isochrones to predict the companion mass and

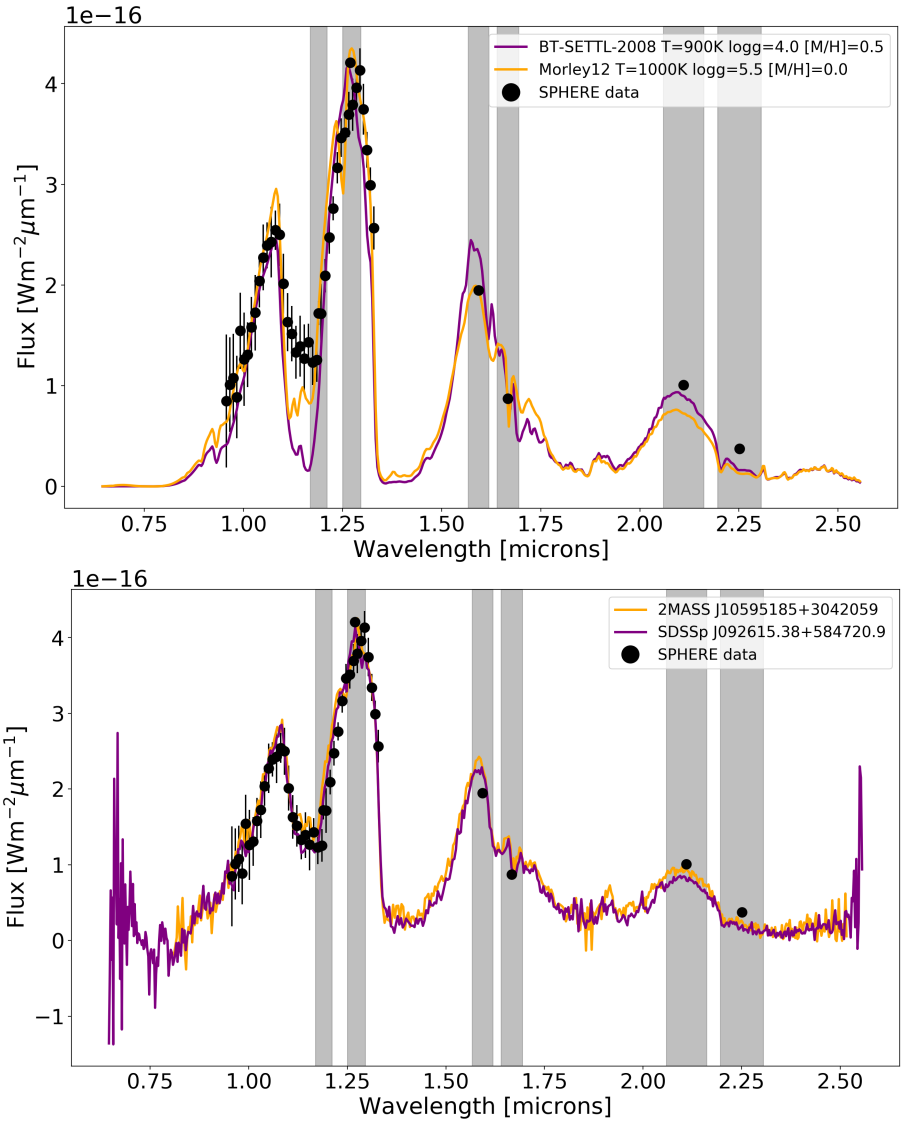

Fig. 4. Atmospheric spectra of HD 13724. The FWHM of the $J23$, $H23$, and $K12$ IRDIS filters are shown with grey bars (*from left to right*). The error bars on the $H2$, $H3$, $K1$, and $K2$ data are present but smaller than the size of the markers on each plot. *Top*: two best-fitting spectra from BT-Settl 2008 models (Allard et al. 2012) and the Morley et al. (2012) models from the SpeX Prism library are overplotted, and the flux is scaled to match HD 13724 B. Fitting was performed to the IFS and IRDIS data simultaneously. *Bottom*: comparison of the observed spectrum of HD 13724 B with the two best fit T4 brown dwarf atmospheres: 2MASS J10595185+3042059 and SDSSp J092615.38+58720.9 fitted using the *splat* package (Burgasser et al. 2016).

temperature as a function of the calculated absolute photometry in each band. The resulting absolute photometric magnitudes, masses, and temperatures are listed in Table 4.

4.4. Spectral and atmospheric analysis

In order to estimate the spectral type of HD 13724 B, we used the SpeX Prism library of near-infrared (NIR) spectra of brown dwarfs (Burgasser 2014) using the *splat* python package (Burgasser et al. 2016) where each spectrum was flux calibrated to the distance of HD 13724. The *splat* package contains a library of observed brown dwarf spectra as well as theoretical models that we use as templates to derive the physical parameters.

Each SpeX Prism spectrum was also converted into the appropriate spectral resolution of each IFS measurement by convolution with a Gaussian. The FWHM used for the convolution was assumed to be twice the separation between each wavelength channel. To fit the spectrophotometry of HD 13724 B with atmospheric models, we converted the contrast measurements into physical fluxes using a model spectrum for the host star ($T_{\rm eff}$ = 5900 K, $\log g$ = 4.5 dex and [Fe/H] = 0.3 dex) from the BT-NextGen library (Allard et al. 2012) and the SPHERE filter transmission curves. The BT-NextGen spectrum is fit to the spectral energy distribution (SED) and is built using data from *Tycho* (Høg et al. 2000), 2MASS (Cutri et al. 2003), WISE (Cutri et al. 2013), and HIPPARCOS (Perryman et al. 1997).

We calculated the $\chi^2_{\rm r}$ of template brown dwarfs in the SpeX Prism library as a function of spectral type. We include the uncertainties of the template spectra in the χ^2 computation. The best-fit object is 2MASS J10595185+3042059 (Cutri et al. 2003) which is classified as a T4 brown dwarf. In Fig. 4 we also plot the second-best fit spectrum of SDSSp J092615.38+584720.9 (Cutri et al. 2003), which is classified as a T4.0/T4.5 brown dwarf. The temperatures of 2MASS J10595185+3042059 and SDSSp J092615.38+584720.9 are not given explicitly but effective temperatures of mid-T dwarfs covers a small range ($T_{\rm eff} \approx$ 1100−1400 K; Kirkpatrick et al. 2000). The T4 spectral type provides the best fit.

We use the $H2$ and $H3$ band values to place HD 13724 B on a colour-magnitude diagram as shown in Fig. 5 which is built using the Spex Prism Library (Burgasser 2014). The placement of HD 13724 B on the colour-magnitude diagram agrees well with the estimated T spectral type.

To further constrain the physical properties of HD 13724 B, we compared the observed SED to synthetic spectra for cool brown dwarfs from Morley et al. (2012) and Allard et al. (2012).

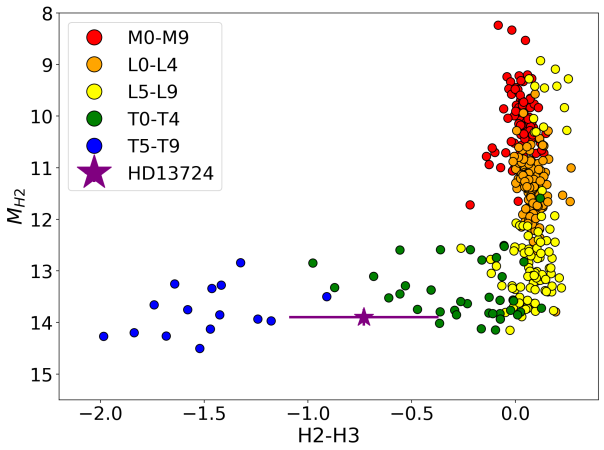

Fig. 5. Colour-magnitude diagram showing the predicted $H2$–$H3$ colours and $H2$ absolute magnitudes for objects in the SpeX Prism Library (Burgasser 2014). The flux of HD 13724 B and the 1σ limit on its $H2$–$H3$ colour are shown. Its position is compatible with objects in the middle of the T sequence.

The biggest difference between these models is that the Morley et al. (2012) models include the condensate sedimentation efficiency coefficients.

We adjusted the Morley et al. (2012) and Allard et al. (2012) models, which sit well within the range of the mid-T dwarf range (see Fig. 4). The Morley et al. (2012) models are the best fit to the data with the following parameters: $T_{\rm eff}$ = 1000 K, $\log g$ = 5.5 cm s^{-2}, $f_{\rm SED}$ = 3, [M/H] = 0.0, and R = 1.01 $R_{\rm Jup}$.

5. Summary and conclusions

In this paper we report the direct detection of a ~50 $M_{\rm Jup}$ brown dwarf using VLT/SPHERE. HD 13724 B serves as an essential benchmark brown dwarf for testing brown dwarf atmospheric and evolutionary models where it joins just a short list of benchmark brown dwarf companions of stars with RV and imaging measurements: HR 7672 B (Liu et al. 2002; Crepp et al. 2012), HD 19467 B (Crepp et al. 2014), HD 4747 B (Sahlmann et al. 2011; Crepp et al. 2016; Peretti et al. 2019), GJ 758 B (Thalmann et al. 2009; Bowler et al. 2018), HD 4113 C (Cheetham et al. 2018), GJ 229 B (Nakajima et al. 1995; Brandt et al. 2019; Feng et al. 2020), and HD 72946 B (Maire et al. 2020).

We obtained images of HD 13724 B in the J, H, and K bands along with its spectrum from IFS data in the Y–J bands. Through comparison with the SpeX Prism Library of brown dwarf spectra (Burgasser 2014), we found that HD 13724 B is most consistent with a spectral type of T4, which also agrees with the position of HD 13724 B on the $H2$–$H3$ colour-magnitude diagram (Fig. 5). It should be noted that in general the template T4 brown dwarf provides a better fit than the synthetic spectra of Morley et al. (2012). This is especially true in the $K1$ and $K2$ bands where we observe more flux than the models would suggest. This might be due to clouds in the atmospheres that tend to increase the flux in the K-band (Marley et al. 1996; Morley et al. 2012). The template adjustment using the Morley et al. (2012) models allowed us to derive a temperature of 1000 K.

We analysed the HD 13724 system by combining RV measurements and high-contrast imaging, enabling us to place constraints on the orbital and physical parameters of HD 13724 B. This suggests a mass of 43–56 $M_{\rm Jup}$, an inclination of 53–60 deg, and a period range of 72–226 yr. We calculated the isochronal mass of HD 13724 B from the COND substellar isochrones (Baraffe et al. 2003) taking into account the age of the star. This gives a mass range of 31–52 $M_{\rm Jup}$ corresponding to an age of 0.5–2 Gyr. This overlaps with the mass range from the observations and suggests that either the star is slightly older than expected or – if the age is correct – some physics is missing from the modelling of the evolution of these substellar objects.

The combination of *Gaia* astrometry with future RV and imaging datasets will allow for much tighter constraints on the orbital and physical parameters of HD 13724 B, which in turn will improve the comparison with atmospheric and evolutionary models.

Many attempts have been made to detect these long-period companions from the CORALIE RV survey through imaging as part of a fifteen-year effort using VLT/NACO, with little success. The VLT/SPHERE is allowing us to now unveil these RV-detected brown dwarfs. We expect that the future upgrade of SPHERE (SPHERE+ Boccaletti 2019) will increase the sample of cool brown dwarfs detected thanks to its higher contrast capabilities at short separations. Ultimately, future instruments like SPHERE+, the *James Webb* Space Telescope, and the upcoming ELT/METIS (Carlomagno et al. 2016) should allow us to bridge the gap between the coolest brown dwarfs and the most massive giant planets.

Acknowledgements. This work has been carried out within the framework of the National Centre for Competence in Research PlanetS supported by the Swiss National Science Foundation. The authors acknowledge the financial support of the SNSF. This publications makes use of The Data & Analysis Center for Exoplanets (DACE), which is a facility based at the University of Geneva (CH) dedicated to extrasolar planets data visualisation, exchange and analysis. DACE is a platform of the Swiss National Centre of Competence in Research (NCCR) PlanetS, federating the Swiss expertise in Exoplanet research. The DACE platform is available at https://dace.unige.ch. This work has made use of data from the European Space Agency (ESA) mission *Gaia* (https://www.cosmos.esa.int/gaia), processed by the *Gaia* Data Processing and Analysis Consortium (DPAC, https://www.cosmos.esa.int/web/gaia/dpac/consortium). Funding for the DPAC has been provided by national institutions, in particular the institutions participating in the *Gaia* Multilateral Agreement. This research has benefitted from the SpeX Prism Library (and/or SpeX Prism Library Analysis Toolkit), maintained by Adam Burgasser at http://www.browndwarfs.org/spexprism. This research made use of the SIMBAD database and the VizieR Catalogue access tool, both operated at the CDS, Strasbourg, France. The original descriptions of the SIMBAD and VizieR services were published in Wenger et al. (2000) and Ochsenbein et al. (2000). This research has made use of NASA's Astrophysics Data System Bibliographic Services.

References

Allard, F., Homeier, D., & Freytag, B. 2012, Phil. Trans. R. Soc. London, Ser. A, 370, 2765
Amara, A., & Quanz, S. P. 2012, MNRAS, 427, 948
Andrieu, C., & Thoms, J. 2008, Stat. Comput., 18, 343
Baraffe, I., Chabrier, G., Barman, T. S., Allard, F., & Hauschildt, P. H. 2003, A&A, 402, 701
Baraffe, I., Homeier, D., Allard, F., & Chabrier, G. 2015, A&A, 577, A42
Beuzit, J. L., Vigan, A., Mouillet, D., et al. 2019, A&A, 631, A155
Boccaletti, A. 2019, in The Very Large Telescope in 2030, 38
Boden, A. F., Torres, G., & Latham, D. W. 2006, ApJ, 644, 1193
Bonnefoy, M., Lagrange, A. M., Boccaletti, A., et al. 2011, A&A, 528, L15
Bowler, B. P., Dupuy, T. J., Endl, M., et al. 2018, AJ, 155, 159
Brandt, T. D., Dupuy, T. J., Bowler, B. P., et al. 2019, AJ, submitted [arXiv:1910.01652]
Burgasser, A. J. 2014, in Astronomical Society of India Conference Series (India: Astronomical Society of India), 11
Burgasser, A. J., Aganze, C., Escala, I., et al. 2016, AAS Meeting Abstracts, 227, 434.08
Carlomagno, B., Absil, O., Kenworthy, M., et al. 2016, SPIE Conf. Ser., 9909, 990973
Cheetham, A., Ségransan, D., Peretti, S., et al. 2018, A&A, 614, A16

Crepp, J. R., Johnson, J. A., Fischer, D. A., et al. 2012, ApJ, 751, 97
Crepp, J. R., Johnson, J. A., Howard, A. W., et al. 2014, ApJ, 781, 29
Crepp, J. R., Gonzales, E. J., Bechter, E. B., et al. 2016, ApJ, 831, 136
Cutri, R. M., Wright, E. L., Conrow, T., et al. 2013, VizieR Online Data Catalog: II/328
Cutri, R. M., Skrutskie, M. F., van Dyk, S., et al. 2003, VizieR Online Data Catalog, II/246
Delisle, J. B., Ségransan, D., Buchschacher, N., & Alesina, F. 2016, A&A, 590, A134
Delisle, J. B., Ségransan, D., Dumusque, X., et al. 2018, A&A, 614, A133
Dohlen, K., Langlois, M., Saisse, M., et al. 2008, Proc. SPIE, 7014, 70143L
Dupuy, T. J., & Liu, M. C. 2017, ApJS, 231, 15
Ekström, S., Georgy, C., Eggenberger, P., et al. 2012, A&A, 537, A146
Feng, F., Butler, R. P., Shectman, S. A., et al. 2020, ApJS, 246, 11
Gaia Collaboration (Brown, A. G. A., et al.) 2018, A&A, 616, A1
Gao, F., & Han, L. 2012, Comput. Optim. Appl., 51, 259
Georgy, C., Ekström, S., Eggenberger, P., et al. 2013, A&A, 558, A103
Haario, H., Saksman, E., & Tamminen, J. 2001, Bernoulli, 7, 223
Hagelberg, J., Ségransan, D., Udry, S., & Wildi, F. 2016, MNRAS, 455, 2178
Hoeg, E., Bässgen, G., Bastian, U., et al. 1997, A&A, 323, L57
Høg, E., Fabricius, C., Makarov, V. V., et al. 2000, A&A, 355, L27
Kirkpatrick, J. D., Reid, I. N., Liebert, J., et al. 2000, AJ, 120, 447
Liu, M. C., Fischer, D. A., Graham, J. R., et al. 2002, ApJ, 571, 519
Maire, A. L., Bonnefoy, M., Ginski, C., et al. 2016a, A&A, 587, A56
Maire, A.-L., Langlois, M., Dohlen, K., et al. 2016b, SPIE Conf. Ser., 9908, 990834
Maire, A. L., Baudino, J. L., Desidera, S., et al. 2020, A&A, 633, L2
Mamajek, E. E., & Hillenbrand, L. A. 2008, ApJ, 687, 1264
Marley, M. S., Saumon, D., Guillot, T., et al. 1996, Science, 272, 1919
Marmier, M. 2014, Ph.D. thesis, Geneva Observatory, University of Geneva, Switzerland
Mayor, M., Pepe, F., Queloz, D., et al. 2003, The Messenger, 114, 20
Mesa, D., Gratton, R., Zurlo, A., et al. 2015, A&A, 576, A121
Morley, C. V., Fortney, J. J., Marley, M. S., et al. 2012, ApJ, 756, 172
Nakajima, T., Oppenheimer, B. R., Kulkarni, S. R., et al. 1995, Nature, 378, 463
Ochsenbein, F., Bauer, P., & Marcout, J. 2000, A&AS, 143, 23
Pavlov, A., Möller-Nilsson, O., Feldt, M., et al. 2008, SPIE Conf. Ser., 7019, 701939
Peretti, S., Ségransan, D., Lavie, B., et al. 2019, A&A, 631, A107
Perryman, M. A. C., Lindegren, L., Kovalevsky, J., et al. 1997, A&A, 323, L49
Queloz, D., Mayor, M., Naef, D., et al. 2000, in From Extrasolar Planets to Cosmology: The VLT Opening Symposium, eds. J. Bergeron & A. Renzini (Berlin: Springer), 548
Rickman, E. L., Ségransan, D., Marmier, M., et al. 2019, A&A, 625, A71
Sahlmann, J., Ségransan, D., Queloz, D., et al. 2011, A&A, 525, A95
Santos, N. C., Israelian, G., & Mayor, M. 2001, A&A, 373, 1019
Santos, N. C., Sousa, S. G., Mortier, A., et al. 2013, A&A, 556, A150
Ségransan, D., Udry, S., Mayor, M., et al. 2010, A&A, 511, A45
Soummer, R., Aime, C., & Falloon, P. E. 2003, A&A, 397, 1161
Soummer, R., Pueyo, L., & Larkin, J. 2012, ApJ, 755, L28
Thalmann, C., Carson, J., Janson, M., et al. 2009, ApJ, 707, L123
Udry, S., Mayor, M., Queloz, D., Naef, D., & Santos, N. 2000, in From Extrasolar Planets to Cosmology: The VLT Opening Symposium, eds. J. Bergeron & A. Renzini (Berlin: Springer), 571
Vigan, A., Moutou, C., Langlois, M., et al. 2010, MNRAS, 407, 71
Vigan, A., Bonnefoy, M., Ginski, C., et al. 2016, A&A, 587, A55
Wenger, M., Ochsenbein, F., Egret, D., et al. 2000, A&AS, 143, 9

Appendix A: MCMC results

Here we provide the full list of parameters adjusted in the MCMC as well as the marginalised 1D and 2D posterior distributions of the parameters corresponding to the global fit of the RV and direct-imaging models.

Table A.1. Parameters corresponding to the combined adjustment of the astrometric and RV observations of HD 13724 B derived from the MCMC posterior distributions.

Var	Units	Max(Proba)	Mode	Med	Std	CI(2.5%)	CI(97.5%)	Priors
$M_\star$	$[M_\odot]$							$N(1.14, 0.06)$
π	[mas]							$N(22.9781,\ \sqrt{0.0277^2 + 0.040^2})$
log (Proba)		−675.516	−685.396	−682.013	2.687	−688.373	−678.024	
$\gamma(H03)$	$[\mathrm{m\,s^{-1}}]$	20833	20885	20806	36	20733	20870	U
$\Delta V(CVL - H03)$ (*)	$[\mathrm{m\,s^{-1}}]$	−229	−303	−234	133	−496	27	$N(0, 300)$
$\Delta V(C98 - H03)$	$[\mathrm{m\,s^{-1}}]$	−37.9	−35.8	−37.6	2.3	−42.2	−33.0	U
$\Delta V(C07 - H03)$	$[\mathrm{m\,s^{-1}}]$	−37.8	−34.2	−41.0	4.5	−49.9	−32.2	U
$\Delta V(C14 - H03)$	$[\mathrm{m\,s^{-1}}]$	−15.1	−21.2	−13.6	4.4	−22.3	−5.0	$N(-20, 5)$
S_{Act}	$[\mathrm{m\,s^{-1}}]$	14.0	20.3	12.5	4.5	3.6	21.4	U
σ_J	$[\mathrm{m\,s^{-1}}]$	7.03	7.17	7.11	0.62	5.98	8.39	U
$\log(P)$	[day]	4.764	4.952	4.654	0.132	4.423	4.917	U
$\log(K)$	$[\mathrm{m\,s^{-1}}]$	2.459	2.483	2.444	0.020	2.400	2.476	U
$\sqrt{e}.\cos\omega$		−0.827	−0.864	−0.792	0.043	−0.862	−0.702	U
$\sqrt{e}.\sin\omega$		−0.070	−0.114	−0.067	0.014	−0.095	−0.039	U
$T_{V\mathrm{min}}$	[bjd] (**)	56033	56038	56034	21	55993	56074	U
Ω	[deg]	17.4	19.2	16.4	4.3	7.3	23.9	U
i	[deg]	58.5	58.6	57.40	1.7	53.6	60.0	U
a_{r}	[mas]	721	945	606	129	421	907	U
K	$[\mathrm{m\,s^{-1}}]$	288	304	278	13	251	299	–
P	[y]	159	245	123	41	72	226	–
e		0.688	0.760	0.632	0.067	0.498	0.747	–
ω	[deg]	184.9	187.5	184.9	1.1	182.8	187.0	–
a_{r}	[au]	31.3	41.2	26.3	5.6	18.3	39.5	–
M_{B}	$[M_{\mathrm{jup}}]$	53.1	56.3	50.5	3.3	43.7	56.4	–
$M_{\mathrm{B}}.\sin(i)$	$[M_{\mathrm{jup}}]$	45.3	48.1	42.5	3.5	35.3	48.6	–

Notes. (*) CVL stands for CORAVEL; (**) the date is expressed as BJD-2 400 000.

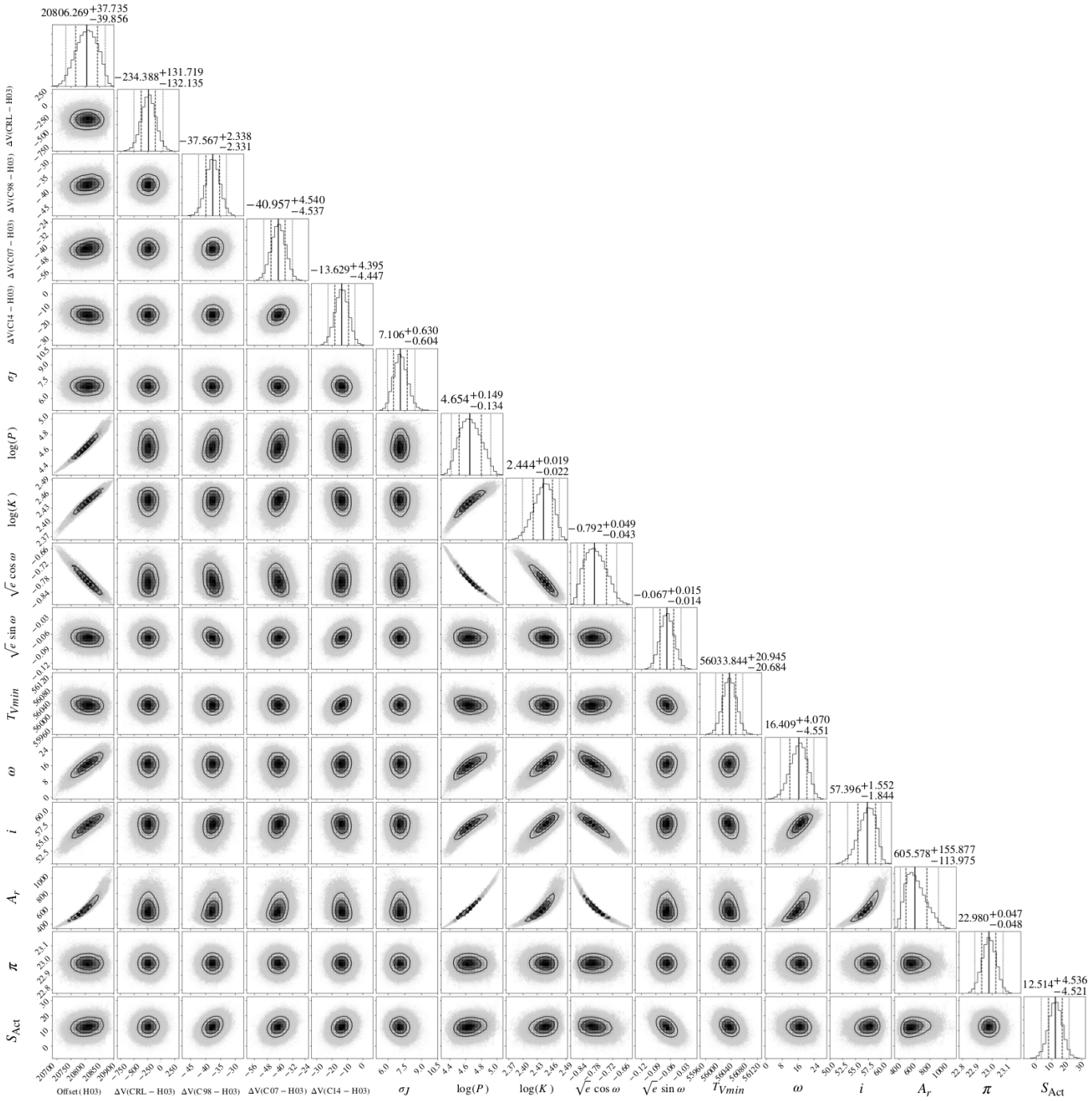

Fig. A.1. Marginalised 1D and 2D posterior distributions of the 16 parameters corresponding to the global fit of the RV and direct-imaging models. Confidence intervals at 2.275, 15.85, 50.0, 84.15, and 97.725% are overplotted on the 1D posterior distributions, while the median $\pm 1\sigma$ values are given at the top of each 1D distribution. Overplotted on the 2D posterior distribution are the 1, 2, and 3σ contour levels. *From left-to-right* and *top-to-bottom*, the list of parameters are: $\gamma(H03)$, $\Delta V(CVL - H03)$, $\Delta V(C98 - H03)$, $\Delta V(C07 - H03)$, $\Delta V(C14 - H03)$, σ_J, $\log(P)$, $\log(K)$, $\sqrt{e}.\cos\omega$, $\sqrt{e}.\sin\omega$, $T_{V_{\min}}$, Ω, i, a_r, π, S_{Act}.

5.3 Summary and conclusions

High-contrast images were taken of the radial-velocity detected brown dwarf HD 13724. A direct detection was made in the H-band with SPHERE IRDIS as well as in data from SPHERE IFS. An additional epoch of observations were taken in the J and K bands just over a year later confirming the companion. Because of the combination of radial velocity and direct imaging data, the inclination of the system can be determined, giving rise to the true mass of the companion. We analysed the spectrum of HD 13724 B from the SPHERE IFS data and detected absorption features due to CH_4 and H_2O. Such features are only present in the atmospheres of ultracool T-type brown dwarfs or giant exoplanets. By comparing the spectrum to observations of field brown dwarfs and models (Morley et al. 2012; Allard et al. 2012) we infer that it is a T4 type brown dwarf with an effective temperature of 1000 K and $\log g = 4.5$. By combining the radial velocity and astrometric information from the imaging data, we determine a mass of $\sim 50\ M_{\rm Jup}$.

It is one of only five known T-type brown dwarfs with a dynamical mass and age estimate from a combination of radial velocity and imaging data. As a result, this brown dwarf serves as a crucial benchmark with measured physical and orbital parameters, including a dynamical mass, effective temperature and surface gravity. Benchmark brown dwarfs provide a wealth of information to make observational comparisons to brown dwarf and giant planet atmospheric models which tie into the formation and evolution of such objects. Furthermore, HD 13724 B helps to populate the mass-luminosity-age relation for brown dwarfs which to date is not constrained. This is due to the low occurrence rate of ultracool brown dwarf companions, and also the difficulty in detecting such faint objects, emphasising the importance of such a detection.

For future work with this target it will be beneficial to obtain a higher resolution spectrum with VLTI/GRAVITY, like recent work that has been carried out by Gravity Collaboration et al. (2019). HD 13724 B is an ideal candidate due to being a bright luminous object at high enough angular separation to resolve. A higher resolution spectrum would bring additional insights into the atmospheric properties of HD 13724 B, increasing its importance as a benchmark brown dwarf.

CHAPTER 6

NACO AND THE NACO-ISPY SURVEY

"Everybody thought I was a bit of an eccentric for wanting to be out there looking at the stars, but I still do."

— Brian May

6.1 NAsmyth Adaptive Optics System (NAOS) - COudé Near Infrared CAmera (CONICA)

The NAsmyth Adaptive Optics System (NAOS) - COudé Near Infrared CAmera (CONICA) (NACO; Lenzen et al. 2003; Rousset et al. 2003), shown in Fig. 6.1, was a near-infrared imager and spectrograph with spectroscopic, polarimetric and coronagraphic capabilities. It was installed in 2001, as the first Adaptive-Optics (AO) instrument installed at the VLT and was originally mounted on UT4's Nasmyth focal point and more recently it was moved to UT1. It had a Wavefront Sensor (WFS) with capabilities of correcting in either the visible or the IR. However, in 2018 the Visible (VIS) WFS broke on NACO, meaning that the AO could only operate corrections in the IR.

NACO has now been decommissioned, with the last images taken in October 2019. NACO was VLT's only imager capable of correcting in the infrared, and this capability will not be possible again until ERIS comes online (Kenworthy et al. 2018).

NACO's capabilities were complementary to SPHERE's (discussed in Chapter 2.2) in that the observing range of NACO is between the $J - M'$ bands, which corresponds to $\lambda_c = 1.27 - 4.78 \mu$m (Kaufer 2008). This means that NACO extends to longer wavelengths than that of SPHERE which can only observe up to the K band at 2.251 μm.

Although NACO is now decommissioned, it played a key role in some important results like the first direct image of an exoplanet (Chauvin et al. 2004), as well as providing the first ever spectrum of a directly observed exoplanet (Janson et al. 2010).

Fig. 6.1 NACO attached to the Nasmyth focal point on VLT's UT1. Image credit: ESO.

6.2 NACO-Imaging Survey for Planets around Young stars (NACO-ISPY)

6.2.1 Overview

The original consortium between Max-Planck-Institut für Astronomie (MPIA) Heidelberg, Zeuntrum für Astronomie der Univeristät Heidelberg - Landessternwarte Königstuhl (ZAH-LSW) and Université de Genève (UNIGE), was to perform an astrometric planet search programme (Launhardt 2009) using the instrument PRIMA (Phase Referenced Imaging and Micro-arcsecond Astrometry, Quirrenbach et al. 2004) with ESO's Very Large Telescope Interferometer (VLTI).

The project, called the Exoplanet Search programme with PRIma (ESPRI), was to build Differential Delay Line (DDLs) for PRIMA (Pepe et al. 2008) and to develop astrometric operation and software tools in return for Guaranteed Time Observations (GTOs) to carry out the exoplanet search programme.

In compensation of the cancellation of the PRIMA project at ESO, we received 120 nights from ESO on one of the VLTs and we had to make an offer for an observing programme related to planets. Therefore, a new survey to use the GTO with VLT/NACO was formed.

The project became the NACO-Imaging Survey for Planets around Young Stars (NACO-ISPY), which is a large Guaranteed Time Observations (GTO) project to directly detect exoplanets in the L'-band (3.8 ± 0.4 μm) using, as the name suggests, VLT/NACO. The survey consists of 120 nights of GTO over $\sim$4 years, which started in December 2015.

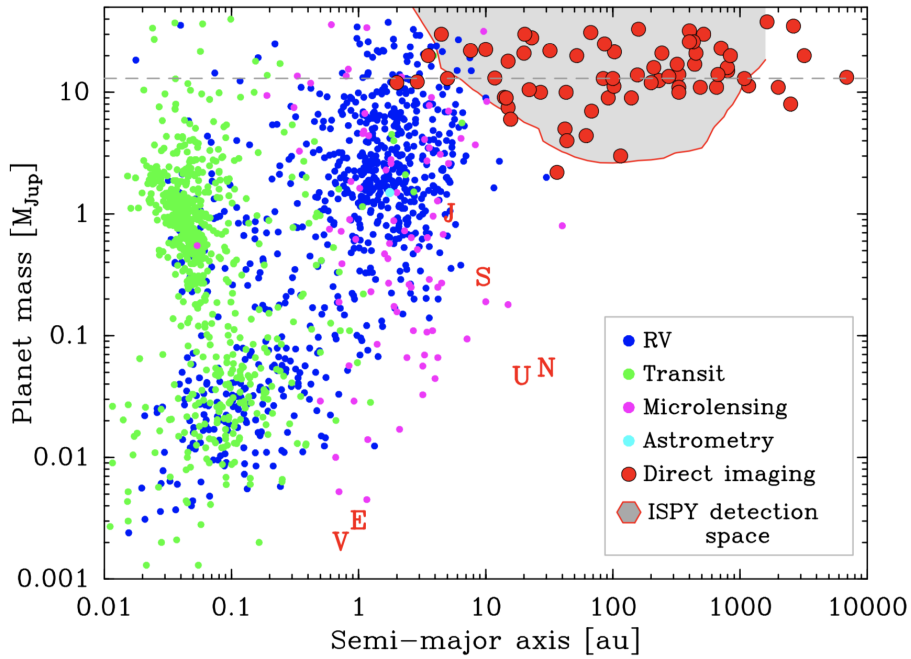

Fig. 6.2 Confirmed exoplanets from the exoplanet.eu database (Schneider et al. 2011) as of the beginning of 2020 with the ISPY detection space highlighted in grey. The Solar System planets are also marked. Figure from Launhardt et al. (2020).

The main scientific aim of this survey is to detect and characterise wide-orbit (>10 AU) giant planets during and shortly after their formation phase within protoplanetary and debris disks around nearby young stars. As seen in Fig. 6.2, the survey probes the parameter space between different exoplanet detection methods, where we start to bridge the gap between RV-detected exoplanets and directly-imaged planets, discussed in Chapter 1.2.

The NACO-ISPY survey is unique from other large direct imaging surveys, for example, the SPHERE-SHINE survey (Chauvin et al. 2017), in that most other surveys operate at wavelengths $\lambda \leq 2.2\mu$m, which makes them optimal for young and massive planets, whereas observing with NACO at 3.8μm allows us to probe very young and still embedded planets as well as cooler (i.e. more evolved) planets around stars that are a few hundred Myr.

When the new programme with NACO was formed, it was thought that it would be competitive with VLT/SPHERE due to exploiting the L'-band capability. This is because when we compare the star-planet contrast (see Fig. 6.3) in the H-band (where most SPHERE observations are carried out) versus the L'-band (where the NACO observations are carried out), we see that the contrast is more favourable, and therefore any companions are easier to detect at longer wavelengths. We gain ~ 2 mags between the H and L'-band when using the hot start evolutionary models (Allard 2014) and a $\sim 2-3$ mags when using the cold start evolutionary models (Spiegel & Burrows 2012). The difference in the contrast expected is crucial in gaining detections in this parameter space, particularly for somewhat older (i.e. a few 100 Myr

old) stars, where the gain in contrast is much more substantial. Furthermore, probing this parameter space is crucial in contributing to our understanding of how giant planets form.

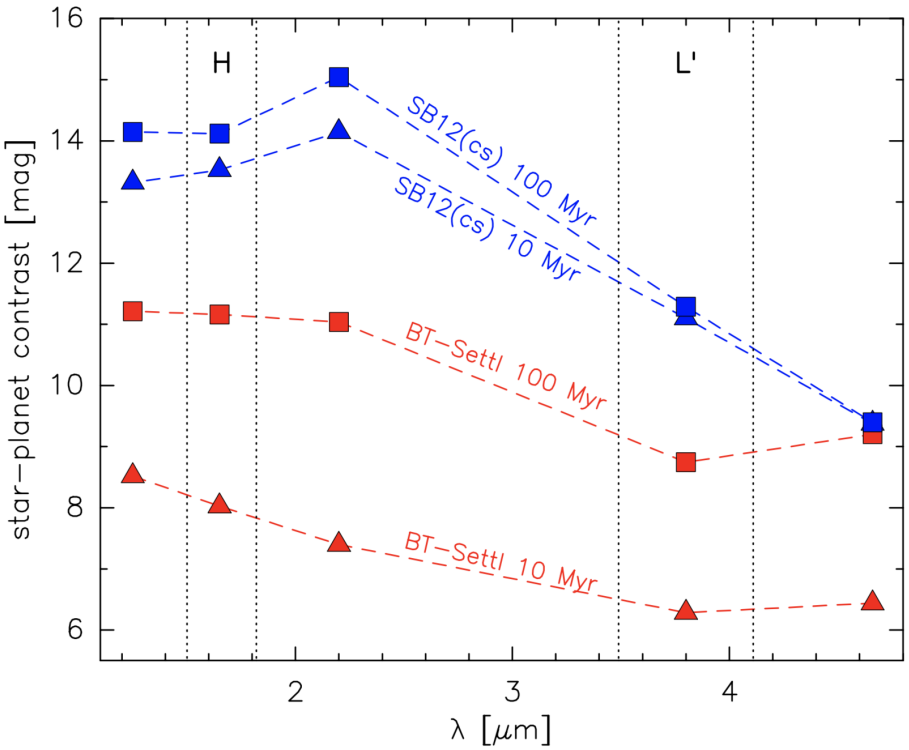

Fig. 6.3 Star-planet contrast for a 1 $M_{\odot}$ star and a 10 $M_{\rm Jup}$ planet as a function of wavelength for two different ages (10 Myr and 100 Myr) and two evolutionary models. Blue (cold start), labelled SB12 (Spiegel & Burrows 2012) and red (hot start), labelled BT-Settl (Allard 2014). Figure from Launhardt et al. (2020).

6.2.2 Target selection

The survey consists of approximately 200 stars that were selected from various databases and the literature, which is discussed in depth in Launhardt et al. (2020) in Section 6.2.6. The selection criteria of the targets were the following:

- Young stars ($\lesssim$ 200 Myr)
- Stars that host either a protoplanetary or debris disk
- Distance $\lesssim$ 160 pc for debris disk targets and $\lesssim$ 1000 pc for protoplanetary disk targets
- Visible from Paranal Observatory (-70 deg $\lesssim$ DEC $\lesssim$ +15 deg)
- Stars with masses between $\sim 0.5 - 5 M_{\odot}$

- Spectral types between M4 and B8
- $K < 10$ mag to ensure good adaptive optics correction for the NACO NIR wavefront sensor
- Stars with no known close (< 1") binaries by searching the literature and catalogues including the Washington Double Star (WDS) catalogue (Mason et al. 2001) and the ninth catalogue of spectroscopic binary orbits (Pourbaix et al. 2004)
- Targets with no archival deep ADI L'-band observations

One unique feature of the NACO-ISPY survey is selecting targets that host either a protoplanetary or debris disk. The reason for this selection of targets with debris disks is that certain sizes of debris disk belts cannot be explained by self-stirring processes, and are best explained by a massive companion in or outside of the disk. These targets were selected where there is a high probability of an internal or external stirring companion, with the possibility of detecting such companions with NACO.

The protoplanetary disk sample consists of extremely young stars where we may expect to directly detect an embedded companion still forming in their disk. For these targets, the primary focus was on Herbig Ae/Be stars. The reason for this is because in these systems gas giant planets might be forming at larger radial separations (Quanz 2015), making them easier to spatially resolve.

6.2.3 Observing strategy

Each target was observed for approximately 3 hours, along with using the AGPM corongraph for bright ($L' \lesssim 6.5$ mag) targets, allowing us to probe much deeper contrast levels than previous L' direct imaging surveys.

The Annular Groove Phase Mask (AGPM) coronagraph (Mawet et al. 2013; Absil et al. 2014) was used for stars bright than $L' \lesssim 6.5$ mag, in order to maximise the achievable contrast, whilst simultaneously minimising the inner working angle (IWA). The limit on whether the coronagraph was used or not varied slightly depending on exact observing conditions at the time of observation.

This limit on when the coronagraph was used was set up for two reasons: the coronagraph came with significant overheads during the observations and therefore should only have been used when necessary; and precisely centring behind the coronagraph was extremely difficult for faint targets ($L' \lesssim 6.5$ mag).

Each target was observed using very deep angular differential imaging in pupil tracking mode (ADI; Marois et al. 2006), which is discussed in Chapter 2.5. With an observing time of $\sim$3 hours, we were able to achieve a field rotation of each target between 70 - 100 deg, which was sufficient to suppress speckles noise and achieve a deep contrast level between the star and any companion candidate.

The observing sequence consisted of taking a non-saturated image of the star to get the Point Spread Function (PSF) of the star at the beginning and at the end of each observation.

As the sky is very bright in the L'-band ($\sim$ 3.9mag[1]), it was necessary to model and correct for the thermal background emission. For the coronagraphic observations, we switched to an offset sky position every $\sim$8 minutes that was used for the sky subtraction in the data reduction.

For the non-coronagraphic observations, the star was positioned at the centre of one quadrant of CONICA and then subsequently moved to the centre of the next quadrant using fixed offsets. Because of this, we were able to observe the star continuously without adding in additional offsets for sky frames.

The typical $5-\sigma$ contrast that we achieve from these observations is $\Delta L' \sim 7$mag at 0.2" and a background detection limit of $\sim$ 16 mag at $>$ 1.5" (Launhardt et al. 2020).

6.2.4 Data reduction and analysis

All of the data reduction has been carried out using the GRAPHIC pipeline by Hagelberg et al. (2016). The key components of GRAPHIC are described in Chapter 2.5.

Some changes were made to the GRAPHIC pipeline to take into account the two different types of observations (coronagraphic and non-coronagraphic) during the cleaning steps of the data. UNIGE played a key role in the processing and reduction of the data. This included Anthony Cheetham, a former UNIGE postdoc and science team member of NACO-ISPY, fully automating the GRAPHIC pipeline on the `NACODRS` server based at UNIGE. In addition, he added several modules to the GRAPHIC pipeline, including a PCA-based sky-subtraction scheme outlined in Hunziker et al. (2018), in addition to a PCA-based algorithm to subtract the flux from the star (Soummer et al. 2012; Amara & Quanz 2012). The full description of the data reduction is given in Launhardt et al. (2020).

An additional and recent approach called Temporal Reference for the Analysis of Planets (TRAP, Samland 2019) was also implemented into the pipeline. TRAP works by overcoming the issue of not being able to use images taken close in time, as a minimum field rotation is necessary to avoid subtraction of the companion signal (discussed in Chapter 2.5), which is especially true at small angular separations. However, it has been shown by Milli et al. (2016) that speckles are correlated over at least two temporal regimes: speckles with correlation times of a few seconds, and speckles decaying over minutes to hours. Using this information, Samland (2019) created a model of the temporal systematics using reference pixels. Simultaneously a model of the planet 'transiting' over the detector is fitted, probing a grid of planetary positions, which is used to create a 2D detection map. The gain in contrast is highest at small angular separations.

The NACO-ISPY data are now currently being reduced with the TRAP reduction in addition to the PCA-based reduction, which allows us to make a comparison of the different reductions, where some features or companion candidates may be visible in one reduction and not the other or vice versa.

I am now responsible for running the pipeline, especially with the recent addition of the TRAP module, and ensuring that all of the imaging data are available to the consortium through DACE. The instructions on how to run the GRAPHIC pipeline for the NACO-ISPY data is given in Appendix B. In Appendix C is a description of how to access the NACO-ISPY data through DACE.

[1] https://www.eso.org/gen-fac/pubs/astclim/paranal/skybackground/.

Furthermore, beyond being responsible for running the data reduction for the survey, I have also had an active part in the image inspection of the processed data to highlight any companion candidates, analyse them and make decisions about the follow-up of these candidates through regular face-to-face meetings and telecons. I have also been one of the main observers for the project, having observed on VLT/NACO for the consortium for a total of 22 nights.

6.2.5 Summary of results

As the data analysis of the survey is still ongoing, the final outcome and results of the survey have not been published yet. Below is a summary of the results that have been published so far. Those of which I have contributed to as part of the collaboration of NACO-ISPY, I have included in Appendix A, except for the survey paper which is outlined below.

The results published so far from the NACO-ISPY survey are:

- 'ISPY-NACO Imaging Survey for Planets around Young stars. Survey description and results from the first 2.5 years of observations', Launhardt et al. (2020)
- 'ISPY-NACO Imaging Survey for Planets around Young stars. A young companion candidate embedded in the R CrA cloud', Cugno et al. (2019)
- 'ISPY-NACO Imaging Survey for Planets around Young stars. Discovery of an M dwarf in the gap between HD 193571 and its debris ring, Musso Barcucci et al. (2019)
- 'Spectral and orbital characterisation of the directly imaged giant planet HIP 65426 b', Cheetham et al. (2019)
- 'Discovery of a planetary-mass companion within the gap of the transition disk around PDS 70', Keppler et al. (2018); Müller et al. (2018)

6.2.6 ISPY-NACO Imaging Survey for Planets around Young stars. Survey description and results from the first 2.5 years of observations

In Launhardt et al. (2020) we discuss the outline of the survey, including the scientific aim and comparison to other large direct imaging surveys. We also discuss in more depth the target selection, observing strategy and data reduction on which I have briefly discussed in this chapter. The paper also includes first results, consisting of 11 images of disks, the analysis of two companion candidates and detection limits from the survey so far. The full description is outlined in Launhardt et al. (2020) below.

A&A 635, A162 (2020)
https://doi.org/10.1051/0004-6361/201937000

Astronomy & Astrophysics

ISPY-NACO Imaging Survey for Planets around Young stars

Survey description and results from the first 2.5 years of observations⋆

R. Launhardt[1], Th. Henning[1], A. Quirrenbach[2], D. Ségransan[3], H. Avenhaus[4,1], R. van Boekel[1], S. S. Brems[2], A. C. Cheetham[1,3], G. Cugno[4], J. Girard[5], N. Godoy[8,11], G. M. Kennedy[6], A.-L. Maire[1,10], S. Metchev[7], A. Müller[1], A. Musso Barcucci[1], J. Olofsson[8,11], F. Pepe[3], S. P. Quanz[4], D. Queloz[9], S. Reffert[2], E. L. Rickman[3], H. L. Ruh[2], and M. Samland[1,12]

[1] Max-Planck-Institut für Astronomie, Königstuhl 17, 69117 Heidelberg, Germany
e-mail: rl@mpia.de
[2] Landessternwarte, Zentrum für Astronomie der Universität Heidelberg, Königstuhl 12, 69117 Heidelberg, Germany
[3] Observatoire Astronomique de l'Université de Genève, 51 Ch. des Maillettes, 1290 Versoix, Switzerland
[4] ETH Zürich, Institute for Particle Physics and Astrophysics, Wolfgang-Pauli-Str. 27, 8093 Zürich, Switzerland
[5] Space Telescope Science Institute, Baltimore 21218, MD, USA
[6] Department of Physics & Centre for Exoplanets and Habitability, University of Warwick, Coventry, UK
[7] The University of Western Ontario, Department of Physics and Astronomy, 1151 Richmond Avenue, London, ON N6A 3K7, Canada
[8] Instituto de Física y Astronomía, Facultad de Ciencias, Universidad de Valparaíso, Av. Gran Bretaña 1111, Playa Ancha, Valparaíso, Chile
[9] Cavendish Laboratory, J J Thomson Avenue, Cambridge, CB3 0HE, UK
[10] STAR Institute, University of Liège, Allée du Six Août 19c, 4000 Liège, Belgium
[11] Núcleo Milenio Formación Planetaria – NPF, Universidad de Valparaíso, Av. Gran Bretaña 1111, Valparaíso, Chile
[12] Department of Astronomy, Stockholm University, Stockholm, Sweden

Received 28 October 2019 / Accepted 4 February 2020

ABSTRACT

Context. The occurrence rate of long-period ($a \gtrsim 50$ au) giant planets around young stars is highly uncertain since it is not only governed by the protoplanetary disc structure and planet formation process, but also reflects both dynamical re-structuring processes after planet formation as well as possible capture of planets not formed in situ. Direct imaging is currently the only feasible method to detect such wide-orbit planets and constrain their occurrence rate.
Aims. We aim to detect and characterise wide-orbit giant planets during and shortly after their formation phase within protoplanetary and debris discs around nearby young stars.
Methods. We carry out a large L'-band high-contrast direct imaging survey for giant planets around 200 young stars with protoplanetary or debris discs using the NACO instrument at the ESO Very Large Telescope on Cerro Paranal in Chile. We use very deep angular differential imaging observations with typically >60° field rotation, and employ a vector vortex coronagraph where feasible to achieve the best possible point source sensitivity down to an inner working angle of about 100 mas. This paper introduces the NACO Imaging Survey for Planets around Young stars (NACO-ISPY), its goals and strategy, the target list, and data reduction scheme, and presents preliminary results from the first 2.5 survey years.
Results. We achieve a mean 5 σ contrast of $\Delta L' = 6.4 \pm 0.1$ mag at 150 mas and a background limit of $L'_{\rm bg} = 16.5 \pm 0.2$ mag at >1.″5. Our detection probability is >50% for companions with $\gtrsim$8 $M_{\rm Jup}$ at semi-major axes of 80–200 au and >13 $M_{\rm Jup}$ at 30–250 au. It thus compares well to the detection space of other state-of-the-art high-contrast imaging surveys. We have already contributed to the characterisation of two new planets originally discovered by VLT/SPHERE, but we have not yet independently discovered new planets around any of our target stars. We have discovered two new close-in low-mass stellar companions around R CrA and HD 193571 and report in this paper the discovery of close co-moving low-mass stellar companions around HD 72660 and HD 92536. Furthermore, we report L'-band scattered light images of the discs around eleven stars, six of which have never been imaged at L'-band before.
Conclusions. The first 2.5 yr of the NACO-ISPY survey have already demonstrated that VLT/NACO combined with our survey strategy can achieve the anticipated sensitivity to detect giant planets and reveal new close stellar companions around our target stars.

Key words. methods: observational – techniques: high angular resolution – surveys – planets and satellites: detection – protoplanetary disks

1. Introduction

We are currently experiencing a golden era of exoplanet research that has led us from the first discovery of a planet orbiting another Sun-like star (Mayor & Queloz 1995)[1] to the realisation that planetary systems are a natural by-product of star formation.

⋆ ESO program IDs 096.C-0679, 097.C-0206, 198.C-612, and 199.C-0065.

[1] The first confirmed discovery of an extrasolar planet was actually published by Wolszczan & Frail (1992), but this planet orbits a neutron star.

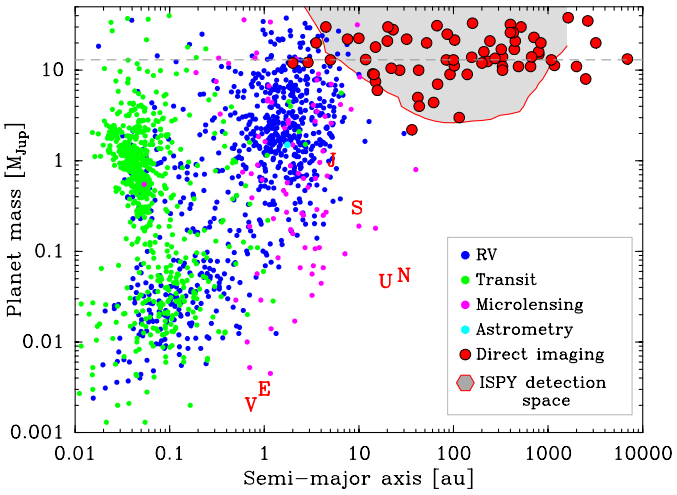

Fig. 1. Distribution of planet mass vs. orbital separation of known exoplanets and candidates as listed on `exoplanet.eu` (Schneider et al. 2011). The main detection methods are marked by different colours. Solar system planets are marked by red letters. The dashed horizontal line marks the approximate deuterium burning mass limit. The grey-shaded area marks the parameter space probed by our NACO-ISPY survey (10% detection probability, cf. Fig. 10).

Indeed, our immediate Galactic environment is richly populated with stars that harbour planetary systems. We are already aware of many stars with known exoplanets within only a few parsecs around the Sun, such as for example, Proxima Centauri at 1.3 pc (Anglada-Escudé et al. 2016), Barnard's Star at 1.8 pc (Ribas et al. 2018), Teegarden's Star at 3.8 pc (Zechmeister et al. 2019), Fomalhaut at 7.7 pc (Kalas et al. 2008)[2], Trappist-1 at 12 pc (Gillon et al. 2017), or β Pictoris at 19 pc (Lagrange et al. 2010, 2019). Most stars in Sun-like environments[3] seem to host planets. We have also learnt that the variety of planets and the architecture of planetary systems can be very different from what we know from our own Solar System. However, significant gaps remain in our knowledge of the occurrence rate and architecture of planetary systems in general and of the origin and evolution of our own Solar System in particular.

The most successful exoplanet discovery techniques thus far are the radial velocity (RV) and transit methods (see also Fig. 1). Although very successful in terms of discoveries and providing statistics, these methods nevertheless have non-negligible detection biases and limitations meaning that important questions remain unanswered. Both methods are intrinsically biased toward short-period planets and both usually avoid young stars because their intrinsic photospheric and chromospheric activity can mask the subtle signals induced by the presence of a planet (Saar & Donahue 1997, Schrijver & Zwaan 2008, Barnes et al. 2017). Astrometry on the other hand, and in particular with the anticipated final release of the *Gaia* data (individual measurements), will provide us with new discoveries that are expected to reveal the still incompletely known giant planet (GP) population in the 3–5 au separation range (Casertano et al. 2008; Perryman et al. 2014) in the near future.

However, we still know very little about the frequency of rocky planets in the habitable zone or the occurrence rate of GPs at orbital separations beyond 5 au. Both are important pieces of the puzzle needed for constraining the uncertain ends in planet formation and evolution models (e.g. Baraffe et al. 2003; Fortney et al. 2008; Spiegel & Burrows 2012; Mordasini et al. 2012; Allard et al. 2013). The occurrence rate of long-period GPs is only poorly constrained since it is not only governed by the structure of the protoplanetary discs in which they form and by the physics of the planet formation process, that is, classical core accretion (Pollack et al. 1996; Ida & Lin 2004), gravitational instability (Boss 1997), or pebble accretion (Johansen & Lacerda 2010; Ormel & Klahr 2010; Bitsch et al. 2015), but also reflects dynamical re-structuring processes taking place well after planet formation. Both migration processes during the gas-rich protoplanetary disc phase and dynamical interactions between planets well after the clearing of the disc can change the architecture of planetary systems dramatically between birth and maturity (e.g. Davies et al. 2014; Morbidelli 2018). Furthermore, an unknown fraction of the giant planet population on wide orbits may actually not originate from the system they are in now, but could have been captured free-floating in space, for example in dense star clusters (Perets & Kouwenhoven 2012).

Therefore, if we want to understand how mature planetary systems like our own are formed, there is an explicit scientific demand to find and characterise GPs in wide orbits around young stars, which cannot be satisfied by the successful indirect detection techniques mentioned above. Because of the long orbital timescales involved, the only currently feasible way to explore the GP population in wide orbits is by direct imaging (DI).

Direct imaging with the currently most advanced instruments allows us to probe exoplanets at separations from the host star down to a few astronomical units (1–10 au, depending on distance and other parameters) and planet masses down to about 1 $M_{\rm Jup}$ (see Fig. 1). In terms of separations, DI is thus truly complementary to the RV and transit methods. However, DI is currently only sensitive to gaseous, self-luminous (i.e. young) GPs, while smaller (and rocky) planets are too faint to be detectable with current instrumentation in the glare of their host stars.

Nevertheless, DI with high-contrast techniques has already provided us with some spectacular discoveries (e.g. Marois et al. 2008, 2010; Lagrange et al. 2010; Rameau et al. 2013a; Kuzuhara et al. 2013; Macintosh et al. 2015; Keppler et al. 2018). Moreover, the recent advancement of very large high-contrast DI planet surveys with several hundred target stars (see Table 5) has provided us with first constraints on the occurrence rate and distribution of massive (1–13 $M_{\rm Jup}$) GPs in wide orbits (20–300 au) around young stars. The derived values for the substellar companion frequency still show a large scatter as they range from <1% up to 10%, depending on sample parameters and models used (e.g. Lafrenière et al. 2007; Biller et al. 2013; Brandt et al. 2014a; Chauvin et al. 2015; Nielsen et al. 2016, 2019; Bowler 2016; Galicher et al. 2016; Vigan et al. 2017; Meshkat et al. 2017; Stone et al. 2018). Overall, these results show that such wide-orbit GPs are rare.

However, most of these surveys operate at wavelengths $\lambda \leq 2.2\,\mu$m and are thus optimised for hot (young and massive) planets. Very deep observations at longer wavelengths are needed to also reveal both very young and still embedded (i.e. reddened) planets and protoplanets as well as more evolved (i.e. cooler) planets around somewhat older (few hundred Myr) stars (Fig. 2). Furthermore, it is also important to probe physical separations down to 5–10 au to bridge the gap between the RV-constrained GP population around mature stars and the very

[2] The nature of the companion candidate to Formalhaut is still debated (Janson et al. 2012).
[3] We still know very little about planets around stars in very different environments, such as for example close to the Galactic centre or in very low-metallicity environments.

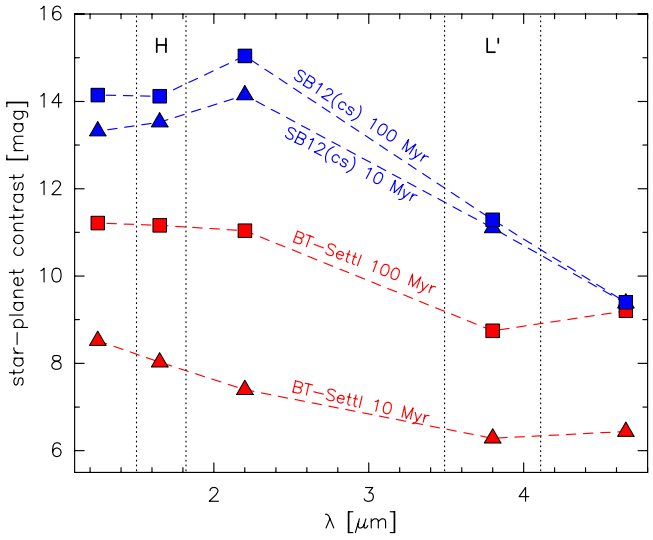

Fig. 2. Star-planet contrast for a 1 $M_{\odot}$ star and a 10 $M_{\rm Jup}$ GP as a function of wavelength for two different ages (10 and 100 Myr) and two evolutionary models (blue: Spiegel & Burrows 2012, cold start; red: Allard 2014, hot start), showing the 2–3 mag contrast advantage of the L'-band vs. H-band which is used for most other large DI surveys.

wide-orbit GP population around very young stars revealed by these DI surveys.

To address these needs, we initiated a large (≈200 stars) L'-band Imaging Survey for Planets around Young stars with NACO (see Sect. 4) at the ESO Very Large Telescope (VLT) on Cerro Paranal in Chile (NACO-ISPY). The survey was launched in December 2015, carried out as guaranteed time observations (GTO) with a total budget of 120 observing nights, and was completed after 4 yr in late 2019. The NACO-ISPY survey is complementary to the largest and most recent other L'-band imaging survey, the Large Binocular Telescope (LBT) Interferometer Exozodi Exoplanet Common Hunt (LEECH; Skemer et al. 2014; Stone et al. 2018), because it covers the southern sky as opposed to the northern sky accessible from the LBT located in Arizona. It is also complementary to most of the other large imaging surveys listed in Table 5 because it is carried out in the L'-band (3.8 μm) as opposed to the most widely used H- and K-bands. Last but not least, our survey is also different from most of the other surveys in that we focus exclusively on nearby stars that are surrounded by either protoplanetary transition discs (PPDs) or debris discs (DEBs).

In this paper, we give a general overview of the NACO-ISPY survey, its goals, strategy and targets, and present preliminary results from the first 2.5 survey years. In Sect. 2 we describe the scientific goals and strategy of the survey. Section 3 gives an overview of the target selection, the master target sample, and the list and properties of targets observed during ESO periods 96 through 100. Observations and data reduction are described in Sects. 4 and 5. The first survey results are presented in Sect. 6 and discussed in Sect. 7. Section 8 summarises and concludes the paper.

2. Survey goals and strategy

Our NACO-ISPY survey is tailored to characterise the wide-separation GP population around nearby young stars during and shortly after the planet formation phase. We exploit the L'-band capability of NACO (see Sect. 4) and focus on young stars, thus making NACO-ISPY complementary to most other current large DI surveys which mostly employ the H-band. In particular, we address the following main scientific questions:

– Can we detect and characterise GPs during their formation phase within PPDs, where indirect methods for shorter-period planets fail?

– What are the properties (luminosity and temperature), location (separation), and occurrence rate of such planets?

– What is the occurrence rate and luminosity and/or separation distribution of long-period GPs in DEBs?

– What is the relation between DEB properties and the presence of wide-separation GPs? Can we constrain stirring models and establish disc properties as planet tracers (see below)?

– How frequent are GPs at separations ≥5 au around young (≲100 Myr) solar-type stars, i.e. closer to what has already been partially constrained by previous imaging surveys?

– Does the distribution change with age and at what age do the most significant changes occur?

– Are the occurrence and properties of wide-orbit GPs correlated with shorter-period GPs such that in-situ formation and outward scattering can be disentangled?

Consequently, our survey is focused on only two types of nearby young stars with circumstellar discs: (a) young (<10 Myr) stars with gas-rich PPDs with direct or indirect evidence for gaps that could be carved by (proto)-planets (transition discs), and (b) somewhat older (up to a few hundred Myr) stars with well-characterised DEBs, where the primordial dust has been processed completely, and the current dust population results from the collisional grinding of larger planetesimals (Wyatt 2008).

We plan to observe approximately 200 stars in total over the planned survey duration of 4 yr and within the time budget of 120 nights (which includes weather losses and second-epoch observations). This total number of survey targets is a compromise between the goal to go deeper than previous surveys, the need for a sufficiently large target list to ensure a robust statistical interpretation of the expected low-number discovery outcome, and the GTO time budget. The entire survey is carried out with the NACO instrument (Rousset et al. 2003; Lenzen et al. 2003, see Sect. 4) and the L' filter at the ESO VLT on Cerro Paranal in Chile. Every target star is observed once with very deep angular differential imaging (ADI; Marois et al. 2006) observations (2–4 h with typically >60° field rotation) and a coronagraph employed (where feasible) to achieve the best possible point-source sensitivity down to the smallest possible separations (see Sect. 4). Second epoch observations are only scheduled where interesting companion candidates discovered in the first epoch image require confirmation.

For the young PPD stars, we exploit the advantage of the L'-band for embedded planets with possible large circumplanetary extinction over the shorter-wavelength near-infrared (NIR) bands. Furthermore, the suspected circumplanetary discs were shown to be very bright at $\lambda > 3\,\mu$m (e.g. Zhu 2015; Eisner 2015; Szulágyi et al. 2019), further helping L'-band observations even where the embedded planets may not be directly detectable. Indeed, L'-band observations were key for detecting the few forming planet candidates that we know of today, namely LkCa 15 b (Kraus & Ireland 2012), HD 100546 b (Quanz et al. 2015), HD 169142 b (Biller et al. 2014; Reggiani et al. 2014), MWC 758 b (Reggiani et al. 2018), and PDS 70 b (Keppler et al. 2018), even though all but the last one are still debated (Currie et al. 2019; Rameau et al. 2017; Ligi et al. 2018; Wagner et al. 2019). Further advantages of the L'-band are, for example, that scattering from circumstellar disc material, which increases the

noise and the probability of false positives, and contamination by background objects are less severe than at shorter wavelengths.

For the older DEB stars, we also exploit the L'-band advantage, but here for cooler, that is, lower-mass and/or older planets. More importantly, our NACO-ISPY survey is clearly distinguished from the SPHERE-SHINE survey (Chauvin et al. 2017a) for example, in that we explicitly target a large sample of well-characterised DEB stars and employ a target selection and survey strategy that will allow us to constrain the relation between DEB properties (e.g. signatures of dynamical excitation, see below) and the occurrence of GPs.

3. Targets

3.1. Target selection

The targets for the ISPY survey were selected from various databases and the literature. In particular, the PPD targets were compiled from catalogues and studies of Herbig Ae/Be stars (e.g. The et al. 1994; Menu et al. 2015) and then complemented with additional lower-mass objects for which high-spatial resolution observations showed substructures in their circumstellar discs possibly indicative of ongoing (gas giant) planet formation (e.g. Andrews et al. 2011, 2018). Here, we could only add objects that were not blocked from other ongoing observing programs. The primary focus on Herbig Ae/Be stars was motivated by the idea that in these systems (more massive) gas giant planets might be forming at larger radial separations (cf. Quanz 2015). Indeed, thus far most candidates for young, embedded planets have been detected around such objects (e.g. Quanz et al. 2013, 2015; Brittain et al. 2014; Biller et al. 2014; Currie et al. 2017; Reggiani et al. 2014, 2018), although not all of these candidates were confirmed in follow-up studies and the origin of some of the detected signals has recently been questioned (e.g. Rameau et al. 2017; Cugno et al. 2019a; Ligi et al. 2018; Huélamo et al. 2018).

The DEB targets were mainly compiled from the *Spitzer* IRS catalogue of Chen et al. (2014), the first comprehensive DEB catalogue based on spectroscopic data. To ensure that we select only stars with significant DEB signals, we re-compiled and re-evaluated the complete spectral energy distributions (SEDs) of all target candidates (see Sect. 3.3), and applied primary cut-offs for the fractional disc luminosity at $L_{\rm IR}/L_{\rm bol} > 3 \times 10^{-6}$ and for the blackbody temperature of the disc excess emission at $T_{\rm d1} < 220$ K. The threshold values are chosen to avoid outliers with non-significant excess or suspiciously high fit temperatures. We also inspected all SED fits individually to identify suspicious cases that could be affected by confusion with background or other objects. The new SED fits were also used to re-derive other disc and stellar parameters (see Sect. 3.3 and Fig. 7). Additional DEB targets were selected from the results of the *Herschel* DEB surveys DUNES (Eiroa et al. 2013; Maldonado et al. 2015) and DEBRIS (Matthews et al. 2010; Booth et al. 2013). In particular, we selected those targets which show indications not only of cold outer debris belts, but also of an additional hot exozodiacal dust belt closer to the host star. The motivation for selecting the latter derives from the speculation that hot inner debris belts are related to the formation of rocky planets and that in such systems more massive gas giant planets might also be forming at larger radial separations. Most of the approximately 30 DEB targets older than 1 Gyr (see Fig. 4) originate from the *Herschel* detections.

In addition to the specific selection criteria mentioned above, we use the following general selection criteria for compiling our master list of target candidates:

– $-70\,\deg \leq$ Dec $\leq +15\,\deg$, to ensure sufficient observability from the location of Paranal observatory (>4 h at air mass <1.5; with a few exceptions);

– distance ≤160 pc (DEB) and ≤1000 pc (PPD) to achieve reasonable spatial resolution;

– avoid extreme (later than M4, earlier than B8) and uncertain spectral types;

– $K < 10$ mag to ensure good adaptive optics (AO) correction for the NACO NIR wavefront sensor;

– no known close (<1″) binaries and multiples around bright stars (data archives, catalogues, and literature checked) that could hamper centring of the coronagraph (see Sect. 4);

– no existing and sufficiently deep ADI L'-band observations available (various archives searched).

With these selection criteria, we compiled a master list consisting of 90 PPD and 300 DEB stars. Distances were inferred from *Gaia* DR2 parallaxes (Gaia Collaboration 2016, 2018) with the method described by Bailer-Jones et al. (2018) and retrieved through VizieR (Ochsenbein et al. 2000), unless stated otherwise in Tables 1 and D.1. Age estimates were compiled from the literature. Many stars have multiple partially contradicting published age estimates derived with different methods. In Tables 1 and D.1, we list only the age value that we consider to be the most reliable one. The listed age reference may not necessarily point to the original age estimate, but can also refer to a paper that compiles and discusses various age estimates. L' magnitudes and their uncertainties are derived from the WISE photometry (Cutri et al. 2013) and black body interpolation between WISE filters W1 (3.35 μm) and W2 (4.6 μm) to L' (3.8 μm).

Since the total time budget for our survey of 120 observing nights permits deep observations of only ≈200 stars (see Sect. 4), the target candidates in this master list were separated into three priority categories: priority 1 targets that will be observed, priority 2 targets that will be observed if time permits, and priority 3 targets that will not be scheduled for observations, unless needed as fillers.

Among the 90 PPD target candidates, we gave the highest priority to nearby (<200 pc) Herbig Ae/Be stars and to transition discs with known gaps and cavities with separations large enough so that L'-band observations with VLT/NACO can probe for embedded sources. Intermediate priority was given to Herbig Ae/Be stars at distances >200 pc and to lower-mass (T Tau) objects with less pronounced or more poorly characterised transition disc signatures. The lowest priority was given to objects where high-contrast L' observations were already available or published or where the discovery space was limited for other reasons. This resulted in a list of 43 priority 1 targets, 33 priority 2 targets, and 14 targets that were discarded from the observing list and not even used as fillers.

To prioritise the DEB target candidates in such a way that we maximise the detection probability (success-oriented) while at the same time preserving an (relatively) unbiased sample, we evaluated what the achievable planet mass detection limit at a projected physical separation of 20 au would be. For this purpose, we used mean $5\,\sigma$ contrast curves achieved during the first few observing runs (Table 2) under good weather conditions with our standard observing procedures with and without the coronagraph. These contrast curves were then scaled to the L' magnitudes of each target candidate in such a way that at small angular separations, the contrast is preserved independently of the stellar brightness ($\Delta L' \approx 6.4$ mag at $\Delta r = 150$ mas), and at large separations (>3″), the mean background limit of $\Delta L' \approx 16.7$ mag is preserved (see Sects. 4 and 6.1 and Fig. 9). The resulting contrast curves are then converted to planet-mass

Table 1. PPD targets observed between December 2015 and March 2018 (P 96 through P 100).

Name [a]	RA(J2000) [b] [hh:mm:ss]	Dec(J2000) [dd:mm:ss]	Dist. [c] [pc]	V [d] [mag]	$\log(L_*)$ [e] [$L_\odot$]	$T_{\rm eff}$ [e] [K]	Age [f] [Myr]	$R_{\rm disc}$ [g] [au]	Refs. [h]
V* V892 Tau	04:18:40.61	28:19:15.6	117 ± 2	14.7	−1.82	4250	5	90	11, 11
HD 283571	04:21:57.41	28:26:35.5	444 ± 50	9.3	1.26	4420	1.8	243 ± 40	12, 41
HD 31648	04:58:46.27	29:50:37.0	161 ± 2	7.7	1.29	7860	8.5 ± 2	634 ± 13	13, 42
HD 34282	05:16:00.48	−09:48:35.4	359 ± 5	9.8	0.95	8250	6.4 ± 2	293 ± 15	14, 43
HD 37411	05:38:14.51	−05:25:13.3	359 ± 4	9.8	1.28	6810	9 ± 4.5	123	3, 1, 44
HD 37806	05:41:02.29	−02:43:00.7	423 ± 11	7.9	2.04	8590	...	141	1, 45
HD 38120	05:43:11.89	−04:59:49.9	402 ± 13	9.1	1.60	9120	...	290 ± 48	43
HD 259431	06:33:05.19	10:19:20.0	711 ± 24	8.8	2.88	6500	0.06 ± 0.03	8.1	15, 46
NX Pup	07:19:28.29	−44:35:11.2	410 ± 82	10.0	1.66	4760	0.05	...	1, 16
HD 58647	07:25:56.10	−14:10:43.5	316 ± 4	6.9	2.23	7228	...	137	45
HD 72106	08:29:34.90	−38:36:21.1	279 ± 88	8.6	1.48	7570	...	40	2, 47
HD 85567	09:50:28.54	−60:58:03.0	1002 ± 29	8.6	2.54	7880	0.01	0.5 ± 0.2	16, 48
TW Hya	11:01:51.91	−34:42:17.0	60 ± 0.2	10.9	−0.5	4240	7.5 ± 0.7	172 ± 11	17, 43
HD 95881	11:01:57.62	−71:30:48.4	1148 ± 44	8.3	2.8	6740	8	200	16, 49
HD 97048	11:08:03.31	−77:39:17.5	184 ± 1	8.5	1.14	6750	6.5 ± 1	866	13, 50
HD 98922	11:22:31.67	−53:22:11.5	662 ± 16	6.7	2.92	8800	0.01	110	16, 51
HD 100453	11:33:05.58	−54:19:28.5	104 ± 0.4	7.8	0.81	7270	10 ± 2	41	18, 52
HD 100546	11:33:25.44	−70:11:41.2	110 ± 0.6	6.8	1.37	9180	3.8 ± 0.5	500	13, 53
HD 101412	11:39:44.46	−60:10:27.7	407 ± 5	9.0	1.43	7840	2 ± 1	92.5	19, 54
HD 104237	12:00:05.09	−78:11:34.6	108 ± 0.7	6.6	1.32	7250	5.5 ± 0.5	66 ± 14	13, 55
PDS 70	14:08:10.16	−41:23:52.6	113 ± 0.5	12.2	−0.46	3970	5.4 ± 1	113	20, 31, 56
HD 139614	15:40:46.38	−42:29:53.5	134 ± 1	8.3	0.90	8020	10 ± 3	94 ± 3	13, 43
HD 141569	15:49:57.75	−03:55:16.3	110 ± 0.6	7.1	1.19	8440	4.7 ± 0.3	279 ± 5	14, 43
IM Lup	15:56:09.18	−37:56:06.1	158 ± 1.4	11.6	0.02	4060	0.75 ± 0.25	...	21
HD 142527	15:56:41.89	−42:19:23.2	157 ± 1	8.3	1.04	5320	2 ± 0.5	257 ± 15	13, 57
HD 144668	16:08:34.29	−39:06:18.3	160 ± 2	7.1	1.14	5860	2.8 ± 1	38 ± 5	13, 45
Elias2-27	16:26:45.03	−24:23:07.8	118 ± 15	20.4 [i]	...	....	0.8	525	23, 58
KK Oph	17:10:08.12	−27:15:18.8	220 ± 7	11.0	1.14	5140	8 ± 2	276	24, 59
HD 319139	18:14:10.48	−32:47:34.5	72.3 ± 0.3	10.7	−0.21	4250	21	362	25, 60
HD 169142	18:24:29.78	−29:46:49.3	114 ± 0.8	8.2	0.76	7320	7.7 ± 2	194	13, 61
R CrA	19:01:53.86	−36:57:08.1	95 ± 7	11.9	1.85	3960	1	...	26, 32
T CrA	19:01:58.79	−36:57:50.3	130	11.7	...	5000	23	...	3, 16
HD 179218	19:11:11.25	15:47:15.6	264 ± 3	7.2	1.83	8490	2.3 ± 0.3	131 ± 22	24, 43
HD 190073	20:03:02.51	05:44:16.7	872 ± 52	7.8	2.73	8380	1	108 ± 4	16, 44

Notes. [a]Where available, we use the HD number as main source ID. [b]ICRS, from *Gaia* (Gaia Collaboration 2018) where available. [c]Distances and their uncertainties are inferred from *Gaia* DR2 parallaxes (Gaia Collaboration 2016, 2018) with the method described by Bailer-Jones et al. (2018) and retrieved through VizieR (Ochsenbein et al. 2000), unless indicated otherwise (references 1 through 3). [d]L' magnitudes are listed in Table 3. [e]$\log(L_*)$ and $T_{\rm eff}$ (rounded to full ten) adopted from *Gaia* DR2 (Gaia Collaboration 2018), unless indicated otherwise (references 31 through 32). [f]Ages compiled here are taken from the literature and derived with different methods and different treatment of uncertainties. Some ages refer to references which only summarise different other age estimation attempts. [g]Outer disc radii are compiled from the literature and originate from different methods. They are corrected for new *Gaia* DR2 distances where necessary. [h]References 1 through 3 refer to distance, 11 through 26 refer to age, 31 through 32 refer to L_* and $T_{\rm eff}$, and 41 through 61 refer to observed disc radius. [i]The *Gaia* G magnitude is listed for Elias 2-27 because no V mag is available.

References. (1) Fairlamb et al. (2015); (2) van Leeuwen (2007); (3) Acke & van den Ancker (2004); (11) Hamidouche (2010); (12) Palla & Stahler (2002); (13) Meeus et al. (2012); (14) Merín et al. (2004); (15) Alecian et al. (2013); (16) Manoj et al. (2006); (17) Ducourant et al. (2014); (18) Collins et al. (2009); (19) Wade et al. (2005); (20) Keppler et al. (2018); (21) Mawet et al. (2012); (22) Canovas et al. (2017); (23) Andrews et al. (2018); (24) Pascual et al. (2016); (25) Kastner et al. (2014); (26) Sicilia-Aguilar et al. (2011); (31) Keppler et al. (2018); (32) Cugno et al. (2019b); (41) Isella et al. (2010); (42) Piétu et al. (2007); (43) Dent et al. (2005); (44) Liu et al. (2011); (45) Mariñas et al. (2011); (46) Kraus et al. (2008); (47) Schegerer et al. (2009); (48) Wheelwright et al. (2013); (49) Verhoeff et al. (2010); (50) Walsh et al. (2016); (51) Caratti o Garatti et al. (2015); (52) Benisty et al. (2017); (53) Tatulli et al. (2011); (54) Geers et al. (2007); (55) Grady et al. (2004); (56) Hashimoto et al. (2012); (57) Fukagawa et al. (2006); (58) Pérez et al. (2016); (59) Kreplin et al. (2013); (60) Rosenfeld et al. (2013); (61) Fedele et al. (2017).

detection limits using the L' magnitudes, ages, and distances of the stars (Tables 1, D.1, 3, and D.2) together with BT-Settl evolutionary models (Allard 2014; Baraffe et al. 2015).

The highest priority was given to DEB stars around which the predicted planet-mass detection limit at 20 au projected physical separation was $\leq 10\,M_{\rm Jup}$. We also gave high priority to DEBs with detectable gas (CO) content (e.g. Zuckerman et al. 1995; Moór et al. 2011, 2015a; Marino et al. 2016, 2017; Greaves et al. 2016; Lieman-Sifry et al. 2016), although it is not a priori clear if the CO gas is of primary or secondary origin, in particular in the discs around A stars (Moór et al. 2017). However, in some cases and in particular in the few later-type CO-rich discs,

Table 2. GTO observing runs during P 96 through P 100.

Period / run ID	Dates	No of nights	Conditions (seeing)	Notes
96 / 096.C-0679(A)	2015, Dec 15 – 19	4	Excellent (0.5″-1″)	11 stars [(a)], no losses
96 / 096.C-0679(B)	2016, Feb 17 – 20	3	Partly cloudy and windy (1″-2″)	4 stars, 28% weather loss [(b)]
97 / 097.C-0206(A1)	2016, May 02 – 11	6	Mostly cloudy and windy (0.5″-2″)	7 stars, 60% weather loss
97 / 097.C-0206(A2)	2016, May 29 – Jun 03	5	Mostly cloudy (0.5″-1.5″)	5 stars, 70% weather loss
97 / 097.C-0206(B)	2016, Jul 30 – Aug 02	3	Partly cloudy and windy (0.4″-1.2″)	7 stars, 18% weather loss
98 / 198.C-0612(A)	2016, Nov 06 –13	5	Good, partly mixed (0.7″-1.6″)	10 stars, no loss
98 / 198.C-0612(C)	2016, Dec 08 – 13	5	Mostly cloudy and windy (0.7″-3″)	7 stars, 60% weather loss [(b)]
98 / 198.C-0612(B)	2017, Mar 14 – 18	4	Mixed, partly high humidity (0.4″-1.5″)	8 stars, 33% weather loss
99 / 199.C-0065(A1)	2017, May 01 – 04	3	Mixed, partly strong wind (0.4″-1.5″)	9 stars, no loss
99 / 199.C-0065(A2)	2017, May 15 – 20	5	Mixed, partly strong wind (0.4″-1.5″)	11 stars, 10% weather loss
99 / 199.C-0065(B)	2017, Jun 16 –Sep 01 [(c)]	8	Mixed, partly high humidity (0.4″-1.7″)	15 stars, 15% weather loss
100 / 199.C-0065(C)	2017, Oct 29 – Nov 04	6	Good, partly windy (0.4″-1.2″)	14 stars, no loss
100 / 199.C-0065(D)	2018, Feb 22 – Mar 03	7	Excellent (0.3″-1.3″)	14 stars, no loss

Notes. [(a)]Number of stars for which good, i.e. useable, data were obtained (one target was observed twice). [(b)]Weather loss includes both closed-dome and bad-weather data with strongly variable photometry. [(c)]Six short, scattered subruns, of which two two-night runs were carried out in VM and four single-night runs in dVM.

the gas is likely to originate from colliding or evaporating icy planetesimals (Kral et al. 2016; Matrà et al. 2019). Intermediate priority was given to DEB stars with predicted 20 au detection limits between 10 and 20 $M_{\rm Jup}$. Lowest priority was given to pre-selected target candidates with predicted mass detection limits >20 $M_{\rm Jup}$, which were only observed if needed as fillers. This selection process resulted in a final list of 177 DEB targets, of which 87 are priority 1, the same number are priority 2, plus three stars for which we re-classified the IR excess as not significant only after they were observed early in the survey.

3.2. Target list

Our final survey target list thus consists of 253 stars, of which 76 stars are surrounded by young PPDs, and 177 stars are surrounded by DEBs (including the three targets mentioned above for which the IR excess was later classified as not significant). Of these 253 targets, we assigned 130 stars as priority 1 (43 PPDs and 87 DEBs).

Figure 3 shows the sky distribution of all 253 ISPY GTO target candidates. Figure 4 shows the distribution of spectral types, ages, distances, and L' magnitudes. Spectral types range from early M to late B, corresponding to $T_{\rm eff} \approx 3000-10000$ K. Ages of the PPD stars range from about 2 to 10 Myr. The majority of the DEB targets have ages of between 10 and 100 Myr with a distribution tail out to a few gigayears (the older ones being mostly *Herschel* detections). Distances to the PPD stars are mostly between 100 and 170 pc, while the DEB targets are located between 3 and 150 pc, with two distribution peaks around 10–50 pc and 100–140 pc. L' magnitudes range from 2.5 to 8.5 mag with very few outliers towards the brighter and fainter ends.

Figure 5 shows the colour-magnitude diagram (CMD) of our target stars with the stellar ages colour-coded and Siess et al. (2000) isochrones overplotted. The zero-age main sequence (ZAMS) is clearly visible as well as the many redder (cooler) and over-luminous (because of their larger radii) pre-main sequence (PMS) stars.

Figure 6 shows the fractional disc-related excess luminosity $L_{\rm disc}/L_* = f_{\rm d}$ (see Sect. 3.3) versus stellar age for all ISPY targets, illustrating the dominance of the disc emission over the stellar contribution for the young PPDs and the relatively faint disc contribution from the more evolved DEBs. Error bars in both dimensions can be substantial, in particular for the ages and for the fractional disc luminosities of the young PPD targets (see below). As ages are compiled from the literature and derived with different methods and assumptions, we have no means of deriving consistent uncertainties for all sources and therefore we refrain from showing error bars here. The PPD and DEB targets appear as two clearly separated groups in this diagram with $f_{\rm d}^{\rm PPD} > 0.01 > f_{\rm d}^{\rm DEB}$, albeit with some age overlap in the range 5–20 Myr. Because stellar luminosities derived from the SED fitting (see Sect. 3.3) were not corrected for extinction, fractional disc luminosities for some of the very young and embedded PPD stars are significantly overestimated and appear unphysically large (>1). For the older DEB stars with typically optically thin discs, where extinction should not play a significant role, the diagram suggests a trend of fractional disc luminosity declining with age as $\log(f_{\rm d}) = -0.5 \times \log(\text{age}) - 3$, albeit with the note of caution that we introduced a selection bias by applying a lower limit to $f_{\rm d} > 3 \times 10^{-6}$. Nevertheless, this trend also holds for the upper envelope of the distribution, which is not affected by the selection bias. Figure 7 shows the flux density distribution of a typical DEB survey target (here HD 203).

3.3. Targets observed during ESO periods 96 through 100

In this section, we describe the 112 target stars (34 PPDs and 78 DEBs) observed during ESO periods 96 throughout 100, which comprise approximately the first half of the survey. The analysis of the complete survey will be presented in a forthcoming paper. Tables 1 and D.1 list the names, coordinates, and other parameters for these stars. The observations are described in more detail in Sect. 4.

Distances and mean uncertainties for all but four targets (marked in Table 1) are derived by inverting *Gaia* parallaxes[4] (Gaia Collaboration 2018). Stellar luminosities and $T_{\rm eff}$ of PPD

[4] A more appropriate way to derive distances from parallaxes for stars more distant and with larger relative parallax uncertainties than our targets is outlined by Bailer-Jones (2015).

Table 3. Observations and achieved contrast values of PPD targets.

Name	Obs date	Seeing	Field rot.	AGPM	L' [(a)]	5 σ contrast [(b)] at r					
						0.″25	0.″5	0.″75	1.″0	2.″0	3.″0
		[arcsec]	[deg]		[mag]	[mag]	[mag]	[mag]	[mag]	[mag]	[mag]
V* V892 Tau	2016-12-10	1.3	50	y	4.75 ± 0.19	5.8	7.8	9.3	9.8	10.6	10.7
HD 283571	2016-12-09	1.0	41	y	5.30 ± 0.20	6.1	8.4	9.1	10.2	11.6	11.8
HD 31648	2017-11-01	1.0	66	y	4.51 ± 0.25	6.9	9.6	10.5	11.1	12.0	12.0
HD 34282	2016-11-07	0.8	118	y	6.59 ± 0.07	5.9	7.6	8.2	8.7	9.4	9.6
HD 37411	2017-11-03	0.8	70	y	6.26 ± 0.09	6.0	7.3	8.6	9.7	10.1	10.1
HD 37806	2017-10-30	0.9	55	y	4.18 ± 0.30	6.9	9.8	10.5	11.3	12.0	12.1
HD 38120	2017-10-29	0.5	66	y	6.25 ± 0.09	6.3	8.6	9.5	9.8	9.9	10.1
HD 259431	2016-12-11	1.6	38	y	3.95 ± 0.35	5.8	8.3	9.2	10.1	11.0	10.8
NX Pup	2018-02-22	0.4	83	y	4.17 ± 0.40	3.7	8.8	10.6	11.3	12.4	12.4
HD 58647	2018-02-23	0.6	127	y	3.85 ± 0.41	7.6	9.9	11.1	11.7	12.6	12.7
HD 72106	2016-12-12	0.9	130	n	6.76 ± 0.04	6.7	7.4	7.6	7.8	10.1	10.2
HD 85567	2018-03-01	0.4	62	y	4.22 ± 0.34	7.9	10.3	11.1	11.4	12.5	12.5
TW Hya	2016-05-03	0.9	134	n	6.96 ± 0.06	5.2	7.9	8.3	9.0	9.4	9.5
HD 95881	2017-03-14	0.7	57	y	4.11 ± 0.25	8.6	10.3	10.7	11.6	12.5	12.5
HD 97048	2016-05-02	1.0	67	y	4.47 ± 0.10	5.8	8.5	9.4	10.0	11.0	11.1
HD 98922	2018-02-22	0.5	86	y	2.90 ± 0.20	6.7	9.8	11.1	12.3	13.8	14.0
HD 100453	2016-05-09	1.2	85	y	4.31 ± 0.35	6.9	9.4	10.0	10.0	11.6	11.7
HD 100546	2017-03-15	1.2	60	y	3.92 ± 0.27	6.5	8.8	10.3	11.1	11.8	12.1
HD 101412	2017-03-17	0.8	69	y	5.70 ± 0.09	8.1	9.3	9.8	10.3	10.7	10.7
HD 104237	2017-05-16	0.8	45	y	3.44 ± 0.45	7.5	10.1	11.0	11.2	13.1	13.3
PDS 70	2016-06-01	0.6	84	n	7.91 ± 0.03	5.2	7.2	8.2	8.3	8.6	8.7
HD 139614	2017-05-01	1.2	101	y	5.64 ± 0.12	7.7	8.6	9.6	10.0	10.4	10.6
HD 141569	2016-05-02	0.7	50	y	6.07 ± 0.08	6.7	8.0	8.4	8.7	9.2	9.3
IM Lup	2017-05-15	1.3	120	n	6.80 ± 0.06	7.1	9.1	9.9	10.1	10.3	10.3
HD 142527	2017-05-17	0.8	107	y	3.92 ± 0.39	7.8	10.0	10.5	11.2	12.6	12.7
HD 144668	2017-06-16	0.7	61	y	3.18 ± 0.16	5.9	8.1	8.6	9.3	10.8	11.2
Elias 2-27	2017-05-18	0.5	173	n	7.20 ± 0.04	5.0	6.9	7.5	8.3	9.2	9.1
KK Oph	2016-08-01	0.7	171	y	4.08 ± 0.31	7.1	9.3	10.2	10.3	11.2	12.1
HD 319139	2016-05-03	0.7	161	n	7.12 ± 0.05	5.9	8.1	8.5	8.8	9.1	9.2
HD 169142	2017-05-18	0.7	110	y	5.99 ± 0.10	6.2	8.2	8.9	9.3	10.1	10.1
R CrA	2017-05-19	0.7	36	y	1.78 ± 0.05	3.6	6.1	7.5	8.8	11.2	11.7
T CrA	2017-05-15	1.2	122	y	6.41 ± 0.05	6.4	8.9	10.3	10.8	11.8	11.8
HD 179218	2016-05-02	0.9	63	y	4.47 ± 0.25	7.5	9.4	10.0	10.7	11.5	11.7
HD 190073	2017-07-01	0.7	58	y	4.34 ± 0.31	8.0	10.2	10.8	11.3	12.3	12.4

Notes. [(a)] L' magnitudes and their uncertainties are derived by interpolation between WISE bands W1 (3.35 μm) and W2 (4.6 μm) to 3.8 μm (Cutri et al. 2013). [(b)] Corrected for AGPM throughput where applicable (see Sect. 4).

targets are also taken from *Gaia* DR2 (Gaia Collaboration 2018), although their values have rather large uncertainties owing to circumstellar extinction, which was not taken into account. Ages and outer disc radii of PPD targets are compiled from the literature with references are given in Table 1.

Stellar luminosities, effective temperatures, and disc radii of DEB targets are derived by fitting stellar (PHOENIX; Husser et al. 2013) and blackbody models to observed photometry and spectra. The photometry is obtained from multiple catalogues and publications, including 2MASS, APASS, HIPPARCOS/*Tycho*-2, *Gaia*, AKARI, WISE, IRAS, *Spitzer*, *Herschel*, JCMT, and ALMA. In some cases, photometry has been excluded, for example due to saturation or confusion with background or other objects. The fitting method uses synthetic photometry of grids of models to find the best-fitting models with the MultiNest code (Feroz et al. 2009), and an example is shown in Fig. 7. We first fit star + single disc component models, but in a few cases the fits were significantly improved by adding a second blackbody component, which we interpret as an indication that the star harbours debris belts at multiple radii (Kennedy & Wyatt 2014). The blackbody radius of the debris belts, $R_{\rm BB}$, is then given by (Pawellek & Krivov 2015):

$$R_{\rm BB} = \left(\frac{278\,{\rm K}}{T_{\rm dust}}\right)^2 \left(\frac{L}{L_\odot}\right)^{1/2}. \quad (1)$$

An estimate of the "true" disc radius, $R_{\rm disc}$, is then obtained by applying a stellar luminosity-dependent correction factor, Γ, which accounts for the radiation pressure blowout grain size,

$$\Gamma = a\,(L_*/L_\odot)^b \quad (2)$$

(Pawellek & Krivov 2015), but using the new coefficients given in Pawellek (2016), namely $a = 7.0$ and $b = -0.39$, and limiting Γ to $\Gamma_{\rm max} = 4.0$ for stars with $L_* \lesssim 4\,L_\odot$.

In addition, we also compile and list in Table D.1 disc radii directly obtained from spatially resolved observations where available. These directly measured disc sizes originate from various different tracers and methods for which properly derived

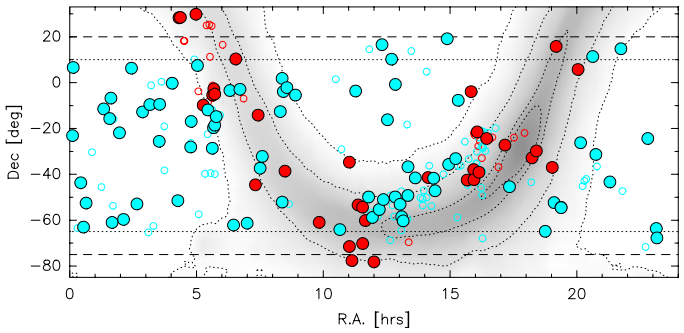

Fig. 3. Sky distribution of all 253 ISPY targets. PPD targets are shown in red, DEB targets in blue. Targets observed in P 96 through P 100 are marked as large filled circles. Targets observed later and with the analysis not yet included in this paper are marked as small empty circles. The grey-shaded area and dotted contours outline the Milky Way disc and bulge as traced by the COBE-DIRBE band 2 (K) zodi-subtracted all-sky map (Hauser et al. 1989). Dotted and dashed horizontal lines mark the approximate declinations for field rotations of 60° and 50°, respectively, achievable with a total observing time of 3 h scheduled around meridian passage of the star.

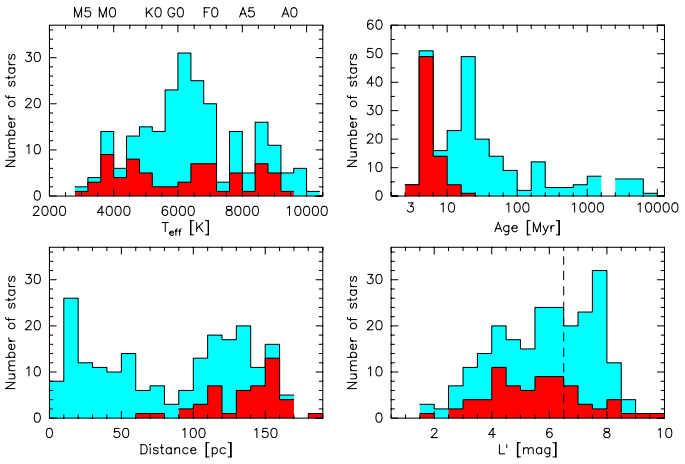

Fig. 4. Histograms showing the distribution of stellar effective temperatures, ages, distances, and L' magnitudes of all 253 ISPY target candidates. PPD targets are shown in red, DEB targets in blue on top of PPD histograms. Spectral types above the first panel correspond to main-sequence stars (Cox 2000). We note that 25 of the PPD targets have distances >200 pc and are thus not contained in the distance distribution histogram. The vertical dashed line in the lower right panel marks the approximate brightness limit up to which the AGPM can be used.

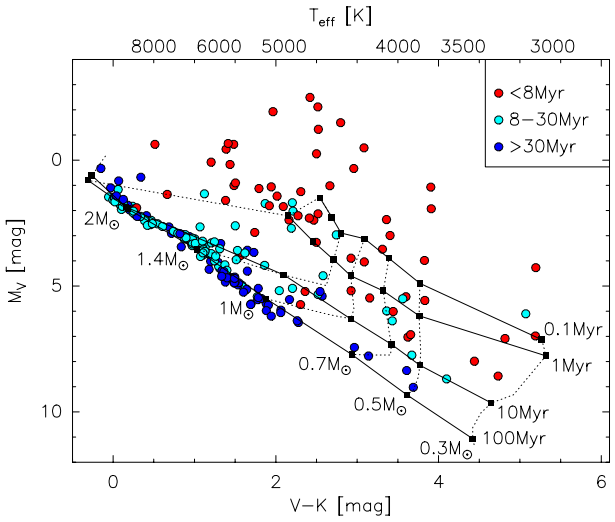

Fig. 5. Colour-magnitude diagram of all NACO-ISPY target candidates. Marked on top are the effective temperatures which a main-sequence star with the corresponding $V - K$ colour would have (Cox 2000). Stellar ages are colour-coded: red: <8 Myr, light blue: 8–30 Myr, dark blue: >30 Myr. Isochrones (Siess et al. 2000) for four stellar ages (counting from the birthline) and for metallicity $Z = 0.02$ are overplotted.

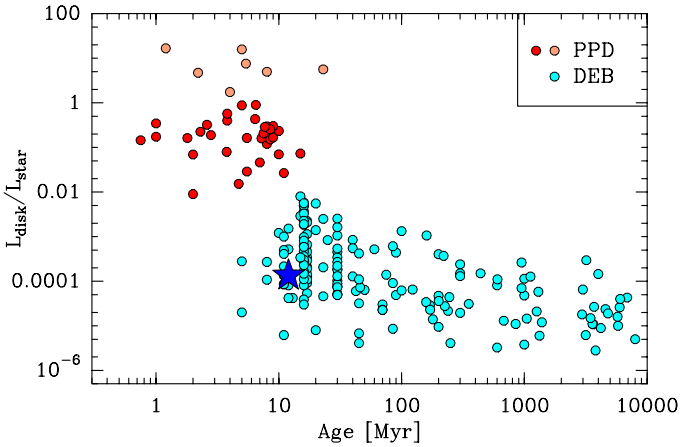

Fig. 6. Fractional disc-related excess luminosity vs. stellar age for all ISPY targets. PPD targets are shown in red, DEB targets in light blue. The large dark blue asterisk marks HD 203 for which we show the SED in Fig. 7. We note that stellar luminosities were not corrected for extinction such that fractional disc luminosities are overestimated and appear unphysically large for some of the very young and embedded PPD stars (>1, light red).

uncertainties are not always available and may therefore not always reflect the "true" outer disc radius. While VIS and NIR observations tracing scattered light and FIR and submm images tracing thermal emission from cold dust should be reliable tracers of the total DEB extent, mid-IR (MIR) observations may trace only hot dust and miss the cold outer dust belts. Nevertheless, these observations provide the best measure we can currently obtain to evaluate the robustness and reliability of the model disc sizes obtained via SED fitting and available for all targets. Figure 8 compares the SED fit-based model radii to the directly observed disc sizes for those 48 targets for which there are known and published disc size measurements available. As can be seen, there is general good agreement between SED-derived and observed disc sizes over a size range of more than two magnitudes. The mean relative discrepancy is ≈50% with the most significant outlier showing a discrepancy of a factor of seven. However, this outlier (HD 38678, see Table D.1) is one of the five stars for which the disc radius was derived from marginally resolved MIR observations which do not trace the cold outer dust belt and thus underestimate the disc size. We therefore conclude that the SED-derived disc radii are, in general, a good proxy for the actual sizes of the cold outer debris belts.

4. Observations

During 13 observing campaigns and 64 observing nights (all in Visitor mode) between December 2015 and March 2018 (see Table 2), we observed and obtained useable data for 112 out of

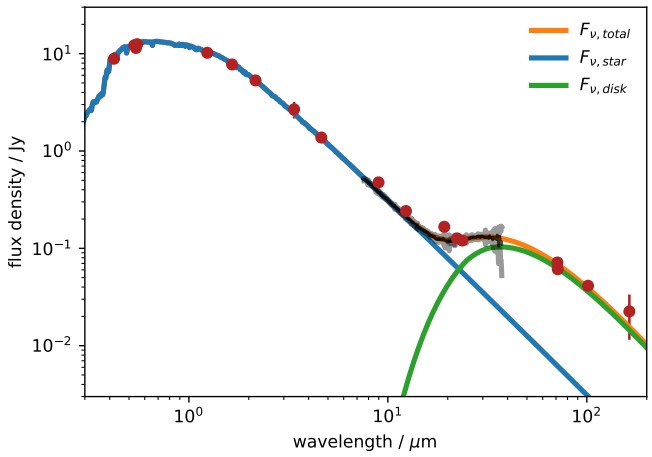

Fig. 7. Flux density distribution for a typical DEB target (HD 203, cf. Fig. 6). Photometric data are shown as red circles, and the *Spitzer* IRS spectrum is shown as a black solid line with uncertainties in grey. The best-fit model (orange line) has stellar (blue) and blackbody (green, for the DEB) components (see Sect. 3.3 for details).

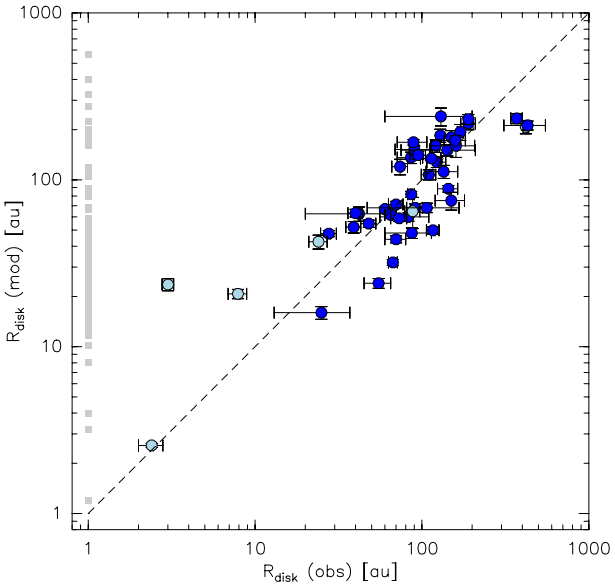

Fig. 8. Debris disc sizes (outer belt radii) obtained via SED fitting and corrected for the luminosity-dependent blowout grain size (Pawellek & Krivov 2015) vs. directly measured disc radii derived from spatially resolved observations (values and references for the stars observed in ESO periods P 96 through 100 are in Table D.1). Disc sizes derived from VIS/NIR or FIR/submm observations are marked in dark blue. Disc sizes derived from MIR observations are marked in light blue. The dashed line marks equality. Marked in light grey at $R_{\rm disc}$(obs) = 1 au are those targets that do not have spatially resolved observations.

the 253 NACO-ISPY target candidates. In total, we obtained 140 datasets of which 105 were obtained with a coronagraph (see below).

For all observations in this survey, we use the AO assisted imager NACO, which is mounted in the Nasmyth A focus at UT1 (Antu) of ESO's VLT on Cerro Paranal in Chile. NACO is equipped with the AO front end, NAOS (Rousset et al. 2003), and the NIR imaging camera CONICA (Lenzen et al. 2003). All stars are observed with the L27 camera of NACO, which provides a pixel scale of 27.2 mas pix^{-1}, and with the L' filter (λ_0 = 3.80 μm, $\Delta\lambda$ = 0.62 μm). The pixel scale corresponds to a sampling of ~3.5 pix per λ/D, the diffraction-limited full width at half maximum (FWHM).

To achieve high contrast between the star and its immediate surroundings, we carry out ADI observations in pupil tracking mode. For ADI, the total time on source time is governed by the need for a field rotation large enough to efficiently remove the speckle noise. Therefore, we observe each star for 2–4 h around its meridian passage, thus typically achieving field rotations of between 70° and 100°. In Fig. A.1 we present histograms displaying the total time on target, field rotation, seeing, and coherence time for all data sets.

To further improve the contrast at small angular separations from bright stars, we use the annular groove phase mask (AGPM) vector vortex coronagraph (Mawet et al. 2013; Absil et al. 2014) for all stars that are bright enough to centre the coronagraph ($L' \lesssim 6.5$ mag). The AGPM effectively suppresses the on-axis starlight by re-directing it outside the pupil, where it is blocked by the Lyot stop. The typical detector integration time (DIT) with AGPM is 0.35 s. To model and correct the thermal background emission, we switch to an offset sky position every eight minutes (13 exposures (NEXPO), 100 detector integration times (NDIT)). We use NACO's cube mode to store each individual image frame for frame selection and sky reconstruction. To properly correct for the off-axis AGPM transmission, we measured the AGPM throughput as described in Appendix B and obtained the radial throughput curve shown in Fig. B.1.

For targets fainter than $L' \approx 6.5$ mag, the AGPM cannot be used because they are too faint for precise centring behind the AGPM. However, we use the same total integration time to achieve similar sensitivity at larger separations. The typical detector integration time (DIT) without AGPM is 0.2 s. The star is positioned at the centre of one quadrant of CONICA and after one exposure (NEXPO = 1, NDIT = 126) is moved to the centre of the next quadrant using fixed offsets. This allows for continuous observation of the star without applying additional telescope offsets for sky frames.

With this approach, we reach a star-planet 5 σ contrast of typically $\Delta L'$ ~7 mag at 0.″2 and a background detection limit of ~16 mag at >1.5″ (see also Sect. 6.1 and Fig. 9). With this strategy for very deep and high-contrast observations and a smallest possible inner working angle (IWA) of ≈100 mas, we are able to observe two to three targets per night on average.

The lower left quadrant of CONICA is strongly affected by bad columns with large constant offset and low sensitivity (see also Sect. 5.1). Until June 2017 every eigth column was affected, but since then, the situation has deteriorated and 38% of this quadrant is affected. Therefore, the lower left quadrant is no longer used in the observing cycle without the AGPM, while the less-severe bad-column problem of a second affected detector quadrant could be handled with post-processing (Sect. 5.1).

The ADI observation is bracketed by unsaturated flux measurements. To avoid saturation, the DIT of CONICA is adjusted depending on the brightness of the star in L'-band, and the star is cycled through the three detector quadrants that are not affected by the bad columns.

An astrometric field is observed at least once per observing run with and without the AGPM to monitor and measure the pixel scale and true north orientation of the detector. The fields are 47 Tucanae and the region around the Orion Trapezium Cluster. The analysis of the astrometric fields is described in Appendix C, and the resulting mean astrometric parameters are listed in Table C.2.

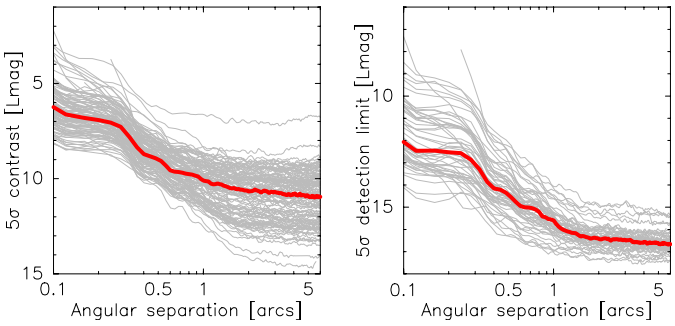

Fig. 9. *Left*: 5σ L' contrast curves for all targets observed during P96 through P100 (light grey, corrected for AGPM throughput where applicable; see Sect. 4) and median contrast (thick red). *Right*: 5σ L' detection limit curves.

5. Data reduction and analysis

All data taken by the ISPY survey are homogeneously reduced using the GRAPHIC pipeline (Hagelberg et al. 2016). While a summary of the philosophy of the pipeline is explained in Hagelberg et al. (2016), substantial changes have been made to many of the steps to optimise them for NACO-ISPY data. Since two types of data are taken during the survey (with and without the AGPM coronagraph), two reduction pathways are used. These steps converge after the data have been cleaned, and the final reduction steps are performed in the same way.

5.1. Cleaning of coronagraphic data

The NACO detector has two quadrants with defective columns. For the first of these, three in every eight columns show a constant value. To avoid problems in subsequent reduction steps, we first correct for these by replacing them with the mean of the four closest non-affected pixels from the same row. Dark frames are then made by median-combining each cube of sky frames. We use the PCA[5]-based sky-subtraction scheme outlined in Hunziker et al. (2018) to remove the background flux, subtracting the first five PCA modes from each image. We then correct for the second quadrant with defective pixels. In this quadrant, one in every eight columns has a dark current offset that varies in time. We correct for this by subtracting the median of each affected column from that column.

To calculate the position of the star behind the AGPM, we use a novel centring routine applied individually to each ∼0.35 s frame. This procedure is summarised here, while a more extensive discussion and a description of its performance will be the subject of a subsequent publication (Godoy et al., in prep.). We perform a two-component fit to the area around the AGPM centre, consisting of a Gaussian for the star and a second profile for the subtraction by the AGPM, which we represent by a Gaussian with negative flux. To improve the stability of the fit, we fix the FWHM and position of the AGPM to the value obtained as described below.

Since the position of the AGPM coronagraph moves on the NACO detector, we use the edges of the 15″ circular aperture around the AGPM to calculate its centre in each image, and use a fixed offset between the centre of this aperture and the position of the AGPM mask calculated from the sky frames. We find that the AGPM moves within a 50×10 pixel region, and its position often changes on hour timescales by several pixels, making this a crucial step in the reduction process. Due to the movement of the AGPM and the presence of significant jitter on short timescales with NACO, we find that this centring procedure outperforms other methods used in the literature.

We remove frames from the reduction that show 5σ outlying values in several criteria using the median absolute deviation as a robust estimator of the standard deviation. First, we use the distance between the measured star position and AGPM position, and then we use the total flux measured in an annulus around the star between 40 and 190 mas, and the scatter of the values in the same annulus.

5.2. Cleaning of non-coronagraphic data

In the same way as for the AGPM coronagraphic data, we first correct the defective columns in the first quadrant as described in the previous section. To subtract the sky background for non-coronagraphic data, we use the three-position dithering pattern used in our observations. Often, the stellar point spread function (PSF) is not clearly visible in the raw frames due to strong dark-current patterns on the detector and so an iterative approach to finding the star position must be taken. We first calculate rough sky frames by taking the mean of the frames in each three-dither sequence. We use the same PCA-based sky subtraction routine as for coronagraphic data, removing the first five modes. We then calculate the star position by performing a Gaussian fit to the PSF, recording the model parameters for each individual exposure.

Using the calculated star positions, we build a robust set of sky frames by again taking the mean of the frames in each three-dither sequence, masking out an area of 40×40 pixels around the calculated star position in each exposure. We then apply the sky subtraction routine a second time using these frames, and repeat the centring procedure to ensure a robust determination of the star position.

We apply automatic criteria to remove bad frames from our data, by removing 5σ outliers in the flux and FWHM measured from the Gaussian fit, calculated across all frames of the entire observing sequence. We also reject 5σ outliers in the star position calculated within each cube (i.e. each dither is treated separately).

5.3. Angular differential imaging and point-source detection limits

The remainder of the reduction procedure is common to both coronagraphic and non-coronagraphic observations. Data are binned by centring each individual exposure and taking the median over each original data cube (roughly 100 frames, or 35 s). We apply a phase ramp to the Fourier transform of each image and take the inverse transform in order to recentre the data.

We then use a PCA-based algorithm to subtract the flux from the star (Soummer et al. 2012; Amara & Quanz 2012). We apply PCA in annuli with a width of 2 $FWHM$. For each frame, we build a reference library using those frames where the change in parallactic angle is sufficiently high that a companion would have moved by more than 0.75 $FWHM$. We perform a number of reductions by subtracting 10–50% of the available PCA modes, using the 30% reduction as our baseline for the detection limit calculation. The frames are then derotated using Fourier transforms and median-combined to produce a final image. By using Fourier transforms to shift and derotate the images, the amplitude and structure of the noise in each image is preserved as well as the amplitude and shape of any potential signals and the stellar

[5] Principal Component Analysis.

PSF. In addition, both steps are reversible when done in this way. This stands in contrast to interpolation-based methods, which have the effect of a low-pass filter and are non-reversible. These benefits were explored by Larkin et al. (1997) and Hagelberg et al. (2016) among others.

Before calculating the detection limits, we first subtract large-scale structures by subtracting the median within a 20×20 pixel box from each pixel. We estimate a 1D noise curve by taking the standard deviation of the pixel values in annuli of $1 \times FWHM$ in width. This is then converted to a detection limit curve using the peak stellar flux corrected for small sample statistics and for the throughput of the PCA algorithm. For correcting for small sample statistics, we follow the approach proposed by Mawet et al. (2014) such that a constant false positive probability of 2.9×10^{-7} (equivalent to $5\,\sigma$ for Gaussian noise) is maintained. The throughput of the PCA algorithm is estimated by injecting the mean stellar PSF into the cleaned, binned images with a signal-to-noise ratio (S/N) of 7 and repeating the PCA reduction. The ratio of input and output flux is then recorded. This is repeated ten times in each annulus, with the azimuth of the injected PSF changed each time. The mean of these values is used to correct the 1D detection limit. The transmission of the AGPM coronagraph was measured on-sky (see Appendix B) and a corresponding correction applied where applicable.

6. Results from the first 2.5 yr of observations

6.1. Overview and detection thresholds

Tables 3 and D.2 list the main observing parameters, L' magnitudes, and achieved $5\,\sigma$ contrast values at six angular separations for all 33 PPD and 78 DEB targets observed during ESO periods 96 through 100. We use the classical $5\,\sigma$ approach here, corrected for both small sample statistics (Mawet et al. 2014) and AGPM throughput, to characterise our detection thresholds and discovery space in a comparable way. At this stage of the survey, we do not employ an automated detection algorithm and therefore do not quantify our detection limits in terms of 95% completeness like, for example, Wahhaj et al. (2013a) or Stone et al. (2018). This must be kept in mind when comparing the detection spaces of different surveys.

We achieve a median $5\,\sigma$ L' contrast at 150 mas of $\Delta L' = 6.4 \pm 0.1$ mag with best and worst values of ~8 mag and ~4 mag, respectively. This contrast close to the IWA is to first order independent of the brightness of the star. The scatter seen in Fig. 9 is mainly caused by variations in the observing conditions. At separations >3″, we achieve a slightly stellar brightness-dependent $5\,\sigma$ detection limit of $L'_{\rm bg} = (15.7 \pm 0.2) + L_* \times (0.16 \pm 0.03)$ mag with best and worst values of 17.5 and 15 mag, respectively (Fig. 9).

To evaluate the companion detection space of our survey, we first convert the $5\,\sigma$ contrast curves (Fig. 9) to planet mass detection limit curves using the L' magnitudes, ages, and distances of the stars (Tables 1, D.1, 3, and D.2) together with the CIFIST2011bc BT-Settl evolutionary model isochrones for the NACO passbands (Allard 2014; Baraffe et al. 2015). The BT-Settl models adopt a "hot start" and solar abundances and employ a cloud model, which puts them in between the two models assuming atmospheric extremes with respect to dust and cloud opacity, COND (no photospheric dust opacity, Baraffe et al. 2003) and DUSTY (maximal dust opacity, Chabrier et al. 2000). We then run Monte-Carlo (MC) simulations in which we assign each star one planet with random mass, semi-major axis (SMA), orbit orientation, and orbital phase, and verify if this planet is above or below the mass detection threshold ($5\,\sigma$) at the respective projected separation. To average down the MC noise, we perform 10^6 mock survey runs. If probability distribution functions (PDF) for planet occurrence rate, masses, and SMA are invoked, the same setup can be used to predict how many planets (and BDs) we should have detected given an assumed underlying PDF. Eccentricities are currently set to zero, but assumptions on the eccentricity distribution will be taken into account for the complete statistical analysis of the entire survey.

Figure 10 shows our resulting detection space in terms of achieved detection probability versus companion mass and SMA[6]. Our detection probability is ≥50% for companions with $M \geq 8\,M_{\rm Jup}$ in the SMA range 80–200 au and $M > 13\,M_{\rm Jup}$ at 30–250 au, but reaches at the 10% level down to $3\,M_{\rm Jup}$ at 40–500 au and out to 5–1000 au for companions with $M > 13\,M_{\rm Jup}$.

6.2. Characterisation of known companions

Within the survey, we have observed and characterised a few stars with previously known companions, have detected and confirmed a number of previously unknown companions, have detected several discs at L'-band, and have identified several companion candidates for which analysis and confirmation is still ongoing. For this reason, we also cannot yet provide a statistical analysis with constraints on the underlying population of GPs and BDs.

Early results on individual targets have been published in separate papers. The discovery of a planetary-mass companion within the gap of the PPD around the pre-main sequence star PDS 70 (V* V1032 Cen) by VLT/SPHERE observations along with L' characterisation by VLT/NACO observations was published by Keppler et al. (2018) and Müller et al. (2018). A detailed characterisation of the SPHERE-discovered warm, dusty giant planet around the young A2 star HIP 65426 via L' NACO and other observations was published by Cheetham et al. (2019).

6.3. New and confirmed companions

The discovery of a close (18.7 au) low-mass stellar companion to the young (1–3 Myr) PPD star R CrA was published by Cugno et al. (2019b). This companion was independently and simultaneously also discovered by SPHERE (Mesa et al. 2019). Another close (11 au) low-mass stellar companion residing within the gap between the host star and its DEB was discovered around HD 193571 by Musso Barcucci et al. (2019).

Around at least two other stars (HD 72660 and HD 92536), we find previously unmentioned close (<1″) low-mass stellar companions, both shown in Fig. 11. For both companions, we can already astrometrically reject the background hypothesis and confirm co-motion. HD 72660 is a ~200 Myr old A0 star with no significant IR excess at a distance of 98.8 ± 0.1 pc (Table D.1). We find a previously unmentioned secondary source at a mean angular separation of $\rho \approx 270$ mas and PA ≈ 55° with $\Delta L' \approx 5.5$ mag (Fig. 11). The background star hypothesis could be rejected and co-motion confirmed via second-epoch observations (Table 4). Using BT-Settl evolutionary models (Allard 2014; Baraffe et al. 2015) and adopting the distance of the primary, the L' brightness and astrometry correspond to a

[6] We note that we consider the true SMA in 3D space together with an arbitrary orbit inclination and arbitrary orbital phase of the companion, such that the detection probability always remains below one.

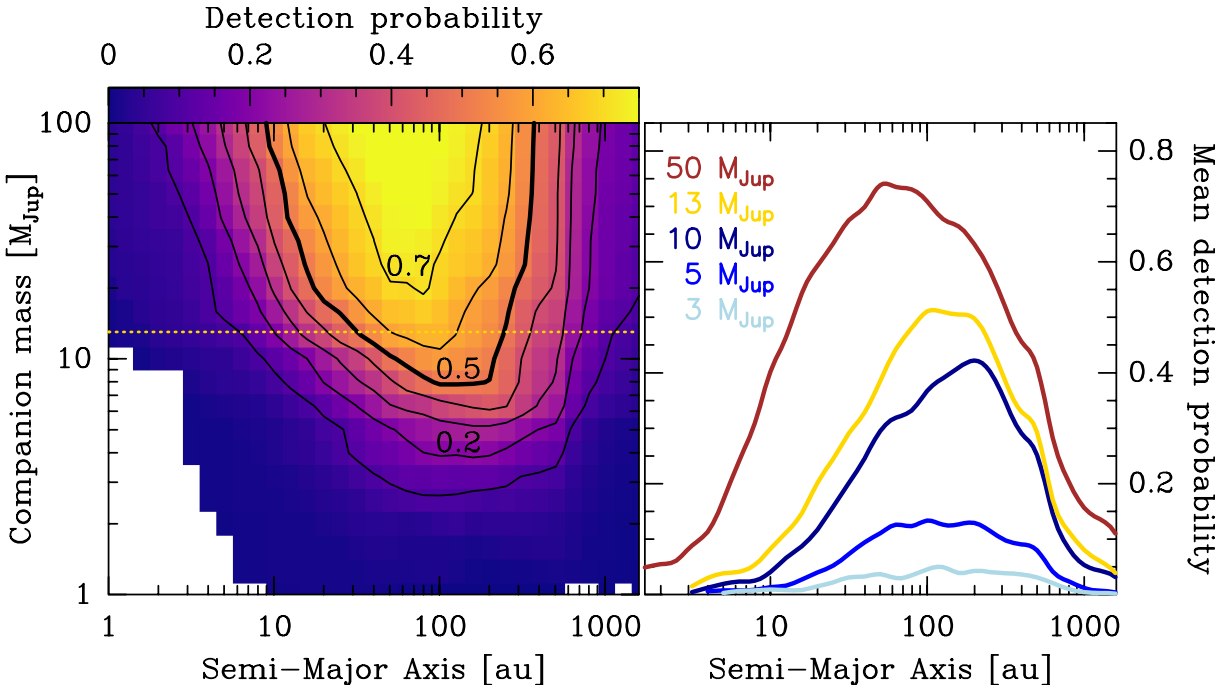

Fig. 10. *Left*: detection probability (colour map) as function of companion mass and semi-major axis for all 112 targets observed during P96 through P100. Contours show detection probabilities from 0.1 to 0.7 (bold: 0.5); the maximum is 0.8 (at SMA ≈ 60 au and $M \gtrsim 60\,M_{\rm Jup}$). The horizontal yellow dotted line marks the approximate boundary between GP and BD ($13\,M_{\rm Jup}$). *Right*: probability curves for different masses as function of SMA.

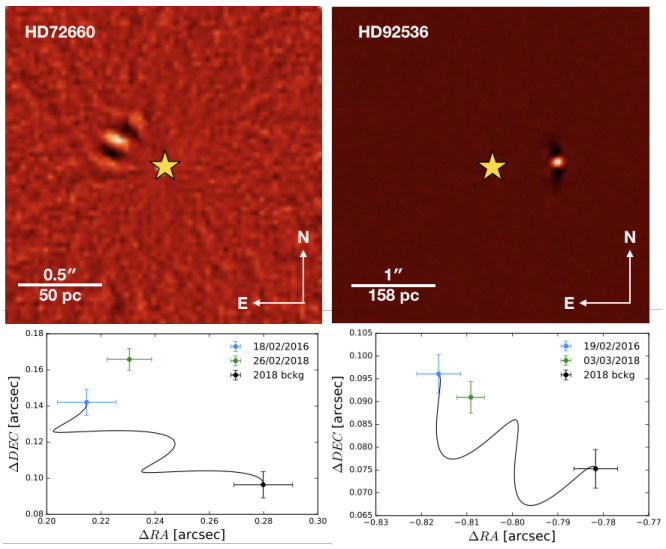

Fig. 11. *Top*: coronagraphic L'-band images of HD 72660 and HD 92536, both with the newly detected low-mass stellar companions. Primary star positions are marked by asterisks. *Bottom*: proper motion analysis of the respective companion candidates. Blue and green data points with error bars show the relative positions of the companions at the two respective epochs. Black points indicate the position the companions would have had at the time of the respective second epoch if they were distant background stars with no proper motion, using the first epoch position as starting point and considering the *Gaia* DR2 proper motion and parallax of the primaries, including their uncertainties (which are however too small to be noticeable).

$0.44 \pm 0.04\,M_\odot$ (M1) companion at a projected separation of $R = 24.4 \pm 0.5$ au. We also detect significant relative motion between primary and secondary with $\Delta\rho \approx 13.5$ mas yr^{-1} and $\Delta\,{\rm PA} \approx 1.1°\,{\rm yr}^{-1}$. Since we only have two astrometric measurements covering only a small orbital arc without any constraint on curvature, we use the prescription provided by Pearce et al. (2015) to verify whether or not the secondary could be in a bound orbit. Adopting a primary mass of $2.4\,M_\odot$ (Chen et al. 2014), the astrometry given in Table 4, and the *Gaia* distance, we derive[7] the dimensionless parameter $B = V_{\rm sky}/V_{\rm esc} = 0.14^{+0.14}_{-0.09}$ (Pearce et al. 2015), indicating that the companion is very likely bound provided the SMA of its (possibly eccentric) orbit is larger than $a_{\rm min} = R/2\,(1-B)^{-1} \approx 14.7$ au[8]. No meaningful constraints can be put on other orbital parameters such as eccentricity or inclination at this point, except that an edge-on orbit can be excluded ($i < 86°$). A chance projection of an unbound object cannot be strictly ruled out as long as there is no constraint on the curvature of motion, for example by third epoch astrometry. However, this is extremely unlikely since no other point source is detected in this field, that is, the local stellar density must be small.

HD 92536 is a ~46 Myr old B8 star at 157.3 ± 1.1 pc with a debris belt at $r_{\rm DD} = 13 \pm 3$ au (Table D.1). We find a previously unmentioned secondary source at $\rho \approx 818$ mas and PA $\approx 276.5°$ with $\Delta L' \approx 5.36$ mag (Fig. 11). The background star hypothesis could be rejected and co-motion confirmed via second-epoch observations (Table 4). Using again the BT-Settl models, the L' brightness and astrometry correspond to a $0.33 \pm 0.05\,M_\odot$ (M2-4) companion at a projected separation of $\sim 129 \pm 1$ au. We also detect significant relative motion between primary and secondary of $\Delta\rho \approx -3.9$ mas yr^{-1} and $\Delta\,{\rm PA} \approx 0.15°\,{\rm yr}^{-1}$. Adopting a primary mass of $3\,M_\odot$ (Chen et al. 2014), we derive $B = 0.15^{+0.43}_{-0.14}$ (Pearce et al. 2015), indicating that also this companion is very likely bound provided $a > a_{\rm min} \approx 76$ au. No meaningful constraints can be put on other orbital parameters at this point, except that an edge-on orbit can be excluded ($i < 85°$).

[7] http://drgmk.com/imorbel/
[8] $B > 1$ would indicate the companion is unbound.

Table 4. Astrometry and photometry of newly identified close stellar companions.

Star	Date	Δ RA [mas]	Δ Dec [mas]	ρ [mas]	PA [deg]	$\Delta L'$ [mag]	m_2 [$M_\odot$]
HD 72600 B	2016-02-17	215 ± 10	142 ± 7	257 ± 10	56.5 ± 0.2	5.36 ± 0.4	0.44 ± 0.04
	2018-02-25	230 ± 8	166 ± 6	284 ± 10	54.3 ± 0.2	5.62 ± 0.2	
HD 92536 B	2016-02-18	−816 ± 5	96 ± 4	822 ± 5	276.7 ± 0.3	5.16 ± 0.03	0.33 ± 0.05
	2018-03-02	−809 ± 3	91 ± 3	814 ± 3	276.4 ± 0.2	5.57 ± 0.04	

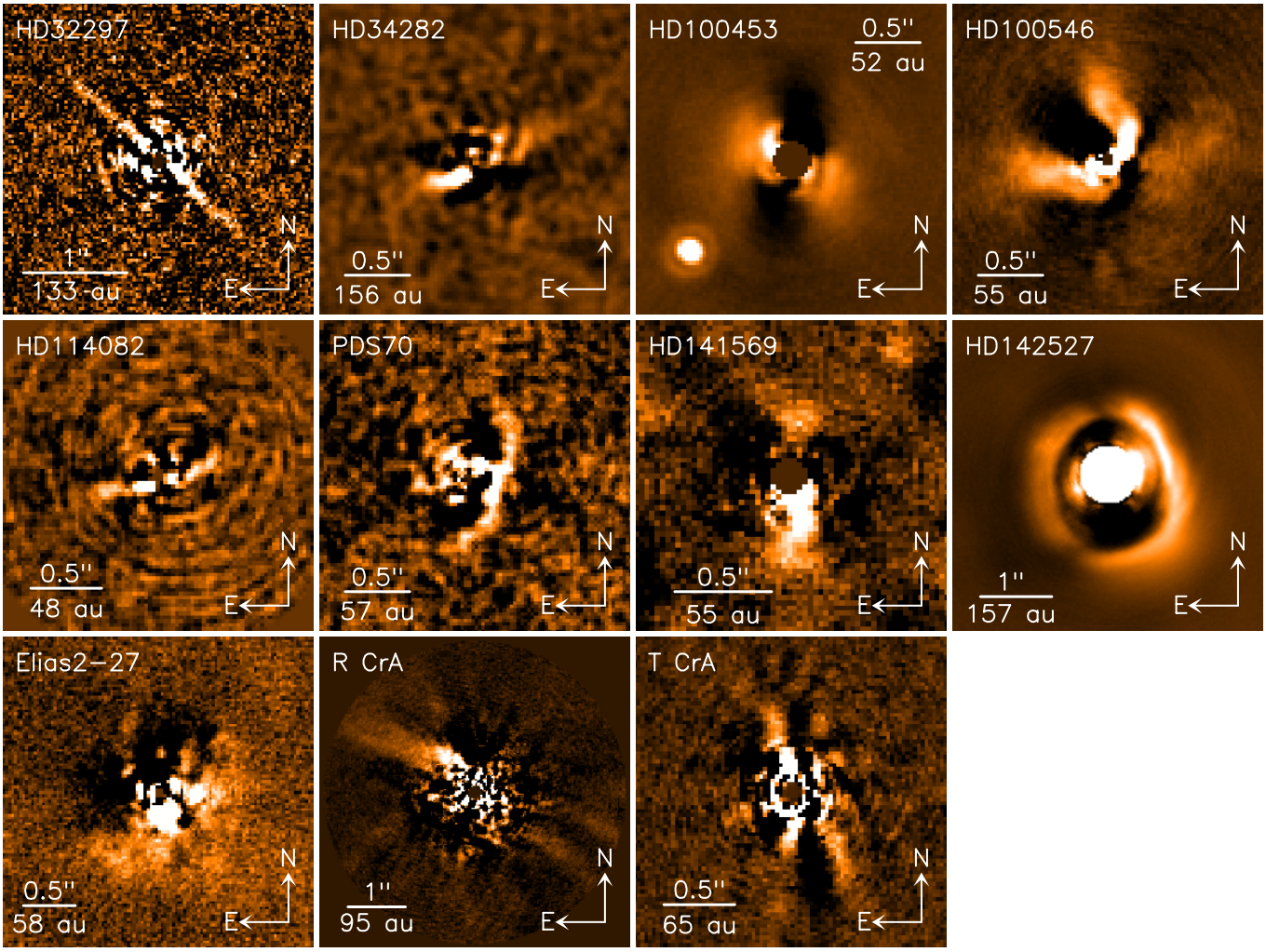

Fig. 12. NACO L'-band images of circumstellar discs.

6.4. Disc detections

Although our ADI observations were not optimised to detect extended emission from circumstellar discs, we have detected scattered light at L'-band from discs around 11 of the 112 target stars observed in P 96 through 100 (Fig. 12). All of these discs except R CrA have been imaged at millimetre wavelengths with ALMA. Five of the eleven discs have already been well-studied and also detected and imaged at L'-band (and shorter NIR bands). These are the discs around the 20 Myr-old A0 DEB star HD 32297 at 133 pc (Schneider et al. 2005; Rodigas et al. 2014; Bhowmik et al. 2019), the 3.8 Myr-old B9 PPD star HD 100546 at 110 pc (Quanz et al. 2013, 2015; Avenhaus et al. 2014; Currie et al. 2014; Sissa et al. 2018), the 5.4 Myr old K5 PPD star PDS 70 at 113 pc (Hashimoto et al. 2012; Keppler et al. 2018), the 4.7 Myr-old B9 PPD star HD 141569 at 111 pc (Currie et al. 2016; Mawet et al. 2017; Perrot et al. 2016), and the 2 Myr-old F6 PPD star HD 142527 at 157 pc (Rameau et al. 2012; Canovas et al. 2017; Avenhaus et al. 2017).

In this paper, we only show the L'-band images of the detected discs without attempting any kind of further analysis, which would require data at other wavelengths and radiative transfer simulations. Since the L'-band scattered light does not necessarily trace the discs in their entirety and our ADI observing mode and data reduction filters out significant parts of the emission, we also do not attempt to derive disc sizes from the images.

7. Discussion

7.1. Detection limits and preliminary statistical analysis

Based on the 5-σ contrast curves shown in Fig. 9, stellar properties (Tables 1 and D.1), and the BT-Settl evolutionary models (Allard 2014; Baraffe et al. 2015), we calculate planet mass detection limit curves for all stars and derive a map of the raw detection probabilities in companion mass – SMA space (Fig. 10). With the same approach, but assuming an underlying companion mass function (CMF) for GPs and BDs from Reggiani et al. (2016) together with a normalisation based on the newest analysis of all existing DI survey results from Galicher et al. (2016), we evaluate how many companions we should have already detected provided the assumptions for the underlying CMF holds for our target stars and provided we would have completed all our ongoing candidate confirmation efforts. We run MC simulations of our survey in which we assign every star a companion (one or none) according to the CMF, place the companion at a random position on a randomly oriented (circular) orbit, and count the expected detections. We find that we should have detected $2.0^{+3.7}_{-1.8}$ companions in the GP-BD mass regime ($0.5^{+1.1}_{-0.3}$ GP and $1.5^{+1.6}_{-0.5}$ BD). While the poisson noise accounts for an uncertainty of the predicted number of companion detections of about ±1.3, the largest part of the uncertainties stated above derives from the uncertainty in our current knowledge of the underlying CMF (see Galicher et al. 2016).

Assuming both the findings reported by Meshkat et al. (2017) as well as their assumption on the functional shape of the underlying CMF, we should have detected $8^{+3.4}_{-2.2}$ companions in the GP-BD mass regime ($2.0^{+1.6}_{-0.9}$ GP and 6^{+3}_{-2} BD). Since verification efforts for several BD as well as GP candidates are still ongoing, we cannot yet draw any robust conclusions on occurrence rates or distinguish between the two different predictions. At the end of our survey (including companion verification efforts), we plan a statistical analysis that does not only include the detection thresholds and detections of our survey, but includes that of other surveys as well.

7.2. Comparison to other surveys

A list of deep imaging surveys of nearby (<100 pc) stars carried out between 2003 and 2013 is conveniently provided by Chauvin et al. (2015). Stone et al. (2018) list L'-band surveys carried out between 2007 and 2017. Bowler (2016) provides a comprehensive overview and description of previous and ongoing large imaging surveys. To put our NACO-ISPY survey into context, we compile in Table 5 a condensed overview of previous and ongoing large DI surveys dedicated to exoplanet searches, which is not complete and does not include many of the early and smaller surveys. In the context of this large variety of big surveys, our NACO-ISPY survey is the largest L'-band survey and the largest survey (including shorter wavelengths) that exclusively targets young stars with either PPDs or DEBs. A direct comparison between different surveys is not straightforward since there is no uniform metric, the detail of information provided by the various publications differs largely, detection limits (if provided) are derived in different ways, and a correction for small-sample statistics (Mawet et al. 2014) is not always applied. Harmonising the results regarding the two latter points would require uniform re-reduction of all data for direct comparison.

We focus our comparison here on the following surveys: (1) Rameau et al. (2013b), a deep L' survey with NACO and with the largest target overlap, (2) LEECH, the newest and deepest L' survey with a small target overlap (northern sky, Stone et al. 2018), the two largest DEB samples from (3) the Gemini/NICI planet-finding campaign (H-band, Wahhaj et al. 2013a) and (4) SEEDS (H-band, Janson et al. 2013), and (5) the first 300 stars from GPIES, which did not explicitly targets DEB stars but still has a large overlap with our DEB sample (H-band, Nielsen et al. 2019). The purpose of the following mostly qualitative comparisons is to present our NACO-ISPY survey in the context of existing, comparable large DI surveys. For the reasons mentioned above and below, performance numbers can mostly not be compared directly and serve only to describe the approximate detection space of the different surveys.

Our NACO-ISPY survey shares the same instrument and filter and the largest overlap (30 targets) with the survey of young, nearby, and dusty stars conducted by Rameau et al. (2013b). In contrast to our observing strategy, Rameau et al. (2013b) did not employ a coronagraph and restricted the time per target to 90 min, irrespective of the field rotation achieved. Their median field rotation is of the order of 25°, while we achieve ~85° (Fig. A.1b). Contrast curves in Rameau et al. (2013b) are given in the classical 5 σ scheme, but are not corrected for small-sample statistics. Nevertheless, a direct comparison between the published curves reveals that we achieve on average 0.5–0.7 mag better contrasts at small angular separations of <300 mas, that is, inside the wings of the PSF where the contrast is almost unaffected by the background limit (which the latter authors do not mention, but which is probably similar to what we achieve). Planet mass detection spaces as published appear similar between NACO-ISPY (Fig. 10) and Rameau et al. (2013b, their Fig. 6), but numbers cannot be compared directly because of different calibrations, target star properties, and evolutionary models used (COND vs. BT-Settl in ISPY). For our anticipated final statistical analysis, we will incorporate the Rameau et al. (2013b) data after re-evaluating the significance of the DEB excess and coherent re-reduction of all data.

The most recently completed and probably deepest L'-band survey, albeit with only a small overlap (eight targets), is the LEECH) survey conducted with the LBT on the northern sky (Skemer et al. 2014; Stone et al. 2018). LEECH also did not employ a coronagraph, but was able to benefit from the excellent LBTI AO system (Bailey et al. 2014), deformable secondary mirrors, and the simultaneous but not interferometric use of two 8.4 m mirrors. LEECH also performed ADI and achieved a mean field rotation of ~65°. Stone et al. (2018) show two sets of contrast curves: the classical 5 σ contrasts without small sample correction and small-sample-corrected contrast curves based on 95% completeness, which they use for the analysis. The "modern" 95% completeness curves produced by these latter authors are on average 0.28 mag less sensitive than their classical 5 σ curves. A direct comparison between the LEECH 5 σ curves and our small-sample-corrected median 5 σ contrasts (Fig. 9) indicates that LEECH achieved significantly better L' contrasts at small angular separations ($\Delta L' \sim 9.0$ mag at $\Delta r = 300$ mas vs. ~7.6 mag for ISPY), but has an IWA of ~250 mas, while the coronagraphic NACO-ISPY observations go down to 100–150 mas. Contrasts at larger angular separations are incomparable since they depend on the contrast between target star brightness and background limit (which we do not know for LEECH). The planet mass detection space of the entire LEECH survey as published by Stone et al. (2018) covers a similar SMA/projected separation range to ours, but the depth cannot

Table 5. Overview of deep exoplanet DI surveys.

Survey or reference	Telescope	Instrument	Filt.	Mode [a]	# of targets [b]	Spectral types	Dist. [c] [pc]	Age [c] [Myr]	Notes [d]
L′-band surveys									
Kasper et al. (2007)	VLT	NACO	L'	Sat-I	22 (4)	FGKM	37	10-30	–
Heinze et al. (2010)	MMT	Clio	L'	ADI	54 (4)	FGKM	11	200	–
Delorme et al. (2012)	VLT	NACO	L'	ADI	16 (1)	M	25	12	–
Rameau et al. (2013b)	VLT	NACO	L'	ADI	59 (30)	BAFGKM	40	30	–
Meshkat et al. (2015)	VLT	NACO	L'	ADI	13 (3)	AF	48	40	–
Lannier et al. (2016)	VLT	NACO	L'	ADI	58 (1)	M	38	21	1
Stone et al. (2018)	LBTI	LMIRcam	L'	ADI	98 (8)	BAFGKM	25	400	2
NACO-ISPY	VLT	NACO	L'	Cor-ADI	200	AFGK	60	30	–
Other surveys									
Masciadri et al. (2005)	VLT	NACO	H, K_S	Sat-I	30 (3)	KM	10–60	10–100	–
Lafrenière et al. (2007)	Gemini-N	NIRI	H	ADI	85 (11)	FGKM	22	10–5000	3
Chauvin et al. (2010)	VLT	NACO	H, K_S	Cor-I	88 (10)	BAFGKM	42	$\lesssim$100	4
Wahhaj et al. (2013a)	Gemini-S	NICI	H	ADI/ASDI	57 (31)	AFGKM	43	100	5, 13
Biller et al. (2013)	Gemini-S	NICI	H	Cor-ASDI	80 (17)	BAFGKM	40	10-200	5, 14
Nielsen et al. (2013)	Gemini-S	NICI	H	Cor-ASDI	70 (23)	BA	$\lesssim$75		5, 15
Janson et al. (2013)	Subaru	HiCIAO	H	ADI	50 (22)	AFGKM	~30	~200	6, 13
Brandt et al. (2014b)	Subaru	HiCIAO	H	ADI	63 (4)	AFGKM	$\lesssim$50	$\lesssim$500	6, 14
Chauvin et al. (2015)	VLT	NACO	H	ADI	85 (4)	FGK	66	100	7
Galicher et al. (2016)	Gemini-N	NIRI	H, K	ADI	292 (33)	BAFGKM	45	120	8
	Gemini-S	NICI	H, K	ADI	–	–	–	–	–
	Keck II	NIRC2	H, K	ADI	–	–	–	–	–
	VLT	NACO	H, K	ADI	–	–	–	–	9
Hinkley et al. (2011)	Hale	Project 1640	J, H	Cor-ASDI	?	...	...	...	10
Nielsen et al. (2019)	Gemini-S	GPI	H	ASDI	300 (**60**)	BAFGK	~30	10–600	11
SHINE	VLT	SPHERE	H, K	ASDI	~600	BAFGKM	...	...	12

Notes. [a]Imaging modes: Sat-I: saturated imaging, ADI: angular differential imaging, Cor-ADI: coronagraphic ADI, ASDI: angular and spectral differential imaging. [b]In brackets the number of targets overlapping with NACO-ISPY. [c]A single number represents the median, otherwise the range is given. [d]Survey notes: (1) MASSIVE, (2) LEECH: LBTI Exozodi Exoplanet Common Hunt (see also Skemer et al. 2014), (3) GDPS: Gemini Deep Planet Survey, (4) NACO Survey of Young Nearby Austral Stars, (5) The Gemini/NICI planet finding campaign (see also Liu et al. 2010), (6) SEEDS: Strategic Exploration of Exoplanets with Subaru (see also Tamura 2016), (7) VLT/NACO-LP: VLT Large Program to Probe the Occurence of Exoplanets and Brown Dwarfs at Wide Orbits (see also Reggiani et al. 2016; Vigan et al. 2017), (8) IDPS: International Deep Planet Search (Vigan et al. 2012), (9) VLT/NACO sub-survey: (Vigan et al. 2012), (10) Project 1640: a Coronagraphic Integral Field Spectrograph at Palomar and ongoing survey with the same name, (11) GPIES: Gemini Planet Imager Exoplanet Survey (600 stars planned), ongoing (see also Marchis et al. 2016; Macintosh et al. 2018), (12) SpHere Infrared survEy, ongoing (Vigan et al. 2016; Chauvin et al. 2017a,b; Keppler et al. 2018; Müller et al. 2018; and others). (13) DEB stars, (14) Young moving group stars, (15) Young B and A stars.

be directly compared without putting all data into the same model. Although LEECH did not explicitly target stars with DEBs and observed in the other hemisphere, our two surveys have eight targets in common. For our final statistical analysis, we incorporate the LEECH data not only of these eight stars, but also of other (northern) targets which prove to have a significant DEB.

The NICI (Wahhaj et al. 2013a) and SEEDS (Janson et al. 2013) DEB surveys targeted 57 and 50 stars, respectively, of which 31 and 22 are in common with NACO-ISPY. The NICI observing campaign employed a semi-transparent flat-topped Gaussian focal plane mask to reduce scattered light from the central star, which provided an effective IWA of 0.″32 for faint companions. Wahhaj et al. (2013a) achieve a mean 95% completeness contrast (which for NICI agrees for most stars well with the traditionally used 5 σ contrast; see Wahhaj et al. 2013b) of $\Delta H \approx 10.5$ mag at 0.″36. In terms of planet mass detection limit (BT-Settl models, Allard 2014; Baraffe et al. 2015), this compares well with the median 5 σ contrast of $\Delta L' \approx 8.5$ mag which we achieve with NACO-ISPY at this angular separation (cf. Figs. 2 and 9). However, with our coronagraphic NACO-ISPY observations, we achieve a significantly smaller IWA of 100–150 mas, which makes the two surveys truly complementary. The other two sub-surveys of the NICI campaign (Biller et al. 2013; Nielsen et al. 2013) that also have certain target overlap with NACO-ISPY have similar detection limits. The SEEDS observations were done in saturated ADI mode with the saturation extending typically out to a radius of 0.″3 and contrasts that typically stay below those achieved by NICI.

Nielsen et al. (2019) recently published a statistical analysis of the first 300 stars observed by the Gemini Planet Imager Exoplanet Survey (GPIES). Although GPIES did not explicitly target DEB stars, the survey has 60 targets (mostly DEB) in common with NACO-ISPY (full sample). GPIES achieves a coronagraphic IWA at H-band of 0.″12, which is very similar to what NACO achieves at L'-band. Nielsen et al. (2019) quantify the achieved contrasts in terms of standard deviation (8 σ at <0.″3 and 6 σ further out) based on the matched-filter algorithm described by Ruffio et al. (2017) and employ the BT-Settl models to convert these to planet detection thresholds. The detection

probability Nielsen et al. (2019) infer for GPIES with the aforementioned thresholds and models (see their Fig. 4) is ≥50% for companions with ≥8 $M_{\rm Jup}$ in the SMA range 10–100 au and reaches down to 3 $M_{\rm Jup}$ at 3–200 au at the 10% level. This compares well to our NACo-ISPY detection space albeit reaching somewhat lower SMA owing to the smaller mean distance of their targets.

Other very large ongoing exoplanet imaging surveys that have not yet published summary papers and for which we therefore cannot compare overlap and detection limits with our NACO-ISPY survey include SPHERE-SHINE (Chauvin et al. 2017a) and Project 1640 (Hinkley et al. 2011). Our sensitivity map shown in Fig. 10 agrees very well (50% contour) with the mean sensitivity map for FGK stars derived by Bowler (2016) from the meta-analysis of 384 stars with published high-contrast imaging observations.

8. Summary and outlook

We present an overview of the NACO-ISPY DI survey for planets around young stars, its scientific goals, observation strategy, targets, and data-reduction scheme. Below we summarise the performance and preliminary results from the first 2.5 yr of observations.

– With NACO-ISPY, we target ≈200 young (median age 30 Myr) and nearby (median distance 60 pc) stars that are either surrounded by a gas-rich PPD with indications for inner holes or gaps (∼50 stars), or by somewhat older well-characterised DEBs (∼150 stars).

– During the first 2.5 yr of the survey, from December 2015 through February 2018 (ESO periods 96 through 100), we observed 112 target stars (34 PPDs and 78 DEBs).

– All observations are carried out with the NACO L27 camera at the VLT, with L' filter and in pupil-tracking ADI mode. For brighter stars ($L' \lesssim 6.5$ mag), the AGPM vector vortex coronagraph is used; fainter stars are observed in saturated mode. The thermal sky background is derived by switching to an offset sky position every 8 min when the AGPM is used. Otherwise, a dither pattern is used. The ADI observation is enclosed by unsaturated flux measurements of the target star itself.

– We typically spend 2–4 h on one source around meridian passage and achieve field rotations of typically 90° ± 20°. With this approach, we reach a mean planet–star 5 σ contrast of $\Delta L' \sim$ 7 mag at 0.″2 and a background detection limit of ∼16.5 mag at >1.5″.

– All data are homogeneously reduced using the GRAPHIC pipeline (Hagelberg et al. 2016), which was optimised for NACO-ISPY data. After initial cleaning and corrections for defective detector columns and pixels, a PCA-based sky-subtraction scheme with five modes is used to remove the background from each image. For the coronagraphic data sets, we employ a novel centring procedure to determine a posteriori the (drifting) position of the AGPM on the detector and the position of the star behind the AGPM. The star position for the non-coronagraphic data is calculated by performing a Gaussian fit to the PSF in each individual exposure. Automatic criteria are used to iteratively remove bad frames and outliers. The data are then centred and median-binned (∼100 frames or 35 s), and a PCA-based algorithm is used to subtract the star. Frames are then derotated using Fourier transforms and median combined to produce the final image.

– One-dimensional noise curves are estimated from the standard deviation of the pixel values in 1 $FWHM$-wide annuli and converted to 5 σ contrast curves using the peak stellar flux from the unsaturated flux images. The contrast curves are corrected for small sample statistics, for the transmission of the AGPM coronagraph measured on-sky, and for the throughput of the PCA algorithm.

– We evaluate the planet mass detection space of our survey by combining the achieved 5 σ $\Delta L'$ contrast curves with actual stellar parameters, BT-Settl evolutionary models, and MC survey simulations. The mean detection probability of our survey is >50% for companions with $M \gtrsim 8\,M_{\rm Jup}$ in the SMA range 80–200 au and $M > 13\,M_{\rm Jup}$ at 30–250 au and compares well to the detection space of other state-of-the-art high-contrast imaging surveys (Bowler 2016).

– While we have not yet been able to independently discover and confirm a new planet in our target sample, our observations have already contributed to the characterisation of two new planets originally discovered by SPHERE: HIP 65426 B (Chauvin et al. 2017b; Cheetham et al. 2019) and PDS 70 B (Keppler et al. 2018; Müller et al. 2018). We discovered two new close-in low-mass stellar companions around the young PPD star R CrA (Cugno et al. 2019b) and within the DEB around HD 193571 (Musso Barcucci et al. 2019). Around at least two other stars (HD 72660 and HD 92536), we find and astrometrically confirm previously unmentioned close (<1″) low-mass co-moving stellar companions.

– We detected scattered light at L'-band around at least nine PPD stars and two DEB stars. Six of these discs had never before been imaged at L'-band.

– As data-reduction improvements, candidate identification, and follow-up characterisation are still ongoing, further discoveries may be revealed even from the data already presented in this paper.

– The NACO-ISPY GTO survey observations with a total budget of 120 nights will be completed in late 2019 with a total of approximately 200 stars imaged at L'-band. A statistical analysis of the entire survey and the synthesis with complementary observations (see below) will be presented in an upcoming paper.

To complement our GP discovery space towards smaller separations (<1–2 au), we are currently carrying out a complementary RV survey for planets around the DEB stars from the NACO-ISPY list (RVSPY, Zakhozhay et al., in prep.). On a timescale of 2–3 yr, the synergy of these two surveys will provide us with the most complete census of GPs around young DEB stars to date, although there will still be a mass sensitivity gap for lower-mass GPs in the DI-probed region (≳10 au) and a general sensitivity gap in the 2–10 au region. This is where astrometry will come into play. The anticipated final full release of the *Gaia* data (individual measurements) will provide us in the near future (no specific release time has yet been given) with the necessary data to reveal the still incompletely known GP population in the 3–5 au separation range (e.g. Casertano et al. 2008).

Acknowledgements. This work has made use of data from the European Space Agency (ESA) mission *Gaia* (https://www.cosmos.esa.int/gaia), processed by the *Gaia* Data Processing and Analysis Consortium (DPAC, https://www.cosmos.esa.int/web/gaia/dpac/consortium). Funding for the DPAC has been provided by national institutions, in particular the institutions participating in the *Gaia* Multilateral Agreement. This publication also makes use of data products from the Wide-field Infrared Survey Explorer, which is a joint project of the University of California, Los Angeles, and the Jet Propulsion Laboratory/California Institute of Technology, funded by the National Aeronautics and Space Administration. This research has made use of the SIMBAD database and the VizieR catalogue access tool, both operated at CDS, Strasbourg, France. The original description of the VizieR service was published in Ochsenbein et al. (2000). This research made use of Astropy[9], a community-developed core Python package for Astronomy (Astropy Collaboration 2013,

[9] http://www.astropy.org

2018). T. H. acknowledges support from the European Research Council under the Horizon 2020 Framework Program via the ERC Advanced Grant Origins 832428. A.M. and A.Q. acknowledge the support of the DFG priority program SPP 1992 "Exploring the Diversity of Extrasolar Planets" (MU 4172/1-1). G.C. and S.P.Q. thank the Swiss National Science Foundation for financial support under grant number 200021_169131. G.M.K. is supported by the Royal Society as a Royal Society University Research Fellow. J.O. and N.G. acknowledge financial support from the ICM (Iniciativa Científica Milenio) via the Núcleo Milenio de Formación Planetaria grant. J.O. acknowledges financial support from the Universidad de Valparaíso, and from Fondecyt (grant 1180395). N.G. acknowledges grant support from project CONICYT-PFCHA/Doctorado Nacional/2017 folio 21170650. Part of this work has been carried out within the framework of the National Centre of Competence in Research PlanetS supported by the Swiss National Science Foundation (SNSF). We acknowledge the financial support of the SNSF. We also acknowledge helpful discussions and direct contributions to various aspects in the survey definition phase and data handling by Ingo Stilz, Carlos Eiroa, Alexander V. Krivov, Nicole Pawellek, Attila Moór, and Esther Buenzli.

References

Absil, O., Mawet, D., Delacroix, C., et al. 2014, Proc. SPIE, 9148, 91480M
Acke, B., & van den Ancker, M. E. 2004, A&A, 426, 151
Alecian, E., Wade, G. A., Catala, C., et al. 2013, MNRAS, 429, 1001
Allard, F. 2014, IAU Symp., 299, 271
Allard, F., Homeier, D., Freytag, B., et al. 2013, Mem. Soc. Astron. It. Suppl., 24, 128
Amara, A., & Quanz, S. P. 2012, MNRAS, 427, 948
Andrews, S. M., Wilner, D. J., Espaillat, C., et al. 2011, ApJ, 732, 42
Andrews, S. M., Huang, J., Pérez, L. M., et al. 2018, ApJ, 869, L41
Anglada-Escudé, G., Amado, P. J., Barnes, J., et al. 2016, Nature, 536, 437
Apai, D., Janson, M., Moro-Martín, A., et al. 2008, ApJ, 672, 1196
Astropy Collaboration (Robitaille, T. P., et al.) 2013, A&A, 558, A33
Astropy Collaboration (Price-Whelan, A. M., et al.) 2018, AJ, 156, 123
Avenhaus, H., Quanz, S. P., Schmid, H. M., et al. 2014, ApJ, 781, 87
Avenhaus, H., Quanz, S. P., Schmid, H. M., et al. 2017, AJ, 154, 33
Bailer-Jones, C. A. L. 2015, PASP, 127, 994
Bailer-Jones, C. A. L., Rybizki, J., Fouesneau, M., Mantelet, G., & Andrae, R. 2018, AJ, 156, 58
Bailey, V. P., Hinz, P. M., Puglisi, A. T., et al. 2014, SPIE Conf. Ser., 9148, 914803
Baraffe, I., Chabrier, G., Barman, T. S., Allard, F., & Hauschildt, P. H. 2003, A&A, 402, 701
Baraffe, I., Homeier, D., Allard, F., & Chabrier, G. 2015, A&A, 577, A42
Barnes, J. R., Jeffers, S. V., Anglada-Escudé, G., et al. 2017, MNRAS, 466, 1733
Benisty, M., Stolker, T., Pohl, A., et al. 2017, A&A, 597, A42
Bhowmik, T., Boccaletti, A., Thébault, P., et al. 2019, A&A, 630, A85
Biller, B. A., Liu, M. C., Wahhaj, Z., et al. 2013, ApJ, 777, 160
Biller, B. A., Males, J., Rodigas, T., et al. 2014, ApJ, 792, L22
Bitsch, B., Lambrechts, M., & Johansen, A. 2015, A&A, 582, A112
Boccaletti, A., Augereau, J.-C., Lagrange, A.-M., et al. 2012, A&A, 544, A85
Bonfanti, A., Ortolani, S., Piotto, G., & Nascimbeni, V. 2015, A&A, 575, A18
Booth, M., Kennedy, G., Sibthorpe, B., et al. 2013, MNRAS, 428, 1263
Boss, A. P. 1997, Science, 276, 1836
Bowler, B. P. 2016, PASP, 128, 102001
Brandt, T. D., McElwain, M. W., Turner, E. L., et al. 2014a, ApJ, 794, 159
Brandt, T. D., Kuzuhara, M., McElwain, M. W., et al. 2014b, ApJ, 786, 1
Brittain, S. D., Carr, J. S., Najita, J. R., Quanz, S. P., & Meyer, M. R. 2014, ApJ, 791, 136
Broekhoven-Fiene, H., Matthews, B. C., Kennedy, G. M., et al. 2013, ApJ, 762, 52
Bryden, G., Beichman, C. A., Carpenter, J. M., et al. 2009, ApJ, 705, 1226
Canovas, H., Hardy, A., Zurlo, A., et al. 2017, A&A, 598, A43
Caratti o Garatti, A., Tambovtseva, L. V., Garcia Lopez, R., et al. 2015, A&A, 582, A44
Carpenter, J. M., Bouwman, J., Mamajek, E. E., et al. 2009, ApJS, 181, 197
Casagrande, L., Schönrich, R., Asplund, M., et al. 2011, A&A, 530, A138
Casertano, S., Lattanzi, M. G., Sozzetti, A., et al. 2008, A&A, 482, 699
Chabrier, G., Baraffe, I., Allard, F., & Hauschildt, P. 2000, ApJ, 542, 464
Chauvin, G., Lagrange, A. M., Bonavita, M., et al. 2010, A&A, 509, A52
Chauvin, G., Vigan, A., Bonnefoy, M., et al. 2015, A&A, 573, A127
Chauvin, G., Desidera, S., Lagrange, A.-M., et al. 2017a, SF2A-2017: Proceedings of the Annual meeting of the French Society of Astronomy and Astrophysics, eds. C. Reylé, P. Di Matteo, F. Herpin, et al., 331
Chauvin, G., Desidera, S., Lagrange, A. M., et al. 2017b, A&A, 605, L9
Cheetham, A. C., Samland, M., Brems, S. S., et al. 2019, A&A, 622, A80
Chen, C. H., Mittal, T., Kuchner, M., et al. 2014, ApJS, 211, 25
Choquet, É., Perrin, M. D., Chen, C. H., et al. 2016, ApJ, 817, L2
Churcher, L., Wyatt, M., & Smith, R. 2011, MNRAS, 410, 2
Close, L. M., Puglisi, A., Males, J. R., et al. 2012, ApJ, 749, 180
Collins, K. A., Grady, C. A., Hamaguchi, K., et al. 2009, ApJ, 697, 557
Corder, S., Carpenter, J. M., Sargent, A. I., et al. 2009, ApJ, 690, L65
Cox, A. N. 2000, Allen's Astrophysical Quantities (New York: Springer)
Cugno, G., Quanz, S. P., Hunziker, S., et al. 2019a, A&A, 622, A156
Cugno, G., Quanz, S. P., Launhardt, R., et al. 2019b, A&A, 624, A29
Currie, T., Muto, T., Kudo, T., et al. 2014, ApJ, 796, L30
Currie, T., Grady, C. A., Cloutier, R., et al. 2016, ApJ, 819, L26
Currie, T., Brittain, S., Grady, C. A., Kenyon, S. J., & Muto, T. 2017, Res. Notes Am. Astron. Soc., 1, 40
Currie, T., Marois, C., Cieza, L., et al. 2019, ApJ, 877, L3
Cutri, R. M., et al. 2013, VizieR Online Data Catalog: II/328
Davies, M. B., Adams, F. C., Armitage, P., et al. 2014, Protostars and Planets VI (Tucson, AZ: University of Arizona Press), 787
Delorme, P., Lagrange, A. M., Chauvin, G., et al. 2012, A&A, 539, A72
Dent, W. R. F., Greaves, J. S., & Coulson, I. M. 2005, MNRAS, 359, 663
Desidera, S., Covino, E., Messina, S., et al. 2015, A&A, 573, A126
Dobbie, P. D., Lodieu, N., & Sharp, R. G. 2010, MNRAS, 409, 1002
Draper, Z. H., Duchêne, G., Millar-Blanchaer, M. A., et al. 2016, ApJ, 826, 147
Ducourant, C., Teixeira, R., Galli, P. A. B., et al. 2014, A&A, 563, A121
Eiroa, C., Marshall, J. P., Mora, A., et al. 2013, A&A, 555, A11
Eiroa, C., Rebollido, I., Montesinos, B., et al. 2016, A&A, 594, L1
Eisner, J. A. 2015, ApJ, 803, L4
Fairlamb, J. R., Oudmaijer, R. D., Mendigutía, I., Ilee, J. D., & van den Ancker, M. E. 2015, MNRAS, 453, 976
Fedele, D., Carney, M., Hogerheijde, M. R., et al. 2017, A&A, 600, A72
Feroz, F., Hobson, M. P., & Bridges, M. 2009, MNRAS, 398, 1601
Fortney, J. J., Marley, M. S., Saumon, D., & Lodders, K. 2008, ApJ, 683, 1104
Fukagawa, M., Tamura, M., Itoh, Y., et al. 2006, ApJ, 636, L153
Gaia Collaboration (Prusti, T., et al.) 2016, A&A, 595, A1
Gaia Collaboration (Brown, A. G. A., et al.) 2018, A&A, 616, A1
Galicher, R., Marois, C., Macintosh, B., et al. 2016, A&A, 594, A63
Geers, V. C., van Dishoeck, E. F., Visser, R., et al. 2007, A&A, 476, 279
Gillon, M., Triaud, A. H. M. J., Demory, B.-O., et al. 2017, Nature, 542, 456
Grady, C. A., Woodgate, B., Torres, C. A. O., et al. 2004, ApJ, 608, 809
Greaves, J. S., Holland, W. S., Matthews, B. C., et al. 2016, MNRAS, 461, 3910
Hagelberg, J., Ségransan, D., Udry, S., & Wildi, F. 2016, MNRAS, 455, 2178
Hamidouche, M. 2010, ApJ, 722, 204
Hashimoto, J., Dong, R., Kudo, T., et al. 2012, ApJ, 758, L19
Hauser, M. G., Kelsall, T., Moseley, S. H., et al. 1989, BAAS, 21, 1219
Heinze, A. N., Hinz, P. M., Sivanandam, S., et al. 2010, ApJ, 714, 1551
Hinkley, S., Oppenheimer, B. R., Zimmerman, N., et al. 2011, PASP, 123, 74
Holland, W. S., Matthews, B. C., Kennedy, G. M., et al. 2017, MNRAS, 470, 3606
Huélamo, N., Chauvin, G., Schmid, H. M., et al. 2018, A&A, 613, L5
Hung, L.-W., Duchêne, G., Arriaga, P., et al. 2015, ApJ, 815, L14
Hunziker, S., Quanz, S. P., Amara, A., & Meyer, M. R. 2018, A&A, 611, A23
Husser, T.-O., Wende-von Berg, S., Dreizler, S., et al. 2013, A&A, 553, A6
Ida, S., & Lin, D. N. C. 2004, ApJ, 616, 567
Isella, A., Carpenter, J. M., & Sargent, A. I. 2010, ApJ, 714, 1746
Janson, M., Carson, J. C., Lafrenière, D., et al. 2012, ApJ, 747, 116
Janson, M., Brandt, T. D., Moro-Martín, A., et al. 2013, ApJ, 773, 73
Johansen, A., & Lacerda, P. 2010, MNRAS, 404, 475
Kalas, P., Graham, J. R., Clampin, M. C., & Fitzgerald, M. P. 2006, ApJ, 637, L57
Kalas, P., Fitzgerald, M. P., & Graham, J. R. 2007, ApJ, 661, L85
Kalas, P., Graham, J. R., Chiang, E., et al. 2008, Science, 322, 1345
Kasper, M., Apai, D., Janson, M., & Brandner, W. 2007, A&A, 472, 321
Kastner, J. H., Hily-Blant, P., Rodriguez, D. R., Punzi, K., & Forveille, T. 2014, ApJ, 793, 55
Kennedy, G. M., & Wyatt, M. C. 2014, MNRAS, 444, 3164
Keppler, M., Benisty, M., Müller, A., et al. 2018, A&A, 617, A44
Kral, Q., Wyatt, M., Carswell, R. F., et al. 2016, MNRAS, 461, 845
Kraus, A. L., & Ireland, M. J. 2012, ApJ, 745, 5
Kraus, S., Preibisch, T., & Ohnaka, K. 2008, ApJ, 676, 490
Kreplin, A., Weigelt, G., Kraus, S., et al. 2013, A&A, 551, A21
Krist, J. E., Stapelfeldt, K. R., Bryden, G., & Plavchan, P. 2012, AJ, 144, 45
Kuzuhara, M., Tamura, M., Kudo, T., et al. 2013, ApJ, 774, 11
Lachaume, R., Dominik, C., Lanz, T., & Habing, H. J. 1999, A&A, 348, 897
Lafrenière, D., Doyon, R., Marois, C., et al. 2007, ApJ, 670, 1367
Lagrange, A.-M., Bonnefoy, M., Chauvin, G., et al. 2010, Science, 329, 57
Lagrange, A. M., Meunier, N., Rubini, P., et al. 2019, Nat. Astron., 421
Lannier, J., Delorme, P., Lagrange, A. M., et al. 2016, A&A, 596, A83
Larkin, K. G., Oldfield, M. A., & Klemm, H. 1997, Opt. Commun., 139, 99
Lenzen, R., Hartung, M., Brandner, W., et al. 2003, Proc. SPIE, 4841, 944
Lestrade, J.-F., Matthews, B. C., Sibthorpe, B., et al. 2012, A&A, 548, A86
Lieman-Sifry, J., Hughes, A. M., Carpenter, J. M., et al. 2016, ApJ, 828, 25

Ligi, R., Vigan, A., Gratton, R., et al. 2018, MNRAS, 473, 1774
Liu, M. C., Wahhaj, Z., Biller, B. A., et al. 2010, SPIE Conf. Ser., 7736, 77361K
Liu, T., Zhang, H., Wu, Y., Qin, S.-L., & Miller, M. 2011, ApJ, 734, 22
Macintosh, B., Graham, J. R., Barman, T., et al. 2015, Science, 350, 64
Macintosh, B., Chilcote, J. K., Bailey, V. P., et al. 2018, SPIE Conf. Ser., 10703, 107030K
Maldonado, J., Martínez-Arnáiz, R. M., Eiroa, C., Montes, D., & Montesinos, B. 2010, A&A, 521, A12
Maldonado, J., Eiroa, C., Villaver, E., Montesinos, B., & Mora, A. 2015, A&A, 579, A20
Mamajek, E. E., & Bell, C. P. M. 2014, MNRAS, 445, 2169
Mamajek, E. E., & Hillenbrand, L. A. 2008, ApJ, 687, 1264
Mamajek, E. E., Bartlett, J. L., Seifahrt, A., et al. 2013, AJ, 146, 154
Manoj, P., Bhatt, H. C., Maheswar, G., & Muneer, S. 2006, ApJ, 653, 657
Marchis, F., Kalas, P. G., Perrin, M. D., et al. 2016, Proc. SPIE, 9910, 99102D
Mariñas, N., Telesco, C. M., Fisher, R. S., & Packham, C. 2011, ApJ, 737, 57
Marino, S., Matrà, L., Stark, C., et al. 2016, MNRAS, 460, 2933
Marino, S., Wyatt, M. C., Panić, O., et al. 2017, MNRAS, 465, 2595
Marois, C., Lafrenière, D., Doyon, R., Macintosh, B., & Nadeau, D. 2006, ApJ, 641, 556
Marois, C., Macintosh, B., Barman, T., et al. 2008, Science, 322, 1348
Marois, C., Zuckerman, B., Konopacky, Q. M., Macintosh, B., & Barman, T. 2010, Nature, 468, 1080
Marshall, J. P., Kirchschlager, F., Ertel, S., et al. 2014, A&A, 570, A114
Masciadri, E., Mundt, R., Henning, T., Alvarez, C., & Barrado y Navascués, D. 2005, ApJ, 625, 1004
Matrà, L., Öberg, K. I., Wilner, D. J., Olofsson, J., & Bayo, A. 2019, AJ, 157, 117
Matthews, B. C., Sibthorpe, B., Kennedy, G., et al. 2010, A&A, 518, L135
Mawet, D., Riaud, P., Absil, O., & Surdej, J. 2005, ApJ, 633, 1191
Mawet, D., Absil, O., Montagnier, G., et al. 2012, A&A, 544, A131
Mawet, D., Absil, O., Delacroix, C., et al. 2013, A&A, 552, L13
Mawet, D., Milli, J., Wahhaj, Z., et al. 2014, ApJ, 792, 97
Mawet, D., Choquet, É., Absil, O., et al. 2017, AJ, 153, 44
Mayor, M., & Queloz, D. 1995, Nature, 378, 355
McLaughlin, D. E., Anderson, J., Meylan, G., et al. 2006, ApJS, 166, 249
Meeus, G., Montesinos, B., Mendigutía, I., et al. 2012, A&A, 544, A78
Menu, J., van Boekel, R., Henning, T., et al. 2015, A&A, 581, A107
Merín, B., Montesinos, B., Eiroa, C., et al. 2004, A&A, 419, 301
Mesa, D., Bonnefoy, M., Gratton, R., et al. 2019, A&A, 624, A4
Meshkat, T., Bailey, V. P., Su, K. Y. L., et al. 2015, ApJ, 800, 5
Meshkat, T., Mawet, D., Bryan, M. L., et al. 2017, AJ, 154, 245
Moerchen, M. M., Telesco, C. M., & Packham, C. 2010, ApJ, 723, 1418
Montes, D., López-Santiago, J., Gálvez, M. C., et al. 2001, MNRAS, 328, 45
Moór, A., Ábrahám, P., Juhász, A., et al. 2011, ApJ, 740, L7
Moór, A., Juhász, A., Kóspál, Á., et al. 2013, ApJ, 777, L25
Moór, A., Henning, T., Juhász, A., et al. 2015a, ApJ, 814, 42
Moór, A., Kóspál, Á., Ábrahám, P., et al. 2015b, MNRAS, 447, 577
Moór, A., Kóspál, Á., Ábrahám, P., et al. 2016, ApJ, 826, 123
Moór, A., Curé, M., Kóspál, Á., et al. 2017, ApJ, 849, 123
Morales, F. Y., Bryden, G., Werner, M. W., & Stapelfeldt, K. R. 2016, ApJ, 831, 97
Morbidelli, A. 2018, Handbook of Exoplanets (Cham: Springer), 145
Mordasini, C., Alibert, Y., Klahr, H., & Henning, T. 2012, A&A, 547, A111
Müller, A., Keppler, M., Henning, T., et al. 2018, A&A, 617, L2
Musso Barcucci, A., Launhardt, R., Kennedy, G. M., et al. 2019, A&A, 627, A77
Nielsen, E. L., Liu, M. C., Wahhaj, Z., et al. 2013, ApJ, 776, 4
Nielsen, E. L., Liu, M. C., Wahhaj, Z., et al. 2016, IAU Symp., 314, 220
Nielsen, E. L., De Rosa, R. J., Macintosh, B., et al. 2019, AJ, 158, 13
Ochsenbein, F., Bauer, P., & Marcout, J. 2000, A&AS, 143, 23
Olofsson, J., Juhász, A., Henning, T., et al. 2012, A&A, 542, A90
Olofsson, J., Samland, M., Avenhaus, H., et al. 2016, A&A, 591, A108
Ormel, C. W., & Klahr, H. H. 2010, A&A, 520, A43
Palla, F., & Stahler, S. W. 2002, ApJ, 581, 1194
Pascual, N., Montesinos, B., Meeus, G., et al. 2016, A&A, 586, A6
Pawellek, N. 2016, PhD Thesis, University of Jena, Germany
Pawellek, N., & Krivov, A. V. 2015, MNRAS, 454, 3207
Pearce, T. D., Wyatt, M. C., & Kennedy, G. M. 2015, MNRAS, 448, 3679
Pecaut, M. J., & Mamajek, E. E. 2016, MNRAS, 461, 794
Perets, H. B., & Kouwenhoven, M. B. N. 2012, ApJ, 750, 83
Pérez, L. M., Carpenter, J. M., Andrews, S. M., et al. 2016, Science, 353, 1519
Perrot, C., Boccaletti, A., Pantin, E., et al. 2016, A&A, 590, L7
Perryman, M., Hartman, J., Bakos, G. Á., & Lindegren, L. 2014, ApJ, 797, 14
Piétu, V., Dutrey, A., & Guilloteau, S. 2007, A&A, 467, 163
Plavchan, P., Werner, M. W., Chen, C. H., et al. 2009, ApJ, 698, 1068
Pollack, J. B., Hubickyj, O., Bodenheimer, P., et al. 1996, Icarus, 124, 62
Quanz, S. P. 2015, Ap&SS, 357, 148
Quanz, S. P., Amara, A., Meyer, M. R., et al. 2013, ApJ, 766, L1
Quanz, S. P., Amara, A., Meyer, M. R., et al. 2015, ApJ, 807, 64
Rameau, J., Chauvin, G., Lagrange, A.-M., et al. 2012, A&A, 546, A24
Rameau, J., Chauvin, G., Lagrange, A.-M., et al. 2013a, ApJ, 779, L26
Rameau, J., Chauvin, G., Lagrange, A.-M., et al. 2013b, A&A, 553, A60
Rameau, J., Follette, K. B., Pueyo, L., et al. 2017, AJ, 153, 244
Reggiani, M., Quanz, S. P., Meyer, M. R., et al. 2014, ApJ, 792, L23
Reggiani, M., Meyer, M. R., Chauvin, G., et al. 2016, A&A, 586, A147
Reggiani, M., Christiaens, V., Absil, O., et al. 2018, A&A, 611, A74
Rhee, J. H., Song, I., Zuckerman, B., & McElwain, M. 2007, ApJ, 660, 1556
Ribas, I., Tuomi, M., Reiners, A., et al. 2018, Nature, 563, 365
Rodigas, T. J., Debes, J. H., Hinz, P. M., et al. 2014, ApJ, 783, 21
Rosenfeld, K. A., Andrews, S. M., Wilner, D. J., Kastner, J. H., & McClure, M. K. 2013, ApJ, 775, 136
Rousset, G., Lacombe, F., Puget, P., et al. 2003, Proc. SPIE, 4839, 140
Ruffio, J.-B., Macintosh, B., Wang, J. J., et al. 2017, ApJ, 842, 14
Saar, S. H., & Donahue, R. A. 1997, ApJ, 485, 319
Schegerer, A. A., Wolf, S., Hummel, C. A., Quanz, S. P., & Richichi, A. 2009, A&A, 502, 367
Schneider, G., Silverstone, M. D., & Hines, D. C. 2005, ApJ, 629, L117
Schneider, G., Silverstone, M. D., Hines, D. C., et al. 2006, ApJ, 650, 414
Schneider, J., Dedieu, C., Le Sidaner, P., Savalle, R., & Zolotukhin, I. 2011, A&A, 532, A79
Schrijver, C. J., & Zwaan, C. 2008, Solar and Stellar Magnetic Activity (Cambridge: Cambridge University Press)
Sicilia-Aguilar, A., Henning, T., Kainulainen, J., & Roccatagliata, V. 2011, ApJ, 736, 137
Siess, L., Dufour, E., & Forestini, M. 2000, A&A, 358, 593
Sissa, E., Gratton, R., Garufi, A., et al. 2018, A&A, 619, A160
Skemer, A. J., Hinz, P., Esposito, S., et al. 2014, Proc. SPIE, 9148, 91480L
Smith, R., Wyatt, M. C., & Haniff, C. A. 2009, A&A, 503, 265
Soummer, R., Pueyo, L., & Larkin, J. 2012, ApJ, 755, L28
Spiegel, D. S., & Burrows, A. 2012, ApJ, 745, 174
Stone, J. M., Skemer, A. J., Hinz, P. M., et al. 2018, AJ, 156, 286
Szulágyi, J., Dullemond, C. P., Pohl, A., & Quanz, S. P. 2019, MNRAS, 487, 1248
Tamura, M. 2016, Proc. Jpn Acad.Ser. B 92, 45
Tatulli, E., Benisty, M., Ménard, F., et al. 2011, A&A, 531, A1
The, P. S., de Winter, D., & Perez, M. R. 1994, A&AS, 104, 315
Tucci Maia, M., Ramírez, I., Meléndez, J., et al. 2016, A&A, 590, A32
van Leeuwen, F. 2007, A&A, 474, 653
Verhoeff, A. P., Min, M., Acke, B., et al. 2010, A&A, 516, A48
Vican, L. 2012, AJ, 143, 135
Vigan, A., Patience, J., Marois, C., et al. 2012, A&A, 544, A9
Vigan, A., Bonnefoy, M., Ginski, C., et al. 2016, A&A, 587, A55
Vigan, A., Bonavita, M., Biller, B., et al. 2017, A&A, 603, A3
Wade, G. A., Drouin, D., Bagnulo, S., et al. 2005, A&A, 442, L31
Wagner, K., Stone, J. M., Spalding, E., et al. 2019, ApJ, 882, 20
Wahhaj, Z., Liu, M. C., Nielsen, E. L., et al. 2013a, ApJ, 773, 179
Wahhaj, Z., Liu, M. C., Biller, B. A., et al. 2013b, ApJ, 779, 80
Wahhaj, Z., Milli, J., Kennedy, G., et al. 2016, A&A, 596, L4
Walsh, C., Juhász, A., Meeus, G., et al. 2016, ApJ, 831, 200
Weise, P., Launhardt, R., Setiawan, J., & Henning, T. 2010, A&A, 517, A88
Wheelwright, H. E., Weigelt, G., Caratti o Garatti, A., & Garcia Lopez, R. 2013, A&A, 558, A116
Wolszczan, A., & Frail, D. A. 1992, Nature, 355, 145
Wyatt, M. C. 2008, ARA&A, 46, 339
Zechmeister, M., Dreizler, S., Ribas, I., et al. 2019, A&A, 627, A49
Zhu, Z. 2015, ApJ, 799, 16
Zuckerman, B., & Song, I. 2004, ApJ, 603, 738
Zuckerman, B., & Song, I. 2012, ApJ, 758, 77
Zuckerman, B., Kim, S. S., & Liu, T. 1995, ApJ, 446, L79
Zuckerman, B., Rhee, J. H., Song, I., & Bessell, M. S. 2011, ApJ, 732, 61

Appendix A: Observing statistics histograms

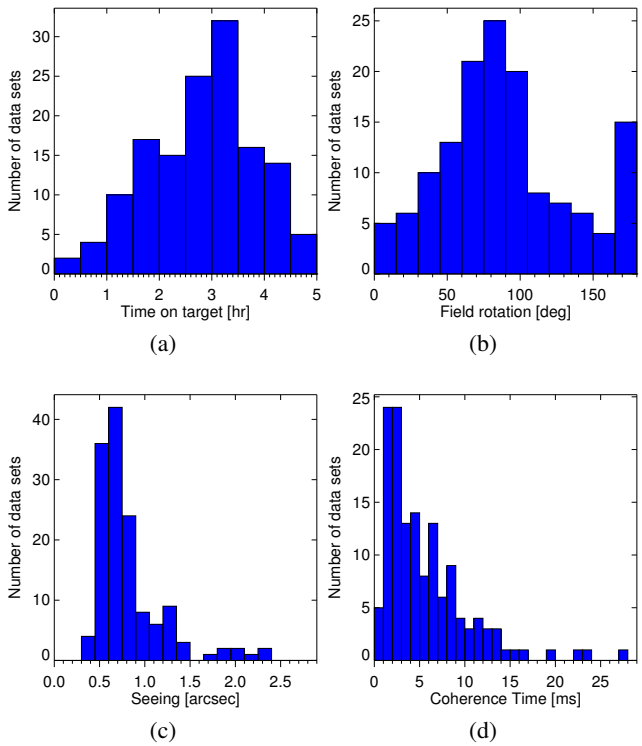

Fig. A.1. Distribution of the main observing characteristics for all targets observed during P96 to P100. (*a*) Total time spent on target. For the majority of our targets we spend between 2 and 4 h to maximise field rotation (*b*).

Appendix B: Off-axis transmission of the annular groove phase mask vector vortex coronagraph

To measure the on-sky off-axis AGPM transmission, two bright stars were observed for comparison. HD 146624 was observed during the night of May 19, 2017, and HIP 98421 was observed during the night of August 31, 2017. The instrument setup and observation are similar to standard AGPM observations. The star was placed manually in vertical and horizontal direction around the AGPM with the goal of a one-pixel sampling. Sampling at different position angles is not necessary because of the perfect circular symmetry of the AGPM. For HD 146624 and HIP 98421, 45 and 30 data cubes were recorded, respectively, each containing 400 frames. Data cubes recorded with the star centred behind the AGPM or of bad data quality were rejected in the analysis, which leaves 40 useful cubes for HD 146624 and 29 for HIP 98421. A sky observation was taken after every five cubes.

The sky frames were cosmetically reduced including dark subtraction, flat field, and bad pixel correction. This was necessary for determining the position of the AGPM centre on the detector. In the sky frames, the AGPM centre appears similar to a (faint) stellar source due to thermal emission. The AGPM centre was fitted by a Moffat function for each frame in each cube. The final position of the AGPM centre per cube was retrieved by computing the median and the standard deviation of the individual measurements.

The data cubes with the object were cosmetically reduced including sky subtraction, flat field, and bad pixel correction. The star in each frame and cube was fitted by a Moffat function to get its position and ultimately its radial distance from the AGPM centre. To measure the flux of a star, aperture photometry

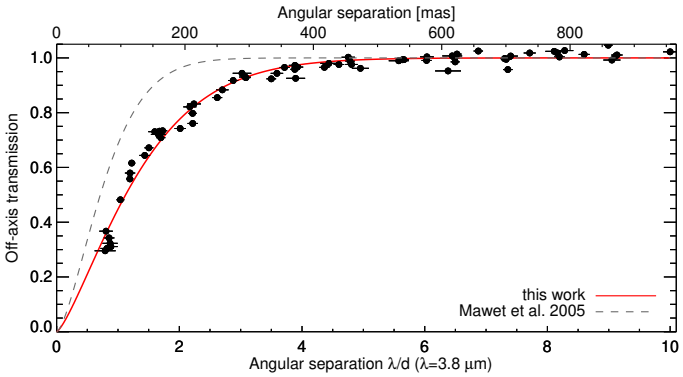

Fig. B.1. Measured off-axis transmission (black points) of the AGPM and the exponential fit (red line) to the data as a function of radial distance from the AGPM centre in resolution elements. The data of both stars are combined after normalising the stellar fluxes (see text for explanation). The error bars of the flux measurements are smaller than the size of the symbols. The exponential fit on simulated data by Mawet et al. (2005) is shown as a dashed grey line for comparison.

was performed using an aperture radius of $4 \times FWHM$[10] for the source, and an annulus of $6\text{–}10 \times FWHM$ for the background. The final flux value for each cube is the weighted average of the individual flux measurements.

The off-axis transmission of the AGPM, $T(r)$, has a theoretical profile of the form $1 - \exp(-2 \cdot r^2)$, where r is the radial distance of the AGPM centre in resolution elements λ/D (Mawet et al. 2005). For measuring the empirical transmission curve, $T^*(r)$, we therefore use the form

$$T^*(r) = 1 - \exp(-a \cdot r^b). \quad \text{(B.1)}$$

As both the position and flux have uncertainties, an MC approach was used to determine the fit parameters a and b. For both stars, the measured flux as a function of radial distance from the AGPM centre was fitted using Eq. (B.1) with the additional flux-scaling parameter c, but without weighting of the data points or taking into account uncertainties. Instead, 10^5 new data sets were generated by randomly drawing new measurements from each data point taking its uncertainty into account. The final fit value for each variable was obtained by computing the bootstrap mean of the 10^5 measurements by generating 10^5 bootstrap samples. The uncertainty in the fit parameters is the standard deviation of all measurements. The explained fitting procedure on the individual stars was used only to determine the fit parameter c, which denotes the stellar flux. This is required before combining both data sets because the stars have different fluxes and c normalises the fluxes of both stars to one. The fitting procedure was then applied to the combined normalised data set (Fig. B.1). The final values and uncertainties of the fit parameters are: $a = 0.586 \pm 0.022$, $b = 1.330 \pm 0.059$.

Appendix C: Astrometric correction

Measurements of the plate scale and the true north orientation on a regular basis are essential to warrant accurate and precise astrometric values of identified candidate companions. The main stellar field used for astrometric calibration is 47 Tuc as it usually provides more than 100 stars under good atmospheric conditions in the field of view of NaCo. An alternative field is the Orion

[10] FWHM is the full width at half maximum and is ≈3.5 px for NaCo observations in L' at 3.8 μm

Table C.1. Parameters and values used for the AGPM and satPSF instrument setup.

Parameter	AGPM	satPSF
naxis [px]	768	1024
DIT [s]	0.35	0.2
NDIT	100	100
N cubes/object	5	5
N cubes/sky	6	5

Trapezium Cluster, but with significantly fewer sources visible in L'.

Astrometric fields are observed since the start of the survey in December 2015 with and without (satPSF) the AGPM. Table C.1 lists typical values used for the instrument setup. The actual values can vary because of the brightness of the sky background. In addition, we refined the observing template with time. The goal during each observing run is to observe an astrometric field with and without the AGPM in both field and pupil tracking mode, respectively.

The image reduction steps for the AGPM and satPSF mode are similar and include: bad pixel and flat field correction, and sky subtraction. Since we are recording up to six sky cubes, the frames and cubes are median-combined to a single image to remove any stellar sources present. Each object cube (the actual astrometric field) is treated individually. The final analysis is based on the average image for each individual cube. If the data were recorded in pupil tracking mode, the frames are derotated before averaging them.

After the cosmetic reduction, stellar sources in the image are identified with a version of DAOPHOT implemented in IDL. Marginal Gaussians are used to find centroids. To refine the result and reject bad detections, each initially found source is fitted with a Gaussian function. The fitted FWHM values of both directions and the fitted position are used to reject non-stellar sources. For the remaining sources, the x and y pixel coordinates are converted into RA and Dec using the WCS information written in the fits header and the separation and position angles between all stars are computed. To compare these values with a reference, we use the catalogue of McLaughlin et al. (2006) for 47 Tuc and the catalogue of Close et al. (2012) for the Trapezium. The catalogue entries (RA, Dec) are corrected for proper motion if present and converted to x,y-coordinates using the WCS information written in the fits header and the separation and position angles between all catalogue stars are computed. This allows us to identify the detected stars in the image with their corresponding catalogue entry. The derived value for the plate scale between one pair of stars is then the distance from the catalogue pair in milliarcseconds divided by the measured distance of the same pair detected in the image. The true north value is computed from the difference between measured position angle of a stellar pair and its respective catalogue entry. For 100 stars detected in the image, there are therefore over 4400 individual measurements available. The final values for plate scale and true north including their uncertainties are listed in Table C.2 and were produced by computing the two-sigma-clipped resistant mean.

Table C.2. Weighted averaged values for plate scale and true north for different instrument setups.

Mode	Pixel scale [mas]	True north [deg]
AGPM	27.208 ± 0.088	0.572 ± 0.178
satPSF	27.193 ± 0.059	0.568 ± 0.115

Appendix D: Additional tables

Table D.1. DEB targets observed between December 2015 and March 2018 (P 96 through P 100).

Name [(a)]	RA(J2000) [hh:mm:ss]	Dec(J2000) [dd:mm:ss]	Dist. [(b)] [pc]	V [mag]	$\log(L_*)$ [(c)] [$L_\odot$]	$T_{\rm eff}$ [(c)] [K]	Age [(d)] [Myr]	$R_{\rm disc}$ [(c)] [au]	Ref. [(e)]
HD 203	00:06:50.02	−23:06:26.7	39.9	6.2	0.63	6800	12 ± 2	47 ± 3	1
HD 377	00:08:25.69	06:37:00.5	38.5	7.6	0.07	5820	90 ± 65	136 ± 11 [(f)] (86)	2, 50
HD 2262	00:26:12.20	−43:40:47.4	22.3	3.9	1.01	7750	200 ± 100	45 ± 5	4
HD 3003	00:32:43.79	−63:01:53.0	45.8	5.1	1.28	9260	30 ± 15	24 ± 2	1

Notes. [(a)]Where available, we use the HD number as main source ID. [(b)]All distances in this table are inferred from *Gaia* DR2 parallaxes (Gaia Collaboration 2016, 2018) with the method described by Bailer-Jones et al. (2018) and retrieved through VizieR (Ochsenbein et al. 2000). Uncertainties are typically <0.6% and exceed in no case 2.6%. [(c)]Stellar L_*, $T_{\rm eff}$, and $R_{\rm disc}$ are derived from SED fitting (see Sect. 3.2). Additional $R_{\rm disc}$ values in brackets refer to directly observed and spatially resolved disc radii compiled from the literature (references 50 through 73). [(d)]Age notes. [(e)]References 1 through 30 refer to age, references 50 through 73 refer to observed disc radius. [(f)]SED fit indicates second hot inner dust belt. [(g)]Disc excess is not significant.

References. (1) Zuckerman & Song (2004); (2) Apai et al. (2008); (3) Weise et al. (2010); (4) Chen et al. (2014); (5) Zuckerman et al. (2011); (6) Zuckerman & Song (2012); (7) Casagrande et al. (2011); (8) Moór et al. (2011); (9) Desidera et al. (2015); (10) Mamajek & Hillenbrand (2008); (11) Bonfanti et al. (2015); (12) Rhee et al. (2007); (13) Maldonado et al. (2010); (14) Meshkat et al. (2015); (15) Carpenter et al. (2009); (16) Moór et al. (2016); (17) Plavchan et al. (2009); (18) Olofsson et al. (2012); (19) Vican (2012); (20) Lachaume et al. (1999); (21) Dobbie et al. (2010); (22) Eiroa et al. (2016); (23) Lafrenière et al. (2007); (24) Mamajek & Hillenbrand (2008); (25) Pecaut & Mamajek (2016); (26) Bryden et al. (2009); (27) Mamajek & Bell (2014); (28) Tucci Maia et al. (2016); (29) Montes et al. (2001); (30) Mamajek et al. (2013); (50) Choquet et al. (2016); (51) Holland et al. (2017); (52) Kalas et al. (2007); (53) Moór et al. (2015b); (54) Moór et al. (2013); (55) Broekhoven-Fiene et al. (2013); (56) Morales et al. (2016); (57) Boccaletti et al. (2012); (58) Moór et al. (2016); (59) Kalas et al. (2006); (60) Olofsson et al. (2016); (61) Smith et al. (2009); (62) Moerchen et al. (2010); (63) Corder et al. (2009); (64) Booth et al. (2013); (65) Draper et al. (2016); (66) Wahhaj et al. (2016); (67) Marshall et al. (2014); (68) Hung et al. (2015); (69) Lestrade et al. (2012); (70) Lieman-Sifry et al. (2016); (71) Schneider et al. (2006); (72) Churcher et al. (2011); (73) Krist et al. (2012).

Table D.1. continued.

Name [a]	RA(J2000) [hh:mm:ss]	Dec(J2000) [dd:mm:ss]	Dist. [b] [pc]	V [mag]	$\log(L_*)$ [c] [$L_\odot$]	$T_{\rm eff}$ [c] [K]	Age [d] [Myr]	$R_{\rm disc}$ [c] [au]	Ref. [e]
HD 3670	00:38:56.70	−52:32:03.4	77.4	8.2	0.40	6390	30 ± 15	160 ± 8	4
HIP 6276	01:20:32.20	−11:28:02.5	35.3	8.4	−0.28	5320	70 ± 25	28 ± 4	5
HD 9672	01:34:37.78	−15:40:34.9	57.0	5.6	1.18	8750	40 ± 10	208 ± 19 [f] (420)	6, 51
HD 10008	01:37:35.37	−06:45:36.7	24.0	7.7	−0.33	5280	3000 ± 2400	56 ± 6	7
HD 10472	01:40:24.07	−60:59:56.6	71.0	7.6	0.56	6710	30 ± 15	180 ± 13 [f]	1
HD 12039	01:57:48.91	−21:54:04.9	41.4	8.1	−0.05	5660	30 ± 15	20 ± 1	3
HD 13246	02:07:26.02	−59:40:45.8	45.5	7.5	0.24	6130	30 ± 15	12 ± 1	3
HD 15115	02:26:16.25	06:17:33.2	48.9	6.8	0.56	6720	12 ± 2	212 ± 13 [f] (315-550)	8, 52
HD 16743	02:39:07.56	−52:56:05.3	57.8	6.8	0.71	6900	200 ± 100	233 ± 16 [f] (370)	4, 53
HD 17925	02:52:31.89	−12:46:09.3	10.4	6.1	−0.40	5180	90 ± 10	20 ± 2	3
HD 19668	03:09:42.23	−09:34:45.6	38.7	8.5	−0.24	5420	100 ± 50	16 ± 2	9
HD 21997	03:31:53.65	−25:36:50.9	69.5	6.4	1.03	8380	30 ± 15	180 ± 18 (150)	4, 54
HD 22049	03:32:56.42	−09:27:29.9	3.20	3.7	−0.47	5073	1000 ± 500	32 ± 2 (67)	10, 11, 51
HD 25457	04:02:36.66	−00:16:05.9	18.8	5.4	0.31	6270	75 ± 25	56 ± 4	2
HD 27290	04:16:01.59	−51:29:11.9	20.4	4.2	0.82	7140	300 ± 250	218 ± 18 (190)	12, 55
HD 30422	04:46:25.75	−28:05:14.8	57.4	6.2	0.93	7700	13 ± 7	128 ± 9 (123)	4, 56
HD 30495	04:47:36.21	−16:56:05.5	13.2	5.5	−0.02	5850	45 ± 10	84 ± 5	13
HD 32297	05:02:27.44	07:27:39.7	132.3	8.1	0.92	7790	20 ± 10	107 ± 8 [f] (110)	12, 57
HD 35850	05:27:04.75	−11:54:03.0	26.9	6.3	0.27	6040	12 ± 15	68 ± 4	3
HD 37484	05:37:39.63	−28:37:34.7	59.0	7.3	0.54	6680	30 ± 10	53 ± 3	14
SAO 150676	05:40:20.74	−19:40:10.8	73.0	9.0	0.06	5620	63 ± 10	3 ± 1	15
HD 38206	05:43:21.67	−18:33:26.9	71.3	5.7	1.49	10380	30 ± 15	194 ± 22 [f] (170)	12, 56
HD 38678	05:46:57.34	−14:49:19.0	21.9	3.5	1.22	8790	12 ± 2	24 ± 2 (3)	4, 62
HD 43989	06:19:08.05	−03:26:20.0	51.9	8.0	0.19	5940	30 ± 15	8 ± 2	5
HD 46190	06:27:48.62	−62:8:59.7	84.3	6.6	1.13	8400	5 ± 5	13 ± 7	4
HD 48370	06:43:01.02	−02:53:19.3	36.0	7.9	−0.11	5580	30 ± 10	168 ± 7 (89)	16, 28
HD 53143	06:59:59.85	−61:20:12.6	18.4	6.8	−0.23	5410	300 ± 100	60 ± 4 (55-110)	12, 59
HD 59967	07:30:42.51	−37:20:21.7	21.8	6.6	−0.05	5790	353 ± 68	68 ± 8	17
HD 61005	07:35:47.50	−32:12:14.7	36.4	8.2	−0.20	5400	30 ± 15	67 ± 2 (60)	3, 60
HD 69830	08:18:23.78	−12:37:47.2	12.6	6.0	−0.22	5420	4000 ± 1000	2.6 ± 0.1 (2.4)	18, 61
HD 70573	08:22:49.90	01:51:33.6	59.2	8.7	0.00	5750	70 ± 15	... [g]	3
HD 71043	08:22:55.16	−52:07:25.4	73.1	5.9	1.38	9260	30 ± 15	16 ± 2	4
HD 71155	08:25:39.63	−03:54:23.1	37.4	3.9	1.60	9890	170 ± 70	65 ± 14 (88)	19, 62
HD 72660	08:34:01.62	−02:09:05.6	98.8	5.8	1.67	9500	200 ± 100	... [g]	4
HD 76151	08:54:17.95	−05:26:04.1	16.8	6.0	−0.01	5830	1047 ± 301	28 ± 2	20
HD 92536	10:39:22.83	−64:06:42.4	157.3	6.3	1.95	10800	46 ± 6.5	13 ± 3	21
HD 98058	11:16:39.70	−03:39:05.8	57.3	4.5	1.62	7500	700 ± 200	... [g]	22
HD 102458	11:47:24.58	−49:53:02.9	113.0	9.1	0.43	5670	8 ± 5	18 ± 2	3
HD 103703	11:56:26.56	−58:49:16.8	107.1	8.5	0.57	6410	17 ± 10	13 ± 1	4
MML 8	12:12:35.77	−55:20:27.3	112.9	10.5	−0.04	4710	5 ± 3	16 ± 1	3
HD 107146	12:19:06.61	16:32:55.2	27.4	7.0	0.00	5830	160 ± 0	134 ± 4 [f] (97-130)	15, 63
HD 107649	12:22:24.86	−51:01:34.4	108.0	8.8	0.45	6290	17 ± 10	24 ± 2	4
HD 109085	12:32:04.23	−16:11:45.6	18.0	4.3	0.69	6940	950 ± 350	230 ± 15 [f] (145)	23, 51
HD 110411	12:41:53.06	10:14:08.3	38.1	4.9	1.18	8780	200 ± 100	112 ± 10 (111)	12, 64
HD 111520	12:50:19.72	−49:51:49.0	108.6	8.9	0.43	6140	17 ± 10	71 ± 4 (70)	4, 65
HD 111631	12:50:43.58	−00:46:01.8	10.6	8.5	−1.00	3993	680 ± 300	400 ± 40	19
MML 28	13:01:50.70	−53:04:58.1	117.5	11.1	−0.29	4620	8 ± 3	25 ± 2	3
HD 113556	13:05:32.61	−58:32:08.0	101.2	8.1	0.65	6840	17 ± 10	167 ± 16 [f]	4
HD 114082	13:09:16.19	−60:18:30.1	95.4	8.2	0.58	6580	17 ± 10	48 ± 2 (27.7)	4, 66
HD 115820	13:20:26.81	−49:13:25.2	115.5	8.0	0.85	7470	17 ± 10	39 ± 3	4
HD 115892	13:20:35.82	−36:42:44.2	17.8	2.7	1.36	9160	45 ± 20	26 ± 3	4
MML 36	13:37:57.30	−41:34:42.0	99.5	10.1	0.00	4960	30 ± 10	16 ± 1	3
HD 125541	14:21:11.54	−41:42:24.9	159.8	8.9	0.76	7160	16 ± 0	29 ± 2	4
HD 126062	14:24:37.00	−47:10:39.9	132.0	7.4	1.23	9100	16 ± 0	325 ± 27 [f]	4
HD 131511	14:53:23.77	19:09:10.1	11.4	6.0	−0.29	5090	1000 ± 300	120 ± 13 (74)	24, 67
HD 131835	14:56:54.47	−35:41:43.7	133.3	7.9	0.98	7690	16 ± 2	150 ± 12 [f] (75-210)	25, 68
HD 134888	15:13:27.96	−33:08:50.2	112.0	8.7	0.50	6320	16 ± 8	88 ± 4	4

Table D.1. continued.

Name [a]	RA(J2000) [hh:mm:ss]	Dec(J2000) [dd:mm:ss]	Dist. [b] [pc]	V [mag]	$\log(L_*)$ [c] [$L_\odot$]	$T_{\rm eff}$ [c] [K]	Age [d] [Myr]	$R_{\rm disc}$ [c] [au]	Ref. [e]
GJ 581	15:19:27.54	−07:43:19.3	6.30	10.6	−1.92	3238	1000 ± 500	16 ± 2 (25)	26, 69
HD 156623	17:20:50.62	−45:25:14.5	111.4	7.3	1.11	8610	16 ± 2	75 ± 10 [f] (150)	25, 70
HD 172555	18:45:26.86	−64:52:15.2	28.3	4.8	0.89	7620	23 ± 3	21 ± 2	27
HD 177171	19:06:19.96	−52:20:27.3	58.8	5.2	1.40	6010	30 ± 15	... [f]	4
HD 181296	19:22:51.18	−54:25:25.4	47.3	5.0	1.43	9440	23 ± 3	43 ± 4 (24)	27, 61
HD 181327	19:22:58.92	−54:32:16.3	48.1	7.0	0.46	6450	23 ± 3	82 ± 4 (86.3)	27, 71
HD 191089	20:09:05.22	−26:13:26.5	50.1	7.2	0.44	6460	12 ± 2	59 ± 3 (73)	1, 72
HD 193571	20:22:27.50	−42:02:58.4	68.3	5.6	1.44	9740	170 ± 70	119 ± 15	4
HD 196544	20:37:49.12	11:22:39.6	59.4	5.4	1.36	9130	225 ± 40	66 ± 7	9
HD 197481	20:45:09.34	−31:20:24.1	9.72	8.6	−1.02	3600	15 ± 10	44 ± 2 (70)	3, 51
HD 202628	21:18:27.27	−43:20:04.8	23.8	6.8	−0.01	5780	604 ± 445	160 ± 24 (162-254)	28, 73
HD 206860	21:44:31.19	14:46:20.0	18.1	6.0	0.06	5970	85 ± 65	40 ± 2	29
NLTT 54872	22:48:04.47	−24:22:07.5	7.67	12.6	−2.33	3011	440 ± 40	48 ± 8	30
HD 218340	23:08:12.24	−63:37:40.8	56.0	8.4	0.06	5810	45 ± 10	200 ± 16	4
HD 218511	23:09:41.44	−67:43:56.3	14.8	8.3	−0.80	4370	1260 ± 600	34 ± 2	19
HD 220825	23:26:55.96	01:15:20.2	48.9	4.9	1.34	9400	70 ± 25	28 ± 4	5
HD 223340	23:48:50.50	−28:07:15.7	44.2	9.3	−0.35	5250	220 ± 100	42 ± 2	19

Table D.2. Observations and achieved contrast values of DEB targets.

Name	Obs date	Seeing	Field rot.	AGPM	L' [a]	5 σ contrast [b] at r					
						0.″25	0.″5	0.″75	1.″0	2.″0	3.″0
		[arcsec]	[deg]		[mag]	[mag]	[mag]	[mag]	[mag]	[mag]	[mag]
HD 203	2017-10-29	0.6	156	y	5.09 ± 0.22	6.0	8.2	8.9	9.5	9.8	9.7
HD 377	2016-07-31	0.4	74	y	6.07 ± 0.12	8.0	9.4	9.7	9.9	10.5	10.6
HD 2262	2017-10-31	0.8	72	y	3.35 ± 0.63	7.6	10.1	11.0	11.8	13.1	13.1
HD 3003	2017-11-01	0.6	94	y	4.88 ± 0.24	8.8	10.0	11.0	11.5	11.9	12.0
HD 3670	2016-08-01	0.6	104	n	7.02 ± 0.06	7.3	9.2	9.6	10.0	10.3	10.2
HIP 6276	2016-12-11	1.4	40	n	6.53 ± 0.08	5.8	8.0	9.1	9.6	10.0	10.0
HD 9672	2016-11-06	0.5	129	y	5.41 ± 0.18	7.8	9.0	9.5	10	10.6	10.9
HD 10008	2016-11-12	0.5	106	y	5.73 ± 0.14	7.2	8.9	9.5	9.8	10.7	10.7
HD 10472	2016-11-07	0.7	71	y	6.61 ± 0.08	7.1	8.3	8.5	9.2	9.7	9.9
HD 12039	2017-11-03	0.7	147	y	6.40 ± 0.08	6.5	8.2	8.6	8.9	9.5	9.6
HD 13246	2017-08-29	0.6	99	y	6.16 ± 0.10	6.7	8.5	9.2	9.4	10.0	10.1
HD 15115	2016-11-08	0.4	91	y	5.75 ± 0.07	8.0	9.1	9.9	10.4	10.9	10.9
HD 16743	2016-11-11	0.7	92	y	5.90 ± 0.14	8.5	9.5	10.1	10.3	10.7	10.9
HD 17925	2015-12-15	1.0	94	y	3.89 ± 0.42	7.6	9.9	10.8	11.5	12.5	12.5
HD 19668	2015-12-18	0.9	79	n	6.66 ± 0.07	7.1	9.6	10.0	10.3	10.3	10.4
HD 21997	2017-11-02	0.6	182	y	6.08 ± 0.11	7.0	8.2	9.0	9.4	10.0	10.2
HD 22049	2017-10-29	0.5	104	y	1.60 ± 0.05	8.4	10.5	11.6	12.6	14.2	14.4
HD 25457	2015-12-17	0.8	79	y	4.06 ± 0.30	8.4	10.1	10.7	11.4	12.5	12.5
HD 27290	2016-12-12	0.6	100	y	3.37 ± 0.55	8.0	9.8	10.9	11.8	13.0	13.0
HD 30422	2016-11-11	0.9	169	y	5.72 ± 0.12	7.9	9.0	9.8	10.2	10.8	10.8
HD 30495	2016-12-11	1.9	48	y	3.89 ± 0.20	6.3	8.6	9.8	10.3	11.4	11.3
HD 32297	2017-11-03	0.5	85	n	7.61 ± 0.04	6.0	7.9	8.9	9.4	9.7	9.7
HD 35850	2015-12-15	0.8	96	y	4.87 ± 0.19	7.1	9.1	10.2	11.0	11.7	11.6
HD 37484	2016-11-12	0.7	183	y	6.23 ± 0.09	7.0	8.1	8.6	9.1	9.8	10.1
SAO 150676	2015-12-18	0.6	133	n	7.41 ± 0.04	7.6	8.5	9.0	9.3	9.5	9.5
HD 38206	2016-11-08	0.6	138	y	5.78 ± 0.15	8.1	9.2	9.7	10.3	10.6	10.7
HD 38678	2015-12-16	0.8	86	y	3.21 ± 0.55	6.5	9.4	10.4	11.4	12.7	12.9
HD 43989	2015-12-17	0.7	79	y	6.44 ± 0.08	7.1	8.9	9.5	9.8	10.2	10.3
HD 46190	2016-11-06	0.4	81	y	6.33 ± 0.10	8.0	9.1	9.8	10.0	10.3	10.4

Notes. [a] L' magnitudes and uncertainties are derived by interpolating between WISE bands W1 (3.35 μm) and W2 (4.6 μm) to 3.8 μm. [b] Corrected for AGPM throughput where applicable (see Sect. 4).

Table D.2. continued.

Name	Obs date	Seeing	Field rot.	AGPM	L' [(a)]	5 σ contrast [(b)] at r					
						0.″25	0.″5	0.″75	1.″0	2.″0	3.″0
		[arcsec]	[deg]		[mag]	[mag]	[mag]	[mag]	[mag]	[mag]	[mag]
HD 48370	2018-03-02	0.5	65	y	6.25 ± 0.09	7.4	8.8	9.4	9.7	10.2	10.3
HD 53143	2015-12-16	0.6	59	y	4.86 ± 0.25	7.5	9.8	10.7	11.1	11.7	11.8
HD 59967	2015-12-15	0.8	96	y	5.01 ± 0.23	7.9	9.5	10.4	10.8	11.3	11.4
HD 61005	2018-02-25	0.9	142	n	6.42 ± 0.09	7.5	9.1	9.8	10.1	10.6	10.6
HD 69830	2017-03-14	0.5	86	y	3.99 ± 0.38	7.3	9.9	10.7	11.0	11.9	12.1
HD 70573	2015-12-18	0.5	78	n	7.12 ± 0.04	6.5	8.7	9.7	9.8	9.9	10.0
HD 71043	2018-02-26	0.8	76	y	5.82 ± 0.15	6.8	8.6	9.5	10.1	10.6	10.7
HD 71155	2017-03-17	0.6	48	y	3.79 ± 0.41	7.6	10.3	10.5	11.5	12.3	12.3
HD 72660	2016-02-17	1.7	53	y	5.76 ± 0.13	5.7	8.2	9.3	9.9	10.2	10.3
HD 76151	2018-02-24	0.4	53	y	4.38 ± 0.36	7.7	10.2	10.7	11.2	12.3	12.4
HD 92536	2016-02-18	1.3	70	y	6.46 ± 0.08	6.3	8.5	8.3	9.0	10.0	10.0
HD 98058	2017-05-01	0.3	92	y	4.04 ± 0.31	6.9	9.4	10.3	11.2	12.3	12.4
HD 102458	2017-05-03	0.6	97	n	7.41 ± 0.04	6.7	8.4	8.9	8.9	9.4	9.4
HD 103703	2017-05-15	0.9	77	n	7.31 ± 0.04	7.2	7.6	6.7	9.0	9.9	9.9
MML 8	2018-02-23	0.6	110	n	8.07 ± 0.03	7.3	8.8	9.2	9.4	9.6	9.6
HD 107146	2018-02-26	0.6	75	y	5.49 ± 0.02	6.9	9.2	10.1	10.4	11.2	11.2
HD 107649	2018-02-25	0.4	112	n	7.60 ± 0.06	7.9	9.1	9.6	9.8	10.1	10.1
HD 109085	2018-02-24	0.7	133	y	3.03 ± 0.45	6.3	8.7	9.9	10.9	12.5	12.8
HD 110411	2016-02-18	1.7	66	y	4.52 ± 0.32	7.7	9.8	10.2	11.0	11.7	11.7
HD 111520	2017-05-17	1.3	58	n	7.52 ± 0.03	6.8	8.5	9.0	9.1	9.3	9.2
HD 111631	2018-03-01	0.5	92	y	4.81 ± 0.26	8.8	10.2	10.8	11.3	12.1	12.3
MML 28	2016-05-31	0.7	51	n	8.70 ± 0.03	4.1	6.2	6.6	6.6	7.0	7.1
HD 113556	2016-06-02	0.7	77	n	7.20 ± 0.04	6.3	8.3	9.0	9.4	9.5	9.6
HD 114082	2018-03-02	1.1	89	n	7.13 ± 0.04	7.3	9.2	9.9	9.9	10.2	10.2
HD 115820	2017-05-02	1.4	74	n	7.29 ± 0.04	6.0	8.2	8.6	8.7	9.1	9.1
HD 115892	2016-02-17	2.0	44	y	2.72 ± 0.20	6.4	8.0	10.3	11.1	12.9	13.0
MML 36	2017-06-17	0.9	102	n	7.80 ± 0.04	6.9	8.6	8.9	9.3	9.4	9.5
HD 125541	2017-03-17	0.6	97	n	8.08 ± 0.03	7.5	8.3	8.5	8.7	8.9	9.0
HD 126062	2017-03-14	0.6	93	n	7.32 ± 0.40	6.8	8.8	8.9	9.1	9.5	9.4
HD 131511	2017-07-01	0.8	58	y	3.77 ± 0.47	6.9	9.6	10.6	11.3	12.4	12.4
HD 131835	2016-05-03	0.4	111	n	7.52 ± 0.04	7.4	9.0	9.3	9.4	9.7	9.8
HD 134888	2017-05-03	0.6	149	n	7.62 ± 0.04	7.1	8.9	9.1	9.1	9.4	9.5
GJ 581	2017-07-13	0.8	107	y	5.62 ± 0.10	7.7	9.7	10.4	10.6	11.1	11.2
HD 156623	2017-05-02	2.0	84	n	6.95 ± 0.06	6.5	9.1	9.5	9.7	9.9	9.9
HD 172555	2017-05-16	1.4	87	y	4.23 ± 0.30	7.7	10.2	11.1	11.5	12.3	12.4
HD 177171	2016-05-31	1.3	63	y	3.67 ± 0.44	7.2	9.2	10.2	11.0	12.1	12.0
HD 181296	2017-05-01	1.2	78	y	4.97 ± 0.16	7.4	9.4	10.2	10.7	11.2	11.2
HD 181327	2016-07-31	0.9	84	y	5.86 ± 0.12	7.7	9.3	9.7	9.9	10.7	10.6
HD 191089	2016-08-01	0.6	184	y	5.99 ± 0.11	7.7	8.8	9.3	9.8	10.3	10.4
HD 193571	2016-05-30	0.7	78	y	5.55 ± 0.15	5.3	7.9	8.9	9.1	9.7	9.8
HD 196544	2017-08-29	0.5	60	y	5.25 ± 0.16	7.4	9.1	9.4	10.0	10.6	10.8
HD 197481	2017-07-13	0.8	131	y	4.28 ± 0.32	6.2	9.6	10.6	11.1	11.9	12.1
HD 202628	2017-08-31	0.6	102	y	5.20 ± 0.15	8.2	9.5	10.1	10.3	10.9	11.1
HD 206860	2017-06-17	0.7	47	y	4.43 ± 0.26	6.8	9.4	10.1	10.6	11.7	11.8
NLTT 54872	2017-07-13	1.0	171	n	6.87 ± 0.05	7.1	8.3	8.6	8.8	9.3	9.0
HD 218340	2016-07-30	0.8	91	n	6.94 ± 0.07	6.9	8.5	9.4	9.9	9.9	10.1
HD 218511	2017-07-01	1.3	44	y	5.23 ± 0.20	7.3	8.9	9.7	10.2	10.8	10.9
HD 220825	2017-11-03	0.8	53	y	4.83 ± 0.29	6.9	9.7	10.5	10.9	11.6	11.6
HD 223340	2017-10-30	0.7	132	y	7.04 ± 0.04	5.9	7.7	8.3	8.8	9.1	9.2

6.3 Summary and conclusions

The NACO-ISPY survey serves as a complementary survey to other large imaging surveys like SPHERE-SHINE (Chauvin et al. 2017) and the Gemini Planet Imager Exoplanet Survey (GPIES, Nielsen et al. 2019). NACO observes at longer wavelengths and therefore covers a different parameter space by exploiting the L'-band sensitivity to embedded (i.e. reddened) planets, as well as relatively cooler (i.e. more evolved) planets. NACO-ISPY also provides a unique sample of targets that host protoplanetary and debris disks, allowing us to investigate young forming planets and stirring mechanisms of debris disks.

In addition, combining observations from NACO in the L' and M' bands, along with SPHERE observations in the $Y-K$ bands allows us to place tighter constraints on exoplanetary detections by obtaining spectra with a greater wavelength coverage, as shown in Cheetham et al. (2019).

As the analysis of the survey is still ongoing, a full statistical analysis of the survey sample is yet to be completed. Even from the first summary of survey results (Launhardt et al. 2020) we already have many disk detections and several interesting companion candidates.

From the ongoing image inspection, 48 new companion candidates have been detected (of which 4 of those have been published from the survey so far), as well as 11 previously known companions have been detected, out of a total of 209 targets observed, corresponding to approximately 28% of the sample having a companion or companion candidate. In addition, 25 disks have been detected, corresponding to approximately 12% of the sample. Most of these targets will require a second epoch observation to confirm that the detected companion candidates are co-moving with the target and are therefore gravitationally bound to the primary star.

When the final data analysis is complete we will be able to make some conclusions of the occurrence rate of planets at wide-separations around young stars with protoplanetary or debris disks.

Chapter 7

Conclusions and Perspectives

"Aperooooooof!"

— Jan Philip Sindel

7.1 Summary

During my PhD I have used the radial velocity and direct imaging techniques to detect and characterise substellar companions. The detection of such companions contributes to our understanding of the occurrence rates of giant planets and brown dwarfs at wide separations (>5 AU), which can help inform the formation scenarios of such objects.

In order to detect these companions, I have coordinated the search for long-period planets with the CORALIE spectrograph and highlighted targets of significant interest that are promising candidates for follow-up high-contrast imaging, some of which are discussed in Rickman et al. (2019). Subsequently, I led several observing campaigns with VLT/SPHERE, and directly detected four new companions. This includes the detection of a new benchmark brown dwarf, for which I carried out a full spectral and atmospheric characterisation discussed in Rickman et al. (2020). Additionally, the non-detections from the VLT/SPHERE observing campaigns constrain the parameter space of the radial-velocity-detected companions by ruling out bright stellar companions.

These detections join just a short list of brown dwarf companions with a known dynamical mass, subsequently contributing to a significant proportion of such objects and populating the unconstrained mass-luminosity-age relation of brown dwarfs. Simultaneously this work also probes a mass-separation parameter space that is not well understood. The crucial element in combining the radial velocity and direct imaging methods is that a true dynamical mass can be obtained that is model independent. Consequently, such detections serve as critical tools for testing models of formation, evolution and their atmospheres.

It should be noted that a similar approach has been taken by the TRENDS survey (Crepp et al. 2012; Gonzales et al. 2020), who have carried out a high-contrast imaging survey using Keck/NIRC2 based on

radial velocity measurements from Keck/HIRES which complements the work presented here, as their focus is on the Northern Hemisphere, whereas this work focuses on the Southern Hemisphere.

Furthermore, I have contributed to the work of the NACO-ISPY survey that targets young stars hosting protoplanetary or debris disks, and serves as a complementary survey to other large imaging surveys like SPHERE-SHINE (Chauvin et al. 2017) and the Gemini Planet Imager Exoplanet Survey (GPIES, Nielsen et al. 2019). Such an extensive survey in the L'-band probes embedded planets, and will provide a unique sample of targets that host protoplanetary and debris disks, allowing us to investigate young forming planets and stirring mechanisms of debris disks.

In the short term, these detections provide important benchmarks to test atmospheric models of ultracool substellar companions, that can serve as analogues for giant gaseous planets (Faherty et al. 2016). These objects subsequently challenge our understanding of physics and chemistry within gas giants. In the long term, moreover, these detections build a clearer picture about the occurrence rate of giant planets and brown dwarfs at separations greater than 5 AU. Both of these factors contribute towards the understanding of giant planet and brown dwarf structure, formation, and evolution (e.g. see, Wittenmyer et al. 2020).

7.2 Future prospects

Going forward I plan to carry out an imaging survey using dynamically informed targets based on astrometric data from *Hipparcos* and *Gaia*, combined with long-baseline radial velocity surveys, to image companions with a high detection rate efficiency. Deriving accurate masses and orbital parameters from *Hipparcos* and *Gaia* data has already shown some success by Brandt (2018) and Kervella et al. (2020), and with its overlap in parameter space with imaging surveys, the use of astrometric data will become a critical technique to probe orbital parameters of long-period companions.

This will produce a statistically significant sample of imaged planets with known masses, orbits, spectra and ages to test models of planet formation and atmospheric chemistry. Such a sample will provide us with benchmark systems to follow-up with new instruments like SPHERE+ (Boccaletti et al. 2020), as well as large characterisation missions like JWST, or to obtain high resolution spectra with VLTI/GRAVITY (Gravity Collaboration et al. 2019). Furthermore, any non-detections with current ground-based facilities of stars with evidence of acceleration due to an unseen companion, would serve as an ideal sample for the the upcoming ELTs, where they will probe a currently inaccessible parameter space ($\sim$0.05-0.2") (Carlomagno et al. 2016).

The goal is to provide a catalogue with multiple astrometric and long-baseline radial-velocity surveys assembled together to hunt for the best candidates to directly image. It will pave the way for a new strategy of discovering widely-separated exoplanets. Because direct imaging is a focal point of future missions, the blind observing strategy needs to be overhauled; defining this sample of promising imaging candidates is a crucial step in that process. Furthermore, it will produce a statistical sample of new imaged planets with known masses, orbits, spectra and ages that is complementary to samples from

short-period radial velocity and transit searches. This will provide a global picture of the occurrence rates of exoplanets which is crucial to test models of planet formation and evolution.

More generally, as the instrumentation of high-contrast imagers is developed in the coming years, the possibility to image less massive planets at smaller and smaller separations becomes a reality. This will create the possibility in the future of imaging an Earth-like planet, making it an even more powerful technique.

APPENDIX A

ADDITIONAL PUBLICATIONS

A.1 NACO-ISPY consortium survey papers

Here I present some published results from the NACO-ISPY survey (discussed in Chapter 6) where I have contributed to the observations, image inspection and/or data reduction of these targets:

1. ISPY - NACO Imaging Survey for Planets around Young stars. A young companion candidate embedded in the R CrA cloud, Cugno et al. (2019)
2. ISPY - NACO Imaging Survey for Planets around Young stars. Discovery of an M dwarf in the gap between HD 193571 and its debris ring, Musso Barcucci et al. (2019)
3. Spectral and orbital characterisation of the directly imaged giant planet HIP 65426 b, Cheetham et al. (2019)

A.1.1 ISPY - NACO Imaging Survey for Planets around Young stars. A young companion candidate embedded in the R CrA cloud

In Cugno et al. (2019) we present the detection of a companion to R CrA. The companion has a mass between $0.1 - 1.03\ M_{\odot}$, where the uncertainty is large due to the uncertainty of the age of the system and of the L' magnitude of the primary star. The companion had already been predicted by several other studies including Takami et al. (2003), Forbrich et al. (2006) and Kraus et al. (2009). In addition, an independent discovery of the companion to R CrA by the SPHERE-SHINE survey was published (Mesa et al. 2019a), confirming the detection of the companion. The full description is outlined in Cugno et al. (2019) below.

A&A 624, A29 (2019)
https://doi.org/10.1051/0004-6361/201935142

Astronomy & Astrophysics

ISPY – NaCo Imaging Survey for Planets around Young stars

A young companion candidate embedded in the R CrA cloud⋆,⋆⋆,⋆⋆⋆

G. Cugno[1], S. P. Quanz[1,⋆⋆⋆⋆], R. Launhardt[2], A. Musso Barcucci[2], S. S. Brems[3], A. Cheetham[4], N. Godoy[5,6], G. M. Kennedy[7,8], T. Henning[2], A. Müller[2], J. Olofsson[5,6], F. Pepe[4], A. Quirrenbach[3], S. Reffert[3], E. L. Rickman[4], and D. Ségransan[4]

[1] ETH Zurich, Institute for Particle Physics and Astrophysics, Wolfgang-Pauli-Strasse 27, 8093 Zurich, Switzerland
e-mail: gabriele.cugno@phys.ethz.ch
[2] Institute for Astronomy (MPIA), Königstuhl 17, 69117 Heidelberg, Germany
[3] Landessternwarte, Zentrum für Astronomie der Universität Heidelberg, Königstuhl 12, 69117 Heidelberg, Germany
[4] Observatoire Astronomique de l'Université de Genève, 51 Ch. des Maillettes, 1290 Versoix, Switzerland
[5] Instituto de Física y Astronomía, Facultad de Ciencas, Universidad de Valparaíso, Av. Gran Bretaña 1111, Playa Ancha, Valparaíso, Chile
[6] Núcleo Milenio Formación Planetaria – NPF, Universidad de Valparaíso, Av. Gran Bretaña 1111, Valparaíso, Chile
[7] Department of Physics, University of Warwick, Gibbet Hill Road, Coventry CV4 7AL, UK
[8] Centre for Exoplanets and Habitability, University of Warwick, Gibbet Hill Road, Coventry CV4 7AL, UK

Received 28 January 2019 / Accepted 10 February 2019

ABSTRACT

Context. Within the NaCo-ISPY exoplanet imaging program, we aim at detecting and characterizing the population of low-mass companions at wide separations ($\gtrsim$10 AU), focusing in particular on young stars either hosting a known protoplanetary disk or a debris disk.
Aims. R CrA is one of the youngest (1–3 Myr) and most promising objects in our sample because of two previous studies that suggested the presence of a close companion. Our aim is to directly image and characterize the companion for the first time.
Methods. We observed R CrA twice with the NaCo instrument at the Very Large Telescope (VLT) in the L' filter with a one year time baseline in between. The high-contrast imaging data were reduced and analyzed and the companion candidate was detected in both datasets. We used artificial negative signals to determine the position and brightness of the companion and the related uncertainties.
Results. The companion is detected at a separation of 196.8 ± 4.5/196.6 ± 5.9 mas (18.7 ± 1.3/18.7 ± 1.4 AU) and position angle of 134.7 ± 0.5°/133.7 ± 0.7° in the first/second epoch observation. We measure a contrast of 7.29 ± 0.18/6.70 ± 0.15 mag with respect to the primary. A study of the stellar proper motion rejects the hypothesis that the signal is a background object. The companion candidate orbits in the clockwise direction and, if on a face-on circular orbit, its period is ∼43−47 yr. This value disagrees with the estimated orbital motion and therefore a face-on circular orbit may be excluded. Depending on the assumed age, extinction, and brightness of the primary, the stellar companion has a mass between 0.10 ± 0.02 $M_\odot$ and $1.03^{+0.20}_{-0.18}$ $M_\odot$ range, if no contribution from circumsecondary material is taken into account.
Conclusions. As already hypothesized by previous studies, we directly detected a low-mass stellar companion orbiting the young Herbig Ae/Be star R CrA. Depending on the age assumptions, the companion is among the youngest forming companions imaged to date, and its presence needs to be taken into account when analyzing the complex circumstellar environment of R CrA.

Key words. techniques: high angular resolution – planets and satellites: formation – planets and satellites: detection

1. Introduction

In recent years, high-contrast high spatial resolution direct imaging has revealed a few planetary mass objects (β Pic b, HR 8799 bcde, HD 95086 b, 51 Eri b, HIP 65426 b, PDS 70 b; Lagrange et al. 2009; Marois et al. 2008, 2010; Rameau et al. 2013; Macintosh et al. 2015; Chauvin et al. 2017b; Keppler et al. 2018). Several surveys (such as NICI, SPHERE-SHINE, IDPS, SEEDS, LEECH, and GPI; Liu et al. 2010; Chauvin et al. 2017a; Vigan et al. 2012; Tamura 2014; Skemer et al. 2014; Macintosh et al. 2014) exploit the capabilities of existing instrumentation to put stronger constraints on the occurrence rate of giant planets (5−13 M_J) at large orbital distance (30−300 AU), which was estimated to be $0.6^{+0.7}_{-0.5}$% by Bowler (2016). Statistically characterizing the giant planet population in wide orbits (>10 AU) is also one of the primary goals of the NaCo Imaging Survey for Planets around Young stars (NaCo-ISPY; Launhardt et al., in prep.). The survey targets nearby young stars that are surrounded by either a protoplanetary or a debris disk. Unlike most other ongoing imaging

⋆ Based on observations collected at the Paranal Observatory, ESO (Chile). Program ID: 199.C-0065(A) and 1101.C-0092(A).
⋆⋆ After this paper was first submitted, another study of R CrA corroborating the reality of its companion, and reaching conclusions largely in agreement with ours, was posted on arXiv (Mesa et al. 2019).
⋆⋆⋆ The data associated with Fig. 1 are only available at the CDS via anonymous ftp to cdsarc.u-strasbg.fr (130.79.128.5) or via http://cdsarc.u-strasbg.fr/viz-bin/qcat?J/A+A/624/A29
⋆⋆⋆⋆ National Center of Competence in Research "PlanetS" (http://nccr-planets.ch)

Table 1. Stellar parameters of R CrA.

Parameter	Values	Reference
RA	$19^h01^m53.68^s$	(1)
Dec	$-36°57'08.14''$	(1)
Sp. type	F5, A5, B8	(2), (3), (4)
Dist. (pc)	94.9 ± 6.3	(1)
$\mu_\alpha \times \cos(\delta)$ (mas yr^{-1})	1.58 ± 1.20	(1)
μ_δ (mas yr^{-1})	−30.83 ± 1.19	(1)
K (mag)	2.858 ± 0.262	(5)
L (mag)	1.78 ± 0.05	(6)
WISE $W3$ (mag)	−1.239 ± 0.390	(7)
Age (Myr)	0.3–3, 1	(8), (9), (10)
A_V (mag)	6.0–8.0, 1.9	(9), (11)
Mass ($M_\odot$)	3.0, 3.5	(10), (11)

References. (1) Gaia Collaboration (2018), (2) Hillenbrand et al. (1992), (3) Chen et al. (1997), (4) Hamaguchi et al. (2005), (5) Cutri et al. (2003), (6) Glass & Penston (1975), (7) Cutri et al. (2013), (8) Meyer & Wilking (2009), (9) Forbrich et al. (2006), (10) Bibo et al. (1992), (11) Lorenzetti et al. (1999).

surveys that focus on shorter wavelengths, ISPY utilizes the L' filter ($\lambda \sim 3.8\,\mu$m) of the NaCo instrument at the Very Large Telescope (VLT) to obtain high-contrast imaging data. At this wavelength, there are four main advantages compared to the near-infrared regime: (1) the contrast requirements are more favorable for a detection; (2) dust extinction from circumstellar material has minimal effects on the observed flux; (3) scattering from circumstellar disk material, which increases the noise and probability of false positives, is less important; and (4) contamination from background objects is less severe because most background stars are not red enough to be easily detected at L' band. Altogether, possibly embedded objects with lower intrinsic luminosity might be detected. The major limiting factor of collecting data in the 3–5 μm range is related to the lower spatial resolution that can be achieved.

Given its age and proximity (see Table 1), R CrA is an ideal target for the ISPY search for companions at small physical separations. R CrA is located in the Coronae Australis molecular cloud, a star-forming region containing several low- to intermediate-mass objects (e.g., Fernández & Comerón 2001; Haas et al. 2008). Its "Coronet" (Taylor & Storey 1984; Wilking et al. 1997) is a deeply embedded cluster of young stars that was extensively studied in recent years across all wavelengths, from radio (e.g., Brown 1987; Feigelson et al. 1998; Forbrich et al. 2006) to X-rays (e.g., Koyama et al. 1996; Neuhäuser et al. 2000), and whose luminosity is dominated by R CrA ($L_{\rm bol} = 70\,L_\odot$, Lorenzetti et al. 1999, but updated with distance from Table 1). Because of the complexity of its circumstellar environment and its known variability, the properties of R CrA are not well constrained (see Table 1).

As an example, the extinction in the R CrA cloud is highly uncertain, and X-ray spectra from Forbrich et al. (2006) suggested $A_V = 6.0$–8.0 mag, but other studies derived lower values (e.g., Lorenzetti et al. 1999, $A_V = 1.9$ mag). Since it was not possible to further constrain this parameter from the available data, we adopted a conservative approach considering A_V in the 1.9–8.0 mag range. Concerning possible companions, Takami et al. (2003) observed R CrA with the Royal Greenwich Observatory (RGO) spectrograph on the Anglo-Australian Telescope (AAT) and the data showed a displacement around the Hα line emission that was best explained with the presence of a companion and an outflow from the primary. Combining their results with previous observations presented in Bailey (1998) and Takami et al. (2003) gave a rough estimate for the position angle (PA) of a possible companion in 1996 and 1999 (~220° and ~200°). Later, Forbrich et al. (2006) hypothesized that a companion was orbiting R CrA based on *Chandra* and *XMM-Newton* data. These authors detected variable X-ray emission but because no X-ray flux is expected from intermediate-mass young stellar objects, they suggested that the emission comes from a low-mass companion. Kraus et al. (2009) analyzed VLTI/AMBER H- and K-band spectro-interferometric observations of R CrA and found no clear evidence for a companion at separations between 0.″02 and 0.″2, despite strong asymmetries in the brightness distribution of the source that could be caused by a second object. They achieved contrast limits of 4.0 mag, so a fainter (i.e., lower mass or more deeply embedded) object would have been missed in their observations. Furthermore, they measured the inclination of the disk surrounding R CrA to be ~35°, (confirming previous results from, e.g., Clark et al. 2000) and its PA to be ~180°–190°.

Table 2. Summary of observations.

Parameter	Epoch 1	Epoch 2
UT date (yyyy/mm/dd)	2017/05/19	2018/06/06
Prog. ID	199.C-0065(A)	1101.C-0092(A)
DIT[a] (s)	0.35	0.1082
# of DITs	12 100	18 401
Par. angle start/end (°)	42.46/78.44	−40.25/80.91
Airmass min/max	1.04/1.19	1.04/1.22
Mean seeing[b] (as)	0.65	0.63
True north[c] (°)	0.39 ± 0.21	0.43 ± 0.18
Plate Scale (mas pix^{-1})	27.21 ± 0.10	27.21 ± 0.08
# unsaturated PSF	2000	2400
DIT unsaturated PSF (s)	0.005	0.004256

Notes. [(a)]DIT = Detector integration time, i.e., exposure time per image frame. [(b)]Mean DIMM seeing measured during the observations. [(c)]Additional rotation in clockwise direction that has to be applied in order for north to point to the top of the images.

In this paper, we present the results of new high-contrast imaging L'-band observations of R CrA that find direct evidence for a stellar companion. In Sect. 2 we summarize the observations and explain the data reduction. In Sect. 3 we present our results and discuss them in Sect. 4. We conclude in Sect. 5.

2. Observations and data reduction

2.1. VLT/NaCo observations

We observed R CrA on 2017 May 19 and 2018 June 06, taking advantage of the AGPM vortex vector coronagraph (Mawet et al. 2013), which enables high-contrast imaging very close to the diffraction limit (~0.″095). For the observations, the L27 camera (pixel scale ~27.2 mas pix^{-1}) was used with the L' filter ($\lambda_c = 3.8\,\mu$m, $\Delta\lambda = 0.62\,\mu$m). The camera derotator was switched off to enable angular differential imaging (ADI; Marois et al. 2006) and the "cube mode" allowed us to save all individual exposures. Both observing runs consisted of series of 13 coronagraphic cubes of images of R CrA (7.6 and 2.3 min for the two epochs) interposed with one cube of sky images to sample the background and subtract it later. In total, for the first and second observations we obtained 70.6/33.2 min of on-source integration time and 36.0/121.2° of field rotation (see Table 2). In addition, unsaturated photometric images were taken at the beginning and

at the end of the observations. These were used later to calibrate, simulate, and insert artificial point spread functions (PSFs) in the data. Table 2 summarizes the observations together with the atmospheric conditions.

2.2. Data reduction

Both datasets were reduced with `PynPoint` (Amara & Quanz 2012; Stolker et al. 2019), an end-to-end modular python pipeline for analyzing high-contrast imaging data. In particular, the PSF subtraction is based on principal component analysis (PCA; Amara & Quanz 2012; Soummer et al. 2012).

After assigning to each frame its parallactic angle by linearly interpolating between the start and end value of each cube, the first ten frames and the last frame of each cube were removed. The first frames suffer from a systematically higher background that drops exponentially (e.g., Stolker et al. 2019). The last frame represents the mean of the cube. The remaining frames were dark-subtracted, and the stripes present in the lower left quadrant due to detector issues were corrected by substituting each pixel value with the mean of the two neighboring values. For the second epoch, where two neighboring bad working columns were present on the detector, the average of the closest functioning right and left pixels were used[1]. Other bad pixels were corrected by 4-sigma clipping (Stolker et al. 2019). Then, using spline interpolation all images were aligned applying cross-correlation and the entire stack was shifted to the exact image center after fitting a 2D Gaussian to the mean of the frames. Next, each background cube was averaged to a single image. From each science frame, the average between the previous and subsequent background image was subtracted. Finally, we binned, i.e., mean-combined, sets of two, five, and ten frames. In this way, three different datasets were created and a frame selection was applied to each of the three stacks rejecting images, where the stellar flux measured in a circular aperture ($r = 1\farcs0$) deviated by more than three standard deviations from the median values of the stack.

For the PSF subtraction, `PynPoint` applies full-frame PCA to reconstruct and then remove the stellar PSF before derotating and combining all the images (Amara & Quanz 2012; Stolker et al. 2019). In order to search for faint high-contrast signals at small separations, several mask radii are applied to cover the central part of the stellar PSF and the number of principal components (PC) used to model and subtract the PSF was varied.

The unsaturated PSF frames underwent a simpler calibration. After dark subtraction and bad pixel cleaning, the background was subtracted using the dithering technique, in which the star is imaged in three different quadrants of the detector[2]. Whenever the star was not present in a quadrant, these cubes served to sample the background. Because the dither position changed every 400 frames, the images were subtracted from each other with an offset of 400 frames, meaning that the nth image of the set was subtracted from the (n+400)th frame and cut ($0\farcs5$ in size) around the positive PSF signal. Then, all frames were aligned, centered, and averaged to obtain a unique PSF template for each epoch.

We looked for differences in the unsaturated images within individual epochs and between them. Since the final PSF template is unique for each dataset, we have to consider variations of the unsaturated images due to changes in weather conditions and possibly in intrinsic stellar flux. This component of the photometric uncertainty was estimated as the standard deviation of the stellar flux measured in each exposure in a circular aperture of $0\farcs19$ ($2\lambda/D$) and it amounts to 0.03 mag for epoch 1 and 0.09 mag for epoch 2. The larger variation in epoch 2 results from a systematic decrease in stellar flux by ∼13% between the beginning and end of the observing sequence. Furthermore, during the first epoch, the central star R CrA appeared on average 0.22 mag brighter than during the second observation[3]. This difference is analyzed in the context of the companion brightness in Sect. 4.

3. Analysis and results

3.1. The detection of a young companion candidate

A strong companion signal is consistently detected in both datasets (see Fig. 1) and, given the baseline of one year, the displacement is in agreement with orbital motion as we discuss in Sect. 4. The companion candidate is detected for a wide range in the number of subtracted PCs (1–20 for Epoch 1 and 4–30 for Epoch 2) applying inner masks of $0\farcs05$ and $0\farcs1$ in radius. To quantify the confidence of the detection, we calculated the false positive fraction (FPF) measuring the signal flux in an aperture of diameter λ/D ($\approx 0\farcs095$) and sampling the residual noise in non-overlapping apertures of the same size at the same separation, but at different azimuthal angles (Mawet et al. 2014). The central position of the signal aperture was determined by fitting a 2D Gaussian to the signal. Using Eqs. (9) and (10) of Mawet et al. (2014) we determined the signal-to-noise ratio (S/N) and the FPF. This approach considers corrections for small sample statistics and utilizes the Student t-distribution to estimate FPFs. We found a best S/N of 9.2 for the first epoch (no frame binning, PC=5, $r_{\rm mask} = 0\farcs05$ as) and 9.6 for the second (bin = 10, PC = 9, $r_{\rm mask} = 0\farcs1$), corresponding to FPFs of 1.7×10^{-6} and 1.17×10^{-6}, respectively.

3.2. Astrometry and photometry

To determine the astrometry and photometry of the companion, two different methods were used, namely the minimization of the determinants of the Hessian matrix (HM) at the position of the signal (Cugno et al. 2019) and a Markov chain Monte Carlo (MCMC) minimization algorithm (Stolker et al. 2019). Both methods are based on the artificial planet technique, in which signals from unsaturated PSFs are subtracted from the data with different combinations of position and contrast to minimize the residuals. Specifically, the HM technique tries to minimize the curvature of the image in the signal region and the MCMC minimizes the flux residuals as performed in Wertz et al. (2017). In both cases a circular region with $r = 0\farcs1425$ ($1.5\lambda/D$) around the companion was considered.

We used the HM characterization algorithm on all combinations of PCs and the mask radius that yielded an FPF $< 3.2\times10^{-5}$ (corresponding to a 4σ confidence) in the bin = 5 and bin = 10 datasets (22 setups for epoch 1 and 56 for epoch 2). To consider systematic effects related to the PSF subtraction parameters, we averaged the best fit solutions to obtain astrometry and photometry of the companion. The uncertainties are represented by the standard deviation of the set of best solutions.

[1] We note, however, that the stripe correction has no influence on the results presented later since the studied region was located in a different quadrant.

[2] We avoided using the quadrant with bad columns.

[3] This value is based on the measured count rate, even though the conditions were not photometric either night.

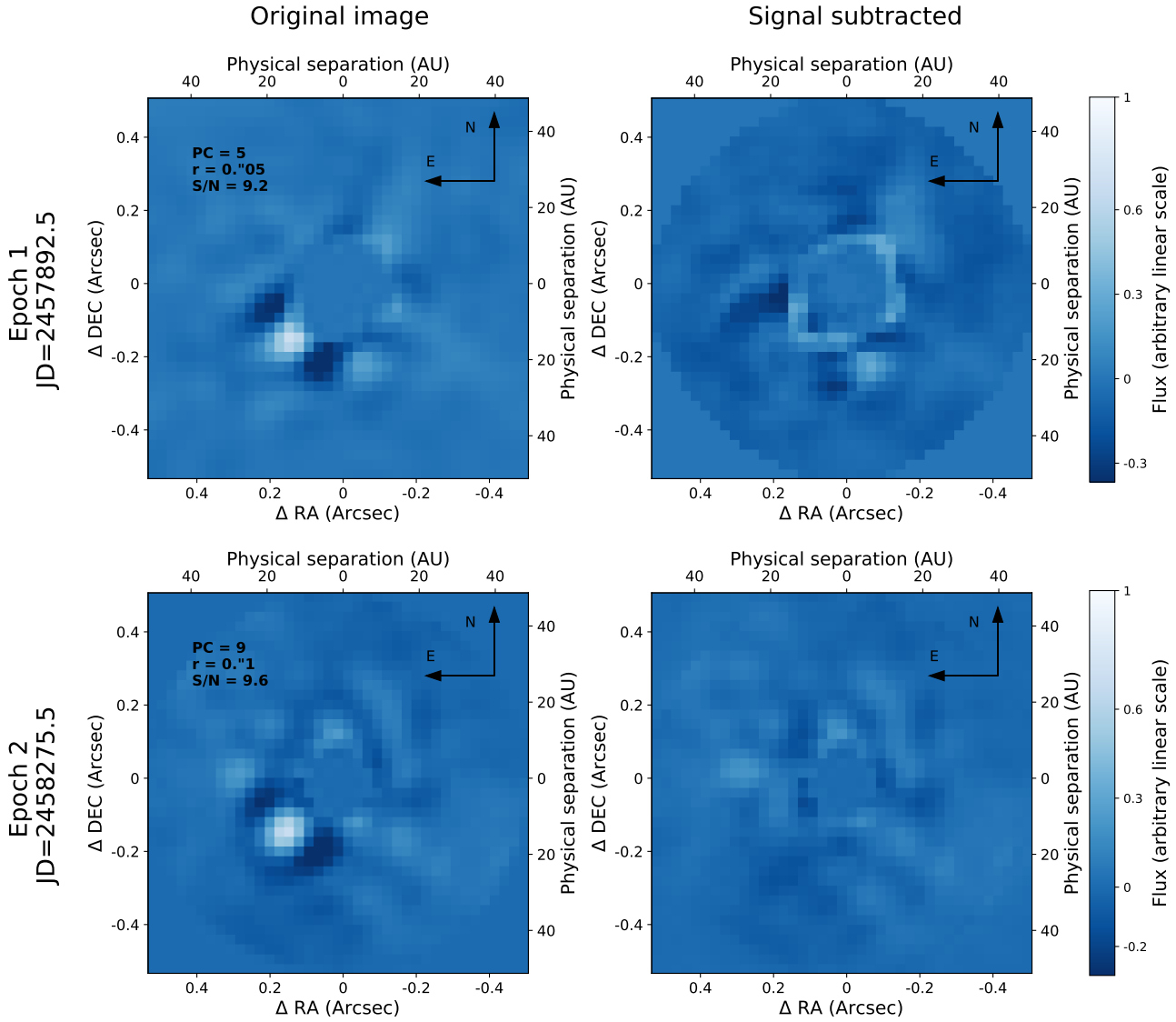

Fig. 1. *Left panel*: first and second epoch detections (*top and bottom panels*, respectively) with the highest S/N (*left panel*) and the corresponding signal-subtracted images (*right panel*). The numbers of subtracted PCs from the central PSF, the applied mask radius, and the S/N are reported in the top left corner of the original images. The same parameters were used for the right panels, where prior to PSF subtraction the HM approach was used to subtract the companion signal.

Table 3. Measured astrometry and photometry of R CrA B.

Epoch 1	Sep (mas)	PA (°)	Contrast (mag)
Hessian matrix	196.8 ± 4.5	134.7 ± 0.5	7.29 ± 0.18
MCMC	192.9 ± 1.0	135.0 ± 0.2	$6.93^{+0.01}_{-0.02}$
Epoch 2			
Hessian matrix	196.6 ± 5.9	133.7 ± 0.7	6.70 ± 0.15
MCMC	186.7 ± 1.1	132.0 ± 0.2	6.48 ± 0.01

The MCMC characterization algorithm was performed for stacks with 10 binned images using the parameter combination that delivered the lowest FPF, namely PC = 3, mask = 0.″05 for epoch 1, and PC = 9, mask = 0.″1 for epoch 2. The parameter space was explored by 200 walkers, each performing a chain of 500 steps.

Astrometric calibration was performed using an astrometric reference field in 47 Tuc taken on 2017 May 19 and on 2018 June 07 and comparing it to the catalog of McLaughlin et al. (2006). The resulting True North correction and platescale are summarized in Table 2. The measured contrasts were corrected for the separation-dependent throughput of the coronagraph (Mawet et al. 2013), which was 0.91 for both epochs. Table 3 summarizes the measurements of the companion for both methods and epochs after those corrections, still without considering photometric variability. The formal errors obtained through the MCMC algorithm do not include any systematic uncertainty and therefore are much smaller than those obtained for HM. For epoch 1, the astrometric results obtained through both methods agree within 1σ error bars, while the measurements obtained for the data of epoch 2 show a larger scatter. For both cases, the MCMC approach measured a lower contrast than the HM. To investigate the presence of systematics, we inserted signals at 0.″2 at three different PAs randomly chosen (but separated by at least 50° from the companion) with 7.3 mag contrast. The analysis shows that neither of the two approaches systematically delivers more accurate results; sometimes the HM algorithm

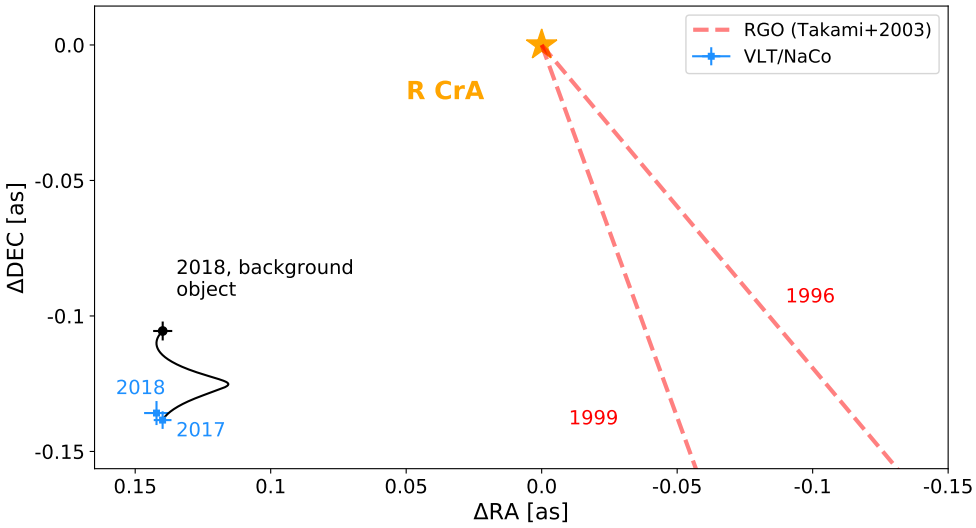

Fig. 2. Astrometry chart of R CrA and its companion candidate. The orange asterisk represents the position of R CrA, the blue squares represent the detected relative positions presented in this work, while the black circle shows the expected position of a stationary background object at the second epoch, given the parallax and proper motion of R CrA as reported in Table 1. The red dashed lines represent the PAs at which the companion was predicted by Takami et al. (2003) from 1996 and 1999 data.

gives values closer to the known ground-truth, sometimes the MCMC sampling. This is most probably because of the presence of residual PSF speckle noise in the image that affects the measurements. Because the HM approach includes at least in part systematic uncertainties, we decided to use these results for the remainder of our analysis.

4. Discussion

4.1. Exclusion of a background source

In Fig. 2 we show in blue squares the relative astrometric position of R CrA B, keeping the primary at a fixed position. The black line and circle represent the path and position we would expect for a stationary background object according to the *Gaia* proper motion of R CrA, which is inconsistent with the observations. Error bars represent uncertainties for the astrometric results obtained with the HM approach and also include the uncertainties in *Gaia* parallax and proper motion for the black circle. However, both the *Gaia* DR2 astrometric excess noise of 3.3 mas and the large unit weight error of ≈31 (UWE; the currently most useful goodness-of-fit indicator for the *Gaia* DR2 five-parameter astrometric solutions; Lindegren et al. 2018) indicate that the single star astrometric solution does not fit the observations well. These inconsistencies could be due to systematic errors not taken into account by the formal uncertainties, but at the given level it is more likely that the companion to R CrA is responsible for the larger than expected residuals to the single star solution.

Combining predictions from Takami et al. (2003) with the new information from NaCo observations, it seems that the secondary source moves west to east and, if bound, it orbits R CrA in a clockwise direction (current projected separation ~18.7 AU). Assuming a face-on circular orbit, its period would be ~43−47 yr (central star mass ~3.0−3.5 $M_\odot$). This value implies an orbital velocity of ~7.7−8.3 deg yr^{-1}. Considering the PAs estimated between 1996 and 2018, the orbital velocity was calculated to be ~4.0 deg yr^{-1}, while that between the ISPY detections is 1 ± 0.9 deg yr^{-1}. Therefore, based on the 22-year-long baseline, the inconsistency allows us to marginally exclude a face-on orbit. Given the lack of uncertainties, confidence levels, and orbital separations in the predictions from Takami et al. (2003), it is not possible to draw more significant conclusions and more precise constraints from the available information.

4.2. Mass of the companion candidate

To estimate the L' brightness of R CrA, we considered the 2MASS (Cutri et al. 2003) K-band photometry and that from the AllWISE Catalog (Cutri et al. 2013) in $W3$ ($\lambda \sim 11.6\,\mu$m) as reported in Table 1. We estimated fluxes in the two bands using filter zero points[4] and interpolated between the two values. The resulting flux was translated into magnitude and we obtained a brightness of 1.5 ± 0.5 mag at 3.8 μm. This method avoids using the highly saturated and therefore rather unreliable measurements taken with the WISE (Wright et al. 2010) $W1$ and $W2$ bands. This estimate agrees with the brightness measured by Glass & Penston (1975), which is 1.78 ± 0.05 mag, where the error is an upper limit for the uncertainty. To be conservative, we considered L' values for the R CrA system to be in the 2.0−1.0 mag range. It is likely that the measured infrared emission is affected by contribution from the circumstellar disk and surrounding material. Nevertheless, the contrast has been measured with respect to the observed flux, and the intrinsic stellar brightness is not relevant for the characterization of the companion. After combining the primary brightness with the measured contrasts, we corrected for extinction (A_V = 1.9−8.0 mag, Table 1) using the extinction curve from Mathis (1990) for R_V = 3.1. This resulted in $A_{L'}$ = 0.09−0.36 mag. Afterward, absolute magnitudes for the companion candidate were computed and compared with the interpolated isochrones from the BT-Settl models (Baraffe et al. 2003) for ages of τ = 1, 2, and 3 Myr. As shown in Fig. 3, depending on the brightness, extinction, and age of the primary at the time of the observations, the companion could have masses ranging from 0.10 ± 0.02 $M_\odot$ to $1.03^{+0.20}_{-0.18}$ $M_\odot$. Considering the particular case in which the brightness of the primary was equal to 1.78 ± 0.05 mag, as measured by Glass & Penston (1975) at 3.5 μm, the companion would have a mass of 0.10−0.38 $M_\odot$ (epoch 1) and 0.19−0.63 $M_\odot$ (epoch 2) for ages in the 1−3 Myr range and L' extinctions in the aforementioned interval. These ranges include 1σ error bars.

As calculated in Sect. 2, R CrA appeared ~0.22 mag brighter in the first observation than in the second. Even if this offset were due to intrinsic stellar variation, the estimated contrasts (Table 3) indicate that the L' brightness of the companion is subject to variability of Δmag ≈ 0.4 ± 0.23 mag, making the mass estimation through model grids particularly difficult. Variability

[4] http://svo2.cab.inta-csic.es/theory/fps3/

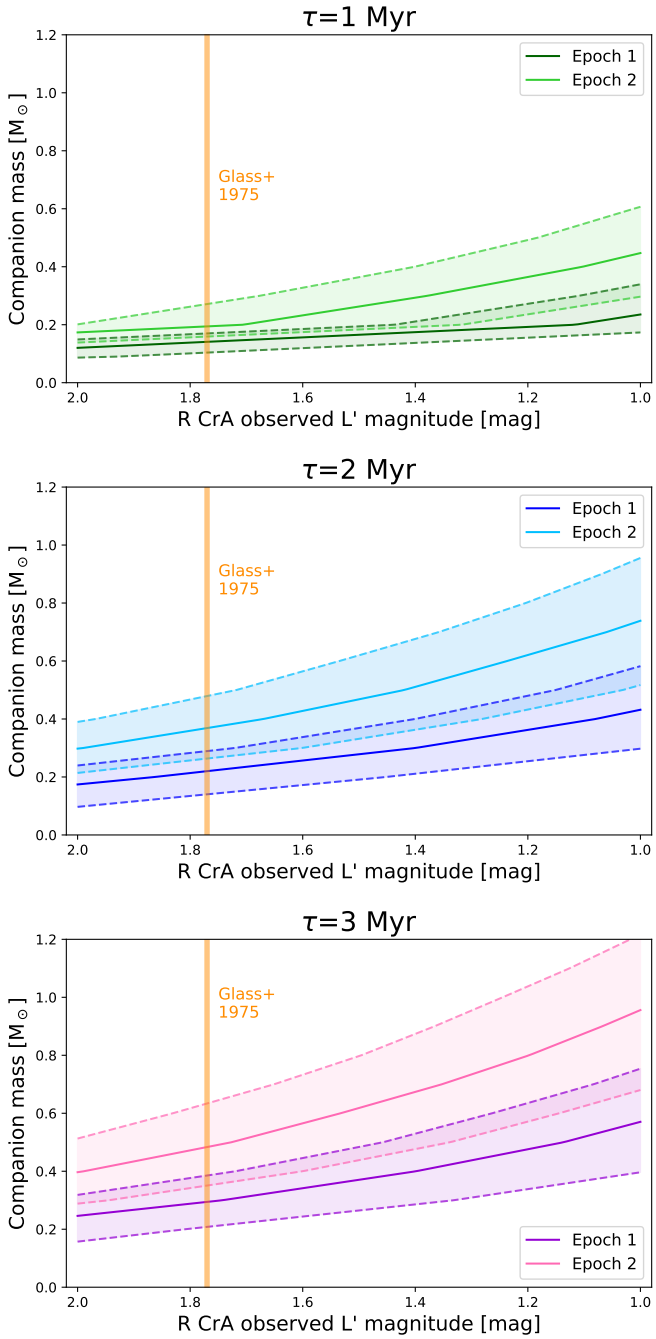

Fig. 3. Companion mass as a function of the primary L' magnitude for $\tau = 1, 2, 3$ Myr (*top to bottom panels*). The shaded regions represent the 1σ uncertainty range coming from contrast, photometric uncertainty of the PSF template, distance, and extinction. The orange solid line indicates the value provided by Glass & Penston (1975).

of this order of magnitude is expected for low-mass young protostars (e.g., Cody & Hillenbrand 2014), in particular if part of the flux is due to accretion processes occurring at varying rates (Wolk et al. 2013) and emitting infrared flux. Another process that might contribute to the observed L' flux is the reprocessing of stellar photons that are absorbed by circumstellar material and re-emitted in the mid-infrared. Unfortunately, with the available data, it is not possible to estimate the fraction of reprocessed L' flux. Accounting for the presence of accreting circumstellar material and a dusty envelope, the estimated mass of the companion should be considered an upper limit.

5. Summary and conclusions

As shown in several previous studies, the environment in the Coronet is extremely complex. Our NaCo high-contrast imaging data revealed an additional physical component of this region, which will need to be taken into account when interpreting the cloud environment harboring R CrA. Follow-up observations with a baseline of a few years will allow to better constrain the orbit of the object and further investigate its time variability. High-contrast observations at shorter wavelengths may shed light on the spectral type of the object and help quantify extinction effects. Finally, the presence of material accreting onto the companion candidate and emitting infrared flux needs to be considered and investigated. In this case, different contributions to the infrared emission should be disentangled and the object mass could be calculated from the true photospheric emission of the object.

Acknowledgements. The authors thank T. Stolker and C. Bailer-Jones for helpful and constructive discussions. Part of this work has been carried out within the frame of the National Center for Competence in Research PlanetS supported by the Swiss National Science Foundation. SPQ acknowledges the financial support of the SNSF. GC and SPQ thank the Swiss National Science Foundation for financial support under grant number 200021_169131. GMK is supported by the Royal Society as a Royal Society University Research Fellow. AM acknowledges the support of the DFG priority program SPP 1992 "Exploring the Diversity of Extrasolar Planets" (MU 4172/1-1). JO and NG acknowledge financial support from the ICM (Iniciativa Científica Milenio) via the Núcleo Milenio de Formación Planetaria grant. JO acknowledges support from the Universidad de Valparaíso, and from Fondecyt (grant 1180395). This research has made use of the SIMBAD database, operated at CDS, Strasbourg, France. This work has made use of data from the European Space Agency (ESA) mission *Gaia* (`https://www.cosmos.esa.int/gaia`), processed by the *Gaia* Data Processing and Analysis Consortium (DPAC, `https://www.cosmos.esa.int/web/gaia/dpac/consortium`). Funding for the DPAC has been provided by national institutions, in particular the institutions participating in the *Gaia* Multilateral Agreement. This publication makes use of data products from the Wide-field Infrared Survey Explorer, which is a joint project of the University of California, Los Angeles, and the Jet Propulsion Laboratory/California Institute of Technology, funded by the National Aeronautics and Space Administration.

References

Amara, A., & Quanz, S. P. 2012, MNRAS, 427, 948
Bailey, J. 1998, MNRAS, 301, 161
Baraffe, I., Chabrier, G., Barman, T. S., Allard, F., & Hauschildt, P. H. 2003, A&A, 402, 701
Bibo, E. A., The, P. S., & Dawanas, D. N. 1992, A&A, 260, 293
Bowler, B. P. 2016, PASP, 128, 102001
Brown, A. 1987, ApJ, 322, L31
Chauvin, G., Desidera, S., Lagrange, A. M., et al. 2017a, in SF2A-2017: Proceedings of the Annual meeting of the French Society of Astronomy and Astrophysics, eds. C. Reylé, P. Di Matteo, F. Herpin, et al., 331
Chauvin, G., Desidera, S., Lagrange, A.-M., et al. 2017b, A&A, 605, L9
Chen, H., Grenfell, T. G., Myers, P. C., & Hughes, J. D. 1997, ApJ, 478, 295
Clark, S., McCall, A., Chrysostomou, A., et al. 2000, MNRAS, 319, 337
Cody, A. M., & Hillenbrand, L. A. 2014, ApJ, 796, 129
Cugno, G., Quanz, S. P., Hunziker, S., et al. 2019, A&A, 622, A156
Cutri, R. M., Skrutskie, M. F., van Dyk, S., et al. 2003, VizieR Online Data Catalog: II/246
Cutri, R. M., Wright, E. L., Conrow, T., et al. 2013, VizieR Online Data Catalog: II/328
Feigelson, E. D., Carkner, L., & Wilking, B. A. 1998, ApJ, 494, L215
Fernández, M., & Comerón, F. 2001, A&A, 380, 264
Forbrich, J., Preibisch, T., & Menten, K. M. 2006, A&A, 446, 155
Gaia Collaboration (Brown, A. G. A., et al.) 2018, A&A, 616, A1
Glass, I. S., & Penston, M. V. 1975, MNRAS, 172, 227
Haas, M., Heymann, F., Domke, I., et al. 2008, A&A, 488, 987
Hamaguchi, K., Yamauchi, S., & Koyama, K. 2005, ApJ, 618, 360
Hillenbrand, L. A., Strom, S. E., Vrba, F. J., & Keene, J. 1992, ApJ, 397, 613
Keppler, M., Benisty, M., Müller, A., et al. 2018, A&A, 617, A44
Koyama, K., Hamaguchi, K., Ueno, S., Kobayashi, N., & Feigelson, E. D. 1996, PASJ, 48, L87

Kraus, S., Hofmann, K.-H., Malbet, F., et al. 2009, A&A, 508, 787
Lagrange, A.-M., Gratadour, D., Chauvin, G., et al. 2009, A&A, 493, L21
Lindegren, L., Hernández, J., Bombrun, A., et al. 2018, A&A, 616, A2
Liu, M. C., Wahhaj, Z., Biller, B. A., et al. 2010, in Adaptive Optics Systems II, Proc. SPIE, 7736, 77361K
Lorenzetti, D., Tommasi, E., Giannini, T., et al. 1999, A&A, 346, 604
Macintosh, B., Graham, J. R., Ingraham, P., et al. 2014, Proc. Natl. Acad. Sci., 111, 12661
Macintosh, B., Graham, J. R., Barman, T., et al. 2015, Science, 350, 64
Marois, C., Lafrenière, D., Doyon, R., Macintosh, B., & Nadeau, D. 2006, ApJ, 641, 556
Marois, C., Macintosh, B., Barman, T., et al. 2008, Science, 322, 1348
Marois, C., Zuckerman, B., Konopacky, Q. M., Macintosh, B., & Barman, T. 2010, Nature, 468, 1080
Mathis, J. S. 1990, ARA&A, 28, 37
Mawet, D., Absil, O., Delacroix, C., et al. 2013, A&A, 552, L13
Mawet, D., Milli, J., Wahhaj, Z., et al. 2014, ApJ, 792, 97
McLaughlin, D. E., Anderson, J., Meylan, G., et al. 2006, ApJS, 166, 249
Mesa, D., Bonnefoy, M., Gratton, R., et al. 2019, A&A, 624, A4
Meyer, M. R., & Wilking, B. A. 2009, PASP, 121, 350
Neuhäuser, R., Walter, F. M., Covino, E., et al. 2000, A&AS, 146, 323
Rameau, J., Chauvin, G., Lagrange, A.-M., et al. 2013, ApJ, 772, L15
Skemer, A. J., Hinz, P., Esposito, S., et al. 2014, in Adaptive Optics Systems IV, Proc. SPIE, 9148, 91480L
Soummer, R., Pueyo, L., & Larkin, J. 2012, ApJ, 755, L28
Stolker, T., Bonse, M. J., Quanz, S. P., et al. 2019, A&A, 621, A59
Takami, M., Bailey, J., & Chrysostomou, A. 2003, A&A, 397, 675
Tamura, M. 2014, in Exploring the Formation and Evolution of Planetary Systems, eds. M. Booth, B. C. Matthews, & J. R. Graham, IAU Symp., 299, 12
Taylor, K. N. R., & Storey, J. W. V. 1984, MNRAS, 209, 5P
Vigan, A., Patience, J., Marois, C., et al. 2012, A&A, 544, A9
Wertz, O., Absil, O., Gómez González, C. A., et al. 2017, A&A, 598, A83
Wilking, B. A., McCaughrean, M. J., Burton, M. G., et al. 1997, AJ, 114, 2029
Wolk, S. J., Rice, T. S., & Aspin, C. A. 2013, AJ, 145, 113
Wright, E. L., Eisenhardt, P. R. M., Mainzer, A. K., et al. 2010, AJ, 140, 1868

A.1.2 ISPY - NACO Imaging Survey for Planets around Young stars. Discovery of an M dwarf in the gap between HD 193571 and its debris ring

In Musso Barcucci et al. (2019) we describe the detection of an M-dwarf companion around the A0 star, HD 193571, that also hosts a debris disk. The companion has a mass between $\sim 0.31 - 0.39\ M_{\odot}$ and it is only the third discovery of a low-mass stellar object within a debris disk after HR 2562 (Konopacky et al. 2016) and HD 206893 (Milli et al. 2017). The paper concludes, by comparing self- and companion-stirring models, that it is likely that the companion is responsible for the stirring of the disk. The full description is outlined in Musso Barcucci et al. (2019) below.

A&A 627, A77 (2019)
https://doi.org/10.1051/0004-6361/201935146

Astronomy & Astrophysics

ISPY – NaCo Imaging Survey for Planets around Young stars

Discovery of an M dwarf in the gap between HD 193571 and its debris ring[⋆,⋆⋆]

Arianna Musso Barcucci[1], Ralf Launhardt[1], Grant M. Kennedy[2], Henning Avenhaus[3], Stefan S. Brems[4], Roy van Boekel[1], F. Cantalloube[1], Anthony Cheetham[1,5], Gabriele Cugno[6], Julien Girard[7], Nicolás Godoy[8,9], Thomas K. Henning[1], Stanimir Metchev[10], André Müller[1], Johan Olofsson[8,9], Francesco Pepe[5], Sascha P. Quanz[6], Andreas Quirrenbach[4], Sabine Reffert[4], Emily L. Rickman[5], Matthias Samland[1], and Damien Segransan[5]

[1] Max Planck Institute for Astronomy (MPIA), Königstuhl 17, 69117 Heidelberg, Germany
e-mail: musso@mpia.de
[2] Department of Physics, University of Warwick, Gibbet Hill Road, Coventry CV4 7AL, UK
[3] Lakeside Labs, Lakeside Park B04b, 9020 Klagenfurt, Austria
[4] Landessternwarte, Zentrum für Astronomie der Universität Heidelberg, Königstuhl 12, 69117 Heidelberg, Germany
[5] Observatoire Astronomique de l'Université de Genève, 51 Ch. des Maillettes, 1290 Versoix, Switzerland
[6] ETH Zürich, Institute for Particle Physics and Astrophysics, Wolfgang-Pauli-Str. 27, 8093 Zürich, Switzerland
[7] European Southern Observatory (ESO), Karl-Schwazschild-Str. 2, 85748 Garching, Germany
[8] Instituto de Física y Astronomía, Facultad de Ciencias, Universidad de Valparaíso, Av. Gran Bretaña 1111, Playa Ancha, Valparaíso, Chile
e-mail: johan.olofsson@uv.cl
[9] Núcleo Milenio Formación Planetaria – NPF, Universidad de Valparaíso, Av. Gran Bretaña 1111, Playa Ancha, Valparaíso, Chile
[10] The University of Western Ontario, Dept. of Physics and Astronomy, 1151 Richmond Avenue, London, ON N6A 3K7, Canada

Received 28 January 2019 / Accepted 20 May 2019

ABSTRACT

Context. The interaction between low-mass companions and the debris discs they reside in is still not fully understood. A debris disc can evolve due to self-stirring, a process in which planetesimals can excite their neighbours to the point of destructive collisions. In addition, the presence of a companion could further stir the disc (companion-stirring). Additional information is necessary to understand this fundamental step in the formation and evolution of a planetary system, and at the moment of writing only a handful of systems are known where a companion and a debris disc have both been detected and studied at the same time.
Aims. Our primary goal is to augment the sample of these systems and to understand the relative importance between self-stirring and companion-stirring.
Methods. In the course of the VLT/NaCo Imaging Survey for Planets around Young stars (ISPY), we observed HD 193571, an A0 debris disc hosting star at a distance of 68 pc with an age between ~60 and 170 Myr. We obtained two sets of observations in L' band and a third epoch in H band using the GPI instrument at Gemini-South.
Results. A companion was detected in all three epochs at a projected separation of ~11 au (~0.17″), and co-motion was confirmed through proper motion analysis. Given the inferred disc size of 120 au, the companion appears to reside within the gap between the host star and the disc. Comparison between the L' and H band magnitude and evolutionary tracks suggests a mass of ~0.31–0.39 $M_{\odot}$.
Conclusions. We discovered a previously unknown M-dwarf companion around HD 193571, making it the third low-mass stellar object discovered within a debris disc. A comparison to self- and companion-stirring models suggests that the companion is likely responsible for the stirring of the disc.

Key words. stars: individual: HD 193571 – planet-disk interactions – planets and satellites: detection – infrared: planetary systems – instrumentation: high angular resolution – techniques: high angular resolution

1. Introduction

Circumstellar discs are the natural by-products of the protostellar accretion process and they are the birthplaces of planetary systems. They evolve with time and undergo a series of processes. After the material that was in the original protoplanetary disc has been dissipated (usually within ~10 Myr, see Ercolano & Pascucci 2017), a new generation of dust is created and continuously replenished via planetesimal collisions, forming a second generation debris disc (DD). These destructive encounters are triggered when the planetesimals are dynamically excited such that their relative velocities increase above a critical value (low-velocity collisions can happen in non-excited DDs as well, but they produce a different and recognisable emission spectrum, see Heng & Tremaine 2010). Three possible stirring processes have been proposed so far that could induce such an excitation in the disc: stellar encounters, self-stirring and companion-stirring. Of these three, the first scenario is the least likely one to be observed, since close stellar encounters are rare (particularly among field stars) and the disc brightness resulting

⋆ The reduced images are only available at the CDS via anonymous ftp to cdsarc.u-strasbg.fr (130.79.128.5) or via http://cdsarc.u-strasbg.fr/viz-bin/qcat?J/A+A/627/A77
⋆⋆ ESO program IDs 097.C-0206 and 1101.C-0092.

from dust production drops too quickly to be detectable (Kenyon & Bromley 2002).

In the self-stirring scenario (Kenyon & Bromley 2008), planetesimals with low relative velocities form increasingly large bodies that in return dynamically excite smaller neighbours above the critical threshold for planetesimal destruction. The planetesimal growth scales with orbital period, resulting in an inside-out collisional cascade. Since a maximum growth speed is set by the host star and disc parameters, at any given time there is a maximum disc size that can be explained by self-stirring.

In the companion-stirring case (Mustill & Wyatt 2009), the planetesimals are excited by the companion's secular perturbations, and the maximum disc size at a given time is a function of the physical properties of both the central star and the companion.

The optimal scenario to investigate these processes is therefore the one in which the disc and the companion(s) are observed and characterised at the same time. At the moment of writing, only a handful of such systems have been found: HR 8799 is one of the most extensively studied (Marois et al. 2008), alongside HD 95086 (Rameau et al. 2013) and β Pic (Lagrange et al. 2010). In addition, only two systems are currently known where the companion is in the stellar mass regime: HR 2562 (Konopacky et al. 2016) and HD 206893 (Milli et al. 2017).

The limited number of systems suitable to investigate the companion-disc interaction does not allow us to fully comprehend this phenomenon, and therefore augmenting this sample is our primary goal.

Detecting and characterising giant planets (GPs) around DD host stars is one of the scientific goals of the Imaging Survey for Planets around Young Stars (ISPY, Launhardt et al., in prep.), currently underway at the Very Large Telescope (VLT). It makes use of the NaCo instrument (Lenzen et al. 2003; Rousset et al. 2003) in L' band, and the Angular Differential Imaging (ADI, Marois et al. 2006).

2. HD 193571

Within the NaCo-ISPY survey, we observed HD 193571 (HR 7779, GJ 969, κ 01 Sgr), an A0V field star at a distance of 68.45 pc (Gaia Collaboration 2018), which is part of a wide-separation (>40″) three-component system[1] (WDS Catalogue, see Mason et al. 2014).

The age of this target is uncertain: David & Hillenbrand (2015) derived stellar parameters for more than 3000 nearby early-type (BAF) field stars, and compared them with stellar isochrones. They computed final ages and masses with both a Bayesian inference approach and classical isochrone interpolation, obtaining 161 Myr and 66 Myr, respectively. They presented criteria to decide between the two values, but for HD 193571 it is unclear which age or mass estimate should be preferred. Throughout this study we use a primary mass of $M = 2.2 \pm 0.1\,M_{\odot}$, which encompasses both the Bayesian inferred mass and the mass derived via interpolation.

The age estimates for HD 193571 are presented in Table 1, together with the main stellar properties.

HD 193571 is known to harbour a debris disc, inferred from its infrared excess ($f = L_{\rm disc}/L_{\star} = 2.3 \times 10^{-5}$). We fit its spectral energy distribution (SED) to derive the stellar luminosity and effective temperature, and the debris belt radius. We fit simultaneously a stellar atmosphere (PHOENIX; Husser et al. 2013) plus a single black-body (BB) model to the observed photometry and the *Spitzer* IRS spectrum. The photometry includes a wide range of filters and wavelengths, from: "Heritage" Stromgren and UBV (Paunzen 2015), 2MASS (Skrutskie et al. 2006), Hipparcos/*Tycho*-2 (ESA 1997), AKARI (Ishihara et al. 2010), WISE (Wright et al. 2010), and *Spitzer* (Chen et al. 2014). The fitting method uses synthetic photometry of grids of models, and finds the best-fitting model with the MultiNest code (Feroz et al. 2009). The SED of HD 193571 is best fit by an A0 stellar model plus a one-temperature BB model locating the dust at a distance of $R_{\rm BB} = 62 \pm 4$ au, with a temperature of 81 ± 3 K. The best fit is shown in Fig. 2.

The BB radius of the dust disc is given by (Pawellek & Krivov 2015)

$$R_{\rm BB} = \left(\frac{278\,{\rm K}}{T_{\rm dust}}\right)^2 \left(\frac{L}{L_{\odot}}\right)^{1/2}.$$

An estimate of the "true" disc radius, $R_{\rm disc}$, is then obtained by applying a stellar luminosity-dependent correction factor, Γ, which accounts for the radiation pressure blowout grain size

$$\Gamma = a\,(L_{*}/L_{\odot})^{b},$$

(Pawellek & Krivov 2015), using the new coefficients given in Pawellek (2016): $a = 7.0$ and $b = -0.39$. After applying this correction, the estimated disc size for HD 193571 is 120 ± 15 au. The disc has never been imaged in scattered light, and additional SPHERE/IRDIS observations were inconclusive in this respect (see Appendix A).

We used the fitted stellar spectrum to derive the stellar H and L' magnitudes (reported in Table 1), integrating over the NaCo H- and L'-band filters. We used zero points of 1.139×10^{-10} erg cm^{-2} s^{-1} Å^{-1} and 5.151×10^{-12} erg cm^{-2} s^{-1} Å^{-1}, respectively[2].

Table 1. Fundamental stellar parameters and properties for HD 193571.

Parameter	Value	Ref.
RA (hh:mm:ss)	20:22:27.50	5
Dec (dd:mm:ss)	−42:02:58.43	5
Parallax (mas)	14.61 ± 0.17	1
Distance (pc)	68.45 ± 0.82	1
Proper motion (mas yr^{-1})	$\mu_{\alpha} \times \cos\delta = 41.31 \pm 0.22$	1
	$\mu_{\delta} = -83.74 \pm 0.19$	1
Sp. type	A0V	6
$T_{\rm eff}$ (K)	9740 ± 100	3
Mass ($M_{\odot}$)	2.2 ± 0.1	2
Radius ($R_{\odot}$)	1.85 ± 0.1	3
$v \sin i$ (km s^{-1})	71	2
L ($L_{\odot}$)	27.7 ± 1	3
$f = L_{\rm disc}/L_{\star}$	$2.3 \times 10^{-5} \pm 1 \times 10^{-6}$	3
Bayesian age (Myr)	161^{+247}_{-35}	2
Interp. age (Myr)	66	2
$m_{L'}$ (mag)	5.614 ± 0.030	4
m_{H} (mag)	5.609 ± 0.030	4

References. (1) Gaia Collaboration (2016, 2018); (2) David & Hillenbrand (2015); (3) this work (see Sect. 2); (4) apparent magnitude of the host star in the L' band, derived from SED fitting (see Sect. 2) and correcting for the NaCo L' band transmission curve; (5) value taken from the online Simbad catalogue; (6) Chen et al. (2014).

[1] The B and C components were observed in 2000 and 1999, and have a distance of 39.30″ and 56.80″, with a PA of 312° and 283°, respectively.

[2] http://svo2.cab.inta-csic.es/svo/theory/fps3/index.php?mode=browse&gname=Paranal&gname2=NACO

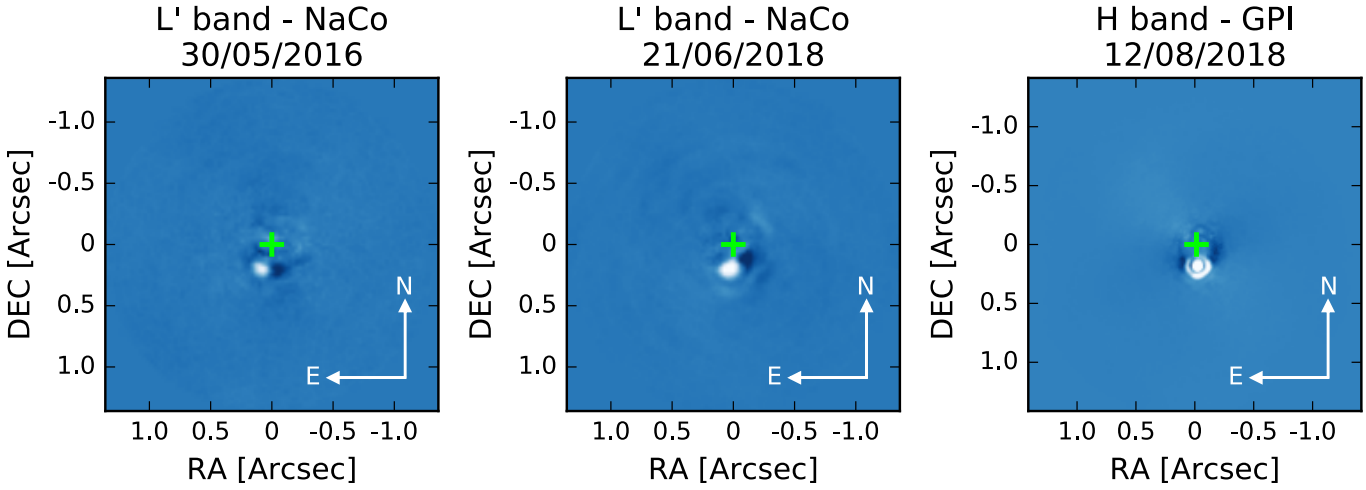

Fig. 1. Classically ADI reduced images for the two NaCo datasets (*left and centre*) and for the GPI dataset (*right*). The images are oriented with north up and east left, and the green cross indicates the position of the central star. The companion is clearly visible close to the centre in all three datasets. The images are normalised and the colour map was chosen for a better visualisation of the data.

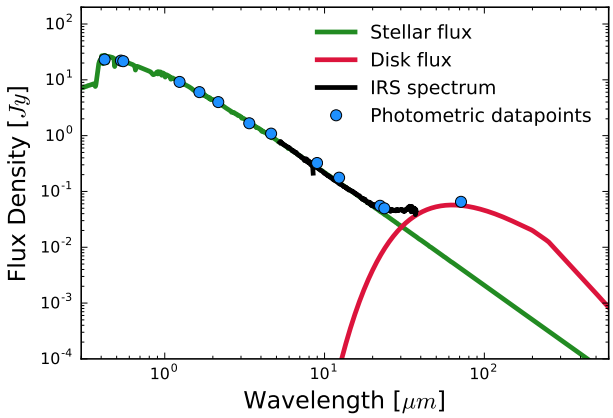

Fig. 2. Flux density distribution of HD 193571, showing the photometric datapoints found in the literature (in blue) and the IRS spectrum (in black), together with the fitted stellar (green) and disc (red) fluxes.

Table 2. VLT/NaCo summary of observations.

Parameter	Epoch 1	Epoch 2
Obs.	30/05/2016	21/06/2018
Prog. ID	097.C-0206	1101.C-0092
#cubes	91	196
Tot. PA	78°	84°
DIT obs. [(a)] (s)	0.35	0.35
DIT flux [(b)] (s)	0.07	0.07
DIMM [(c)]	~1.″0	~1.″1
Tot. time [(d)] (m)	53	114
Sky time [(e)] (m)	4.1	9.3

Notes. [(a)]Detector Integration Time for the observations, chosen to avoid saturation outside ~0.″1. [(b)]Detector Integration Time for the non-coronographic flux measurements. [(c)]Mean DIMM seeing during the observations. [(d)]Total on-source integration time, in minutes. [(e)]Total on-sky time, in minutes: 7 sky visits for the 2016 dataset and 16 sky visits for the 2018 dataset.

3. Observations and data reduction

HD 193571 was observed at two different epochs with NaCo at the Very Large Telescope (VLT), and an additional third epoch was obtained with the Gemini Planet Imager (GPI, Macintosh et al. 2014) through the Fast Turnaround observing mode (Program ID: GS-2018A-FT-111).

3.1. VLT/NaCo

Coronagraphic ADI observations of HD 193571 were obtained in May 2016 and June 2018 in L' band (see Table 2), making use of the Annular Groove Phase Mask (AGPM, Mawet et al. 2013) vector vortex coronagraph to suppress as much as possible the diffraction pattern from the host star. We used cube-mode, saving 100 frames per cube. The observations were interlaced with frequent sky observations for background subtraction (every ~8 min) and bracketed with non-coronagraphic flux measurements to create an unsaturated point spread function (PSF) reference. The data was reduced with the ISPY end-to-end modular reduction pipeline GRAPHIC (Hagelberg et al. 2016). The main reduction steps comprise background subtraction, flat field correction, bad pixel cleaning, and centring. Each cosmetically reduced cube is then median combined. For a more detailed explanation on how the data reduction is performed we refer to the ISPY overview paper (Launhardt et al., in prep.). The observations are summarised in Table 2.

3.2. Gemini/GPI

HD 193571 was observed in the H band with GPI in coronagraphic ADI mode on 12 August 2018, obtaining 76 frames and achieving a total field rotation of 88°. The integration time for each exposure was 60 s.

The photometry of GPI data can be calibrated using the satellite spots, which are four reference spots created by diffraction of the central star light from a square grid superimposed on the pupil plane (Wang et al. 2014). They can be used to extract the photometry and spectroscopy of the central star. During the observations there was a misalignment of the grid that produces the satellite spots, resulting in a diffraction spike above two of the four satellite spots, thus rendering them unusable for photometric calibration. Therefore, in the following analysis, when referring to the satellite spots, we only refer to the two unbiased ones.

Table 3. Astrometry and photometry of the companion candidate for all three datasets.

Date of obs.	FPF 5σ	Separation (arcsec)	PA (deg)	Projected semi-major axis (au)	Abs. mag. (mag)
30/05/2016	4.4×10^{-4}	0.180 ± 0.014	152.35 ± 4.46	12.30 ± 0.97	$M_{L'} = 6.12 \pm 0.14$
21/06/2018	3.6×10^{-5}	0.167 ± 0.014	170.27 ± 4.81	11.42 ± 0.97	$M_{L'} = 6.28 \pm 0.11$
12/08/2018	1.00×10^{-13}	0.155 ± 0.012	176.90 ± 3.71	10.60 ± 0.83	$M_H = 6.89 \pm 0.06$

Notes. Given the small angular separation of the companion, the false probability fraction (FPF) values were evaluated on the classically ADI reduced images following the prescription in Mawet et al. (2014), which accounts for small sample statistics. The final magnitudes are absolute values calculated taking into account the distance to the target and its uncertainties.

The data were reduced making use of the publicly available GPI Data Pipeline (Maire et al. 2010), with the following reduction steps:

- Calibration files were created using the "Dark" and "Wavelength Solution 2D" recipes, applied to the dark frame and the Argon lamp calibration snapshot taken as part of the observations;
- A bad pixel map was created combining the results of the "Hot Bad Pixel Map" and "Cold Bad Pixel Map" recipes, which have been applied respectively to a set of 15 dark frames and a set of 5 daytime Wollaston disperser flat frames for each filter (Y, J, H, $K1$, and $K2$). The calibration files were chosen from the Gemini Data Archive to be the closest in time to the observations;
- The data were reduced applying the "Calibrated Datacube Extraction" recipe, using the above-mentioned newly created calibration files. This recipe also includes an automatic search and characterisation of the four satellite spots, storing in the header the location and peak flux (in ADU) of all the spots, for each wavelength channel;
- The flux-calibrated cubes were oriented using the internal GPI recipe "Rotate North Up".

4. Analysis and results

The final classically ADI reduced images for all the three epochs are shown in Fig. 1. A close-in companion is clearly visible in all three epochs south of the star.

4.1. Astrometry and photometry

To analyse the two NaCo datasets we used the *ANDROMEDA* (Cantalloube et al. 2015)[3] package, which uses a maximum likelihood estimation approach together with negative fake signal injection to evaluate the astrometry and photometry of a companion in an ADI dataset. The algorithm needs as inputs the reduced frames (corrected for the AGPM throughput), the parallactic angles, and an unsaturated and exposure time-scaled image of the central star. Since we were interested in analysing only the known companion, we set the Inner Working Angle and Outer Working Angle keywords to $0.2\,\lambda/D$ and $20\,\lambda/D$, respectively (we refer to Cantalloube et al. 2015 for a detailed explanation of the *ANDROMEDA* package). The final x and y offsets (and relative 3σ uncertainties) were converted into separation and position angle using a platescale for NaCo of $27.2\,\mathrm{mas\,pix^{-1}}$, assuming a conservative error of 0.5 pixels on the centring of the frames, and correcting for the true north offset of $0\overset{\circ}{.}486 \pm 0\overset{\circ}{.}180$ (Launhardt et al., in prep.). Given the target's distance and L' band magnitude (see Table 1), we converted the flux evaluated with *ANDROMEDA*, and relative 3σ uncertainties, into an absolute L' magnitude for both epochs accounting for the uncertainties on the host star magnitude and distance from the system. The final astrometry and photometry values for the two NaCo epochs, as well as the GPI epoch, are given in Table 3.

For the GPI dataset we evaluated astrometry and photometry of the companion in a slightly different way since no unsaturated exposure of the central star was obtained.

For the astrometry, we made use of the satellite spots (visible in all the reduced frames) to create a PSF reference: we first averaged the two satellite spots in each frame, and then we averaged over the 76 frames, obtaining a PSF for each spectral channel. We use this PSF, together with the *ANDROMEDA* package, to obtain the astrometry of the companion (as was done for the NaCo datasets) in each spectral cube. The final astrometry is the weighted mean of the astrometric positions at each wavelength, and is given in Table 3 taking into account the GPI pixel scale of $14.166\,\mathrm{mas\,pix^{-1}}$, the additional true north offset of $0.10 \pm 0.13°$ as reported in Rosa et al. (2015), and a conservative error on the centring of 0.5 pixels.

To obtain the photometry of the companion we calibrated the cubes extracted in Sect. 3.2 in the following way:

- For each spectral channel, we averaged the satellite spots peak flux (stored in the header), obtaining a mean satellite flux in ADU, and relative standard deviation;
- We then converted the frame from ADU to physical units, using the following equation (as detailed on the GPI website[4]):

$$\mathrm{frame[units]} = \frac{\mathrm{frame[ADU]}}{\mathrm{Satellite\ spectrum[ADU]}} \times \frac{\mathrm{Star\ Spectrum\ [units]}}{\mathrm{Star-to-Satellite\ Flux\ ratio}}$$

  The "Star-to-Satellite Flux ratio" was calibrated by the GPI team[5], and it is $= (2 \times 10^{-4})^{-1}$. The "Star Spectrum" (in the desired flux units) is obtained from the stellar spectrum fitted in Sect. 2. We accounted for the uncertainty on the "Star-to-Satellite Flux ratio", the uncertainties on the stellar spectrum, and the standard deviation of the satellite spots flux;
- To account for possible contamination from the stellar halo, we median combined all the frames in each spectral channel, and then subtracted this median from each photometrically calibrated cube;
- We then extracted a spectrum for the companion from each median-subtracted, photometrically calibrated cube, fitting a Gaussian to the companion to get the peak flux. The final spectrum is the weighted average of the spectra in all cubes.

The final spectrum of the companion is shown in Fig. 4. We integrated this spectrum over the NaCo H-band filter, obtaining a

[3] http://www.theses.fr/2016GREAY017

[4] http://docs.planetimager.org/pipeline/usage/tutorial_spectrophotometry.html

[5] See footnote 4.

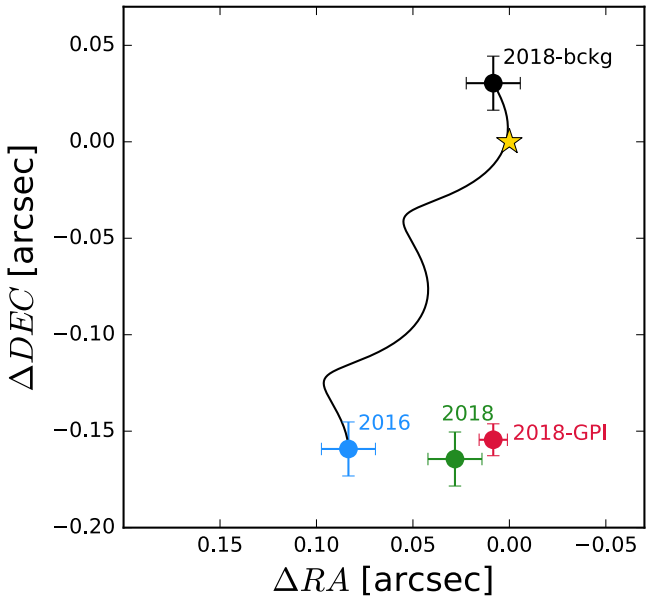

Fig. 3. Proper motion analysis of the companion showing the astrometry for the three epochs. The black data point is the position that the companion would have at the epoch of the GPI observation if it were a background star with no motion, using its position in 2016 as starting point and considering the proper motion of the host star. The companion is clearly co-moving with the star (shown in yellow).

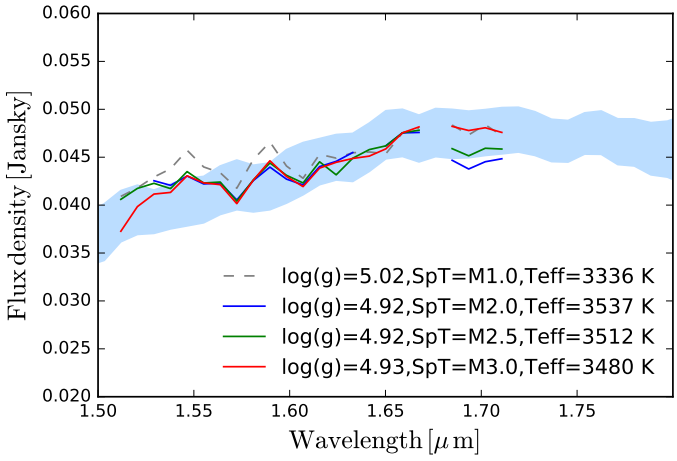

Fig. 4. Comparison between the spectrum of the companion and observed spectra of early M dwarfs. The blue shaded area is the flux density of the companion in the GPI H-band, in Jansky. The spectrum is the weighted average of the spectra extracted from the 76 GPI datacubes and the area encompass the uncertainties (derived from the uncertainty on the flux of the host star). The solid lines are three spectra from the CARMENES stellar spectral library, for various $T_{\rm eff}$ and log g values (evaluated in Hintz et al. 2019) and the dotted grey line is an additional spectrum of an M1 object.

NaCo H-band apparent magnitude of 11.07 ± 0.06. This corresponds to an absolute magnitude of 6.89±0.06. The final astrometry and photometry for the companion is given in Table 3.

The close separation makes it unlikely for the companion to be a background star. Nevertheless, we evaluated the position that the object would have on the sky at epoch 2018, starting from its position in epoch 2016, if it were a background object with no significant proper motion. The results are shown in Fig. 3. The object is clearly co-moving with the host star, at a projected separation of ∼11 au.

4.2. Physical properties

We compared the GPI H-band spectrum with observed spectra of early M dwarfs from the stellar spectral library[6] of the CARMENES survey (Reiners et al. 2018), which is the first large library of M dwarfs with high-resolution spectra in the infrared. We plot three of the best matching spectra (binned to the GPI H-band resolution) in Fig. 4, a non-matching spectrum (dotted grey line) for comparison, and the H-band spectrum of HD 193571 B. From the comparison, we can infer a surface gravity of log g ∼ 4.9, a temperature of ∼3500 K, and a spectral type between M3 and M2, which seem to fit the data reasonably well. However, a high-resolution and/or broader band spectrum would be needed to properly constrain the surface gravity and spectral type of the companion.

We estimated the mass of the companion using the BT-Settl evolutionary tracks (Allard et al. 2012)[7], by comparing them with the observed L'- and H-band photometry. In the colour-magnitude diagram of Fig. 5 we show the companion L'-band absolute photometry of 6.19 ± 0.08 mag (evaluated as the weighted mean of the two NaCo epochs), as well as evolutionary tracks for two representative ages of 60 Myr (dashed line) and 150 Myr (solid line). As shown in Fig. 5, the photometry does not allow us to distinguish between the two age estimates, so we use both age values in the rest of the paper. We interpolated the BT-Settl models to estimate the mass of the companion for both L'- and H-band photometry, in mass steps of 0.034 dex. Taking into account the photometric uncertainty in both bands, we obtained a weighted mass of 0.395 ± 0.007 $M_\odot$ for an age of 161 Myr, and 0.305 ± 0.025 $M_\odot$ for an age of 66 Myr.

4.3. Orbital motion

The astrometry of the companion between the three epochs shows signs of orbital motion. Following the prescription in Pearce et al. (2015), we can explore the possible orbital solutions for a companion imaged over a short orbital arc, using the dimensionless parameter B ($\sqrt{B} = V_{\rm sky}/V_{\rm esc}$ is the sky-plane velocity of the companion divided by the escape velocity), and the direction of motion φ, where $\varphi = 0°$ is motion along a vector from the primary to the companion.

We assumed a total system mass of 2.6 ± 0.1 $M_\odot$ (for an age of 161 Myr) and 2.55 ± 0.1 $M_\odot$ (for an age of 66 Myr) and we derived[8] B and φ for the three epochs (NaCo 2016, NaCo 2018, and GPI 2018). For both age estimates the values agree within the uncertainties, and we obtain $B = 0.25^{+0.16}_{-0.11}$ and $\varphi = 100 \pm 15°$, which leads to a minimum semi-major axis of $a_{\rm min} = 8.20 \pm 1.77$ au (see Eq. (5) in Pearce et al. 2015). Following Pearce et al. (2015), we can draw the following conclusions:

– Even considering the uncertainties, the B value is <1, so the companion's sky-plane motion is below the escape velocity. While the object could be unbound if the line of sight velocity (or separation) is high, this is unlikely;
– We cannot place constraints on the eccentricity of the orbit, meaning that a circular orbit cannot be ruled out (this will have an impact on our stirring mechanisms study in Sect. 4);

[6] http://carmenes.cab.inta-csic.es/gto/jsp/reinersetal2018.jsp
[7] http://svo2.cab.inta-csic.es/theory/newov/
[8] http://drgmk.com/imorbel/

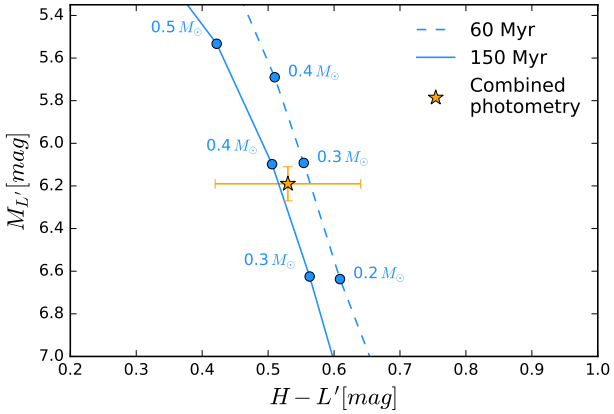

Fig. 5. Colour-magnitude diagram showing the weighted mean L'-band magnitude derived from the 2016 and 2018 NaCo datasets, together with the H-band magnitude derived from the GPI dataset. We plot the evolutionary tracks for the BT-Settl models from Allard et al. (2012), for ages of 60 and 150 Myr. The photometry does not allow us to distinguish between the two age estimates.

– We can place a loose upper limit of ∼80° on the inclination.

We also explored the possible orbital motion parameters using the python package `orbitize`[9] with the Orbit For The Impatient (OFTI) algorithm detailed in Blunt et al. (2017) (see Appendix C). While the uncertainties on the astrometry and the limited amount of datapoints do not place any meaningful constraints on the orbital elements, the periastron distance is restricted to $\lesssim$15 au. This result is confirmed by exploring the possible orbital parameters using the method of Pearce et al. (2015). Therefore, if the companion's orbit is nearly coplanar with the disc, the entire orbit should be interior to the disc, otherwise the companion would have disrupted the disc on a dynamical timescale. Assuming a circular orbit and a semi-major axis of 11 au, the companion would have a minimum period of ∼23 years, implying that a baseline of several years would be needed before any additional astrometric datapoint could provide better constraints on the orbital elements. The companion is massive enough that even in the unlucky case of an almost face-on orbit ($i \sim 1°$) it would produce a radial velocity signal strong enough to be detected (semi-amplitude $K \gtrsim 120\,\mathrm{m\,s^{-1}}$); however, this would also require a time baseline of many years.

5. Stirring mechanisms

The relative importance of self- and companion-stirring mechanisms is a non-trivial problem. It depends on the companion's physical and orbital parameters, the host star age and mass, and the disc mass in solids. The equations used in this section are from Wyatt (2008) and Mustill & Wyatt (2009), and are summarised in Appendix B. We note that to be consistent with the underlying assumptions of these two papers, we use the black-body disc radius of 62 au while working with equations from Wyatt (2008), and the corrected disc radius of 120 au for the Mustill & Wyatt (2009) equations (see Appendix B). That is, the model in Wyatt (2008) uses parameters derived by fitting to black-body radii, while the model of Mustill & Wyatt (2009) uses orbital dynamics, so is based on physical disc radii.

Assuming that the mutual inclination between the plane of the orbit and the disc is not too large, there are two conditions that need to be satisfied for a companion to dominate the stirring process at a certain distance from the star, and at a given time: (a) the companion must be able to stir planetesimals, at that location, to relative destructive velocities and (b) the timescale for companion-stirring at that distance must be greater than the self-stirring timescale.

The first condition is encapsulated by Eqs. (B.2) and (B.3), which give the maximum distance at which a companion with a given semi-major axis $a_{\rm pl}$ and eccentricity $e_{\rm pl}$ can stir planetesimals above the disruption threshold velocity $v_{\rm rel}$. This velocity is a function of the planetesimal size R and, as shown by Eq. (B.2), has a minimum at $R \sim 80$ m. We set this maximum distance equal to the estimated true disc radius of 120 au, and we plotted the $a_{\rm pl}$–$e_{\rm pl}$ relationship in Fig. 6 for the $R = 80$ m case (solid light blue curve). The companion would not be able to stir planetesimals at that distance if its semi-major axis and eccentricity were below this curve. The planetesimals might be smaller or larger than 80 m, and this would increase $v_{\rm rel}$ and push the light blue curve rightwards and upwards. While R has a definite minimum (particles smaller than a certain size, typically around few μm, would be blown away by radiation pressure from the central star) it is not straightforward to define a maximum R value. We proceeded as follows:

– At any given time, there is a maximum size of planetesimals that participate in the collisional cascade (because larger objects will have collision timescales longer than the stellar age). This maximum size $R_{\rm max}$ can be evaluated by inverting Eq. (B.1). For a disc size of 62 au, and with a fractional luminosity of the disc f, stellar mass and stellar luminosity as in Table 1, we have $R_{\rm max} = 132$ m. This is the maximum value for R, assuming that the disc has been stirred for all of its life ($t_{\rm stir} = t_{\rm age} = 66$ Myr. In the 161 Myr case we obtain $R_{\rm max} = 790$ m);
– An internal perturber can influence the timescale of orbit crossings for planetesimals, and thus $t_{\rm stir}$ might be less than the stellar age (i.e. the disc was stirred more recently). We use Eq. (B.4) to calculate this orbit crossing timescale $t_{\rm cross}$ as a function of the perturber properties (eccentricity, semi-major axis, and mass);
– We now have a revised value for the total time the disc has been stirred as $t_{\rm stir} = t_{\rm age} - t_{\rm cross}$, and consequently a revised $R_{\rm max}$ value as a function of the perturber properties (i.e. we have a relationship between $R_{\rm max}$, $a_{\rm pl}$, and $e_{\rm pl}$);
– Combining this relationship with Eqs. (B.2) and (B.3), we can trace $R_{\rm max}$ in the ($a_{\rm pl}$, $e_{\rm pl}$) parameter space.

As can be seen in Fig. 6, when we plot this for the 66 Myr case, $R_{\rm max}$ is relatively small (∼132 m along the curve) and almost overlaps with the $R = 80$ m case. The $R_{\rm max}$ in the 161 Myr case is plotted with a dashed grey curve. The companion can stir the disc over most of the shown parameter space.

The second condition requires that, at a given time and distance, the companion-stirring timescale is shorter than the self-stirring timescale. Mustill & Wyatt (2009) made such a study and defined the parameter Φ as the distance at which self and companion-stirring times are equal (see Appendix B). It is a function of the companion's properties (mass $m_{\rm pl}$, semi-major axis $a_{\rm pl}$, and eccentricity $e_{\rm pl}$), the central star's mass, and the disc's mass in solids (expressed by the dimensionless parameter $x_{\rm m}$, see Appendix B). Since we are interested in which stirring process is dominant at the location of the debris belt, we set $\Phi = 120$ au and obtain the equilibrium relationship between self- and planetary-stirring. Tracing this line in the ($a_{\rm pl}$, $e_{\rm pl}$) parameter space marks the boundary between the domination of the two stirring processes, thus allowing us to investigate the combination of $a_{\rm pl}$ and $e_{\rm pl}$ for which the disc is dominated by self-stirring.

[9] https://orbitize.readthedocs.io/en/latest/

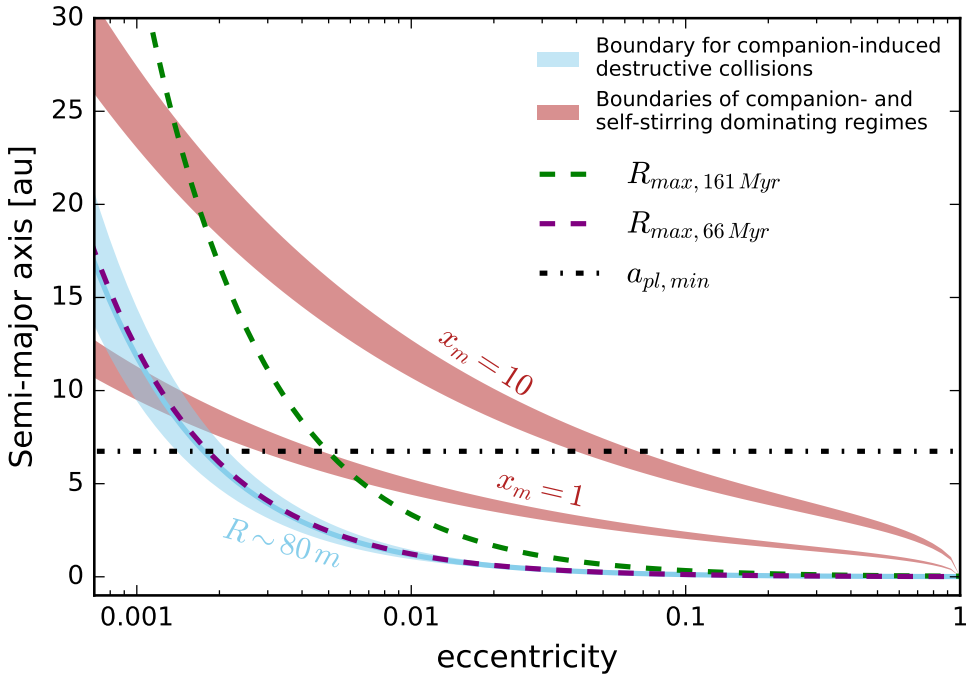

Fig. 6. Boundaries between a self-stirring and companion-stirring dominated disc. The light blue lines mark the ($a_{\rm pl}$, $e_{\rm pl}$) parameter space in which the companion would be able to stir planetesimals of size R to destruction velocities at a distance of 120 au. The shaded area around the solid light blue (R = 80 m) line takes into account the errors on the disc size and the stellar mass. The dashed purple line shows the $R_{\rm max}$ for 66 Myr (close to the solid light blue line) and the dashed green line shows the $R_{\rm max}$ value for the 161 Myr case. The shaded red areas indicate the boundaries between the self-stirring and companion-stirring dominated cases, for a fixed distance and companion mass, and for two representative $x_{\rm m}$ values; accounting for errors on disc size, stellar mass, and companion mass (the areas encompass both age estimates). The horizontal dotted black line is the lowermost boundary of the minimum possible companion semi-major axis calculated in Sect. 4.3. The companion dominates the stirring process only for combinations of $a_{\rm pl}$ and $e_{\rm pl}$ lying above the light blue curve (the companion can stir planetesimals at the disc distance) and the red curve (the companion stirs the disc faster than the disc stirs itself).

Since there is a dependence on the $x_{\rm m}$ value as well, in Fig. 6 we plotted two representative values for $x_{\rm m}$ of 1 and 10 (solid red lines). The curve for $x_{\rm m}$ = 10 lies above the $x_{\rm m}$ = 1 case because a more massive disc forms large planetesimals more quickly, and can thus self-stir earlier. As discussed in Mustill & Wyatt (2009), $x_{\rm m} \gtrsim 10$ discs may be problematic as their high masses imply gravitationally unstable discs at earlier times when the gas was present. Thus, it is likely that the $x_{\rm m}$ = 10 line in Fig. 6 represents an upper limit to where the disc could be self-stirred. Given an $x_{\rm m}$ value and fixing the companion mass to 0.25 $M_{\odot}$, any combination of eccentricity and semi-major axis above the curve would imply that companion-stirring is quicker than self-stirring at the distance of the disc, hence the companion-stirring would dominate the stirring process. An additional constraint can be placed on the minimum semi-major axis, as discussed in Sect. 4.3, which is shown by the dashed black line in Fig. 6.

It is important to note that both conditions must be satisfied for the companion to dominate the stirring process, and this is true only for certain combinations of eccentricity and semi-major axis. In the plot it is clear how, given an eccentricity $\gtrsim$0.1, any semi-major axis places the companion above both curves, and thus the companion would dominate. For eccentricities $\gtrsim$0.002, any $a_{\rm pl}$ would lie above the light blue curves (both for the $R \sim$ 80 m and for the $R_{\rm max}$ case), but only certain $a_{\rm pl}$ would satisfy the criterion for companion-induced stirring dominating over self-stirring (depending on the $x_{\rm m}$ value), so low-eccentricity companions must be closer to the disc to dominate the stirring. Finally, for extremely low eccentricities ($\lesssim$0.002) and small semi-major axes, the companion would not be able to stir planetesimals at the distance of the disc (below the light blue curve), and in any case the self-stirring would be dominant at that distance (below the red curve).

As shown in Fig. 6, it is most likely that the companion is dominating the stirring process, and self-stirring is relevant only when the companion has a very low eccentricity (in combination with a small semi-major axis).

6. Conclusions

We presented the first detection of a close low-mass stellar companion around the A0 star HD 193571. The three epochs obtained with VLT/NaCo and GPI confirm that the companion is co-moving with the host star, showing the potential of multi-band/multi-instrument follow-up to confirm direct imaging candidates. Comparing M_H and $M_{L'}$ band photometry to evolutionary tracks suggests a mass of $\sim$0.305 $\pm$ 0.025 $M_{\odot}$ for an age of 66 Myr ($\sim$0.395 $\pm$ 0.007 $M_{\odot}$ for the 161 Myr case), which would make it an M2-2.5 dwarf. Comparison to observed spectra seems to suggest a surface gravity of $\sim$4.9 and a temperature of $\sim$3500 K. The orbital motion detected in the three epochs is not enough to place solid constraints on the orbital parameters, but allows us to confirm the co-motion with the host star and to exclude an edge-on orbit.

Given the projected separation of $\sim$11 au and a maximum periastron of $\sim$15 au, the companion appears to orbit interior to the circumstellar debris belt (inferred via SED IR-excess to be at $\sim$120 au). We investigated the plausibility that both self- and companion-stirring mechanisms are responsible for the currently observed debris belt radius. Since no constraints can be put on

the eccentricity, we cannot exclude a fully self-stirring scenario for the disc. However, a small deviation from a circular orbit would result in the disc being dominated by companion-stirring (as shown in Fig. 6) and if the orbit is sufficiently eccentric the disc will appear eccentric as well. The companion is likely responsible for the stirring of a disc that appears to be an order of magnitude further away, showing how a massive companion can influence a debris disc at large distances.

At the moment, only a handful of systems are suited for a study of stirring mechanisms, and the HD 193571 system represents an important addition, containing the third known M-dwarf companion to a young star discovered to be orbiting within the primary's circumstellar disc, and the first one found around an A0-type star. In the future, radial velocity observations as well as a resolved image of the disc could be useful in deepening our understanding of this system.

Acknowledgements. A.M.B. thanks Christian Ginsky for the help in reducing the SPHERE/IRDIS data and the useful discussion afterwards, and Wolfgang Brandner for the help in reducing the GPI data. A.M.B. would also like to thank the anonymous referee for the useful and constructive comments. G.M.K. is supported by the Royal Society as a Royal Society University Research Fellow. G.C. and S.P.Q. thank the Swiss National Science Foundation for the financial support under the grant number 200021_169131. J.O. and N.G. acknowledge financial support from the ICM (Iniciativa Científica Milenio) via the Núcleo Milenio de Formación Planetaria grant. J.O. acknowledges financial support from the Universidad de Valparaíso, and from Fondecyt (grant 1180395). N.G. acknowledges support from project CONICYT-PFCHA/Doctorado Nacional/2017 folio 21170650. A.M. and A.Q. acknowledge the support of the DFG priority program SPP 1992 "Exploring the Diversity of Extrasolar Planets" (MU 4172/1-1 and QU 113/6-1). This research has made use of the Washington Double Star Catalog maintained at the U.S. Naval Observatory, and of data products from the Two Micron All Sky Survey, which is a joint project of the University of Massachusetts and the Infrared Processing and Analysis Center/California Institute of Technology, funded by the National Aeronautics and Space Administration and the National Science Foundation. This work has made use of data from the European Space Agency (ESA) mission *Gaia* (`https://www.cosmos.esa.int/gaia`), processed by the *Gaia* Data Processing and Analysis Consortium (DPAC, `https://www.cosmos.esa.int/web/gaia/dpac/consortium`). Funding for the DPAC has been provided by national institutions, in particular the institutions participating in the *Gaia* Multilateral Agreement. This research made use of Astropy (`http://www.astropy.org`), a community-developed core Python package for Astronomy (Astropy Collaboration 2013, 2018).

References

Allard, F., Homeier, D., & Freytag, B. 2012, Trans. R. Soc. London Ser. A, 370, 2765
Astropy Collaboration (Robitaille, T. P., et al.) 2013, A&A, 558, A33
Astropy Collaboration (Price-Whelan, A. M., et al.) 2018, AJ, 156, 123
Blunt, S., Nielsen, E. L., De Rosa, R. J., et al. 2017, AJ, 153, 229
Cantalloube, F., Mouillet, D., Mugnier, L. M., et al. 2015, A&A, 582, A89
Chen, C. H., Mittal, T., Kuchner, M., et al. 2014, ApJS, 211, 25
David, T. J., & Hillenbrand, L. A. 2015, ApJ, 804, 146
Ercolano, B., & Pascucci, I. 2017, Roy. Soc. Open Sci., 4, 170114
ESA 1997, VizieR Online Data Catalog: I/239
Feroz, F., Hobson, M. P., & Bridges, M. 2009, MNRAS, 398, 1601
Gaia Collaboration (Prusti, T., et al.) 2016, A&A, 595, A1
Gaia Collaboration (Brown, A. G. A., et al.) 2018, A&A, 616, A1
Ginski, C., Stolker, T., Pinilla, P., et al. 2016, A&A, 595, A112
Hagelberg, J., Ségransan, D., Udry, S., & Wildi, F. 2016, MNRAS, 455, 2178
Heng, K., & Tremaine, S. 2010, MNRAS, 401, 867
Hintz, D., Fuhrmeister, B., Czesla, S., et al. 2019, A&A, 623, A136
Husser, T., Wende-Von Berg, S., Dreizler, S., et al. 2013, A&A, 553, A6
Ishihara, D., Onaka, T., Kataza, H., et al. 2010, A&A, 514, A1
Kenyon, S. J., & Bromley, B. C. 2002, AJ, 123, 1757
Kenyon, S. J., & Bromley, B. C. 2008, ApJS, 179, 451
Konopacky, Q. M., Rameau, J., Duchêne, G., et al. 2016, ApJ, 829, L4
Lagrange, A. M., Bonnefoy, M., Chauvin, G., et al. 2010, Science, 329, 57
Lenzen, R., Hartung, M., Brandner, W., et al. 2003, in Instrument Design and Performance for Optical/Infrared Ground-based Telescopes, eds. M. Iye, & A. F. M. Moorwood, Proc. SPIE, 4841, 944
Macintosh, B., Graham, J. R., Ingraham, P., et al. 2014, Proc. Natl. Acad. Sci., 111, 12661
Maire, J., Perrin, M. D., Doyon, R., et al. 2010, in Ground-based and Airborne Instrumentation for Astronomy III, Proc. SPIE, 7735, 773531
Marois, C., Lafreniere, D., Doyon, R., Macintosh, B., & Nadeau, D. 2006, ApJ, 641, 556
Marois, C., Macintosh, B., Barman, T., et al. 2008, Science, 322, 1348
Mason, B. D., Wycoff, G. L., Hartkopf, W. I., Douglass, G. G., & Worley, C. E. 2014, AJ, 122, 3466
Mawet, D., Absil, O., Delacroix, C., et al. 2013, A&A, 552, L13
Mawet, D., Milli, J., Wahhaj, Z., et al. 2014, ApJ, 792, 97
Milli, J., Hibon, P., Christiaens, V., et al. 2017, A&A, 597, L2
Mustill, A. J., & Wyatt, M. C. 2009, MNRAS, 399, 1403
Paunzen, E. 2015, A&A, 580, A23
Pawellek, N. 2016, PhD Thesis, University of Jena
Pawellek, N., & Krivov, A. V. 2015, MNRAS, 454, 3207
Pearce, T. D., Wyatt, M. C., & Kennedy, G. M. 2015, MNRAS, 448, 3679
Rameau, J., Chauvin, G., Lagrange, A.-M., et al. 2013, ApJ, 772, L15
Reiners, A., Zechmeister, M., Caballero, J. A., et al. 2018, A&A, 612, A49
Rosa, R. J. D., Nielsen, E. L., Blunt, S. C., et al. 2015, ApJ, 814, L3
Rousset, G., Lacombe, F., Puget, P., et al. 2003, in Adaptive Optical System Technologies II, eds. P. L. Wizinowich, & D. Bonaccini, Proc. SPIE, 4839, 140
Schmid, H. M., Joos, F., & Tschan, D. 2006, A&A, 452, 657
Skrutskie, M. F., Cutri, R. M., Stiening, R., et al. 2006, AJ, 131, 1163
Wang, J. J., Rajan, A., Graham, J. R., et al. 2014, in Ground-based and Airborne Instrumentation for Astronomy V, SPIE Conf. Ser., 9147, 914755
Wright, E. L., Eisenhardt, P. R. M., Mainzer, A. K., et al. 2010, AJ, 140, 1868
Wyatt, M. C. 2008, Annu. Rev. Astron. Astrophys., 46, 339

Appendix A: IRDIS disc non-detection

We observed the target with SPHERE/IRDIS at the VLT in coronagraphic Differential Polarisation Imaging (DPI) mode on 26 September 2018, using the H broad-band filter.

We took eight polarimetric cycles, each consisting of four data cubes, one per half wave plate (HWP) position. Each data cube consisted of four individual exposures with exposure times of 32 s. The science observations were bracketed with 2 s exposures, to create an unsaturated PSF reference for the central star.

The data were reduced following the prescription in Ginski et al. (2016), obtaining the radial Stokes components Q_Φ and U_Φ (see Schmid et al. 2006), where Q_Φ would contain any polarisation signal coming from dust scattered light, and it is shown in Fig. B.1. No emission is visible at the expected location of the disc (~1.″75) or anywhere else. The faint emission from the centre is due to the stellar halo, and the spider is vaguely visible extending approximately in the north-south direction.

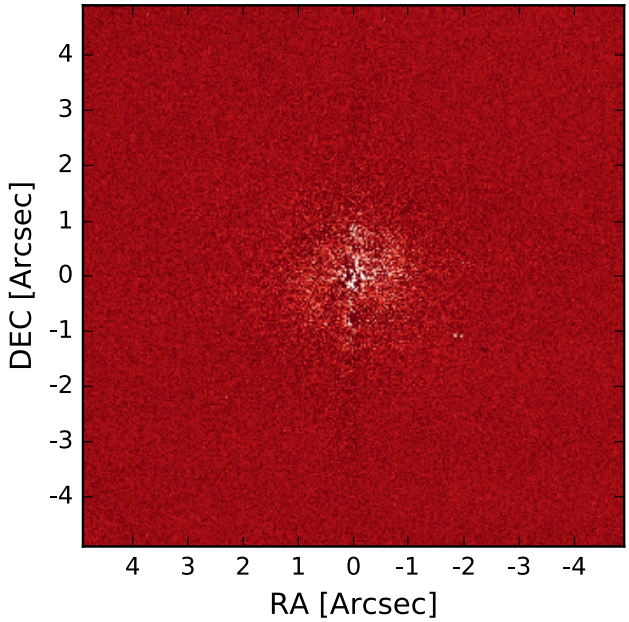

Fig. B.1. DPI data taken with SPHERE/IRDIS, with a total field of view of ~10″ × 10″, given a pixel scale for IRDIS of 12.25 mas pix^{-1}. No polarised signal from the disc scattered light is visible. The image is oriented with north up and east left.

Appendix B: Stirring mechanisms

B.1. Self-stirring

From Wyatt (2008) the maximum fractional luminosity $f_{\max}$ of a planetesimal belt at distance r around a star of mass $m_\star$, luminosity $L_\star$, and age $t_{\rm age}$ is

$$f_{\max} = 0.58 \times 10^{-9} r^{7/3}\,(\mathrm{d}r/r)\,R_{\max}^{0.5} Q_{\rm D}^{\star 5/6} e^{-5/3} m_\star^{-5/6} L_\star^{-0.5} t_{\rm age}^{-1}, \quad \text{(B.1)}$$

where $R_{\max}$ is the maximum size of the planetesimals that are participating in the cascade at that given time (called $D_{\rm c}$ in Wyatt 2008), $Q_{\rm D}^\star$ is the planetesimal strength in Jkg^{-1}, e is the mean planetesimal eccentricity, and $\mathrm{d}r/r$ is the relative width of the planetesimal belt. It was found (see Wyatt 2008) that the population of debris discs around A stars can be fitted assuming $Q_{\rm D}^\star = 150\,\mathrm{J\,kg^{-1}}$, $e = 0.05$, and $\mathrm{d}r/r = 0.5$. All of this assumes that the disc has been stirred for its whole lifetime (i.e. $t_{\rm stir} = t_{\rm age}$). The disc evolution model developed in Wyatt (2008) is SED-based, and therefore the planetesimal belt distance r refers to the black-body radius $R_{\rm BB}$ of 62 au, inferred via SED fitting.

B.2. Companion-stirring

From Mustill & Wyatt (2009), the threshold velocity above which collisions between planetesimal of size R become destructive is

$$v_{\rm rel}^\star(R) = \left[0.8\left(\frac{R}{80\,\mathrm{m}}\right)^{-0.33} + 0.2\left(\frac{R}{80\,\mathrm{m}}\right)^{1.2}\right]^{0.83} \mathrm{ms^{-1}}. \quad \text{(B.2)}$$

A companion of mass $m_{\rm pl}$ internal to the disc on an orbit of semi-major axis $a_{\rm pl}$ and eccentricity $e_{\rm pl}$, around a primary of mass $m_\star$, would be able to stir planetesimals to catastrophic collisions only up to a maximum distance $a^\star$:

$$a^\star(R) = 3.8\,\mathrm{au}\left(\frac{e_{\rm pl}}{0.1}\right)^{2/3}\left(\frac{m_\star}{1\,M_\odot}\right)^{1/3}\left(\frac{a_{\rm pl}}{1\,\mathrm{au}}\right)^{2/3}\left(\frac{v_{\rm rel}^\star(R)}{1\,\mathrm{km\,s^{-1}}}\right)^{-2/3}. \quad \text{(B.3)}$$

In addition, it is possible to calculate the timescale for orbit crossing of planetesimals at a distance a as

$$t_{\rm cross} \sim 1.53 \times 10^3 \frac{\left(1-e_{\rm pl}^2\right)^{3/2}}{e_{\rm pl}}\left(\frac{a}{10\,\mathrm{au}}\right)^{9/2} \times \left(\frac{m_\star}{M_\odot}\right)^{1/2}\left(\frac{m_{\rm pl}}{M_\odot}\right)^{-1}\left(\frac{a_{\rm pl}}{1\,\mathrm{au}}\right)^{-3}\mathrm{yr}. \quad \text{(B.4)}$$

B.3. Companion-stirring versus self-stirring

Mustill & Wyatt (2009) also defined the parameter Φ as the distance boundary between self-stirring and companion-stirring at a fixed age as

$$\Phi = 630\,\mathrm{au}\left(1-e_{\rm pl}^2\right)^{-1} e_{\rm pl}^{2/3}\left(\frac{m_{\rm pl}}{M_\odot}\right)^{2/3} \times \left(\frac{a_{\rm pl}}{1\,\mathrm{au}}\right)^{2}\left(\frac{m_\star}{M_\odot}\right)^{-4/3} x_{\rm m}^{-0.77}, \quad \text{(B.5)}$$

where the dimensionless parameter $x_{\rm m}$ is a scaling factor relating the disc surface density to the minimum mass solar nebula density (see Mustill & Wyatt 2009 and Kenyon & Bromley 2008).

The model developed in Mustill & Wyatt (2009) is a dynamic model that depends on the physical structure of the disc, and therefore on the real disc size of 120 au (see Sect. 2).

Appendix C: Orbital constraints with OFTI

We explored the possible orbital motion parameters using the python package `orbitize` with the Orbit For The Impatient (OFTI) algorithm detailed in Blunt et al. (2017). We used two total mass estimates: $2.6 \pm 0.1\,M_{\odot}$ (for an age of 161 Myr) and $2.5 \pm 0.1\,M_{\odot}$ (for an age of 66 Myr). We used a uniform prior for the semi-major axis, and in the epoch of periastron passage and argument of periastron. We used a $\sin(i)$ prior for the inclination angle, and a linearly descending prior for the eccentricity, with a slope of -2.18. For both age estimates, the results agree within the error bar, and in Fig. C.1 we show the posterior distribution function for the 161 Myr case. As shown in the figure, the uncertainties on the astrometry and the limited number of datapoints do not allow us to place any meaningful constraints on the orbital elements, but the periastron distance q is restricted to $\lesssim$15 au.

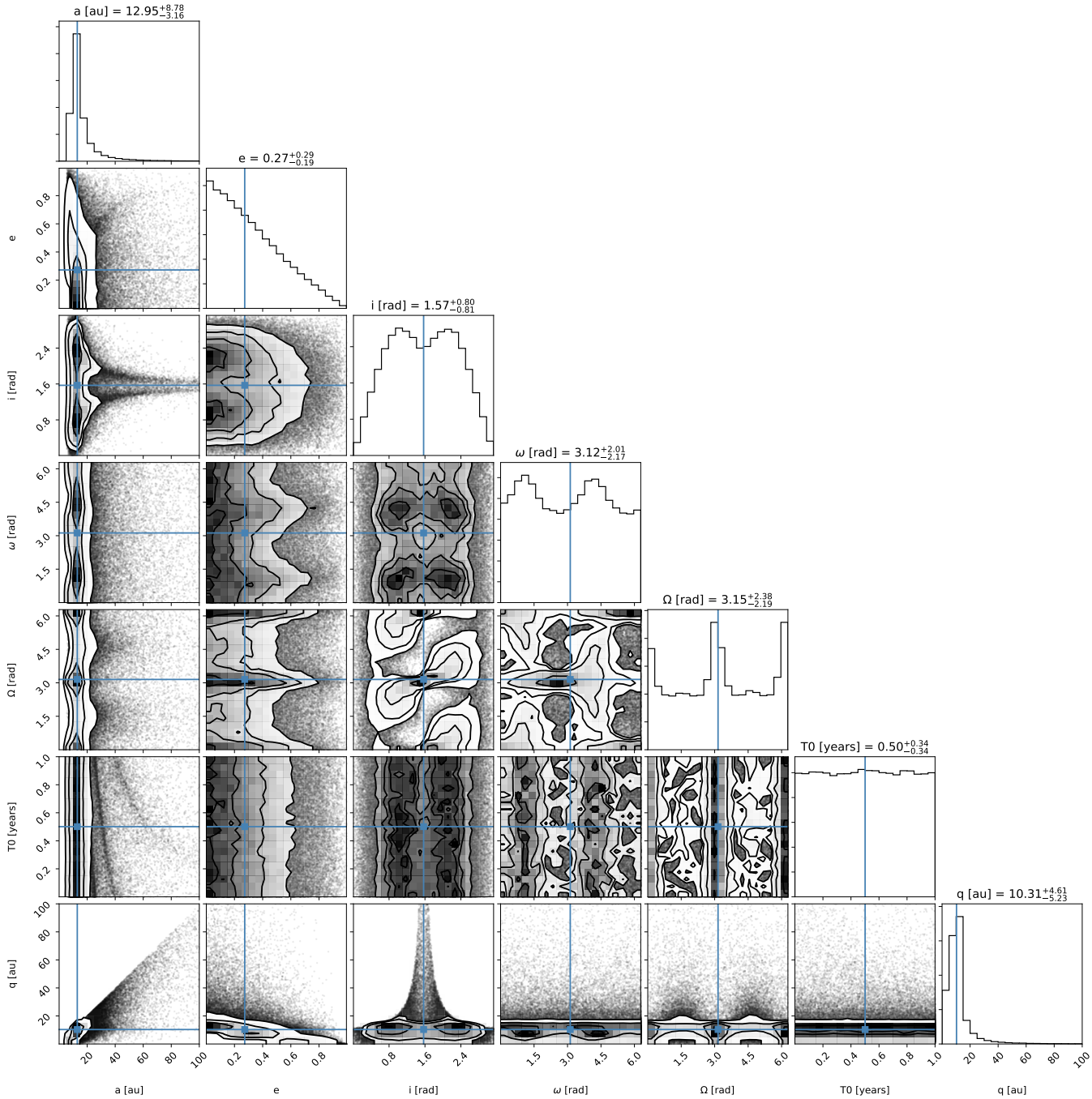

Fig. C.1. Posterior distribution function for the orbital parameters derived with the `orbitize` package using the OFTI implementation.

A.1.3 Spectral and orbital characterisation of the directly imaged giant planet HIP 65426 b

In Cheetham et al. (2019) we combined data from the SPHERE-SHINE survey with the NACO-ISPY survey to characterise the spectrum and orbit of the recently discovered exoplanet, HIP 65426 b, by Chauvin et al. (2017). By combining the data taken in the L' and M' bands by NACO, along with the SPHERE $Y-H$ band spectrum, we were able to better constrain the mass, temperature, radius, and surface gravity than previous estimates. We were able to obtain a mass estimate of $8 \pm 1 M_{\rm Jup}$, an effective temperature of 1618 ± 7 K, and place first constraints on the orbital period of 800^{+1200}_{-400} years. The full description is outlined in Cheetham et al. (2019) below.

A&A 622, A80 (2019)
https://doi.org/10.1051/0004-6361/201834112

Astronomy & Astrophysics

Spectral and orbital characterisation of the directly imaged giant planet HIP 65426 b⋆

A. C. Cheetham[1], M. Samland[2], S. S. Brems[3], R. Launhardt[2], G. Chauvin[4,5], D. Ségransan[1], T. Henning[2], A. Quirrenbach[3], H. Avenhaus[2], G. Cugno[6], J. Girard[7], N. Godoy[8,9], G. M. Kennedy[10], A.-L. Maire[2], S. Metchev[3,11,12], A. Müller[2], A. Musso Barcucci[2], J. Olofsson[8,9], F. Pepe[1], S. P. Quanz[6], D. Queloz[13], S. Reffert[3], E. Rickman[1], R. van Boekel[2], A. Boccaletti[14], M. Bonnefoy[4], F. Cantalloube[2], B. Charnay[14], P. Delorme[4], M. Janson[2,15], M. Keppler[2], A.-M. Lagrange[4], M. Langlois[16,17], C. Lazzoni[18], F. Menard[4], D. Mesa[18,19], M. Meyer[20], T. Schmidt[14], E. Sissa[18], S. Udry[1], and A. Zurlo[16,21,22]

(Affiliations can be found after the references)

Received 20 August 2018 / Accepted 18 December 2018

ABSTRACT

HIP 65426 b is a recently discovered exoplanet imaged during the course of the SPHERE-SHINE survey. Here we present new L' and M' observations of the planet from the NACO instrument at the VLT from the NACO-ISPY survey, as well as a new Y–H spectrum and K-band photometry from SPHERE-SHINE. Using these data, we confirm the nature of the companion as a warm, dusty planet with a mid-L spectral type. From comparison of its SED with the BT-Settl atmospheric models, we derive a best-fit effective temperature of $T_{\rm eff} = 1618 \pm 7$ K, surface gravity $\log g = 3.78^{+0.04}_{-0.03}$ and radius $R = 1.17 \pm 0.04\,R_{\rm J}$ (statistical uncertainties only). Using the DUSTY and COND isochrones we estimate a mass of $8 \pm 1\,M_{\rm J}$. Combining the astrometric measurements from our new datasets and from the literature, we show the first indications of orbital motion of the companion (2.6σ significance) and derive preliminary orbital constraints. We find a highly inclined orbit ($i = 107^{+13}_{-10}$ deg) with an orbital period of 800^{+1200}_{-400} yr. We also report SPHERE sparse aperture masking observations that investigate the possibility that HIP 65426 b was scattered onto its current orbit by an additional companion at a smaller orbital separation. From this data we rule out the presence of brown dwarf companions with masses greater than $16\,M_{\rm J}$ at separations larger than 3 AU, significantly narrowing the parameter space for such a companion.

Key words. stars: individual: HIP 65426 – planets and satellites: atmospheres – techniques: high angular resolution – planets and satellites: detection – planetary systems

1. Introduction

The number of exoplanets that can be studied through direct imaging is steadily growing (e.g. Macintosh et al. 2015; Chauvin et al. 2017a; Keppler et al. 2018), and each object can provide a wealth of information about their formation, evolution and atmospheres. For studies of giant planet atmospheres, the mid-infrared wavelength range covers a critical regime that is particularly sensitive to cloud properties, and contains strong molecular absorption bands from CH_4 and CO (Sharp & Burrows 2007). Since young giant planets still retain the heat of their formation, this wavelength range also offers favourable flux ratios between planet and host star. This has led to the majority of the directly imaged planets being discovered or studied in this wavelength range, particularly in the L-band (e.g. Chauvin et al. 2004; Marois et al. 2008, 2010; Lagrange et al. 2010; Rameau et al. 2013; Skemer et al. 2014; Macintosh et al. 2015; Müller et al. 2018). However, the increasing thermal background at longer wavelengths makes detections beyond the L-band much more difficult and only a few planets have published M-band photometry, including HR 8799 b,c,d (Galicher et al. 2011), β Pic b (Bonnefoy et al. 2013) and 51 Eri b (Rajan et al. 2017). JWST will be a critical tool for studying such objects at mid-infrared wavelengths, with the NIRCAM and MIRI instruments having high-contrast coronagraphic imaging capabilities across 1.8–25 μm (Krist et al. 2007; Boccaletti et al. 2015).

One planet that has yet to be studied in the mid-infrared is HIP 65426 b, recently discovered by the SHINE (SpHere INfrared survey for Exoplanets) survey utilising the SPHERE instrument at the VLT (Chauvin et al. 2017b). Analysis of its 1–2.3 μm spectrum shows a likely L5-L7 spectral type, effective temperature of $T_{\rm eff} = 1300$–1600 K, low surface gravity and a luminosity consistent with a 6–12 $M_{\rm J}$ planet. Given its placement in the mid-L spectral sequence, it provides an important opportunity to study the atmospheric physics of young giant planets in a regime where complex cloud/dust physics and non-equilibrium chemistry play key roles (e.g. Galicher et al. 2011; Skemer et al. 2014; Currie et al. 2014). This object is also a primary target of a JWST Early Release Science program (Hinkley et al. 2017), which will provide additional photometry in the near- and mid-infrared.

In this paper, we present the results of new mid-infrared imaging taken during the ISPY survey (Imaging Survey for Planets around Young stars; Launhardt et al. 2018, in prep.) with the NACO instrument at the VLT, as well as new near-infrared coronagraphic and Sparse Aperture Masking (SAM) observations obtained with SPHERE. We adopt the stellar parameters of HIP 65426 from Chauvin et al. (2017a). In particular we assume

⋆ Based on observations collected at the European Organisation for Astronomical Research in the Southern Hemisphere under ESO programmes 199.C-0065 (PI: Launhardt), 198.C-0209 (PI: Beuzit) and 1100.C-0481 (PI: Beuzit).

Table 1. Observing log.

UT Date	Instrument	Filter	NDIT[a] × DIT[b] (s)	NDIT[a] × DIT[b] (Flux[c]) (s)	$\Delta\pi^d$ (°)	True North (°)	Pixel scale (mas pixel^{-1})
2017-05-18	NACO	L'	30 114 × 0.2	2400 × 0.1	113	−0.44 ± 0.10	27.20 ± 0.05
2017-05-19	NACO	M'	71 200 × 0.05	2400 × 0.04	96	−0.44 ± 0.10	27.20 ± 0.05
2017-05-03	SPHERE-IFS	Y–H + SAM	384 × 4		49.5	1.78 ± 0.05	7.46 ± 0.02
2017-05-03	SPHERE-IRDIS	K_1 + SAM	720 × 2		49.5	1.78 ± 0.05	12.267 ± 0.01
2017-05-03	SPHERE-IRDIS	K_2 + SAM	720 × 2		49.5	1.78 ± 0.05	12.263 ± 0.01
2018-05-12	SPHERE-IFS	Y–H	40 × 96	47 × 2	31.7	1.76 ± 0.06	7.46 ± 0.02
2018-05-12	SPHERE-IRDIS	K_1	40 × 96	101 × 0.84	31.7	1.76 ± 0.06	12.267 ± 0.01
2018-05-12	SPHERE-IRDIS	K_2	40 × 96	101 × 0.84	31.7	1.76 ± 0.06	12.263 ± 0.01

Notes. [(a)]NDIT refers to the total number of integrations. [(b)]DIT refers to the integration time of each image. [(c)]Flux refers to the sequence of images taken to measure the number of detector counts and PSF shape of the primary star. [(d)]$\Delta\pi$ is the maximum change in parallactic angle during the sequence.

a solar metallicity, an effective temperature of 8840 ± 200 K estimated from HARPS spectroscopy, as well as a primary mass of 1.96 ± 0.04 $M_\odot$ and age of 14 ± 4 Myr from comparison of isochrones with the photometry of HIP 65426 and that of neighbouring stars. However, we update its parallax and distance using the results of the *Gaia* DR2 (Gaia Collaboration 2016, 2018). This yields a distance of 109.2 ± 0.7 pc (c.f. 111.4 ± 3.8 pc from Chauvin et al. 2017a), and an updated projected separation for the companion of 90 AU.

2. Observations and data analysis

2.1. NACO imaging

HIP 65426 was observed as part of the NACO-ISPY survey (Launhardt et al. 2018, in prep) on 2017-05-18 and 2017-05-19 using the L' (3.8 μm) and M' (4.8 μm) filters respectively of the NACO instrument (Lenzen et al. 1998; Rousset et al. 2003). The majority of our observing time consisted of short exposure images with no coronagraph, dithering the star between 3 quadrants of the NACO detector[1]. Despite the short integration time, the stellar PSF was partially saturated on the detector in L'. More details of the observing sequence can be found in Table 1. We also acquired a separate set of shorter exposure images to measure the stellar flux at the beginning and end of the sequence.

The data were reduced independently using the GRAPHIC (Hagelberg et al. 2016), PynPoint (Amara & Quanz 2012), and IPAG-ADI (Chauvin et al. 2012) packages. These pipelines follow similar approaches for data cleaning. Similar results were obtained, and so we report the results of the GRAPHIC pipeline. Briefly, first the frames were sky subtracted using principal component analysis (PCA) following the approach of Hunziker et al. (2018). The position of the star was then measured in each frame by fitting a Gaussian profile. We then compared the fitted parameters (amplitude, position and width) across the observing sequence and removed outliers more than 5 median absolute deviations from the median of each parameter. Frames were shifted to be centred on the star using Fourier transforms. The cleaned datacubes were then PSF (point spread function) subtracted using PCA (Soummer et al. 2012; Amara & Quanz 2012). The cleaning procedure was also performed on the unsaturated, shorter exposure images to measure the stellar flux and as a reference for the unsaturated PSF shape.

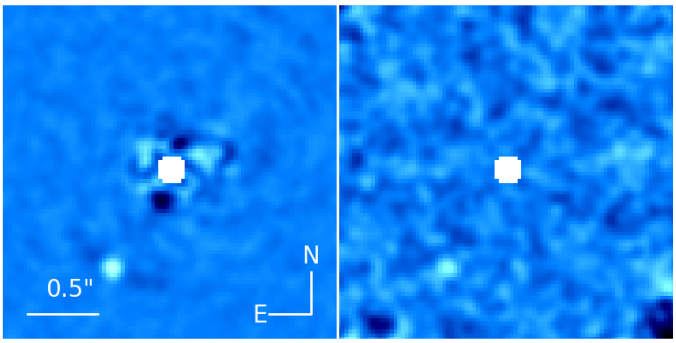

Fig. 1. Final PSF-subtracted images from the two NACO datasets in L' (*left panel*) and M' (*right panel*). The companion is detected in both datasets. While we find a lower contrast ratio in M', the high thermal background leads to a lower overall SNR.

For the GRAPHIC reduction, the data were first binned in groups of 126 frames for the L' data and groups of 200 frames for the M' data. PCA was applied to annular sections of the image, each with a width of 2 $FWHM$ (full width at half maximum, measured from the stellar PSF). For each frame, a reference library was constructed using only those frames where the field rotation was large enough for a companion to have moved by 0.75 $FWHM$. 30% of the available PCA modes were then subtracted from the data. The PSF-subtracted frames were then derotated using Fourier transforms (Larkin et al. 1997) and median-combined to produce the final images in Fig. 1.

To extract the astrometry and photometry of the companion, we used the negative PSF injection technique (Lagrange et al. 2010). For each set of parameters, we inject a negative copy of the unsaturated PSF into the raw frames with the appropriate position and flux. We then calculate the likelihood from the residuals in a small (10 pixel) box around the companion position. We assume Gaussian distributed residuals with a standard deviation measured from the values in an annulus at the same separation taken from the initial reduction, after masking out the companion. The same values were used to verify the Gaussianity with a one-sided Kolmogorov–Smirnov test ($D = 0.022$, $p = 0.45$ and $D = 0.019$, $p = 0.56$ for L' and M', respectively). The likelihood was measured on a grid of parameters around the best-fit position, and we extracted the uncertainties from the marginal likelihood distribution of each parameter.

[1] We avoided the detector quadrant with persistent striping present since the recommissioning of NACO in 2014–2015. This quadrant is in the lower left, containing pixel (0,0).

Table 2. Measured photometry of HIP 65426 b and derived masses.

Instrument	Filter	Δmag	App. mag	Abs. mag	App. flux ($Wm^{-2}\mu m^{-1}$)
SPHERE	H_2	11.14 ± 0.05	17.94 ± 0.05	12.75 ± 0.05	$(8.6 \pm 0.4) \times 10^{-17}$
SPHERE	H_3	10.78 ± 0.06	17.58 ± 0.06	12.39 ± 0.06	$(10.1 \pm 0.6) \times 10^{-17}$
SPHERE	K_1	10.19 ± 0.10	17.01 ± 0.09	11.82 ± 0.09	$(7.5 \pm 0.6) \times 10^{-17}$
SPHERE	K_2	9.82 ± 0.10	16.79 ± 0.09	11.60 ± 0.09	$(7.1 \pm 0.6) \times 10^{-17}$
NACO	L'	8.47 ± 0.14	15.26 ± 0.15	10.07 ± 0.15	$(4.1 \pm 0.5) \times 10^{-17}$
NACO	M'	8.2 ± 0.4	15.1 ± 0.5	9.9 ± 0.5	$(2.1 \pm 0.8) \times 10^{-17}$

In addition to the uncertainties resulting from the fit, we explored the effect of different PCA parameters, varying the protection angle between 0.5–1.5 $FWHM$ and the number of PCA modes from 10 to 40% of the number of binned frames. The scatter of the best-fit values was added in quadrature to our astrometric and photometric uncertainties. We also added an additional term to the photometric uncertainty (13% in L' and 3% in M') due to the change in flux of the primary star measured during the short-exposure sequence at the start and end of the observing sequence, caused by variations in the observing conditions and adaptive optics correction. The larger variation seen in L' was caused by the presence of thin clouds during the sequence.

To verify the robustness of the uncertainties calculated from this approach, we injected synthetic companions using the PSF of another star observed during the same night. First, we used the best-fit parameters of HIP 65426 b to remove the companion from the data and generate a clean datacube. We then injected companions with randomly drawn parameters, using fluxes and separations centred on that of HIP 65426 b, and with random position angles. For each iteration we performed the same procedure to measure the parameters of the injected companion. This was repeated 50 times for each filter. We then calculated the difference between the injected and measured parameters. The root-mean-square of these residuals were within 10% of our uncertainties for HIP 65426 b, and so we conclude that they are representative of our measurement accuracy.

To convert the contrast measurements of HIP 65426 b to physical fluxes we produced a synthetic spectrum by scaling a BT-NextGen spectrum (Allard et al. 2012) with an effective temperature $T_{\rm eff} = 8800$ K, surface gravity $\log g = 4.5$ and solar metallicity to the photometry of HIP 65426 compiled from 2MASS, *Tycho*-2, HIPPARCOS and WISE (Skrutskie et al. 2006; Høg et al. 2000; van Leeuwen 2007; Wright et al. 2010). The contrast ratio measurements were then multiplied by the predicted flux of the primary star in each filter. We then used the *Gaia* DR2 distance of 109.2 ± 0.7 pc (Gaia Collaboration 2016, 2018) to convert to absolute flux, with the results given in Table 2.

2.2. SPHERE coronagraphic imaging

As part of the SHINE exoplanet survey (Chauvin et al. 2017b), HIP 65426 was re-observed on 2018-05-12 with deep coronagraphic imaging to improve the Y–H spectrum and K-band photometry of the companion, and to monitor its relative astrometry. We used the infrared dual-band imager and spectrograph (IRDIS; Dohlen et al. 2008) and integral field spectrograph (IFS; Claudi et al. 2008) modules of SPHERE (Beuzit et al. 2008). Data were obtained using the IRDIFS_EXT mode. In this configuration, IRDIS and IFS operate simultaneously, with IRDIS in dual-band imaging mode (Vigan et al. 2010) using the K_1 and K_2 filters (2.100 and 2.251 μm, respectively) and IFS covering the Y–H bands (0.96–1.64 μm).

The data processing follows the same procedure as in Chauvin et al. (2017a). The data were first cleaned using the SPHERE Data Reduction and Handling (DRH) pipeline (Pavlov et al. 2008), consisting of background subtraction, flat fielding and extraction of the spectral data cube. Additional cleaning steps for IFS were performed using the routines described in Mesa et al. (2015), consisting of bad pixel correction, spectral cross-talk correction and an improved wavelength calibration procedure.

The SpeCal pipeline (Galicher et al. 2018) was used to perform the starlight subtraction and companion analysis. The TLOCI (Marois et al. 2014) algorithm was used to perform the starlight subtraction, and we used the PSF model approach described in Galicher et al. (2018) to measure the companion position and flux in each filter.

2.3. SPHERE aperture masking

During the SHINE survey, HIP 65426 was also observed with the sparse aperture mask (SAM) mode of SPHERE (Cheetham et al. 2016) on 2017-05-03, using a 7-hole mask. This mode turns the telescope pupil into an interferometric array, allowing the use of observables such as the closure phase (Jennison 1958) that are robust to optical aberrations. This results in SAM being a useful technique for studying high-contrast structure or companions at small angular separations that would otherwise be inaccessible. While it was expected that HIP 65426 b would not be detectable with SAM due to the large separation and high contrast, the data were obtained to search for additional companions that would be undetectable with other techniques. The observations were taken with the IRDIFS_EXT mode, the same filter combination as the coronagraphic imaging data. Further details of the observing sequence can be found in Table 1.

To clean the data, a different approach was taken for the IFS and IRDIS modules. The IFS data were cleaned using the same approach as the SPHERE coronagraphic data, while the IRDIS data were cleaned using a custom set of *IDL* routines consisting of background subtraction, flat fielding and bad pixel correction.

The cleaned datacubes were processed with a similar procedure to that outlined in Tuthill et al. (2000) and Kraus et al. (2008), with modifications made to deal with multi-wavelength data (39 channels for IFS and 2 for IRDIS). Briefly, images were centred and windowed with a super-Gaussian function to limit sensitivity to read-noise. Closure phases were then measured from the Fourier transforms of the images, and calibrated using a weighted sum of those measured on the reference star HD 116664, which was observed alternately with HIP 65426

Table 3. Measured astrometry of HIP 65426 b.

UT Date	Instrument	Filter	ρ (mas)	ρ (AU)	θ (deg)	Reference
2016-05-30	SPHERE	H_2	830.4 ± 4.9	90.7 ± 0.8	150.28 ± 0.22	Chauvin et al. (2017a)
2016-06-26	SPHERE	H_2	830.1 ± 3.2	90.7 ± 0.7	150.14 ± 0.17	Chauvin et al. (2017a)
2017-02-07	SPHERE	H_2	827.6 ± 1.5	90.4 ± 0.6	150.11 ± 0.15	Chauvin et al. (2017a)
2017-02-09	SPHERE	K_1	828.8 ± 1.5	90.5 ± 0.6	150.05 ± 0.16	Chauvin et al. (2017a)
2017-05-18	NACO	L'	832 ± 3	90.8 ± 0.7	149.52 ± 0.19	This work
2017-05-19	NACO	M'	850 ± 20	93 ± 2	148.5 ± 1.6	This work
2018-05-12	SPHERE	K_1	822.9 ± 2.0	89.9 ± 0.6	149.85 ± 0.15	This work
2018-05-12	SPHERE	K_2	826.4 ± 2.4	90.2 ± 0.6	149.89 ± 0.16	This work

during the same sequence. Correlations between wavelengths (for both IFS and IRDIS) were not considered in this analysis, and so the detection limits are expected to be slightly optimistic.

To determine the limits for companion detection, a Monte-Carlo approach was taken. We generated 10 000 simulated closure phase datasets using the measured uncertainties. For each combination of separation, contrast and position angle on a grid of values, we counted the number of non-detections, defined as those simulations where a point source model fit the data better than the corresponding binary model. After marginalising over position angle, we calculated 3.3σ detection limits for each separation as the contrast at which 99.9% of noise simulations result in a non-detection. These were then converted to 5σ limits for consistency with the NACO and SPHERE imaging data.

3. Results

3.1. Astrometry

To calibrate the NACO data, we compared L' observations of an astrometric reference field in 47 Tuc taken on 2017-05-19 to the catalog of McLaughlin et al. (2006), resulting in the pixel scale and True North offset reported in Table 1. The final measured astrometry of HIP 65426 b is given in Table 3. The measured NACO L' separation of 832 ± 3 mas corresponds to a projected physical separation of 90.9 ± 0.7 AU using the updated distance to HIP 65426. For the SPHERE coronagraphic imaging data, we used the astrometric calibration scheme outlined in Maire et al. (2016a), with the pixel scale and True North offset also reported in Table 1.

Between the SPHERE epochs, we see the first indications of orbital motion, with the observed position changing consistently in the same direction and a maximum of 2.6σ deviation between the datapoints. To investigate the orbital parameters consistent with the observed motion, we used the Orbits for the Impatient (OFTI) method of Blunt et al. (2017), based on Bayesian rejection sampling. We applied uniform priors in the epoch of periastron passage T_0 and argument of periastron ω, a $\sin i$ prior in inclination i, and a linearly decreasing prior in the eccentricity e based on the results of Nielsen et al. (2008). To choose the semi-major axis a and position angle of nodes Ω, a single datapoint was chosen randomly and sampled with its given uncertainties, and the orbit scaled and rotated to pass through this point. The period was then calculated assuming a primary mass of $1.96\,M_\odot$. Each parameter set was accepted or rejected by comparing its likelihood to a number randomly drawn from a uniform probability distribution over the range (0,1). This process was repeated until 10 000 orbits had been selected, from which we derived our posterior distributions. As in Blunt et al. (2017), we increased the fraction of accepted orbits by normalising the likelihood function by the maximum likelihood found from an initial run of the algorithm. We find a 0.5° offset in position angle between the NACO and SPHERE datasets taken in 2017, much larger than the expected change due to orbital motion and inconsistent with the 2016 and 2018 SPHERE measurements. Similar systematic offsets have been found in other datasets, and may originate from the different choice of astrometric reference fields and star catalogs used for the two instruments. To avoid any problems this may cause, we used only the SPHERE epochs to calculate the likelihood of potential orbits. In addition, we used only the astrometry measured in the IRDIS H_2 and K_1 filters, leading to 5 datapoints.

A sample of the resulting orbits are shown in Fig. 2, while the full posterior distributions are shown in Fig. 3. From the posterior distributions, significant constraints can be placed on several of the orbital parameters, and the measured values are given in Table 4. We find an orbital period of $\log(P[d]) = 5.51^{+0.37}_{-0.25}$ ($P = 800^{+1200}_{-400}$ yr), implying a semi-major axis of $a = 110^{+90}_{-30}$ AU. Orbits close to edge-on are preferred, with a peak at $i = 107^{+13}_{-10}$. While the $\sin i$ prior favours highly inclined orbits, the posterior distribution is significantly narrower than the distribution of generated orbits, showing that the inclination measurement is not dominated by the prior. Two families of solutions are found, with consistent parameters except for a 180° change in both Ω and ω. This corresponds to our lack of knowledge as to whether HIP 65426 b is moving towards or away from us on its orbit. Due to the short time baseline compared to the orbital period and the lack of curvature in the observed motion, the eccentricity is essentially unconstrained, with the posterior distribution reflecting the linear prior used to draw sample orbits. Since we used a linear prior, the peak occurs at $e = 0$ and we instead express the eccentricity as a 1σ upper limit ($e < 0.43$). In addition, the orbital eccentricity shows significant correlations with several other parameters, with high eccentricity solutions preferring larger inclinations and shorter periods, for example. A different choice of prior would impact many of the orbital parameters.

3.2. Atmospheric models

To estimate the physical parameters of HIP 65426 b we compared the observed spectrum to atmospheric models. We used the Markov chain Monte Carlo procedure described in Samland et al. (2017) to explore the likelihood distribution, interpolating the grid of spectral models at each step.

When comparing to the BT-Settl models (Baraffe et al. 2015), we found best-fit values similar to those of Chauvin et al. (2017a), with $T_{\rm eff} = 1618 \pm 7$ K, $\log g = 3.78^{+0.04}_{-0.03}$ dex and radius $R = 1.17 \pm 0.04\,R_{\rm J}$. This model is compared to the observed SED (spectral energy distribution) of HIP 65426 b in Fig. 4.

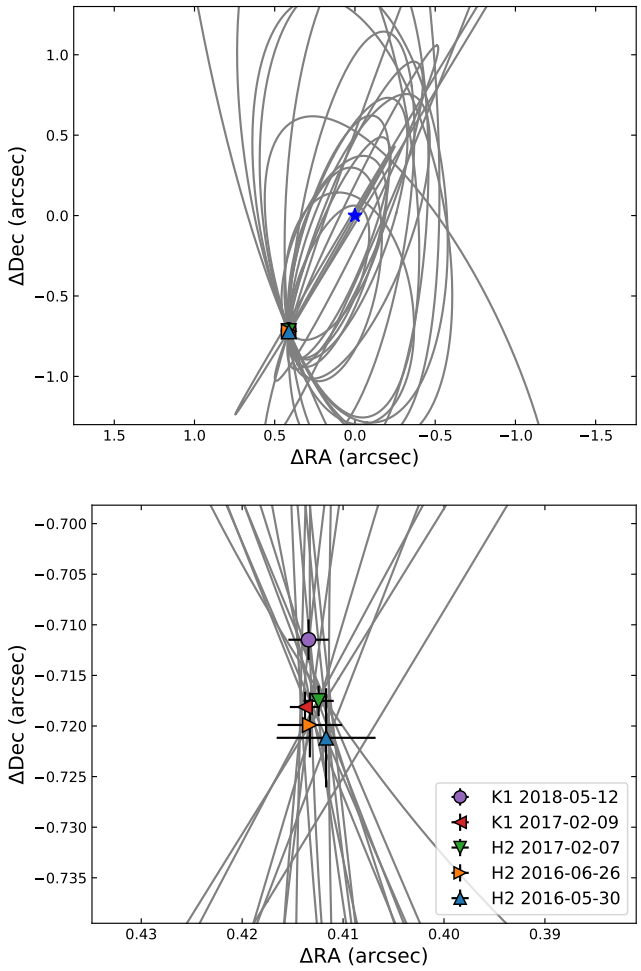

Fig. 2. Observed SPHERE-IRDIS astrometry of HIP 65426 b compared to 20 orbits drawn randomly from the 250 best-fitting orbits in the OFTI output sample. The position of the primary star is shown with a blue star. A close up of the region around the present position of HIP 65426 b is shown separately in the bottom plot.

Combining the temperature and radius measurements results in a luminosity estimate for HIP 65426 b of $\log(L/L_\odot) = -4.05 \pm 0.03$, while the radius and surface gravity produce a mass esimate of $M = 3.32 \pm 0.4\,M_J$. The listed uncertainties are optimistic, since they do not account for uncertainties in the modelling of these objects, and different models are likely to show systematic differences in the measured parameters that are larger than the given uncertainties. A number of free parameters are also not included in this analysis, including metallicity and cloud properties, that may impact the results.

We repeated the same procedure as above using the cloudy atmosphere petitCODE models, described in Mollière et al. (2017). We found that the best-fit solution converged to low temperatures (~1200 K) with unphysically large radii ($>2\,R_J$), although a second likelihood peak at higher temperatures (~1800 K) provided a similar fit to the data with different physical parameters. This set of models failed to simultaneously reproduce the shape of the J-band peak and the K-band flux, and so we concentrate on the BT-Settl results.

3.3. Empirical comparison

Using the measured photometry, we placed HIP 65426 b on colour–colour and colour-magnitude diagrams. We compiled spectra of field dwarfs from Leggett et al. (2010), the IRTF spectral library of M, L and T dwarfs (Cushing et al. 2005; Rayner et al. 2009) and the SpeX Prism Library (Burgasser 2014). For targets where no parallax or distance was provided, we used the Database of Ultracool Parallaxes maintained by Trent Dupuy (Dupuy & Liu 2012; Dupuy & Kraus 2013) and the results of Dahn et al. (2017), where available. We also included photometry from Dupuy & Liu (2012). For targets without L' magnitudes, we converted WISE W1 (3.5 μm) absolute magnitudes to L' (3.8 μm) absolute magnitudes using a relation calculated from a linear fit to the targets with photometry in both bands. To compare the photometry of HIP 65426 b with those of other young targets, we included a range of directly imaged companions from the literature (Chauvin et al. 2004; Bonnefoy et al. 2013, 2016; Mawet et al. 2015; Lagrange et al. 2016; Maire et al. 2016b; Mesa et al. 2016; Rajan et al. 2017; Cheetham et al. 2018).

From the colour-magnitude diagrams in Fig. 5, we can see that HIP 65426 b occupies a similar position to mid-late L-dwarfs. HIP 65426 b is redder and more luminous than the sequence of field dwarfs with similar spectral types. This property is typical for young field dwarfs (Faherty et al. 2012; Liu et al. 2013), which contract and cool over time.

The position of HIP 65426 b on colour-magnitude diagrams is similar to that of PDS 70 b (Keppler et al. 2018; Müller et al. 2018). At wavelengths longer than 1.4 μm, their absolute magnitudes are similar. However, HIP 65426 b is significantly brighter in the J-band and displays systematically bluer colours than PDS 70 b, suggesting a higher temperature. Given that PDS 70 is also significantly younger than HIP 65426 (~5 and ~14 Myr, respectively; Keppler et al. 2018; Chauvin et al. 2017a), the mass of HIP 65426 b is expected to be larger.

Compared to other planetary-mass companions, HIP 65426 b sits clearly between the early L-dwarfs (e.g. β Pic b and HD 106906 b) and the L/T transition objects (e.g. HR 8799 c,d,e and 2M 1207 b). Together, these targets will be useful to study the atmospheric properties of young giant exoplanets across the L spectral sequence.

3.4. Mass

To estimate the mass of HIP 65426 b, we compared the predictions of the DUSTY (Chabrier et al. 2000) and COND (Baraffe et al. 2003) isochrones to the absolute magnitudes presented in Table 2. We used a Monte Carlo procedure to include the uncertainty on the age of the HIP 65426 system, drawing 10 000 samples from a Gaussian distribution consistent with the estimated age of 14 ± 4 Myr. We interpolated the isochrones at each age and found the mass that gave the best match to the observed photometry, and took the median and standard deviation of these values as the mass and its uncertainty. With this method, the majority of samples fall below the minimum mass on the DUSTY model grid of 7.3 M_J, and so we estimate a 1σ upper limit of 8.4 M_J. From the COND models we estimate a mass of $7.5 \pm 0.9\,M_J$.

We also used the luminosity estimated from the BT-SETTL model fit of $\log(L/L_\odot) = -4.05 \pm 0.03$, with the estimated age of 14 ± 4 Myr. We find values of $8.2 \pm 1.1\,M_J$ and $8.3 \pm 0.9\,M_J$ for the DUSTY and COND grids respectively.

We find that the colours of HIP 65426 b are systematically redder than those predicted by the COND isochrones. When placed on a range of colour-magnitude diagrams, such as the one in Fig. 6, the position of HIP 65426 b falls closer to the DUSTY tracks, suggesting the dusty nature of the companion.

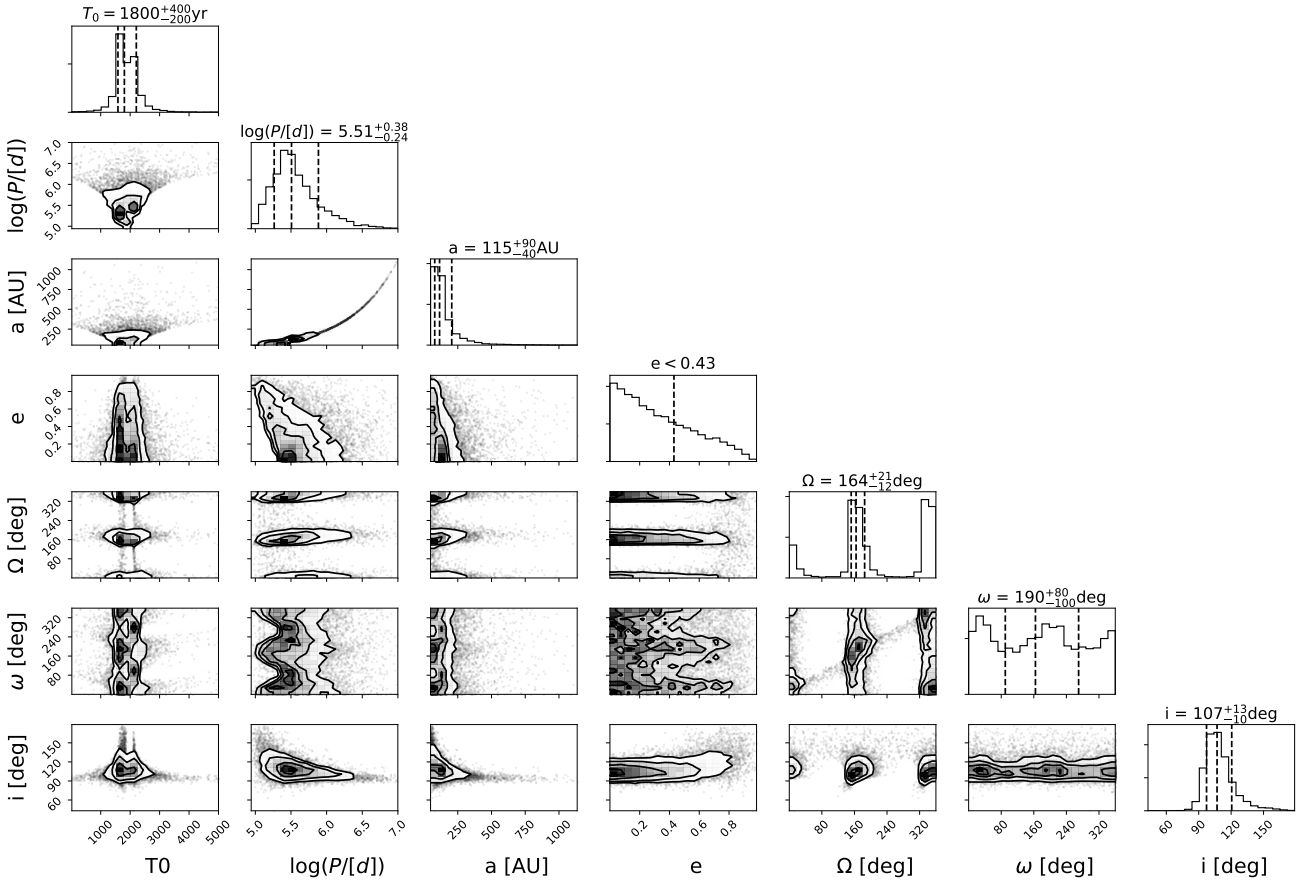

Fig. 3. Posterior distributions for the orbital parameters of HIP 65426 b around its host star. The dotted lines show the median value and 1σ uncertainties for each parameter. For Ω and ω, the value and uncertainties of one of the two solution families is plotted with a dotted line. For the eccentricity e, only the 1σ limit is plotted.

Table 4. Measured orbital parameters of HIP 65426 b.

Parameter	Solution family 1	Solution family 2
log(P[d])	$5.51^{+0.37}_{-0.25}$	$5.50^{+0.38}_{-0.23}$
a (AU)	120^{+90}_{-40}	110^{+90}_{-30}
T_0 (yr)	1800^{+400}_{-200}	1800^{+400}_{-200}
e	<0.43	<0.43
Ω(°)	164^{+21}_{-12}	344^{+20}_{-12}
ω(°)	190^{+80}_{-100}	20^{+80}_{-90}
i(°)	107^{+13}_{-10}	107^{+13}_{-10}

An in-depth comparison of the photometry of HIP 65426 b with the BERN exoplanet cooling models by Marleau et al. (2019) resulted in mass estimates of $11.1^{+1.1}_{-2.2}$ M_J and $10.4^{+0.6}_{-2.6}$ M_J for their cold-start and hot-start simulations, suggesting a higher mass than the COND and DUSTY models.

3.5. Limits on further companions

We detect no additional companions in the NACO or SPHERE data. The SPHERE SAM detection limits probe a new parameter space not explored by Chauvin et al. (2017a). The 5σ detection limits are displayed in Fig. 7. Combining the detection limits with the DUSTY isochrones, we can rule out objects with masses larger than 20 M_J at separations of >2 AU, and 16 M_J at >3 AU, with a significance of 5σ.

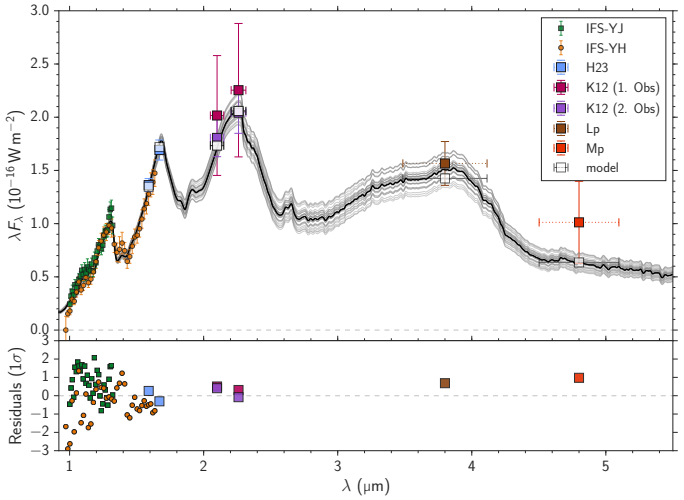

Fig. 4. Observed spectrum of HIP 65426 b (coloured squares) compared to the best-fit spectral model from the BT-Settl grid, with $T_{\rm eff}$ = 1618 K, log g = 3.78 and R = 1.17 R_J. The horizontal error bars show the width of the SPHERE and NACO filters, and the grey squares show the predicted flux calculated using the filter transmission curves. Several models drawn from the MCMC posterior distributions are also shown in grey.

4. Summary and conclusions

In this paper we have presented the first L' and M' images of the planetary companion HIP 65426 b, extending the coverage

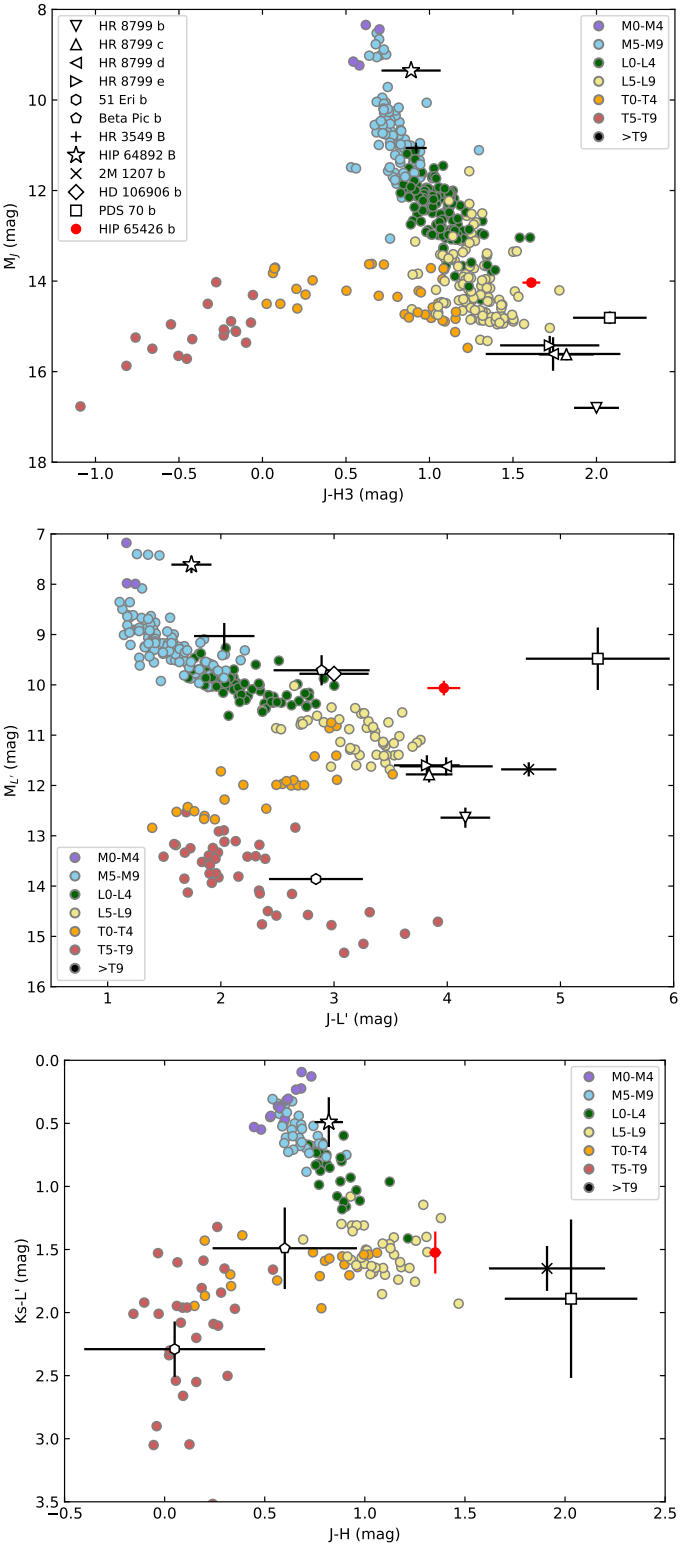

Fig. 5. Colour-magnitude and colour–colour diagrams showing the sequence of field dwarfs (coloured circles), a range of young, imaged brown dwarf and exoplanet companions (black symbols) and HIP 65426 b (red circle). HIP 65426 b falls near objects with mid-L spectral types, but is more luminous and with redder colours than the field sequence. This matches the trend seen for other young objects with similar spectral type.

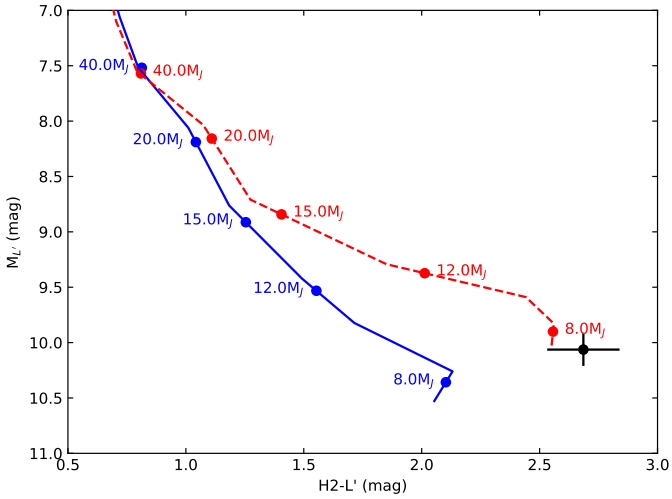

Fig. 6. Colour-magnitude diagram showing the COND (blue) and DUSTY (red) evolutionary models compared to HIP 65426 b. We find that the colours of HIP 65426 b match the DUSTY models more closely than the COND predictions.

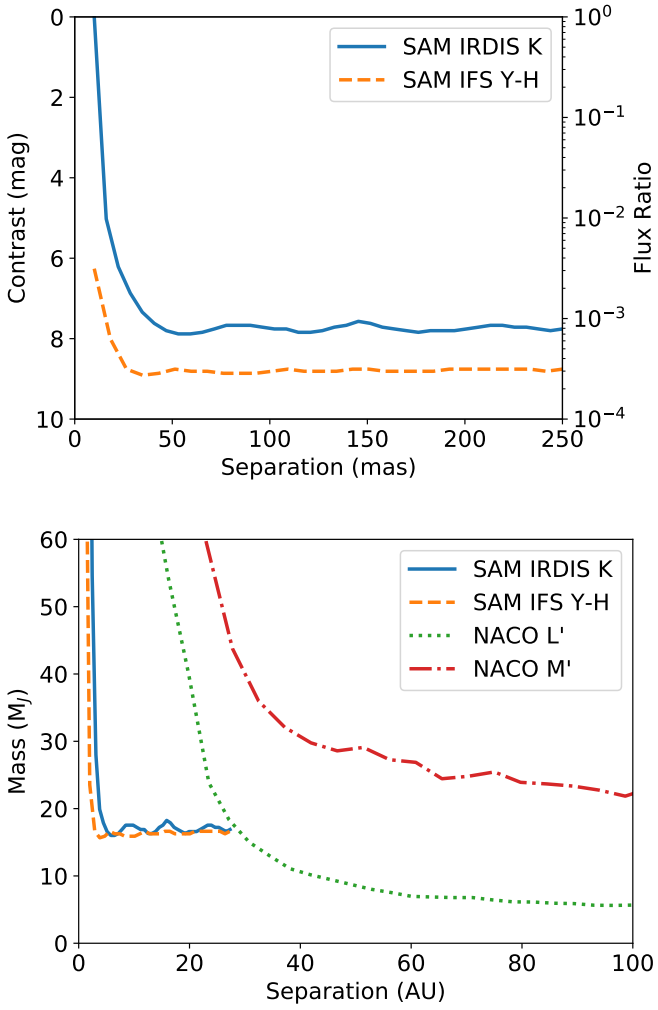

Fig. 7. Detection limits on further companions around HIP 65426. *Top panel*: detection limits from the SPHERE-SAM data in contrast and angular separation. *Bottom panel*: mass limits for the SPHERE-SAM and NACO data expressed as projected physical separations. The limits in contrast were converted to masses using the DUSTY isochrones.

of its SED to the mid-infrared. The photometry extracted from these data are consistent with the conclusions of Chauvin et al. (2017a), confirming the nature of HIP 65426 b as a dusty, warm giant planet with a mid-L spectral type. Through comparison with the BT-Settl models, we find best-fit values of $T_{\rm eff} = 1618$ K, surface gravity of $\log g = 3.78$ and radius of $R = 1.17\,R_{\rm J}$. The observed SED is not fit well by the cloudy petitCODE models, with the grid unable to simultaneously reproduce the features seen at the J and K bands. Using the new thermal-infrared photometry, we update the estimated mass of HIP 65426 b, yielding a value of $8 \pm 1\,M_{\rm J}$ from the DUSTY and COND isochrones. Among these two models, we find that its colours more closely match the predictions of the DUSTY models. This mass estimate is consistent with the results of Marleau et al. (2019) using the Bern exoplanet cooling models.

From the two-year time baseline between datasets, we have obtained the first indications of orbital motion of HIP 65426 b. We performed a preliminary orbital fit, with the present data preferring a close to edge-on orbit ($i = 107^{+13}_{-10}$) with an orbital period of $P = 800^{+1200}_{-400}$ yr. Due to the large orbital period, a significantly longer time baseline will be needed for a full determination of its orbital parameters.

By placing HIP 65426 b on colour-magnitude and colour–colour diagrams, we show that it fits in the sequence of other young giant planets. It displays redder colours and a higher luminosity than the field sequence, a trend typical of young, low gravity, and dusty objects. Amongst the other imaged planets, the recently discovered object PDS 70 b provides a close match to the observed spectrum of HIP 65426 b and may be a useful analog. These objects join a growing number of planetary-mass objects with L spectral types that have now been imaged. Given that low-surface gravity objects are expected to have cloud layers higher in their atmospheres (Marley et al. 2012), the L-T transition occurs at lower effective temperatures in young planets than field brown dwarfs. In this context, HIP 65426 b is an important object for understanding the atmospheric physics of young giant planets across the L spectral type where clouds are thought to play an important role, and for comparing their properties to that of the better-understood field brown dwarfs.

As discussed in Chauvin et al. (2017a), the large separation of HIP 65426 b and its high mass are not consistent with in situ formation via core accretion. However, the authors raised the possibility that it may have formed at a much smaller separation and experienced a scattering event with another companion, leading to its present wide orbit. This scenario was explored in detail by Marleau et al. (2019), who found that planet–planet scattering remains a viable pathway to produce objects like HIP 65426 b. Our SPHERE-SAM observations significantly narrow the parameter space for an additional massive object to occupy, ruling out the presence of $>16\,M_{\rm J}$ brown dwarf companions at projected separations of >3 AU. However, the current observations cannot discount the scenario of scattering caused by one or more additional giant planets on shorter-period orbits interior to that of HIP 65426 b.

Acknowledgements. This work has been carried out within the frame of the National Centre for Competence in Research "PlanetS" supported by the Swiss National Science Foundation (SNSF). A.M. acknowledges the support of the DFG priority program SPP 1992 "Exploring the Diversity of Extrasolar Planets" (MU 4172/1-1). J.O. and N.G. acknowledge financial support from the ICM (Iniciativa Científica Milenio) via the Núcleo Milenio de Formación Planetaria grant. J.O. acknowledges financial support from the Universidad de Valparaíso, and from Fondecyt (grant 1180395). A.Z. acknowledges support from the CONICYT + PAI/ Convocatoria nacional subvención a la instalación en la academia, convocatoria 2017 + Folio PAI77170087. N.G. acknowledges support from project CONICYT-PFCHA/Doctorado Nacional/2017 folio 21170650.

SPHERE is an instrument designed and built by a consortium consisting of IPAG (Grenoble, France), MPIA (Heidelberg, Germany), LAM (Marseille, France), LESIA (Paris, France), Laboratoire Lagrange (Nice, France), INAF – Osservatorio di Padova (Italy), Observatoire Astronomique de l'Université de Genève (Switzerland), ETH Zurich (Switzerland), NOVA (Netherlands), ONERA (France), and ASTRON (Netherlands) in collaboration with ESO. SPHERE was funded by ESO, with additional contributions from CNRS (France), MPIA (Germany), INAF (Italy), FINES (Switzerland), and NOVA (Netherlands). SPHERE also received funding from the European Commission Sixth and Seventh Framework Programmes as part of the Optical Infrared Coordination Network for Astronomy (OPTICON) under grant number RII3-Ct-2004-001566 for FP6 (2004-2008), grant number 226604 for FP7 (2009-2012), and grant number 312430 for FP7 (2013-2016). This work has made use of the SPHERE Data Centre, jointly operated by OSUG/IPAG (Grenoble), PYTHEAS/LAM/CeSAM (Marseille), OCA/Lagrange (Nice), and Observatoire de Paris/LESIA (Paris) and supported by a grant from Labex OSUG@2020 (Investissements d'avenir - ANR10 LABX56). This publication makes use of data products from the Two Micron All Sky Survey, which is a joint project of the University of Massachusetts and the Infrared Processing and Analysis Center/California Institute of Technology, funded by the National Aeronautics and Space Administration and the National Science Foundation. This research has benefitted from the SpeX Prism Spectral Libraries, maintained by Adam Burgasser at `http://pono.ucsd.edu/~adam/browndwarfs/spexprism`. This work has made use of data from the European Space Agency (ESA) mission *Gaia* (`https://www.cosmos.esa.int/gaia`), processed by the *Gaia* Data Processing and Analysis Consortium (DPAC, `https://www.cosmos.esa.int/web/gaia/dpac/consortium`). Funding for the DPAC has been provided by national institutions, in particular the institutions participating in the *Gaia* Multilateral Agreement.

References

Allard, F., Homeier, D., & Freytag, B. 2012, Phil. Trans. R. Soc. London, Ser. A, 370, 2765
Amara, A., & Quanz, S. P. 2012, MNRAS, 427, 948
Baraffe, I., Chabrier, G., Barman, T. S., Allard, F., & Hauschildt, P. H. 2003, A&A, 402, 701
Baraffe, I., Homeier, D., Allard, F., & Chabrier, G. 2015, A&A, 577, A42
Beuzit, J.-L., Feldt, M., Dohlen, K., et al. 2008, Proc. SPIE, 7014, 701418
Blunt, S., Nielsen, E. L., De Rosa, R. J., et al. 2017, AJ, 153, 229
Boccaletti, A., Lagage, P.-O., Baudoz, P., et al. 2015, PASP, 127, 633
Bonnefoy, M., Boccaletti, A., Lagrange, A.-M., et al. 2013, A&A, 555, A107
Bonnefoy, M., Zurlo, A., Baudino, J. L., et al. 2016, A&A, 587, A58
Burgasser, A. J. 2014, ASI Conf. Ser., 11, 7
Chabrier, G., Baraffe, I., Allard, F., & Hauschildt, P. 2000, ApJ, 542, 464
Chauvin, G., Lagrange, A.-M., Dumas, C., et al. 2004, A&A, 425, L29
Chauvin, G., Lagrange, A.-M., Beust, H., et al. 2012, A&A, 542, A41
Chauvin, G., Desidera, S., Lagrange, A.-M., et al. 2017a, A&A, 605, L9
Chauvin, G., Desidera, S., Lagrange, A.-M., et al. 2017b, in SF2A-2017: Proceedings of the Annual Meeting of the French Society of Astronomy and Astrophysics, eds. C. Reylé, P. Di Matteo, F. Herpin, et al., 331
Cheetham, A. C., Girard, J., Lacour, S., et al. 2016, in Optical and Infrared Interferometry and Imaging V, Proc. SPIE, 9907, 99072T
Cheetham, A., Bonnefoy, M., Desidera, S., et al. 2018, A&A, 615, A160
Claudi, R. U., Turatto, M., Gratton, R. G., et al. 2008, in Ground-Based and Airborne Instrumentation for Astronomy II, Proc. SPIE, 7014, 70143E
Currie, T., Burrows, A., Girard, J. H., et al. 2014, ApJ, 795, 133
Cushing, M. C., Rayner, J. T., & Vacca, W. D. 2005, ApJ, 623, 1115
Dahn, C. C., Harris, H. C., Subasavage, J. P., et al. 2017, AJ, 154, 147
Dohlen, K., Langlois, M., Saisse, M., et al. 2008, in Ground-Based and Airborne Instrumentation for Astronomy II, Proc. SPIE, 7014, 70143L
Dupuy, T. J., & Kraus, A. L. 2013, Science, 341, 1492
Dupuy, T. J., & Liu, M. C. 2012, ApJS, 201, 19
Faherty, J. K., Burgasser, A. J., Walter, F. M., et al. 2012, ApJ, 752, 56
Gaia Collaboration (Prusti, T., et al.) 2016, A&A, 595, A1
Gaia Collaboration (Brown, A. G. A., et al.) 2018, A&A, 616, A1
Galicher, R., Marois, C., Macintosh, B., Barman, T., & Konopacky, Q. 2011, ApJ, 739, L41
Galicher, R., Boccaletti, A., Mesa, D., et al. 2018, A&A, 615, A92
Hagelberg, J., Ségransan, D., Udry, S., & Wildi, F. 2016, MNRAS, 455, 2178
Hinkley, S., Skemer, A., Biller, B., et al. 2017, High Contrast Imaging of Exoplanets and Exoplanetary Systems with JWST, JWST Proposal ID 1386, Cycle 0 Early Release Science
Høg, E., Fabricius, C., Makarov, V. V., et al. 2000, A&A, 355, L27
Hunziker, S., Quanz, S. P., Amara, A., & Meyer, M. R. 2018, A&A, 611, A23
Jennison, R. C. 1958, MNRAS, 118, 276
Keppler, M., Benisty, M., Müller, A., et al. 2018, A&A, 617, A44

Kraus, A. L., Ireland, M. J., Martinache, F., & Lloyd, J. P. 2008, ApJ, 679, 762
Krist, J. E., Beichman, C. A., Trauger, J. T., et al. 2007, in Techniques and Instrumentation for Detection of Exoplanets III, Proc. SPIE, 6693, 66930H
Lagrange, A.-M., Bonnefoy, M., Chauvin, G., et al. 2010, Science, 329, 57
Lagrange, A.-M., Langlois, M., Gratton, R., et al. 2016, A&A, 586, L8
Larkin, K. G., Oldfield, M. A., & Klemm, H. 1997, Opt. Commun., 139, 99
Leggett, S. K., Burningham, B., Saumon, D., et al. 2010, ApJ, 710, 1627
Lenzen, R., Hofmann, R., Bizenberger, P., & Tusche, A. 1998, in Infrared Astronomical Instrumentation, ed. A. M. Fowler, Proc. SPIE, 3354, 606
Liu, M. C., Dupuy, T. J., & Allers, K. N. 2013, Astron. Nachr., 334, 85
Macintosh, B., Graham, J. R., Barman, T., et al. 2015, Science, 350, 64
Maire, A.-L., Langlois, M., Dohlen, K., et al. 2016a, in Ground-Based and Airborne Instrumentation for Astronomy VI, Proc. SPIE, 9908, 990834
Maire, A.-L., Bonnefoy, M., Ginski, C., et al. 2016b, A&A, 587, A56
Marleau, G.-D., Coleman, G. A. L., Leleu, A., & Mordasini, C. 2019, A&A, in press
Marley, M. S., Saumon, D., Cushing, M., et al. 2012, ApJ, 754, 135
Marois, C., Macintosh, B., Barman, T., et al. 2008, Science, 322, 1348
Marois, C., Zuckerman, B., Konopacky, Q. M., Macintosh, B., & Barman, T. 2010, Nature, 468, 1080
Marois, C., Correia, C., Véran, J.-P., & Currie, T. 2014, IAU Symp., 299, 48
Mawet, D., David, T., Bottom, M., et al. 2015, ApJ, 811, 103
McLaughlin, D. E., Anderson, J., Meylan, G., et al. 2006, ApJS, 166, 249
Mesa, D., Gratton, R., Zurlo, A., et al. 2015, A&A, 576, A121
Mesa, D., Vigan, A., D'Orazi, V., et al. 2016, A&A, 593, A119
Mollière, P., van Boekel, R., Bouwman, J., et al. 2017, A&A, 600, A10
Müller, A., Keppler, M., Henning, T., et al. 2018, A&A, 617, L2
Nielsen, E. L., Close, L. M., Biller, B. A., Masciadri, E., & Lenzen, R. 2008, ApJ, 674, 466
Pavlov, A., Möller-Nilsson, O., Feldt, M., et al. 2008, in Advanced Software and Control for Astronomy II, Proc. SPIE, 7019, 701939
Rajan, A., Rameau, J., De Rosa, R. J., et al. 2017, AJ, 154, 10
Rameau, J., Chauvin, G., Lagrange, A.-M., et al. 2013, ApJ, 772, L15
Rayner, J. T., Cushing, M. C., & Vacca, W. D. 2009, ApJS, 185, 289
Rousset, G., Lacombe, F., Puget, P., et al. 2003, in Adaptive Optical System Technologies II, eds. P. L. Wizinowich & D. Bonaccini, Proc. SPIE, 4839, 140
Samland, M., Mollière, P., Bonnefoy, M., et al. 2017, A&A, 603, A57
Sharp, C. M., & Burrows, A. 2007, ApJS, 168, 140
Skemer, A. J., Marley, M. S., Hinz, P. M., et al. 2014, ApJ, 792, 17
Skrutskie, M., Cutri, R., Stiening, R., et al. 2006, AJ, 131, 1163
Soummer, R., Pueyo, L., & Larkin, J. 2012, ApJ, 755, L28
Tuthill, P. G., Monnier, J. D., Danchi, W. C., Wishnow, E. H., & Haniff, C. A. 2000, PASP, 112, 555
van Leeuwen, F. 2007, A&A, 474, 653
Vigan, A., Moutou, C., Langlois, M., et al. 2010, MNRAS, 407, 71
Wright, E. L., Eisenhardt, P. R. M., Mainzer, A. K., et al. 2010, AJ, 140, 1868

[1] Département d'Astronomie, Université de Genève, 51 chemin des Maillettes, 1290, Versoix, Switzerland
e-mail: anthony.cheetham@unige.ch

[2] Max Planck Institute for Astronomy, Königstuhl 17, 69117 Heidelberg, Germany
[3] Landessternwarte, Zentrum für Astronomie der Universität Heidelberg, Königstuhl 12, 69117 Heidelberg, Germany
[4] Université Grenoble Alpes, CNRS, IPAG, 38000 Grenoble, France
[5] Unidad Mixta Internacional Franco-Chilena de Astronomía, CNRS/INSU UMI 3386 and Departamento de Astronomía, Universidad de Chile, Casilla 36-D, Santiago, Chile
[6] Institute for Particle Physics and Astrophysics, ETH Zurich, Wolfgang-Pauli-Strasse 27, 8093 Zurich, Switzerland
[7] Space Telescope Science Institute, 3700 San Martin Dr. Baltimore, MD 21218, USA
[8] Instituto de Física y Astronomía, Facultad de Ciencias, Universidad de Valparaíso, Av. Gran Bretaña 1111, Playa Ancha, Valparaíso, Chile
[9] Núcleo Milenio Formación Planetaria – NPF, Universidad de Valparaíso, Av. Gran Bretaña 1111, Valparaíso, Chile
[10] Department of Physics, University of Warwick, Gibbet Hill Road, Coventry, CV4 7AL, UK
[11] Department of Physics and Astronomy, Centre for Planetary Science and Exploration, The University of Western Ontario, London, ON N6A 3K7, Canada
[12] Department of Physics and Astronomy, Stony Brook University, Stony Brook, NY 11794-3800, USA
[13] Astrophysics Group, Cavendish Laboratory, J.J. Thomson Avenue, Cambridge CB3 0HE, UK
[14] LESIA, Observatoire de Paris, PSL Research University, CNRS, Sorbonne Universités, UPMC Université Paris 06, Université Paris Diderot, Sorbonne Paris Cité, 5 place Jules Janssen, 92195 Meudon, France
[15] Department of Astronomy, Stockholm University, AlbaNova University Center, 10691, Stockholm, Sweden
[16] Aix-Marseille Université, CNRS, LAM (Laboratoire d'Astrophysique de Marseille) UMR 7326, 13388 Marseille, France
[17] CRAL, UMR 5574, CNRS, Université de Lyon, Ecole Normale Supérieure de Lyon, 46 Allée d'Italie, 69364 Lyon Cedex 07, France
[18] INAF – Osservatorio Astronomico di Padova, Vicolo dell' Osservatorio 5, 35122, Padova, Italy
[19] INCT, Universidad De Atacama, calle Copayapu 485, Copiapó, Atacama, Chile
[20] Department of Astronomy, University of Michigan, 1085 S. University Ave, Ann Arbor, MI 48109-1107, USA
[21] Núcleo de Astronomía, Facultad de Ingeniería y Ciencias, Universidad Diego Portales, Av. Ejercito 441, Santiago, Chile
[22] Escuela de Ingeniería Industrial, Facultad de Ingeniería y Ciencias, Universidad Diego Portales, Av. Ejercito 441, Santiago, Chile

A.2 SPHERE-SHINE consortium survey papers

Here I include publications from the SPHERE-SHINE survey (briefly discussed in Chapter 2.4) that I contributed to which were outside of the scope of this thesis:

1. Exploring the R CrA environment with SPHERE. Discovery of a new stellar companion, Mesa et al. (2019a)
2. Hint of curvature in the orbital motion of the exoplant 51 Eridani b using 3 yr of VLT/SPHERE monitoring, Maire et al. (2019)
3. Two cold belts in the debris disk around the G-type star NZ Lupi, Boccaletti et al. (2019)
4. SPHERE view of the jet and the envelope of RY Tauri, Garufi et al. (2019)
5. Determining the mass limits around HD 163296 through SPHERE direct imaging data, Mesa et al. (2019c)
6. Investigating the nature of the extended structure around the Herbig star RCrA using integral field and high-resolution spectroscopy, Rigliaco et al. (2019)
7. VLT/SPHERE exploration of the young multiplanetary system PDS 70, Mesa et al. (2019b)
8. HD 117214 debris disk: scattered light images and constraints on the presence of planets, Engler et al. (2020)
9. RefPlanets: Search for reflected light from extra-solar planets with SPHERE/ZIMPOL, Hunziker et al. (2020)
10. Searching for the near infrared counterpart of Proxima c using multi-epoch high contrast SPHERE data at VLT, Gratton et al. (2020)
11. Orbital and spectral characterization of the benchmark T-type brown dwarf HD 19467 B, Maire et al. (2020)

A&A 624, A4 (2019)
https://doi.org/10.1051/0004-6361/201834682

Astronomy & Astrophysics

Exploring the R CrA environment with SPHERE

Discovery of a new stellar companion⋆,⋆⋆

D. Mesa[1,2], M. Bonnefoy[3], R. Gratton[1], G. Van Der Plas[3], V. D'Orazi[1], E. Sissa[1], A. Zurlo[4,5,6], E. Rigliaco[1], T. Schmidt[7,8], M. Langlois[9,6], A. Vigan[6], M. G. Ubeira Gabellini[10], S. Desidera[1], S. Antoniucci[11], M. Barbieri[2], M. Benisty[12,3], A. Boccaletti[8], R. Claudi[1], D. Fedele[13], D. Gasparri[2], T. Henning[14], M. Kasper[15], A.-M. Lagrange[3], C. Lazzoni[1], G. Lodato[10], A.-L. Maire[14], C. F. Manara[15], M. Meyer[16], M. Reggiani[17], M. Samland[14], M. Van den Ancker[15], G. Chauvin[3], A. Cheetham[18], M. Feldt[14], E. Hugot[6], M. Janson[14,19], R. Ligi[20], O. Möller-Nilsson[14], C. Petit[21], E. L. Rickman[18], F. Rigal[22], and F. Wildi[18]

(Affiliations can be found after the references)

Received 19 November 2018 / Accepted 6 February 2019

ABSTRACT

Aims. R Coronae Australis (R CrA) is the brightest star of the Coronet nebula of the Corona Australis (CrA) star forming region. This star is very red in color, probably due to dust absorption, and is strongly variable. High-contrast instruments allow for an unprecedented direct exploration of the immediate circumstellar environment of this star.

Methods. We observed R CrA with the near-infrared (NIR) channels (IFS and IRDIS) of SPHERE at the Very Large Telescope (VLT). In this paper, we used four different epochs, three of which are from open time observations while one is from SPHERE guaranteed time. The data were reduced using the data reduction and handling pipeline and the SPHERE Data Center. We implemented custom IDL routines on the reduced data with the aim to subtract the speckle halo. We have also obtained pupil-tracking H-band (1.45−1.85 μm) observations with the VLT/SINFONI NIR medium-resolution ($R \sim 3000$) spectrograph.

Results. A companion was found at a separation of 0.156″ from the star in the first epoch and increasing to 0.184″ in the final epoch. Furthermore, several extended structures were found around the star, the most noteworthy of which is a very bright jet-like structure northeast from the star. The astrometric measurements of the companion in the four epochs confirm that it is gravitationally bound to the star. The SPHERE photometry and SINFONI spectrum, once corrected for extinction, point toward a spectral type object that is early M with a mass between 0.3 and 0.55 $M_{\odot}$. The astrometric analyis provides constraints on the orbit paramenters: $e \sim 0.4$, semimajor axis at 27–28 au, inclination of ∼70°, and a period larger than 30 yr. We were also able to put constraints of few $M_{\rm Jup}$ on the mass of possible other companions down to separations of few tens of au.

Key words. instrumentation: spectrographs – methods: data analysis – techniques: imaging spectroscopy – stars: pre-main sequence – stars: individual: R CrA

1. Introduction

Nowadays young stars surrounded by a protoplanetary disk are considered as the primary environment in which to study the formation of giant exoplanets (see, e.g., Chen et al. 2012; Marshall et al. 2014). In addition, it is clear that giant planets at large separations are more frequently found around intermediate mass stars than around solar-mass stars (see, e.g., Johnson et al. 2010; Bowler 2016). Herbig AeBe (HAeBe) stars (Herbig 1960; Hillenbrand et al. 1992) are young (<10 Myr), intermediate mass (1.5−8 $M_{\odot}$) and typically with A, B, F spectral types. These stars are characterized by a strong infrared excess (The 1994) owing to the presence of a circumstellar protoplanetary disk. They are also experiencing accretion processes and their spectral line profiles are very complex. These characteristics make these objects very valuable in the field of extrasolar planets given that they allow the exploration of the very first stages of the formation of planetary systems.

The HAeBe star R Coronae Australis (R CrA – HIP 93449) is the brightest star in the very young, compact (∼1 pc in diameter), and obscured Coronet protostar cluster (Taylor & Storey 1984). This cluster is characterized by a very high and spatially variable extinction with A_V up to 45 mag (Neuhäuser & Forbrich 2008). This nebula is located toward the center of the Corona Australis (CrA) molecular clouds complex (Graham 1992), one of the nearest star forming region with a distance of ∼130 pc (Neuhäuser & Forbrich 2008). More recently, Dzib et al. (2018), using the mean trigonometric parallax obtained from *Gaia* Data Release 2 (Gaia Collaboration 2018), estimated a distance of 154 ± 4 pc. The presence of emission line objects was also signaled in the vicinity of R CrA (Graham 1993). The CrA region was explored through deep infrared imaging by Wilking et al. (1997), who identified hundreds of point-like sources. Moreover, these authors gave particular relevance to the study of the region of the Coronet nebula where they identified extensive reflective nebulae, dust-free cavities, and Herbig–Haro objects. More recently, Meyer & Wilking (2009) obtained the infrared spectra for a magnitude limited sample of stars of the CrA region allowing their characterization.

⋆ Based on observations made with European Southern Observatory (ESO) telescopes at Paranal Observatory in Chile, under programs ID 095.C-0787(A), 097.C-0591(A), 1100.C-0481(H), 0101.C-0350(A) and 2101.C-5048(A).

⋆⋆ The SPHERE and SINFONI images are only available at the CDS via anonymous ftp to cdsarc.u-strasbg.fr (130.79.128.5) or via http://cdsarc.u-strasbg.fr/viz-bin/qcat?J/A+A/624/A4

A&A 624, A118 (2019)
https://doi.org/10.1051/0004-6361/201935031

Astronomy & Astrophysics

Hint of curvature in the orbital motion of the exoplanet 51 Eridani b using 3 yr of VLT/SPHERE monitoring[⋆,⋆⋆]

A.-L. Maire[1,2,⋆⋆⋆], L. Rodet[3], F. Cantalloube[1], R. Galicher[4], W. Brandner[1], S. Messina[5], C. Lazzoni[6,7], D. Mesa[6,8], D. Melnick[9], J. Carson[9,1], M. Samland[1,⋆⋆⋆⋆], B. A. Biller[10,1], A. Boccaletti[4], Z. Wahhaj[11,12], H. Beust[3], M. Bonnefoy[3], G. Chauvin[3,13], S. Desidera[6], M. Langlois[14,12], T. Henning[1], M. Janson[15,1], J. Olofsson[16,17,1], D. Rouan[4], F. Ménard[3], A.-M. Lagrange[3], R. Gratton[6], A. Vigan[12], M. R. Meyer[18,19], A. Cheetham[20], J.-L. Beuzit[12,3], K. Dohlen[12], H. Avenhaus[1,19], M. Bonavita[10,6], R. Claudi[6], M. Cudel[3], S. Daemgen[19], V. D'Orazi[6], C. Fontanive[10], J. Hagelberg[3,19], H. Le Coroller[12], C. Perrot[4,16,17], E. Rickman[20], T. Schmidt[4,21], E. Sissa[6], S. Udry[20], A. Zurlo[22,23,12,6], L. Abe[24], A. Origné[12], F. Rigal[25], G. Rousset[4], A. Roux[3], and L. Weber[20]

(Affiliations can be found after the references)

Received 7 January 2019 / Accepted 15 March 2019

ABSTRACT

Context. The 51 Eridani system harbors a complex architecture with its primary star forming a hierarchical system with the binary GJ 3305AB at a projected separation of 2000 au, a giant planet orbiting the primary star at 13 au, and a low-mass debris disk around the primary star with possible cold and warm components inferred from the spectral energy distribution.
Aims. We aim to better constrain the orbital parameters of the known giant planet.
Methods. We monitored the system over three years from 2015 to 2018 with the Spectro-Polarimetric High-contrast Exoplanet REsearch (SPHERE) instrument at the Very Large Telescope (VLT).
Results. We measure an orbital motion for the planet of ∼130 mas with a slightly decreasing separation (∼10 mas) and find a hint of curvature. This potential curvature is further supported at 3σ significance when including literature Gemini Planet Imager (GPI) astrometry corrected for calibration systematics. Fits of the SPHERE and GPI data using three complementary approaches provide broadly similar results. The data suggest an orbital period of 32^{+17}_{-9} yr (i.e., 12^{+4}_{-2} au in semi-major axis), an inclination of 133^{+14}_{-7} deg, an eccentricity of $0.45^{+0.10}_{-0.15}$, and an argument of periastron passage of 87^{+34}_{-30} deg [mod 180°]. The time at periastron passage and the longitude of node exhibit bimodal distributions because we do not yet detect whether the planet is accelerating or decelerating along its orbit. Given the inclinations of the orbit and of the stellar rotation axis (134–144°), we infer alignment or misalignment within 18° for the star–planet spin-orbit. Further astrometric monitoring in the next 3–4 yr is required to confirm at a higher significance the curvature in the motion of the planet, determine if the planet is accelerating or decelerating on its orbit, and further constrain its orbital parameters and the star–planet spin-orbit.

Key words. planetary systems – methods: data analysis – stars: individual: 51 Eridani – techniques: high angular resolution – planets and satellites: dynamical evolution and stability – techniques: image processing

1. Introduction

The giant planet 51 Eridani b is the first of its kind discovered in the Gemini Planet Imager (GPI) exoplanet imaging survey (Macintosh et al. 2015). The methane-rich planet is a bound companion to the young star 51 Eridani, which is a member of the 24-Myr β Pictoris moving group (Zuckerman et al. 2001; Torres et al. 2008; Bell et al. 2015). The star is located at 29.78 ± 0.15 pc, inferred from the inverse of the parallax measured by *Gaia* (Gaia Collaboration 2018). It is in good agreement with the value derived with an optimized approach (29.76 ± 0.12 pc, Bailer-Jones et al. 2018). Our uncertainty of 0.15 pc includes in addition to the statistical error of 0.12 pc an uncertainty term of 0.1 mas to account for potential parallax systematics[1]. The star forms a hierarchical system with the M-dwarf binary GJ 3305AB with separation ∼10 au located at a projected separation of 2000 au (Feigelson et al. 2006; Montet et al. 2015). Simon & Schaefer (2011) measured a stellar radius of 1.63 ± 0.03 $R_\odot$ with the Center for High Angular Resolution Astronomy (CHARA) interferometer and inferred a stellar mass of 1.75 ± 0.05 $M_\odot$. The primary star also harbors a debris disk inferred from the spectral energy distribution (SED; Riviere-Marichalar et al. 2014; Patel et al. 2014). Riviere-Marichalar et al. (2014) estimated a low infrared (IR) fractional luminosity $L_{\rm IR}/L_\odot = 2.3 \times 10^{-6}$ from *Herschel* photometry. Since their analysis is based on fitting a three-parameter model of a modified blackbody to three data points with excess IR emission at wavelengths $\geq 70\,\mu$m, the resulting value for

⋆ The fitted orbits and the histogram distributions of the orbital parameters are only available at the CDS via anonymous ftp to cdsarc.u-strasbg.fr (130.79.128.5) or via http://cdsarc.u-strasbg.fr/viz-bin/qcat?J/A+A/624/A118

⋆⋆ Based on observations collected at the European Organisation for Astronomical Research in the Southern Hemisphere under ESO programmes 095.C-0298, 096.C-0241, 198.C-0209, and 1100.C-0481.

⋆⋆⋆ F.R.S.-FNRS Postdoctoral Researcher.

⋆⋆⋆⋆ International Max Planck Research School for Astronomy and Cosmic Physics, Heidelberg, Germany.

[1] https://www.cosmos.esa.int/web/gaia/dr2

A&A 625, A21 (2019)
https://doi.org/10.1051/0004-6361/201935135

Astronomy & Astrophysics

Two cold belts in the debris disk around the G-type star NZ Lupi[⋆,⋆⋆]

A. Boccaletti[1], P. Thébault[1], N. Pawellek[3], A.-M. Lagrange[2], R. Galicher[1], S. Desidera[4], J. Milli[2,5], Q. Kral[1], M. Bonnefoy[2], J.-C. Augereau[2], A. L. Maire[3,6], T. Henning[3], H. Beust[2], L. Rodet[2], H. Avenhaus[7], T. Bhowmik[1], M. Bonavita[4,8], G. Chauvin[2], A. Cheetham[9], M. Cudel[2], M. Feldt[3], R. Gratton[4], J. Hagelberg[2], P. Janin-Potiron[10], M. Langlois[10,11], F. Menard[2], D. Mesa[4], M. Meyer[7,12], S. Peretti[9], C. Perrot[1,13,14], T. Schmidt[1], E. Sissa[4], A. Vigan[10], E. Rickman[9], Y. Magnard[2], D. Maurel[2], O. Moeller-Nilsson[3], D. Perret[1], and J.-F. Sauvage[15]

(Affiliations can be found after the references)

Received 25 January 2019 / Accepted 25 March 2019

ABSTRACT

Context. Planetary systems hold the imprint of the formation and of the evolution of planets especially at young ages, and in particular at the stage when the gas has dissipated leaving mostly secondary dust grains. The dynamical perturbation of planets in the dust distribution can be revealed with high-contrast imaging in a variety of structures.
Aims. SPHERE, the high-contrast imaging device installed at the VLT, was designed to search for young giant planets in long period, but is also able to resolve fine details of planetary systems at the scale of astronomical units in the scattered-light regime. As a young and nearby star, NZ Lup was observed in the course of the SPHERE survey. A debris disk had been formerly identified with HST/NICMOS.
Methods. We observed this system in the near-infrared with the camera in narrow and broad band filters and with the integral field spectrograph. High contrasts are achieved by the mean of pupil tracking combined with angular differential imaging algorithms.
Results. The high angular resolution provided by SPHERE allows us to reveal a new feature in the disk which is interpreted as a superimposition of two belts of planetesimals located at stellocentric distances of ~85 and ~115 au, and with a mutual inclination of about 5°. Despite the very high inclination of the disk with respect to the line of sight, we conclude that the presence of a gap, that is, a void in the dust distribution between the belts, is likely.
Conclusions. We discuss the implication of the existence of two belts and their relative inclination with respect to the presence of planets.

Key words. stars: individual: NZ Lup – planet-disk interactions – techniques: high angular resolution – techniques: image processing

1. Introduction

Debris disks correspond to a late stage in the evolution of planetary systems when the primordial material has been expelled out of the systems or incorporated into planets and other bodies. The observed dust results from collisions among the rocky planetesimals or is deposited by comets. Planets, if already formed, are expected to produce indirect signatures in the form of a departure from a pure axisymmetrical disk morphology. Recently, the advance of high-contrast imaging, in particular with the installation of Spectro-Polarimetic High contrast imager for Exoplanets REsearch (SPHERE, Beuzit et al. 2019) and Gemini Planet Imager (GPI, Macintosh et al. 2008), has yielded a significant number of new discoveries in this field either revealing new disks (Lagrange et al. 2016; Kalas et al. 2015; Currie et al. 2015; Bonnefoy et al. 2017; Sissa et al. 2018) or new structures in known disks (Boccaletti et al. 2015; Perrin et al. 2015; Garufi et al. 2016; Perrot et al. 2016; Milli et al. 2017). These observations are definitely pointing to the presence of planets.

Of particular interest is the ever-growing number of disks in which multiple belts are observed due to significant gain in angular resolution and contrast, both in the thermal emission and scattered light regimes. On the one hand, the sub-millimeter interferometer Atacama Large Millimeter Array (ALMA) has revealed obvious cases of gaps in several protoplanetary disks likely sculpted by sub-Jupiter-like planets (Dipierro et al. 2015; Nomura et al. 2016), as well as in one debris disk (Marino et al. 2018). On the other hand, at shorter wavelengths in scattered light, gaps were also found in the protoplanetary disks of TW Hya (Rapson et al. 2015a; van Boekel et al. 2017) and V4046 Sgr (Rapson et al. 2015b), for instance. A few cases featuring an alternance of gaps and belts were also observed in some debris disks such as HD 131835 (Feldt et al. 2017) and HD 141569 (Perrot et al. 2016). However, these disks contain gas (Kral et al. 2017), which might also be responsible for developing belts (Takeuchi & Artymowicz 2001; Kral et al. 2018) or arcs (Lyra & Kuchner 2013; Richert et al. 2018). Despite the fact that a double-belt structure has been inferred for several systems from analyses of spectral energy distribution (SED; Pawellek et al. 2014; Pawellek & Krivov 2015), so far a single gasless debris disk featuring two belts has been unambiguously imaged around HIP 67497 by Bonnefoy et al. (2017). This potentially new class of debris disks is different from the

⋆ Reduced images of Fig. 1 are only available at the CDS via anonymous ftp to cdsarc.u-strasbg.fr (130.79.128.5) or via http://cdsarc.u-strasbg.fr/viz-bin/qcat?J/A+A/625/A21

⋆⋆ Based on data collected at the European Southern Observatory, Chile under programs 097.C-0523, 097.C-0865, 198.C-0209.

A&A 628, A68 (2019)
https://doi.org/10.1051/0004-6361/201935546

Astronomy & Astrophysics

SPHERE view of the jet and the envelope of RY Tauri*

A. Garufi[1], L. Podio[1], F. Bacciotti[1], S. Antoniucci[2], A. Boccaletti[3], C. Codella[1,4], C. Dougados[4], F. Ménard[4], D. Mesa[5], M. Meyer[6], B. Nisini[2], H. M. Schmid[7], T. Stolker[7], J. L. Baudino[8], B. Biller[9], M. Bonavita[9], M. Bonnefoy[4], F. Cantalloube[10], G. Chauvin[4], A. Cheetham[11], S. Desidera[5], V. D'Orazi[5], M. Feldt[10], R. Galicher[3], A. Grandjean[4], R. Gratton[5], J. Hagelberg[7], A. M. Lagrange[4], M. Langlois[12], J. Lannier[4], C. Lazzoni[13], A. L. Maire[14], C. Perrot[3,15,16], E. Rickman[11], T. Schmidt[3], A. Vigan[17], A. Zurlo[17,18,19], A. Delboulbé[4], D. Le Mignant[17], D. Fantinel[5], O. Möller-Nilsson[10], L. Weber[11], and J.-F. Sauvage[17]

(Affiliations can be found after the references)

Received 26 March 2019 / Accepted 17 June 2019

ABSTRACT

Context. Jets are rarely associated with pre-main sequence intermediate-mass stars. This contrasts with the frequent detection of jets in lower mass or younger stars. Optical and near-IR observations of jet-driving sources are often hindered by the presence of a natal envelope.

Aims. Jets around partly embedded sources are a useful diagnostic to constrain the geometry of the concealed protoplanetary disk. We intend to clarify how the jet-driving mechanisms are affected by both spatial anisotropies and episodic variations at the (sub-)au scale from the star.

Methods. We obtained a rich set of high-contrast VLT/SPHERE observations from 0.6 to 2.2 μm of the young intermediate-mass star RY Tau. Given the proximity to the Sun of this source, our images have the highest spatial resolution ever obtained for an atomic jet (down to ~4 au).

Results. Optical observations in polarized light show no sign of the protoplanetary disk detected by ALMA. Instead, we observed a diffuse signal resembling a remnant envelope with an outflow cavity. The jet is detected in the Hα, [S II] at 1.03 μm, He I at 1.08 μm, and [Fe II] lines in the 1.25 μm and 1.64 μm. The jet appears to be wiggling and its radial width increasing with the distance is complementary to the shape of the outflow cavity suggesting a strong interaction with jet and envelope. Through the estimated tangential velocity (~100 km s^{-1}), we revealed a possible connection between the launching time of the jet substructures and the stellar activity of RY Tau.

Conclusions. RY Tau is at an intermediate stage toward the dispersal of the natal envelope. This source shows episodic increases of mass accretion and ejection similarly to other known intermediate-mass stars. The amount of observed jet wiggle is consistent with the presence of a precessing disk warp or misaligned inner disk that would be induced by an unseen planetary or sub-stellar companion at sub- or few-au scales respectively. The high disk mass of RY Tau and of two other jet-driving intermediate-mass stars, HD 163296 and MWC480, suggests that massive, full disks are more efficient at launching prominent jets.

Key words. ISM: jets and outflows – planet-disk interactions – stars: variables: T Tauri, Herbig Ae/Be – protoplanetary disks – infrared: stars

1. Introduction

The formation history of planets is closely connected to the global evolution of protoplanetary disks. Our knowledge of disk morphology has greatly advanced in the last few years thanks to the high-contrast and high-resolution imaging in both the visible and near-IR (NIR) and the (sub-)mm offered by new instruments like Spectro-Polarimetric High-contrast Exoplanet REsearch instrument at the Very Large Telescope (VLT/SPHERE), Gemini Planet Imager (GPI), and Atacama Large Millimeter Array (ALMA). However, if on one hand ALMA also has access to younger, embedded sources (see, e.g., Sheehan & Eisner 2017), the optical and NIR imaging has important limitations in this regard because of the much higher extinction of these young sources. In fact, the protoplanetary disks of well-studied pre-main sequence (PMS) stars like HL Tau (Takami et al. 2007) or DG Tau B (Podio et al. 2011) have not been imaged at short wavelengths, and the whole sample of disks with available NIR images is biased toward more evolved sources with no remnant envelope (Garufi et al. 2018).

Among the various physical processes that affect the morphology of protoplanetary disks, the removal of mass and angular momentum through jets and outflows may play a fundamental role (see the review by Frank et al. 2014) since it can limit the increase of stellar rotation and allows a high accretion rate for a large fraction of the protoplanetary disk lifetime. Given the importance of this element for the star formation process, it is crucial to establish if the ejection of jets is a general phenomenon for forming stars of all masses and evolutionary stages. Jets are also a useful diagnostic of the innermost disk regions being closely connected to the accretion processes and the interplay of the star and disk.

It is known that jets are almost ubiquitous in protostars (see, e.g., Nisini et al. 2015). However, jets are often observed in more evolved PMS stars, and in particular around the low-mass

* Based on observations performed with VLT/SPHERE under program ID 096.C-0241(C), 096.C-0241(F), 096.C-0248(A), 096.C-0454(A), and 1100.C-0481(A).

Monthly Notices of the ROYAL ASTRONOMICAL SOCIETY

MNRAS **488,** 37–46 (2019) doi:10.1093/mnras/stz1662
Advance Access publication 2019 June 18

Determining mass limits around HD 163296 through SPHERE direct imaging data

D. Mesa,[1,2]★ M. Langlois,[3,4] A. Garufi,[5] R. Gratton,[1] S. Desidera,[1] V. D'Orazi,[1] O. Flasseur,[6] M. Barbieri,[2] M. Benisty,[7,8] T. Henning,[9] R. Ligi,[10] E. Sissa,[1] A. Vigan,[4] A. Zurlo,[4,11,12] A. Boccaletti,[13] M. Bonnefoy,[7] F. Cantalloube,[8] G. Chauvin,[7] A. Cheetham,[14] V. De Caprio,[15] P. Delorme,[8] M. Feldt,[9] T. Fusco,[4,16] L. Gluck,[8] J. Hagelberg,[17] A.-M. Lagrange,[8] C. Lazzoni,[1] F. Madec,[4] A.-L. Maire,[9,18] F. Menard,[8] M. Meyer,[17,19] J. Ramos,[9] E.L. Rickman,[14] D. Rouan,[13] T. Schmidt[13,20] and G. Van der Plas[7]

Affiliations are listed at the end of the paper

Accepted 2019 June 12. Received 2019 June 10; in original form 2019 April 24

ABSTRACT

HD 163296 is a Herbig Ae/Be star known to host a protoplanetary disc with a ringed structure. To explain the disc features, previous works proposed the presence of planets embedded into the disc. We have observed HD 163296 with the near-infrared (NIR) branch of SPHERE composed by IRDIS (InfraRed Dual-band Imager and Spectrograph) and IFS (integral field spectrograph) with the aim to put tight constraints on the presence of substellar companions around this star. Despite the low rotation of the field of view during our observation we were able to put upper mass limits of few M_{Jup} around this object. These limits do not allow to give any definitive conclusion about the planets proposed through the disc characteristics. On the other hand, our results seem to exclude the presence of the only candidate proposed until now using direct imaging in the NIR even if some caution has to be taken considered the different wavelength bands of the two observations.

Key words: instrumentation: spectrographs – methods: data analysis – techniques: imaging spectroscopy – (stars:) planetary systems, HD 163296.

1 INTRODUCTION

The most promising environments to search for in-formation planetary systems are protoplanetary discs around very young stars (see e.g. Chen et al. 2012; Marshall et al. 2014). These systems can be probed both with high-contrast imaging in the near-infrared (NIR) through instruments like SPHERE (Beuzit et al. 2019), GPI (Macintosh et al. 2014), Keck/NIRC2 (Mawet et al. 2017), and CHARIS at Subaru Telescope (Groff et al. 2015) and at submillimetre wavelengths with instruments like ALMA. One noteworthy example of the first case is the recently discovered planet around the disc hosting star PDS 70 (Keppler et al. 2018; Müller et al. 2018). On the other hand, in recent years an increasing number of protoplanetary disc with gaps and rings have been imaged through ALMA (e.g. ALMA Partnership et al. 2015; Andrews et al. 2016; Loomis et al. 2017; Ansdell et al. 2018; Fedele et al. 2018; Huang et al. 2018; Pinilla et al. 2018). One of the most promising model to explain these structures implies that they are due to the interactions between the disc and planetary mass objects (e.g. Bryden et al. 1999; Jin et al. 2016). However, plenty of alternative models have been proposed to explain these structures including dust accumulations at the snowlines (e.g. Zhang, Blake & Bergin 2015), zonal flows (e.g. Béthune, Lesur & Ferreira 2017), or secular gravitational instability (e.g. Takahashi & Inutsuka 2014). Clearly, having the possibility to directly image the foreseen planetary companions into these discs or, alternatively, to put tight limits on the masses of these objects could help to disentangle between the proposed models.

HD 163296 (HIP 87819) is an A1V spectral-type (Mora et al. 2001) Herbig Ae/Be star at a distance of 101.5 ± 1.2 pc from the Sun (Gaia Collaboration et al. 2018). Recently, its stellar parameters were defined by Setterholm et al. (2018) fitting its *H*- and *K*-band flux with the *PARSEC* models (Bressan et al. 2012) and finding an age of 10.4 Myr and a mass of 1.9 $M_{\odot}$. We will assume these

★ E-mail: dino.mesa@inaf.it

A&A 632, A18 (2019)
https://doi.org/10.1051/0004-6361/201936707

Astronomy & Astrophysics

Investigating the nature of the extended structure around the Herbig star RCrA using integral field and high-resolution spectroscopy

E. Rigliaco[1], R. Gratton[1], D. Mesa[1], V. D'Orazi[1], M. Bonnefoy[2], J. M. Alcalà[3], S. Antoniucci[4], F. Bacciotti[5], M. Dima[1], B. Nisini[4], L. Podio[5], M. Barbieri[6], R. Claudi[1], S. Desidera[1], A. Garufi[5], E. Hugot[7], M. Janson[8,9], M. Langlois[10], E. L. Rickman[11], E. Sissa[1], M. Ubeira Gabellini[12], G. van der Plas[2], A. Zurlo[13,14,8], Y. Magnard[15], D. Perret[16], R. Roelfsema[17], and L. Weber[18]

[1] INAF/Osservatorio Astronomico di Padova, Vicolo dell'osservatorio 5, 35122 Padova, Italy
e-mail: elisabetta.rigliaco@inaf.it
[2] Université Grenoble Alpes, CNRS, IPAG, 38000 Grenoble, France
[3] INAF – Osservatorio Astronomico di Capodimonte, Salita Moiariello 16, 80131 Napoli, Italy
[4] INAF – Osservatorio Astronomico di Roma, Via di Frascati 33, 00078 Monte Porzio Catone, Italy
[5] INAF – Osservatorio Astrofisico di Arcetri, Largo E. Fermi 5, 50125 Firenze, Italy
[6] INCT, Universidad De Atacama, calle Copayapu 485, Copiapó, Atacama, Chile
[7] Aix-Marseille Université , CNRS, CNES LAM, Marseille, France
[8] Max-Planck-Institut für Astronomie, Königstuhl 17, 69117 Heidelberg, Germany
[9] AlbaNova University Center, Stockholm University, Stockholm, Sweden
[10] Université Lyon, Université Lyon 1, ENS de Lyon, CNRS, CRAL UMR 5574, 69230 Saint-Genis-Laval, France
[11] Geneva Observatory, University of Geneva, Chemin des Maillettes, Switzerland
[12] Dipartimento di Fisica, Universitá Degli Studi di Milano, Via Celoria, 16, 20133 Milano, Italy
[13] Nucleo de Astronomia, Facultad de Ingenieria y Ciencias, Universidad Diego Portales, Av. Ejercito 441, Santiago, Chile
[14] Escuela de Ingenieria Industrial, Facultad de Ingenieria y Ciencias, Universidad Diego Portales, Av. Ejercito 441, Santiago, Chile
[15] Université Grenoble Alpes, CNRS, IPAG, 38000 Grenoble, France
[16] LESIA, Observatoire de Paris, Université PSL, CNRS, Sorbonne Université, Université Paris Diderot, Sorbonne Paris Cité, 5 place Jules Janssen, 92195 Meudon, France
[17] NOVA Optical Infrared Instrumentation Group, Oude Hoogeveensedijk 4, 7991 PD Dwingeloo, The Netherlands
[18] Geneva Observatory, University of Geneva, Chemin des Mailettes 51, 1290 Versoix, Switzerland

Received 16 September 2019 / Accepted 28 September 2019

ABSTRACT

Context. We present a detailed analysis of the extended structure detected around the young and close-by Herbig Ae/Be star R CrA. This is a young triple system with an intermediate mass central binary whose separation is of the order of a few tens of the radii of the individual components, and an M-star companion at about 30 au.
Aims. Our aim is to understand the nature of the extended structure by means of combining integral-field and high-resolution spectroscopy.
Methods. We conducted the analysis based on FEROS archival optical spectroscopy data and adaptive optics images and integral-field spectra obtained with SINFONI and SPHERE at the VLT.
Results. The observations reveal a complex extended structure that is composed of at least two components: a non-uniform wide cavity whose walls are detected in continuum emission up to 400 au, and a collimated wiggling-jet detected in the emission lines of helium and hydrogen. Moreover, the presence of [Fe II] emission projected close to the cavity walls suggests the presence of a slower moving wind, most likely a disk wind. The multiple components of the optical forbidden lines also indicate the presence of a high-velocity jet co-existing with a slow wind. We constructed a geometrical model of the collimated jet flowing within the cavity using intensity and velocity maps, finding that its wiggling is consistent with the orbital period of the central binary. The cavity and the jet do not share the same position angle, suggesting that the jet is itself experiencing a precession motion possibly due to the wide M-dwarf companion.
Conclusions. We propose a scenario that closely agrees with the general expectation of a magneto-centrifugal-launched jet. These results build upon the extensive studies already conducted on R CrA.

Key words. stars: pre-main sequence – protoplanetary disks – Herbig-Haro objects – ISM: jets and outflows – ISM: individual objects: R CrA

1. Introduction

Herbig Ae/Be stars (Herbig 1960) are pre-main sequence stars of intermediate mass covering the range between low-mass T Tauri stars (TTSs), and the embedded massive young stellar objects. They are considered the high-mass counterparts of pre-main sequence T Tauri stars (Strom et al. 1972; Cohen & Kuhi 1979; Finkenzeller & Mundt 1984). These stars, like T Tauri stars, show rich emission-lines spectra, infrared continuum excess and veiled photospheric absorption. The formation of stars in the

A&A 632, A25 (2019)
https://doi.org/10.1051/0004-6361/201936764

Astronomy & Astrophysics

VLT/SPHERE exploration of the young multiplanetary system PDS70★,★★

D. Mesa[1], M. Keppler[2], F. Cantalloube[2], L. Rodet[3], B. Charnay[4], R. Gratton[1], M. Langlois[5,6], A. Boccaletti[4], M. Bonnefoy[3], A. Vigan[6], O. Flasseur[7], J. Bae[8], M. Benisty[3,9], G. Chauvin[3,9], J. de Boer[10], S. Desidera[1], T. Henning[2], A.-M. Lagrange[3], M. Meyer[11], J. Milli[12], A. Müller[2], B. Pairet[13], A. Zurlo[14,15,6], S. Antoniucci[16], J.-L. Baudino[17], S. Brown Sevilla[2], E. Cascone[18], A. Cheetham[19], R. U. Claudi[1], P. Delorme[3], V. D'Orazi[1], M. Feldt[2], J. Hagelberg[19], M. Janson[20], Q. Kral[4], E. Lagadec[21], C. Lazzoni[1], R. Ligi[22], A.-L. Maire[2,23], P. Martinez[21], F. Menard[3], N. Meunier[3], C. Perrot[4,24,25], S. Petrus[3], C. Pinte[26,3], E. L. Rickman[19], S. Rochat[3], D. Rouan[4], M. Samland[2,20], J.-F. Sauvage[27,6], T. Schmidt[4,28], S. Udry[19], L. Weber[19], and F. Wildi[19]

(Affiliations can be found after the references)

Received 23 September 2019 / Accepted 24 October 2019

ABSTRACT

Context. PDS 70 is a young (5.4 Myr), nearby (~113 pc) star hosting a known transition disk with a large gap. Recent observations with SPHERE and NACO in the near-infrared (NIR) allowed us to detect a planetary mass companion, PDS 70 b, within the disk cavity. Moreover, observations in H_α with MagAO and MUSE revealed emission associated to PDS 70 b and to another new companion candidate, PDS 70 c, at a larger separation from the star. PDS 70 is the only multiple planetary system at its formation stage detected so far through direct imaging.

Aims. Our aim is to confirm the discovery of the second planet PDS 70 c using SPHERE at VLT, to further characterize its physical properties, and search for additional point sources in this young planetary system.

Methods. We re-analyzed archival SPHERE NIR observations and obtained new data in Y, J, H and K spectral bands for a total of four different epochs. The data were reduced using the data reduction and handling pipeline and the SPHERE data center. We then applied custom routines (e.g., ANDROMEDA and PACO) to subtract the starlight.

Results. We re-detect both PDS 70 b and c and confirm that PDS 70 c is gravitationally bound to the star. We estimate this second planet to be less massive than 5 $M_{\rm Jup}$ and with a $T_{\rm eff}$ around 900 K. Also, it has a low gravity with $\log g$ between 3.0 and 3.5 dex. In addition, a third object has been identified at short separation (~0.12″) from the star and gravitationally bound to the star. Its spectrum is however very blue, meaning that we are probably seeing stellar light reflected by dust and our analysis seems to demonstrate that it is a feature of the inner disk. We cannot however completely exclude the possibility that it is a planetary mass object enshrouded by a dust envelope. In this latter case, its mass should be of the order of a few tens of $M_\oplus$. Moreover, we propose a possible structure for the planetary system based on our data, and find that this structure cannot be stable on a long timescale.

Key words. instrumentation: spectrographs – methods: data analysis – techniques: imaging spectroscopy – planetary systems – stars: individual: PDS70

1. Introduction

PDS 70 is a K7 pre-main sequence star of 5.4 ± 1.0 Myr in age (Müller et al. 2018) that is part of the Upper Centaurus-Lupus group (Pecaut & Mamajek 2016) at a distance of 113.43 ± 0.52 pc (Gaia Collaboration 2016, 2018). In the course of the VLT/SPHERE SHINE survey (Chauvin et al. 2017), Keppler et al. (2018) discovered a planetary mass companion, PDS 70 b, located in the transition disk surrounding this young star. The presence of a circumstellar disk was first inferred by Metchev et al. (2004) due to the detection of a strong mid-infrared (MIR) excess and of a strong emission at millimeter wavelengths. The disk was first resolved in K_s band by Riaud et al. (2006) using VLT/NACO. The first detection of a gap in the disk was obtained by Hashimoto et al. (2012) exploiting H-band polarized data obtained through the Subaru/HiCIAO instrument. Using the same data, Dong et al. (2012) estimated, assuming a distance of 140 pc for the system, a gap size of around 65 au in which the dust is depleted by a factor of approximately 1000 with respect to the outer part of the disk. These latter authors also found evidence of an inner disk with dimensions of the order of few astronomical units detecting a weak near-infrared (NIR) excess in the spectral energy distribution (SED); they estimated a total dust mass of $\sim 10^{-4}$ $M_\odot$ for the disk. PDS 70 was also observed at millimeter wavelengths by Hashimoto et al. (2015) using the Submillimeter Array (SMA) and, more recently, by Long et al. (2018) using ALMA. The ALMA observations were performed both at 0.87 mm continuum and at HCO^+ and CO gas emission lines. These allowed the presence of a radial gap between the inner and the outer disk at 15–60 au of separation to be defined in the dust continuum, assuming a distance of 140 pc, and different substructures to be imaged, such as a bridge-like feature and an azimuthal gap in the HCO^+ emission

★ The reduced images are also available at the CDS via anonymous ftp to cdsarc.u-strasbg.fr (130.79.128.5) or via http://cdsarc.u-strasbg.fr/viz-bin/cat/J/A+A/632/A25

★★ Based on observation made with European Southern Observatory (ESO) telescopes at Paranal Observatory in Chile, under programs ID 095.C-0298(B), 1100.C-0481(D), 1100.C-0481(L) and 1100.C-0481(M).

A&A 635, A19 (2020)
https://doi.org/10.1051/0004-6361/201936828

Astronomy & Astrophysics

HD 117214 debris disk: scattered-light images and constraints on the presence of planets⋆,⋆⋆

N. Engler[1], C. Lazzoni[2], R. Gratton[2], J. Milli[5], H. M. Schmid[1], G. Chauvin[3,15], Q. Kral[4], N. Pawellek[6,7], P. Thébault[4], A. Boccaletti[4], M. Bonnefoy[3], S. Brown[3], T. Buey[4], F. Cantalloube[3], M. Carle[9], A. Cheetham[8], S. Desidera[2], M. Feldt[8], C. Ginski[10], D. Gisler[11], Th. Henning[8], S. Hunziker[1], A. M. Lagrange[3], M. Langlois[9,13], D. Mesa[2], M. R. Meyer[1,14], O. Moeller-Nilsson[8], J. Olofsson[15,8,16], C. Petit[19], S. Petrus[9], S. P. Quanz[1], E. Rickman[12], E. Stadler[3], T. Stolker[1], A. Vigan[9], F. Wildi[12], and A. Zurlo[17,18,9]

(Affiliations can be found after the references)

Received 2 October 2019 / Accepted 9 January 2020

ABSTRACT

Context. Young stars with debris disks are the most promising targets for an exoplanet search because debris indicate a successful formation of planetary bodies. Debris disks can be shaped by planets into ring structures that give valuable indications on the presence and location of planets in the disk.

Aims. We performed observations of the Sco-Cen F star HD 117214 to search for planetary companions and to characterize the debris disk structure.

Methods. HD 117214 was observed with the SPHERE subsystems IRDIS, IFS, and ZIMPOL at optical and near-IR wavelengths using angular and polarimetric differential imaging techniques. This provided the first images of scattered light from the debris disk with the highest spatial resolution of 25 mas and an inner working angle <0.1″. With the observations with IRDIS and IFS we derived detection limits for substellar companions. The geometrical parameters of the detected disk were constrained by fitting 3D models for the scattering of an optically thin dust disk. Investigating the possible origin of the disk gap, we introduced putative planets therein and modeled the planet–disk and planet–planet dynamical interactions. The obtained planetary architectures were compared with the detection limit curves.

Results. The debris disk has an axisymmetric ring structure with a radius of 0.42(±0.01)″ or ∼45 au and an inclination of 71(±2.5)° and exhibits a 0.4″ (∼40 au) wide inner cavity. From the polarimetric data, we derive a polarized flux contrast for the disk of $(F_{\rm pol})_{\rm disk}/F_* = (3.1 \pm 1.2) \times 10^{-4}$ in the *RI* band.

Conclusions. The fractional scattered polarized flux of the disk is eight times lower than the fractional IR flux excess. This ratio is similar to the one obtained for the debris disk HIP 79977, indicating that dust radiation properties are similar for these two disks. Inside the disk cavity we achieve high-sensitivity limits on planetary companions with a mass down to ∼4 $M_{\rm J}$ at projected radial separations between 0.2″ and 0.4″. We can exclude stellar companions at a radial separation larger than 75 mas from the star.

Key words. planetary systems – planet-disk interactions – stars: individual: HD 117214 – stars individual: HIP 65875 – techniques: high angular resolution – techniques: polarimetric

1. Introduction

Circumstellar debris disks around young stars (∼10−100 Myr) are often considered to be the remains of protoplanetary disks and are seen as a direct evidence for the presence of large planetesimals and planets because the large amount of dust observed in these stellar systems is thought to be generated in destructive collisions between large solid bodies (e.g., Wyatt 2008; Krivov 2010; Hughes et al. 2018, and references therein). When they orbit a star, planets scatter planetesimals away and gravitationally attract small rocks and tiny dust grains. This clears out large surrounding areas around the planets (e.g., Faber & Quillen 2007; Dipierro et al. 2016; Geiler & Krivov 2017, and references therein). In this way, planets can create wide empty gaps in dusty disks and shape them into ring structures. This scenario for the evolution of a planetary system provides one possible explanation for the multiple concentric rings observed in protoplanetary disks (e.g., Andrews et al. 2018) and debris disks (Golimowski et al. 2011; Perrot et al. 2016; Feldt et al. 2017; Bonnefoy et al. 2017; Marino et al. 2018; Engler et al. 2019; Boccaletti et al. 2019). Large amount of gas in the disks (Kral et al. 2018) can also lead to similar results (Lyra & Kuchner 2013; Richert et al. 2018). However, the idea of a planetary origin of the ring structure is supported by the planets that have been discovered in the gaps of protoplanetary disks (Keppler et al. 2018; Haffert et al. 2019) and between two debris belts (Marois et al. 2010; Rameau et al. 2013). For this reason, debris disks, especially those that are supposed to consist of at least two planetesimal belts (Lazzoni et al. 2018; Kennedy & Wyatt 2014), are the primary targets in searches for extrasolar planets.

The Scorpius-Centaurus OB association (Sco-Cen) is one preferred region for surveys searching for debris disks and young exoplanets near the Sun. The region is divided into three large subgroups and contains hundreds of young stars located at distances of ∼100−200 pc (Gaia Collaboration 2018). The F6V

⋆ The reduced images (FITS files) are only available at the CDS via anonymous ftp to cdsarc.u-strasbg.fr (130.79.128.5) or via http://cdsarc.u-strasbg.fr/viz-bin/cat/J/A+A/635/A19

⋆⋆ Based on data collected at the European Southern Observatory, Chile under program 1100.C-0481.

A&A 634, A69 (2020)
https://doi.org/10.1051/0004-6361/201936641

Astronomy & Astrophysics

RefPlanets: Search for reflected light from extrasolar planets with SPHERE/ZIMPOL⋆

S. Hunziker[1], H. M. Schmid[1], D. Mouillet[3,4], J. Milli[5], A. Zurlo[17,18,15], P. Delorme[3], L. Abe[12], H. Avenhaus[13,1], A. Baruffolo[14], A. Bazzon[1], A. Boccaletti[10], P. Baudoz[10], J. L. Beuzit[15], M. Carbillet[12], G. Chauvin[3,16], R. Claudi[14], A. Costille[15], J.-B. Daban[12], S. Desidera[14], K. Dohlen[15], C. Dominik[9], M. Downing[19], N. Engler[1], M. Feldt[13], T. Fusco[15,20], C. Ginski[11], D. Gisler[7,8], J. H. Girard[24,3], R. Gratton[14], Th. Henning[13], N. Hubin[19], M. Kasper[19], C. U. Keller[11], M. Langlois[21,15], E. Lagadec[12], P. Martinez[12], A. L. Maire[13,23], F. Menard[3,4], M. R. Meyer[25], A. Pavlov[13], J. Pragt[2], P. Puget[3], S. P. Quanz[1], E. Rickman[22], R. Roelfsema[2], B. Salasnich[14], J.-F. Sauvage[15,20], R. Siebenmorgen[19], E. Sissa[14], F. Snik[11], M. Suarez[19], J. Szulágyi[6], Ch. Thalmann[1], M. Turatto[14], S. Udry[22], R. G. van Holstein[11], A. Vigan[15], and F. Wildi[22]

(Affiliations can be found after the references)

Received 5 September 2019 / Accepted 24 November 2019

ABSTRACT

Aims. RefPlanets is a guaranteed time observation programme that uses the Zurich IMaging POLarimeter (ZIMPOL) of Spectro-Polarimetric High-contrast Exoplanet REsearch instrument at the Very Large Telescope to perform a blind search for exoplanets in wavelengths from 600 to 900 nm. The goals of this study are the characterisation of the unprecedented high polarimetic contrast and polarimetric precision capabilities of ZIMPOL for bright targets, the search for polarised reflected light around some of the closest bright stars to the Sun, and potentially the direct detection of an evolved cold exoplanet for the first time.

Methods. For our observations of α Cen A and B, Sirius A, Altair, ϵ Eri and τ Ceti we used the polarimetric differential imaging (PDI) mode of ZIMPOL which removes the speckle noise down to the photon noise limit for angular separations $\gtrsim 0.6''$. We describe some of the instrumental effects that dominate the noise for smaller separations and explain how to remove these additional noise effects in post-processing. We then combine PDI with angular differential imaging as a final layer of post-processing to further improve the contrast limits of our data at these separations.

Results. For good observing conditions we achieve polarimetric contrast limits of 15.0–16.3 mag at the effective inner working angle of ∼0.13″, 16.3–18.3 mag at 0.5″, and 18.8–20.4 mag at 1.5″. The contrast limits closer in ($\lesssim 0.6''$) display a significant dependence on observing conditions, while in the photon-noise-dominated regime ($\gtrsim 0.6''$) the limits mainly depend on the brightness of the star and the total integration time. We compare our results with contrast limits from other surveys and review the exoplanet detection limits obtained with different detection methods. For all our targets we achieve unprecedented contrast limits. Despite the high polarimetric contrasts we are not able to find any additional companions or extended polarised light sources in the data obtained so far.

Key words. instrumentation: high angular resolution – methods: data analysis – methods: observational – techniques: polarimetric – techniques: image processing – planets and satellites: detection

1. Introduction

High-contrast imaging is a key technique for the search and classification of extrasolar planets, which is one of the primary goals in modern astronomy. However, the technical requirements are very challenging and up to now only about a dozen young, giant planets have been directly imaged (e.g., Macintosh et al. 2015; Bowler 2016; Schmidt et al. 2016; Chauvin et al. 2017; Keppler et al. 2018). Young, self-contracting giant planets are hot, with temperatures of $T \approx 1000-2000$ K (e.g. Baraffe et al. 2003; Spiegel & Burrows 2012). Therefore, they are bright in the near-infrared (NIR) and the required contrast $C = F_{\rm pl}/F_{\rm star} \approx 10^{-5\pm1}$ is within reach of modern extreme adaptive optics (AO) systems, like the Spectro-Polarimetric High-contrast Exoplanet REsearch instrument (SPHERE; Beuzit et al. 2008) at the Very Large Telescope (VLT), the Gemini Planet Imager (GPI; Macintosh et al. 2014), the Natural Guide Star (NGS) AO system (van Dam et al. 2004) at Keck or the Subaru Coronagraphic Extreme Adaptive Optics (SCExAO; Jovanovic et al. 2015). Unfortunately, young stars with planets are rare in the solar neighbourhood. Furthermore, for the young stars in the nearest star forming regions at $d \approx 150$ pc the expected angular separations of planets tend to already be quite small and therefore these objects are difficult to detect in observations.

Most old planets, including all habitable planets, are cold and therefore produce only scattered light in the visual to NIR (<2 μm) wavelength range (Sudarsky et al. 2003). Light-scattering by the atmosphere of a planet produces a polarisation signal that can be distinguished from the unpolarised light of the much brighter central star (Seager et al. 2000; Stam et al. 2004; Buenzli & Schmid 2009). The contrast of this reflected light from extrasolar planets with respect to the brightness of their host stars is very challenging ($C \lesssim 10^{-7}$), but polarimetric

⋆ Based on observations made with ESO Telescopes at the La Silla Paranal Observatory under programme IDs: 095.C-0312(B), 096.C-0326(A), 097.C-0524(A), 097.C-0524(B), 098.C-0197(A), 099.C-0127(A), 099.C-0127(B), 0102.C-0435(A).

A&A 638, A120 (2020)
https://doi.org/10.1051/0004-6361/202037594

Astronomy & Astrophysics

Searching for the near-infrared counterpart of Proxima c using multi-epoch high-contrast SPHERE data at VLT⋆,⋆⋆

R. Gratton[1], A. Zurlo[2,3,4], H. Le Coroller[4], M. Damasso[5], F. Del Sordo[6,7], M. Langlois[8,4], D. Mesa[1], J. Milli[9], G. Chauvin[10,11], S. Desidera[1], J. Hagelberg[12], E. Lagadec[13], A. Vigan[4], A. Boccaletti[14], M. Bonnefoy[10], W. Brandner[15], S. Brown[15], F. Cantalloube[15], P. Delorme[10], V. D'Orazi[1], M. Feldt[15], R. Galicher[14], T. Henning[15], M. Janson[16], P. Kervella[13], A.-M. Lagrange[10], C. Lazzoni[1], R. Ligi[17], A.-L. Maire[15,18], F. Ménard[10], M. Meyer[19], L. Mugnier[20], A. Potier[14], E. L. Rickman[12], L. Rodet[10], C. Romero[10], T. Schmidt[14,21], E. Sissa[1], A. Sozzetti[5], J. Szulágyi[22], Z. Wahhaj[9], J. Antichi[23], T. Fusco[20], E. Stadler[10], M. Suarez[24], and F. Wildi[12]

(Affiliations can be found after the references)

Received 28 January 2020 / Accepted 14 April 2020

ABSTRACT

Context. Proxima Centauri is the closest star to the Sun and it is known to host an Earth-like planet in its habitable zone; very recently a second candidate planet was proposed based on radial velocities. At quadrature, the expected projected separation of this new candidate is larger than 1 arcsec, making it a potentially interesting target for direct imaging.

Aims. While identification of the optical counterpart of this planet is expected to be very difficult, successful identification would allow for a detailed characterization of the closest planetary system.

Methods. We searched for a counterpart in SPHERE images acquired over four years through the SHINE survey. In order to account for the expected large orbital motion of the planet, we used a method that assumes the circular orbit obtained from radial velocities and exploits the sequence of observations acquired close to quadrature in the orbit. We checked this with a more general approach that considers Keplerian motion, called K-stacker.

Results. We did not obtain a clear detection. The best candidate has signal-to-noise ratio $(S/N) = 6.1$ in the combined image. A statistical test suggests that the probability that this detection is due to random fluctuation of noise is <1%, but this result depends on the assumption that the distribution of noise is uniform over the image, a fact that is likely not true. The position of this candidate and the orientation of its orbital plane fit well with observations in the ALMA 12 m array image. However, the astrometric signal expected from the orbit of the candidate we detected is 3σ away from the astrometric motion of Proxima as measured from early *Gaia* data. This, together with the unexpectedly high flux associated with our direct imaging detection, means we cannot confirm that our candidate is indeed Proxima c.

Conclusions. On the other hand, if confirmed, this would be the first observation in imaging of a planet discovered from radial velocities and the second planet (after Fomalhaut b) of reflecting circumplanetary material. Further confirmation observations should be done as soon as possible.

Key words. planets and satellites: detection – planets and satellites: individual: Proxima c – stars: individual: Proxima – planets and satellites: terrestrial planets – instrumentation: high angular resolution – techniques: image processing

1. Introduction

Proxima Centauri (hereafter Proxima) is the closest star to the Sun (1.3012 ± 0.0003 pc: Benedict et al. 1999; van Leeuwen 2007; Gaia Collaboration 2018) and its planetary system is among the most likely to allow a detailed investigation of an Earth-like planet. Anglada-Escudé et al. (2016) discovered a close-in Earth-like planet, Proxima b, using radial velocities (RV). This planet was confirmed by Damasso & Del Sordo (2017) and a more accurate estimate of the mass of $m_b \sin i_b = 1.0 \pm 0.1\ M_\oplus$ was obtained by Damasso et al. (2020). This planet is in the habitable zone, but it is too close to the star for direct imaging with current instrumentation (projected semi-major axis $a \sim 37$ mas). In the near future, a combination of high-resolution spectroscopy and high-contrast imaging might facilitate the detection of its signal and ultimately the study of the composition of its atmosphere (Snellen et al. 2015; Lovis et al. 2017). Through additional RVs, Damasso et al. (2020) found evidence of a second planet (Proxima c) with a minimum mass of $5.8 \pm 1.9\ M_\oplus$ on a roughly circular orbit with period of 1900^{+96}_{-82} days $= 5.21^{+0.26}_{-0.22}$ yr, and semimajor axis of 1.48 ± 0.08 au, corresponding to a maximum angular separation of 1.14 ± 0.06 arcsec. This planet is compatible with the upper limit set from astrometry (Benedict et al. 1999; Lurie et al. 2014). Hereafter, we use the epoch, period, and semimajor axis of the circular orbit solution by Damasso et al. (2020) to fine-tune our search for Proxima c.

Given its large apparent separation from the star, direct detection of Proxima c might be perhaps feasible, though difficult,

⋆ The reduced images are only available at the CDS via anonymous ftp to cdsarc.u-strasbg.fr (130.79.128.5) or via http://cdsarc.u-strasbg.fr/viz-bin/cat/J/A+A/638/A120

⋆⋆ Based on data collected at the European Southern Observatory, Chile (ESO Programs 095.D-0309, 096.C-0241, 096.D-0252, 097.C-0865, 198.C-D0209, 099.D-0098, 099.C-0127.

A&A 639, A47 (2020)
https://doi.org/10.1051/0004-6361/202037984

Astronomy & Astrophysics

Orbital and spectral characterization of the benchmark T-type brown dwarf HD 19467B⋆,⋆⋆

A.-L. Maire[1,2,⋆⋆⋆], K. Molaverdikhani[2,⋆⋆⋆⋆], S. Desidera[3], T. Trifonov[2], P. Mollière[2], V. D'Orazi[3], N. Frankel[2], J.-L. Baudino[4,5], S. Messina[6], A. Müller[2], B. Charnay[5], A. C. Cheetham[2], P. Delorme[7], R. Ligi[8], M. Bonnefoy[7], W. Brandner[2], D. Mesa[3], F. Cantalloube[2], R. Galicher[5], T. Henning[2], B. A. Biller[9,2], J. Hagelberg[10,7], A.-M. Lagrange[7], B. Lavie[10], E. Rickman[10], D. Ségransan[10], S. Udry[10], G. Chauvin[7,11], R. Gratton[3], M. Langlois[12,13], A. Vigan[13], M. R. Meyer[14], J.-L. Beuzit[13], T. Bhowmik[5], A. Boccaletti[5], C. Lazzoni[3,15], C. Perrot[16,17,5], T. Schmidt[18,5], A. Zurlo[19,20,13], L. Gluck[7], J. Pragt[21], J. Ramos[2], R. Roelfsema[21], A. Roux[7], and J.-F. Sauvage[22,14]

(Affiliations can be found after the references)

Received 19 March 2020 / Accepted 16 May 2020

ABSTRACT

Context. Detecting and characterizing substellar companions for which the luminosity, mass, and age can be determined independently is of utter importance to test and calibrate the evolutionary models due to uncertainties in their formation mechanisms. HD 19467 is a bright and nearby star hosting a cool brown dwarf companion detected with radial velocities and imaging, making it a valuable object for such studies.

Aims. We aim to further characterize the orbital, spectral, and physical properties of the HD 19467 system.

Methods. We present new high-contrast imaging data with the SPHERE and NaCo instruments. We also analyze archival data from the instruments HARPS, NaCo, HIRES, UVES, and ASAS. Furthermore, we use proper motion data of the star from HIPPARCOS and *Gaia*.

Results. We refined the properties of the host star and derived an age of $8.0^{+2.0}_{-1.0}$ Gyr based on isochrones, gyrochronology, and chemical and kinematic arguments. This age estimate is slightly younger than previous age estimates of ∼9–11 Gyr based on isochrones. No orbital curvature is seen in the current imaging, radial velocity, and astrometric data. From a joint fit of the data, we refined the orbital parameters for HD 19467B, including: a period of 398^{+95}_{-93} yr, an inclination of $129.8^{+8.1}_{-5.1}$ deg, an eccentricity of 0.56 ± 0.09, a longitude of the ascending node of 134.8 ± 4.5 deg, and an argument of the periastron of $64.2^{+5.5}_{-6.3}$ deg. We assess a dynamical mass of 74^{+12}_{-9} M_J. The fit with atmospheric models of the spectrophotometric data of the companion indicates an atmosphere without clouds or with very thin clouds, an effective temperature of 1042^{+77}_{-71} K, and a high surface gravity of $5.34^{+0.08}_{-0.09}$ dex. The comparison to model predictions of the bolometric luminosity and dynamical mass of HD 19467B, assuming our system age estimate, indicates a better agreement with the Burrows et al. (1997, ApJ, 491, 856) models; whereas, the other evolutionary models used tend to underestimate its cooling rate.

Key words. brown dwarfs – methods: data analysis – stars: individual: HD 19467 – techniques: high angular resolution – planets and satellites: dynamical evolution and stability – techniques: image processing

1. Introduction

The mass of most substellar companions found around stars with high-contrast imaging techniques is inferred from the comparison of their measured luminosity and estimated age to evolutionary models (e.g., Burrows et al. 1997; Baraffe et al. 2003, 2015; Marley et al. 2007). However, uncertainties in the age estimates and in the initial conditions during the formation of these objects produce large uncertainties in the mass estimates, especially at the boundary of the planet and brown dwarf regimes. To test and calibrate the evolutionary models, the detection and the characterization of benchmark low-mass companions, for which the luminosity, mass, and age can be derived from independent methods, is of paramount importance.

HD 19467 is a G3 main-sequence star located at 32.03 ± 0.11 pc[1] (Gaia Collaboration 2016, 2018). Crepp et al. (2014) infer an age of 4.6–10 Gyr from isochrones and gyrochronology, and a subsolar metallicity of [Fe/H] = −0.15 ± 0.04 dex. Mason et al. (2001) did not find evidence for stellar binarity from speckle interferometry. Crepp et al. (2014) report the discovery of a cool brown dwarf companion from a radial velocity (RV) trend measured with the Keck High Resolution Echelle Spectrometer (HIRES) and subsequently confirmed with near-infrared (NIR) high-contrast imaging with the Keck Near-InfraRed Camera (NIRC2). HD 19467B has an

⋆ The reduced images shown in Fig. 3 are only available at the CDS via anonymous ftp to cdsarc.u-strasbg.fr (130.79.128.5) or via http://cdsarc.u-strasbg.fr/viz-bin/cat/J/A+A/639/A47

⋆⋆ Based on observations collected at the European Organisation for Astronomical Research in the Southern Hemisphere under ESO programmes 1100.C-0481, 0100.C-0234, 096.C-0602, 072.C-0488, 183.C-0972, 084.D-0965, 188.C-0265, 192.C-0852, and 0100.D-0444.

⋆⋆⋆ F.R.S.-FNRS Postdoctoral Researcher.

⋆⋆⋆⋆ International Max Planck Research School for Astronomy and Cosmic Physics, Heidelberg, Germany.

[1] The uncertainty includes an additional uncertainty of 0.1 mas to account for potential parallax systematics, https://www.cosmos.esa.int/web/gaia/dr2

APPENDIX B

RUNNING THE GRAPHIC PIPELINE FOR THE NACO-ISPY SURVEY

The instructions to run the GRAPHIC pipeline (Hagelberg et al. 2016) for the NACO-ISPY data, discussed in Chapter 6.2, are outlined below. There are seven steps required to process the data from their raw form to being ready for the DACE platform. They are the following:

1. Download data
2. Sort and check consistency
3. Process flux frames
4. Process target frames
5. Run PCA and contrast curve
6. Run DICPM / TRAP
7. Copy to DACE

B.1 Important information

A few things to note before the steps are outlined. The code to run the pipeline is in on the `nacodrs`:

`~/code/naco_ispy/`

where `~/` means `/home/local/nacodrs` on the `nacodrs` server. The `git` repository is at https://gitlab.unige.ch/Anthony.Cheetham/naco_ispy and mirrored at https://github.com/AnthonyCheetham/naco_ispy.

The processing scripts that launch GRAPHIC are here:

`~/code/naco_ispy/processing_scripts/`

The high level python scripts (e.g. to queue reductions for multiple targets at once) are here:

`~/code/naco_ispy/data_handling_scripts/`

GRAPHIC itself is in:

`~/code/graphic_git/3.3/`

Step 1 is performed on the `obstr01` server as the `trmgr` user. Steps 2-6 are performed on `nacodrs` as the `nacodrs` user. To log in as `nacodrs` and process the data, first log into the `nacodrs` machine with your own username, then type:

```
su -l nacodrs
```

This uses the "automated" pipeline, which tracks datasets and whether they have been processed, and launches GRAPHIC processing scripts as background jobs for any remaining tasks. The status of each dataset is stored in a .csv file/table, which needs to be updated regularly (or else the same dataset may be processed twice, or you won't be able to launch the processing for new data):

`/data/NACO/obs_table.dat`

All of the "automated" scripts are in:

`~/code/naco_ispy/data_handling_scripts`

The actual job queuing is done by `queue_analysis.py`. It has options `-flux`, `-targ`, `-pca`, `-dicpm` for the different steps you would want to launch. By default it launches the processing on all datasets that have not been processed yet.

- To print out what it will queue without queuing it (it is always a good idea to run this first) use the option:

  `-dry_run`

- To ignore whether the dataset has already been processed, and launch it anyway, use the option:

  `-reprocess`

- To only consider datasets up to number `X` (when ordered by date) use the option:

  `--num X`

- To only consider datasets from number `X` (when ordered by date) use the option:

  `--skip X`

- For example, to process the target frames on datasets 20 to 40:

  ```
  python queue_analysis.py --num 40 --skip 20 -targ
  ```

B.2 Steps to run GRAPHIC

1 Download data

- Log onto `trmgr@obstr01`. Then:

  `cd /home/trmgr/TRESO/`

  `python EsoTransfert.py -i NACO -n 2019-01-18 -ac True`
- Can run as batch process using `"at now"`, or by first logging into `login01.astro.unige.ch` and using the ‘‘`screen`’’ command to run it in the background.

2 Sort and check consistency

- Sort the data using `copy_sort_data.py` in the `data_handling_scripts` directory:

  `python copy_sort_data.py`
- Data is sorted into `/data/NACO/Science/Date/Target/`and then `Flux`, `Sky` or `Targ` depending on the type.
- Add the data to the observations table using `update_obs_table.py`:

  `python update_obs_table.py`
- It will print the location of dataset and whether it is consistent, with a `TRUE` or `FALSE` for the `Flux` and `Sky/Targ` files. For example:

  `/data/NACO/Science/2015-12-15/HD17925/`

  `Final status: True True`

  This means `Flux=TRUE`, `Targ=TRUE` so both are consistent and ready to process.

If a problem is detected, it will say what the problem is and you need to fix it and repeat this step. A common problem might be that the exposure time was changed at the start of the sequence. If so, remove the few files with the wrong exposure time at the start. Or there might be too many or too few flux frames (there must be a multiple of 3), and the ones that were taken accidentally need to be removed.

3 Process flux frames

- Queue up the analysis using `queue_analysis.py` in the `data_handling_scripts` directory. It will only queue sequences that pass the consistency test. It calls `flux.slurm` in the `processing_scripts` directory:

  `python queue_analysis.py -flux`
- Other options include `--num X` to only look at first `X` files, `--skip Y` to ignore the first `Y` files, `-dry_run` to print what it would do without `-dry_run` instead of launching the reduction, `-reprocess` to force the pipeline to run on data that has already been processed.

- Each job will be launched with `"at"` or `"batch"` and put in the queue to be started once the previous job finishes.
- Output goes into `ADI/`

4 Process target frames

- Queue up the analysis using `queue_analysis.py` in the `data_handling_scripts` directory:

  `python queue_analysis.py -targ`
- It has the same procedure and options as the flux queueing. It calls `agpm_graphic.slurm` or `saturated_psf_graphic.slurm` from the `processing_scripts` directory, depending on whether or not the AGPM was inserted.
- Output goes into `ADI/`

5 Run PCA and contrast curve

- Update the `obs_table` so that the pipeline knows it is ready for PCA:

  `python update_obs_table.py`
- Queue up the analysis using `queue_analysis.py` in the `data_handling_scripts` directory:

  `python queue_analysis.py -pca`
- It has the same procedure and options as the flux queuing. It calls `pca_graphic_agpm.slurm` or `pca_graphic_satpsf.slurm` from the `processing_scripts` directory, depending on whether or not the AGPM was inserted.
- Output goes into `ADI/GRAPHIC_PCA/` and `ADI/cADI/`.

6 Run DICPM (aka TRAP)

- Queue up the analysis using `queue_analysis.py` in the `data_handling_scripts` directory:

  `python queue_analysis.py -dicpm`
- It has the same procedure and options as the flux queuing. It calls `dicpm_reduction.slurm` from the `processing_scripts` directory.
- Output goes into `ADI/DICPM/`
- **NOTE:** `update_obs_table.py` does not track whether TRAP has been run before! So be careful before launching jobs.

7 Copy to DACE

- Copy using `copy_for_dace` in the `data_handling_scripts` directory:

  `python copy_for_dace.py`

- Copies the results from `ADI/GRAPHIC_PCA/` to `data/NACO/NACO-ISPYDRS/DRS-1.0/reduced/`, after converting into a DACE-friendly format.
- Request to the DACE team to update the NACO data on DACE.

B.3 Additional information

B.3.1 Known issues

- If GRAPHIC has a problem while running, it can occasionally fail to close some of the processes, which can lead to some MPI threads running in the background at 100% CPU until forced to close using the ‘‘`kill`’’ command. So you need to occasionally check how many processes remain in the queue (using `atq`) to ensure it is progressing, and fix any problems in GRAPHIC that may cause this.
- The processing does not currently do bad pixel or flat field correction. The vast majority of bad pixels are removed by the PCA sky subtraction, which is probably an unreliable way to do it. The main problem has always been cosmic rays and blinking pixels, which were not fixed by GRAPHIC until recently. The flat fields were not implemented because it was difficult to find a good solution to detecting the right one and getting GRAPHIC to use it, and because tests showed that it makes no significant difference to the results.
- The flat fields can be processed using `queue_cal_analysis.py` in the `data_handling_scripts` directory, but it is not yet linked to the database or the rest of the pipeline. One solution might be to have a script that copies the closest flat in time into each target directory before queuing the target analysis.
- In late 2018, there were some upgrades made to the bad pixel code. This could be tested and implemented into the ISPY processing scripts. It will significantly increase the time to process the data though (earlier tests showed it roughly doubles the processing time).

B.3.2 Notes about GRAPHIC

GRAPHIC is a collection of python scripts that do specific reduction steps (e.g. sky subtraction, binning, calculating the star position). Bash scripts have been made that run the steps in the right order and with the right options. The reduction is split into several steps. Each step is designed to be run in the `/data/NACO/Science/Date/TargetName/` directory for each target. The bash scripts are in:

`~/code/naco_ispy/processing_scripts/`

The scripts assume that the data have been downloaded and sorted into `Flux`, `Sky` and `Targ` directories (which is done by `copy_sort_data.py` as described in step 2 in Section B.2).

B.3.3 Cleaning

The outputs of these scripts are automatically put into the corresponding `/data/NACO/Science/Date/TargetName/ADI` directory.

- To process the flux files:

  `flux.slurm`

- To clean the AGPM files:

  `agpm_graphic.slurm`

- To clean the saturated PSF files:

  `saturated_psf_graphic.slurm`

B.3.4 PSF subtraction

The outputs of these scripts are automatically put into the corresponding `/data/NACO/Science/Date/TargetName/ADI/ReductionAlgorithm` directory.

- To run PCA and cADI with the FoV tuned for the AGPM data:

  `pca_graphic_agpm.slurm`

- To run PCA and cADI with the FoV tuned for the saturated PSF data:

  `pca_graphic_satpsf.slurm`

- To run DICPM/TRAP on a 1.4" FoV:

  `dicpm_reduction.slurm`

Appendix C

Running the DACE Python API for the NACO-ISPY survey

The data from the NACO-ISPY survey, discussed in Chapter 6.2, can be accessed directly through the DACE website (Buchschacher et al. 2015; Buchschacher & Alesina 2019) from:

https://dace.unige.ch/observationSearch/?observationType=[%22imaging%22]

Alternatively, one can use the recently developed Python API through DACE to access the data. Below is an example of accessing NACO-ISPY data through the Python API:

```
from dace.imaging import Imaging

#query the observation database and search for ISPY observations
observedTargets = Imaging.query_database(limit=10000, filters={'prog_id':
 ↪ {'contains': 'NACO-ISPY'}})

#list the different fields (corresponding to the columns in the web interface
 ↪ https://dace.unige.ch/observationSearch/
for key in observedTargets.keys():
    print(key)

#print the values of several of the fields
for j in range(len(observedTargets['obj_id_catname'])):
    print('%3d %12s %10s %30s' %(j,observedTargets['obj_id_catname'][j],
     ↪ observedTargets['date_night'][j], observedTargets['file_rootpath'][j]))

#download all of the reduced data of one night for the ISPY programme
Imaging.download('all',filters={'date_night':  {'contains':
 ↪ '2017-10-29'},'prog_id': {'contains': 'NACO-ISPY'}},
 ↪ output_full_file_path='/tmp/ISPY-2017-10-29.tar.gz')
```

```
16
17 #download all of the reduced data of a target for the ISPY programme
18 Imaging.download('all',filters={'obj_id_catname':  {'contains':
    ↪  'HD38120'},'prog_id': {'contains': 'NACO-ISPY'}},
    ↪  output_full_file_path='/tmp/ISPY-HD38120.tar.gz')
19
20 #get a specific reduced image
21 Imaging.get_image('NACO.2017-10-30T09:15:20.189_gpca.fits',file_type='HC',
    ↪  output_full_file_path='/tmp/NACO.2017-10-30T09:15:20.189_gpca_hc.fits')
```

REFERENCES

Absil, O., Mawet, D., Delacroix, C., et al. 2014, Society of Photo-Optical Instrumentation Engineers (SPIE) Conference Series, Vol. 9148, The VORTEX project: first results and perspectives, 91480M

Absil, O., Milli, J., Mawet, D., et al. 2013, A&A, 559, L12

Adams, F. C. & Benz, W. 1992, Astronomical Society of the Pacific Conference Series, Vol. 32, Gravitational Instabilties in Circumstellar Disks and the Formation of Binary Companions, ed. H. A. McAlister & W. I. Hartkopf, 170

Aguilera-Gómez, C., Ramírez, I., & Chanamé, J. 2018, A&A, 614, A55

Ahn, C. P., Alexandroff, R., Allende Prieto, C., et al. 2012, ApJS, 203, 21

Akeson, R. L., Chen, X., Ciardi, D., et al. 2013, PASP, 125, 989

Alibert, Y., Mordasini, C., Benz, W., & Winisdoerffer, C. 2005, A&A, 434, 343

Allard, F. 2014, in IAU Symposium, Vol. 299, Exploring the Formation and Evolution of Planetary Systems, ed. M. Booth, B. C. Matthews, & J. R. Graham, 271–272

Allard, F., Hauschildt, P. H., Alexander, D. R., Tamanai, A., & Schweitzer, A. 2001, ApJ, 556, 357

Allard, F., Homeier, D., & Freytag, B. 2012, Philosophical Transactions of the Royal Society of London Series A, 370, 2765

Amara, A. & Quanz, S. P. 2012, MNRAS, 427, 948

Andrews, S. M., Huang, J., Pérez, L. M., et al. 2018, ApJL, 869, L41

Bailey, J. 2014, PASA, 31, e043

Bailey, V., Meshkat, T., Reiter, M., et al. 2014, ApJL, 780, L4

Baluev, R. V. 2008, MNRAS, 385, 1279

Baraffe, I., Chabrier, G., & Barman, T. 2010, Reports on Progress in Physics, 73, 016901

Baraffe, I., Chabrier, G., Barman, T. S., Allard, F., & Hauschildt, P. H. 2003, A&A, 402, 701

Baraffe, I., Homeier, D., Allard, F., & Chabrier, G. 2015, AAP, 577, A42

Baranne, A., Queloz, D., Mayor, M., et al. 1996, A&AS, 119, 373

Basri, G. & Marcy, G. W. 1995, AJ, 109, 762

Basri, G., Marcy, G. W., & Graham, J. R. 1996, ApJ, 458, 600

Bensby, T., Feltzing, S., & Oey, M. S. 2014, A&A, 562, A71

Beuzit, J.-L., Mouillet, D., Lagrange, A.-M., et al. 1998, Society of Photo-Optical Instrumentation Engineers (SPIE) Conference Series, Vol. 3353, Coupling adaptive optics and coronography: the ADONIS coronograph, ed. D. Bonaccini & R. K. Tyson, 233–240

Beuzit, J. L., Vigan, A., Mouillet, D., et al. 2019, A&A, 631, A155

Boccaletti, A., Chauvin, G., Mouillet, D., et al. 2020, arXiv e-prints, arXiv:2003.05714

Boccaletti, A., Thébault, P., Pawellek, N., et al. 2019, A&A, 625, A21

Bodenheimer, P., Grossman, A. S., Decampli, W. M., Marcy, G., & Pollack, J. B. 1980, Icarus, 41, 293

Boeshaar, P. C. 1976, PhD thesis, Ohio State University, Columbus.

Bonnefoy, M., Lagrange, A. M., Boccaletti, A., et al. 2011, A&A, 528, L15

Borucki, W. J., Koch, D., Basri, G., et al. 2010, Science, 327, 977

Boss, A. P. 1997, Science, 276, 1836

Boss, A. P. 2006, ApJL, 637, L137

Boss, A. P., Basri, G., Kumar, S. S., et al. 2003, in IAU Symposium, Vol. 211, Brown Dwarfs, ed. E. Martín, 529

Boss, A. P., Fisher, R. T., Klein, R. I., & McKee, C. F. 2000, ApJ, 528, 325

Bouchy, F., Hébrard, G., Udry, S., et al. 2009, A&A, 505, 853

Bowler, B. P. 2016, PASP, 128, 102001

Bowler, B. P., Blunt, S. C., & Nielsen, E. L. 2020, AJ, 159, 63

Bowler, B. P., Dupuy, T. J., Endl, M., et al. 2018, AJ, 155, 159

Brandt, T. D. 2018, ApJS, 239, 31

Brandt, T. D., Dupuy, T. J., Bowler, B. P., et al. 2019, arXiv e-prints, arXiv:1910.01652

Buchschacher, N. & Alesina, F. 2019, Astronomical Society of the Pacific Conference Series, Vol. 521, DACE: New Available Visualisation and Analysis Tools for Exoplanet Research, ed. M. Molinaro, K. Shortridge, & F. Pasian, 757

Buchschacher, N., Ségransan, D., Udry, S., & Díaz, R. 2015, Astronomical Society of the Pacific Conference Series, Vol. 495, Data and Analysis Center for Exoplanets, ed. A. R. Taylor & E. Rosolowsky, 7

Burgasser, A. J. 2007, ApJ, 659, 655

Burgasser, A. J. 2014, in Astronomical Society of India Conference Series, Vol. 11, Astronomical Society of India Conference Series

Burgasser, A. J., Aganze, C., Escala, I., et al. 2016, in American Astronomical Society Meeting Abstracts, Vol. 227, American Astronomical Society Meeting Abstracts #227, 434.08

Burgasser, A. J., Geballe, T. R., Leggett, S. K., Kirkpatrick, J. D., & Golimowski, D. A. 2006, ApJ, 637, 1067

Burgasser, A. J., Kirkpatrick, J. D., Brown, M. E., et al. 1999, ApJL, 522, L65

Burrows, A., Hubbard, W. B., Lunine, J. I., & Liebert, J. 2001, Reviews of Modern Physics, 73, 719

Burrows, A., Hubbard, W. B., Saumon, D., & Lunine, J. I. 1993, ApJ, 406, 158

Burrows, A., Marley, M., Hubbard, W. B., et al. 1997, ApJ, 491, 856

Burrows, A., Sudarsky, D., & Hubeny, I. 2006, ApJ, 640, 1063

Burrows, A., Sudarsky, D., & Lunine, J. I. 2003, ApJ, 596, 587

Butler, R. P. & Marcy, G. W. 1996, ApJL, 464, L153

Butler, R. P., Marcy, G. W., Vogt, S. S., & Apps, K. 1998, PASP, 110, 1389

Butler, R. P., Marcy, G. W., Williams, E., Hauser, H., & Shirts, P. 1997, ApJL, 474, L115

Butler, R. P., Vogt, S. S., Laughlin, G., et al. 2017, AJ, 153, 208

Butler, R. P., Wright, J. T., Marcy, G. W., et al. 2006, ApJ, 646, 505

Cameron, A. G. W. 1978, Moon and Planets, 18, 5

Carlomagno, B., Absil, O., Kenworthy, M., et al. 2016, Society of Photo-Optical Instrumentation Engineers (SPIE) Conference Series, Vol. 9909, End-to-end simulations of the E-ELT/METIS coronagraphs, 990973

Casagrande, L., Schönrich, R., Asplund, M., et al. 2011, A&A, 530, A138

Chabrier, G. & Baraffe, I. 2000, Annu. Rev. Astron. Astrophys., 38, 337

Chabrier, G., Baraffe, I., Allard, F., & Hauschildt, P. 2000, ApJ, 542, 464

Chabrier, G., Baraffe, I., Leconte, J., Gallardo, J., & Barman, T. 2009, in American Institute of Physics Conference Series, Vol. 1094, 15th Cambridge Workshop on Cool Stars, Stellar Systems, and the Sun, ed. E. Stempels, 102–111

Chabrier, G., Johansen, A., Janson, M., & Rafikov, R. 2014, in Protostars and Planets VI, ed. H. Beuther, R. S. Klessen, C. P. Dullemond, & T. Henning, 619

Chabrier, G., Mazevet, S., & Soubiran, F. 2019, ApJ, 872, 51

Charbonneau, D., Allen, L. E., Megeath, S. T., et al. 2005, ApJ, 626, 523

Charbonneau, D., Brown, T. M., Latham, D. W., & Mayor, M. 2000, ApJL, 529, L45

Charbonneau, D., Brown, T. M., Noyes, R. W., & Gilliland, R. L. 2002, ApJ, 568, 377

Chauvin, G., Desidera, S., Lagrange, A. M., et al. 2017, A&A, 605, L9

Chauvin, G., Lagrange, A. M., Dumas, C., et al. 2004, A&A, 425, L29

Cheetham, A., Bonnefoy, M., Desidera, S., et al. 2018a, A&A, 615, A160

Cheetham, A., Ségransan, D., Peretti, S., et al. 2018b, A&A, 614, A16

Cheetham, A. C., Samland, M., Brems, S. S., et al. 2019, A&A, 622, A80

Christou, J. C., Marchis, F., Ageorges, N., Bonaccini, D., & Rigaut, F. J. 1998, Society of Photo-Optical Instrumentation Engineers (SPIE) Conference Series, Vol. 3353, Deconvolution of ADONIS images, ed. D. Bonaccini & R. K. Tyson, 984–993

Claudi, R. U., Turatto, M., Gratton, R. G., et al. 2008, Society of Photo-Optical Instrumentation Engineers (SPIE) Conference Series, Vol. 7014, SPHERE IFS: the spectro differential imager of the VLT for exoplanets search, 70143E

Close, L. M., Males, J. R., Morzinski, K., et al. 2013, ApJ, 774, 94

Close, L. M., Puglisi, A., Males, J. R., et al. 2012, ApJ, 749, 180

Close, L. M., Wildi, F., Lloyd-Hart, M., et al. 2003, ApJ, 599, 537

Cosentino, R., Lovis, C., Pepe, F., et al. 2012, Society of Photo-Optical Instrumentation Engineers (SPIE) Conference Series, Vol. 8446, Harps-N: the new planet hunter at TNG, 84461V

Crepp, J. R., Johnson, J. A., Howard, A. W., et al. 2012, ApJ, 761, 39

Cugno, G., Quanz, S. P., Launhardt, R., et al. 2019, A&A, 624, A29

Cushing, M. C., Kirkpatrick, J. D., Gelino, C. R., et al. 2011, ApJ, 743, 50

Cutri, R. M. & et al. 2012, VizieR Online Data Catalog, II/311

Cutri, R. M. & et al. 2013, VizieR Online Data Catalog, II/328

Cutri, R. M. & et al. 2014, VizieR Online Data Catalog, II/328

Cutri, R. M., Skrutskie, M. F., van Dyk, S., et al. 2003, VizieR Online Data Catalog, II/246

Davies, R. & Kasper, M. 2012, Annu. Rev. Astron. Astrophys., 50, 305

de Boer, J., Langlois, M., van Holstein, R. G., et al. 2020, A&A, 633, A63

Delfosse, X., Forveille, T., Beuzit, J. L., et al. 1999a, A&A, 344, 897

Delfosse, X., Forveille, T., Mayor, M., et al. 1998, A&A, 338, L67

Delfosse, X., Tinney, C. G., Forveille, T., et al. 1999b, A&AS, 135, 41

Delgado Mena, E., Tsantaki, M., Adibekyan, V. Z., et al. 2017, A&A, 606, A94

Delisle, J. B., Ségransan, D., Buchschacher, N., & Alesina, F. 2016, A&A, 590, A134

Delisle, J. B., Ségransan, D., Dumusque, X., et al. 2018, A&A, 614, A133

DENIS Consortium. 2005, VizieR Online Data Catalog, II/263

Díaz, R. F., Almenara, J. M., Santerne, A., et al. 2014, MNRAS, 441, 983

Díaz, R. F., Ségransan, D., Udry, S., et al. 2016, A&A, 585, A134

Dohlen, K., Langlois, M., Saisse, M., et al. 2008, in Proc. SPIE, Vol. 7014, Ground-based and Airborne Instrumentation for Astronomy II, 70143L

Dumusque, X., Lovis, C., Ségransan, D., et al. 2011, A&A, 535, A55

Dupuy, T. J. & Liu, M. C. 2012, ApJS, 201, 19

Dupuy, T. J., Liu, M. C., & Ireland, M. J. 2014, ApJ, 790, 133

Einstein, A. 1905, Annalen der Physik, 322, 891

Ekström, S., Georgy, C., Eggenberger, P., et al. 2012, A&A, 537, A146

Engler, N., Lazzoni, C., Gratton, R., et al. 2020, A&A, 635, A19

Epchtein, N., de Batz, B., Capoani, L., et al. 1997, The Messenger, 87, 27

Faherty, J. K., Rice, E. L., Cruz, K. L., Mamajek, E. E., & Núñez, A. 2013, AJ, 145, 2

Faherty, J. K., Riedel, A. R., Cruz, K. L., et al. 2016, ApJS, 225, 10

Fegley, Bruce, J. & Lodders, K. 1996, ApJL, 472, L37

Fischer, D. A., Marcy, G. W., Butler, R. P., Vogt, S. S., & Apps, K. 1999, PASP, 111, 50

Fischer, D. A., Marcy, G. W., Butler, R. P., et al. 2001, ApJ, 551, 1107

Fischer, D. A., Marcy, G. W., & Spronck, J. F. P. 2014, ApJS, 210, 5

Fontanive, C., Biller, B., Bonavita, M., & Allers, K. 2018, MNRAS, 479, 2702

Forbrich, J., Preibisch, T., & Menten, K. M. 2006, A&A, 446, 155

Fortney, J. J., Ikoma, M., Nettelmann, N., Guillot, T., & Marley, M. S. 2011, ApJ, 729, 32

Forveille, T., Beuzit, J.-L., Delfosse, X., et al. 1999, A&A, 351, 619

Fried, D. L. 1966, Journal of the Optical Society of America (1917-1983), 56, 1372

Gaia Collaboration, Brown, A. G. A., Vallenari, A., et al. 2018, A&A, 616, A1

Gaia Collaboration, Brown, A. G. A., Vallenari, A., et al. 2016a, A&A, 595, A2

Gaia Collaboration, Prusti, T., de Bruijne, J. H. J., et al. 2016b, A&A, 595, A1

Garufi, A., Podio, L., Bacciotti, F., et al. 2019, A&A, 628, A68

Gay, J. & Rabbia, Y. 1996, Academie des Sciences Paris Comptes Rendus Serie B Sciences Physiques, 3, 265

Georgy, C., Ekström, S., Eggenberger, P., et al. 2013, A&A, 558, A103

Gizis, J. E., Reid, I. N., Knapp, G. R., et al. 2003, AJ, 125, 3302

Goldman, B., Bouy, H., Zapatero Osorio, M. R., et al. 2008, A&A, 490, 763

Gonzales, E. J., Crepp, J. R., Bechter, E. B., et al. 2020, ApJ, 893, 27

Goodwin, S. P. & Whitworth, A. 2007, A&A, 466, 943

Gratton, R., Zurlo, A., Le Coroller, H., et al. 2020, A&A, 638, A120

Gravity Collaboration, Lacour, S., Nowak, M., et al. 2019, A&A, 623, L11

Grether, D. & Lineweaver, C. H. 2006, ApJ, 640, 1051

Grossman, A. S., Hays, D., & Graboske, H. C., J. 1974, A&A, 30, 95

Guyon, O. 2018, Annu. Rev. Astron. Astrophys., 56, 315

Guyon, O., Pluzhnik, E. A., Kuchner, M. J., Collins, B., & Ridgway, S. T. 2006, ApJS, 167, 81

Hagelberg, J. 2014, PhD thesis, UNIGE, iD: unige:48240

Hagelberg, J., Ségransan, D., Udry, S., & Wildi, F. 2016, MNRAS, 455, 2178

Halbwachs, J. L., Mayor, M., Udry, S., & Arenou, F. 2003, A&A, 397, 159

Hauschildt, P. H., Allard, F., Ferguson, J., Baron, E., & Alexander, D. R. 1999, ApJ, 525, 871

Helling, C., Ackerman, A., Allard, F., et al. 2008, MNRAS, 391, 1854

Helling, C. & Casewell, S. 2014, A&ARv, 22, 80

Hennebelle, P. & Chabrier, G. 2008, ApJ, 684, 395

Henry, G. W., Marcy, G. W., Butler, R. P., & Vogt, S. S. 2000, ApJL, 529, L41

Henyey, L. G., Lelevier, R., & Levée, R. D. 1955, PASP, 67, 154

Hinkley, S., Oppenheimer, B. R., Soummer, R., et al. 2007, ApJ, 654, 633

Høg, E., Fabricius, C., Makarov, V. V., et al. 2000, A&A, 355, L27

Hunziker, S., Quanz, S. P., Amara, A., & Meyer, M. R. 2018, A&A, 611, A23

Hunziker, S., Schmid, H. M., Mouillet, D., et al. 2020, A&A, 634, A69

Ida, S. & Lin, D. N. C. 2004, ApJ, 604, 388

Janson, M., Bergfors, C., Goto, M., Brandner, W., & Lafrenière, D. 2010, ApJL, 710, L35

Jeans, J. H. 1902, Philosophical Transactions of the Royal Society of London Series A, 199, 1

Joergens, V. 2014, 50 Years of Brown Dwarfs: From Prediction to Discovery to Forefront of Research, Vol. 401

Kaufer, A. 2008, Very Large Telescope NaCo User Manual

Kenworthy, M. A., Snik, F., Keller, C. U., et al. 2018, in Proc. SPIE, Vol. 10702, Society of Photo-Optical Instrumentation Engineers (SPIE) Conference Series, 1070246

Keppler, M., Benisty, M., Müller, A., et al. 2018, A&A, 617, A44

Kervella, P., Arenou, F., & Schneider, J. 2020, A&A, 635, L14

Kirkpatrick, J. D., Gelino, C. R., Cushing, M. C., et al. 2012, ApJ, 753, 156

Kirkpatrick, J. D., Henry, T. J., & McCarthy, Donald W., J. 1991, ApJS, 77, 417

Kirkpatrick, J. D., Reid, I. N., Liebert, J., et al. 1999, ApJ, 519, 802

Kirkpatrick, J. D., Schneider, A., Fajardo-Acosta, S., et al. 2014, ApJ, 783, 122

Koch, D. G., Borucki, W. J., Basri, G., et al. 2010, ApJL, 713, L79

Kolmogorov, A. 1941, Akademiia Nauk SSSR Doklady, 30, 301

Konopacky, Q. M., Rameau, J., Duchêne, G., et al. 2016, ApJL, 829, L4

Kraus, S., Hofmann, K. H., Malbet, F., et al. 2009, A&A, 508, 787

Kroupa, P. 1998, Astronomical Society of the Pacific Conference Series, Vol. 134, The Stellar Mass Function (invited review), ed. R. Rebolo, E. L. Martin, & M. R. Zapatero Osorio, 483

Kumar, S. 1995, Astronomical Society of the Pacific Conference Series, Vol. 74, Planets and Black Dwarfs, ed. G. S. Shostak, 231

Kumar, S. S. 1962a, Models for Stars of Very Low Mass, Institute for Space Studies Report Number X-644-62-78 (1962

Kumar, S. S. 1962b, AJ, 67, 579

Kumar, S. S. 1963a, ApJ, 137, 1126

Kumar, S. S. 1963b, ApJ, 137, 1121

Kumar, S. S. 1972, APSS, 17, 453

Kumar, S. S. 1974, APSS, 28, 173

Kumar, S. S. 1994, APSS, 212, 57

Kuzuhara, M., Tamura, M., Kudo, T., et al. 2013, ApJ, 774, 11

Labeyrie, A. 1970, A&A, 6, 85

Lacombe, F., Marco, O., Geoffray, H., et al. 1998, PASP, 110, 1087

Lagrange, A. M., Bonnefoy, M., Chauvin, G., et al. 2010, Science, 329, 57

Lagrange, A. M., Langlois, M., Gratton, R., et al. 2016, A&A, 586, L8

Lane, B. F., Zapatero Osorio, M. R., Britton, M. C., Martín, E. L., & Kulkarni, S. R. 2001, ApJ, 560, 390

Launhardt, R. 2009, NAR, 53, 294

Launhardt, R., Henning, T., Quirrenbach, A., et al. 2020, A&A, 635, A162

Lawrence, A., Warren, S. J., Almaini, O., et al. 2007, MNRAS, 379, 1599

Leggett, S. K., Dupuy, T. J., Morley, C. V., et al. 2019, ApJ, 882, 117

Lenzen, R., Close, L., Brandner, W., Biller, B., & Hartung, M. 2004, Society of Photo-Optical Instrumentation Engineers (SPIE) Conference Series, Vol. 5492, A novel simultaneous differential imager for the direct imaging of giant planets, ed. A. F. M. Moorwood & M. Iye, 970–977

Lenzen, R., Hartung, M., Brandner, W., et al. 2003, Society of Photo-Optical Instrumentation Engineers (SPIE) Conference Series, Vol. 4841, NAOS-CONICA first on sky results in a variety of observing modes, ed. M. Iye & A. F. M. Moorwood, 944–952

Levee, R. D. 1953, ApJ, 117, 200

Liu, M. C., Magnier, E. A., Deacon, N. R., et al. 2013, ApJL, 777, L20

Luhman, K. L. 2014, ApJL, 786, L18

Luhman, K. L., Wilson, J. C., Brandner, W., et al. 2006, ApJ, 649, 894

Lyot, B. 1939, MNRAS, 99, 580

Ma, B. & Ge, J. 2014, MNRAS, 439, 2781

Macintosh, B., Poyneer, L., Sivaramakrishnan, A., & Marois, C. 2005, Society of Photo-Optical Instrumentation Engineers (SPIE) Conference Series, Vol. 5903, Speckle lifetimes in high-contrast adaptive optics, ed. R. K. Tyson & M. Lloyd-Hart, 170–177

Macintosh, B. A., Graham, J. R., Palmer, D. W., et al. 2008, Society of Photo-Optical Instrumentation Engineers (SPIE) Conference Series, Vol. 7015, The Gemini Planet Imager: from science to design to construction, 701518

Madhusudhan, N., Burrows, A., & Currie, T. 2011, ApJ, 737, 34

Maire, A.-L., Langlois, M., Dohlen, K., et al. 2016, Society of Photo-Optical Instrumentation Engineers (SPIE) Conference Series, Vol. 9908, SPHERE IRDIS and IFS astrometric strategy and calibration, 990834

Maire, A. L., Molaverdikhani, K., Desidera, S., et al. 2020, arXiv e-prints, arXiv:2005.10312

Maire, A. L., Rodet, L., Cantalloube, F., et al. 2019, A&A, 624, A118

Marcy, G. W. & Butler, R. P. 2000, PASP, 112, 137

Marcy, G. W., Butler, R. P., Vogt, S. S., et al. 2001, ApJ, 555, 418

Marley, M. S., Fortney, J. J., Hubickyj, O., Bodenheimer, P., & Lissauer, J. J. 2007, ApJ, 655, 541

Marley, M. S., Seager, S., Saumon, D., et al. 2002, ApJ, 568, 335

Marmier, M., Ségransan, D., Udry, S., et al. 2013, A&A, 551, A90

Marois, C., Doyon, R., Racine, R., et al. 2005, JRASC, 99, 130

Marois, C., Lafrenière, D., Doyon, R., Macintosh, B., & Nadeau, D. 2006, ApJ, 641, 556

Marois, C., Macintosh, B., Barman, T., et al. 2008, Science, 322, 1348

Marois, C., Zuckerman, B., Konopacky, Q. M., Macintosh, B., & Barman, T. 2010, Nature, 468, 1080

Martinache, F. 2019, Diffraction-dominated observational astronomy, ed. N. Nardetto, Y. Lebreton, & E. Lagadec, 16–54

Mason, B. D., Wycoff, G. L., Hartkopf, W. I., Douglass, G. G., & Worley, C. E. 2001, AJ, 122, 3466

Mata Sánchez, D., González Hernández, J. I., Israelian, G., et al. 2014, A&A, 566, A83

Mawet, D., Absil, O., Delacroix, C., et al. 2013, A&A, 552, L13

Mawet, D., David, T., Bottom, M., et al. 2015, ApJ, 811, 103

Mawet, D., Riaud, P., Absil, O., & Surdej, J. 2005, ApJ, 633, 1191

Mayor, M., Marmier, M., Lovis, C., et al. 2011, arXiv e-prints, arXiv:1109.2497

Mayor, M., Pepe, F., Queloz, D., et al. 2003, The Messenger, 114, 20

Mayor, M. & Queloz, D. 1995, Nature, 378, 355

Mayor, M. & Udry, S. 2000, Astronomical Society of the Pacific Conference Series, Vol. 219, Mass Function and Distributions of the Orbital Elements of Substellar Companions (Invited Review), ed. G. Garzón, C. Eiroa, D. de Winter, & T. J. Mahoney, 441

Mayor, M., Udry, S., Naef, D., et al. 2004, A&A, 415, 391

Mesa, D., Bonnefoy, M., Gratton, R., et al. 2019a, A&A, 624, A4

Mesa, D., Keppler, M., Cantalloube, F., et al. 2019b, A&A, 632, A25

Mesa, D., Langlois, M., Garufi, A., et al. 2019c, MNRAS, 488, 37

Metchev, S. A. 2006, PhD thesis, California Institute of Technology, California, USA

Milli, J., Banas, T., Mouillet, D., et al. 2016, Society of Photo-Optical Instrumentation Engineers (SPIE) Conference Series, Vol. 9909, Speckle lifetime in XAO coronagraphic images: temporal evolution of SPHERE coronagraphic images, 99094Z

Milli, J., Hibon, P., Christiaens, V., et al. 2017, A&A, 597, L2

Minniti, D., Butler, R. P., López-Morales, M., et al. 2009, ApJ, 693, 1424

Montagnier, G. 2008, Thesis, Université Joseph-Fourier - Grenoble I

Mordasini, C. 2013, A&A, 558, A113

Mordasini, C., Alibert, Y., Klahr, H., & Henning, T. 2012, A&A, 547, A111

Mordasini, C., Klahr, H., Alibert, Y., Benz, W., & Dittkrist, K.-M. 2010, arXiv e-prints, arXiv:1012.5281

Morley, C. V., Fortney, J. J., Marley, M. S., et al. 2012, ApJ, 756, 172

Morley, C. V., Marley, M. S., Fortney, J. J., et al. 2014, ApJ, 787, 78

Morley, C. V., Skemer, A. J., Allers, K. N., et al. 2018, ApJ, 858, 97

Müller, A., Keppler, M., Henning, T., et al. 2018, A&A, 617, L2

Musso Barcucci, A., Launhardt, R., Kennedy, G. M., et al. 2019, A&A, 627, A77

Nakajima, T., Oppenheimer, B. R., Kulkarni, S. R., et al. 1995, Nature, 378, 463

Nielsen, E. L., De Rosa, R. J., Macintosh, B., et al. 2019, AJ, 158, 13

Noyes, R. W., Jha, S., Korzennik, S. G., et al. 1997, ApJL, 483, L111

Oppenheimer, B. R., Kulkarni, S. R., Matthews, K., & Nakajima, T. 1995, Science, 270, 1478

Padoan, P. & Nordlund, Å. 2004, ApJ, 617, 559

Pepe, F., Mayor, M., Queloz, D., et al. 2004, A&A, 423, 385

Pepe, F., Queloz, D., Henning, T., et al. 2008, Society of Photo-Optical Instrumentation Engineers (SPIE) Conference Series, Vol. 7013, The ESPRI Project: differential delay lines for PRIMA, 70130P

Pepe, F. A., Cristiani, S., Rebolo Lopez, R., et al. 2010, Society of Photo-Optical Instrumentation Engineers (SPIE) Conference Series, Vol. 7735, ESPRESSO: the Echelle spectrograph for rocky exoplanets and stable spectroscopic observations, 77350F

Peretti, S., Ségransan, D., Lavie, B., et al. 2019, A&A, 631, A107

Perrier, C., Sivan, J. P., Naef, D., et al. 2003, A&A, 410, 1039

Perryman, M. 2011, The Exoplanet Handbook

Perryman, M. 2012, European Review, 20, 276

Perryman, M. 2018, The Exoplanet Handbook

Perryman, M., Hartman, J., Bakos, G. Á., & Lindegren, L. 2014, ApJ, 797, 14

Perryman, M. A. C., de Boer, K. S., Gilmore, G., et al. 2001, A&A, 369, 339

Perryman, M. A. C., Lindegren, L., Kovalevsky, J., et al. 1997, A&A, 323, L49

Pollack, J. B., Hubickyj, O., Bodenheimer, P., et al. 1996, Icarus, 124, 62

Pourbaix, D., Tokovinin, A. A., Batten, A. H., et al. 2004, A&A, 424, 727

Poyneer, L., van Dam, M., & Véran, J.-P. 2009, Journal of the Optical Society of America A, 26, 833

Quanz, S. P. 2015, APSS, 357, 148

Queloz, D., Mayor, M., Naef, D., et al. 2000, in From Extrasolar Planets to Cosmology: The VLT Opening Symposium, ed. J. Bergeron & A. Renzini, 548

Quirrenbach, A., Henning, T., Queloz, D., et al. 2004, Society of Photo-Optical Instrumentation Engineers (SPIE) Conference Series, Vol. 5491, The PRIMA Astrometric Planet Search project, ed. W. A. Traub, 424

Racine, R., Walker, G. A. H., Nadeau, D., Doyon, R., & Marois, C. 1999, PASP, 111, 587

Rameau, J., Chauvin, G., Lagrange, A. M., et al. 2013, ApJL, 772, L15

Rebolo, R., Zapatero Osorio, M. R., & Martín, E. L. 1995, Nature, 377, 129

Reid, I. N. & Gizis, J. E. 1997, AJ, 113, 2246

Ricker, G. R., Winn, J. N., Vanderspek, R., et al. 2015, Journal of Astronomical Telescopes, Instruments, and Systems, 1, 014003

Rickman, E. L., Ségransan, D., Hagelberg, J., et al. 2020, A&A, 635, A203

Rickman, E. L., Ségransan, D., Marmier, M., et al. 2019, A&A, 625, A71

Rigaut, F., Neichel, B., Boccas, M., et al. 2014, MNRAS, 437, 2361

Rigaut, F., Rousset, G., Kern, P., et al. 1991, A&A, 250, 280

Rigaut, F., Salmon, D., Arsenault, R., et al. 1998, PASP, 110, 152

Rigliaco, E., Gratton, R., Mesa, D., et al. 2019, A&A, 632, A18

Roddier, F. 1981, Progess in Optics, 19, 281

Roddier, F. & Roddier, C. 1997, PASP, 109, 815

Rosenthal, E. D., Gurwell, M. A., & Ho, P. T. P. 1996, Nature, 384, 243

Rousset, G., Lacombe, F., Puget, P., et al. 2003, Society of Photo-Optical Instrumentation Engineers (SPIE) Conference Series, Vol. 4839, NAOS, the first AO system of the VLT: on-sky performance, ed. P. L. Wizinowich & D. Bonaccini, 140–149

Sahlmann, J., Lovis, C., Queloz, D., & Ségransan, D. 2011a, A&A, 528, L8

Sahlmann, J., Ségransan, D., Queloz, D., et al. 2011b, A&A, 525, A95

Samland, M. 2019, PhD thesis, Max-Planck-Institut für Astronomie

Samland, M., Mollière, P., Bonnefoy, M., et al. 2017, A&A, 603, A57

Santos, N. C., Mayor, M., Naef, D., et al. 2001, A&A, 379, 999

Saumon, D., Chabrier, G., & van Horn, H. M. 1995, ApJS, 99, 713

Saumon, D., Hubbard, W. B., Burrows, A., et al. 1996, ApJ, 460, 993

Saumon, D., Marley, M. S., Abel, M., Frommhold, L., & Freedman, R. S. 2012, ApJ, 750, 74

Schmid, H. M., Bazzon, A., Roelfsema, R., et al. 2018, A&A, 619, A9

Schneider, J., Dedieu, C., Le Sidaner, P., Savalle, R., & Zolotukhin, I. 2011, A&A, 532, A79

Ségransan, D., Delfosse, X., Forveille, T., et al. 2003, in IAU Symposium, Vol. 211, Brown Dwarfs, ed. E. Martín, 413

Ségransan, D., Delfosse, X., Forveille, T., et al. 2000, A&A, 364, 665

Ségransan, D., Udry, S., Mayor, M., et al. 2010, A&A, 511, A45

Showman, A. P. & Kaspi, Y. 2013, ApJ, 776, 85

Sivaramakrishnan, A., Koresko, C. D., Makidon, R. B., Berkefeld, T., & Kuchner, M. J. 2001, ApJ, 552, 397

Skrutskie, M. F., Cutri, R. M., Stiening, R., et al. 2006, AJ, 131, 1163

Soto, M. G. & Jenkins, J. S. 2018, A&A, 615, A76

Soummer, R. 2005, ApJL, 618, L161

Soummer, R., Pueyo, L., & Larkin, J. 2012, ApJL, 755, L28

Sousa, S. G., Santos, N. C., Mayor, M., et al. 2008, A&A, 487, 373

Spiegel, D. S. & Burrows, A. 2012, ApJ, 745, 174

Takami, M., Bailey, J., & Chrysostomou, A. 2003, A&A, 397, 675

Tarter, J. C. 1975, PhD thesis, California Univ., Berkeley.

Thalmann, C., Carson, J., Janson, M., et al. 2009, ApJL, 707, L123

Thatte, N., Abuter, R., Tecza, M., et al. 2007, MNRAS, 378, 1229

Tinney, C. G. 1995, ApJ, 445, 1017

Tinney, C. G. 1999, Nature, 397, 37

Tremblin, P., Amundsen, D. S., Chabrier, G., et al. 2016, ApJL, 817, L19

Tremblin, P., Amundsen, D. S., Mourier, P., et al. 2015, ApJL, 804, L17

Tremblin, P., Chabrier, G., Baraffe, I., et al. 2017, ApJ, 850, 46

Udry, S., Mayor, M., Naef, D., et al. 2002, A&A, 390, 267

Udry, S., Mayor, M., Queloz, D., Naef, D., & Santos, N. 2000, in From Extrasolar Planets to Cosmology: The VLT Opening Symposium, ed. J. Bergeron & A. Renzini, 571

Udry, S. & Santos, N. C. 2007, Annu. Rev. Astron. Astrophys., 45, 397

van Holstein, R. G., Girard, J. H., de Boer, J., et al. 2020, A&A, 633, A64

Vigan, A., Bonavita, M., Biller, B., et al. 2017, A&A, 603, A3

Vigan, A., Langlois, M., Moutou, C., & Dohlen, K. 2008, A&A, 489, 1345

Vigan, A., Moutou, C., Langlois, M., et al. 2010, MNRAS, 407, 71

Vogt, S. S. 1987, PASP, 99, 1214

Vogt, S. S., Allen, S. L., Bigelow, B. C., et al. 1994, Society of Photo-Optical Instrumentation Engineers (SPIE) Conference Series, Vol. 2198, HIRES: the high-resolution echelle spectrometer on the Keck 10-m Telescope, 362

Vogt, S. S., Marcy, G. W., Butler, R. P., & Apps, K. 2000, ApJ, 536, 902

Wagner, K., Apai, D., & Kratter, K. M. 2019, ApJ, 877, 46

Wetherill, G. W. 1980, Annu. Rev. Astron. Astrophys., 18, 77

Wheatley, P. J., Pollacco, D. L., Queloz, D., et al. 2013, in European Physical Journal Web of Conferences, Vol. 47, European Physical Journal Web of Conferences, 13002

Whitehouse, S. C. & Bate, M. R. 2006, MNRAS, 367, 32

Whitworth, A., Bate, M. R., Nordlund, Å., Reipurth, B., & Zinnecker, H. 2007, in Protostars and Planets V, ed. B. Reipurth, D. Jewitt, & K. Keil, 459

Whitworth, A. P. & Zinnecker, H. 2004, A&A, 427, 299

Wilson, O. C. 1963, ApJ, 138, 832

Wilson, O. C. 1968, ApJ, 153, 221

Witte, S., Helling, C., Barman, T., Heidrich, N., & Hauschildt, P. H. 2011, A&A, 529, A44

Wittenmyer, R. A., Clark, J. T., Zhao, J., et al. 2019, MNRAS, 484, 5859

Wittenmyer, R. A., Endl, M., Cochran, W. D., Levison, H. F., & Henry, G. W. 2009, ApJS, 182, 97

Wittenmyer, R. A., Horner, J., Tuomi, M., et al. 2012, ApJ, 753, 169

Wittenmyer, R. A., Wang, S., Horner, J., et al. 2020, MNRAS, 492, 377

Wright, E. L., Eisenhardt, P. R. M., Mainzer, A. K., et al. 2010, AJ, 140, 1868

York, D. G., Adelman, J., Anderson, John E., J., et al. 2000, AJ, 120, 1579